PNNL-15443

Pacific Northwest
National Laboratory
Operated by Battelle for the
U.S. Department of Energy

Vadose Zone Transport Field Study Summary Report

Author:
A. L. Ward[a]

Collaborators:
M.E. Conrad[b]
W.D. Daily[c]
J.B. Fink[d]
V.L Freedman[a]
G.W. Gee[a]
G.M. Hoverston[b]
M.J. Keller[a]
E.L. Majer[b]
C.J. Murray[a]
M.D. White[a]
S.B Yabusaki[a]
Z.F. Zhang[a]

(a) Pacific Northwest National Laboratory, Richland, WA 99352
(b) Lawrence Berkeley National Laboratory, Berkeley, CA 94720
(c) Lawrence Livermore National Laboratory, Livermore, CA 94550
(d) HydroGEOPHYSICS, Inc., 2302 North Forbes Blvd., Tucson, AZ 85745

July 2006

Prepared for the U.S. Department of Energy
under Contract DE-AC05-76RL01830

PACIFIC NORTHWEST NATIONAL LABORATORY
operated by
BATTELLE MEMORIAL INSTITUTE
for the
UNITED STATES DEPARTMENT OF ENERGY
under Contract DE-AC05-76RL01830

Printed in the United States of America

Available to DOE and DOE contractors from the
Office of Scientific and Technical Information,
P.O. Box 62, Oak Ridge, TN 37831-0062;
ph: (865) 576-8401
fax: (865) 576 5728
email: reports@adonis.osti.gov

Available to the public from the National Technical Information Service,
U.S. Department of Commerce, 5285 Port Royal Rd., Springfield, VA 22161
ph: (800) 553-6847
fax: (703) 605-6900
email: orders@nits.fedworld.gov
online ordering: http://www.ntis.gov/ordering.htm

Vadose Zone Transport Field Study Summary Report

Author:
A. L. Ward[a]

Collaborators:
M.E. Conrad[b]
W.D. Daily[c]
J.B. Fink[d]
V.L Freedman[a]
G.W. Gee[a]
G.M. Hoverston[b]
M.J. Keller[a]
E.L. Majer[b]
C.J. Murray[a]
M.D. White[a]
S.B Yabusaki[a]
Z.F. Zhang[a]

(a) Pacific Northwest National Laboratory, Richland, WA 99352
(b) Lawrence Berkeley National Laboratory, Berkeley, CA 94720
(c) Lawrence Livermore National Laboratory, Livermore, CA 94550
(d) HydroGEOPHYSICS, Inc., 2302 North Forbes Blvd., Tucson, AZ 85745

July 2006

Prepared for
the U.S. Department of Energy
under Contract DE-AC05-76RL01830

Pacific Northwest National Laboratory
Richland, Washington 99352

Summary

A series of field studies were conducted at the Hanford Site, near Richland, Washington, from FY 2000 through FY 2003 at two different locations to develop data sets to test models of flow and transport in the vadose zone. The field studies were also done to investigate advanced monitoring techniques for evaluating flow-and-transport mechanisms and delineating contaminant plumes in the vadose zone at the Hanford Site. The studies were conducted as part of the Groundwater/Vadose Zone Integration Project Science and Technology Project, now known as the Remediation and Closure Science Project, managed by the Pacific Northwest National Laboratory (PNNL) and supported by the U.S. Department of Energy, Richland Operations Office. This report summarizes the key findings from the field studies and demonstrates how data collected from these studies are being used to improve conceptual models and develop numerical models of flow and transport in Hanford's vadose zone. Results from the field studies and associated analysis have appeared in more than 46 publications generated over the past 4 years. These publications include test plans and status reports in addition to numerous technical notes and papers.

Two major field campaigns were performed, one at a well injection test site and a second at a clastic dike test site. Both field studies have resulted in field-scale transport parameters for Hanford conditions, which are useful for improving predictions of subsurface flow and transport at the Hanford Site. In addition, advanced geophysical methods, including high resolution electrical resistivity measurements, were successfully tested and are now being deployed at Hanford for subsurface investigations and tank retrieval detection. The most useful information gained from these studies has been a better understanding of flow and transport in the vadose zone, and this has been specifically related to the impact of small-scale stratigraphic features (e.g., sediment layering) on water flow and contaminant transport. Conceptual models have been developed that take into account the lateral spreading of water and contaminants observed in the field studies. Numerical models of unsaturated flow and transport have been revised to account for lateral spreading of subsurface contaminant plumes.

The key results from these studies include:

1) Greater understanding of the complexity of plume migration in the vadose zone at Hanford. Fine-scale geologic heterogeneities, including grain fabric and lamination, were observed to have a strong effect on the large-scale behavior of contaminant plumes, primarily through increased lateral spreading resulting from anisotropy.

2) Observations of anion exclusion in Hanford sediments. Anion exclusion is a mechanism by which negatively charged ions are repelled from the surfaces of negatively charged soil particles, thereby increasing their velocity. Thus, the travel time of ions like pertechnetate, the stable form of ^{99}Tc found in oxidized environments, may decrease over that of unsaturated water flow.

3) Development of a new and robust model for describing saturation-dependent anisotropy in strongly heterogeneous soils. This model is based on the concept that key pore geometrical factors such as shape, size distribution, and tortuosity all interact to produce what is effectively a directional-dependent pore connectivity. This tensorial connectivity gives rise to permeability contrasts that are direction dependent. The concept of a connectivity tensor has been incorporated into PNNL's Subsurface Transport Over Multiple Phases (STOMP) simulator, which is currently being used to

understand plume behavior at a number of sites where lateral spreading may have dominated waste migration.

4) Development of large datasets of coupled flow and transport behavior for both conservative and reactive solutes that reflect the complex interplay of physical, hydrologic, and geochemical heterogeneities in very complex flow fields that are needed to model calibration.

5) Development of inverse modeling capabilities for time-dependent, subsurface, variably saturated flow using an automated optimization algorithm. This was accomplished by coupling STOMP with the non-linear parameter estimation code, UCODE.

6) Development of a parameter-scaling methodology for incorporating the effects of layering into model parameterization. This technique allows layered soils to be described by a single set of reference parameters and scale factors and has made it possible, for the first time, to invert field-scale unsaturated flow in layered soils.

7) Development of a coupled parameter scaling and inverse technique (CPSIT) for calculating field-scale hydraulic parameters that are needed to describe subsurface flow in heterogeneous soils and sediments. Applying this technique to the analysis of the injection test significantly reduced the simulation time needed for the inverse modeling and resulted in a notable improvement in predictions of infiltration and redistribution of water in the subsurface.

8) Development of inverse modeling capabilities for time-dependent, subsurface, reactive transport with transient flow fields using an automated optimization algorithm. This was accomplished by coupling the reactive transport code, CRUNCH, with the non-linear parameter estimation code, UCODE. Currently, four reactive transport parameters, including cation exchange capacity, solid-solution ratio, kinetic rate constant for mineral reaction, and the exponent representing species dependence on the far-from-equilibrium reaction rate, can be estimated with CRUNCH-UCODE.

9) Development of two new upscaling approaches for estimating field-scale hydraulic properties. The first approach falls into the category of volume averaging or homogenization techniques and estimates the plume-scale hydraulic properties from temporal differences in the spatial moments of an infiltrating water plume. The second approach combines the newly developed parameter scaling, which overcomes the problem of scaling vertical heterogeneity, with inverse modeling to estimate field-scale parameters that are implicitly anisotropic.

10) Development of pedotransfer functions for describing fine-scale hydrogeochemical heterogeneity and for incorporating this heterogeneity into reactive transport models. This approach is based on grain-size statistics and can be used to describe heterogeneity in hydraulic properties and sorption properties, such as the cation exchange capacity and the specific surface area of Hanford sediments.

11) Confirmation of recharge estimates needed for transport calculations by evaluating long-term drainage records. Water fluxmeters and lysimeters provide both short- and long-term estimates of recharge at waste sites, particularly those that have been kept free of vegetation.

12) Demonstrated advanced vadose-zone monitoring techniques for providing high-resolution information of the subsurface to support plume delineation and detailed information on the subtle

changes in lithology and bedding surfaces. High-resolution resistivity is now being used for detecting saline plumes at several waste sites at Hanford.

Acknowledgements

This work is a part of the Remediation and Closure Project managed by the Pacific Northwest National Laboratory (PNNL) and sponsored by the U. S. Department of Energy, Richland Operations Office, under contract DE-AC05-76RL01830. Mark Freshley, manager of the Remediation and Closure Project and John Morse, DOE-RL, have provided constant encouragement. We thank the many collaborators who have assisted in these studies. We also acknowledge the valuable technical support received from PNNL staff, including Ray Clayton, Karen Waters-Husted, Chris Strickland, George Last, Phil Meyer, Jeff Serne, Alex Mitroshkov, and interns Eric McGarrah, Mike Murray, LaShane Carter, and Aaron Graham. Management and clerical support from Aleta Busselman, Pat Gibbons, and Elizabeth LaMar is also greatly appreciated and last but not least the editorial support of Wayne Cosby.

Acronyms

1-D, 2-D, 3-D	One, Two, or Three Dimensional
AGU	American Geophysical Union
AT	advanced tensiometer
BHI	Bechtel Hanford Incorporated
BTC	breakthrough curve
CD-Coarse	coarse fraction
CDE	convective dispersive equation
CD-Fine	fine fraction
CEC	cation exchange capacity
CEMI	crosshole electromagnetic imaging
CI	confidence interval
CLT	complex load time
CMP	common midpoint
CPSIT	coupled parameter scaling and inverse technique
CPT	cone penetrometer
CRUNCH	multicomponent strontium ion exchange model
CSS	composite scaled sensitivity
DC	direct current
DOE	U.S. Department of Energy
DOE/RL	U.S. Department of Energy-Richland Operations
EHM	effective homogenous medium
EM	electromagnetic
EMI	electromagnetic induction

EMSP	Environmental Management Science Program
ERT	electrical resistance tomography
FIR	field investigation report
GAO	General Accounting Office
GIMRT	Global Implicit Multicomponent Reactive Transport
GPR	ground-penetrating radar
GSLIB	Geostatistical Software Library
GSSI	Geophysical Survey Systems, Inc.
HRR	high-resolution resistivity
IC	ion chromatography
ICP	inductively coupled plasma
IDF	Integrated Disposal Facility
ILAW	immobilized low activity waste
LBNL	Lawrence Berkeley National Laboratory
LCI	Linear Confidence Interval
MSR	mean-squared residual
NMO	normal movement
NRC	National Research Council
NSM	non-similar media
OEP	optical emission spectrometry
OS3D	Operator Splitting 3-Dimensional Reactive Transport
PNNL	Pacific Northwest National Laboratory
PTF	pedotransfer function
PUREX	plutonium-uranium extraction
PVC	polyvinyl chloride

RMSE	root-mean-squared-error
RPP	River Protection Project
SCT	seismic crosshole tomography
SI	simultaneous inversion
SSR	sum of squared residual
SSWR	sum of the squared weighted residual
STOMP	Subsurface Transport Over Multiple Phases
TCT	connectivity-tortuosity (concept)
TDR	time-domain reflectometry
USDA	U.S. Department of Agriculture
VEA	vertical electrode array
VZTFS	Vadose Zone Transport Field Study
XRD	X-ray diffraction

Contents

Figures

Tables

1.0 Introduction

At the U.S. Department of Energy's (DOE's) Hanford Site near Richland, Washington, a primary pathway for contaminants to reach receptors is through the vadose zone and groundwater. Mobile contaminants, such as chromate, technetium, tritium, and nitrate, among others, have been found at elevated concentrations in groundwater beneath some waste sites. Yet, at other sites that received similar, and at times larger, waste water discharges of similar chemical composition and recharge, the downward migration of mobile contaminants has been quite different. At these sites, mobile contaminants are still relatively high above the water table. There is mounting evidence that the differences in transport behavior between waste sites may be caused mostly by the complex effects of subsurface heterogeneity and anisotropy.

Heterogeneity and anisotropy in natural soils are known to result from sediment depositional processes and have been shown to have a strong impact on contaminant fate and transport in the vadose zone. Simplified conceptual models, coupled with limited parameterization, are perhaps the largest source of uncertainty in predicting subsurface transport behavior at complex sites like Hanford. In recognition of these issues, the National Research Council (NRC 2000) identified the reduction of the uncertainty associated with vadose zone processes as a critical need for the Hanford Site. These concerns have also led DOE to seek ways to improve the conceptual models of vadose transport, to build and test numerical models that can predict the fate and transport of the legacy wastes discharged to Hanford sediments, and to collect the data necessary to parameterize these models.

In FY 2000, the Vadose Zone Transport Field Study (VZTFS) was conceived as part of DOE's Science and Technology (now known as Remediation and Closure Science) project. The objective was to address major uncertainties regarding vadose zone flow and transport. The scope included laboratory and field investigations to generate data that would lead to an improved understanding of field-scale transport as well as to develop and/or identify efficient and cost effective characterization methods (DOE 1998a). This report provides a summary of the experimental studies conducted in the laboratory and field as well as developments in numerical techniques and geophysical characterization tools that occurred over a 3-year period from FY 2000 through FY 2003 that were associated with this scope.

1.1 Technical Background

There is much evidence implicating the effects of heterogeneity and anisotropy on flow-and-transport behavior at the Hanford Site. Recent sampling at the 216-B-26 Trench shows a zone of high ^{99}Tc concentrations between 18 and 53 m (59 and 174 ft) with no reported groundwater contamination (Ward et al. 2004). The transport behavior at this site is caused mostly by subsurface heterogeneity and anisotropy resulting from the depositional environment. Thus, predicting transport under these conditions requires approaches for dealing with the effects of heterogeneity and anisotropy.

Information on heterogeneity is critical for accurately predicting contaminant spreading (Russo 1993) and for evaluating the effectiveness of remediation strategies (Berglund and Cvetkovic 1996). Studies of the orientation and intensity of sedimentary structures, like capillary breaks and clastic dikes, on flow fields should provide insight into the effects of layered heterogeneity and anisotropy on subsurface flow and transport. However, such studies have been limited mostly to laboratory flow cells and numerical

experiments. Large-scale infiltration experiments are useful to characterize field-scale spatial variability of hydraulic properties (van Wesenbeeck and Kachanoski 1991; Youngs 1991). Important vadose zone transport processes have been identified in the few large-scale transport studies conducted internationally during the last decade. Studies include transport tests in the United States at Las Cruces, New Mexico (Wierenga et al. 1990; Hills et al. 1991; Rockhold et al. 1996); at Idaho National Engineering Laboratory in Idaho Falls, Idaho (Wood and Norrell 1996); and at Maricopa, Arizona (Young et al. 1996). Studies outside of the United States include studies in Canada (Kachanoski et al. 1990; van Wesenbeeck and Kachanoski 1994) and in Europe (Schulin et al. 1987; Hammel and Roth 1998).

The field studies performed at other sites have consistently shown that flow-and-transport processes are controlled, to a large extent, by site-specific hydrologic properties and subsurface structural features such as layering, sediment discontinuities, and fracture zones. There were essentially two features common to these studies (Hammel and Roth 1998). First, the local vertical dispersion of solute strongly appears to depend on the measuring volume; it is generally smaller for small volumes such as boreholes than for the volume at which results are desired. Second, horizontal redistribution of solutes may lead to accumulation in areas of local water flux convergence and depletion in divergent areas. These features have mostly been attributed to subsurface heterogeneity and textural discontinuities (Ward et al. 2006).

Part of the complexity in field-scale unsaturated transport arises from natural capillary breaks that form when fine-textured layers are underlain by coarser sediments. During unsaturated flow, these structures direct flow laterally until the matric potential in the fine layer is sufficient to overcome the entry pressure of the underlying coarse layer. Anisotropy, also a nonlinear behavior, can subdue or enhance predicted migration rates, depending on local stratigraphy. A prerequisite for improving fate and transport predictions is to develop conceptual models that take into account the effects of heterogeneity and anisotropy.

The ability to detect subsurface changes in sediment characteristics resulting from heterogeneity and to predict contaminant migration through Hanford's vadose zone is limited by characterization tools and hydrogeologic data. A large database (ROCSAN) of some 40,000 grain-size distributions exists for the Hanford Site as well as a database of borehole geophysical logs, both of which provide information about sediment characteristics but have been rarely used for this purpose.

Over the years, contaminant plumes in tank farms and other past-practice disposal sites have been routinely characterized using gross gamma and spectral gamma techniques. Temporal changes in these logs and observation of contaminants in groundwater monitoring wells have been used to some extent to infer contaminant migration rates (e.g., DOE 1996). Whereas borehole logs provide detailed information for naturally occurring gamma emitters (^{40}K, ^{238}U, ^{232}Th) and gamma-emitting contaminants (e.g., ^{137}Cs, ^{90}Sr), which typically have low mobility because of strong sorption onto vadose zone sediments, they do not provide information for mobile contaminants such as technetium, tritium, or nitrate. The inability to detect these species highlights the need for technologies to detect and monitor the migration of appropriate surrogates for the high-risk contaminants in the vadose zone (GAO 1989). Innovative geophysical techniques that can be used in an environment populated with steel-cased wells and contaminated with hypersaline wastes are needed for identifying mobile contaminants and calculating their rate of migration through the vadose zone (NRC 2000).

1.2 Scope of the Problem

The occurrence and impact of spatial and temporal variability in hydrologic properties of natural soils is well established (Roth et al. 1991; Wierenga et al. 1991; Russo and Bouton 1992). Soil-forming processes typically result in structures whose properties vary with 1) the scale of observation, 2) space (heterogeneity), and 3) orientation (anisotropy). Differences in space and orientation can lead to complex variations in hydrologic properties that strongly affect the migration of water and contaminants through the vadose zone. Thus, the nature of contaminant distributions and the differences observed between waste sites in Hanford's vadose zone are to be expected. The Hanford formation, which is the uppermost sedimentary unit where a significant portion of vadose zone contaminants resides, consists of highly heterogeneous glacial-fluvial sediments. Figure 1.1 shows an outcrop located about 1 km from the 299-E-111 test site in the 200 East Area and the type of hierarchical heterogeneity that typically exists. Multi-scale sedimentological bedforms, including fine-scale laminations, gravel inclusions, cross beds, and ripples embedded in large-scale architectural elements, are common. These multi-scale heterogeneities are discrete with different geometrical shapes, bedding inclinations, and anisotropy structures at each scale.

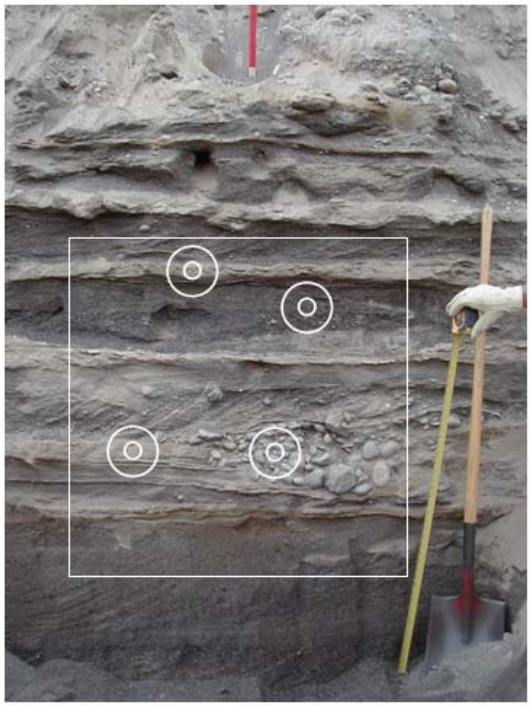

Figure 1.1. Exposed Trench Face Showing Layered Heterogeneity in Hanford's 200 Area near the 299-E24-111 Test Site. The white square represents the typical 1-m (3.3 ft) grid block used for numerical simulations; the white concentric circles represent the typical 5-cm (2-in.) and 15-cm (5.9-in.) diameter samples used to characterize hydraulic properties.

Multi-scale heterogeneities with sub-vertical to vertical structures, commonly known as clastic dikes, are common (Figure 1.2) and are often accompanied by horizontal structures of a similar texture known as sills (Figure 1.3). The origin of clastic dikes is a source of ongoing debate (Bjornstad et al. 1987; Pogue 1998; Fecht et al. 1999), and there has been much speculation about their effect on field-scale flow and transport processes (Jacobs 1997, 1998a, b; Murray et al. 2003).

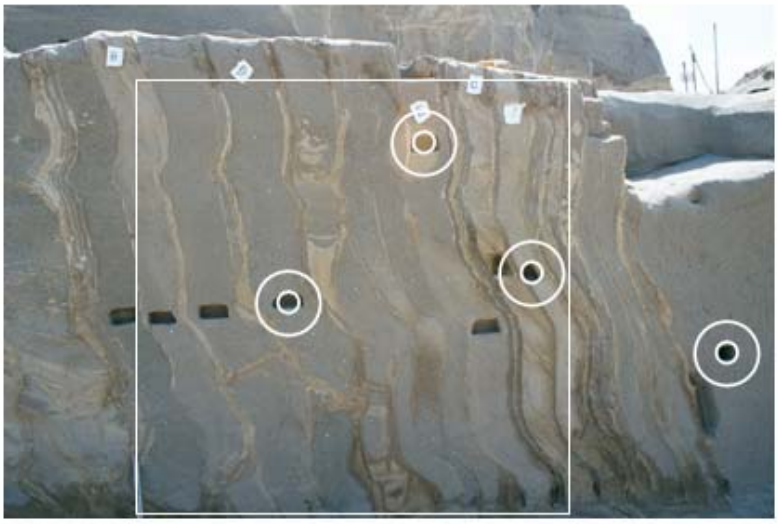

Figure 1.2. Vertical Exposure of a Dike at the Army Loop Road Site in the Sand-Dominated Facies of the Hanford Formation Showing Silt Linings, Coarse Infilling Sediments, and Small-Scale Slumps. Dikes can vary in thickness from a few centimeters to hundreds of meters, and their vertical extent is usually several times greater than their width. The rectangular holes are areas where soil samples were taken for particle-size analysis. The white square represents the typical 1-m (3.3-ft) grid block used for numerical simulations; the white concentric circles represent the typical 5-cm (2-in.) and 15-cm (5.9-in.) diameter samples used to characterize hydraulic properties.

The simulation of fluid flow in these complex formations is of considerable practical importance for predicting contaminant transport and fate to support decision making in relation to remedial actions and long-term stewardship. Of particular interest in these formations are the embedded fine-scale features and how they impact field-scale flow and transport. The realistic simulation of unsaturated flow sediments demands discretization of the domain, at least at the support scale, and the assignment of hydraulic and biogeochemical properties to each grid cell. However, traditional soil-characterization methods provide, at best, spatially and temporally integrated parameter estimates that are inadequate for predicting flow. It is also known that any sort of linear averaging of individual fine-scale relationships to derive effective relationships, the current norm with core analysis, will produce incorrect results (Ferrand and Celia 1992; Zhang et al. 2003b; Stewart et al. 2006). Even if the individual fine-scale relationships could be measured directly, the scale of the typical problem is hundreds of meters, and full three-dimensional (3-D) simulations that capture multi-scale flow processes would be computationally constrained.

A major challenge, therefore, is how to account for the multi-scale heterogeneity and anisotropy in field-scale models. Scientists have employed a variety of methods to reduce the complexity of flow

Figure 1.3. Vertical Exposure Showing a Sill Adjacent to the Dike at Army Loop Road. Sill thickness typically ranges from a few to several centimeters but can exceed 0.5 m (1.6 ft) where liquefaction was severe.

models. One approach is to incorporate only the large-scale architectural elements into the flow model and reduce the dimension of the problem from 3-D to one-dimensional (1-D) or two-dimensional (2-D). Flow in stratified sediments is inherently 3-D because of vertical heterogeneity, fluid properties, and anisotropy. Whereas 2-D and 3-D flows are qualitative similar, 1-D flow is both qualitatively and quantitatively different, and straightforward extrapolation from lower to higher dimensions in highly heterogeneous formations will lead to significant errors (Dagan 1989; Murray et al. 2001, 2003; Ward et al. 2004).

Adequate representation of small-scale features such as those shown in Figure 1.1 to Figure 1.3 therefore remains a challenge when modeling unsaturated flow at large spatial scales. Upscaling methods offer an opportunity to reduce the size of the problem by decreasing the spatial resolution needed to adequately represent the simulation problem. As stated by de Marsily et al. (2005) and demonstrated by several authors (e.g., Renard and de Marsily 1997; Ewing 1998; Gautier et al. 1999), the goal of upscaling is to average the fine-scale properties such that flow calculations made at the upscaled level using the upscaled parameters provide a solution as close as possible to the one that could have been calculated in a high-resolution simulation on the finer grid with the original parameter values. Thus, the solution to this problem may lie in the development of appropriate upscaling methodologies. A number of authors have published comprehensive reviews of the various methods for upscaling flow behavior in porous media (Sanchez-Vila et al. 1995; Wood 2000; Cushman et al. 2002). Most of these methods were developed for saturated porous media that were often assumed to be isotropic at a local scale and may have limited applicability to unsaturated or variably saturated anisotropic porous media. When considering unsaturated systems, a particularly difficult problem in implementing these methods is related to the non-linearity of the constitutive relations between permeability ($\boldsymbol{k}$), saturation (S), and capillary pressure (P_c). Common approaches to upscaling can be summarized into the following four basic methods: 1) stochastic, 2) renormalization, 3) volume averaging, and 4) homogenization. As pointed out by Wood (2000), each of these approaches has advantages and disadvantages. Although there have been attempts

to analyze the upscaling process (e.g., King 1989), so far these methods have not been used to determine whether an upscaled value provides a good or bad approximation. Recent advances in applied mathematics and DOE's investment in high-performance computing are leading to renewed interest in high-resolution and multiscale modeling, but a remaining challenge is to parameterize these models and generate accurate datasets for calibration and validation.

Regardless of the method chosen to simulate a waste site, model validation and calibration will require characterization methods that can be used to estimate the transport properties at the scale of interest, or ideally at multiple scales. Characterizing soil hydraulic and transport behavior at large scales using traditional methods can be time-consuming and very costly. An efficient and relatively inexpensive approach to estimating hydrogeochemical parameters is the pedotransfer function (PTF) approach that estimates the required parameters from easily measurable or available soil physical data. At a much larger scale, the geophysical properties of porous media are influenced by a variety of pore-scale characteristics, including the spatial distribution of constituent minerals, pore morphology and topology, saturation, contaminant concentrations, and even temperature. Not only do the transport properties of electrical conductivity, dielectric constant, and permeability depend on porosity, but they are also strongly influenced by the micro-structure of the porous medium and the connectivity of the pore space.

An important step in the direction of validating modeling approaches is to establish a mechanistic link between the physical phenomena controlling transport at the local scale (e.g., particle-size, permeability, porosity) and the larger scale response of geophysical sensors (e.g., neutron probe, high-resolution resistivity [HRR], ground-penetrating radar). Developing robust, physically based relationships requires simultaneous measurements of hydrologic, geochemical, and geophysical responses in the same transport volume. Such datasets will eventually allow sparse hydraulic property measurements to be combined with geophysical responses to characterize multi-dimensional field-scale distributions of flow-and-transport parameters, a required step for interpreting existing contaminant plumes and predicting future behavior.

1.3 Scope of the Study

The scope of VZTFS was to conduct a series of tests to evaluate how water and dissolved contaminants move in heterogeneous anisotropic sediments representative of Hanford's vadose zone and to identify or develop minimally invasive technologies for subsurface characterization. To address current data gaps related to the behavior of water and mobile contaminants, experiments were designed to allow *in situ* measurement of the variables of interest, or surrogates when appropriate, using proven and emerging characterization technologies. The research focused on 1) characterization investigations of uncontaminated sites with goals of identifying the dominant transport processes for unsaturated water and solute movement, 2) generation of databases for validation of multi-dimensional numerical models of vadose zone flow and transport, and 3) parameter identification and upscaling. In addition to the established monitoring techniques, a number of emerging technologies with potential for application to vadose zone characterization, leak detection, and plume delineation were also investigated as part of the scope. Two types of experiments were conducted under this scope of work:

1) **Subsurface Leak Experiments**. These experiments were designed to provide an improved understanding of flow and transport from a source small in size relative to the observation area, such as might occur from a subsurface leak. The focus was on the effects of layered heterogeneity on flow

asymmetry and the 3-D spatial correlation structure of flow variables. Monitoring was done by nondestructive means, and the experiments were conducted at an existing instrumented site that has undergone some prior characterization. Transport experiments were first conducted with a dilute tracer mixture. Experiments were subsequently repeated with a hypersaline tracer to determine any effects of fluid properties. The results of these experiments are applicable to leaks from buried point sources and are expected to provide crucial information about the near-field behavior of contaminants released from tanks, transfer lines within tank farms, and buried water lines.

2) **Near-Surface Leak Experiments**. These experiments were designed to develop an improved understanding of flow and transport from surface or near-surface sources. Two important objectives were to differentiate the effects of physical and chemical heterogeneities on the transport behavior of reactive contaminants and to quantify the horizontal correlation structure of hydraulic parameters. To accomplish these objectives, experiments were conducted on a 60-m (197-ft) long transect at a clastic dike outcrop. Transport experiments were first conducted with a tracer mixture that had been modified to prevent the sorption of Sr^{2+}. Experiments were subsequently repeated with a tracer mixture that would verify the sorption of Sr^{2+}, and the results were compared to those for non-sorbing solutes. An important aspect was to study the effect of the transverse solute displacement such that the relationship between transverse and longitudinal dispersivity could be quantified. Monitoring was done by nondestructive testing during the experiment with destructive sampling at the end. The results of these experiments are applicable to surface spills and line-source waste discharges such as those occurring from ditches, cribs, and trenches.

1.4 Objectives

The objective of the VZTFS was to conduct controlled transport experiments at field sites chosen to:

1) Identify mechanisms controlling transport processes in soils typical of the hydrogeologic conditions of Hanford's waste disposal sites

2) Observe flow and transport at multiple characteristic length scales to support the development and validation of upscaling methods

3) Develop a detailed and accurate database of flow and transport observations to validate 3-D forward models and investigate the feasibility of joint inversions of hydrological and geophysical data

4) Identify and evaluate advanced, cost-effective characterization methods with the potential to function within the existing infrastructure and to assess changing conditions in the vadose zone, particularly as surrogates of high-risk contaminants that are currently difficult to detect without destructive sampling

5) Develop improved conceptual models for vadose zone flow and transport.

1.5 Experimental Sites

Experiments were planned for two different uncontaminated sites to simulate flow and transport, first from a subsurface leak and then from a near-surface discharge. The strategy for VZTFS site selection was based partly on the analogous site concept used in the 200 Areas Remediation Strategy (DOE 1998b) to minimize the need for site characterization and evaluation. In the analogous site concept, a site that

represents the main waste disposal scenario is chosen after taking into account location, geology, waste site history, and contaminants. Because the VZTFS was concerned with the uncertainty associated with contaminant source distributions and hydrogeologic controls of transport, greater emphasis was placed on the hydrogeologic component and the degree to which sites had been previously characterized. Between FY 2000 and FY 2003, four field tests were conducted.

1.5.1 299-E24-111 Test Site

In FY 2000 and FY 2001, two injection experiments were conducted in Hanford's 200 East Area at the 299-E24-111 test facility, commonly known as the Sisson and Lu site. The test facility is located between the immobilized low activity waste (ILAW) disposal site (now known as the Integrated Disposal Facility [IDF] site) to the west, the 216-A-38-1 crib to the east, and the plutonium-uranium extraction (PUREX) facility to the northeast. This site was chosen primarily because of its characterization history, the presence of layered heterogeneity, and existing monitoring infrastructure. The site underwent extensive sampling and geophysical logging during an earlier set of experiments as reported by Sisson and Lu (1984). The site was subsequently logged in 1993 to map the location of tracers injected in the 1980 experiments and to obtain information on the physical properties (Fayer et al. 1993, 1995). The area immediately west and south (part of the ILAW facility) has been studied in experiments to characterize surface sediments and the upper Hanford formation in support of the Hanford ILAW performance assessment.[(a)] Sediment samples from boreholes located farther southwest, adjacent to the planned ILAW disposal facility, have been analyzed to determine lithologic, geochemical, and hydraulic properties as part of the ILAW performance assessment (Reidel and Horton 1999; Fayer et al. 1995). The site was also the subject of a number of modeling investigations before this study, including attempts to upscale hydraulic properties based on the renormalization methods (Rockhold et al. 1999). Conducting new experiments at this site leveraged characterization efforts of the previous 20 years.

The site's physical layout, particularly the concentric array of steel-cased wells, made it ideal for investigating the 3-D behavior of simulated subsurface leaks and the spatial correlation structure of features with a range greater than the inter-well spacing. The presence of these wells also allowed the evaluation of a variety of geophysical characterization technologies with respect to their potential for imaging the subsurface in electrically noisy environments. Such technologies are needed to reduce the uncertainty in source contaminant distributions and for leak detection and monitoring applications during waste retrieval from tanks. Continuous logging between the surface and the maximum depth allowed determination of the vertical correlation structure.

Figure 1.4 shows a plan view of the well configuration at the test site, including the location of new instrumentation and boreholes installed in the FY 2000 and FY 2001 field campaigns. The injection well used in the FY 2000 test is located adjacent to H2. An additional 32 observation wells, constructed by welding together sections of 0.15-m (6-in.) diameter schedule 40 steel casing, are arranged in a concentric pattern around the injection well. The details of the well placements and monitoring array configurations are provided by Ward and Gee (2000; 2001).

(a) AL Ward, RE Clayton, and JC Ritter. 1998. *Hanford Low-Level Tank Waste Performance Assessment Activity: Determination of In Situ Hydraulic Parameters of Hanford Sediments.* Letter Report for Activity 4b, submitted to Lockheed Martin Hanford Company, September 1998.

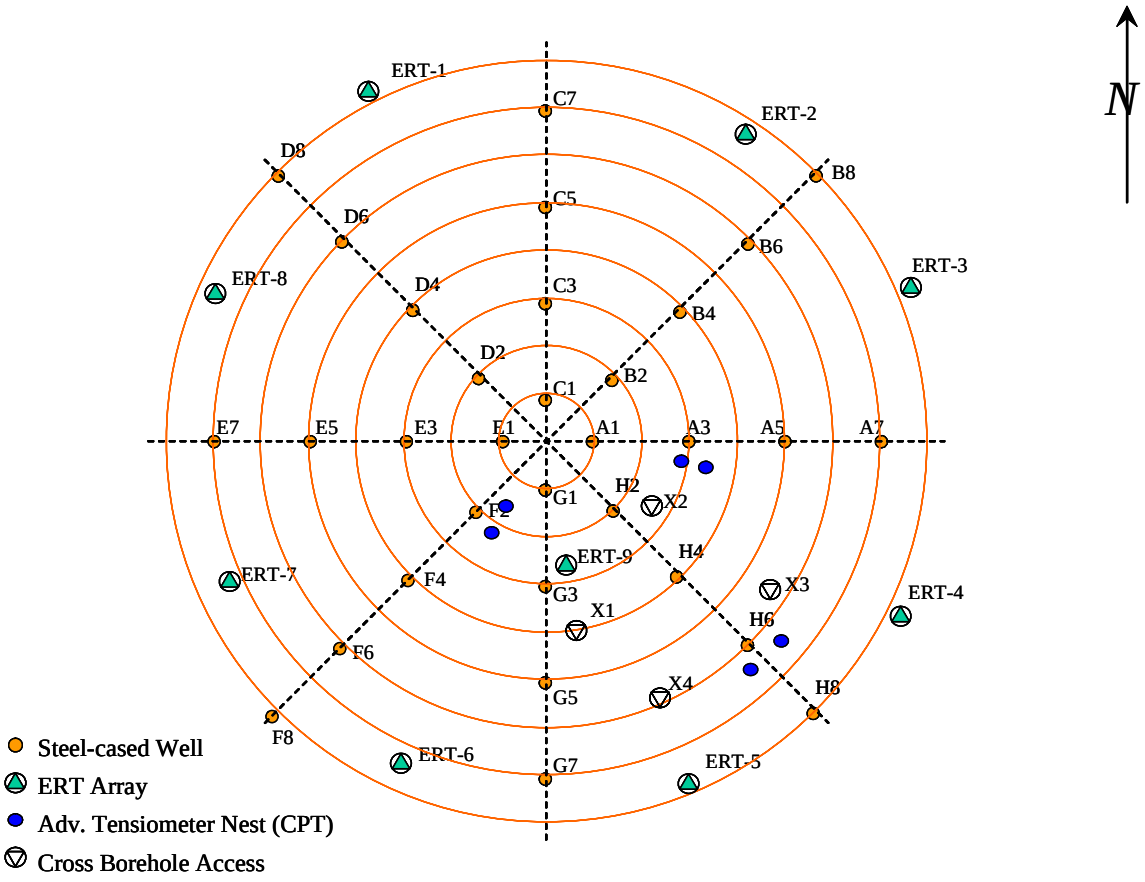

Figure 1.4. Plan View of 299-E24-111 Test facility Used in the FY 2000 and FY 2001 Field Experiments Showing Locations of Access Tubes, Vertical Electrode Arrays, and Injection and Core Sampling Points

For the FY 2000 experiment, a series of new boreholes and instruments were installed using a combination of auguring and cone penetrometer methods. The locations of these new installations are also shown in Figure 1.4. A new injection well was installed about 0.3 m (1 ft) northwest of local Well H2 (Hanford Well E24-104). In addition, eight vertical electrode arrays (VEAs) were installed by cone penetrometer at a radial distance of 8.0 m (26 ft) from the central injection site to facilitate electrical resistance tomography (ERT) imaging of the subsurface. These VEAs consisted of 15 stainless steel tubes (0.15 m [0.5 ft] long, 3.175 cm [1.25 in.] diameter) spaced at 1-m (3.3-ft) intervals with the first electrode located 5 m (16 ft) below the surface. An additional VEA was located 2 m (6.6 ft) south of the central injection well, i.e., between local Wells G-1 and G-3. Three advanced tensiometer (AT) nests were also installed to monitor soil matric potential and collect pore-water samples for laboratory analysis. Tensiometers were installed to different depths by rotary auger with the first located 30 cm (1 ft) north of local Wells H2 (Hanford Well E24-104), H4 (Hanford Well E24-105), and H6 (Hanford Well E24-106). Three additional AT nests were installed by cone penetrometer, including one about 0.3 m (1 ft) south of local Wells A-3 (Hanford Well E24-77), one south east of local Well F-2 (Hanford Well E24-96), and one south west of local Well H-6 (Hanford Well E24-106). In the nest near A-3, one AT was driven to a depth of 6 m (20 ft) while the second was driven to a depth of 8.2 m (27 ft). In the nest near F-2, one AT was driven to a depth of 5.8 m (19 ft) while the second was driven to a depth of 9.5 m (31 ft). In the nest

near H-6, one AT was driven to a depth of 5.8 m (19 ft) while the second was driven to a depth of 10.9 m (36 ft).

Four polyvinyl chloride (PVC) access-tubes (X-1 through X-4) were installed by cone penetrometer to facilitate monitoring by cross well radar, high frequency electromagnetic (EM) impedance measurements, and crosshole seismic. Tube X-1 was located 1.0 m (3.3 ft) southeast of local Well G-3 (Hanford Well E24-101). Tube X-2 was located 1.0 m (3.3 ft) south southeast of local Well H-2 (Hanford Well E24-104); tube X-3 was located 1.5 m (5 ft) east southeast of local Well H-4 (Hanford Well E24-105); whereas tube X-4 was located 4 m (13 ft) west southwest of local Well H-4 (Hanford Well E24-105). Soil samples were also retrieved to analyze physical and chemical properties and to determine water contents and tracer concentrations during and after the test. All installations were in accordance with the technical procedures and specifications described in the FY 2000 test plan (Ward and Gee 2000).

The Hanford formation at the test site extends to about 60 m below the surface, and the water table is over 100 m deep in places. The surface soil at the site is coarse sand, locally known as a Quincy sand, associated with the Quincy soil series (mixed, mesic, Xeric Torripsamments). The soil has a high infiltration capacity (>50 mm hr^{-1}), and thus precipitation infiltrates readily with little or no runoff. The vegetation at the site before the experiment was the typical modified shrub steppe ecosystem with a mixture of sagebrush and cheatgrass. The shrubs on the site were removed in March 1980, before the first series of experiments, and since then, the site has been dominated by a sparse cover of cheatgrass, tumble mustard, and tumbleweed. Figure 1.5 is a photograph of the site during instrumentation and coring in May 2000.

Precipitation at the Hanford Meteorological Station, located about 10 km west of the test site, has averaged 174 mm yr^{-1} since 1946. Nearly half of the precipitation comes in the winter months (November through February). The average monthly temperature ranges from 1.5°C in January to 25°C in July. The humidity ranges from 75% in winter to 35% or less in summer.

Figure 1.5. Vadose Zone Transport Field Study Test Site at 299-E24-111 on May 31, 2000, During Instrumentation and Sampling

1.5.2 Army Loop Road Clastic Dike Site

The FY 2002 and FY 2003 field experiments were conducted at a test site located south of Army Loop Road, and east of Goose Egg Hill. This site was chosen because of the occurrence of several clastic dike outcrops. Surface outcrops of clastic dikes and the presence of near-surface sills made this site ideal for studying the impact of layered heterogeneity derived from a different depositional environment. Clastic dikes generally consist of laminated sand and silt, often with sand at the center and silt along the

outer edges (Figure 1.2). Dikes are easily recognized from aerial and satellite photos as polygonal ground crack patterns (Figure 1.6). The dikes in these networks typically range from 3 cm (1.2 in.) to 1 m (3.3 ft) in width, from 2 m (6.6 ft) to greater than 55 m (180 ft) in depth, and from 1.5 to 100 m (5.0 to 328 ft) along the strike.

The surface expressions of clastic dikes are polygonal shapes that are hosted by lush stands of vegetation (Figure 1.7). In Figure 1.7, the lush-green shrub on the dike borders is tumble mustard (*Sisymbrium altissimum*), an exotic winter annual with a rooting depth of 1 m (3.3 ft) or greater. The tall grass is cheatgrass (*Bromus tectorum*), a winter annual with roots to 0.75 m (2.5 ft), and the low profile grass is a mixture of Sandberg's bluegrass, (*Poa secunda*), a native perennial bunchgrass with roots to 0.45 m (1.5 ft), and bulbous bluegrass (*Poa bulbosa*), a non native biennial grass with roots to 0.25 m (0.8 ft). These stands are supported late into the dry season by higher plant-available water resulting from the larger water-holding capacity of the fine-textured intrusions. The material adjacent to the clastic dikes in this area is sand to gravelly sand with low water holding capacity. As a result, the plants that typically grow on these sediments are native bunch grasses and other non-native grass species. These species have growth cycles that take advantage of the winter precipitation with flowering-induced dormancy occurring in the late spring to early summer.

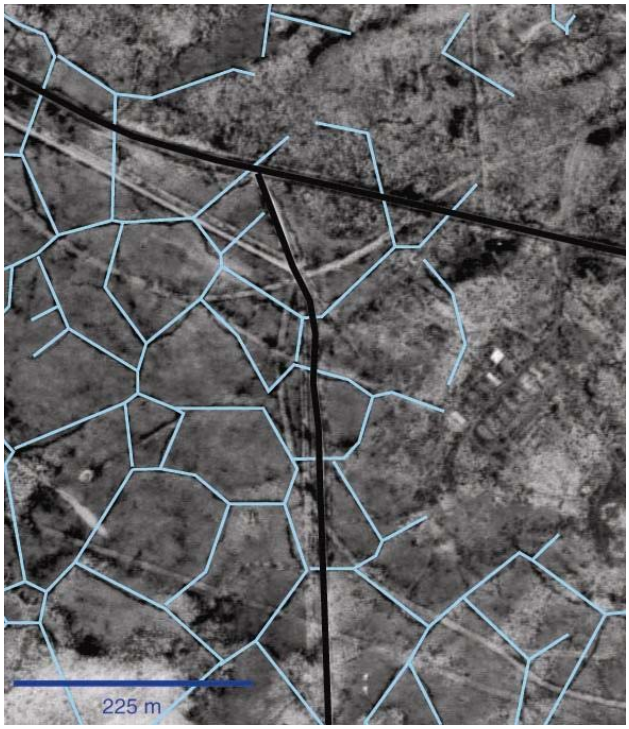

Figure 1.6. ICONOS 1-m (3.3-ft) Resolution Satellite Image of a Portion of DOE Hanford Site with Lines Drawn to Illustrate Locations of Dikes (blue) and Roads (black)

Figure 1.7. The Borders of Typical Vegetation Polygons at the Army Loop Road Site Showing Tumble Mustard with Dormant Grasses Inside the Polygons

The surface soil at the Army Loop Road clastic dike site is a coarse sand, locally known as a Quincy sand, which is associated with the Quincy soil series (mixed, mesic, Xeric Torripsamments). The sand matrix has a high infiltration capacity (>50 mm [>2 in.] hr^{-1}); thus, precipitation infiltrates readily with little or no runoff. However, the subsurface is highly heterogeneous with manifestations over a wide range of length scales. Efforts to measure the hydraulic properties of clastic dikes have been limited. Until recently, the only known measurements were those reported by Fecht et al. (1998), who used laboratory and small-scale field tests to determine the hydraulic conductivity of clastic dikes and their host sediments. At the center of dikes, the average saturated hydraulic conductivity was reported to be about 10^{-5} m s^{-1}. Across the clay linings, the saturated hydraulic conductivity varied from 10^{-6} to 10^{-9} m s^{-1}. The saturated hydraulic conductivity of the host sediment was about 10^{-5} m s^{-1}. Given the range of particle-size distributions and the strong dependence of hydraulic properties on particle-size distributions, sharp contrasts in porosity, pore size, and pore continuity can be expected. The general climatology at this site is essentially the same as at the 299-E24-111 site, although localized precipitation events are known to occur.

Some monitoring infrastructure was present at the site, installed as part of an Environmental Management Science Program (EMSP) study in FY 1999 through FY 2000 (Murray et al. 2001, 2003). There had been some moderate site characterization, consisting mainly of *in situ* air and water permeabilities, particle-size distributions, and ground-penetrating radar measurements to map lithology.

1.5.3 Monitoring Methods

A variety of monitoring methods were used to document tracer distributions and migration rates at the test sites. These included neutron logging, ERT, HRR, EM imaging, crosshole radar, crosshole seismic,

advanced tensiometers, tracers, and coring). The neutron probe and crosshole radar were used for soil moisture measurements; ERT, HRR, and crosshole electromagnetic imaging (CEMI) were used to monitor changes in electrical resistivity resulting from changing concentrations of the ionic tracers and, to some extent, the moisture front; seismic crosshole tomography (SCT) was used for lithologic characterization. The ERT electrodes and access tubes for the crosshole radar were installed by cone penetrometer. Additional methods included tracers (including isotopes) and coring. The details of each of the nine methods selected and the collaborators who deployed the selected methods are listed in the VZTFS test plan (Ward and Gee 2000). During the course of the experiment, four boreholes were installed southeast of local Well C0 at a spacing of about 2 m (6.6 ft). These boreholes were used to obtain continuous split-spoon samples from the surface to a depth of 18 m (59 ft). Selected portions of these samples are being analyzed for their chemical, radiological, and physical characteristics at Pacific Northwest National Laboratory (PNNL) and at the U.S. Salinity Laboratory. Some 60 undisturbed samples were analyzed to determine grain-size distributions and hydraulic properties (Schaap et al. 2003).

1.6 Report Structure

Significant progress was made towards satisfying the objectives of the VZTFS. This report is a summary of the research and development activities performed as part of the VZTFS from FY 2000 through FY 2004. Many of the findings from these studies have been published in peer-reviewed journals and presented at national and international conferences. In the following sections, brief descriptions of laboratory and field tests, the key scientific findings from these tests, and the synopsis and implications of these results are summarized in relation to the objectives described above. The key portions of scientific progress are summarized in a number of distinct categories in Section 2. The data resulting from this study are intended to improve conceptual and numerical models of vadose zone flow and transport and to calibrate field-scale transport models. Section 3 summarizes the conclusions resulting from these studies. With the improved understanding of vadose zone transport processes derived from the studies at uncontaminated sites, methods have been developed to allow the extrapolation of these findings to contaminated sites to guide characterization, monitoring, management, and the selection of remedial and closure actions for the vadose zone at the Hanford Site. Sections 4, 5, and 6 provide listings of VZTFS reports, conference proceedings, and related publications, respectively.

2.0 Scientific Findings

This section describes the effects of layered heterogeneity on subsurface flow, the evidence of anion exclusion during vadose zone transport, and the effects of fluid properties in subsurface flow and transport. It also describes pedotransfer functions to quantify 1) variable hydraulic properties, 2) variability in sorption parameters, and 3) variable transport properties. Multicomponent transport on a laboratory scale is illustrated as well as microscale modeling of variably saturated flow and field-scale reactive transport in a clastic dike. Field-scale observations of coupled flow and reactive transport are described as well as a robust model for saturation-dependent anisotropy. The following measurement methods were used: surface-based ground penetrating radar, SCT, crosshole ground-penetrating radar, crosshole EM induction, HRR, and ERT. The statistical and spatial correlation structure of flow variables is explained as well as the inverse modeling of field-scale unsaturated flow and multicomponent reactive transport. Field-scale hydraulic properties from spatial moments and the combined parameter scaling inverse technique for upscaling flow are described. Finally, the various upscaling methods for Hanford sediments are compared.

2.1 Effects of Layered Heterogeneity on Subsurface Flow

In FY 2000, PNNL and collaborators initiated the first of four injection experiments designed to simulate a subsurface leak of contaminants. These experiments were designed to provide improved understanding of flow and transport from a source small in size relative to the observation area. This experiment is representative of subsurface leaks and discharges into heterogeneous, anisotropic, unsaturated sediments. This study underscores a long-standing issue in the DOE complex in general and at Hanford in particular: a limited ability to characterize properties and simulate subsurface processes at resolutions that are meaningful to understanding the long-term fate of high-risk contaminants in the field. These issues could be particularly important in the 200 East Area given the growing body of evidence suggesting that the field-scale transport behavior is controlled fine-scale (0.1- 10 cm [0.4 – 4 in]) variations in sediment texture that typically fall below the resolution of standard hydrogeologic characterization techniques and size of the typical model grid block. An improved understanding of the effects of fine-scale features on field-scale flow and the response of borehole and surface geophysical sensors is important in developing conceptual models of vadose zone flow as well as interpreting existing contaminant distributions.

For the experiments conducted in FY 2000, a baseline set of volumetric water-content distributions, $\theta(\mathbf{x}; t)$, was obtained on May 5, 2000. A series of five fluid injections were made starting on June 1, 2000. During each injection, 4000-L (1057-gal) aliquots of water were metered into the 5-m (16-ft) deep injection well over a 6-hour period. Subsequent injections occurred weekly for a period of 5 weeks. Following the initial five injections, one additional 4000-L (1057-gal) injection was made on September 18 in an attempt to obtain *in situ* hydrologic properties using a combination of matric potential measurements and neutron-probe water-content measurements at the same depth. The 32 steel-cased wells surrounding the injection well were generally logged with neutron probe within 24 hours of each injection. Because of a wildfire on June 26, logging was postponed until July 7. Subsequently, two more readings of the 32 wells were completed during July. On some occasions, it was impossible to log all of the wells in a single shift, and logging was completed on the following day. After the September

injection, the frequency of neutron-probe measurements decreased with measurements being made at only a few select locations. All other geophysical measurements were discontinued.

Wells were logged with two neutron probes with counts accumulated over a 16-s interval. The spatial distribution of water content, $\theta(x,y,z)$, was determined using the calibration function reported by Ward and Gee (2000). Discontinuous $\theta(z)$ obtained at the discrete sampling wells along the various transects were interpolated by kriging to produce continuous 2-D and 3-D distributions of $\theta(x,y,z)$ for the monitoring times. Measurements were also interpolated over time to produce continuous distributions for data collected over 2 days. Neutron-probe counts from the 32 wells were converted to $\theta(x,y,z)$ for each transect and interpolated using a kriging algorithm in the Tecplot® software package.

If, as hypothesized, small-scale heterogeneity controls flow and transport, point values of water content and tracer concentrations would be subject to large uncertainties because of the complex spatial structure of the hydraulic properties. Analysis of the point values using a state variable model would therefore be subject to some error, particularly if the transport mechanisms are not known *a priori*. To minimize the error, we focused on the integral behavior of the wetting fronts using spatial moments to characterize their behavior. Spatial moments arise naturally in the parameterization of flow-and-transport models (Freyberg 1986). They allow a simple, physically meaningful description of overall plume behavior with a lesser degree of uncertainty than point values (Dagan 1990). A major advantage of this method is that it is direct and makes no assumptions about flow-and-transport processes. Ward et al. (2002) showed that the time-dependence of 3-D spatial moments can be used to characterize an infiltrating water plume. The effects of multi-scale heterogeneity on the distribution of water were examined in detail by calculating the time dependence of the spatial moments of the water plume. For a 3-D water-content distribution, measured at time t, the ijk^{th} plume-scale moment is defined as (Ward et al. 2002)

$$M_{ijk}(t) = \int_{-\infty}^{\infty}\int_{-\infty}^{\infty}\int_{-\infty}^{\infty} \theta(x,y,z,t)\, x^i, y^j, z^k \, dx\, dy\, dz \tag{2.1}$$

where $\theta(x,y,z;t)$ is the water-content field above background, $\theta(x,y,z;t_0)$, and x, y, z are the spatial coordinates. For this study, the values of superscripts *i, j, k* are limited to 0, 1, and 2, representing the zeroth, first, and second moments, respectively. The zeroth moment is unique in that, under conditions when it exists, its value is proportional to the total mass contained in the system. Thus, from Equation (2.1), the mass of water in the plume at time *t* is calculated as $\rho_w \cdot M_{000}(t)$ where ρ_w is the fluid density. In a closed system, $\rho_w \cdot M_{000}(t)$ should remain equal to the injected mass of water. The first central spatial moment describes the position of the plume centroid as a function of time $[x_c(t), y_c(t), z_c(t)]$ and is calculated as

$$x_c(t) = \frac{M_{100}(t)}{M_{000}(t)};\ y_c(t) = \frac{M_{010}(t)}{M_{000}(t)};\ z_c(t) = \frac{M_{001}(t)}{M_{000}(t)} \tag{2.2}$$

Water flows in response to potential gradients that include gravitational potential and matric potential gradients. In the application of moment analysis to locating the center of mass for the water plume, we focus on z_c. This is because an assumption of unit gradient conditions is applicable given that flow is

driven only by gravity. The mean plume-scale velocity in the vertical direction may be calculated from Equation (2.2) as

$$V_z = \frac{dz_c}{dt} \tag{2.3}$$

The second central moment defines the spatial covariance tensor, σ, of which the components of the main diagonal are defined as

$$\sigma_{xx}^2(t) = \frac{M_{200}(t)}{M_{000}(t)} - x_c^2;\ \sigma_{yy}^2(t) = \frac{M_{010}(t)}{M_{000}(t)} - y_c^2;\ \sigma_{zz}^2(t) = \frac{M_{001}(t)}{M_{000}(t)} - z_c^2 \tag{2.4}$$

The second moments in Equation (2.4) are physically related to the spread of the water plume about the center of mass in response to matric potential gradients. Thus, the time history of spatial moments may be useful for describing the behavior of the infiltrating plume without any assumptions about the flow process.

2.1.1 Results

Neutron moderation theory predicts relatively low count ratios (low θ) in coarse-textured soils and relatively high count ratios (high θ) in finer textured soils, such as fine sands, silts, and clays. Thus, in the Hanford formation, spikes in water content are generally coincident with silty fine-to-medium fine sand. A comparison of neutron logs of water content with lithologic logs derived from the sediment cores for the test site confirmed this relationship. Neutron-probe counts from the 32 wells were converted to θ(x;t) for each transect, and data were interpolated using an anisotropic kriging algorithm. Figure 2.1 shows the θ (x,t) on June 02, 2000, after the injection of 4000 L of river water. Recall that the injection point is located at a depth of 5 m, near Well H2 (Figure 1.4). Even at such an early stage of the injection, the wetting front is rather asymmetric beneath the injection point. In homogenous, isotropic porous media, water infiltrating from a buried point source tends to form a symmetrical wetting bulb that becomes more elongated in the vertical direction as the texture of the soil becomes coarser. This wetting front is clearly dominated by advection in the longitudinal and transverse horizontal directions. Movement is predominantly in the region of the finer textured sediments at 5 to 6 m.

A comparison of lithologic logs and neutron-probe data shows a continuous layer of higher θ, indicative of a fine-textured layer, between 5.5 and 7.0 m (Figure 2.1). A similar layer occurs between 10.5 and 11.5 m (Figure 2.2). Localized capillary breaks formed by the occurrence of fine-textured sediment over coarse-textured sediments tend to enhance lateral flow within the fine-textured layers until the water entry pressure of the coarser soils is exceeded. Most of the increase in θ occurs along the D-H transect (Figure 1.4), suggesting that the water is flowing preferentially in a southeasterly direction. The fine-textured soil overlaying the coarse material is therefore acting as a capillary barrier impeding vertical advection and enhancing lateral flow. By this time, a secondary wetting bulb had also developed beneath the primary plume region along D-H. This suggests that the matric potential was already high enough to

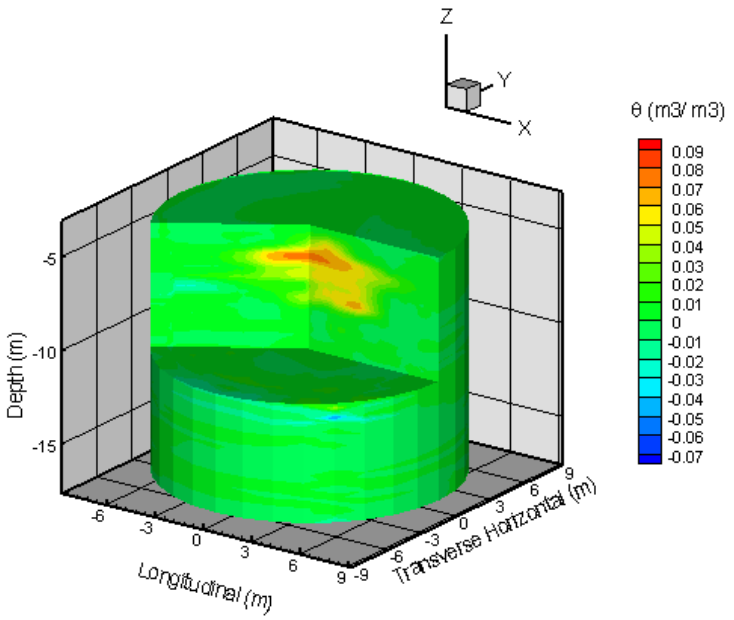

Figure 2.1. Spatial Distribution at Soil Water Content, θ(x,y,z) Interpolated from Neutron-Probe Measurements in the 32 Wells on June 02, 2000, After an Injection of 4,000 L (1057 gal) of Columbia River Water

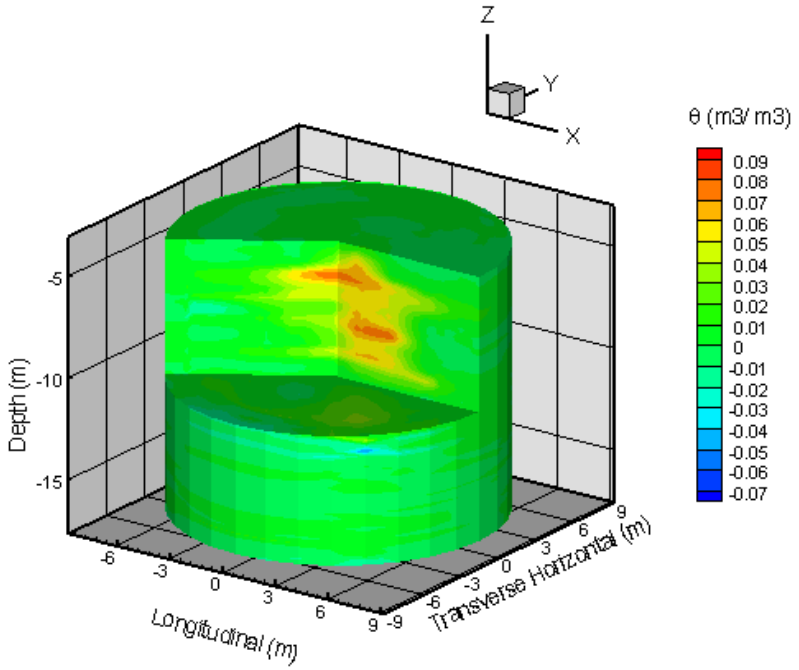

Figure 2.2. Spatial Distribution at Soil Water Content, θ(x,y,z) Interpolated from Neutron-Probe Measurements in the 32 Wells on June 23, 2000, After an Injection of 16,000 L (4227 gal) of Columbia River Water

overcome the entry pressure of the underlying layer, leading to breakthrough into the coarser layer in a much localized region. This observation could have implications on interpreting the behavior of subsurface leaks. Fine-scale layering at scales smaller than the main architectural elements can reduce the vertical migration of water and contaminants while enhancing lateral flow. If there is any slope to these layers, preferential movement could continue to result in the funneling of water and localized deep penetration once the entry pressure of the confining layer is exceeded. Given that the maximum θ observed in this study was generally around 0.25 m^3 m^{-3}, this mechanism could become important with relatively small volumes of water. Figure 2.2 shows that the lower fine-textured layer acted as an impeding layer and led to enhanced lateral movement out of the monitored domain. The experiment was discontinued after a total injection of 20,000 L of water; at that point, none of the injected water had penetrated the lower fine-textured layer.

To gain further insight into the stratigraphic effects on the behavior of the water plume, the time dependence of the zeroth spatial moments was calculated. Figure 2.3 compares the time dependence of the recovered mass of water with the injected mass of water in kilograms. Until the third injection, injected mass and the recovered mass were in good agreement. During the test, the target pump rate was steady for the duration of the test, and the cumulative injected mass approximated a straight line. A total of 11,983.37 kg of water was injected by the end of the third injection on June 15, 2000, and a total of 19,972.29 kg was injected by June 28, 2000. Mass recovery from the June 16, 2000, logging accounted for 11,404 kg or 95.2 percent of the injected mass. Given the 24-hour delay in measurement and the error in the neutron probe resulting from using a single calibration curve for a layered system, the mass

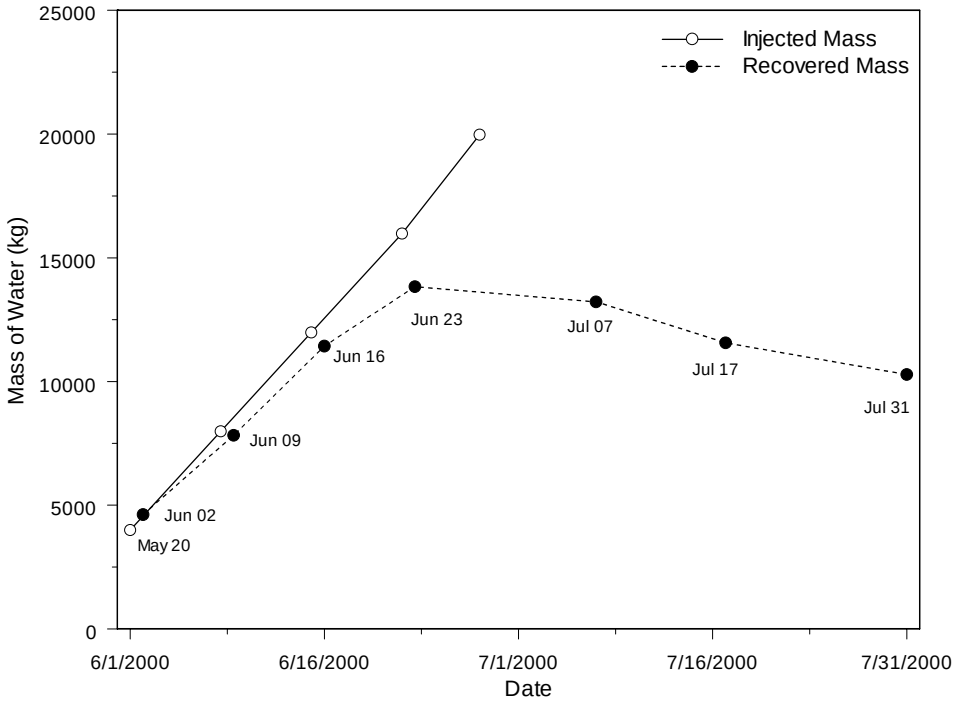

Figure 2.3. Comparison of the Injected and Recovered Mass of Water. Recovered mass was determined from the zeroth moments, $M_{000}(t)$.

recovery is quite remarkable. By the fourth injection, 15,977.8 kg of water had been injected, but the recovered mass was only 13,803 or 86.4 percent. From this point on, there is increasing discrepancy between the injected and recovered mass. By the end of the monitoring period on June 31, 2000, mass recovery was only 10,262 kg, or 51.4 percent of the amount initially injected. The only possible explanation for the divergence between the injected and recovered mass is water leaving the monitored domain. While the boreholes used for monitoring extend to a maximum of 8 m from the injection point, there is no physical subsurface boundary, so the water is free to redistribute in 3-D space in response to the potential gradients.

Figure 2.4 shows the change in water content on June 22, 2000, after the injection of 15,978 kg (35,225 lbs) of water. Figure 2.5 shows the change in water content on June 28, 2000, after the injection of 19,972 kg (44,031 lbs) of water. These plots are cross sections of 3-D plots similar to Figure 2.1 taken at the depth of the plume centroid. The top of the figures is to the north (0^o); the plume is moving in a predominantly southeasterly direction. At this time, water had started to leave the monitoring volume (Figure 2.3). There were minimal changes in $\theta(x,y,z;t)$ for the other orientations, suggesting that most of the water exited the domain to the southeast. This observation has important implications for field-scale predictive and inverse modeling for parameter estimation. Clearly, the zero flux boundary condition typically used for water on the vertical side (north, east, south, and west) boundaries is inappropriate unless they are extended significant distances from the monitored boundary. Using $\theta(x,y,z;t)$ measurements without considering the loss of mass from the monitored domain would lead to erroneous parameter estimates, particularly with respect to the vertical rate of movement. Figure 2.5 also shows that the water-content changes induced by the large water injection were near zero by late June and were totally gone by the end of monitoring in late July.

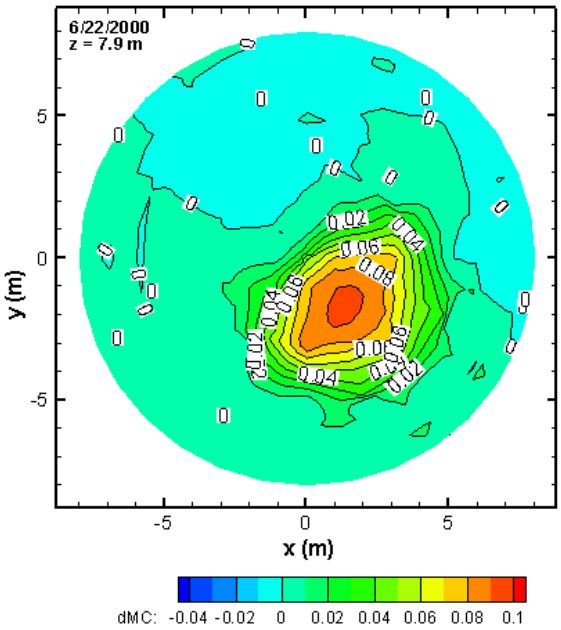

Figure 2.4. Plume Distribution at the Vertical Location of the Centroid on June 22, 2000, after the Injection of 15,978 kg (35,225 lbs) of Columbia River Water. The dMC is equal to $\Delta\theta(x,y,z)$.

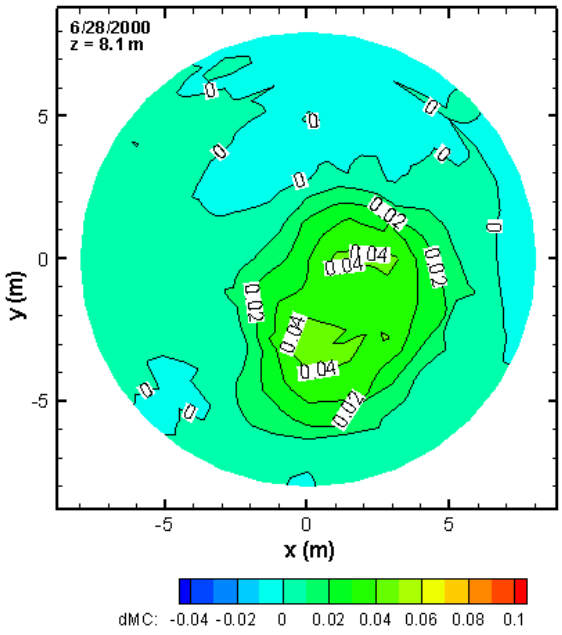

Figure 2.5. Plume Distribution at the Vertical Location of the Centroid on June 28, 2000, after the Injection of 19,972 kg (44,031 lbs) of Columbia River Water. The dMC is equal to $\Delta\theta(x,y,z)$.

2.1.2 Synopsis and Implications

The synopsis of findings for the subsurface leak simulation tests and their implications are as follows:

- The Hanford formation is not uniform, homogeneous, or isotropic and as a result, hydraulic properties appear to vary in the three principal directions. Results of a field-scale injection at the 299-E24-111 test site show a complex interplay between layered heterogeneity and saturation dependent anisotropy that appear to control the movement of water at the test site.

- Spatial moment analysis of water content shows a deviation between the injected and recovered water mass that was attributed to water leaving the monitoring domain via laminated fine-textured layers.

- In stratified sediments, the extent to which an asymmetric flow field develops is controlled partly by the geometry, scale, and continuity of textural contrasts that give rise to heterogeneity in the permeability field.

- Infiltration at the 299-E24-111 test site is 3-D because of multi-scale heterogeneities and anisotropy. Modeling this and similar sites without considering subgrid features would produce conservative results (enhanced vertical migration), which could lead to the over-engineering of remedial actions.

- Field observations show that the 299-E24-111 test site retained little memory of large injection events in terms of elevated water contents. Forensic analysis and history matching will have to rely on sorbed contaminants to map the path of the water front, which will require an improved understanding of reactive transport.

- Construction of the stratigraphic models should include tilted layers to accommodate the natural slope to the formation and an appropriate representation of saturation-dependent anisotropy that can capture lateral spreading along multiple strata with contrasting physical properties. The model to capture flow and transport at the 299-E24-111 test site should incorporate methods to account for sub-grid heterogeneities and the connectivity of these structures.

2.2 Evidence of Anion Exclusion During Vadose Zone Transport

There have been several reported instances in which anion exclusion has been hypothesized to play a role in the flux of solutes though the vadose zone (Biggar and Nielsen 1962; Krupp et al. 1972; Wierenga and van Genuchten 1989). Anion exclusion occurs when negatively charged species (solutes, colloids, microbes) are electrostatically repelled by negatively charged solid surfaces to travel at velocities in excess of those of the migrating fluids. These species are essentially excluded from water associated with the diffuse double layer and move entirely in the free fluid. The exclusion of chloride relative to tritium has been observed to affect recharge estimates based on chloride mass balance. Although the mechanism has been observed mostly in soils with high clay content, there is evidence that it may occur in a wider range of soils. Under oxidizing conditions, ^{99}Tc exists as the soluble heptavalent pertechnetate ion, TcO_4^- which is highly mobile in soils and groundwater. Measurements in a wide range of soils, including alluvium, suggest that TcO_4^- also exhibits anion exclusion effects (Lieser and Bauscher 1987; Zhuang et al. 1988; Schroeder et al. 1993). Neglecting this mechanism could result in overestimating vadose zone water flux and recharge rates to the groundwater based on chloride mass balance, underestimating the impact of colloids, and underestimating the migration rates of high-risk contaminants like ^{99}Tc.

As part of the field experiment at the 299-E24-111 test site, tracers were selected such that a comparative analysis of their transport behavior would provide insight into the relative importance of anion exclusion. Thus, the objectives of this study were to determine the importance of anion exclusion and quantify the uncertainty in transport velocities caused by the anion exclusion process, if active. During the FY 2000 infiltration tests, a tracer cocktail consisting of 3 g $NaH^{13}CO_3$, 25 mg ^{87}Sr, 1 mg ^{145}Nd, 1 mg ^{179}Hf, 3 mg ^{207}Pb, 1000 ppm of Br^-, and 2 kg of D_2O was added to river water during the third injection. Sampling was limited to a series of sediment cores obtained by split spoon and wireline sampling at various times after the injection. The spread of the tracers over time was monitored by measuring the isotope ratios and bromide concentrations in samples of the pore water extracted from a series of boreholes.

A series of boreholes were installed in the southwestern quadrant of the well field (see Figure 1.4) to obtain samples for analyses. Borehole S2 was installed approximately 2 m (6.5 ft) from the injection well 21 days after injecting the tracer solution, and 8 days after the final aliquot of river water was injected. Borehole S3 was also installed about 2 m (6.5 ft) from the injection well but 4 days after the installation of S2. A third borehole, S5, was installed about 2 m (6.5 ft) from the injection well 88 days after release of the tracer. Two additional boreholes, S7 and S8, were installed 281 days after the tracer injection. S7 was installed 3 m (10 m) from the injection well whereas S8 was installed 8 m (26 m) from the injection

well. Core samples were collected in 15-cm (6-in) Lexan® liners, which were immediately capped at both ends on retrieval. Three subsequent sampling campaigns were conducted using cone penetrometer with a wireline sampler. A series of 30-cm (12-in.) long samples were collected from each of three boreholes, S5, S7, and S8, using a 2.5-cm (1-in.) diameter sampling unit. Samples were removed from the sampler and immediately placed in a sealed Ziploc bag and refrigerated for transport to the laboratory. Subsamples of about 200 g (7 oz) were removed for isotopic analyses and sealed in plastic sample bottles. Pore waters were extracted in 1:1 extracts and analyzed for ionic tracers at PNNL. Pore water for isotopic (δD and δ18O) was vacuum-distilled from the samples and analyzed for stable isotope composition at the Lawrence Berkeley National Laboratory (LBNL). Soil water contents were calculated from the weights before and after vacuum extraction.

2.2.1 Results

Figure 2.6 shows plots of depth profiles of relative concentrations of deuterium and bromide as well as soil water content in S5. Solute concentrations in this core were similar to those observed for the earlier cores. The locations of the tracer peaks are also similar to those observed in the earlier boreholes S2 and S3. However, the concentrations of the tracers are somewhat lower. The peak deuterium concentration in S5 was only 34% of the input concentration. Furthermore, the bromide concentrations in S5 were significantly lower than the deuterium concentrations (~ 50%). Although bromide concentrations were generally lower in the S2 and S3, the differences were not as pronounced. The δ18O data for the S5 pore waters are plotted on the right-hand side of Figure 2.7. As in the earlier cores, a shift in δ18O values of the S5 pore waters within the deeper fine-textured layer shows evidence of having been contacted by the injected water. However, there was no evidence of tracers. A similar shift is evident in the upper fine-textured layer at 6 to 7 m (20 to 23 ft). These results and data from the remaining cores confirm that most of the water injected during the tests remained in the depth interval between 4.5 m (15 ft) and about and 11 m (36 ft), spreading out laterally along fine-textured layers. The tracer data also show that there was only minor mixing between the separate aliquots of water leaked into the subsurface, even 9 months after the test was completed. More importantly, the deuterium data suggest that there was little interaction between the pre-existing pore fluids beneath the lower fine-textured layer and the tracer solution, confirming that the bulk of the injected water left the monitored domain by lateral spreading.

In addition to deuterium and bromide, several cations (^{87}Sr, ^{145}Nd, ^{179}Hf, and ^{207}Pb) were included in the tracer solution. For the cations, only the strontium isotope ratios were measured in all of the cores. The ^{87}Sr/^{86}Sr ratio of a pore water sample from core S1 was 0.714 compared to the ^{87}Sr/^{86}Sr ratio of 1.3 in the tracer solution. For Sr concentrations of 1.6 ppm in the pore water and 100 ppb in the tracer solution and a C/Co of 0.5, the ^{87}Sr/^{86}Sr ratio of the pore water in the peak deuterium samples in S2 and S3 should be about 0.75 if strontium was acting conservatively. However, the ^{87}Sr/^{86}Sr ratios in both cores were no different than the background. In the later cores, there was a slight increase in the ^{87}Sr/^{86}Sr ratios up to about 0.715, but the values were still well within the range of values that have been measured for pore water samples from the Hanford formation (0.714 to 0.721). These results suggest that strontium was strongly sorbed onto the sediments immediately adjacent to the injection point, and there was little or no transport even after 9 months.

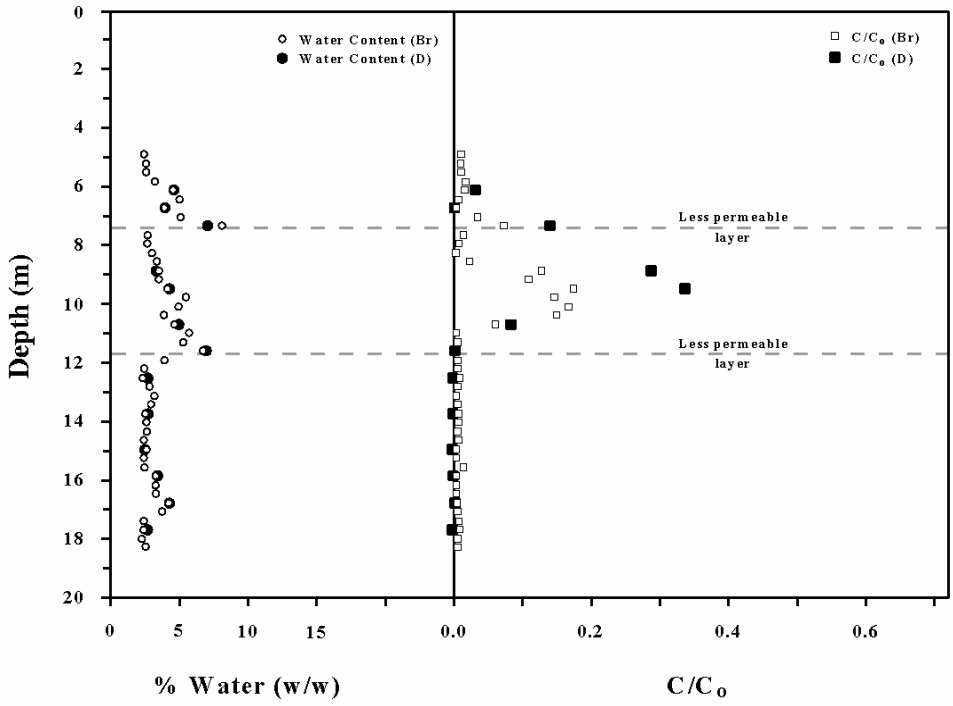

Figure 2.6. Analytical Results from Core S5 Showing Depth Profiles of Soil Water Contents and Relative Concentrations of Deuterium and Bromide

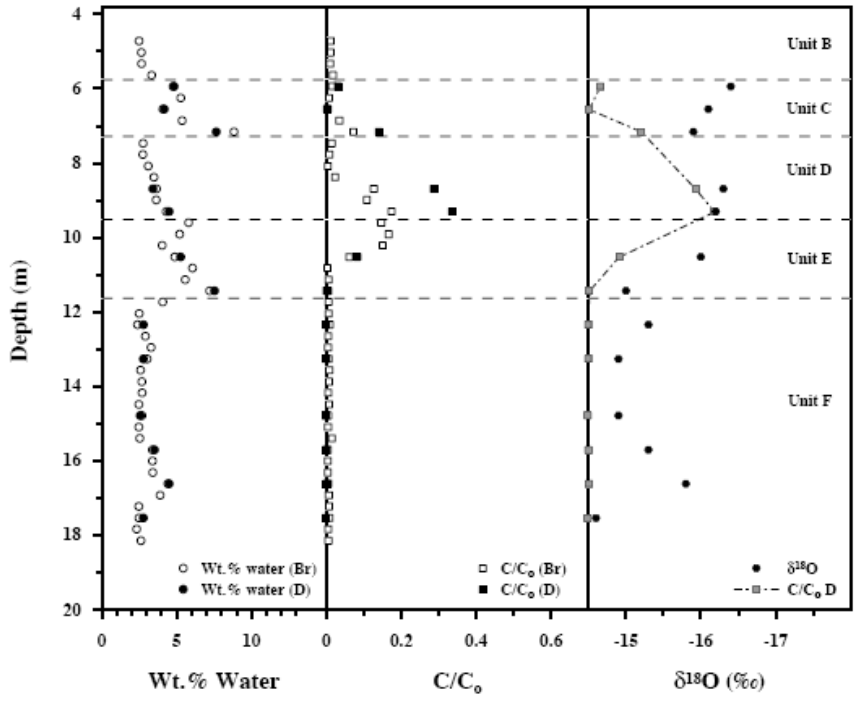

Figure 2.7. Analytical Results from Core S5 Showing Depth Profiles of Moisture Contents, Relative Concentrations of Bromide and Deuterium, and δ18O. The dashed line on the δ18O Plot Represents the Deuterium Concentrations for Comparison.

Comparisons between the deuterium and bromide data show the opposite relationship. The peak concentrations for both are co-located, but the relative peaks are much different. Figure 2.8 shows a plot of the peak concentrations of deuterium and bromide plotted versus elapsed time (after tracer injection). There are two sets of data for borehole S3 because the peak concentrations of deuterium and bromide were in different samples. The trend lines for the two tracers begin at the average concentrations for S2 and both S3 samples and then pass through the data for S5 and S7. The most striking feature is the sharper decrease in the peak bromide concentration relative to the deuterium peak. In the first two cores, the relative bromide concentration was approximately 25% lower than the deuterium concentration. After 9 weeks, the bromide peak was about 50% of the deuterium peak, and by 9 months, bromide was down to approximately 32% of deuterium peak. These relative differences between the deuterium and bromide concentrations were generally the same for other non-peak samples within each borehole, although it was difficult to confirm, given the limited number of deuterium samples. These data suggest that the bromide is moving ahead of the water. This is unlikely to be due simply to different rates of molecular diffusion because the relative concentrations remain fairly consistent at all depths within each borehole. If the discrepancy was due solely to diffusion, then bromide concentrations would have been higher, relative to deuterium, in the samples collected outside of the peak tracer zones. However, it appears that the bromide was moving out laterally more quickly than the deuterium and therefore ahead of the water. This hypothesis is supported by the higher relative proportions of bromide in the cores from S8 versus S7. The S8 well was drilled at the same time as S7, but was located further away from the injection point (8 m versus 3 m). The peak deuterium concentration dropped from 0.25 in S7 to 0.06 in S8, indicating that the

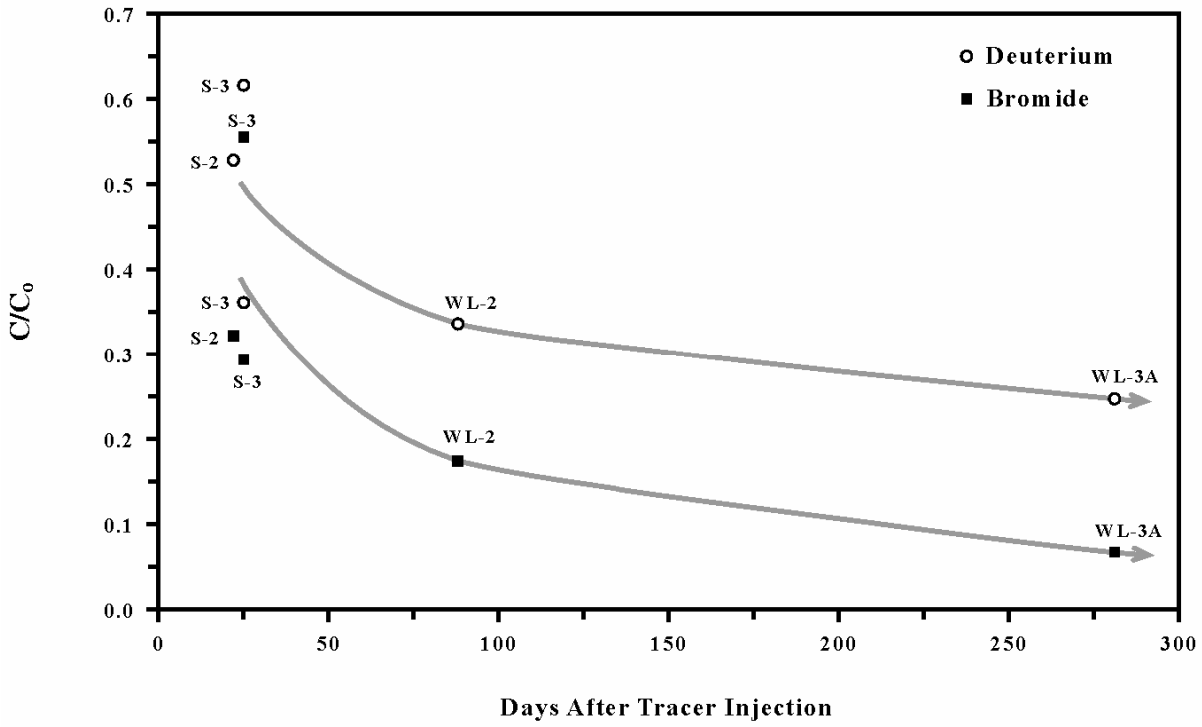

Figure 2.8. Peak Concentrations of Bromide and Deuterium in the Four Boreholes Drilled 2 to 3 m (7 to 10 ft) from the Injection Well. Two sets of data are shown from S3 because different physical samples contained the peak concentrations of deuterium and bromide.

center of mass for the deuterium tracer was located closer to S7 than S8. The peak bromide concentrations in S7 and S8 were both 0.08, indicating that the center of mass for the bromide tracer was located about midway between the two boreholes. This shift from a Br/D_2O ratio of 0.32 in the closer core to 1.25 in the more distant core supports a faster lateral dispersion rate for the bromide. These results provide clear evidence of an active anion exclusion mechanism. Because the bromide ions were essentially excluded from water associated with the diffuse double layer, they were forced to move entirely in the free fluid, which would have been in the larger pores where the pore water velocity was much higher.

2.2.2 Synopsis and Implications

The synopsis of findings for this study of the dominant vadose zone transport mechanisms and their implications are as follows:

- The concentrations of contaminants reaching groundwater are determined by the amount, concentration, and nature of contaminants present in vadose zone sources, the rate of release from the sources, and the action of a number of geochemical processes (e.g., diffusion, ion exchange, and sorption). There is evidence that additional processes, including colloid-facilitated transport and anion exclusion, can enhance the transport of contaminants like ^{99}Tc. These processes are difficult to quantify, and the extent to which they are active in Hanford's vadose zone has not been determined.

- The analysis of $^{87}Sr/^{86}Sr$ ratios of pore waters extracted from the 299-E24-111 test site showed essentially no change from background in pore water samples extracted from cores as little as 2 m (6 ft) from the tracer injection. Measured $^{87}Sr/^{86}Sr$ ratios were about 0.714 compared to a ratio of 1.3 in the tracer solution and a range of 0.714 to 0.721 in pore waters extracted across the site. There was no evidence of any of the other isotopic tracers injected in the cocktail. These results suggest that strontium was strongly sorbed onto the sediments immediately adjacent to the injection point, and there was little or no transport even after 9 months.

- The analysis of bromide and deuterium concentrations from the field experiments at the 299-E24-111 test site provided clear evidence of an active anion-exclusion mechanism.

- The implication of this study is that the anion-exclusion mechanism excludes negatively charged species, including colloids, microbes, and solutes, from the water associated with the diffuse double layer, forcing them to move entirely in the free fluid, which is typically in larger pores. The result is a higher velocity relative to water. This mechanism can potentially impact anionic contaminants (e.g., nitrates, chloride, chromate, pertechnetate) and anionic complexes [e.g., $UO_2(CO_3)^-$].

2.3 Effects of Fluid Properties in Subsurface Flow and Transport

Compared with water, hypersaline liquid wastes ($NaNO_3$ > 10 N) from the reduction-oxidation (REDOX) process at the Hanford Site have elevated viscosity (μ > 1.2 cP), density (ρ > 1400 kg m^{-3}), and surface tension (γ_L > 100 mN m^{-1}). Such liquids have infiltrated into the vadose zone at Hanford from leaking underground storage tanks, but the migration behavior of saturated or hypersaline salt solutions

through unsaturated soils is largely unknown. Laboratory tests with tank-waste simulants suggest that the elevated density, viscosity, and surface tension properties of these liquids can influence the wetting front behavior, altering its shape and migration rate. Conditions under which these mechanisms are active in the field and the extent to which they contribute to transport through the vadose zone are largely unknown, making it impossible to accurately predict the post-leak distribution of these fluids in the field.

In FY 2001, another set of subsurface leak simulation experiments was initiated to provide improved understanding of effects of fluid-properties transport in heterogeneous, anisotropic, unsaturated sediments. Although it is well recognized that the properties of high-level waste fluids and discharged waste water are dissimilar to those of pure water, very few studies have attempted to evaluate the effects of fluid properties on subsurface flow and transport at Hanford (Ward et al. 1997; White and Ward 2001). Discharged water and other waste fluids were known to be rich in inorganic salts. Elevated salt concentrations are known to increase density, viscosity, and surface tensions as high as 110 mN m^{-1} (Ward et al. 1997). Owing to these changes, there has been much speculation about fluid effects with some expectation that these fluids could potentially move faster and deeper than water and dilute solutions when subjected to the same boundary conditions during transport in similar sediments. The FY 2001 experiment at the 299-E-111 test site was designed to study the relative impacts of heterogeneity and fluid properties on transport behavior. Thus, the injected fluids were modified by adding 0.5 wt% of sodium chloride, NaCl, and 40 wt% sodium thiosulfate pentahydrate ($Na_2S_2O_3 \cdot 5\ H_2O$) before injection. Sodium thiosulfate was chosen because it could increase the density, viscosity, and surface tension to the required levels at much lower concentrations than would be required with other salts and because it was one of the few salts approved for injection by the regulators.

The baseline $\theta(x,y,z)$ distributions at the 299-E24-111 test site were obtained on March 21, 2001. The injection experiment commenced on March 30, 2001, and included 10 injections of 36 wt% of sodium thiosulfate solution. The solution was injected at a rate of 5 L per minute (1.4 gpm) such that 1892 L (500 gal) were added with each injection over a 5-week period. After the saline fluid was applied, there was a 1-week break after which Columbia River water was applied in three increments of 3785 L (1000 gal), each over a 2-week period. The injections totaled 18,925 L (5000 gal) of saline solution followed by 11,355 L (3000 gal) of Columbia River water. Wells were also logged with two neutron probes using a 16-s count interval. The spatial distribution of water content, $\theta(x,y,z)$, was determined using the calibration function reported by Ward et al. (2000). Discontinuous $\theta(z)$ obtained at the discrete sampling wells along the various transects were interpolated by kriging to produce continuous 2-D and 3-D distributions of $\theta(x,y,z)$ for the different monitoring times. Measurements were also interpolated over time to produce continuous distributions for data collected over 2 days. As with in the FY 2000 experiment, discrete $\theta(z)$ measurements in the 32 wells were interpolated for the different monitoring times and locations. Given that the subsurface formation remained unchanged and that the moisture contents rapidly returned to the pre-injection conditions, changes between this and the first experiment can be attributed to the effects of fluid properties. As in the first set of experiments, the distribution of the water plume was examined in detail by calculating the time dependence of the spatial moments.

2.3.1 Results

Figure 2.9 shows θ (x,y,z) on April 04, 2001, after the injection of 3,827 L (1011 gal) of water with sodium thiosulfate. Owing to the similarity in the injected mass, the results from the salt-free water injection (4000 L [1057 gal]) shown in Figure 2.1 are used for comparison. Compared to the salt-free

water, moisture contents are somewhat higher near the injection point. Perhaps the most striking difference at this stage is the compact symmetric nature of the water plume. The larger increase in moisture and the apparent mounding of water may be related to properties of the fluid that increased the difficulty of the injection. Unlike the river water injection, ponding was observed in the injection well during the early stages of the hypersaline injection. Subsequent distributions show more extensive lateral movement than the salt-free plume.

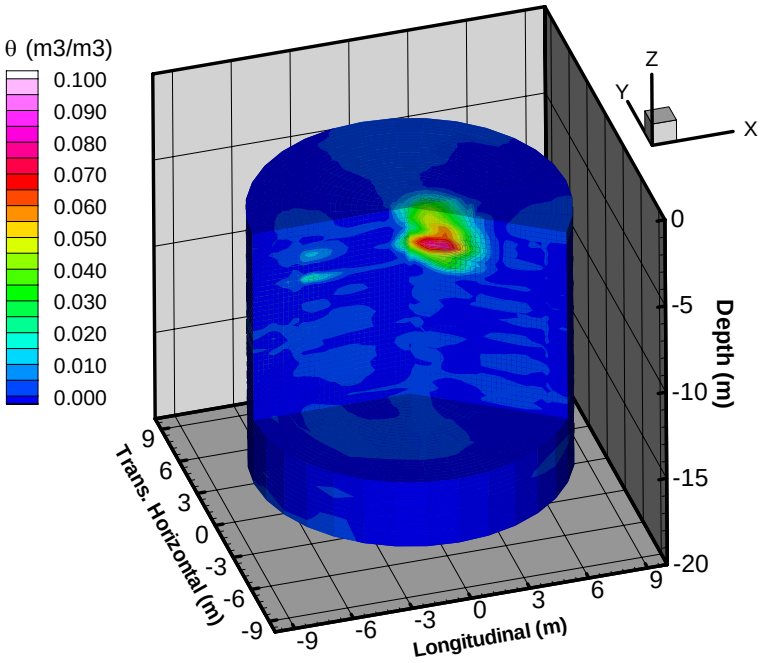

Figure 2.9. Spatial Distribution at Soil Water Content, θ(x,y,z), Interpolated from Neutron-Probe Measurements in the 32 Wells on April 04, 2001, After an Injection of 3,827 L (1011 gal) of Hypersaline Water

The initial compactness of the plume followed by delayed penetration into the underlying coarser sediments may be caused by buoyancy effects resulting from a higher viscosity and surface tension. Such changes in the fluid properties could affect the soil hydraulic properties. Laboratory measurements suggest that the differences in properties of hypersaline fluids may lead to an increase in the entry pressure relative to salt-free water. Surface tension, viscosity, contact angle, and mean pore diameter are all important in controlling the penetration of liquids into the porous media through the Young-Laplace equation

$$P_c = \frac{2\gamma_L \cos\varphi_A}{r} \tag{2.5}$$

where P_c is capillary pressure, γ_L is surface tension of the liquid, and r is the mean radius of the capillary. A liquid will enter the capillary spontaneously only if P_c is positive. The sign of P_c is determined by the term cos φ_A; P_c is positive when $\varphi_A < 90^o$, zero when $\varphi_A = 90^o$, and negative when $\varphi_A > 90^o$. Laboratory measurements show that the contact angle increases with increasing salt concentration. Both increases in

φ_A and decreases in *r* will cause the magnitude of P_c to increase. If the entry pressure initially increased because of elevated salinity, such an effect could be expected to decrease over time as the infiltrating fluid became diluted by the antecedent moisture. However, the relationship between fluid properties and parameters of the water-retention function, particularly the entry pressure, is not well understood for hypersaline fluids, and the time required for these effects to disappear are unknown at this stage.

Figure 2.10 shows the moisture distributions after 26,610 L (7,030 gal) of water had been injected. These data show evidence of the lower fine-textured layer being penetrated along transect E-A with complete breakthrough near well H6 on the D-H transect. This is the first recorded evidence of water penetrating the lower fine-textured layer during experiments at this site. To gain further insight into the relative importance of stratigraphic effects and fluid properties on the behavior of the water plume, we calculated the time dependence of the zeroth spatial moments for the infiltrating plume.

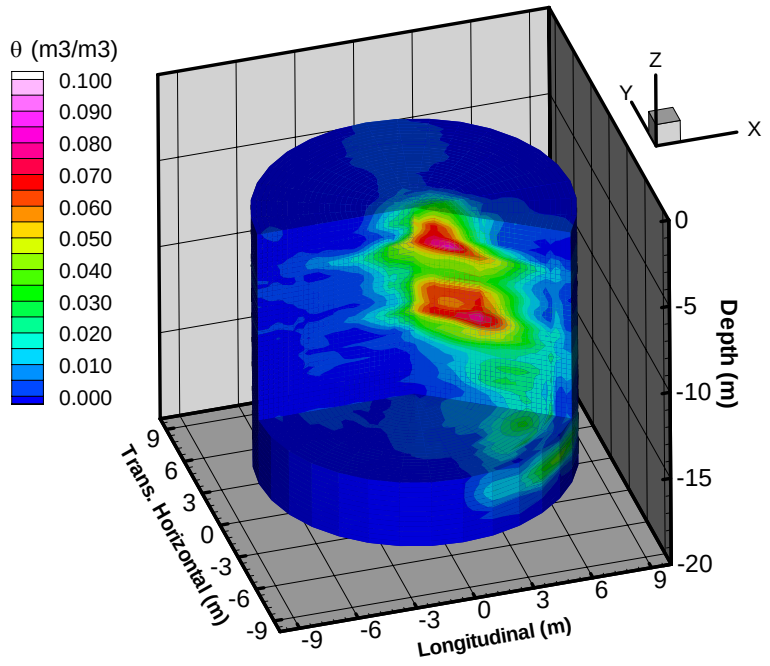

Figure 2.10. Spatial Distribution at Soil Water Content, θ(x,y,z), Interpolated from Neutron-Probe Measurements in the 32 Wells on May 10, 2001, After an Injection of 26,610 L (7,030 gal) of Hypersaline Water

Figure 2.11 compares the time dependence of the recovered mass of saline water with the injected mass in kilograms. Until the fifth injection, injected and recovered water mass were in good agreement. The injection was a bit more difficult to control than in the salt-free injection, and the cumulative injected mass shows some variation about the desired straight-line relationship. A total of 11,338 kg of water had been injected by end of the sixth injection on April 12, 2001, when the injected and recovered mass started to diverge. This is very similar to the 11,938 kg of river water that had been injected before the injected and recovered masses diverged in the salt-free injection (Figure 2.3). The rate of recovery continued to decline over time, and shortly after the last injection on May 9, 2001, the recovered mass

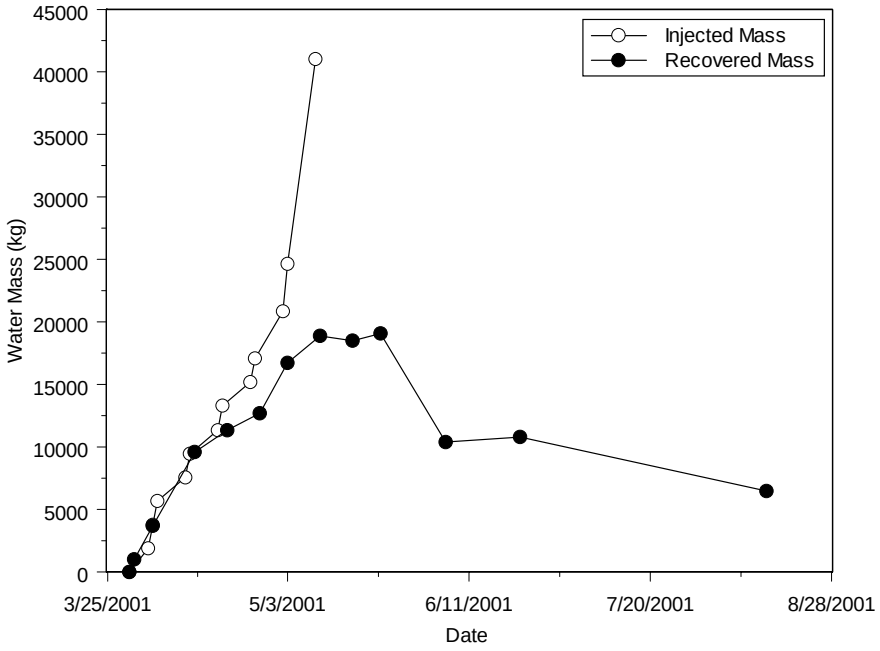

Figure 2.11. Comparison of the Injected and Recovered Mass of Hypersaline Water. Recovered mass was determined from the zeroth moments, $M_{000}(t)$.

(18,889 kg) was less than 50 percent of the total amount of water injected. As with the salt-free injection, the only possible explanation for the divergence between the injected and recovered mass is water leaving the monitored domain. The behavior of the plume centroid was also analyzed to understand the contribution of fluid properties to the overall plume behavior.

Figure 2.12 shows the vertical trajectory of the plume centroid as a function of elapsed time. As with the salt-free plume, the vertical centroid showed a nonlinear dependence on elapsed time. However, a major difference between the two injections is the behavior of the plume center of mass. Unlike the salt-free injection, the vertical movement of the centroid is not monotonic, but shows at least three different rates. The center of mass also appeared to move upward about 25 days after the start of the experiment. These behaviors may be due partly to the effect of the fluid properties on the hydraulic behavior of the sediments, a hypothesis that is supported by the characteristics of the plume. The plume was initially compact with much higher water contents than the salt-free plume after injection of a similar volume. The compact nature may be related to a reduced capability to enter pore space much beyond the injection point. This combined with the increased density would contribute to an increased rate of downward movement once the mass of the plume became large enough. Figure 2.12 shows that the initial rate of vertical descent was similar to the salt-free plume, except for days 3, 20, and again after day 47. Periodic decreases in the rate of decent would occur in the salt plume as new sediments with different entry pressures were encountered as the plume was diluted by antecedent moisture. As the plume became more dilute, the difference between the salt-free and saline plume would decrease, and the mean velocity would increase. The rate of migration of the centroid in the vertical direction continued to increase over time for the hypersaline fluid. After 20,000 kg, the centroid of the hypersaline plume had traveled 35 percent farther in the vertical direction that the salt-free plume.

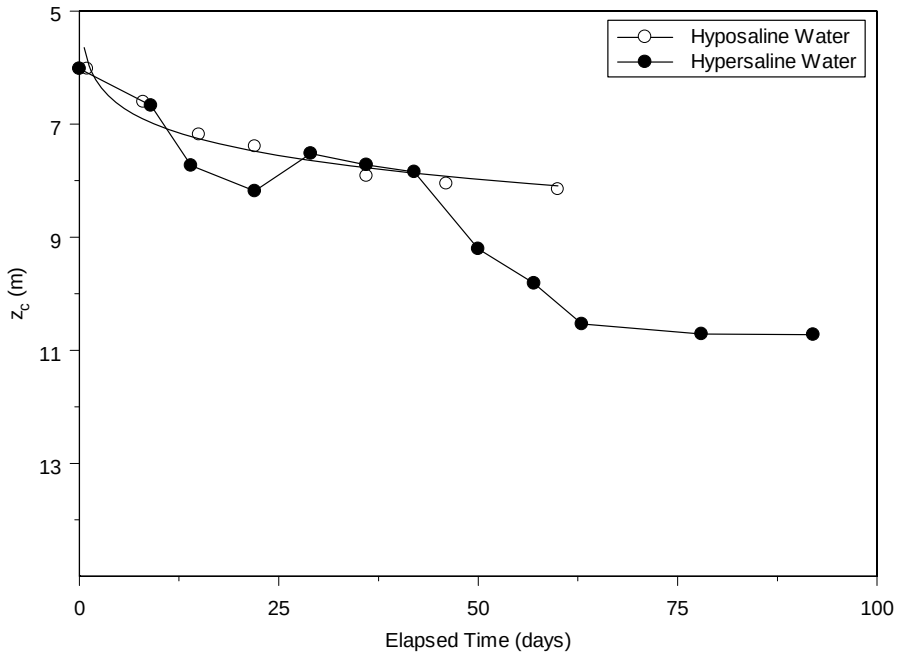

Figure 2.12. Measured Vertical Displacement of the Centroid of the Water Plume Versus Time. The solid line represents the least squares regression with $z_c(t)= 5.8718\ t^{0.0783}$; $R^2 = 0.953$.

For the salt-free injection, the transverse horizontal variance initially increased slowly and showed a nonlinear dependence on travel time, approaching a plateau towards the end of the experiment, but neither of the injections appeared to reach a constant variance. For the hypersaline plume, transverse horizontal variance was less well behaved with several fluctuations (Figure 2.13). The trends in the longitudinal (Figure 2.14) and vertical (Figure 2.15) variance show similar trends with an initial decrease followed by a somewhat erratic increase over time. The vertical variance of the hypersaline plume also showed an initial decrease but, in contrast to the transverse horizontal and longitudinal variance, started to increase after about 37 days to reach a plateau. This is qualitatively similar to the salt-free injection, which also approached a plateau. When analyzed in relation to travel distance, the occurrence of the plateaus appears to coincide with the depths of the fine-textured layers. In the case of the salt-free injections, the variance approached a maximum at around 5 m, similar to the depth of the upper fine-textured layer that controlled lateral movement. The hypersaline plume initially decreased to a minimum at around 5 m, followed by an increase to a maximum at around 15 m. The 5-m and 12-m depths are consistent with the two fine-textured layers that impacted flow. In both injections, the upper fine-textured layer at 5.0 m initially restricted downward movement until the capillary pressure exceeded the entry pressure of the coarser layers. The vertical centroid of the salt-free water reached a maximum of 8 m and was never really impacted by the deeper fine-textured layer. However, the data show that the hypersaline plume reached this depth and was mostly contained until breakthrough occurred near well H8.

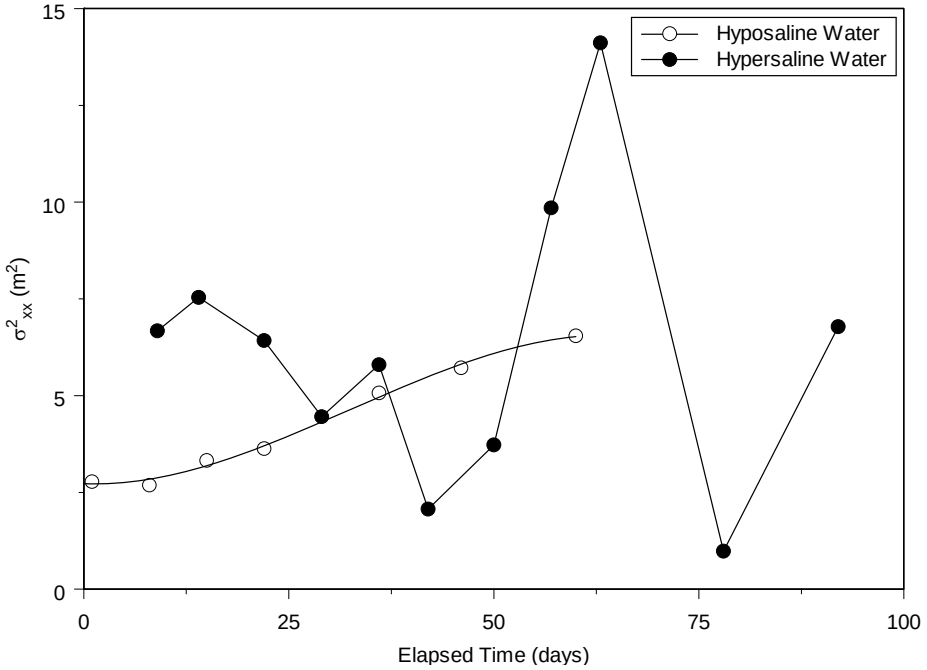

Figure 2.13. A Comparison of the Temporal Dependence of the Transverse Horizontal Variance for the Salt-Free and Hypersaline Plumes

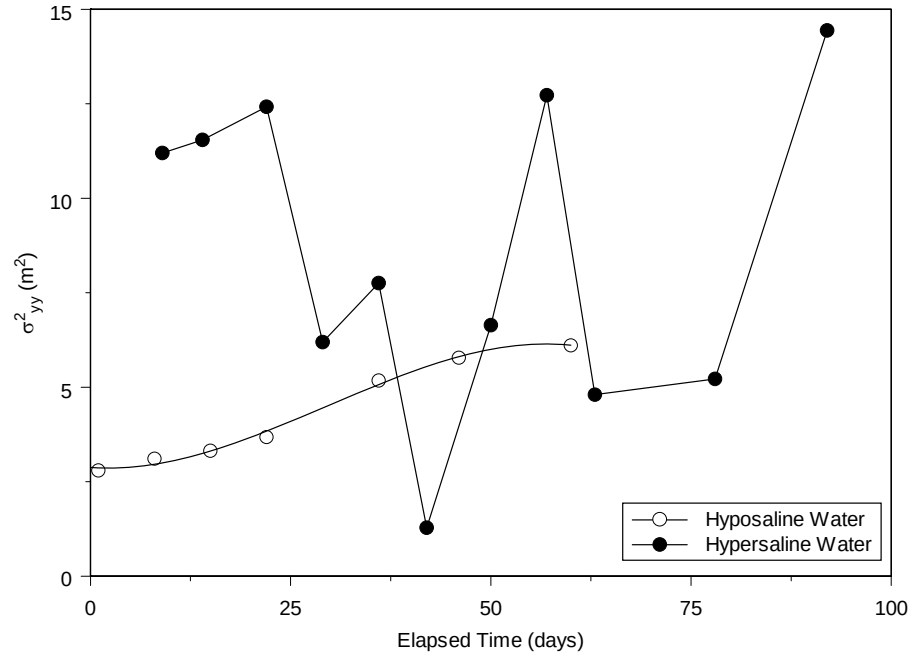

Figure 2.14. A Comparison of the Temporal Dependence of the Longitudinal Variance of the Salt-Free and Hypersaline Plumes

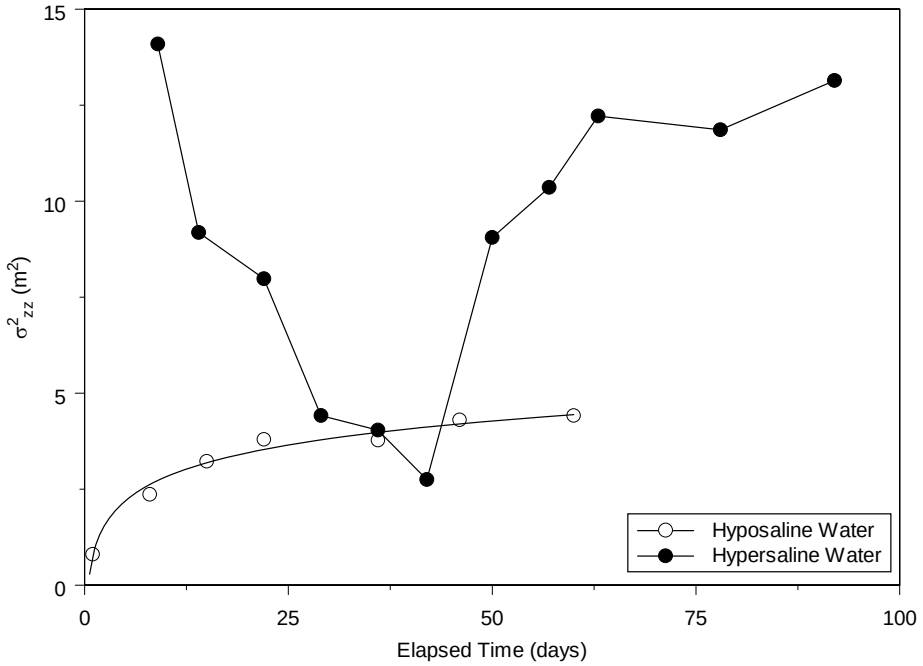

Figure 2.15. A Comparison of the Temporal Dependence of the Vertical Variance of the Salt-Free and Hypersaline Plume

The differences in variance, relative to the salt-free injection, could be caused by a combination of factors. The much higher variance with the hypersaline plume could be expected because this plume covered more of the domain. As it expanded laterally, it would have encountered increased heterogeneity. The apparently erratic nature could be related to the more variable injection rate during the hypersaline injection, which would have translated into a non-steady flow in the subsurface. The initial moisture conditions could have also played a role as these conditions were somewhat different in the two experiments. Infiltration is known to be very sensitive to the initial condition, and even though the initial water contents at the start of the second experiment were similar to that at the beginning of the first experiment, there could have been enough differences to have impacted the behavior of the water plume.

A large initial variance is consistent with spatial variability in the moisture content, the effects of which would have been enhanced by the recently concluded experiment. As the new injection started, spatial differences in moisture would have been smaller with the largest gradient remaining at the wetting front, so a decrease in variance could be expected. The later trends in variance are more difficult to explain but could be related to the effects of the fluid properties. An increase in entry pressure would result in the accumulation and unpredictable redistribution of moisture until pores large-enough to accommodate flow were encountered by the fluid. Given the differences in plume behavior between the two experiments, a complex interplay between initial conditions, fluid properties, and heterogeneity appear to control the subsurface behavior of the plume. Owing to the similarity in initial conditions and the fact that the two experiments were conducted in the same domain, fluid properties may be the main contributor to the observed differences. Experimental confirmation of these effects would be very difficult in the field given that there was a 20-yr difference between the last set of experiments and the injection tests in FY 2000. However, these effects could be easily investigated with a numerical model based on a conceptual model incorporating the required mechanisms.

To this end, the Subsurface Transport Over Multiple Phases (STOMP) simulator was updated to incorporate the effects of fluid properties (i.e., density, viscosity, surface tension, vapor-pressure lowering) on the subsurface transport of hypersaline fluids (White and Ward 2001). Figure 2.16 shows the nonlinear dependence of the predicted mass fraction of aqueous sodium thiosulfate ($Na_2S_2O_3$) on temperature.

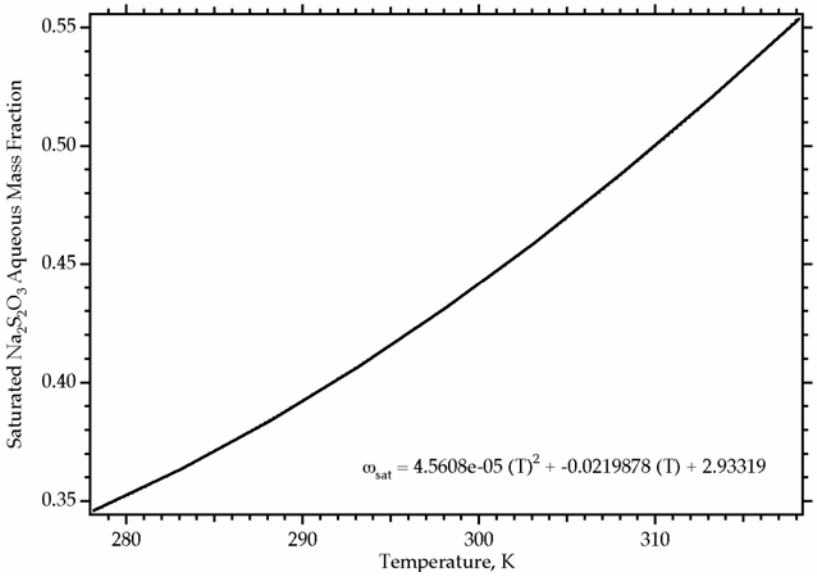

Figure 2.16. Mass Fraction as a Function of Temperature for an Aqueous Sodium Thiosulfate ($Na_2S_2O_3$) Solution

Figure 2.17 compares the predicted saturated aqueous vapor pressure of $Na_2S_2O_3$ as a function of temperature with that of pure water. The variation in vapor pressure is nonlinear with significant lowering, relative to water, even at 298 K. The measured density of $Na_2S_2O_3$ is a linear function of both temperature and molarity, but the dependence on aqueous mass fraction exhibits a nonlinear relationship (Figure 2.18). The measured viscosity shows an even stronger nonlinear relationship, and predicted values are comparable to within 5% of reported values. It is well known that surfactants lower the surface tension of water. This is caused by their attraction for surface water molecules at forces exceeding the weak bulk water hydrogen bonding. At low concentration (< 1 mM) of chaotropic ions (e.g., Cl^-), the surface tension drops with increasing concentration. Higher concentrations of such salts (e.g., KCl) disproportionately increase the bulk fluid salt concentration, thereby increasing the attractive forces on the surface water molecules and increasing the surface tension. Kosmotropic ions (Na^+) tend to remain fully hydrated in the bulk solution, thereby increasing surface tension by the latter mechanism at all concentrations. Thus, the surface tension of hypersaline wastes should be expected to increase with concentration, and this is illustrated in Figure 2.19.

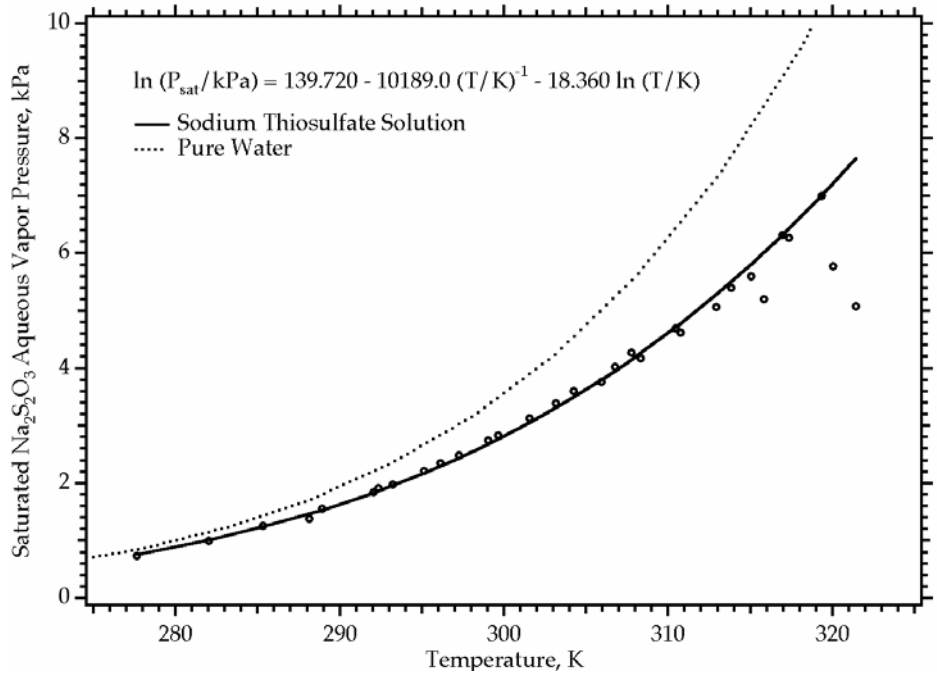

Figure 2.17. Saturated Aqueous Vapor Pressure of Sodium Thiosulfate ($Na_2S_2O_3$) as a Function of Temperature

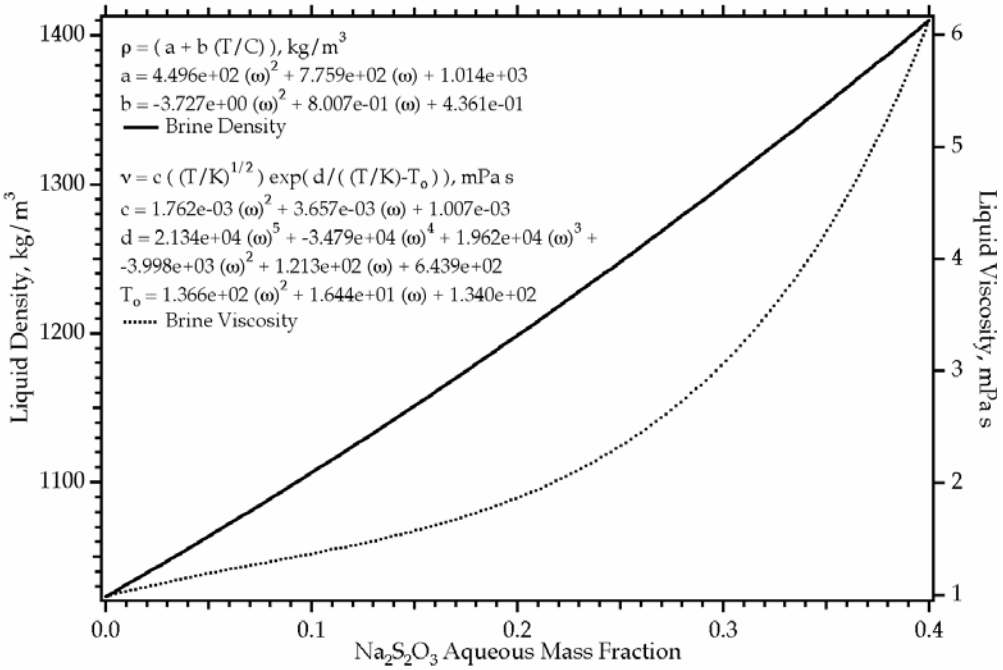

Figure 2.18. Predicted Liquid Density and Viscosity as Functions of Aqueous Sodium Thiosulfate ($Na_2S_2O_3$) Mass Fraction

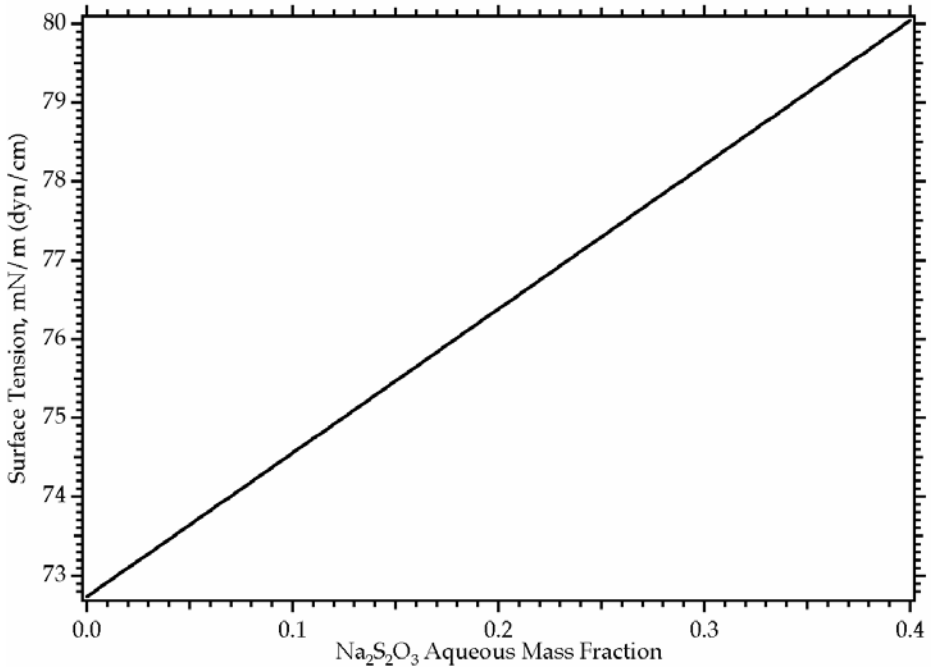

Figure 2.19. Predicted Surface Tension as Function of Aqueous Sodium Thiosulfate ($Na_2S_2O_3$) Mass Fraction

A series of 3-D, multifluid (i.e., aqueous and gas phases) numerical simulations were conducted that systematically considered the effects of elevated density, viscosity, surface tension, and reduced vapor pressure of $Na_2S_2O_3$ on vadose-zone transport. Four different simulations were performed in which different conservation equations were solved. In the base case, only the water mass conservation equations were solved for the migration of a water plume with water density being the only property allowed to vary. In one set of brine simulations, the water mass and salt mass conservation equations were solved. Brine properties, namely density, viscosity, and surface tension, were allowed to vary. In another brine simulation, the water mass, air mass, and salt mass conservation equations were solved with variable brine density, viscosity, surface tension, and vapor pressure lowering. In the final set of simulations, only the conservation equations for water mass and salt mass were solved, and brine properties considered included density and surface tension. In all simulations, soil-moisture characteristics were described by the Brooks-Corey model (Brooks and Corey 1964) whereas relative permeability was described by the Mualem conductivity function. Hydrologic properties were determined from cores collected at the field site and calibrated using river-water injection experiments. Isothermal conditions were assumed for the simulations; however, the effects of salt concentration on water vapor migration were considered. Simulated distributions of water, thiosulfate, and chloride ions (injected as sodium chloride at 0.5% concentration as a tracer with $Na_2S_2O_3$) are compared against field distributions of water, determined by neutron probe, and ion concentrations, determined from the analysis of soil cores.

Simulation results show that surface-tension elevation and vapor-pressure lowering moved soil moisture toward the brine plume. Brine fingering occurred vertically and horizontally into finer textured sediments (Figure 2.20). Water vapor transport from the sediment antecedent moisture into the infiltrating brine was evident and resulted in increased lateral transport relative to simulations with pure

water. However, simulations did not predict the extent of lateral movement of the brine plume observed in the field. In general, simulations with density, viscosity, surface tension, and vapor-pressure lowering effects showed good agreement with experimentally determined first (Figure 2.21) and second (Figure 2.22) moments for vertical movement but less so for transverse horizontal and longitudinal movement. The absence of the erratic behavior may be caused by an inadequate representation of heterogeneity.

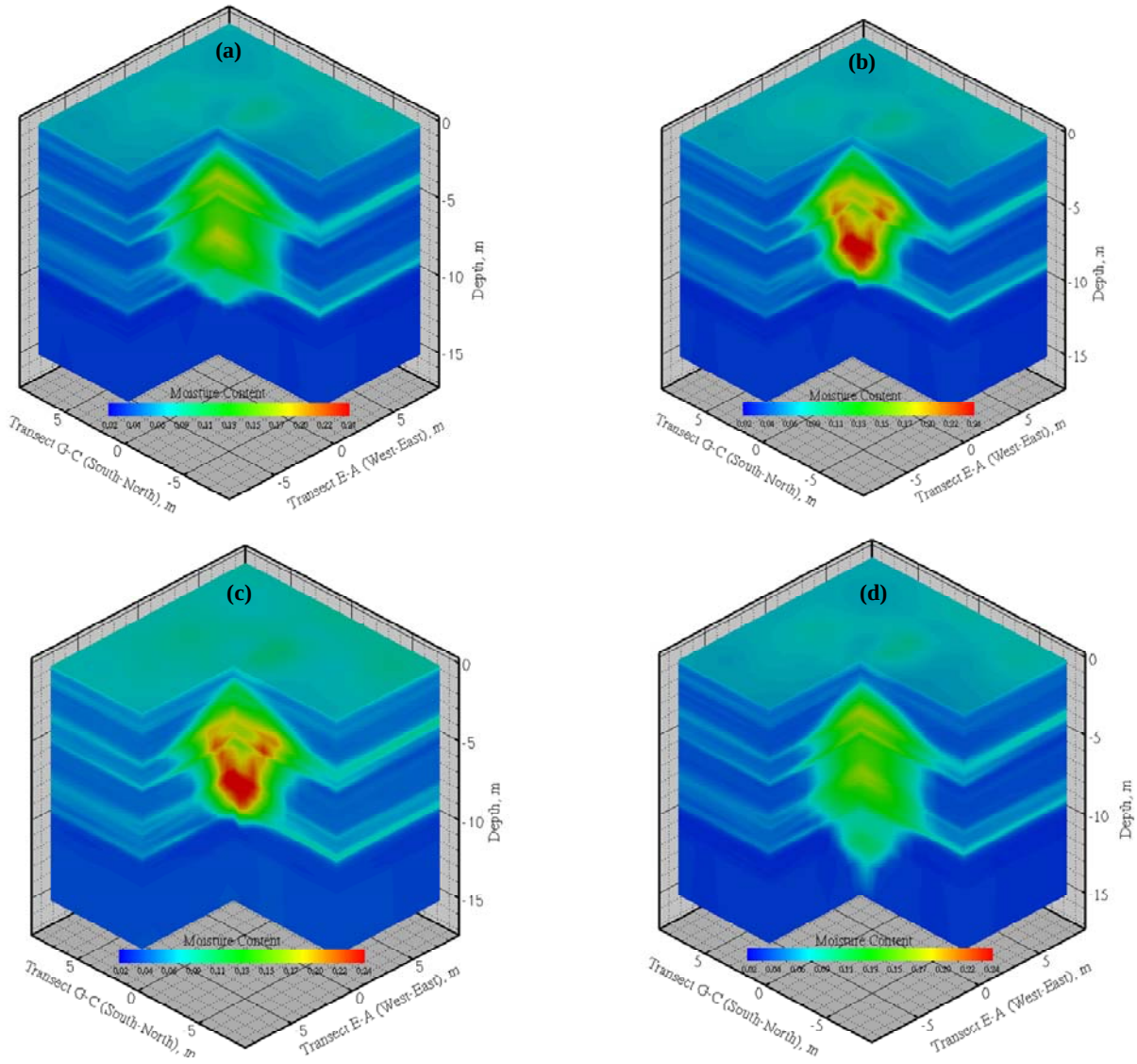

Figure 2.20. Predicted Moisture Content Distributions after 1020 hrs Resulting from the Injection of Water and Sodium Thiosulfate Brine: (a) Water, (b) Water and Salt Mass Equations Density, Viscosity, and Surface Tension Effects, (c) Water, Air, and Salt Mass Equations with Density, Viscosity, Surface Tension, and Vapor Pressure Effects, and (d) Water and Salt Mass Equations with Density and Surface Tension Effects

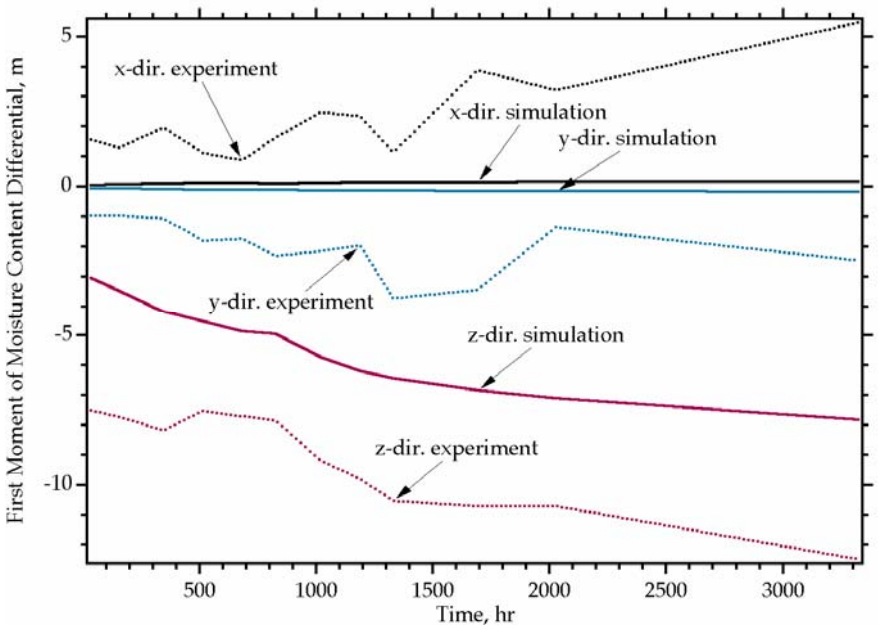

Figure 2.21. First Moment of Predicted Sodium Thiosulfate Plume Simulated Using the Water, Air, and Salt Mass Conservation Equations with Density, Viscosity, Surface Tension, and Vapor Pressure Effects

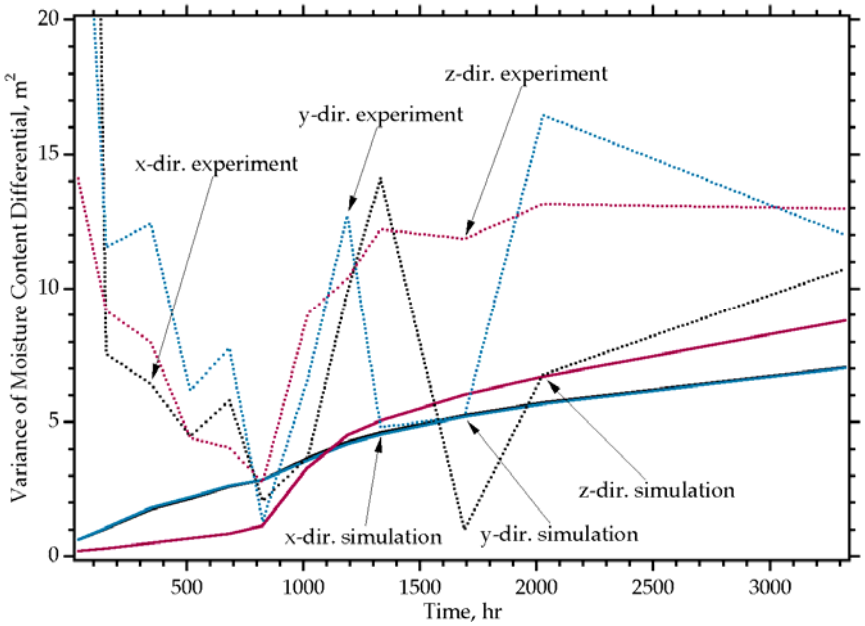

Figure 2.22. Second Moment of Predicted Sodium Thiosulfate Plume Simulated using the Water, Air, and Salt Mass Conservation Equations with Density, Viscosity, Surface Tension, and Vapor Pressure Effects

2.3.2 Synopsis and Implications

The synopsis of findings for the subsurface leak simulation tests and their implications are as follows:

- A set of experiments was designed to gain an understanding of the relative contributions of heterogeneities and fluid properties on subsurface transport
- A spatial moment analysis of water content shows a deviation between the injected and recovered water mass at the 299-E24-111 test site that was attributed to water leaving the monitoring domain via laminated fine-textured layers. This was enhanced in the brine injections.

Brine fingering occurred vertically and horizontally into finer textured soils at the 299-E24-111 test site. Simulations of the field injection experiments did not predict the extent of lateral movement of the plume.

- Simulation results suggest that osmotic potential and vapor pressure lowering should be taken into account when predicting the transport of hypersaline solutions through the vadose zone.

2.4 Pedotransfer Functions to Quantify Variable Hydraulic Properties

Analyzing subsurface flows in complex formations typically involves evaluating soil water infiltration and redistribution and the effects of heterogeneity of flow behavior. Ideally, simulating fluid flow in these systems requires discretization of the domain at the support scale of the input parameters and the assignment of hydraulic properties to each grid cell. These properties include the relative permeability-capillary pressure-saturation relationships, all of which are quite variable and typically depend on soil characteristics such as texture and structure. The sampling and characterization of subsurface stratigraphic units in coarse unconsolidated fluvial formations like those shown in Figure 1.1 are difficult because of the large grain size, the multi-scale nature of the sedimentary structures, and the fact that traditional vadose zone characterization methods provide, at best, spatially integrated parameter estimates. As a result, measuring the required hydraulic properties is costly, difficult, and often impractical. Often the only recourse to model parameterization is to estimate parameter values based on the generalities of existing characterization data.

Because hydraulic properties are affected by other sediment granulometric and physical properties, such as particle size distribution, texture, bulk density, and organic matter content, it may be possible to develop empirical relationships to predict the required properties. Bouma and van Lanen (1987) introduced the term pedotransfer function (PTF) in the broad context of relating different land characteristics and soil properties to one another. Studies over the last two decades have shown that statistical correlations between easily measured properties like soil texture, bulk density, and organic matter can be used to provide estimates of the required parameters that are sufficiently accurate to assess flow and transport behavior. The definition has since been narrowed, in the context of soil hydraulic properties, to mean predictive functions having as arguments basic soil data (e.g., particle-size distribution, bulk density, and organic matter content) that yield the water retention and hydraulic conductivity functions, including saturated hydraulic conductivity (Tietje and Tapkenhinrichs 1993).

These relationships have led to the development of rapid, inexpensive techniques to estimate hydraulic and transport properties using PTFs based on correlations between hydraulic parameters and easily measurable or readily available basic sediment properties (Rawls and Brackensiek 1982; Wösten et al. 2001; Pachepsky et al. 1999; Romano and Palladino 2002). However, these studies have focused largely on agricultural soils, most of which have been homogenized by cultivation over the last several

decades. In relation to waste management and environmental remediation, interpretation of the large data sets on sediment characteristics for use in hydrologic analyses is not always readily apparent. Often at these sites, the information is quite limited and may not include data that are routinely collected in agricultural surveys. At Hanford, for example, the ROCSAN database contains over 40,000 particle-size distribution curves, but no information on organic matter content or volumetric properties like density, porosity needed to apply existing PTFs. Even if these data were available, many of the sediments are now saline because of waste releases; many contain large gravel fractions and have undergone some degree of compaction.

Grain size (texture) is a basic physical characteristic of soils and sediments, and its detailed study often yields information about the physical mechanisms that occurred during transport, deposition, and digenesis. Because various sized particles have different physical and chemical characteristics, the properties of different mineral soils are strongly influenced by the particular fraction that is present in the larger amount. It is mostly because of this dependence that grain size distributions have been widely used to estimate hydraulic and geochemical properties. The objective of this study was to investigate classes of site-specific PTFs, based on grain size distribution properties, that could be applied across the relatively wide range of sediment types commonly encountered at Hanford for predicting hydraulic properties for flow and transport simulations. The properties of interest for parameterizing flow simulations include porosity or saturated water content, bulk density, saturated hydraulic conductivity, bubbling pressure, pore size distribution index, and the residual water content, whereas dispersivity is required for transport simulations. To determine the feasibility of PTFs based on such an approach, existing databases containing both grain size distribution data and hydraulic properties were analyzed for possible relationships. Rawls and Brackensiek (1982) summarized the hydraulic properties of 5371 samples representing all of the major soil textural classes in the U.S. Department of Agriculture (USDA) classification system.

2.4.1 Results

Table 2.1 summarizes the mean Brooks and Corey (1964) parameters for water retention and saturated hydraulic conductivity for 11 textural classes from the United States and represents 1323 soils with approximately 5350 horizons compiled from data of nearly 400 soil scientists (Rawls and Brackensiek 1982). Figure 2.23 shows the range of soil textures included in the Rosetta database (Schaap and Bouten 1996). The range of textures is reasonably wide compared to Hanford sediments that are dominated by sand and gravelly sand. The sand content ranged from 46.3 to 99.9%; silt ranged from 0 to 50.9%, whereas clay ranged from 0 to 10.7%. The silt fraction (0.002 to 0.053 mm) showed the highest variation with a mean value of 3.78 to 7.5%.

Parameters for each texture include porosity (equal to saturated water content, θ_s); residual water content, θ_r; air entry (bubbling) pressure, ψ_b; pore size distribution index, λ; water retained at -33 kPa (θ_{33}) and -1500 kPa (θ_{1500}); and the saturated hydraulic conductivity, K_s. Texture information was used to calculate grain size distribution statistics, namely the geometric mean grain diameter, d_g, and the geometric standard deviation, σ_g, according to the method of Campbell (1974). This method determines the contribution of each of the textural fractions of sand, silt, and clay after calculating the equivalent diameters of each fraction. The geometric mean diameter was then calculated as

$$d_g = \exp(a) \tag{2.6}$$

Table 2.1. Summary Soil Texture, Water Retention, and Hydraulic Conductivity for Major Soil Textural Classes

Soil Type	Sample Size	Sand (%)	Silt (%)	Clay (%)	θ_s ($cm^3\ cm^{-3}$)	θ_r ($cm^3\ cm^{-3}$)	ψ_b (kPa)	λ (-)	θ -33 kPa ($cm^3\ cm^{-3}$)	θ -1500 kPa ($cm^3\ cm^{-3}$)	K_s ($cm\ hr^{-1}$)
Sand	762	92.70	4.40	2.90	0.437	0.020	0.726	0.592	0.091	0.033	21
Loamy sand	338	80.90	12.70	6.40	0.437	0.035	0.869	0.474	0.125	0.055	6.11
Sandy Loam	666	63.40	25.50	11.10	0.453	0.041	1.466	0.322	0.207	0.095	2.59
Loam	383	40.00	40.30	19.70	0.463	0.027	1.115	0.220	0.270	0.117	1.32
Silt Loam	1206	16.60	64.90	18.50	0.501	0.015	2.076	0.211	0.330	0.133	0.68
Sandy Clay Loam	498	54.30	18.30	27.40	0.398	0.068	2.808	0.250	0.255	0.148	0.43
Clay Loam	366	29.80	37.60	32.60	0.464	0.075	2.589	0.194	0.318	0.197	0.23
Silty Clay Loam	689	7.60	59.20	33.20	0.471	0.040	3.256	0.151	0.366	0.208	0.15
Sandy Clay	45	47.50	11.50	41.00	0.430	0.109	2.917	0.168	0.339	0.239	0.12
Silty Clay	127	6.10	47.60	46.30	0.479	0.056	3.419	0.127	0.387	0.250	0.09
Clay	291	14.90	29.90	55.20	0.475	0.090	3.730	0.131	0.396	0.272	0.06

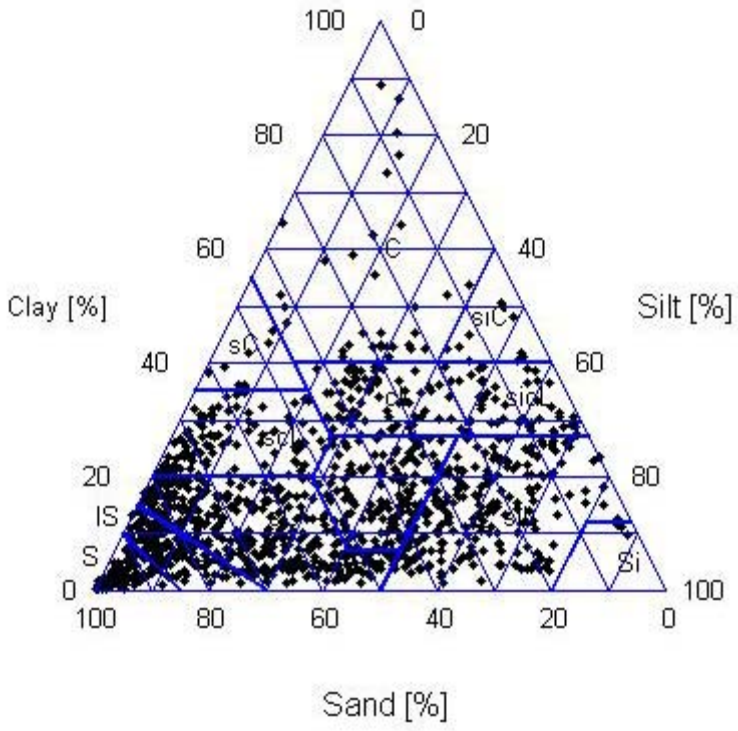

Figure 2.23. Textural Composition of the Rosetta Database

where a is derived from the summation of contribution of d_i over the three classes:

$$a = \sum_i m_i \ln(d_i) \tag{2.7}$$

and m_i is the mass fraction of particle i, and d_i is the arithmetic mean diameter of class i. Here, the equivalent diameter for each class is equal to 0.001 mm for clay, 0.026 mm for silt, and 1.025 mm for sand. The geometric standard deviation was calculated as

$$\sigma_g = \exp(b) \tag{2.8}$$

where

$$b = \left\{ \sum_i m_i \left[\ln(d_i)\right]^2 - a^2 \right\}^{0.5} \tag{2.9}$$

When the entire grain size distribution curve is available, d_g and s_g are calculated from the fitted size distribution.

Fundamental hydraulic and transport properties depend on both d_g and σ_g, which are collinear, and as a result, spatial interpolation could prove difficult. To overcome this potential problem, we introduce the

fredle index. The fredle index is the geometric mean adjusted for distribution of sediment particle sizes and has the same length units as d_g. It is calculated as (Lotspeich and Everest 1981)

$$F_i = \frac{d_g}{\sigma_g} \tag{2.10}$$

When the geometric means of different sediments are similar, a high fredle index indicates a sediment consisting largely of particle sizes near the mean value d_g whereas a low fredle index indicates more evenly distributed particle sizes. The fredle index has been used extensively in studies of salmon habitat and is known to be positively correlated with the substrate permeability to water and hence to dissolved oxygen transport within the sediment. It has also been shown to be positively correlated with the emergence of salmonid alevins (Lotspeich and Everest 1981).

Figure 2.24 shows a plot of air entry pressure as a function of texture and grain size statistics. The air entry pressure is the pressure at which a saturated soil starts to drain under applied pressure. The largest pores start to empty first with increasingly smaller pores emptying as the pressure becomes more negative. Thus, ψ_b can be expected to decrease with increasing sand content as the portion of large pores would increase (Figure 2.24a). Air-entry pressure increased with the increasing silt (Figure 2.24b) and clay content (Figure 2.24c). Although these data show relationships between texture and ψ_b, they are not strong enough for predictive purposes and are complicated by the cross correlation between the different size fractions. As the median grain diameter increases, the median pore size increases, and the pressure required to initiate drainage would decrease. Such a relationship between ψ_b and the median diameter, d_g, is evident in Figure 2.24d. Conversely, as the sediment becomes less well sorted (σ_g increases), large pores are filled by smaller particles, causing a reduction in mean pore size and an increase in ψ_b (Figure 2.24e). Figure 2.24f shows that ψ_b is negatively correlated to the fredle index. This relationship is physically consistent, capturing the combined effects of d_g and σ_g. A high fredle index is indicative of a particle size distribution with particle sizes near d_g (i.e., well sorted or poorly graded) whereas a low fredle index indicates more evenly distributed sediment sizes (i.e., poorly sorted or well graded). Thus, ψ_b would be expected to decrease as F_i increases. Predicting the complete water-retention function also requires a method to independently estimate the slope of the $\theta(\psi)$ curve. This slope can be estimated from the water retained at -33 kPa and -1500 kPa.

Figure 2.25 shows a plot of the water retained at -33 kPa whereas Figure 2.26 shows a similar plot for the water retained at -1500 kPa. Although the water retained shows some dependence on sand (Figure 2.27a, Figure 2.26a), silt (Figure 2.27b, Figure 2.26b); and clay (Figure 2.27c, Figure 2.26c) content, the predictive ability is limited in soils with high silt content like Hanford sediments. The relationship between water retained and median diameter (Figure 2.27d, Figure 2.26d) is a significant improvement over those predicted from textural fractions. As can be expected, the water retained decreases as d_g increases, which is consistent with the experimental observations that increasing coarseness leads to lower water retention at a given pressure in well sorted sediments. However, as a sediment becomes less well sorted, the σ_g increases to produce a better gradation of particle sizes and a wide range of pore sizes. The net effect is an increase in the amount of water retained at a given pressure, and this can be seen in Figure 2.27e and Figure 2.26e.

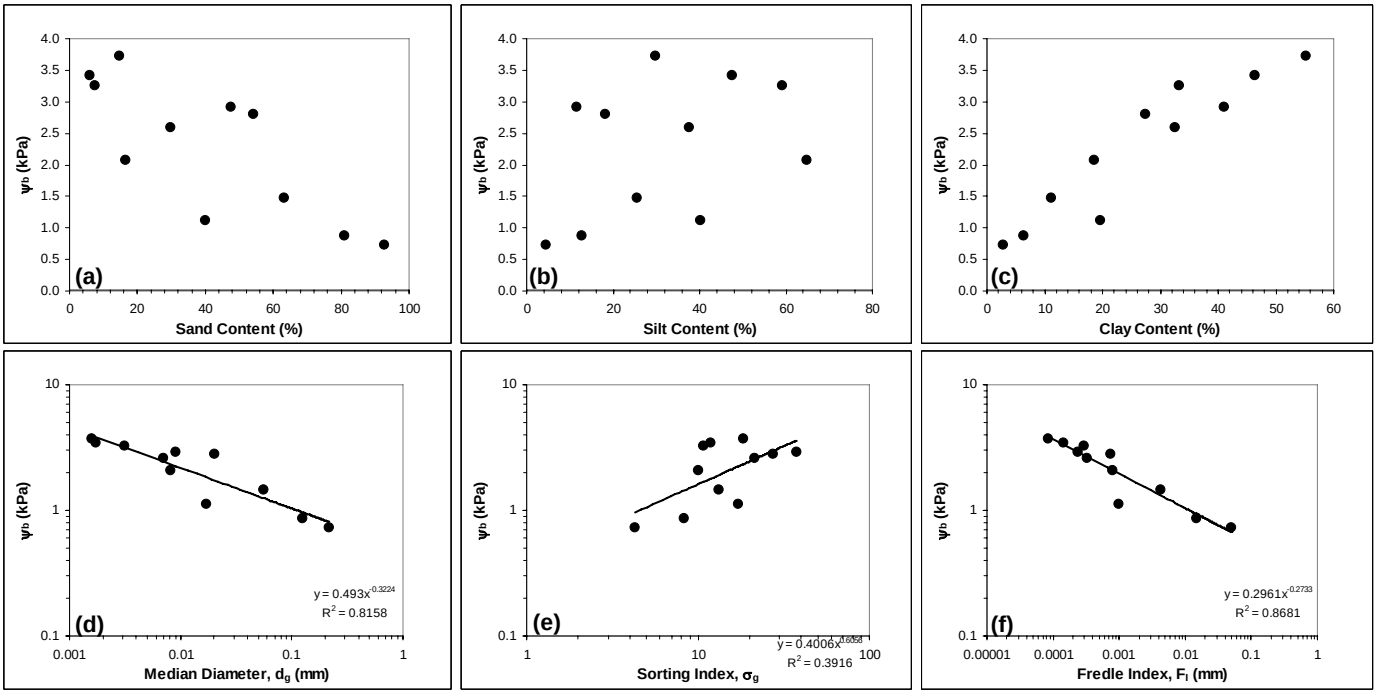

Figure 2.24. Dependence of Air-entry Pressure on Soil Texture and Size Distribution Statistics, (a) Sand Content, (b) Silt Content, (c) Clay Content, (e) Median Particle Diameter, (e) Sorting Index, and (f) Fredle Index

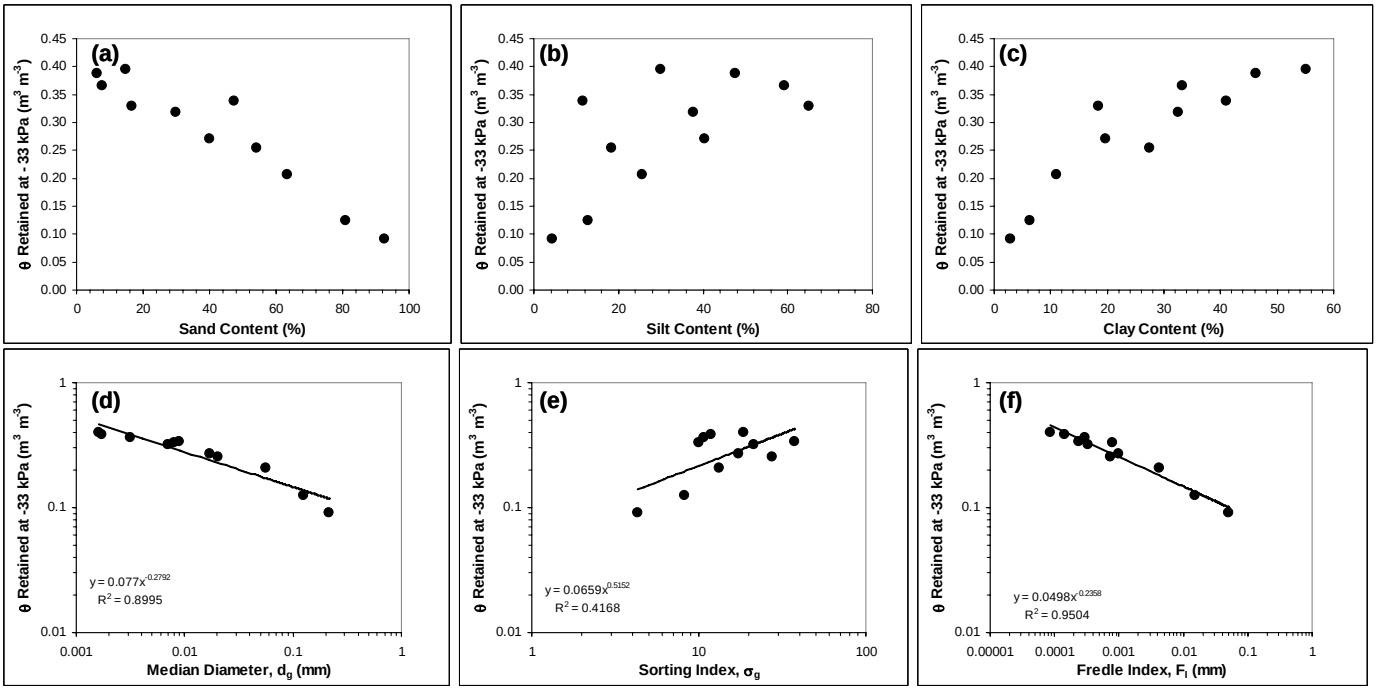

Figure 2.25. Dependence of Water Retained at -33 kPa on Soil Texture and Size Distribution Statistics, (a) Sand Content, (b) Silt Content, (c) Clay Content, (e) Median Particle Diameter, (e) Sorting Index, and (f) Fredle Index

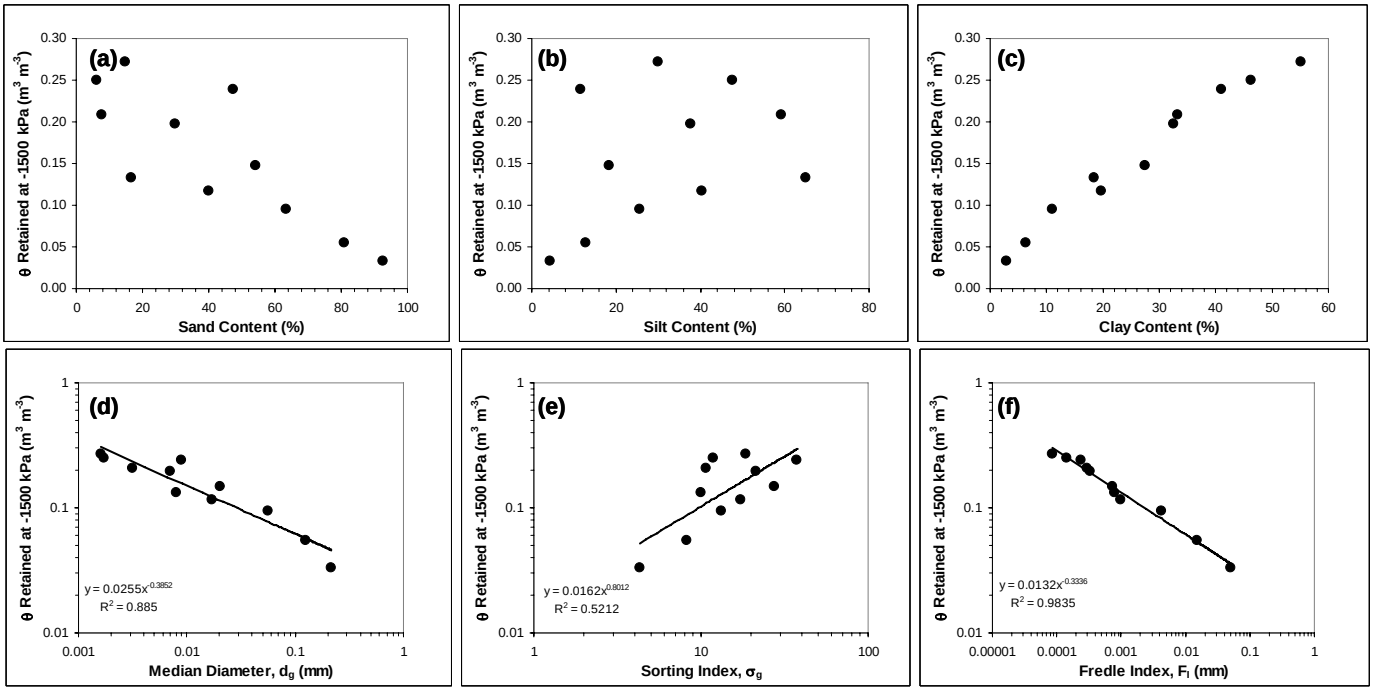

Figure 2.26. Dependence of Water Retained at -1500 kPa on Soil Texture and Size Distribution Statistics, (a) Sand Content, (b) Silt Content, (c) Clay Content, (e) Median Particle Diameter, (e) Sorting Index, and (f) Fredle Index

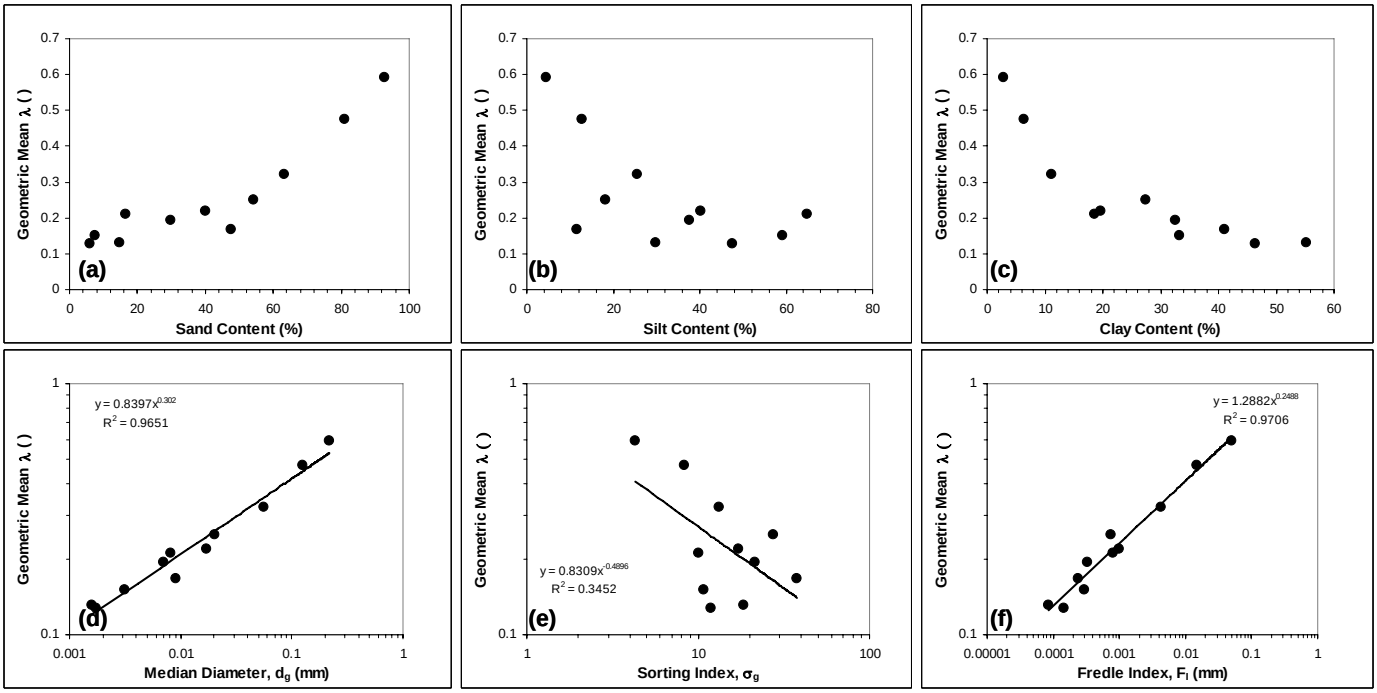

Figure 2.27. Dependence of Pore-size Distribution Index on Soil Texture and Size Distribution Statistics, (a) Sand Content, (b) Silt Content, (c) Clay Content, (e) Median Particle Diameter, (e) Sorting Index, and (f) Fredle Index

Both plots show an inverse relation between the amount of water retained and the fredle index. An increasing fredle index is indicative of sediment whose size distribution is approaching the median diameter or better sorted, which would lead to a narrowing of the pore size range and a decrease in water retained. Thus, the result is physically consistent with the expected behavior for both θ_{33} and θ_{1500}. The relationship between water retained and the fredle index is shown for θ_{33} and θ_{1500} in Figure 2.25f and Figure 2.26f. Not only is the water retained at θ_{33} larger than θ_{1500} at a given value of F_i, but comparing Figure 2.25f and Figure 2.26f and the fitted functions shows that the slope of the θ_{1500}-F_i is larger than that of the θ_{33}–F_i relationship. Although it is clear from these data that the shape and range of the soil-moisture characteristic curve is controlled by texture, the structure also plays an important role. At low (ψ < -33 kPa) and intermediate (-33 kPa < ψ < -100 kPa) pressures, water retention is controlled by capillary effects and the pore-size distribution and hence is strongly affected by soil structure. At the higher pressures, water retention is influenced less by structure and more by texture and the rate of decrease in the water retained increases as the sediment becomes less well sorted.

Several functions have been proposed for describing the dependence of soil water content on the matric potential. One form of the water-retention relationship that can take advantage of these parameters is written as

$$\frac{\theta-\theta_r}{\theta_s-\theta_r}=\left(\frac{\psi_b}{\psi}\right)^{2+L+\frac{2}{\lambda}};\qquad \psi\geq\psi_b \tag{2.10}$$

In the Campbell (1974) form of this equation, $\theta_r = 0$, whereas in the Brooks and Corey (1964) form, $\theta_r > 0$. Typical values of *L* are 1.0 (Burdine 1953); -2.0 (Miller and Miller 1956), and 0.5 (Mualem 1976). The slope of the water retention function is the pore size distribution index, λ, which can be estimated from the 33 and 1500 kPa moisture values as

$$\lambda=\frac{\ln(\theta_{33})-\ln(\theta_{1500})}{\ln(33)-\ln(1500)} \tag{2.11}$$

Figure 2.27 shows the relationship between the pore size distribution index, texture, and grain size statistics. The geometric mean λ increased with increasing sand content (Figure 2.27a) and decreased with silt (Figure 2.27b) and clay (Figure 2.27c) content. Again, the collinear relationships among the textural fractions would complicate predictions based on these fractions, especially in soils with low clay content. The dependence on size statistics shows much stronger relationships, increasing with d_g (Figure 2.27e), decreasing with σ_g (Figure 2.27e), and increasing with F_i (Figure 2.27f). The λ parameter is needed to predict $\psi(\theta)$, as shown in Equation 2.10, and the hydraulic conductivity, $K(\theta)$. There are several equations for predicting $K(\theta)$, but one form that is complementary to the form of $\psi(\theta)$ in Equation 2.10 may be written as

$$\frac{K(\theta)}{K_s}=\left(\frac{\theta-\theta_r}{\theta_s-\theta_r}\right)^{\left(2+L+\frac{2}{\lambda}\right)} \tag{2.12}$$

As in the $\psi(\theta)$ equation, $\theta_r = 0$ in the Campbell (1974) formulation whereas in the Brooks and Corey (1964) formulation, $\theta_r > 0$. Values of θ_r are often inferred from θ_{1500}, and typical values of L can be 1.0 (Burdine 1953), -2.0 (Miller and Miller 1956), or 0.5 (Mualem 1976). Estimating $K(\theta)$, therefore, requires knowledge of K_s and λ.

Figure 2.28 shows the relationship between the saturated hydraulic conductivity, K_s, texture, and grain-size statistics. The geometric mean K_s also increased with sand content, increased with increasing sand content (Figure 2.28a), and decreased with silt (Figure 2.28b) and clay (Figure 2.28c) content. These trends are consistent with experimental observations. As in the previous relationships with grain size statistics, K_s shows a much stronger dependence on d_g (Figure 2.28e), increasing as d_g increased and decreasing as σ_g increased (Figure 2.28f). These effects are consistent with theoretical and experimental studies of particle packing and the resulting effects on hydraulic conductivity. Increasing d_g at a given σ_g results in larger pore sizes, but increasing σ_g causes the infilling of large pores, resulting in a reduction in hydraulic conductivity. A low F_i is indicative of a poorly sorted sediment, and K_s is relatively small (Figure 2.28f). As the sediment becomes better sorted, F_i increases and so does K_s. Thus, it should be now possible to predict $K(\theta)$ for any sediment whose grain-size distribution or size distribution statistics are known.

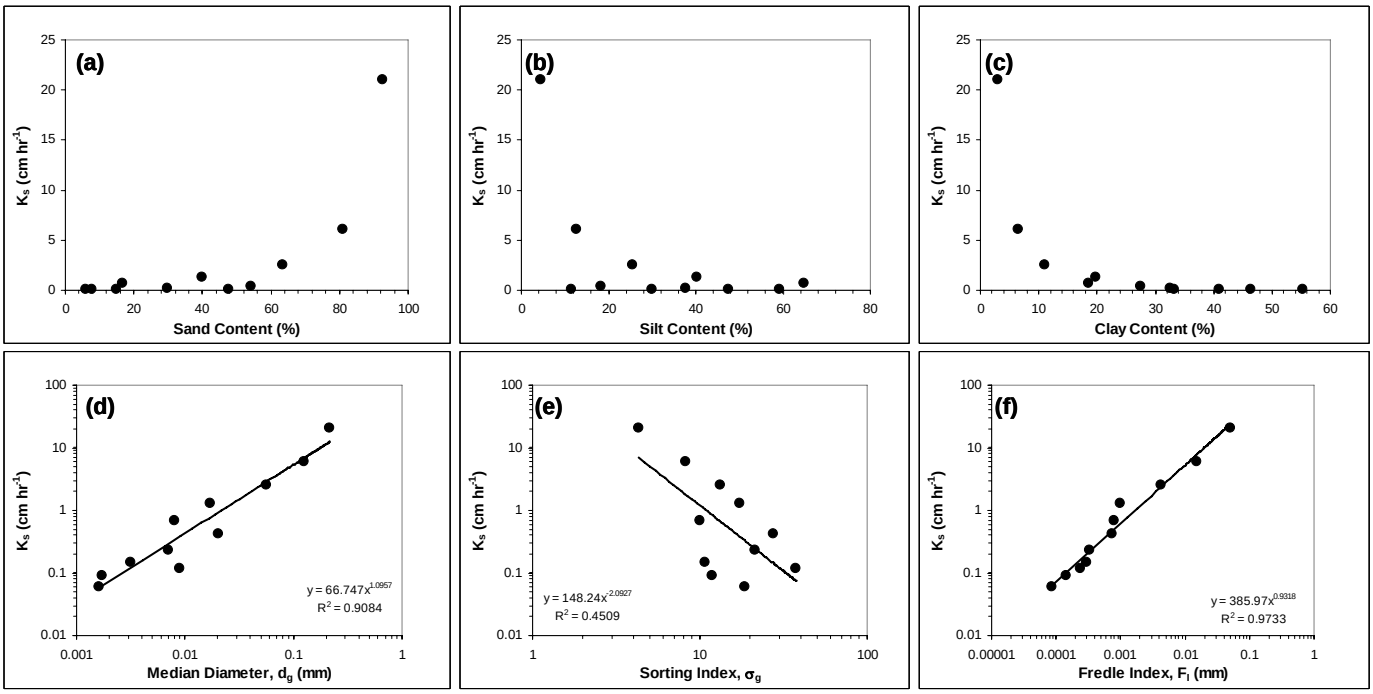

Figure 2.28. Dependence of Saturated Hydraulic Conductivity on Soil Texture and Size Distribution Statistics, (a) Sand Content, (b) Silt Content, (c) Clay Content, (e) Median Particle Diameter, (e) Sorting Index, and (f) Fredle Index

2.4.2 Synopsis and Implications

The synopsis of findings for this study of physically based pedotransfer functions and their implications are as follows:

- Studies over the last two decades have demonstrated the existence of statistical correlations between easily measured properties like soil texture, bulk density, and organic matter and hydraulic properties.

- Predictive tools like PTFs developed from national databases may have limited utility for site-specific Hanford problems because of the narrow range of size distributions of existing samples and the large fraction of > 2-mm sediments (i.e., gravel).

- Estimates of hydraulic parameters can be derived from particle size distribution statistics that are based on the entire distribution curve. The resulting functions are mostly log-log linear with high coefficients of determination and may be summarized as follows:

  Air-entry pressure: $\psi_b = 0.2961 F_i^{-0.2733}$; $R^2 = 0.8681$

  Water content retained at -33 kPa: $\theta_{33} = 0.0498 F_i^{-0.2358}$; $R^2 = 0.9504$

  Water content retained at -1500 kPa: $\theta_{1500} = 0.0132 F_i^{-0.3336}$; $R^2 = 0.9835$

  Saturated hydraulic conductivity: $K_s = 385.97 F_i^{0.9318}$; $R^2 = 0.9733$

  These relationships may not adequately account for the effects of pedogenesis. Porosity loss through compaction can also affect the relationships among texture, particle size statistics, and hydraulic properties.

- Cementation can also alter the effect of texture or size statistics, and bulk density is perhaps the second most important factor affecting hydraulic properties after texture. Adjustments to existing PTFs may therefore be needed for below- and above-average bulk densities.

- The strong correlation between water retained at -33 kPa and -1500 kPa suggests that antecedent moisture in a drained profile is controlled mostly by texture. Thus, high-resolution measurements of antecedent moisture using borehole logs may provide insight into the effects of small-scale textural changes on subsurface flow and transport behavior.

2.5 Pedotransfer Functions to Quantify Variability in Sorption Parameters

Many solutes, including pesticides, plant nutrients, metals, and radioisotopes, are sorbed in natural soils and sediments. Heavy metals and radionuclides are of particular concern at Hanford and are strongly sorbed to the solid phase. Spatial variability makes it impractical to perform comprehensive tests on all contaminants of interest under relevant conditions. Mathematical simulation models have been developed to predict sorption and ion exchange behavior in soils and sediments. When coupled with adsorption indices (e.g., the organic carbon distribution coefficient, K_{oc} used for nonpolar organics; the distribution coefficient, K_d for metals and radionuclides), these models can be used to evaluate the

mobility of different contaminants in the wide range of soils that may exist at a given waste site (e.g. Figure 1.1). However, using these indices to represent transport through natural soils suffers from several limitations, including the use of batch equilibrium measurement techniques and the effects of spatial variability at the field scale. Although simple indices coupled with transport models have been successful in describing laboratory phenomena, laboratory values typically do not provide accurate predictions of field-scale transport behavior, especially under conditions where heterogeneities cause local-scale variations in sorption that cannot be represented with an average coefficient. These indices often vary greatly between contaminants and with aqueous- and solid-phase chemistry.

Mechanistic concepts were incorporated into transport models to provide more robust and scientifically defensible tools for transport predictions. However, field application of these models, especially in heterogeneous sediments, remains limited. In the context of these mechanistic models, heterogeneity refers to the variability in surface reactivity to which iron oxide minerals and coatings contribute greatly. These models typically require more input data, including the characterization of reactive surface areas and cation exchange capacity. A variety of approaches have been developed to represent the spatial distribution of sorption sites. However, many of these approaches are based on measurements on the < 2-mm soil fractions.

The objectives of this study were to 1) develop a robust approach for quantifying variability in sorption parameters, 2) determine the extent to which this approach may or may not be adequate to quantitatively characterize sorption under realistic field conditions, and 3) determine the degree to which laboratory-scale correlations remain valid at the field scale. The proposed concept is based on using PTFs. Predicting hydraulic and transport properties using PTFs based on basic physical and chemical properties is a relatively well established procedure. Assessing reactive properties using PTFs, in contrast, is less well developed. PTFs have been used to predict the buffering functions from basic soil properties, the spatially variable distribution coefficient K_d, and phosphate adsorption-desorption curves. We propose a PTF based on grain size statistics. PTFs based on grain size distribution statistics provide the means for bridging the gap between sediment properties and sorption properties. They also represent an excellent tool for handling multi-scale phenomena affected by packing geometry. However, a more fundamental and systematic study was needed to account for the effects of the whole soil and packing in multi-component systems so as to relate the size distribution statistics of whole soils to measurable properties.

To test the feasibility of such an approach, we used published data and measurements made as part of the field transport studies to investigate relationships between size statistics and indices of sorption. The concept is illustrated using a dataset published by Banin and Amiel (1969). This dataset was chosen because all of the parameters were measured directly rather than determined from modeling or inversion procedures. Banin and Amiel (1969) reported data on the chemical and physical properties, i.e., cation exchange capacity, organic matter content, $CaCO_3$ content, clay, silt, and sand percentages, hydrogroscopic moisture content, and moisture content at -1500kPa and at -33kPa as well as saturated paste states and specific surface area. The measurements were made on a total of 33 soils.

Texture information was used to calculate grain size distribution statistics, namely the geometric mean grain diameter, d_g, and the geometric standard deviation, σ_g, according to the method of Campbell (1974). This method determines the contribution of each of the textural fractions of sand, silt, and clay after calculating the equivalent diameters of each fraction. The geometric mean diameter, d_g, and

standard deviation, σ_g, can then be calculated as described previously using Equations (2.6) and (2.8), respectively. Fundamental hydraulic and transport properties depend on both d_g and σ_g, which are collinear, and as a result, spatial interpolation could prove difficult. Using both d_g and sorting index, σ_I, to predict sorption parameters is avoided by invoking the fredle index, F_i (Lotspeich and Everest 1981), but to the best of our knowledge, this index has never been used to characterize the geochemical properties of soils. It is calculated simply as the ratio of d_g to σ_g as shown previously in Equation (2.10). These statistics were used to explore relationships between sediment physical and geochemical properties related to sorption.

2.5.1 Results

Figure 2.29 shows a plot of specific surface area, $A_{s,}$, measured by the ethyleneglycol monoethly ether method as a function of textural composition. Figure 2.29a shows a highly significant correlation between surface areas with the surface area decreasing as the sand content increased. Figure 2.29c shows a similarly strong relationship between specific surface area and clay content, with the surface area increasing as the clay content increased. The absence of a significant relationship with silt content (Figure 2.29b) is quite noticeable but is inconsistent with studies on U.S. soils, particularly Hanford sediments. An analysis of over 60 soils from Hanford's 200 East Area collected as part of this study found that the silt content was the prime component for determining moisture holding capacity and saturated hydraulic conductivity. These findings are probably caused by the relatively small amount of clay and large amount of silt present in this group of soils compared to those studied by Banin and Amiel (1969), which were considerably higher in clay content. It should be noted that a statistical correlation between a pair of soil properties does not necessarily indicate which soil property is the dependent variable and which is the independent variable. This problem becomes even more complicated when correlations are based on specific size fractions rather than the whole soil. The specific surface area is controlled largely by the amount of clay, and indeed, a highly significant linear relationship is shown in (Figure 2.29c). In fact, these results could be used as the basis of PTFs for other soil scapes, provided the clay composition is similar and homogeneous. However, the co-linearity between sand and clay content and the large regions occupied by these fractions on the textural triangle could pose problems for spatial interpolation and prediction.

We proposed to use the size statistics as the basis of any relationship as they are theoretically more correct and perhaps more robust. This is because a PTF based on the size statistics considers the information content of the entire grain size distribution. Figure 2.29d shows a plot of specific surface area as a function of the geometric mean diameter d_g. The specific surface shows a very strong negative log-linear relationship with the geometric mean grain diameter, a parameter that accounts for the entire grain size distribution. This can be expected as the surface area is known to decrease with increasing grain size. In contrast, a specific surface area shows a positive log-linear relationship with the sorting coefficient (Figure 2.29e). Again, this is consistent with our current knowledge of specific surface area. As a coarse sediment becomes less well sorted, the large pores of the coarse sediment become filled with materials of a finer texture, resulting in a net increase in specific surface area. This information is lost in a PTF based simply on the content of specific fractions that ignore those that may not show strong correlations. To account fully for the co-linearity between d_g and σ_I, the specific surface area was plotted against the fredle index (Figure 2.29d). This relationship, which considers all of the information content of the grain size distribution, is clearly superior to one based on the analysis of a single size fraction. The relationship is log-linear with a coefficient of determination (R^2) of 0.896 compared to a value of 0.81 when regressed

on d_g alone and 0.796 when regressed on σ_I alone. This relationship suggests that if the grain size distribution or textural information is available, a reasonable estimate of specific surface area can be determined.

Figure 2.30 shows a similar analysis for the cation exchange capacity (CEC). These regressions also show a strong negative log-linear relationship between CEC and d_g (R^2=0.84), a positive correlation between CEC and σ_I (R^2=0.78), and a strong negative correlation between CEC and the fredle index (R^2=0.91). These relationships can be expected, given that both specific area and CEC are controlled by the fine-textured component. In fact, the regression of the specific area on CEC also shows a very strong linear relationship (R^2=0.87). As with the specific surface area, knowledge of the grain size distribution or textural information should permit estimation of reasonably accurate values of the CEC.

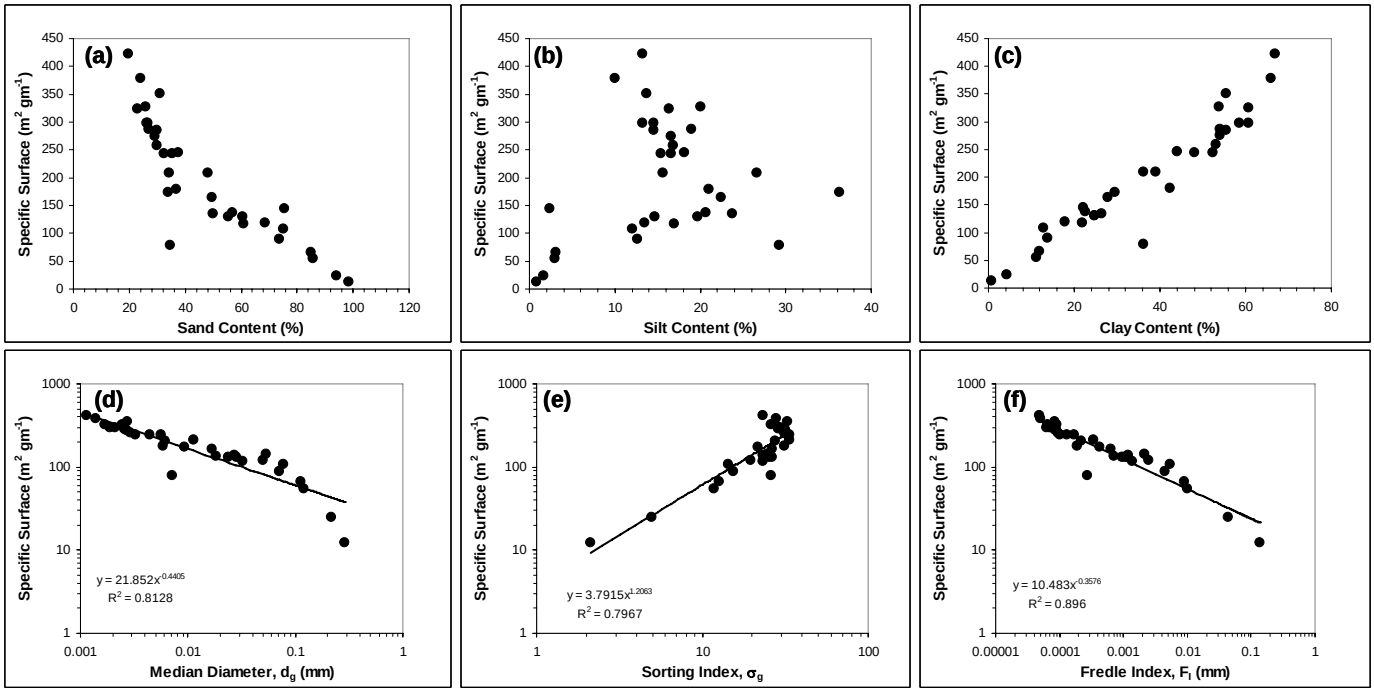

Figure 2.29. Dependence of Specific Surface Area on Soil Texture and Size Distribution Statistics, (a) Sand Content, (b) Silt Content, (c) Clay Content, (e) Median Particle Diameter, (e) Sorting Index, and (f) Fredle Index

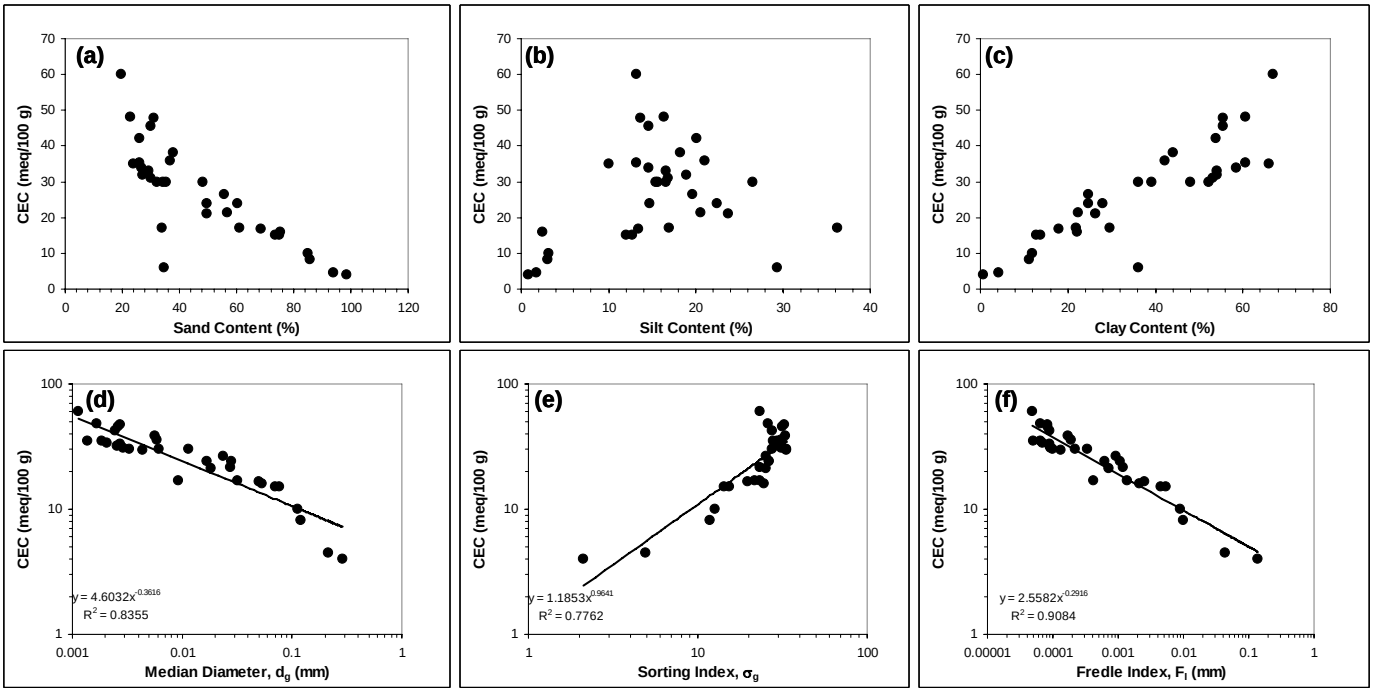

Figure 2.30. Dependence of Cation Exchange Capacity on Soil Texture and Size Distribution Statistics, (a) Sand Content, (b) Silt Content, (c) Clay Content, (e) Median Particle Diameter, (e) Sorting Index, and (f) Fredle Index

The relationships between existing mineralogy data and grain size statistics were also investigated. The calcite content is known to exert considerable influence on the chemical state of several chemical constituents of soils and sediments. The calcite content was regressed on all textural components and grain size statistics for the data set discussed above. Figure 2.31 shows a plot of $CaCO_3$ content as a function of silt content, which showed the strongest relationship. It appears that when $CaCO_3$ is present, it is mostly associated with the silt fraction. In most of the soils containing significant quantities of $CaCO_3$, the silt fraction is composed mostly of $CaCO_3$ with about 0.6% of the silt fraction being contributed by 1% of the $CaCO_3$. Similar observations have been made with Hanford sediments, which show a strong correlation between $CaCO_3$ and moisture content, perhaps because of the presence of silt. Nevertheless, data from the Hanford Site suggest that sediments from similar depositional environments may have similar mineralogy, even in the presence of large differences in grain size distributions (Murray et al. 2003). In an analysis of sediments obtained from a clastic dike at Hanford, the clay content ranged from < 1% in the sand matrix to a high of 23% in the dike. Yet, mineralogical composition of the clay fraction did not differ substantially from the coarse-textured matrix to the fine-textured dike. In all cases, smectite and illite were the minerals present in the greatest abundance. Thus, accounting for mineralogy may not be that important to the development of pedotransfer functions for reactive properties.

Most PTFs have been developed from site-specific databases, although recent developments have seen the derivation of PTFs based on national databases. While the concept of a general PTF rule appears promising, the validation of existing PTFs, although fundamental, is mostly lacking. This is particularly problematic when PTF predictions are used for input to predictive models used to evaluate remedial

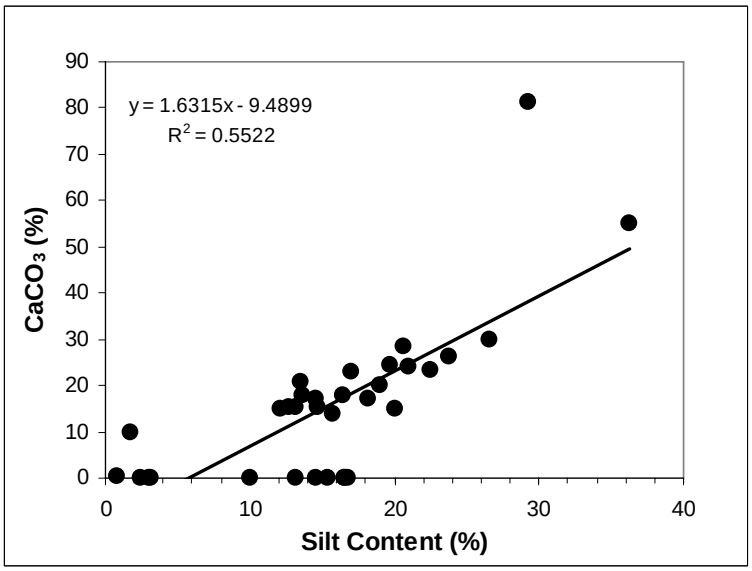

Figure 2.31. Dependence of $CaCO_3$ Content on Silt Content

options or risk assessment. The relationships between the cation exchange capacity, specific surface and size statistics, or the fredle index, which accounts for co-linearity in the mean and standard deviation, suggest that a PTF based on a size index would be very effective for predicting local-scale reactive transport parameters. The fact that these relationships are based on the size statistics means that they can be scaled up and down to handle any size class. We propose that PTFs based on grain size statistics are not only capable of describing the local-scale hydraulic properties and sorptive behavior, but would also allow more efficient description of the spatial distributions of the properties of interest. The concept of scaling across size classes is illustrated using data from Hanford.

Figure 2.32 shows plots of CEC for selected samples from the Army Loop Road site as functions of soil textural components. Figure 2.32a is a plot of CEC as a function of clay content. There is a reasonably good correlation up to about 10% clay, but the paucity of data above 10% may impose some limits on the quality of the fit. The nonlinear relationship observed in these data with a high standard error is inconsistent with other published reports. Banin and Amiel (1969) reported a linear relationship between CEC and clay with R^2 over 0.80. Petersen et al. (1996) also reported a linear relationship with a slightly lower R^2 of around 0.65. The discrepancy between our observations and other published reports may be caused by the amount and type of clays in Hanford sediments. In the study by Petersen et al. (1996), the clay content reached as high as 70% whereas the Banin and Amiel (1969) study used samples with clay contents as high as 75%. In the VZTFS, the highest clay content in the Hanford sediments was about 30% with the control sample (Lucky MC soil) containing 50%. Clay particles and organic matter are the main contributors to the CEC. In Hanford sediments, organic-matter content is typically small but can exist as coatings on mineral surfaces.

Figure 2.32b shows a plot of CEC (meq $[100\ g]^{-1}$) as a function of silt content. The relationship is somewhat better with an R^2 of 0.85. None of the published studies reported on the relationship between CEC and silt content. However, the improved fit may be related to the larger silt content of the sediments

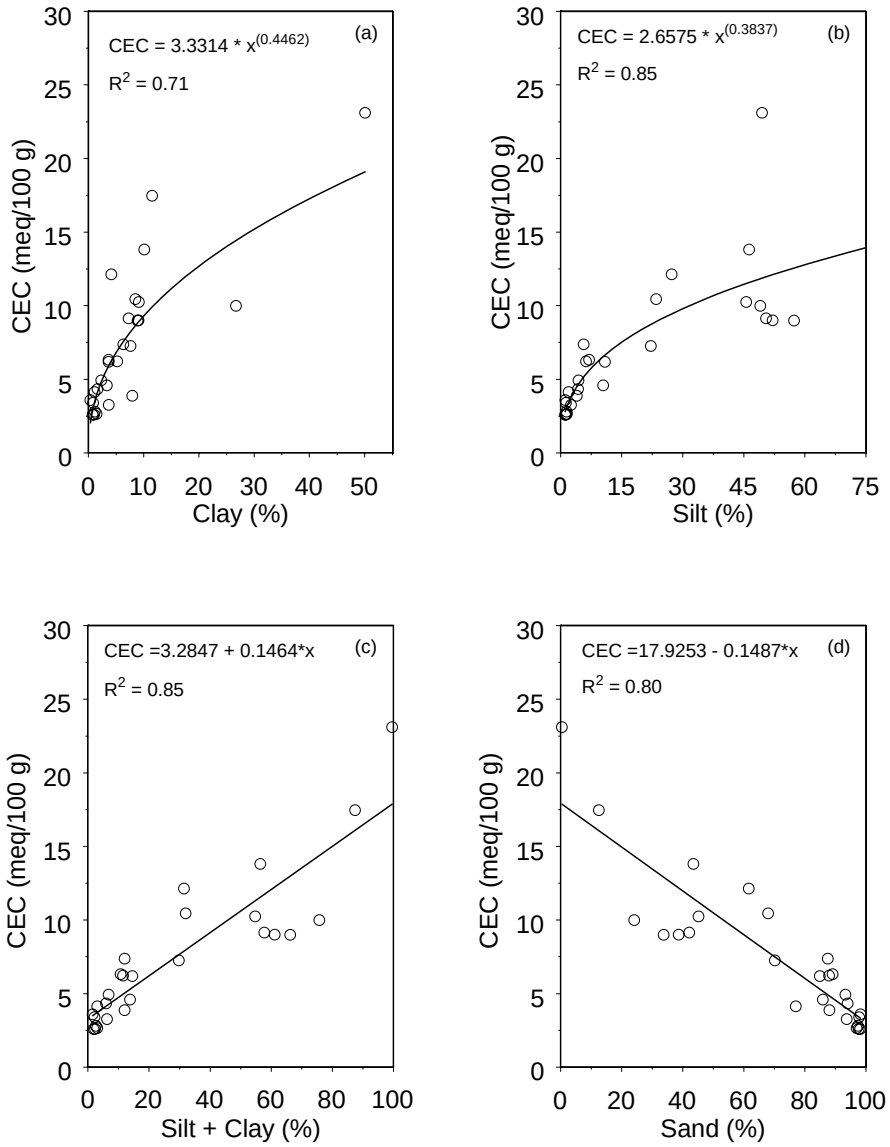

Figure 2.32. Relationships Between Various Soil Properties and the Cation Exchange Capacity in Hanford Sediments from the Army Loop Road Site, (a) Clay Content, (b) Silt Content, (c) Silt + Clay Content, and (d) Sand Content

tested. Many of the samples collected during the installation of boreholes in the waste management areas onsite were analyzed by dry sieving and reported the mud content, which is a combination of clay and silt fractions. Figure 2.32c shows CEC as a function of mud content, which is best described by a linear relationship with reasonably good correlation. It is well established that the fine-textured fraction is the main contributor to the CEC. Thus, as expected, the CEC is negatively correlated with sand content as shown in Figure 2.32d.

An important observation in the sand relationship is the small but non-zero CEC at 100% sand. The cation exchange capacity is typically measured on the < 2-mm fraction of the composite sediments. However, to account for the particle-size distribution of the whole sample, inclusive of the material

> 2 mm, CEC values are often corrected for the > 2-mm fraction (Serne et al. 2002). This correction is based on the assumption that the < 2-mm material constitutes all the exchange capacity, and the > 2-mm material has no exchange sites. If this were the case, we would expect the CEC to approach zero for coarser sediments. Figure 2.32d suggests that this may not be the case. Figure 2.33a shows a plot of CEC as a function of the geometric mean grain size derived from the particle-size distributions. The relationship is best described by a logarithmic function with R^2 of 0.76. The relationship shows the largest CEC values occurring at the smallest d_g with values decreasing as d_g increases. Figure 2.33b shows a plot of CEC versus the sorting index, derived from the graphic inclusive standard deviation of the grain-size distribution. As the soil becomes less well sorted, fines can be expected to fill in the pores formed between the larger particles, leading to an increase in CEC. Thus, the CEC should increase as the sorting index increases, and this is clearly shown in the data. Figure 2.33c shows a plot of CEC versus F_i. Like the d_g dependence, the relationship is still best described by a logarithmic function but with an improvement in R^2. These results clearly show that the CEC can be predicted reasonably well from the mean grain size and sorting index or a ratio of the two. It takes care of the effects of both diameter and sorting index.

The existence of reasonable relationships between textural properties, grain-size statistics, and CEC for the limited number of samples from the Army Loop Road site was the motivation to explore the larger database of historic CEC measurements. A database of over 1200 CEC measurements exists for a variety of Hanford sediments (McHenry 1957; Rouston and Fecht 1979). The approach followed was identical to that used for the samples from the test site. Textural composites were used to calculate grain-size statistics, including the mean diameter and sorting index, from which the fredle index was calculated. Figure 2.34 shows plots of CEC versus a variety of textural parameters for data from Rouston and Fecht (1979). About 500 measurements are included in this database with samples coming from 12 wells across the Hanford Site. In general, these data show very weak correlations between CEC and the textural properties as shown in Figure 2.34a, b, c, and d. The relationships between CEC and the grain-size statistics d_g and σ_I are also quite poor (Figure 2.34e. Even the relationship to F_i shows poor correlation with little predictive capability (Figure 2.34f).

As with the Army Loop Road samples, most of these samples in the Hanford CEC database were relatively low in clay content. The sand content ranged from 47 to 99%, silt ranged from 0 to 33%, and clay ranged from 0 to 20%. Given that CEC is typically measured on the < 2-mm fraction of the composite sediments, the raw CEC values were corrected for sand content. It was assumed that the < 2-mm material constitutes all the exchange capacity, and the > 2-mm material has no exchange sites. A corrected cation exchange capacity, designated as CEC^*, was calculated as $CEC^* = CEC - CEC(0.01 \times sand)$. Figure 2.35a shows a significant improvement when the CEC^* is plotted as a function of d_g. The same can be said of the plot of CEC* versus σ_I and F_i. The trends are identical to those observed with the Army Loop Road samples with CEC* decreasing as d_g increased and increasing with σ_I and F_i. The relationship with F_i is best described by a power function with a reasonably good R^2 of 0.66. Nevertheless, this function could prove invaluable for predicting CEC for the heterogeneous sediments representative of the Hanford vadose zone.

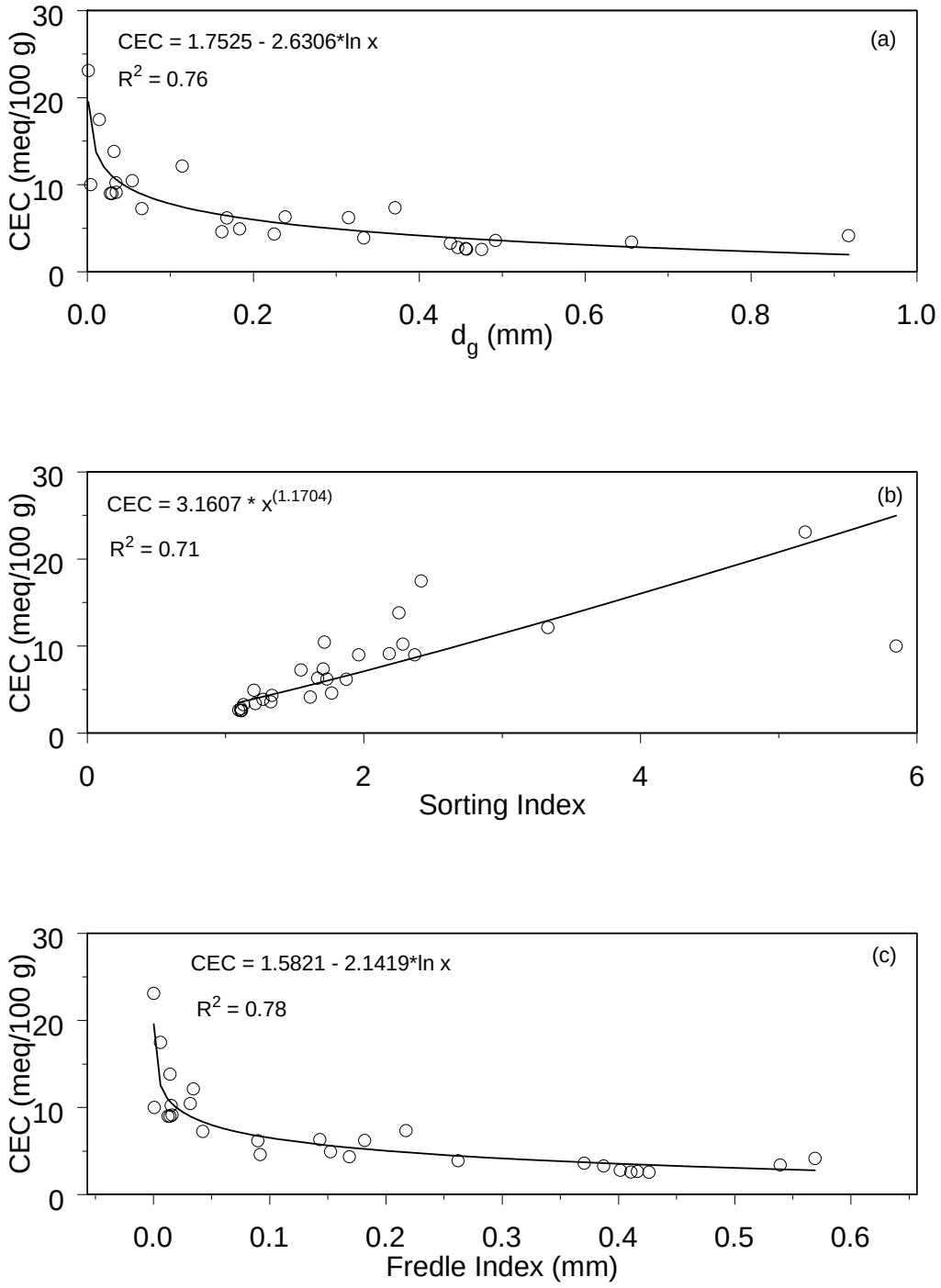

Figure 2.33. Relationships of Grain-Size Statistics and the Cation Exchange Capacity in Hanford Sediments from the Army Loop Road Site, (a) Geometric Mean Diameter, d_g, (b) Sorting Index, σ_I, and (c) Fredle Index, d_g/σ_I

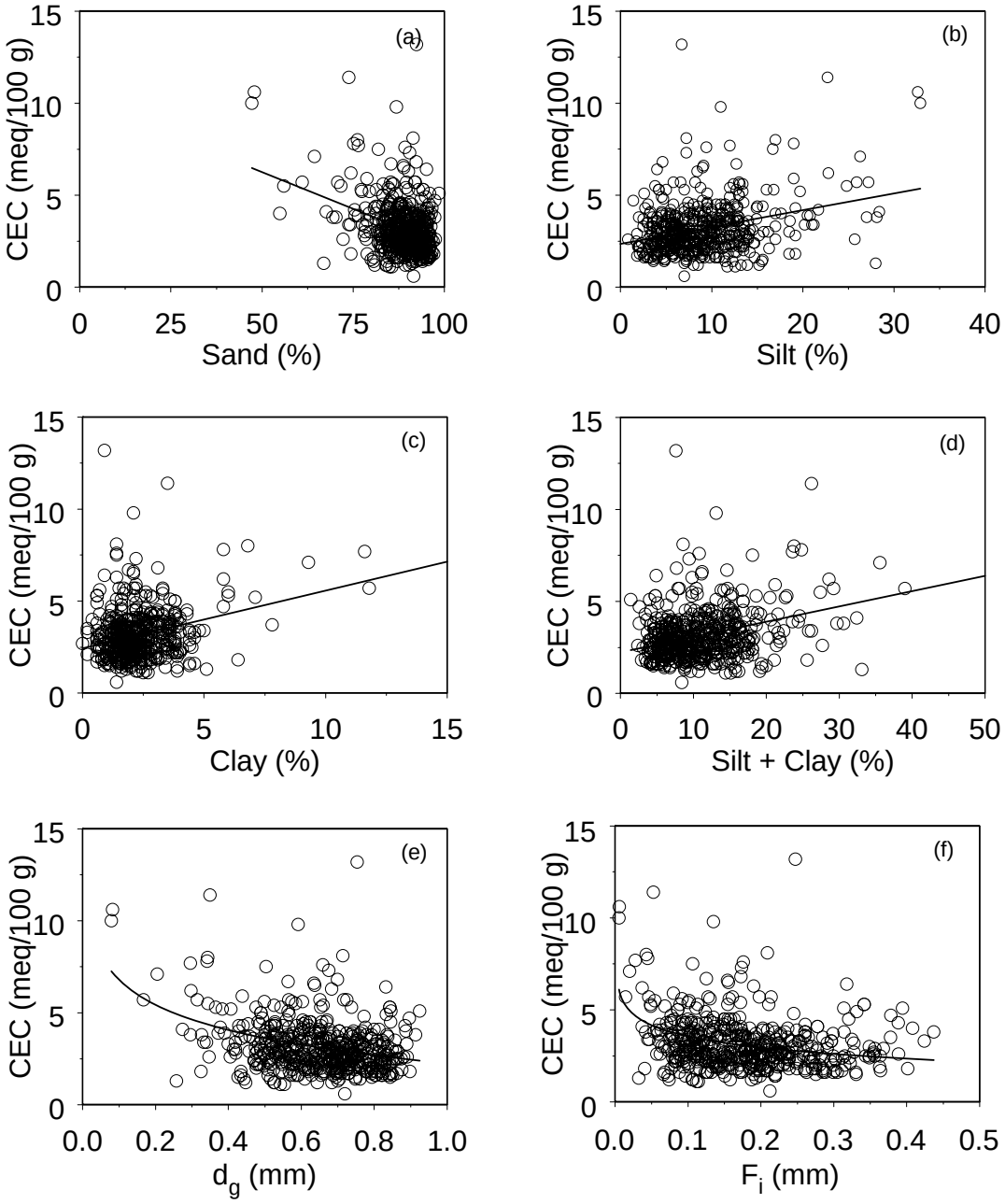

Figure 2.34. Relationships Between Grain-Size Statistics and the Cation Exchange Capacity in Hanford Sediments from the Army Loop Road Site, (a) Sand Percent, (b) Silt Percent (c) Clay Percent, (d) Silt + Clay Percent, (e) Geometric Mean, d_g, and (f) Fredle Index, d_g/σ_I

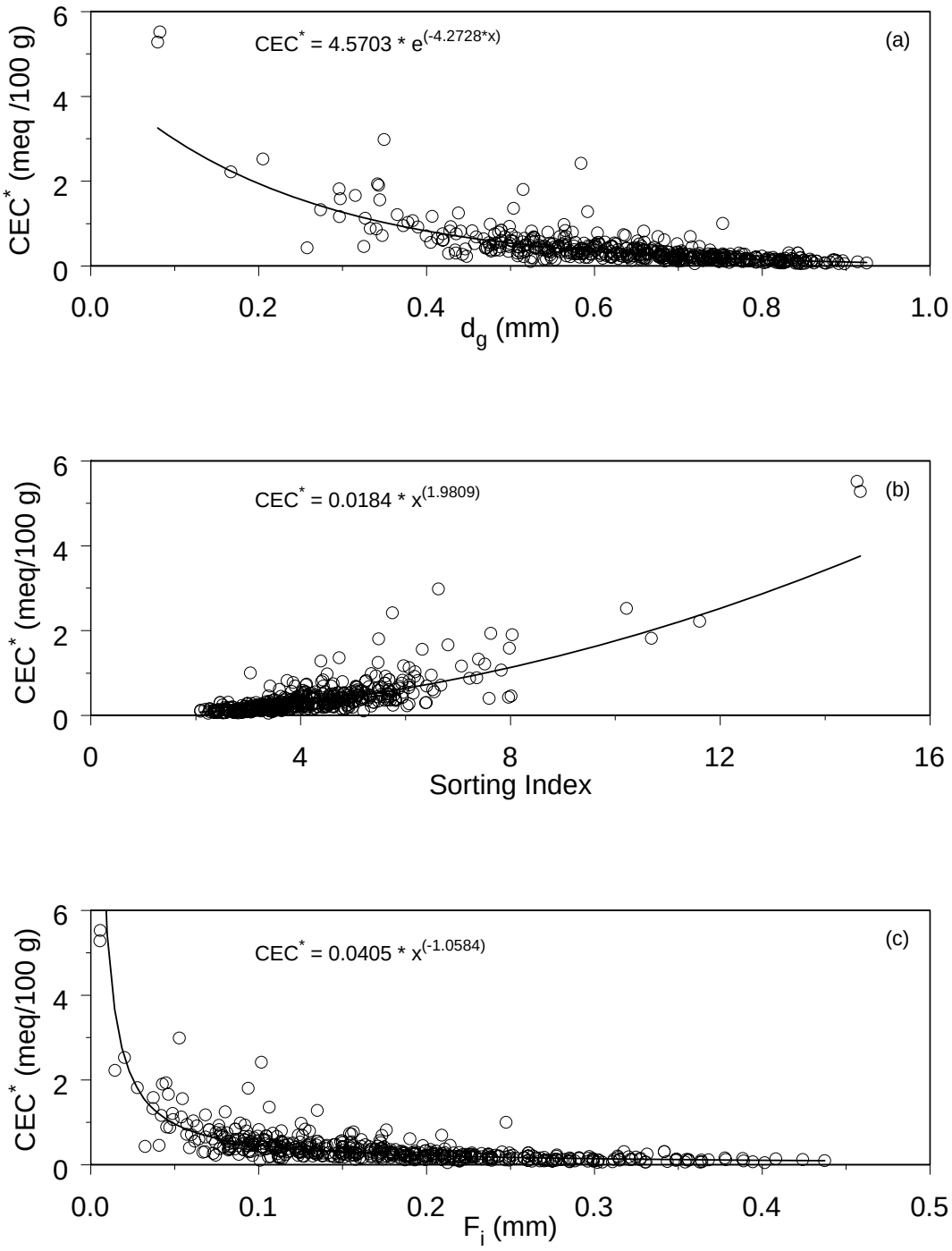

Figure 2.35. Relationships Between Grain-Size Statistics and the Corrected Cation Exchange Capacity, CEC^*, from 12 Wells Across the Hanford Site; (a) Geometric Mean Diameter, d_g, (b) Sorting Index, σ_I, and (c) Fredle Index, d_g/σ_I

An important question in attempting to use CEC from the historic databases relates to the quality of these data, given that they were obtained using a variety of methods. A set of representative samples was selected from the Army Loop Road test site to compare CEC measurement methods with the goal of validating the quality of historic data. Figure 2.36 compares the CEC determined by the three methods. The dialysis method of Amrhein and Suarez (1990) and the sodium acetate method produced similar CEC values. CEC values derived from the Polemio and Rhoades (1977) method were much smaller than those determined by the other two methods. The similarity of results for the Amrhein and Suarez (1990) and sodium acetate methods suggests that CEC values derived from these two methods may be the most reliable. Caution is needed when using CEC results from the Polemio and Rhoades (1977) method. With this finding, the range of the physically based PTFs developed above for CEC values can be expanded to include the historic data. However, historic CEC measurements using the Polemio and Rhoades (1977) method should not be included.

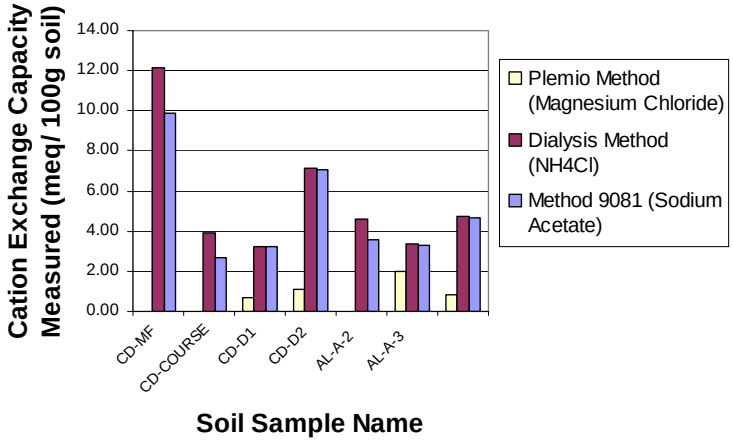

Figure 2.36. Comparison of Results from Three Different CEC Measurement Procedures

To apply these PTF-based methods to the field scale, a method for regionalization is still needed. Previous researchers have used variogram modeling and other geostatistical tools to regionalize water retention and soil buffering functions (Scheinost et al. 1997). In strongly heterogeneous sediments, variogram modeling can sometimes smooth out the effects of small-scale textural changes. A more accurate approach may be to simulate grain-size distributions or measure indirectly from geophysical tools or high-resolution images. Sediment grain-size distributions can be represented in a discrete form, as vectors of co-regionalized size-class abundances (Desbarats 2001). However, the number of classes can become quite large, and the abundances in adjacent classes are often cross-correlated, limiting the simulation of grain-size distributions for heterogeneous systems. Such difficulties would limit the use of grain-size distribution or textural fractions to predict spatially variable CEC in heterogeneous sediments. The same problems would limit the use of grain-size distribution and texture to the regionalization of cation exchange capacity. It has been shown that high-resolution infrared and visible images can be used to derive grain-size statistics and the corresponding hydraulic properties over multiple spatial scales (Ward et al. 2002; Murray et al. 2003). Based on the analyses presented above, using the fredle index, F_i, which accounts for the effect of both the grain diameter and the sorting index, provides a reasonable alternative for regionalization of CEC. This approach was recently demonstrated in the regionalization of CEC for the multicomponent reactive transport simulation of Na^+, K^+, Ca^{2+}, Sr^{2+}, and Mg^{2+} (Ward et al. 2003; Yabusaki and Ward 2004).

Figure 2.37 shows the predicted spatial variability in CEC distribution on a cut face at the Army Loop Road dike site based on infrared and visible images. Casual observation of this cut face showed a relatively undifferentiated sand deposit with a clastic dike down the middle. The conventional approach would have been to assign a single average value of CEC derived from a homogenized sample. Here, photogrammetric methods were used to derive grain-size distributions and grain-size statistics from images with a resolution of 1.1 mm. The PTFs developed above were used to predict CEC in 2D space (Figure 2.37). Reactive transport simulations with this distribution during unsaturated flow resulted in preferential dissolution of calcite and highly heterogeneous sorption of Sr^{2+} and other cations (Yabusaki and Ward 2004).

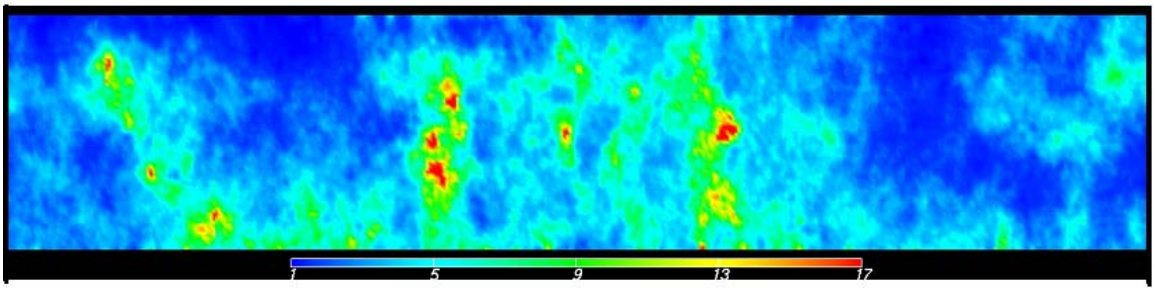

Figure 2.37. Regionalized CEC Using a Physically-Based Pedotransfer Function and High-Resolution Infrared and Visible Images

A similar development is proposed for the specific surface area, A_s. However, very little surface area data exist for Hanford sediments. Given that A_s is controlled by texture, which also controls the equilibrium or antecedent moisture content, θ_i, a relation between A_s and θ_i was sought. The percentage and type of clay in sediment plays an important role in the adsorption and desorption of moisture. A number of researchers have reported good correlation between A_s and moisture content at 0.1 and 15 bar (Banin and Amiel 1969; Campbell and Shiozawa 1992; Petersen et al. 1996). Again, these were typically soils with higher clay content and higher surface areas. Although antecedent moisture appears to be a reasonably good predictor of A_s, caution should be exercised in the use of this variable, especially when high levels of accuracy are required. The amount of water present in a soil could be influenced by the type of exchangeable ion as well as the vapor pressure and more so than the amount of gas adsorbed during the measurement of A_s. One possible solution could be to use the air-dried moisture content in the relationship. Nevertheless, relationships between A_s, CEC, and θ_i for the same soils used in the study are shown in Figure 2.38. As can be expected, there is a relatively strong correlation between A_s and CEC ($R^2 = 0.92$). Compared to other studies, the R^2 is fairly high. Petersen et al. (1996) reported a linear relationship with $R^2 = 0.66$ whereas Banin and Amiel (1969) reported $R^2 = 0.87$ also with a linear relationship. If the Lucy MC soil is excluded from the regression, a linear relationship, $A_s = 3.1288 \times CEC - 2.2468$, results with $R^2 = 0.69$. With this relationship, each $m^2\ g^{-1}$ of A_s contributes about 0.22 meq $(100\ g)^{-1}$ to the CEC, which is about twice the 0.12 reported by Banin and Amiel (1969). The amount and type of clay and organic matter are typically the greatest contributors to CEC. Owing to the low organic matter in Hanford sediments, the CEC can be attributed mostly to clay content, which is also quite low. Samples from the Army Loop Road site contained mainly smectite (44%), illite (36%), chlorite (10.7%), and kaolinite (9.3%). Consequently, most of the Hanford samples fall in the CEC range of 2 to 6 meq $(100\ g)^{-1}$.

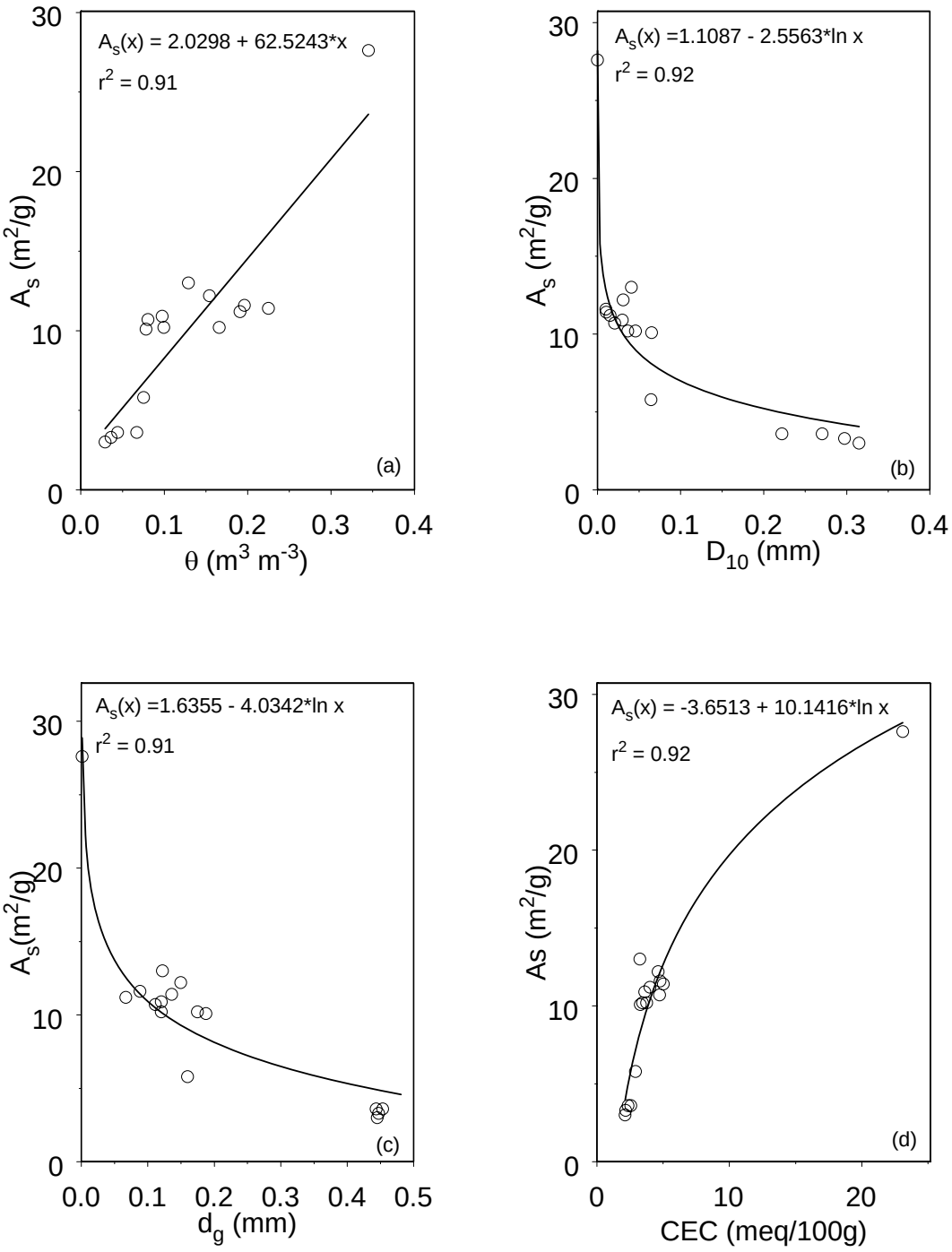

Figure 2.38. Relationships Between Various Soil Properties and the Specific Surface of Sediments from the Army Loop Road Site, (a) Antecedent Moisture Content, (b) D_{10}, (c) Geometric Mean Diameter, and (d) Cation Exchange Capacity

2.5.2 Synopsis and Implications

The synopsis of findings for this study of physically based pedotransfer functions for variable geochemical properties and their implications are as follows:

- Studies over the last two decades have demonstrated the existence of statistical correlations between easily measured properties like soil texture, bulk density, and organic matter and hydraulic properties that form the basis of pedotransfer functions. However, there has been little work done on developing pedotransfer functions for variable sorption parameters.

- Reasonable estimates of geochemical parameters can be derived from particle size distribution statistics that are based on the entire distribution curve. The resulting functions are mostly log-log linear with high coefficients of determination and may be summarized as follows:

  Specific surface area: $S_A = 10.483 F_i^{-0.3576}$; $R^2 = 0.896$

  Cation exchange capacity: $CEC = 2.5582 F_i^{-0.2916}$; $R^2 = 0.9084$

  These relationships inherently allow scaling across particle size classes. However, it should be noted that these relationships may not adequately account for the effects of pedogenesis.

- The existence of reasonable relationships between grain-size statistics and sorption parameters (CEC and A_s) for the limited number of samples from the Army Loop Road site was the motivation to explore the larger database of historic CEC measurements. These data were assessed for quality by comparing CEC values derived from different measurement methods. The dialysis method of Amrhein and Suarez (1990) and the sodium acetate method produced similar CEC values. CEC values derived from the Polemio and Rhoades (1977) method were much smaller than those determined by the other two methods. Using this historic database to develop PTFs for CEC should not include the historic CEC measurements made with the Polemio and Rhoades (1977) method.

- To apply PTF-based methods to the field scale, a method for regionalization is needed. Previous researchers have used variogram modeling and other geostatistical tools to regionalize water retention and soil buffering functions. Geophysical methods offer the opportunity to identify the correlation structure needed to develop these variograms. The concept of regionalization was successfully tested on a cut face from the Army Loop Road site using grain size statistics derived from digital images. This approach allowed reasonable accurate prediction of CEC measurements at a resolution of around 2 mm.

- Simple relationships between existing mineralogy data and size statistics were sought. It appears that when calcite ($CaCO_3$) is present, it is mostly associated with the silt fraction. In most of the soils containing significant quantities of $CaCO_3$, the silt fraction is composed mostly of $CaCO_3$ with about 0.6% of the silt fraction being contributed by 1% of the $CaCO_3$.

- Accounting for mineralogy may not be critical to the development of PTFs for reactive properties as data from the Army Loop Road dike suggest that sediments from similar depositional environments tend have similar mineralogy even in the presence of large differences in grain size distributions.

- To apply PTF-based methods to the field scale, a method for regionalization is needed. Previous researchers have used variogram modeling and other geostatistical tools to regionalize water retention and soil buffering functions. Geophysical methods offer the opportunity to identify the correlation structure needed to develop these variograms.

- The implication of this study is that because of spatial variability, comprehensive tests cannot be performed on all contaminants of interest under relevant conditions to determine sorption indices. The proposed approach provides a possible method to obtain reasonable estimates of two important parameters needed in mechanistic models for multicomponent reactive transport, the specific surface area and the cation exchange capacity.

2.6 Pedotransfer Functions to Quantify Variable Transport Properties

The analysis of reactive transport in subsurface formations also involves evaluating transport behavior along the complex flow paths and the effects of heterogeneity of this transport behavior. As with flow simulations, the ideal transport simulation requires discretization of the domain at the scale of support of the transport properties and the assignment of transport parameters to each grid cell. These properties include the relative permeability-capillary pressure-saturation relationships, all of which are quite variable and typically depend on soil characteristics such as texture and structure. In Section 2.4, simple approaches were developed for estimating hydraulic properties to account for heterogeneities. Accurate predictions of transport in heterogeneous systems also require the means for describing the geochemical heterogeneity. In the context of reactive transport where ion exchange and sorption processes are important, chemical heterogeneity refers to the variability in surface reactivity. In Section 2.5, simple approaches for estimating sorption indices in heterogeneous sediments were developed and tested. One of the remaining challenges is to estimate transport properties, particularly dispersivity, for heterogeneous sediments.

Robust methods for estimating local-scale dispersivity from easily measured or readily available sediment properties have been the subject of research for several decades. Studies conducted in the 1960s and 1970s have also shown the dispersivity to vary with mean grain diameter, d_{50} (Harleman and Rumer 1963; Bruch 1970). Most of these studies focused on permeability and dispersion in packs of uniform spheres and sieved sand. Harleman and Rumer (1963) observed a strong correlation between intrinsic permeability and the median grain size, d_{50}, and between dispersivity and d_{50}. No data were reported for nonuniform media. Han et al. (1985) also showed a relationship between particle size distribution and longitudinal dispersivity. They found that in the case of the wide size distributions, longitudinal dispersivities were larger than in case of uniform particles, and they required a longer dispersion length to achieve a constant value. This suggested a characteristic length for dispersion larger than the mean hydraulic radius and the presence of larger scale nonuniformities that strongly influence the longitudinal dispersion behavior. Lateral dispersivities were found to be insensitive to the distribution of particle sizes or the location in the packed bed.

These studies suggest that, like hydraulic properties, transport properties are affected by sediment granulometric and physical properties such as particle size distribution. Thus, the objective of this study was to identify empirical relationships to predict the transport properties as a function of sediment characteristics. Owing to the scale-dependence of dispersivity, such estimates would be limited to the local-scale values that would then require upscaling to the model grid block of interest. To investigate the feasibility of these relationships, several published dataset sets were analyzed. For the purpose of illustration, we focus on the dataset published by Perfect et al. (2002). In that study, the effects of texture on dispersion coefficients were investigated and showed the dispersion coefficient increasing linearly with the Campbell *b* parameter. This relationship suggested that dispersivity should increase as the sediment texture became finer, or as the median diameter decreases. These data provide the motivation to explore relationships between dispersivity and grain size statistics.

The same approach used in Sections 2.4 and 2.5 was followed. Texture information was used to calculate grain size distribution statistics, namely the geometric mean grain diameter, d_g, and the geometric standard deviation, σ_g, according to the method of Campbell (1974). This method determines the contribution of each of the textural fractions of sand, silt, and clay after calculating the equivalent diameters of each fraction. The geometric mean diameter, d_g, and the standard deviation, σ_g, can then be calculated as described previously using Equations (2.6) and (2.8), respectively. Fundamental hydraulic and transport properties depend on both d_g and σ_g, which are collinear, and as a result, spatial interpolation could prove difficult. Using both d_g and the sorting index, σ_I, to predict sorption parameters is avoided by invoking the fredle index, F_i, calculated simply as the ratio of d_g to σ_g. The resulting statistics were used to explore relationships between sediment physical and transport properties.

2.6.1 Results

Figure 2.39 shows a plot of longitudinal dispersivity, α_L, calculated from the reported dispersion coefficients, as a function of textural composition. Figure 2.39a shows a significant correlation between α_L and sand content with α_L decreasing as sand content increased. Figure 2.39c shows an even stronger relationship between α_L and clay content, with the α_L area increasing as the clay content increased. However, as shown in Figure 2.39b, there is no significant relationship with silt content. This could be problematic for Hanford sediments in which silt content has been shown to be the prime component controlling hydraulic and sorption properties. These findings are probably due to the relatively small amount of silt and large amount of clay present in the group of soils that were used in this study. Nevertheless, these results suggest that texture information, in the form of grain size statistics that account for the entire range of the particle size distribution, could be used as the basis of PTFs for transport properties.

Figure 2.39d shows a plot of α_L as a function of the geometric mean diameter, d_g. The longitudinal dispersivity shows a strong negative log-linear relationship with the geometric mean grain diameter. Although there is some divergence from the log-linear fit at larger values of d_g, the resulting coefficient of determination is still quite high with a value of 0.85. Figure 2.39e plots the same values of α_L as a function of the sorting index, σ_g. This plot shows a positive correlation between α_L and σ_g (R^2=0.52), which is consistent with published findings of studies in packed beds which generally show that as the particle size distribution widens (i.e., σ_g increases), longitudinal dispersivities also increase. To account for the simultaneous decrease in α_L with increasing d_g and the increase with increasing σ_g, the α_L was plotted as a function of the fredle index (Figure 2.39f). The increase in the quality of the fit is self evident

with R^2 increasing to 0.96. These data show a clear relationship between grain size statistics and the longitudinal dispersivity. No data were available to evaluate the relationship between the transverse dispersivity, α_T, and grain size distribution. However, Han et al. (1985) reported a lack of sensitivity of this parameter to the distribution of particle sizes. In the absence of data to assess these relationships, the convention of defining α_T as 0.1 α_L is recommended.

2.6.2 Synopsis and Implications

The synopsis of findings for this study of physically based pedotransfer functions for predicting transport properties and their implications are as follows:

- Studies over the last two decades have demonstrated the existence of statistical correlations between easily measured properties like soil texture, bulk density, and organic matter and hydraulic properties, but there has been only one study aimed at identifying relationships between these properties and transport properties.

- This study was aimed at identifying simple but robust relationships between sediment textural properties and dispersivities that could be used to describe local-scale transport properties in heterogeneous sediments.

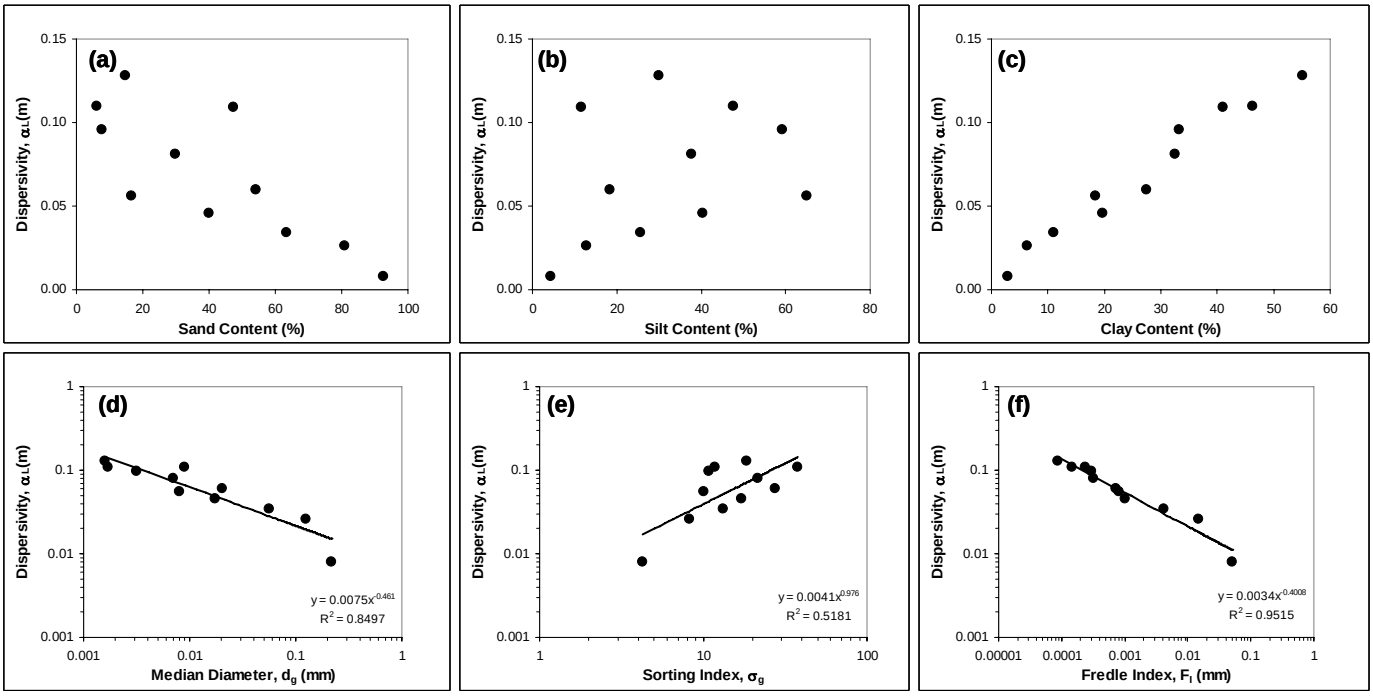

Figure 2.39. Dependence of Longitudinal Dispersivity on Soil Texture and Size Distribution Statistics, (a) Sand Content, (b) Silt Content, (c) Clay Content, (e) Median Particle Diameter, (e) Sorting Index, and (f) Fredle Index

- Reasonable estimates of the longitudinal dispersivity, α_L, can be derived from particle size distribution statistics that are based on the entire distribution curve. The resulting function is log-linear with a high coefficient of determination and may be written as follows:

  Longitudinal dispersivity: $\alpha_L = 0.0034 F_i^{-0.4008}$; $R^2 = 0.9515$

  Transverse dispersivity: $\alpha_L = 0.1\alpha_L$

- The range of textures on which this relationship is based represents the 11 major soil textural classes that are dominant in the United States.

- The implication of this study is that apart from field data collected as part of the vadose zone transport field studies, there are essentially no data for dispersivities at the Hanford Site. This approach is a first step that allows the estimation of dispersivity, based on particle size distributions of which there are some 40,000 available for sediments across the Hanford Site.

2.7 Laboratory-Scale Multicomponent Transport

Multicomponent models for coupled flow and reactive transport models are becoming more widely used for analyzing contaminant fate and transport in complex, physically and chemically heterogeneous porous media. A major challenge in understanding these processes is to identify the parameters needed to describe the physical and chemical processes controlling the movement of the contaminants. Laboratory column experiments play an important role in the model parameterization. The disparity between the scales of measurement of laboratory columns and the typical grid block for numerical simulations of field-scale transport limit the use of laboratory data for field-scale predictions. The upscaling of geochemical parameters, such as distribution coefficients, kinetic reaction constants, cation exchange capacity, and reactive surface area, remains a significant challenge. Transport and ion exchange parameters extracted from column experiments can therefore provide valuable insight into the dominant transport and reaction processes and can be useful as initial parameter estimates for model calibration using field measurements.

Parameter relationships often depend on experimental conditions; thus, an understanding of the relation between media physical properties, boundary conditions, and the parameters describing transport and reactions is needed to develop a link between laboratory and field parameters. To this end, a set of column experiments was conducted to investigate the effect of soil texture on multicomponent competitive transport of five major cations, Na^+, K^+, Ca^{2+}, Sr^{2+}, and Mg^{2+}, in Hanford sediments. These experiments were intended to generate a data set to calibrate a multicomponent reactive transport model for field application and to test the applicability of the Steefel (2004) ion-exchange model for strontium developed for the SX-Tank Farm (White et al. 2001).

For the column experiments, bulk sediments were collected from the Army Loop Road dike site, sieved, dried, and homogenized. Samples were then separated into a coarse fraction (CD-Coarse) and classified as a sand, and a fine fraction (CD-Fine) was classified as a sandy loam. Two PVC columns of 10.64 cm i.d. and 60 cm long were prepared and fitted with screens and end caps that drained into tipping buckets via fiberglass wicks. Fiberglass wicks of 1.27 cm (0.5 in.) diameter and 60 cm (1.96 ft) long

were flared at one end and inserted through the bottoms of the end caps. The wicks served to maintain constant tension at the bottom of the column to maintain steady state unsaturated flow. Each wick terminated in a tipping bucket to allow drainage monitoring. Each column was packed to a height of 50 cm (19.68 in), with a single soil fraction. The CD-Coarse column was packed to an average bulk density of 1.6 g cm^{-3} whereas the CD-Fine column was packed to an average bulk density of 1.4 g cm^{-3}. Each column was fitted with horizontally installed 10-cm (3.94 in.) long Time-Domain Reflectometry (TDR) probes at 20 cm (7.9 in.) and 40 cm (15.7 in.) below the soil surface. Probes were connected to a Campbell Scientific 10-port SDMX 50 multiplexer via 370-cm (12.14-ft) long coaxial cables. TDR measurements of water content and electrical conductivity were made at hourly intervals during the course of the experiment. Suction lysimeters were installed at the same depths as the TDR probes but offset by 45^{o}. The lysimeters served a dual purpose, alternating between solution samplers and tensiometers. The multiplexer, TDR unit, and pressure transducers on the tensiometers were controlled by a Campbell CR10 datalogger.

The two columns were wetted from the bottom to equilibrium moisture conditions by placing the columns in buckets of river water overnight. After wetting overnight, the columns were allowed to drain, and river water was applied to the surface using a Kloehn pump drawing water from a single source container. The water was divided among the two columns until steady-state flow conditions were achieved. The targeted steady-state application was 1.5 cm (0.6 in.) d^{-1} per column, which, based on the column dimensions, is equivalent to a flow rate of about 133.4 mL d^{-1} for each column of 273.6 mL d^{-1} for the two columns. Two separate tracer experiments were run after steady-state flow conditions were achieved. In the first experiment, a tracer consisting of 0.5% SrCl and 5% $MgCl_2$ was applied for 1.5 d at a flux of 1.5 cm (0.6 in.) d^{-1} followed by 19.5 d of river water applied at the same rate. The second tracer consisted of 0.5% SrCl applied under the same protocol as in the first experiment. The tracers were chosen to allow comparison of Sr behavior under conditions that promoted high mobility (Mg present) and high sorption (Mg absent). Mg and Solution samples were collected from the suction lysimeters, and effluent samples were collected from the base of the column (50 cm), both on a daily basis. All water samples were analyzed by inductively coupled plasma-optical emission spectrometry (ICP-OEP) for Ca, Mg, Sr, Na, and K. Samples were also analyzed by ion chromatography (IC) for F, Cl, Br, N, P, and S. At the end of the tracer experiments, the columns were immediately dissected, and soil samples were collected in 2-cm increments in the 0- to 20-cm depth and in 5-cm increments in the 20- to 50-cm depth. Water contents were determined by gravimetry after which the samples were analyzed to determine concentrations of carbonate, total carbon, and strontium and to determine cation exchange capacity. Strontianite content was determined by X-Ray Diffraction (XRD).

2.7.1 Results

One of the advantages of well-designed laboratory column experiments is the ability to control boundary conditions, which in turn simplifies the analysis of the experimental results. However, results of this experiment suggest that there were problems controlling the upper and lower boundaries. The average delivery rate of the pump over the 35-d course of the experiment was 248.4 mL d^{-1}, compared to the desired 266.7 mL d^{-1}. Based on the design of the application system, it was assumed that the same volume of water was applied to each column, resulting in an estimated flow rate of 124.2 mL d^{-1} or a flux density of 1.4 cm d^{-1}. The average outflow rate from the CD-Coarse column was 128 mL d^{-1}, about 3% higher than the average input rate, whereas the average outflow from the CD-Fine column was only 89 mL d^{-1}, some 39% less than the mean input rate. The CD-Fine column took longer to reach equilibrium, only beginning to level off at about day 25. Regression of the outflow from day 25 to day 35

shows a mean outflow rate of 115 mL d^{-1}. Adding this rate to the CD-Fine rate, we obtain a total of 243 mL d^{-1}, which is 5 mL d^{-1} lower than the inflow rate. The discrepancy could be caused by evaporation, data collection errors, or calibration errors for the tipping bucket. The assumption of equal delivery on each column may not be valid.

The mean water content, θ, following the initial wetting of the columns was 0.15 m^3 m^{-3} in the CD-Coarse and 0.25 m^3 m^{-3} in the CD-Fine column. TDR measurements show a mean θ of 0.168 m^3 m^{-3} in the CD-Coarse column and 0.301 m^3 m^{-3} in the CD-Fine column, and these remained quite steady during the course of the experiment. The mean θ derived from destructive sampling at the end of the experiments was 0.140 m^3 m^{-3} in the CD-Coarse and 0.341 m^3 m^{-3} in the CD-Fine. Figure 2.40 compares TDR-measured breakthrough curves, based on an electrical conductivity measurement, with those derived from chloride concentration in solution samples. The TDR provided very good temporal resolution and proved ideal for the simultaneous measurement of water content and electrical conductivity from which breakthrough curves were derived, even in the fine-textured sediments. To limit sampling effects on the flow field, pore water samples were collected less frequently than TDR measurements, and this is reflected in the coarser temporal resolution of the breakthrough curves. Nevertheless, the TDR, solution sampler, and effluent data were of good enough quality to allow estimation of the local-scale transport parameters by fitting the electrical conductivity and/or anion data to the convection-dispersion equation. Both types of data show the expected increase in travel time and dispersion with depth. The temporal resolution of these data was good enough to allow fitting to the convection-dispersion equation to determine transport parameters. Measured chloride breakthrough curves were fitted to an analytical solution of the convection-dispersion equation to determine the transport parameters for the CD-Coarse and CD-Fine columns. Figure 2.41 and Figure 2.42 show examples of the measured and fitted curves for the 20- and 40-cm (7.9- and 15.7-in.) depths in the two columns. The fitted curve is based on the 1-D convection-dispersion equation for a pulse input with a zero concentration initial condition and a pulse width of 1.5 d. In general, there was good agreement between the analytical solution and the observed data. Table 2.2 summarizes the results of these analyses.

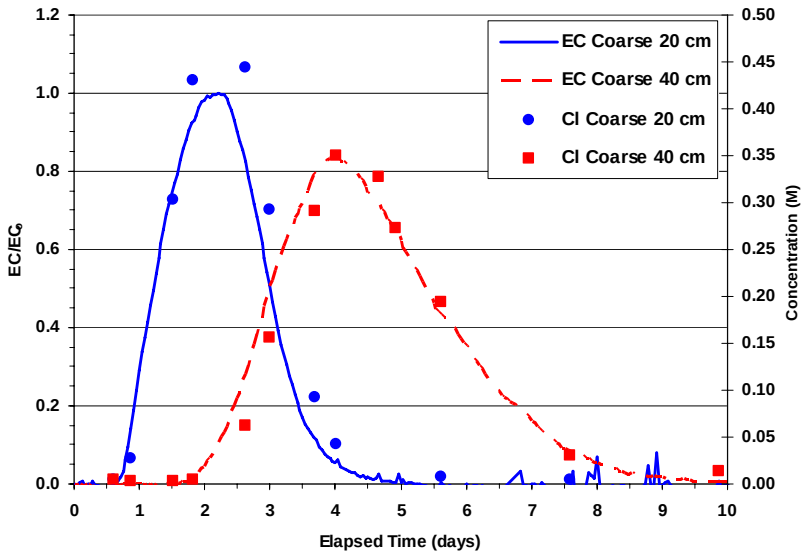

Figure 2.40. A Comparison of TDR-Measured Breakthrough Curves Based on Electrical Conductivity with Those Derived from Chloride Concentration in Solution Samples for the First Tracer Experiment

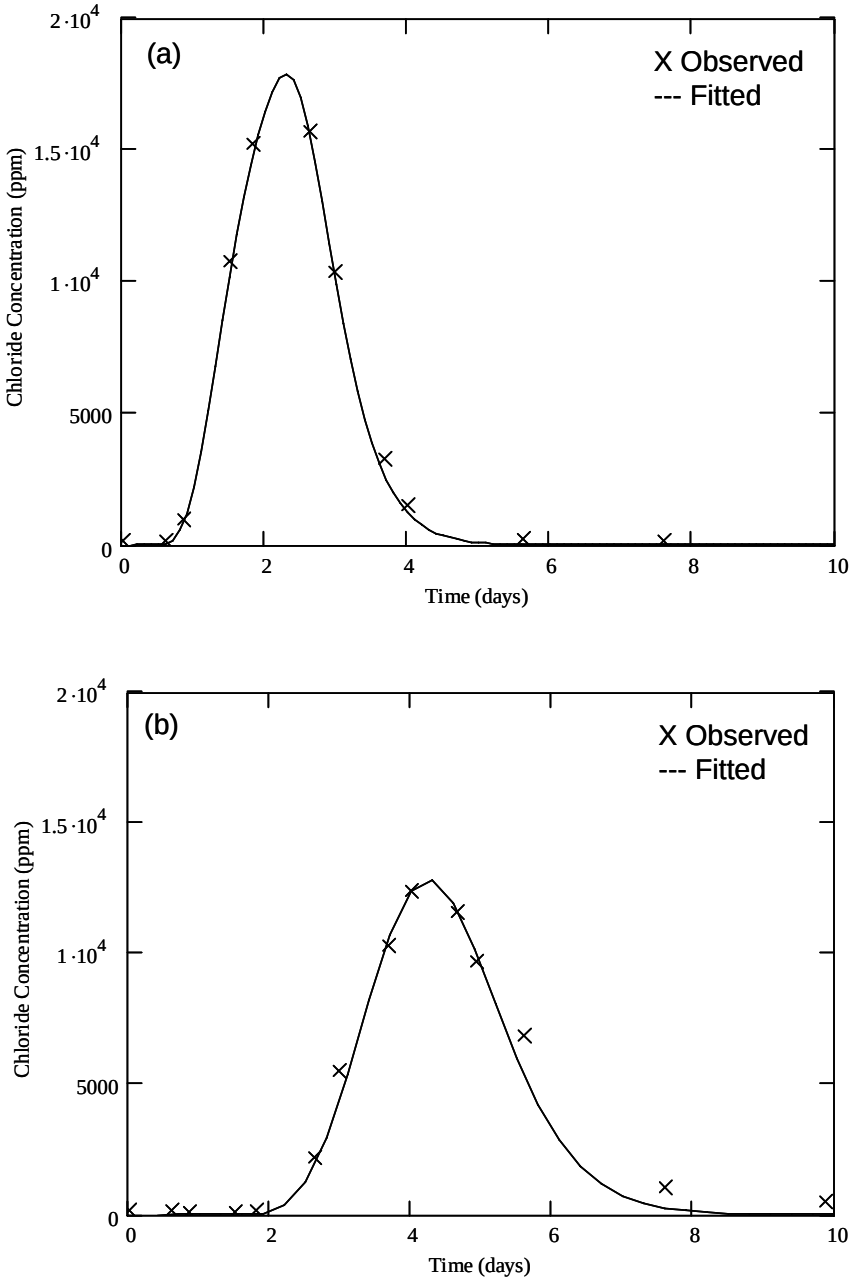

Figure 2.41. Measured and Fitted Chloride Breakthrough Curves for Experiment 1 in CD-Coarse Column Experiment, (a) 20-cm (7.9-in.) Depth, and (b) 40-cm (15.7-in.) Depth

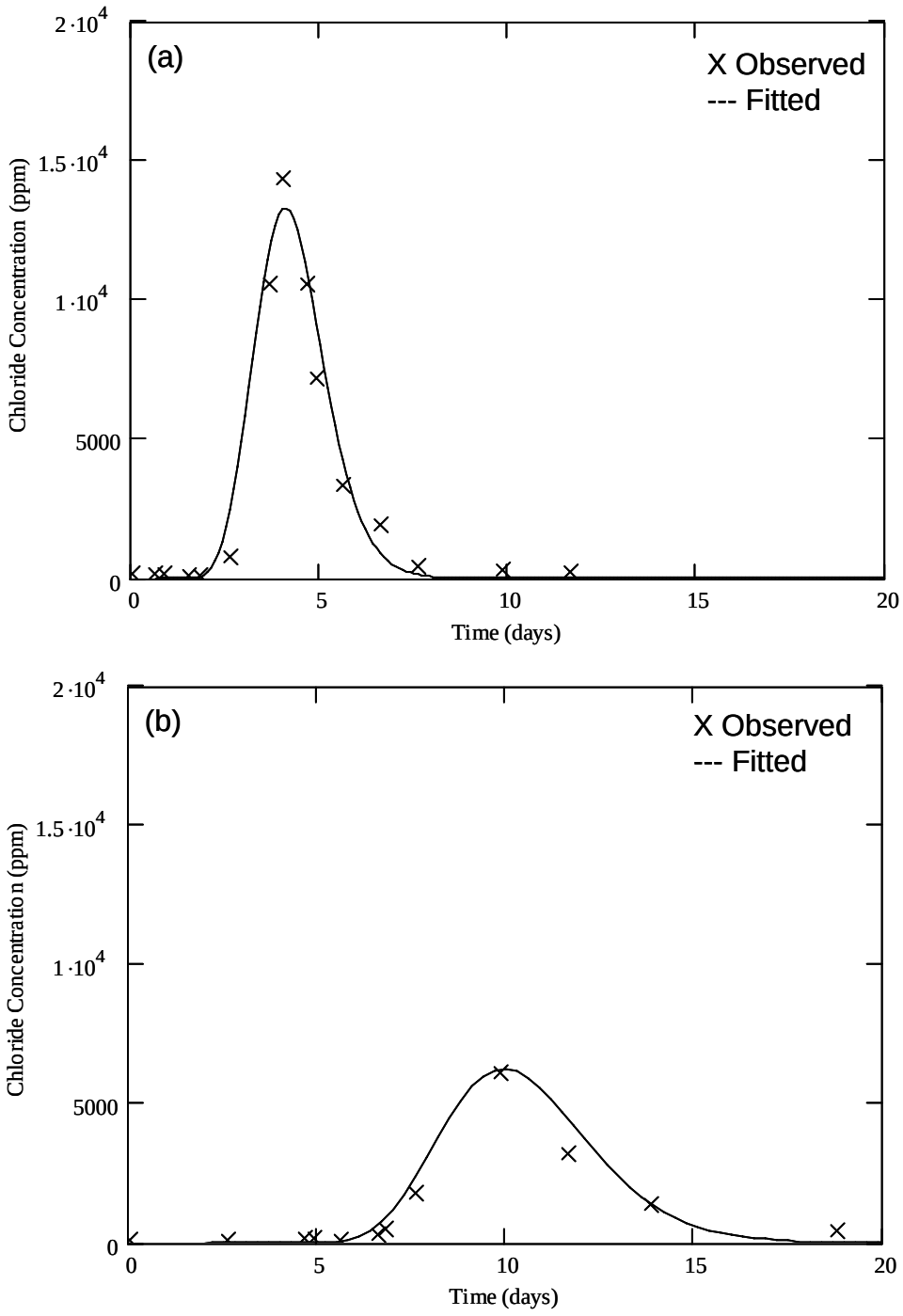

Figure 2.42. Measured and Fitted Chloride Breakthrough Curves for Experiment 1 in CD-Fine Column Experiment, (a) 20-cm (7.9-in.) Depth, and (b) 40-cm (15.7-in.) Depth

Table 2.2. Fitted Transport Parameters for Chloride Breakthrough Curves from the 1-D Column Experiments

Texture	Tracer	Depth (m)	Velocity, v ($m\ d^{-1}$)	Dispersivity α (m)	Dispersion Coefficient D ($m^2\ d^{-1}$)	Mean θ ($m^3\ m^{-3}$)	Transport Volume, θ_t ($m^3\ m^{-3}$)
Coarse	$MgCl_2$ +$SrCl_2$	0.20	0.128	$8.34 \cdot 10^{-3}$	$1.07 \cdot 10^{-3}$	0.1405	0.1130
Coarse	$MgCl_2$ +$SrCl_2$	0.40	0.112	$1.02 \cdot 10^{-2}$	$1.19 \cdot 10^{-3}$	0.1473	0.1298
Coarse	$MgCl_2$ +$SrCl_2$	0.50	0.109	$1.13 \cdot 10^{-2}$	$1.23 \cdot 10^{-3}$	0.1260	0.1330
Fine	$MgCl_2$ +$SrCl_2$	0.20	0.059	$4.50 \cdot 10^{-3}$	$2.64 \cdot 10^{-4}$	0.3333	0.2220
Fine	$MgCl_2$ +$SrCl_2$	0.40	0.042	$7.38 \cdot 10^{-3}$	$3.12 \cdot 10^{-4}$	0.3493	0.3080
Fine	$MgCl_2$ +$SrCl_2$	0.50	0.042	$3.32 \cdot 10^{-3}$	$1.39 \cdot 10^{-4}$	0.3670	0.3110
Coarse	$SrCl_2$	0.20	0.104	$3.16 \cdot 10^{-2}$	$2.25 \cdot 10^{-2}$	0.1405	0.1260
Coarse	$SrCl_2$	0.40	0.082	$1.57 \cdot 10^{-2}$	$1.29 \cdot 10^{-3}$	0.1473	0.1589
Coarse	$SrCl_2$	0.50	0.085	$1.76 \cdot 10^{-2}$	$1.51 \cdot 10^{-3}$	0.1260	0.1531
Fine	$SrCl_2$	0.20	0.038	$1.08 \cdot 10^{-2}$	$4.10 \cdot 10^{-4}$	0.3333	0.3429
Fine	$SrCl_2$	0.40	0.040	$8.07 \cdot 10^{-3}$	$3.25 \cdot 10^{-4}$	0.3493	0.3233
Fine	$SrCl_2$	0.50	0.044	$6.25 \cdot 10^{-3}$	$2.75 \cdot 10^{-4}$	0.3670	0.2961

A discrepancy was observed between the measured and expected velocity based on the steady flux density and the measured water content. In both columns, the velocity in the top 20 cm (7.9 in.) was higher than predicted from the ratio of flux to water content, which suggests that movement of the tracer occurred in a transport volume, θ_t, less than the water-filled pore space, θ. This type of discrepancy has been previously reported in the literature and is usually attributed to non-equilibrium flow because of pore bypass or fingering. The difference between θ_t and mean θ, $\overline{\theta}$, could also be attributed to pore bypass, except in this case, the bypass is more likely caused by experimental error than the traditional causes. Using filter paper to disperse influent over the surface may have resulted in an uneven distribution such that the surface boundary condition was more like a point source than a distributed source. Flow from the point source would have occurred over a smaller effective surface area, resulting in a higher initial flux density and, in effect, a higher velocity. A flow rate of 124 mL d^{-1} was measured for the CD-Coarse column whereas a rate of 115 mL d^{-1} was measured for the CD-Fine column. Knowing the cross-sectional area of the column ($A=8.825 \cdot 10^{-3}\ m^2$), along with the bulk density and water content, the average pore-water velocity in the columns was estimated at 0.097 m (0.318 ft) d^{-1} and 0.041 m (0.135 ft) d^{-1} in the coarse and fine columns, respectively. Table 2.2 shows velocities of 0.128 m (0.42 ft) d^{-1} in the 0- to 20-cm (0- to 7.9-in.) depth of the coarse column and 0.059 m (0.2 ft) d^{-1} in the fine column during the first experiment. The discrepancy decreased with depth, suggesting that flow became more uniform beyond the top 20 cm (7.9 in.) of the column. Both experiments (Tracer 1 and Tracer 2) exhibited these phenomena.

These discrepancies can be accounted by defining a transport volume $\theta_t < \overline{\theta}$. Conceptually, this is equivalent to either (1) defining an effective travel distance that is less than the actual observation depth or (2) defining a cross-sectional area for the flux that is less than actual area. Either method can be applied to scale concentrations of nonreactive solutes without a loss of generality. However, the impact on reactive transport involving ion exchange is much less certain, and the best approach for scaling is presently unknown. This is because the accessible exchange capacity of the sediments and the solid-to-solution ratio, key factors in the migration of exchangeable cations, are both impacted by the nonuniform

moisture content distribution, and either approach will impact the number and distribution of reactive surfaces. These issues will be more critical when dealing with field-scale transport where physical and chemical heterogeneities could cause variability in flow and access to reactive surfaces for sorption.

A rational prerequisite for the selectivity coefficients derived in the laboratory to account for cation mobility in the field was to test the adequacy in describing cation transport in the field sediments. The data from the column experiment were analyzed using the multicomponent strontium ion exchange model (CRUNCH) developed by Steefel et al. (2003). The CRUNCH model was coupled with UCODE to perform an automatic inversion of the data. In addition to the cations used in the tracer, H^+, NO_3^-, HCO_3^-, Cl^-, and SO_4^- were also included as primary components in the modeled reaction network (Yabusaki and Ward 2004). The resulting model, based on measured cation exchange capacity and the selectivity coefficients derived in the laboratory (Zachara et al. 2002; Steefel et al. 2003), was used to predict the multicomponent transport behavior. Transport parameters independently obtained from the chloride breakthrough curves were used to describe dispersivity and pore water velocity for the column. Figure 2.43 shows the results of the multicomponent transport experiment in the coarse-textured column. Experimental data are shown as symbols whereas model predictions occur as smooth curves.

Although the peak was missed by the sampling frequency at the 0.20-m (7.9-in.) and 0.40-m (15.7-in.) depth, the measured chloride concentration peaks are adequately described at all three depths. Apart from the 0.20-m (7.9-in.) depth, spreading was slightly underpredicted by the model (Figure 2.43a). The increase in discrepancy between observations and predictions with increasing depth is because of the dispersivity value fitted to the 0.20-m (7.9-in.) depth to describe transport in the entire column. Table 2.2 shows a clear increase in longitudinal dispersivity with depth in both the coarse- and fine-textured columns. Spreading at the 0.5-m (19.7 in.) depth may have been increased by the wick sampling method that could have resulted in increased mixing.

Figure 2.43b shows the measured and predicted concentrations for Mg^{2+}. The predicted peaks and spreading in Mg^{2+} breakthrough are also in good agreement with observations, except at 0.40 m (15.7 in.). The peak Mg^{2+} concentration at 0.40 cm (15.7 in.) decreased about 33% relative to that at 0.20 m (7.9 in.). The peak at 0.50 cm (19.7 in.) decreased another 25% from the peak at 0.40 cm (15.7 in.), but a notable observation is the delay in the arrival of the Mg^{2+} peak relative to Cl^-. These observations are consistent with ion exchange; some of the Mg^{2+} entering system liberates Ca^{2+} from the exchange sites while the remainder continued to move through the system. An increasing amount of the Mg^{2+} is adsorbed as it moves deeper into the profile, and this is well described by the model. The marked preference of the system for Mg^{2+} over Ca^{2+} resulted in a Ca^{2+} breakthrough identical to that of Cl^- (Figure 2.43c). The model did not do as good a job of timing the peak Ca^{2+} as in matching the Mg^{2+} and Cl^- predictions at 0.20 m (7.9 in.). This may be related to the low frequency of points near the peak. Ca^{2+} concentrations were also under predicted, most likely because using a single cation exchange capacity for the entire column and a value that was perhaps too low. The Ca^{2+} peak results from the liberation of native Ca^{2+} from the sediment, so this observation is consistent with an under estimation of cation exchange capacity. Nevertheless, the Ca^{2+} peak increased by about 10% from the 0.20-cm (7.9-in.) to 40-cm (15.7-in.) port, but decreased slightly at 0.50 m (19.7 in.). The occurrence of the Ca^{2+} slightly in advance of Cl^- peak and the similarity in Ca^{2+} peaks at the three depths suggest that Ca^{2+} in solution is Ca^{2+} liberated from the exchange sites by Mg^{2+}. As Ca^{2+} moves through the system, it would continue to displace other cations (e.g., Na, K) and depending on the concentration of CO_3^-, excess Ca^{2+} could be precipitated as calcite, $CaCO_3$.

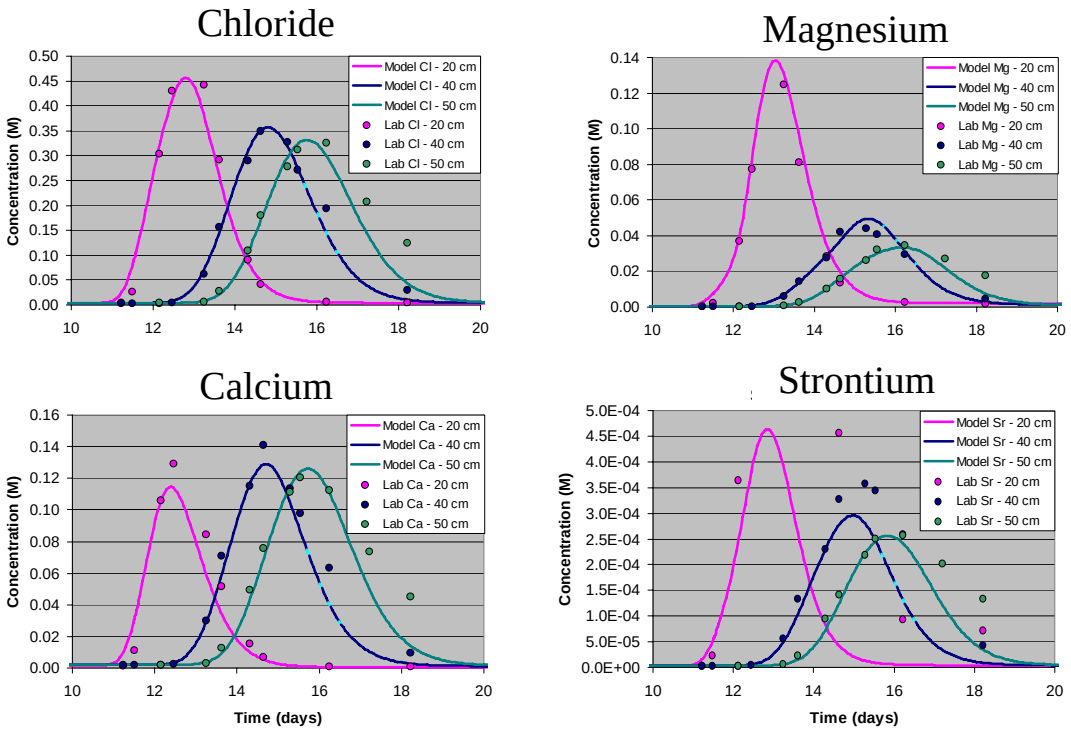

Figure 2.43. Measured and Fitted Cation Breakthrough Curves for Experiment 1 in the CD-Coarse Column Experiment

Figure 2.43d shows the measured and predicted concentrations for Sr^{2+}. The breakthrough of Sr^{2+} was essentially identical to the conservative Cl^-. This result was expected, given that Mg^{2+} was added to alter the behavior of Sr^{2+}. The low concentration of Sr^{2+} relative to the input value suggests that Sr^{2+} was also involved in the ion exchange reactions liberating Ca^{2+} from the exchange complex. The peak Sr^{2+} concentration decreased significantly from 0.20 m (7.9 in.) to 0.40 m (15.7 in.) in a manner similar to Mg^{2+} with the peak at 0.50 m (19.7 in.), decreasing another 10% from the peak at 0.40 m (15.7 in.). The measured Sr^{2+} curves also showed a significant discrepancy between measurements and predictions. The measured curves exhibited much greater spreading than was predicted by the model, and an integrated mass appeared larger than the input mass.

Most of the discrepancy in the model predictions in the top 0.20 m (7.9 in.) were corrected by assuming an effective transport distance less than the 20-cm (7.9-in.) observation depth for the top part of the column. Yabusaki and Ward (2004) also reported an improved fit when the cation exchange capacity of the sediment was increased to 42 μeq g^{-1} in a manual calibration. The measured cation exchange capacity at the dike site ranged from 25.7 μeq g^{-1} in coarse-textured sediments to 230 μeq g^{-1} in fine-textured sediments. The mean cation exchange capacity measured on sediments in the CD-Coarse column was 33 μeq g^{-1} whereas the mean for the CD-Fine column was 121.3 μeq g^{-1}. Despite differences in the sediments used, the range of cation exchange capacities, and the use of unsaturated flow conditions, predictions with the strontium multicomponent ion exchange model developed for SX tank farm sediments under saturated flow conditions performed reasonably well. Nevertheless, inverse analysis

showed that the system was relatively insensitive to the rate of magnesite precipitation. This, plus the observation that the solid solution ratio did not have a significant impact on the total concentration of magnesium, suggests that the selectivity coefficient and b-dot parameters used to describe the competitive adsorption behavior for ion exchange may be inappropriate for these sediments. Further optimization to include the selectivity coefficients and/or b-dot parameters currently assumed known may be required to reduce the discrepancy between observations and predictions.

2.7.2 Synopsis and Implications

The synopsis of findings in the laboratory multicomponent reactive transport experiment and their implications are as follows:

- There was evidence of bypass flow in both the coarse- and fine-textured sediments, although it appears to have been caused mostly by experimental error in maintaining the upper boundary condition.

- Experimental measurements provided good temporal resolution and allowed fitting of transport parameters to anion breakthrough. In the fine-textured sediment, water contents were higher, pore water velocities lower, and dispersivity was lower than in the coarse-textured sediment.

- Strontium, in the presence of a high magnesium concentration, mimicked the behavior of chloride, showing essentially no sorption. In general, the experiment generated a data set with known boundary conditions and good quality transport measurements that can be used for model calibration.

- In the analysis of cation transport, the inability of the model to fit the transport behavior of Cl^- at all depths suggests the need for a depth-dependent dispersivity, which is supported by fitting the individual Cl^- curves to the convective-dispersive equation. The inability to describe features of the different cations equally well suggests that the selectivity coefficient and b-dot parameters used to describe ion exchange, which were derived for SX tank farm sediments, may be inappropriate for the Army Loop Road sediments. It may be necessary to optimize these parameters using the inverse model.

- An important implication relates to the description of transport volume based on nonreactive tracers. Two approaches were investigated for chloride—a smaller effective surface area and a smaller effective travel depth—and both gave essentially the same result. The analysis of reactive transport could be more complicated as the chosen method dictates the amount of reactive surface accessed to the cations. Discrepancies between observations and predictions using parameters developed for the SX Tank Farm sediments suggest the need for further model validation.

2.8 Microscale Modeling of Variably Saturated Flow in a Clastic Dike

In typical depositional environments, sediments are laid down in a predominantly horizontal fashion. Occasionally horizontal seams filled with different kinds of sediments than the host material have been observed within these horizontal layers near vertical cracks. These are typically planar structures filled by

a forceful injection of sediment either from below or above and are known as clastic intrusions. Intrusions may be bedding discordant (dikes), filled with multiple layers of sand, silt, clay, and minor debris (Figure 1.2). The internal morphology can be quite complex and ranging from nearly structureless, to fining-upward, to tubular, to strongly tabular in the vertical direction. Dikes are often accompanied by bedding concordant intrusions, or sills (Figure 1.3). Sills are usually thin in relation to their length and are commonly observed along the base of the lowermost fine-grained stratum.

Although peculiar, clastic dikes are not unusual in occurrence, having been observed in a variety of geological settings. Dikes have been reported extensively in Canada (Dreimanis and Rappol 1997), Japan (Hayashi 1966), Europe (Mangerud et al. 1981), and the United States (Newsom 1903; Shrock 1948; Peterson 1968). In the United States, dikes are particularly ubiquitous in the rhythmically bedded slackwater deposits of the Late Pleistocene Missoula floods known as the Touchet Beds (Bjornstad et al. 1987; Pogue 1998; Fecht et al. 1999). Clastic dikes in the Touchet Beds of the Pasco Basin, which encompasses DOE's Hanford Site (Bjornstad et al. 1987; Fecht et al. 1999), are of particular interest because of their potential to influence subsurface vertical and lateral migration of water and contaminants. Clastic dikes on the Hanford Site typically exceed 2 meters in width and have been observed at depths in excess of 70 m in waste management areas (Fecht et al. 1999; Bjornstad et al. 1987). Because of the higher capillarity and water-holding capacity of the intrusions, plant-available water remains high late into the summer. It has been speculated that the abundance of deep-rooted plant species in or near these structures could also contribute to surface contamination by subsurface waste. The question that naturally arises is whether clastic intrusions are conduits for facilitated transport of contaminants through the unsaturated zone to the water table and to regions outside of waste management areas or whether they are natural barriers inhibiting contaminant spread.

Microscale simulation is a widely used approach to investigate relationships between heterogeneity and subsurface flow behavior. The objective of this study was to quantify the potential impact of clastic intrusions on the flow of water through the vadose zone. To meet this objective, water flow was simulated on a 2-D vertical outcrop of the dike with dimensions 4.7 m long and 1 m deep using the water operational mode of the STOMP simulator, STOMP-W. The grid cells in the domain were upscaled from a grid spacing of 1.11 mm (over $3.59 \cdot 10^6$ nodes) at the measurement scale to 2.22 mm ($8.97 \cdot 10^5$ nodes) on the model grid. In the majority of simulations, a Neumann condition was imposed at the top boundary with $j_w^0 \in \{1, 10, 10^2, 10^3\}$ mm yr^{-1}, representing the range of recharge rates observed at the Hanford Site. A recharge of 1 to 10 mm yr^{-1} is typical of areas of undisturbed shrub steppe onsite; 10^2 mm yr^{-1} is typical of bare soils and gravel-covered tank farms, while 10^3 mm yr^{-1} is the estimated recharge near the periphery of storage tanks because of the umbrella effect of the impermeable tank domes. Pedotransfer functions, based on grain-size distributions, were used to derive hydraulic properties at a resolution of 1.11 mm based on photo mosaics of the outcrop. This approach allowed development of detailed, high-resolution data sets, which typically cannot be obtained from field experiments, even with the best of vadose zone instrumentation.

2.8.1 Results

Figure 2.44a,b shows examples of the spatial variability in texture inferred from photo mosaics of visible and infrared images of a dike outcrop at the Army Loop Road site. The spatial resolution of these images is ~ 0.1 cm per pixel. The cooler temperatures represent areas with higher moisture content, which typically were occupied by silts and silt loams. Figure 2.44c shows the distribution of the vertical

saturated hydraulic conductivity for the same outcrop; the dike is located between 1.8 and 3.6 m along the transect (horizontal distance). The approach used for parameterization is distinct from previous approaches in that the fields of hydraulic properties are derived from high-resolution measurements on an outcrop rather than from geostatistical simulation.

Figure 2.45 shows typical subsurface distributions of θ(x,z) resulting from steady input fluxes, j_w^0, ranging from 1.0 mm yr^{-1} to 10^3 mm yr^{-1}. Water content is not a component of the driving force but reflects the distribution of this force, namely the gradient in the matric potential, $\nabla\psi$. Although ψ varies slowly in space, the internal flux, j_w, will vary to minimize ψ. Consequently, θ adjusts spatially to match j_w and to minimize $\nabla\psi$. The distribution of θ therefore reflects the underlying structure of the heterogeneity, and the degree to which this heterogeneity is expressed depends on j_w^0. Simulated θ clearly covers a wide range of values, even though j_w^0 is constant. At j_w^0 = 1 mm yr^{-1}, θ ranged from 0.05 to 0.24 m^3 m^{-3}; at 10 mm yr^{-1}, the range was 0.07 to 0.27 m^3 m^{-3}; at j_w^0 = 10^2 mm yr^{-1}, the range was

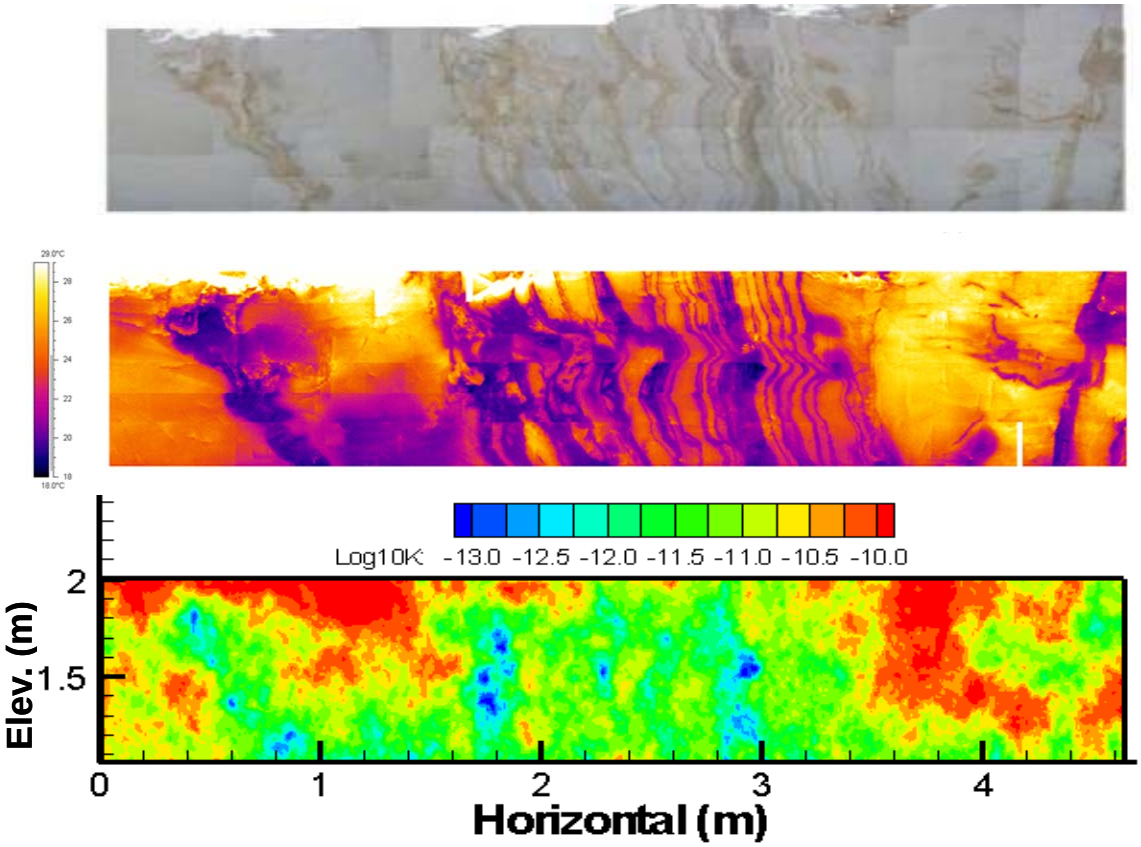

Figure 2.44. Spatial Variability in Texture and Associated Properties in an Outcrop at the Army Loop Road Dike, (a) Photo Mosaic Showing Textural Variations; the Dike Is Located Between 1.8 and 3.6 m; (b) Photo Mosaic of Measured Infrared Temperatures (lower temperature corresponds to higher moisture), and (c) Upscaled Vertical Saturated Hydraulic Conductivity Derived from the Relationship Between Grain-Size Statistics and air Permeability

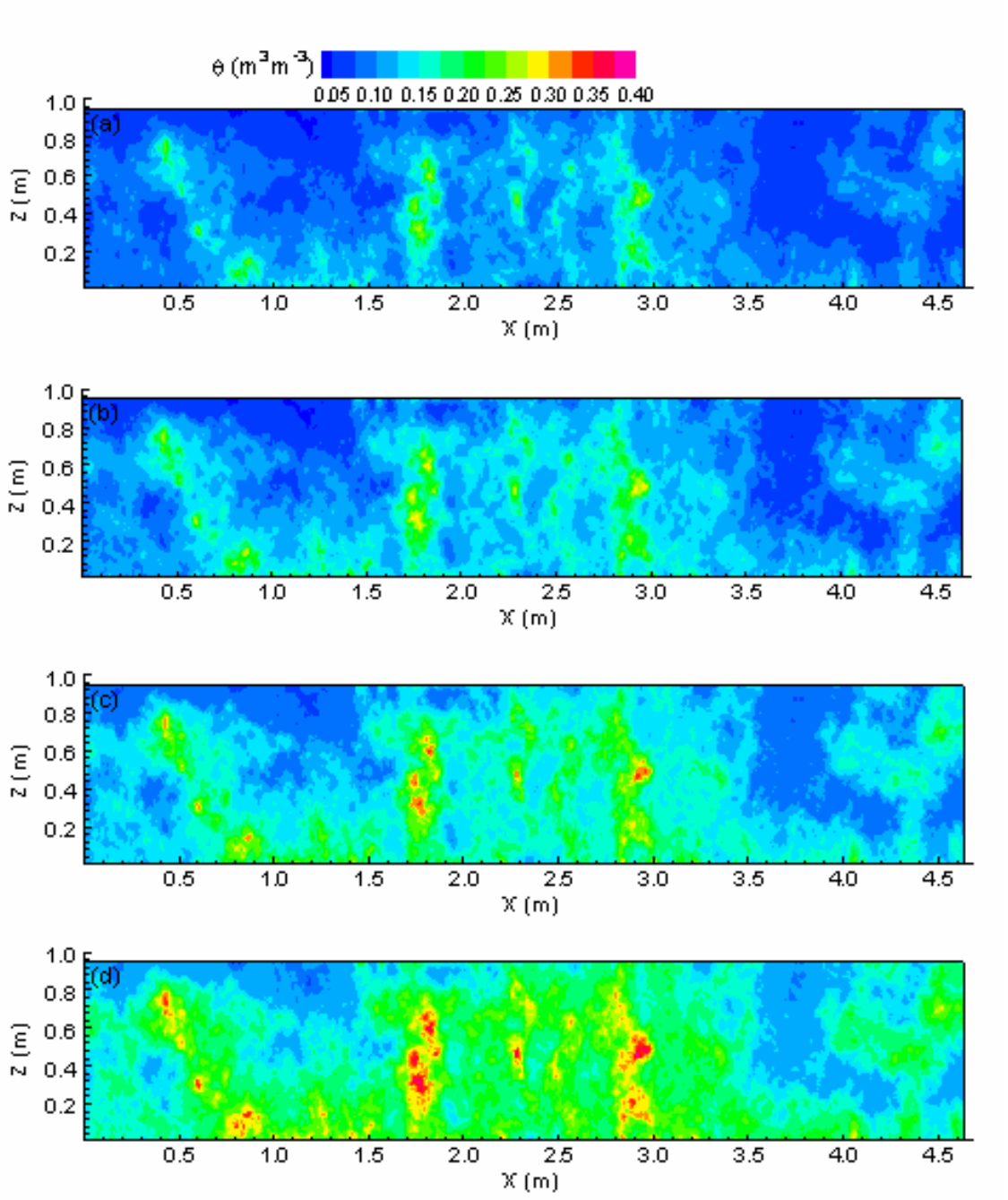

Figure 2.45. Distributions of Volumetric Water Content During Steady Infiltration Under a Constant Surface Flux of (a) 1.0 mm yr^{-1}, (b) 10 mm yr^{-1}, (c) 10^2 mm yr^{-1}, and (d) 10^3 mm yr^{-1}. Domain properties were upscaled to a 2-cm grid.

0.08 to 0.30 $m^3\ m^{-3}$; whereas the entire range of possible θ values was covered at j_w^0 = 10^3 mm yr^{-1}. As the surface flux is increased, the effect of the fine-scale heterogeneities on θ becomes less apparent. This is clearly seen in Figure 2.45b, c, and d within the dike (around $1.8 \leq x \leq 3.6$ m). At low values of j_w^0, θ is a clear reflection of the fine-scale structure, including the range of textures in the dike itself. At these low fluxes, water is easily redirected around less-permeable regions, and only the very smallest of coarse-textured inclusions are penetrated (Figure 2.45a,b). At these values of j_w^0, θ reflects the multiple scales of heterogeneity. As the flux increases, more water is available to start wetting larger, less permeable areas by funneling and bypass flow. Consequently, more of the local-scale heterogeneity is masked (Figure 2.45c) until finally at the highest j_w^0, only the large scale structures are evident (Figure 2.45d).

Elevated water contents have been observed on several occasions during excavations of clastic dikes. When coupled with the obvious lack of water stress in plants growing on these structures, even when adjacent plants on the host matrix were dead, intuition suggested that they might act as rapid flow paths. Interpreting distributions of θ without considering the unsaturated flow dynamics can be misleading as higher θ does not necessarily mean high transport velocities in the vadose zone. This apparent paradox is best illustrated with a plot of subsurface distributions of the dimensionless flux, $\log_{10}\left(\left|\boldsymbol{j}_w\right| / \boldsymbol{j}_w^0\right)$, where j_w is the simulated node centered flux. Distributions of $\log_{10}\left(\left|\boldsymbol{j}_w\right| / \boldsymbol{j}_w^0\right)$ are shown in Figure 2.46. At j_w^0 = 1 mm yr^{-1}, the sediments are mostly unsaturated with $\log_{10}(-\psi)$ around 2.9. At this value of ψ, K(ψ) is highest in the fine-textured sediments, and as a result, flow channels form near the upper boundary, predominantly in the fine-textured sediments, and propagate downward following the paths of highest conductivity Figure 2.46. In the early stages of infiltration, the distribution of the flow paths is clearly dependent on the underlying structure of the heterogeneity as water is redirected or funneled from regions of low conductivity to regions of high conductivity. At the low fluxes, there is insufficient water to overcome the entry pressure of the coarser sediments, and these regions are essentially bypassed, except for the small isolated inclusions.

Following the formation of a channel, and depending on its size, the channel may conduct enough water to overcome the entry pressure of low-permeability regions, resulting in wetting of small isolated regions. Larger regions of low permeability, however, require larger amounts water to initiate wetting than might be available from these channels, and consequently, flow is diverted around the coarse textured regions at low input fluxes. This can be clearly seen in Figure 2.46a and b in the region near 3.7 m where water is diverted around the coarse region until the input flux reaches 10^2 mm yr^{-1} (Figure 2.46c) while smaller coarse-textured regions within the dike, e.g., at x=2.5 m, show increasing velocities at much lower fluxes. As the input flux increases, the $\log(-\psi)$ continues to decrease and the K(ψ) of the coarse-textured regions eventually surpasses that of the fine-textured regions (Figure 2.46b). The high conductivity regions can now carry more water, and larger areas of the coarse sediments start to wet up with a corresponding increase in j_w. The result is a decrease in the difference in j_w between the fine and coarse textures. This trend continues until a critical value of j_w^0 where K(ψ) for the coarse and fine sediments intersect, and the difference in flux between the fine and coarse textures essentially disappears (Figure 2.46c). As the j_w^0 increases further, the K(ψ) of the coarse sediments surpasses that of the fine sediments, and a reversal in the distribution of $\log_{10}\left(\left|\boldsymbol{j}_w\right| / \boldsymbol{j}_w^0\right)$ becomes apparent (Figure 2.46b).

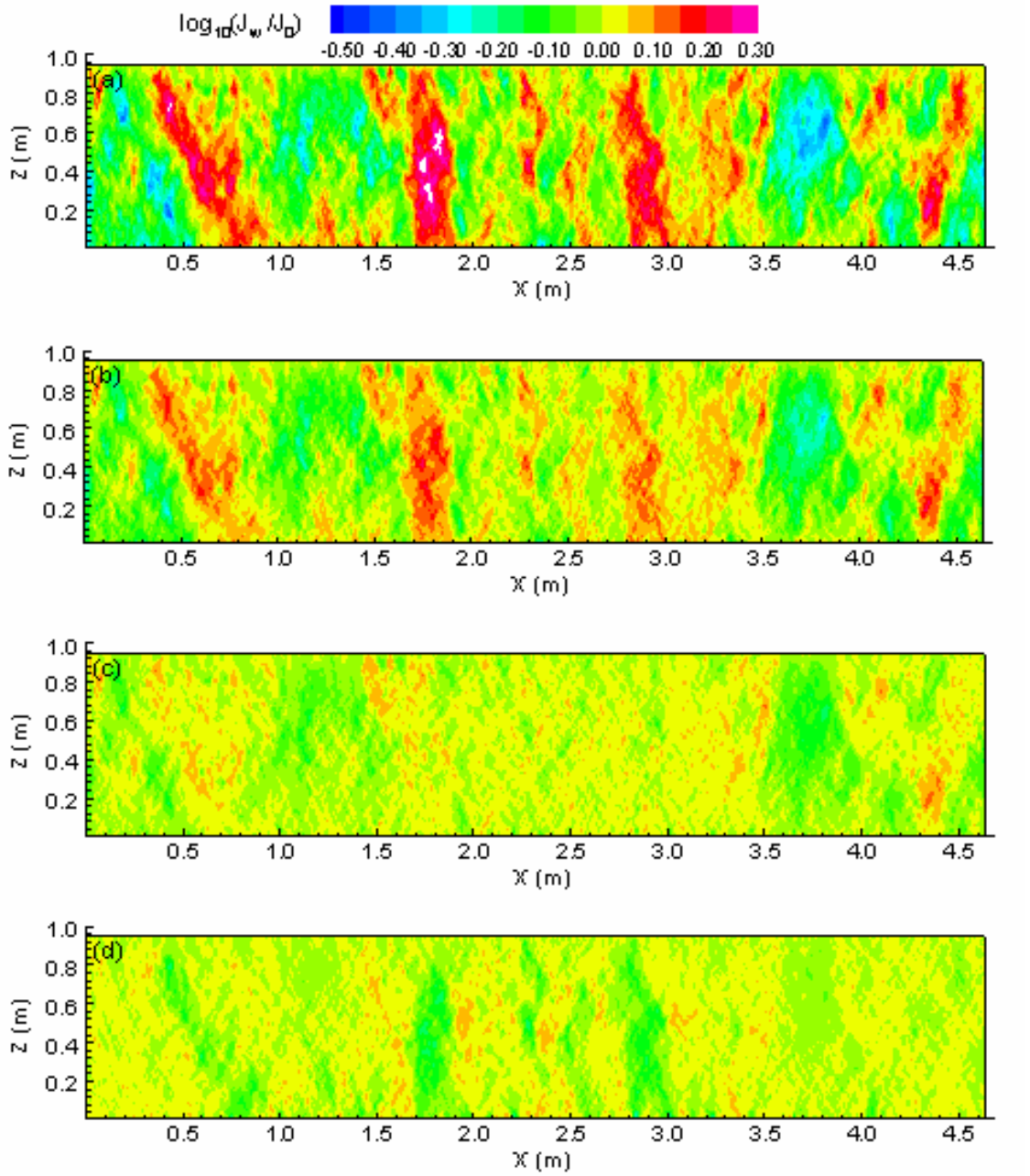

Figure 2.46. Distributions of Dimensionless Water Flux, $\log_{10}\left(\left|j_w\right| / j_w^0\right)$, During Steady Infiltration Under a Constant Surface Flux of (a) 1.0 mm yr^{-1}, (b) 10 mm yr^{-1}, (c) 10^2 mm yr^{-1}, and (d) 10^3 mm yr^{-1}. Domain properties were upscaled to a 2-cm grid.

Regions that were being bypassed earlier because of lower permeability become the dominant regions of transport. There exists two distinct but complementary flow networks, the operation of which is dependent on saturation and hence j_w^0. At fluxes less that the critical j_w^0, the dominant network is the high-permeability, fine-textured regions of the dike. At fluxes equal to the critical j_w^0, the difference between the networks decreases, but is never eliminated. This is because with the range of soils observed in the dike, there is no single ψ at which $K(\psi)$ would be equal for all the soils observed. At j_w^0 greater than the critical flux, the dominant network becomes the high-permeability, coarse textured region that is mostly the host matrix, but also includes the regions of the dike filled by coarser sediments. These complementary flow networks can totally mask the underlying heterogeneity as water is redirected around regions of different texture, depending on j_w^0 and θ. The phenomenon is a reflection of a fundamental characteristic of flow in heterogeneous systems and cannot be replicated with simplified models or systems in which the dike is treated as an equivalent homogeneous medium by assigning field-averaged hydraulic properties. Attempting to model a dike with a 1-D model or conceptualizing it as a thin, vertical structure with effective properties chosen to maximize permeability would fail to show any impact of a dike on subsurface flow. Given the existence of complementary flow networks, the choice of properties to maximize flux under one set of conditions would invariably lead to the minimization of fluxes under the other, and unless an adequate range on input fluxes was simulated, one could easily conclude that dikes had no effect on flow.

Figure 2.47a shows plots of the spatial distribution of θ and $\log_{10}\left(\left|\boldsymbol{j}_w\right| / \boldsymbol{j}_w^0\right)$ at a hypothetical compliance plane located at L = 0.5 m. The distribution of $\theta(x,L)$ clearly reflects the heterogeneity at all levels of j_w^0. In the fine-textured regions of the dike, θ was typically higher with increased flux. As expected, $\theta(x,L)$ was highest at the highest flux with a condition of "near saturated" across the domain. Nevertheless, using measured $\theta(x,L)$ alone to estimate flux would lead to erroneous results. As shown in Figure 2.47b, the distribution of flux along the plane is determined by the input flux. At low input fluxes, water moves faster in the fine-textured regions than in the coarse-textured regions, although the rate may be quite small as it is controlled by the unsaturated hydraulic conductivity function. At high fluxes, the reversal in the flow network is evident as the velocities become higher in the coarse sediments and decrease dramatically in the fine-textured regions.

2.8.2 Synopsis and Implications

The synopsis of findings for this modeling study of the impact of clastic dikes on subsurface flow and their implications are as follows:

- Clastic intrusions, particularly dikes, are common across the Hanford Site, but little is known about their impact of vadose zone flow. In this study, an approach was developed to parameterize a numerical model of a dike outcrop by combining pedotransfer functions with photo mosaics to obtain high-resolution, multi-parameter data sets.

- Model simulations show the existence of two complementary flow networks whose function and structure depends on the input flux and saturation. Under constant flux conditions, the formation of preferential channels is controlled by the structure of small-scale heterogeneity. While this

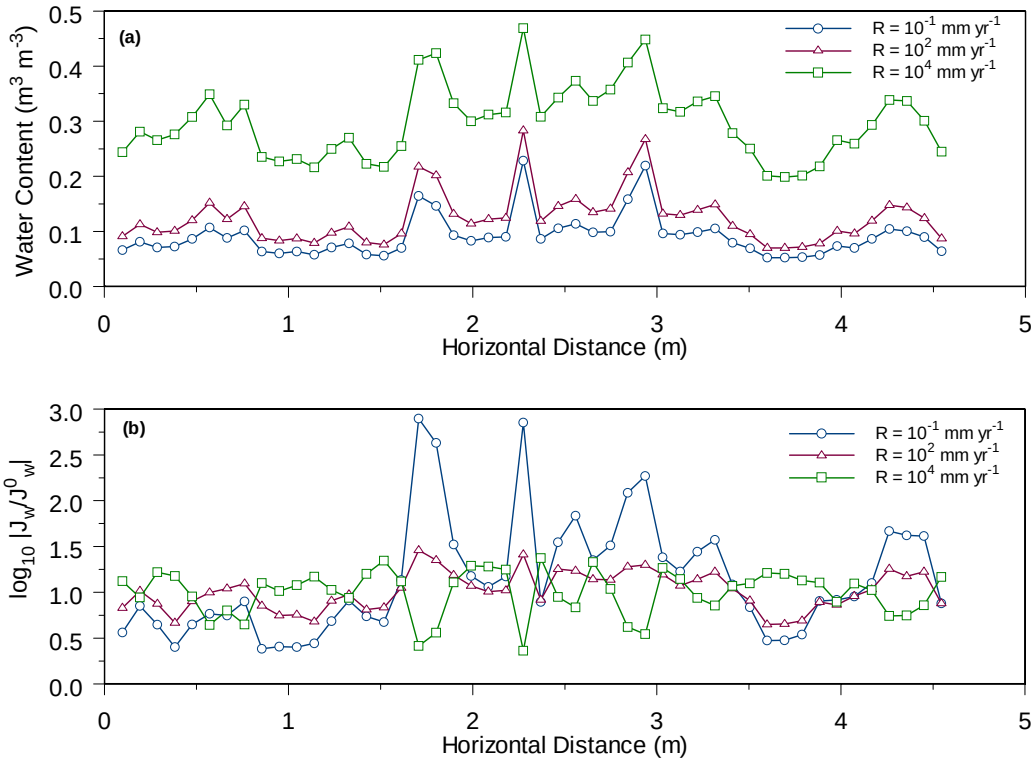

Figure 2.47. The Effect of Surface Input Flux on the Distribution of Water Content and Flux at a Hypothetical Compliance Plane at a Depth L = 0.5 m, (a) Volumetric Water Content, θ(x,L), (b) Dimensionless Water Flux, $\log_{10}\left(\left|\boldsymbol{j}_w\right| / \boldsymbol{j}_w^0\right)$

heterogeneity leads to the development of a complicated flow network with little reflection of the distribution of θ, the resulting flow networks may mask the underlying structure of the heterogeneity as water is redirected around coarse-textured, low conductivity regions. While formation of the networks near the surface is controlled by small-scale heterogeneity, propagation and persistence is somewhat more complex and appears to be dominated by heterogeneities at the larger scale, as these tend to redirect flow at low fluxes.

- The strong dependence of flow structure on saturation suggests that caution is needed for interpreting field-scale tracer tests especially when: 1) boundary conditions vary over time (e.g. constant flux vs. constant head from snow melt, etc.), 2) there are significant differences between wet and dry seasons, and 3) large water table fluctuations have been known to occur. Changes in saturation can completely reverse the flow network, thereby influencing the spatial correlation structure of relative permeability and the location of fast paths.

- The dependence of flow structure on saturation may also affect the distribution of radionuclides and other sorbing contaminants in the vadose zone. Contaminants deposited under a large influx of fluid, for example, may show little subsequent movement unless similar conditions reoccur. Of course, the reoccurrence of similar conditions would result in remobilization of these contaminants and the possible breakthrough at a compliance plane. More importantly, it appears

that modifying the structure of the flow networks (e.g., by changing the infiltration rate) may have some potential for minimizing access to existing contaminants in addition to reducing the rate of migration through the vadose zone.

2.9 Microscale Modeling of Field-Scale Reactive Transport in a Clastic Dike

Field observations of flow and transport in a clastic dike outcrop show complex infiltration patterns and extreme variability in solute transport. Flow simulations predict the existence of complementary flow networks whose function and structure depends on the input flux, saturation, and the underlying fine-scale heterogeneity. An important question therefore relates to the impact of these phenomena on advective, dispersive, and sorptive processes. The strong dependence of flow structure on saturation can be expected to influence the transport of reactive solutes as it could lead to multi-region transport and spatially variable access to mineral surfaces where sorption occurs. This, coupled with spatially variable geochemical properties that control sorption (e.g., exchange capacity, specific surface area) and reaction rates, could impact the spatial distribution of radionuclides and other sorbing contaminants though exclusion at multiple scales. Contaminants deposited under a particular set of conditions could very well become inaccessible to the natural fluxes of water that would typically be unable to access flow networks created under large fluxes typical of subsurface leaks from point sources.

Owing to the lack of proven methodologies for upscaling geochemical parameters, such as distribution coefficients, exchange capacity, reactive surface areas, and kinetic constants, there is much uncertainty in field-scale simulations of reactive transport based on laboratory-measured properties. High-resolution simulations can be useful tools to quantitatively investigate the complex interplay of flow, transport, and reaction processes. However, the general lack of realistically detailed data sets and an inability to directly measure highly resolved model parameters in the field setting have limited widespread use of this method for reactive transport. The objectives of this study were to develop an improved understanding of fundamental relationships between high-resolution characterization information and model parameters of interest and to use microscale or high-resolution simulations to gain an improved understanding of multi-scale heterogeneity on reactive transport. To meet these objectives, pedotransfer functions for geochemical properties, namely exchange capacity and specific surface, were combined with high-resolution images as a means of representing heterogeneous properties at different scales. These data were combined with the flow fields resulting from the STOMP simulations of flow to predict the distribution of reactive solutes in the dike outcrop.

A multicomponent exchange model for strontium was used to predict transport and reactions using the CRUNCH reactive transport simulator. A total of 10 component species, including NO_3^-, Sr^{2+}, H^+, HCO_3^-, Ca^{2+}, Na^+, K^+, Cl^-, Mg^{2+}, and SO_4^-, were included in the model. In addition, 30 secondary aqueous complexes were considered, including CO_2 (aq), CO_3^{2-}, $CaCO_3$ (aq), $CaCl^+$, $CaCl_2$(aq), $CaHCO_3^+$, $CaNO_3^+$, $CaOH^+$, $CaSO_4$ (aq), $SrCl^+$, $SrOH^+$, $SrSO_4$ (aq), $SrCO_3$ (aq), $SrNO_3^+$, HCl(aq), HNO_3 (aq), KCl(aq), KSO_4^-, $MgCO_3$ (aq), $MgCl^+$, $MgHCO_3^+$, MgSO4 (aq), $NaCO_3^-$, NaCl(aq), $NaHCO_3$ (aq), NaOH(aq), $NaSO_4^-$, OH^-, $NaNO_3$ (aq), and $MgNO_3^+$. Equilibrium reaction stoichiometry and thermodynamics were obtained from the EQ3/6 database. Four minerals were considered as potential precipitates—calcite, strontianite, brucite, and gypsum—assuming the same intrinsic reaction rates from previous studies and transition-state theory. Spatially variable cation exchange capacities and specific surface areas were assumed to be applicable. These were derived from pedotransfer functions based on

grain size distributions and selectivity coefficients determined in the column experiments. Transport was simulated on a 2-D vertical outcrop of the dike with dimensions 4.7 m long × 1 m deep with a grid spacing of about 1 mm (> 3×10^6 nodes). The 2-D distributions of moisture contents and velocities for input fluxes j_w^0 of 1, 10, 10^2, and 10^3 mm yr^{-1} resulting from the STOMP simulations were used in the transport simulations. Calcite was assumed to be uniformly distributed throughout the profile with a 1% volume fraction, and strontium was assumed to be initially absent. A constant influx of tracer consisting of 4.7 g L^{-1} of strontium chloride and 47.5 g L^{-1} magnesium chloride dissolved in Columbia River water was applied at the surface.

2.9.1 Results

Figure 2.48a shows a photo mosaic of the dike outcrop derived from visible images whereas Figure 2.48b shows the mosaic resulting from infrared images. These data were combined with pedotransfer functions for hydraulic and geochemical properties to generate high-resolution distributions of porosity (Figure 2.48c) and cation exchange capacity (Figure 2.48d) as well as specific surface area. Zones of fine texture in Figure 2.48a correspond to zones of higher antecedent moisture and cooler temperatures (Figure 2.48b) because of the higher water-holding capacity of these zones. The higher porosities derived for these regions are also consistent with the expectation of higher porosities in sediments of finer texture.

Figure 2.48d shows the distribution of cation exchange capacity predicted at unmeasured locations using pedotransfer functions and physical properties derived from the photo mosaics. Published analyses of basic soil physical properties show high correlations between surface area and both clay content and cation exchange capacity. In dry soils, the surface reactivity is dominated by the clay-size fraction; thus, higher cation exchange capacities can be expected in zones of higher moisture (finer texture).

Although several examples of the application of reactive transport modeling to field-scale transport have been published, there have been few successful applications of laboratory-derived parameters to the field. The approach giving rise to the results in Figure 2.48d provides an opportunity to estimate the required field parameters at multiple scales. Figure 2.49 shows the initial distribution of adsorbed cations in equivalents per bulk volume in m^3. The maximum concentration of aqueous strontium occurs in the upper regions of the profile, decreasing with depth. The total specific area has been observed to control many of the physical and geochemical properties of natural sediments, and this is supported by the spatial correlation between geochemical and physical heterogeneities.

Figure 2.50 shows the predicted cation and mineral concentrations after 40 d. The aqueous strontium front is non-uniform but somewhat smoother than anticipated, given the scale of the heterogeneities (Figure 2.50a). Some distance ahead of the main plume, the front becomes much less uniform. This is more apparent in Figure 2.50b, which shows the distribution of adsorbed strontium. The highest concentrations of strontium are co-located with zones of finer texture, and the nonuniformity of the front reflects the heterogeneity in sorption and water flux. Calcite ($CaCO_{3(s)}$), strontianite ($SrCO_{3(s)}$), brucite ($Mg(OH)_{2(s)}$), and gypsum ($CaSO_{4(s)}$) were considered as potential precipitates, but they remained under saturated during the simulation. Figure 2.50c shows the distribution of calcite ($CaCO_{3(s)}$) after 40 d.

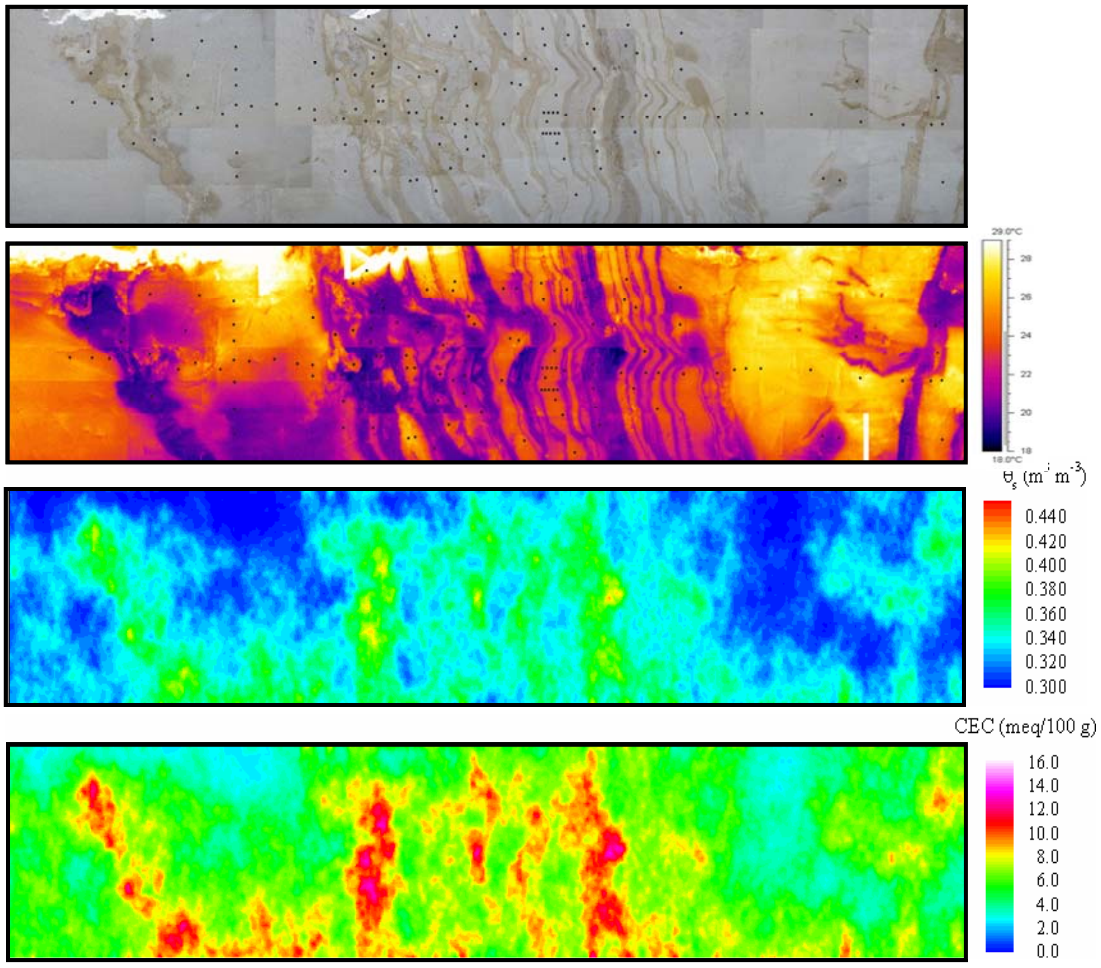

Figure 2.48. Observed Spatial Heterogeneity in Texture and Predicted Variations in Flow and Reaction Parameters (a) Photo Mosaic from High-Resolution Digital Photographs, (b) Photo Mosaic from Infrared Photographs, (c) Saturated Soil Water Content, Assumed Equal to Porosity, and (d) Cation Exchange Capacity

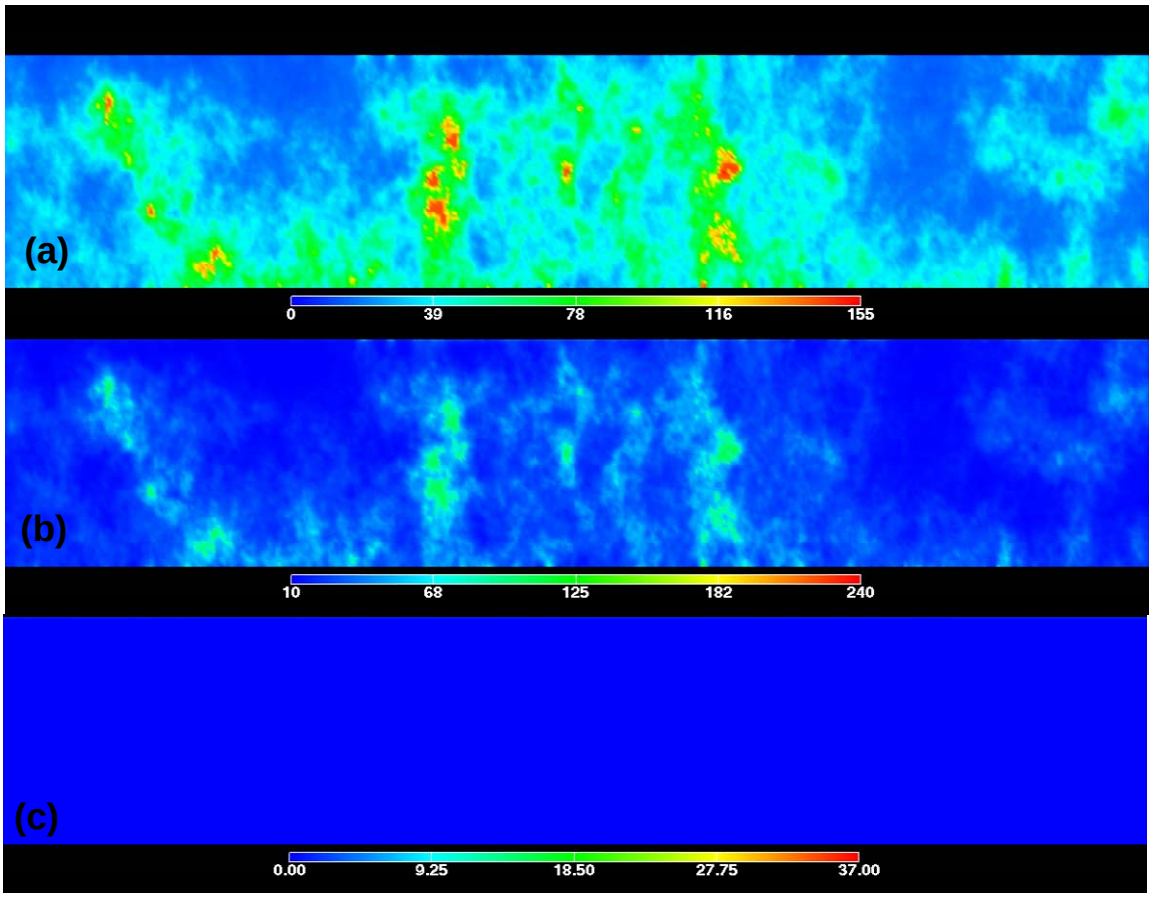

Figure 2.49. Initial Distribution of Adsorbed Cations, (a) Calcium, (b) Magnesium, and (c) Strontium

Only 1% of calcite was initially present in the sediments, and as the tracer solution migrated through and carbonate (CO_3^{2-}) became more available in the system, calcite dissolved and was leached down through the profile (Figure 2.50c). Although the dissolution front appears relatively uniform, distinct zones of elevated calcite concentrations are evident and appear to be correlated with the flow network. The increased availability of carbonate also led to the formation of magnesite ($MgCO_{3(s)}$) and strontianite (Figure 2.49d). The nonuniform calcite dissolution controls strontianite precipitation and mobility through competition for exchange sites and the creation of conditions ideal for strontianite precipitation. The shape of the strontianite precipitation front is qualitatively similar to that of the calcite dissolution front.

In addition to mineral precipitation and dissolution, competitive ion exchange involving Mg^{2+}, Ca^{2+}, Sr^{2+}, K^+, and Na^+ was also predicted. Figure 2.51 shows the predicted aqueous concentrations of calcium (Figure 2.51a), magnesium (Figure 2.51b), and strontium (Figure 2.51c). The predicted spatial distributions of adsorbed cations after 40 d are shown in Figure 2.52. Both the aqueous and adsorbed phases show significant effects of the multiscale physical and geochemical heterogeneities. There is clear evidence of a preferential flow network as flow bypasses regions of low permeability to find regions of higher permeability. These results are consistent with field observations at experimental sites and in waste sites where well-defined chromatographic separation of cations has been observed.

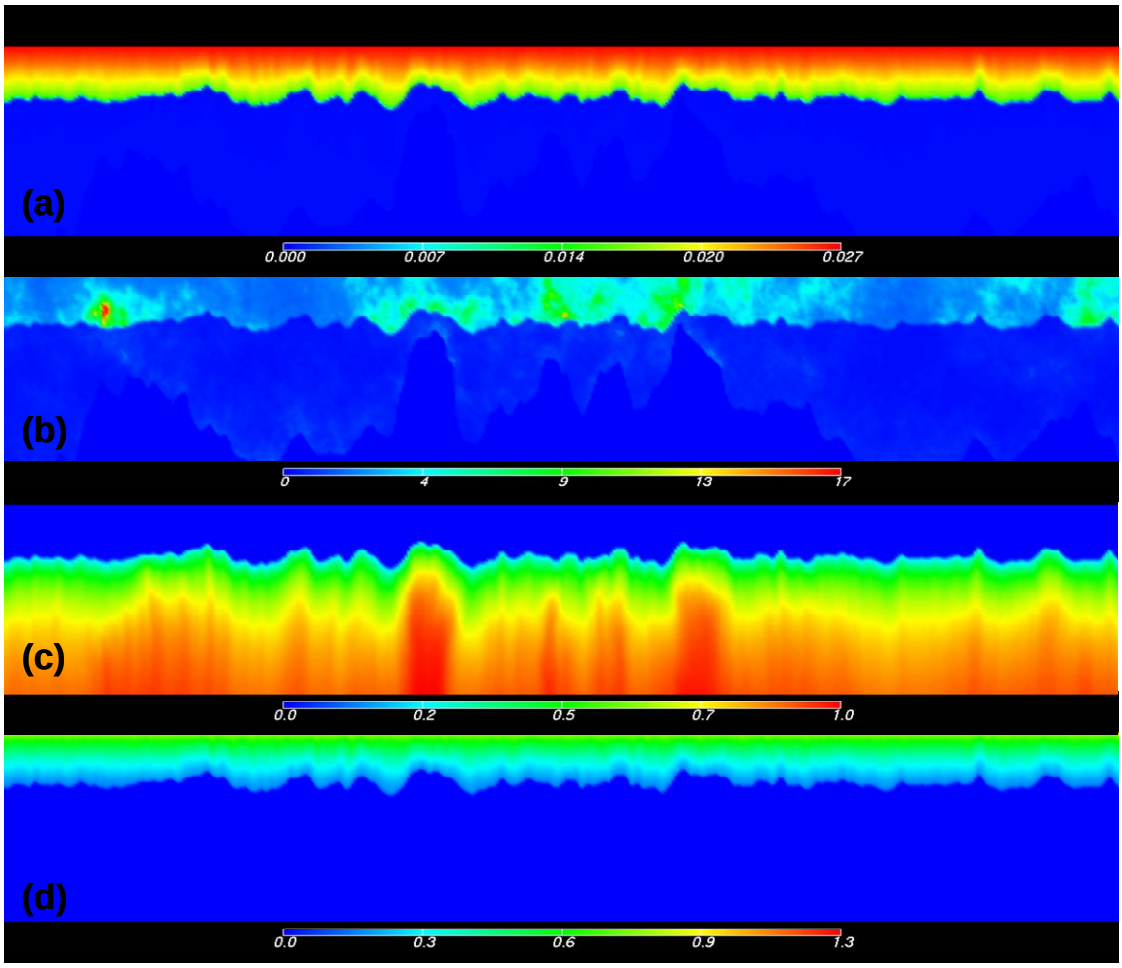

Figure 2.50. Predicted Cation and Mineral Concentrations after 40 d, (a) Aqueous Strontium, (b) Adsorbed Strontium, (c) Calcite, and (d) Strontianite

2.9.2 Synopsis and Implications

The synopsis of findings for microscale simulations of multicomponent reactive transport in heterogeneous sediments and their implications are as follows:

- Unsaturated flow in heterogeneous sediments from a clastic dike outcrop shows the existence of two complementary flow networks whose function and structure depends on the input flux and saturation. The formation of these networks is controlled by multi-scale heterogeneity in physical properties that are also correlated with geochemical properties.

- The strong dependence of flow structure on saturation can be expected to influence the transport of reactive solutes as it could lead to multi-region transport and spatially variable access to mineral surfaces where sorption occurs.

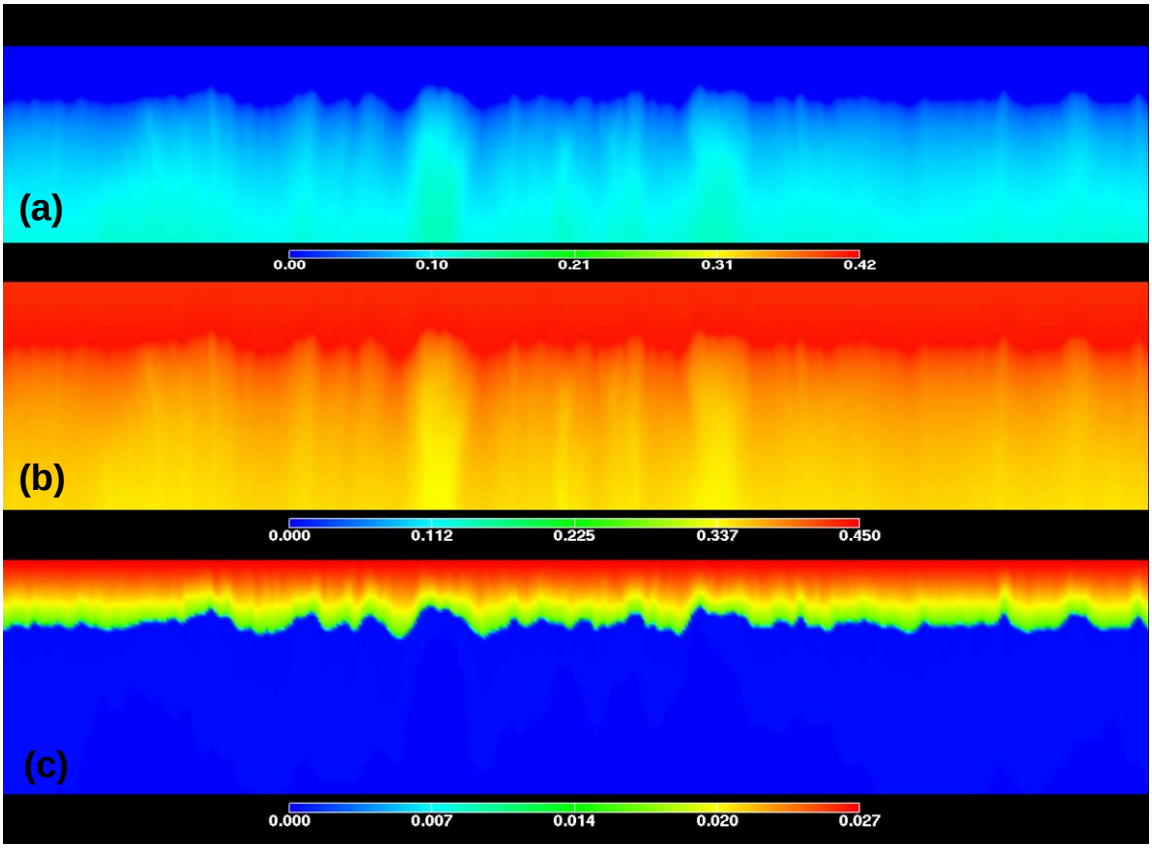

Figure 2.51. Predicted Aqueous Concentrations after 40 d, (a) Calcium, (b) Magnesium, and (c) Strontium

- Spatially variable geochemical properties that control sorption (e.g., exchange capacity, specific surface area) can be predicted from spatially variable physical properties represented by grain-size statistics providing a means for realistic parameterization of high-resolution transport models for the first time.

- High-resolution multicomponent reactive transport modeling is a useful tool for understanding the interplay between flow, transport, and reactions in heterogeneous sediments. Simulation results show the impacts of small-scale heterogeneities that are accentuated at higher recharge rates. Nonuniform access to exchange sites resulted in spatially variable migration of the retarded strontium front. Furthermore, the mobility of the strontium front and its concentration were controlled by the nonuniform dissolution of calcite.

- These findings may have implications for the interpretation of contaminant distributions and the design of remedial actions. Multicomponent reactive transport is sensitive to the hydraulic behavior of the system and properties used to describe the unsaturated properties. Accessing zones of high contaminant concentrations in the subsurface may lead to consideration of the conditions that led to the distributions.

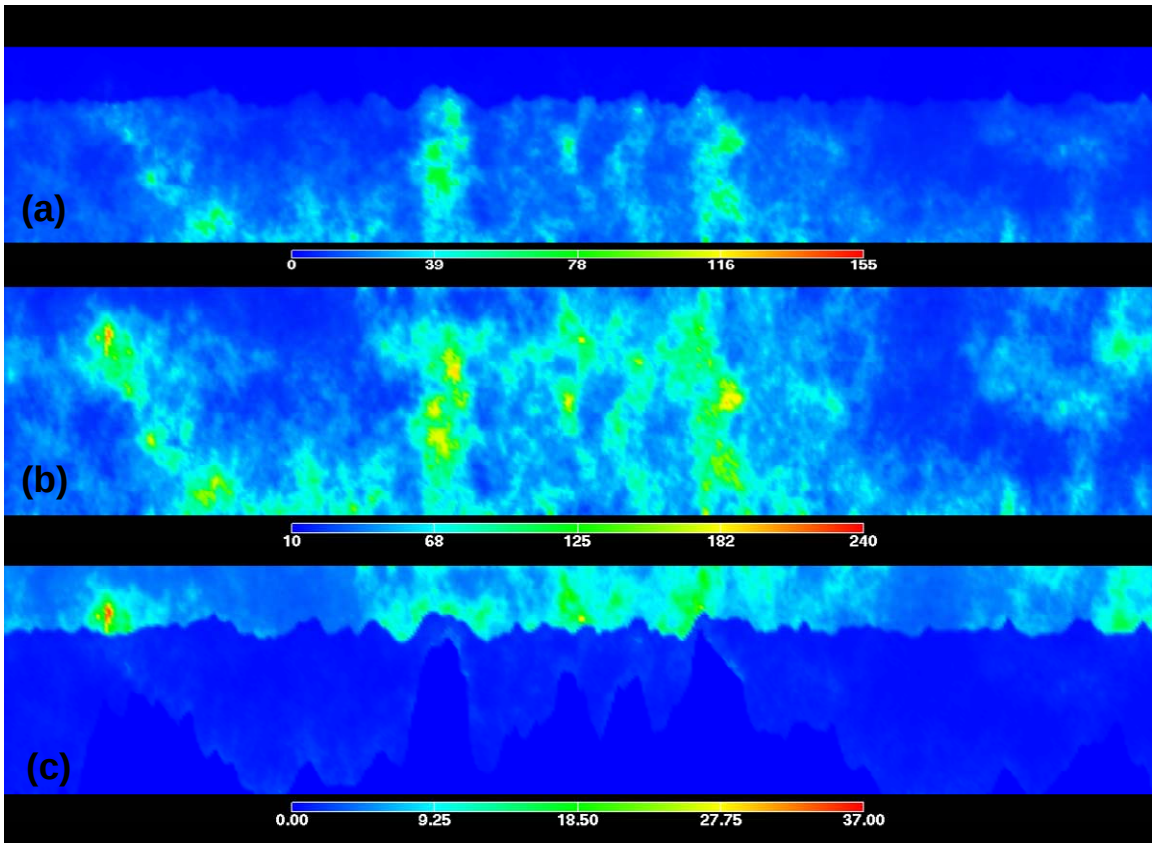

Figure 2.52. Predicted Spatial Distribution Adsorbed Cations after 40 d, (a) Calcium, (b) Magnesium, and (c) Strontium

2.10 Field-Scale Observations of Coupled Flow and Reactive Transport

The migration of radionuclides through the vadose zone involves interactions between complex highly concentrated ionic solutions and heterogeneous sediments. Field-scale reactive transport behavior is therefore affected by physical and geochemical heterogeneities under varying water contents. Multicomponent sorption models that include time-varying solution compositions rather than constant K_d models may be more appropriate for describing the transport of reactive contaminants because of the competition for sorption sites. Yet, little has been done to develop characterization tools to obtain the parameters required to apply these models at the field scale. Laboratory studies conducted under the VZTFS have identified, for example, correlations between cation exchange capacity and grain-size statistics, and it is known that responses of many geophysical modalities are influenced by sediment properties. Traditional laboratory-scale experiments and characterization studies at the batch and column scale are fundamental components in developing a mechanistically predictive understanding of reactive transport. Field experiments provide a bridge between parameter relationships developed in small-scale laboratory studies of limited dimensionality to the field-scale transport behavior. It is only through the study of transport behavior across multiple scales that techniques for parameter upscaling can be developed for the multi-scale systems typical of the field.

The objectives of this study were to 1) obtain a dataset of couple flow and multicomponent reactive transport observations at the field scale to support model calibration and 2) determine the relative contributions of physical and geochemical heterogeneities on the transport of multiple interacting chemical species in field-scale transport. The experiment was designed to compare the transport behavior of strontium with and without a competing cation and at two different flow rates. The experiments were conducted at the Army Loop Road clastic dike site.

A 60-m (197-ft) long transect was cleared, leveled, and instrumented with twin-rod TDR probes, installed at 0.5-m (1.6-ft) intervals along the transect to depths of 1.0 m (3.3 ft), 0.8 m (2.6 ft), 0.4 m (1.3 ft), and 0.2 m (0.7 ft). The probes were constructed of 0.25-in stainless steel rods, spaced 7.6 cm (3 in.) apart parallel to the transect (Figure 2.53). Probes were spaced 0.15 m (0.5 ft) apart, perpendicular to the transect. The longest (1-m [3.3-ft]) probe was installed along the mid line of the transect, near the line source, with probes of decreasing length installed with increasing distance from the line source. At the outer edge of the transect, a second set of 1-m (3.3-ft) long probes were installed to capture any deeper lateral movement from the line source. At 2-m (6.6-ft) intervals along the transect, one stainless steel rod of the 2-wire TDR probe was replaced with a stainless steel suction lysimeter configured to form a multipurpose TDR probe (Baumgartner et al. 1994).

In the spring of 2003, 0.2-m (0.65-ft) deep multipurpose TDR probes were installed for use with the existing 0.4-m and 0.8-m (1.3-ft and 2.6-ft) deep multi-purpose probes. The probes served the dual purpose of monitoring matric potential, ψ, and collecting pore water samples for tracer analysis. At a location 30 m (98 ft) along the transect, a set of bimetallic thermocouples were installed to depths of 0.1 m (0.3 ft), 0.2 m (0.7 ft), 0.4 m (1.3 ft), 0.5 m (1.6 ft), and 1.0 m (3.3 ft) to monitor soil temperature. Eight 2-in.-diameter PVC tubes remained as part of the monitoring system from a previous experiment and were used for neutron-probe access tubes. Figure 2.54 illustrates the layout of the transect, including the location of instrumentation and the PVC access tubes.

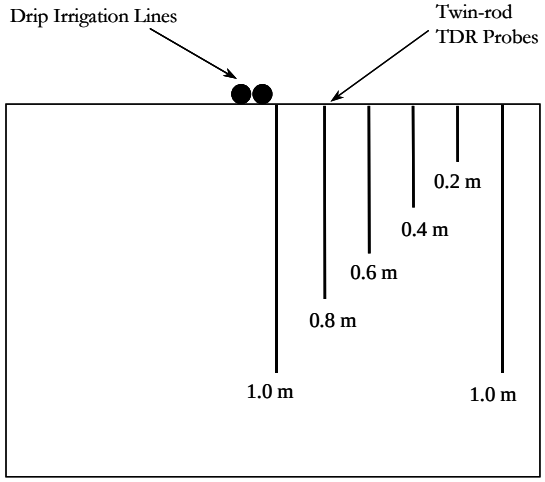

Figure 2.53. Schematic of Probe Installations. Each probe consists of a two-rod TDR probe with a 5-cm (2-in.) inter rod spacing. Probes are spaced 0.5 m (1.6 ft) apart, parallel to the long axis of the trench, and 15 m (50 ft), perpendicular to the long axis.

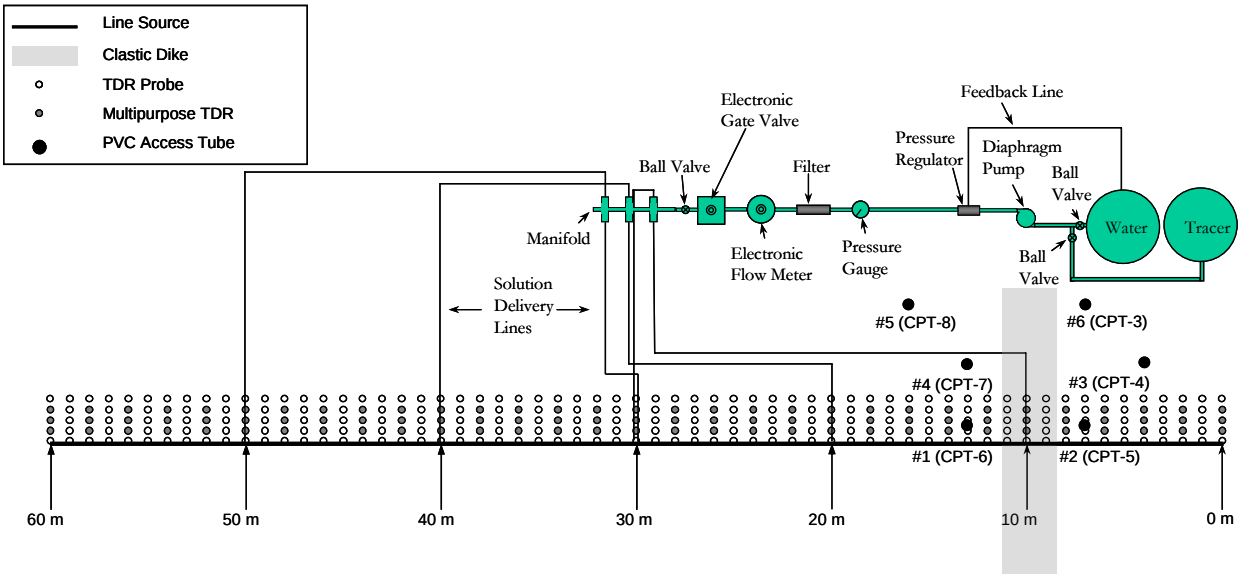

Figure 2.54. Schematic of Experimental Layout Showing TDR Probes and PVC Access Tubes (cone penetrometer [CPT]-#) Used for Crosshole Radar and Neutron-Probe Measurements

Figure 2.55 shows the field site during instrumentation in May 2002. This photo was taken from the west end of the transect (x = 60 m [197 ft]) looking east to the start of the transect (x= 0 m). The clastic dike is centered at x = 10 m (33 ft) and was about 2 m (6.6 ft) wide. The TDR probes were installed at 50-cm (20-in.) spacing, but measurements were made at 1.0-m (3.3-ft) spacing. Multipurpose TDR (TDR + tensiometer) probes were installed on a 2.0-m (6.6-ft) spacing. Using the tensiometers alternated between suction lysimeters for pore water sampling and tensiometers for matric potential measurement.

The entire transect was first covered with a polyethylene sheet, which was laid directly on the surface to minimize evaporation, keep out natural precipitation, and insulate electrical connections from contact with the soil surface. All electrical connections were then made on top of the sheet and covered with a heavy-duty reflective tarp to protect the soil and instruments against diurnal heating and cooling. A drip irrigation line located about 3 cm (1.2 in.) from the center 1.0-m (3.3-ft) deep probe (Figure 2.53) was used to apply water and tracers to the transect. The surface-line source was fed by a 12-V diaphragm pump with a split connection to a 757-L (200-gal) water tank and a 757-L (200-gal) tracer solution tank. The pump operation was controlled by a Campbell Scientific 23X datalogger. The application rate was monitored using a pre-calibrated digital flow meter. The application rate was controlled by adjusting application time or changing line pressure by way of a feedback valve. The 757-L (200-gal) water tank received additional water from an 11,356-L (3000-gal) water tank located onsite. The large water tank was filled approximately every 3 weeks by tanker truck carrying water pumped from the nearby Columbia River. After each tank refill, household bleach (6% sodium hypochlorite) was added at a rate of 102 ppm to minimize the growth of algae and minimize plugging of the drip emitters.

Figure 2.55. The Field Site During FY2003 Instrumentation Looking in an Easterly Direction Along the Transect. The TDR Probes were installed at a 50-cm (19.7-in.) spacing. Weather resistant enclosures containing dataloggers, 16-channel TDR multiplexers, and the 11,356-L (3000-gal) water tank are shown in the background at the left.

During FY 2002, two infiltration experiments were conducted under constant-flux surface-boundary conditions. In the first experiment, water application started on May 14, 2002, with calibration of the irrigation system at a site about 50 m north of the plot. The irrigation system was moved into place on May 31, 2002, and water application started at an average rate of 243 L d^{-1} (64 gpd) on June 1, 2002, for the first experiment. By June 25, 2002, a total of 16,644 L (4397 gal) had been added, and, based on TDR measurements of water content, the system was determined to be at steady state. At this time, a tracer solution consisting of 1.0 g L^{-1} potassium bromide and 7.5 g L^{-1} sodium thiosulfate was applied at the same rate as the irrigation water over a period of 3 days, starting on June 25, 2002. Household bleach (6% sodium hypochlorite) was added at a rate of 260 ppm to the irrigation tank and 120 ppm to the main water tank to minimize the growth of algae and minimize plugging of the drip emitters. Problems with the pump system led to termination of irrigation over the weekend of July 26, 2002, after adding 24,018 L (6,345 gal) of water. Irrigation resumed on July 28 at a similar rate and continued for another 12 days, applying a total volume of 28,558 L (7544 gal) through August 7, 2002. On July 31, 2002, the irrigation rate was increased to 485 L d^{-1} (128.1 gpd) for the second injection experiment. The plot reached steady-state conditions on August 8, 2002, at which time the irrigation source was switched from the water tank to the tracer tank. For this second experiment, the tracer consisted of 1.0 g L^{-1} potassium bromide, 10.0 g L^{-1} sodium thiosulfate, and 1.3 g L^{-1} of deuterium. Clorox bleach was added to the main water tank at 116 ppm to control algal growth. The injection protocol was similar to the first experiment, except that injection occurred over a period of 2 days.

In FY 2003, a series of three infiltration experiments were conducted also under constant-flux surface boundary conditions. Water application from the line source began on May 22, 2003, with an average application rate of 485 L d^{-1} (128 gpd). By June 6, 2003, a total of 7325 L (1935 gal) had been added, and, based on TDR measurements of water content, the system was determined to be at steady state. Beginning at 12:00 PM on June 6, 2003, a tracer solution consisting of 4.7 g L^{-1} strontium chloride and 47.5 g L^{-1} magnesium chloride was inadvertently applied to the transect. The tracer application was at the same rate as the irrigation water. Application of the tracer mixture continued until June 8, 2003, when all 757 L (200 gal) of the contents of the tracer tank had been applied to the transect or returned to the irrigation water tank through the pressure feedback line. Application to the transect did not continue until 4:00 AM on June 9, 2003, when the application line was switched over to the irrigation water tank containing the diluted tracer solution. Approximately 140 L (37 gal) of the diluted tracer solution was then applied to the transect before the presence of the diluted tracer solution became apparent and the irrigation tank was disconnected, drained, rinsed, and filled with tracer-free water. The irrigation tank was reconnected and application of tracer-free water was resumed. The second tracer injection began on July 7, 2003. The tracer again consisted of 4.7 g L^{-1} strontium chloride and 47.5 g L^{-1} magnesium chloride. The injection occurred over a 2-day period and at the same rate as the irrigation water. Before starting the tracer injection, the feedback line was connected to the tracer tank. A total of 730 L (193 gal) of tracer solution was applied to the transect before the application line was switched back over to tracer-free water. For the third experiment, the tracer consisted solely of 5.0 g L^{-1} strontium chloride. Tracer injection began on August 7, 2003, and followed the same injection protocol as the second experiment, applying approximately 757 L (200 gal). In addition, for all three experiments, the tracer solution contained sodium hypochlorite, from commercial bleach, at a concentration of 102 ppm.

The tracers used in the first and second experiments consisted of 4.7 g L^{-1} strontium chloride and 47.5 g L^{-1} magnesium chloride. Household bleach (6% sodium hypochlorite) was also present at a concentration of 102 ppm to control algal growth. In the third experiment, the tracer contained 4.9 g L^{-1} strontium chloride and 102 ppm of bleach solution (6% sodium hypochlorite). In all the experiments, tracer salts were dissolved in river water in a separate tank plumbed into the pump system (Figure 2.5). Tracer distributions were determined from pore water samples obtained from the suction lysimeters and analyzed by auto analyzer.

During wetting, the soil profile was monitored for water content, θ, and matric potential, ψ, at 1-hour intervals. Measurements were also made during subsequent drainage phases to obtain data for the drainage branch of $\psi(\theta)$ curve. Movement of the wetting front was monitored using a combination of TDR, neutron probe, and crosshole and surface ground-penetrating radar (GPR). In addition, bulk electrical conductivity was measured using TDR techniques, and these data were used to construct breakthrough curves of the mobile species. Pore water samples are also collected at predetermined sampling times. Sampling was made possible by withdrawing the water from tensiometers and converting them to suction lysimeters. All water samples were analyzed by ICP-OEP for Ca, Mg, Sr, Na, and K. Samples were also analyzed by IC for F, Cl, Br, N, P, and S. At the end of the tracer experiments, a trench was excavated adjacent to the transect, and sediment cores were taken to determine the sorbed concentration of tracers, the mineral composition, and the grain size distributions.

2.10.1 Results

Initially, the TDR response was influenced by diurnal temperature fluctuations that resulted in an over estimation of θ. The problem was ultimately corrected by burying the cables, thereby removing them from direct exposure to the sun. Following this, the data became essentially stable over time.

Figure 2.56 shows examples of the soil water content, θ, measured during the course of the second infiltration experiment in FY 2003. These data are a subset of measurements made with the 0.4-m (1.3-ft) probes located 0.3 m (1 ft) from the line source (see Figure 2.53). Figure 2.56a shows θ(t) at 2.0 m (6.6 ft) along the transect, a region where the soil was mostly a medium sand. The long-term average water content, $\overline{\theta}$, was around 0.20 m^3 m^{-3} and very similar to measurements at 9.0 m (29.5 ft) as shown in Figure 2.56d. Figure 2.56c shows θ(t) at 9.5 m (31.2 ft) where the sediments changed from the sand host material to the dike that was composed of vertical layers of fine sand and silt. The measured θ(t) was much higher with a mean value of around 0.32 m^3 m^{-3} and also much noisier. The increased θ is caused by the finer texture of the dike sediments that tend to have a higher porosity and water-holding capacity because of the finer texture. The finer texture also results in a higher surface electrical conductivity that has been shown to reduce the signal-to noise ratio in TDR measurements, particularly when using long cables. The transition from the dike back to a sand resulted in a sharp decrease in θ, as seen in Figure 2.56d. Measurements shown in Figure 2.56d were made 12 m (35.2 ft) along the transect where the sand was somewhat coarser than near the start of the transect. The change in texture is reflected in reduction in $\overline{\theta}$ to around 0.14 m^3 m^{-3} compared to the measurements at 2.0 m (6.6 ft). These results are consistent with the laboratory column measurements described in Section 2.7. These results show that TDR is a robust approach for fully automated long-term monitoring of water content in Hanford's vadose zone. Measurements can be made at intervals of 1 hour or less, depending on the total number of probes.

Another advantage of the TDR system is its ability to monitor changes in bulk electrical conductivity *in situ*, which in these experiments was used to track the movement of mobile solutes. This is particularly useful in unsaturated flow experiments where the removal of pore fluids for analysis with a high-enough sampling frequency could disrupt the flow field and ultimately affect transport. Figure 2.57 shows examples of breakthrough curves (BTCs) derived from bulk electrical conductivity measurements made using TDR. The discontinuity around DOY 197-198 resulted from a system shut down to accommodate HRR measurements. All the BTC measurements were also made with the 0.4-m (1.3-ft) long probes at various locations along the transect. The variety of shapes of the BTCs illustrates the variability in transport behavior, even over short distances, and shows clear differences between the sand host sediments and the dike. All the curves show the classic increase and decrease in electrical conductivity as the tracer contacts the probe and is then leached out of the influence of the probe, but this is where the similarity ends. Figure 2.57a,b, and d are highly asymmetric, initially showing the characteristic sharply descending limb that changes to a slower rate of decrease after about 194 days. This type of BTC is indicative of multi-region transport in which part of the solute mass travels with the water through the larger pores, and another part is trapped in smaller pores to be released later at a slower rate. This type of preferential movement is typically observed in structured soils (e.g., fine textured, aggregated soils) and often at relatively high moisture contents. Figure 2.57c shows a classic BTC with a slow rise in conductivity to a peak followed by a slow steady decrease to the initial value. Figure 2.57e, f were measured in the dike region and show a more extreme form of multi-region transport. Both curves show an early sharp increase in electrical conductivity followed by a sharp decrease, quickly followed by another sharp increase. This behavior may be expected in the dike, given the structure (see Figure 1.2).

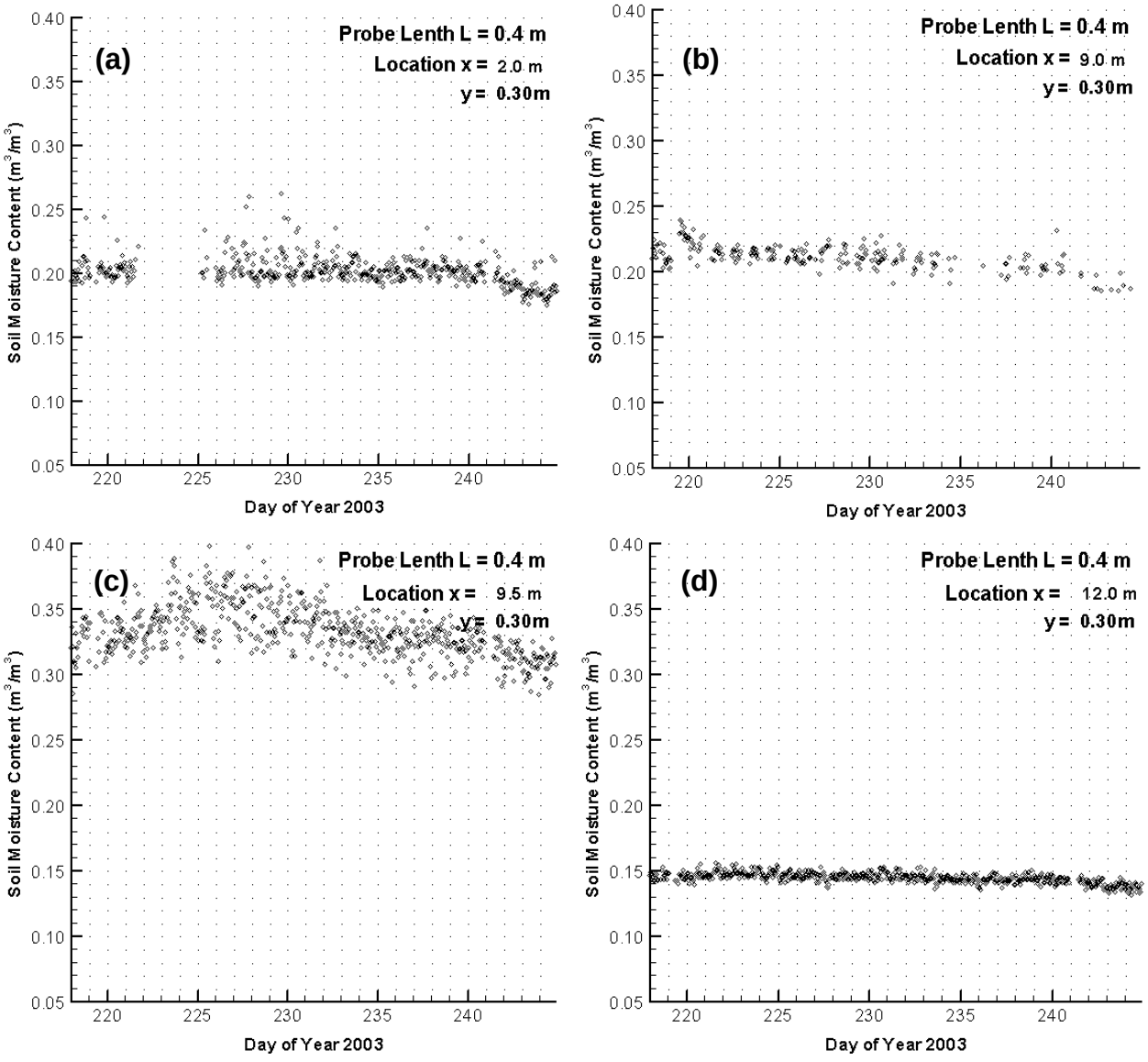

Figure 2.56. TDR-Measured Soil Water Content During the Second Infiltration Experiment in 2003 at Various Distances Along the 60-m (197-ft) Transect at the Army Loop Road Dike Test Site. TDR probe length = 0.4 m (1.3 ft); location = 0.3 m (1 ft) from the line source.

Clastic dikes at Hanford typically consist of laminated sand and silt, often with coarse infilling sediments at the center and silt along the outer edges (silt/clay skins). Transport in the coarse infilled sediments would be qualitatively similar to transport in the host sandy sediments and hence the similarity in the leading edge of the BTCs. The migration of solute in the silt/clay skins and infillings of finer sand would result in bimodal BTCs as solutes were released at a slower rate from these regions. These features would be missed because of low sampling frequency.

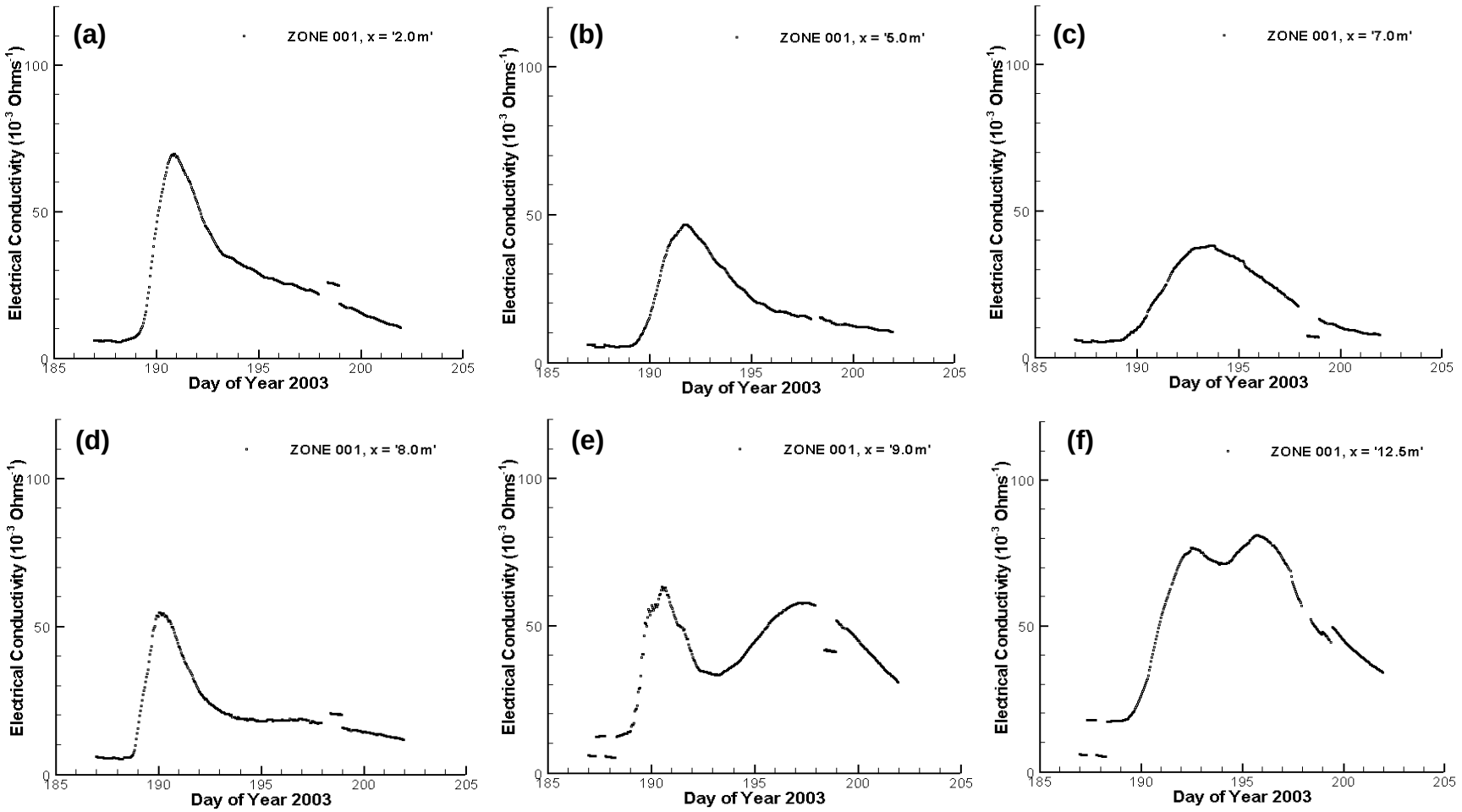

Figure 2.57. TDR-measured Solute Breakthrough Curves During the Second Infiltration Experiment in 2003 at Various Spatial Locations Along the 60-m (197-ft) Transect at the Army loop Road Dike Test Site. TDR probe length = 0.4 m (1.3 ft); location = 0.3 m (1 ft) from the line source.

These results suggest that preferential flow can also be an important transport mechanism in both unstructured soils at relatively low moisture contents and in structured sediments at water contents less than saturation. In both cases, but more so in the dike sediments, a significant portion of the solute was trapped and released over a long period of time. In fact, none of the asymmetric BTCs showing this type of multiregion transport behavior returned to background levels of electrical conductivity by the end of the experiment. This observation could have implications for interpreting groundwater plumes emanating from vadose zone sources, especially when an enhanced infiltration event or a rising water table renews contact with the sediments in which contaminants may be trapped. These trapped sediments could serve as a source of contaminants for a long period.

Figure 2.58 through Figure 2.65 show plots of the 3-D space-time matrix of solute breakthrough at two different depths and distances from the water line source. These data based on solution samples collected using the suction lysimeters spaced 2 m (6.6 ft) apart during the course of the experiment. Thus, measurements were made at only 30-m locations, typically in a daily basis, compared to hourly measurements at over 60 locations with the TDR system. These curves clearly reflect the degree of heterogeneity and its impact on the spatial variability in solute velocity and solute mass recovery. Figure 2.58 shows the space-time distribution of chloride at 40 cm (15.7 in.) deep whereas Figure 2.59 shows the distribution at a depth of 80 cm (31.5 in.). Because of the decrease in $\overline{\theta}_L$ with distance from a line source, the travel time shows an inverse square dependence (see Figure 2.53). As a result of this dependence, the chloride tracer appeared sooner at the 0.8-m (2.6-ft) depth than at the 0.4-m (1.3-ft) depth. Breakthrough curves in the dike sediments (10 m [33 ft]) showed very different responses for the 40- and 80-cm (15.7- and 31.5-in.) depths. At the 80-cm (31.5-in.) depth, the mass recovery of Cl^- was quite low in the dike, and the peak concentrations were about $^1/_{12}$ of those measured in the sandy regions of the profile. The 40-cm (15.7-in.) curves showed less variation in peak concentrations, although the highest concentrations were observed in or near the dike. Given that the 80-cm (31.5-in.) probe is closer to the line source, the water content would have been higher and the mean pore water velocity less than at the 40-cm (15.7-in.) probe, which was farther away. These data show that in the dike itself, the lateral movement of the chloride tracer was much higher than the vertical movement, resulting in higher concentrations and mass recovery at the 40-cm (15.7-in.) probe. Breakthrough curves in the clastic dike were also quite asymmetric, showing a rapid early breakthrough, followed by a decline in concentration and a later increase in a bimodal fashion. Such asymmetry is typical of fractured or aggregated media and is a reflection of some portion of the pore space being initially bypassed. These observations are consistent with the TDR-measured BTCs, although the lower temporal resolution increased the difficulty in parameter estimation. Another striking observation was the absence of heterogeneity effects in the field-averaged curve plotted at 80 m (262 ft) along the horizontal axis. Transport parameters obtained by fitting the average curves to established transport models show an increase in variance or spreading in the transition from the local scale (individual locations) to the field scale (average of all locations). This increase in travel time variance can be attributed entirely to the horizontal variability in the local-scale average solute travel times resulting from the 3-D nature of flow.

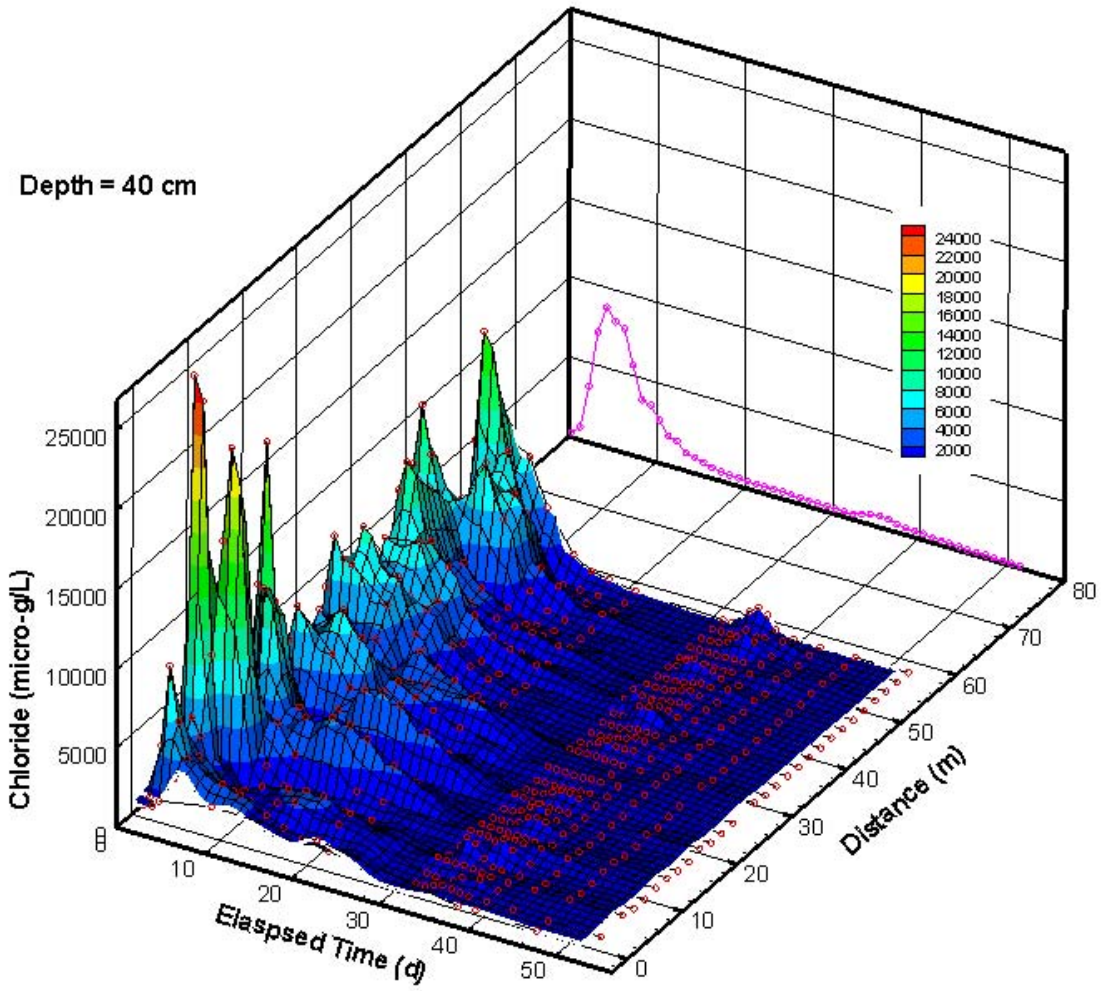

Figure 2.58. Measured Pore Water Chloride Concentration as a Function of Spatial Location and Time at the 40-cm (15.7-in.) Observation Depth at the Army Loop Road Dike Test Site. The field-scale averaged distribution is shown at 80 along the distance axis.

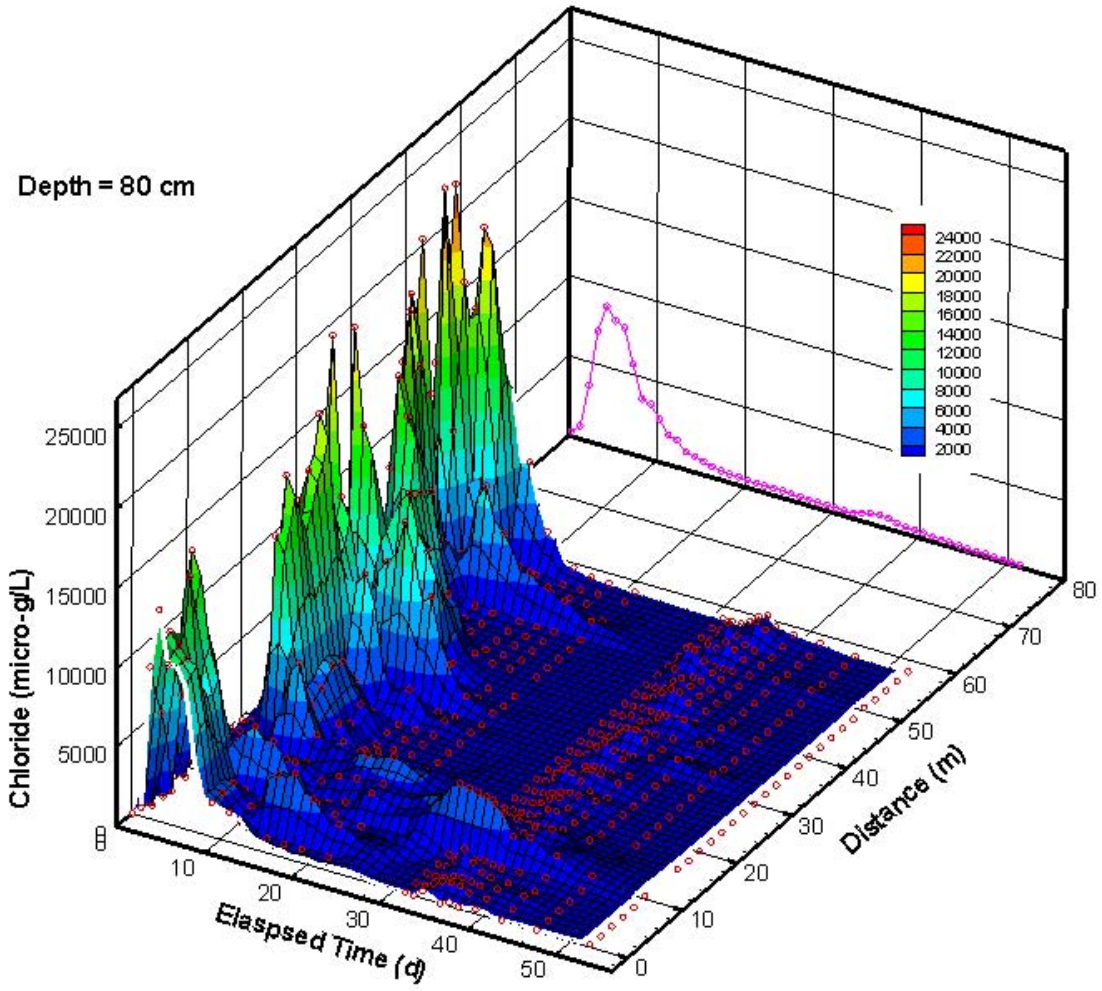

Figure 2.59. Measured Pore Water Chloride Concentration as a Function of Spatial Location and Time at the 80-cm (31.5-in.) Observation Depth at the Army Loop Road Dike Test Site. The field-scale averaged distribution is shown at 80 along the distance axis.

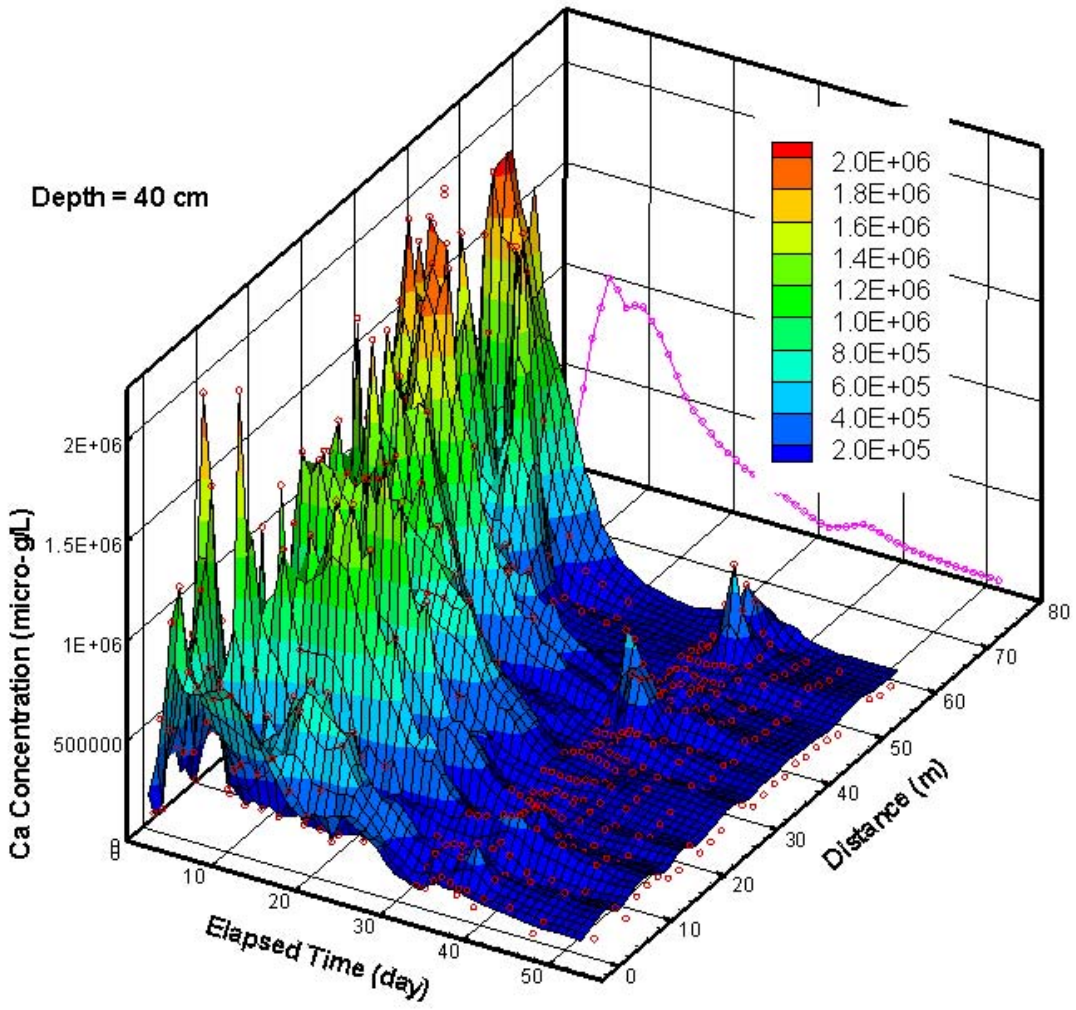

Figure 2.60. Measured Pore Water Calcium Concentration as a Function of Spatial Location and Time at the 40-cm (15.7-in.) Observation Depth at the Army Loop Road Dike Test Site. The field-scale averaged distribution is shown at 80 along the distance axis.

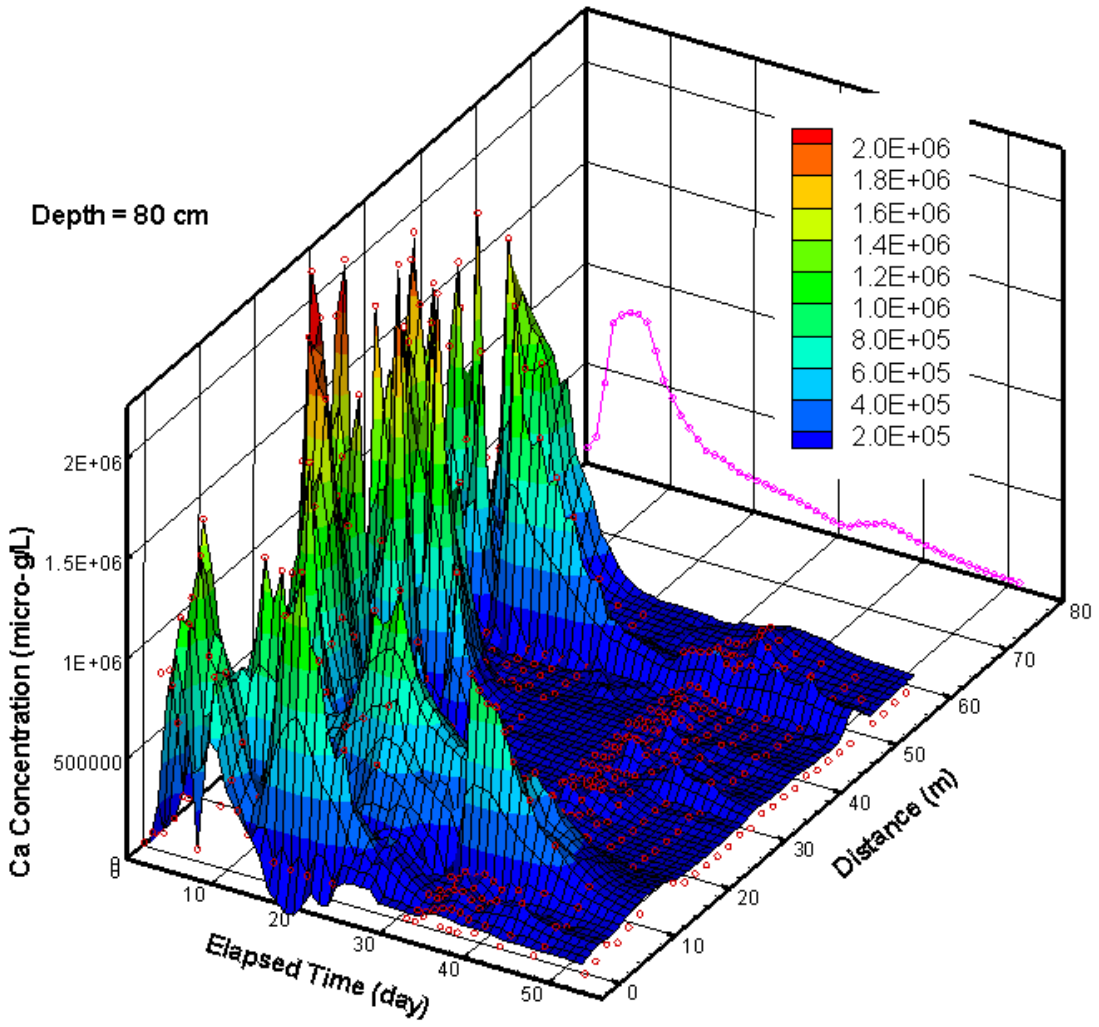

Figure 2.61. Measured Pore Water Calcium Concentration as a Function of Spatial Location and Time at the 80-cm (31.5-in.) Observation Depth at the Army Loop Road Dike Test Site. The field-scale averaged distribution is shown at 80 along the distance axis.

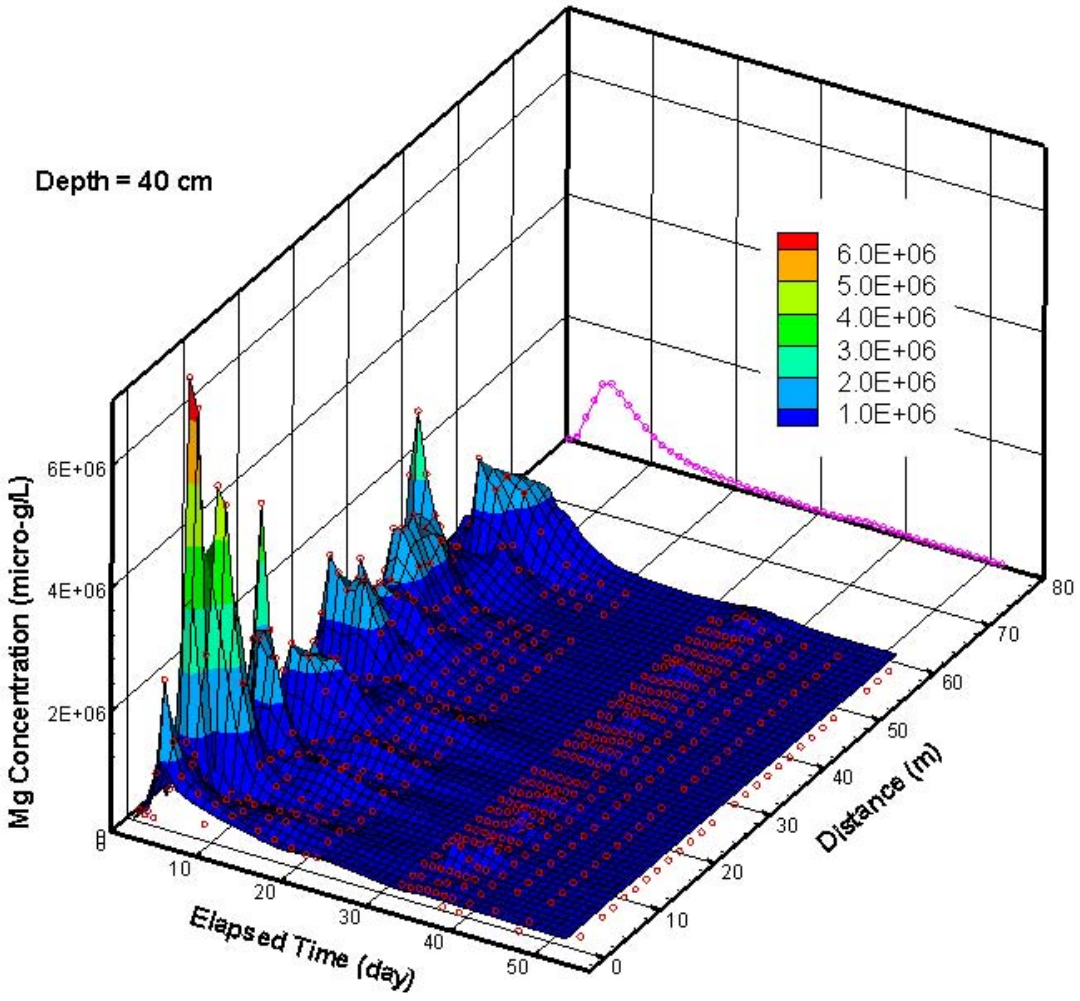

Figure 2.62. Measured Pore Water Magnesium Concentration as a Function of Spatial Location and Time at the 40-cm (15.7-in.) Observation Depth at the Army Loop Road Dike Test Site. The field-scale averaged distribution is shown at 80 along the distance axis.

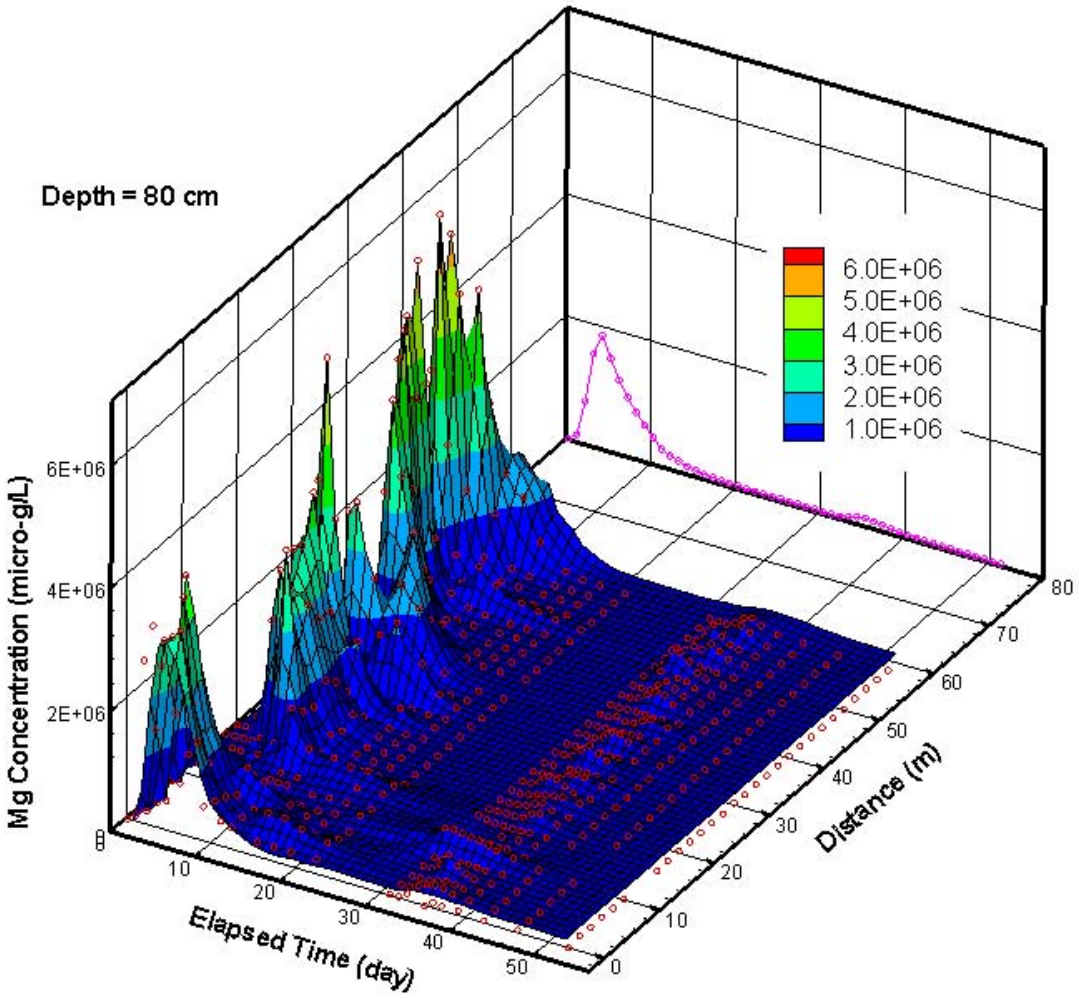

Figure 2.63. Measured Pore Water Magnesium Concentration as a Function of Spatial Location and Time at the 80-cm (31.5-in.) Observation Depth at the Army Loop Road Dike Test Site. The field-scale averaged distribution is shown at 80 along the distance axis.

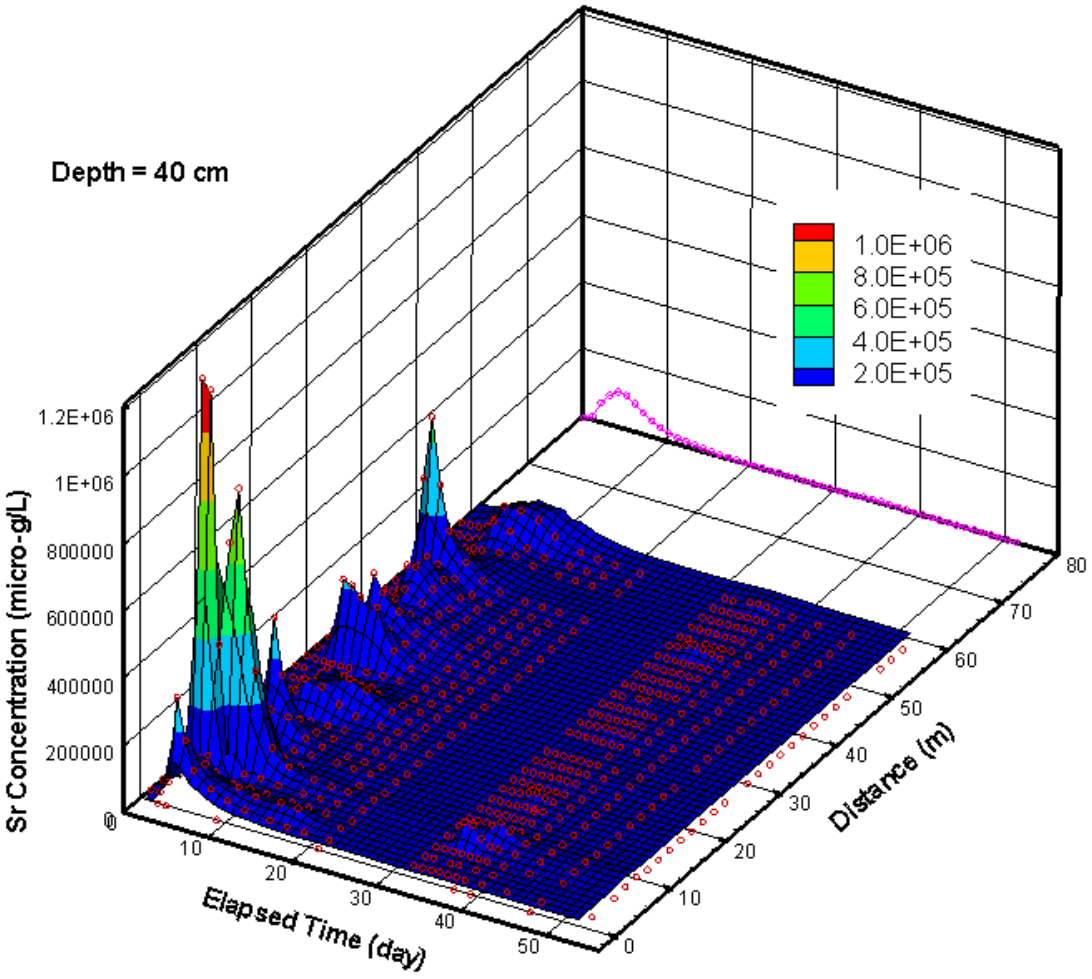

Figure 2.64. Measured Pore Water Strontium Concentration as a Function of Spatial Location and Time at the 40-cm (15.7-in.) Observation Depth at the Army Loop Road Dike Test Site. The field-scale averaged distribution is shown at 80 along the distance axis.

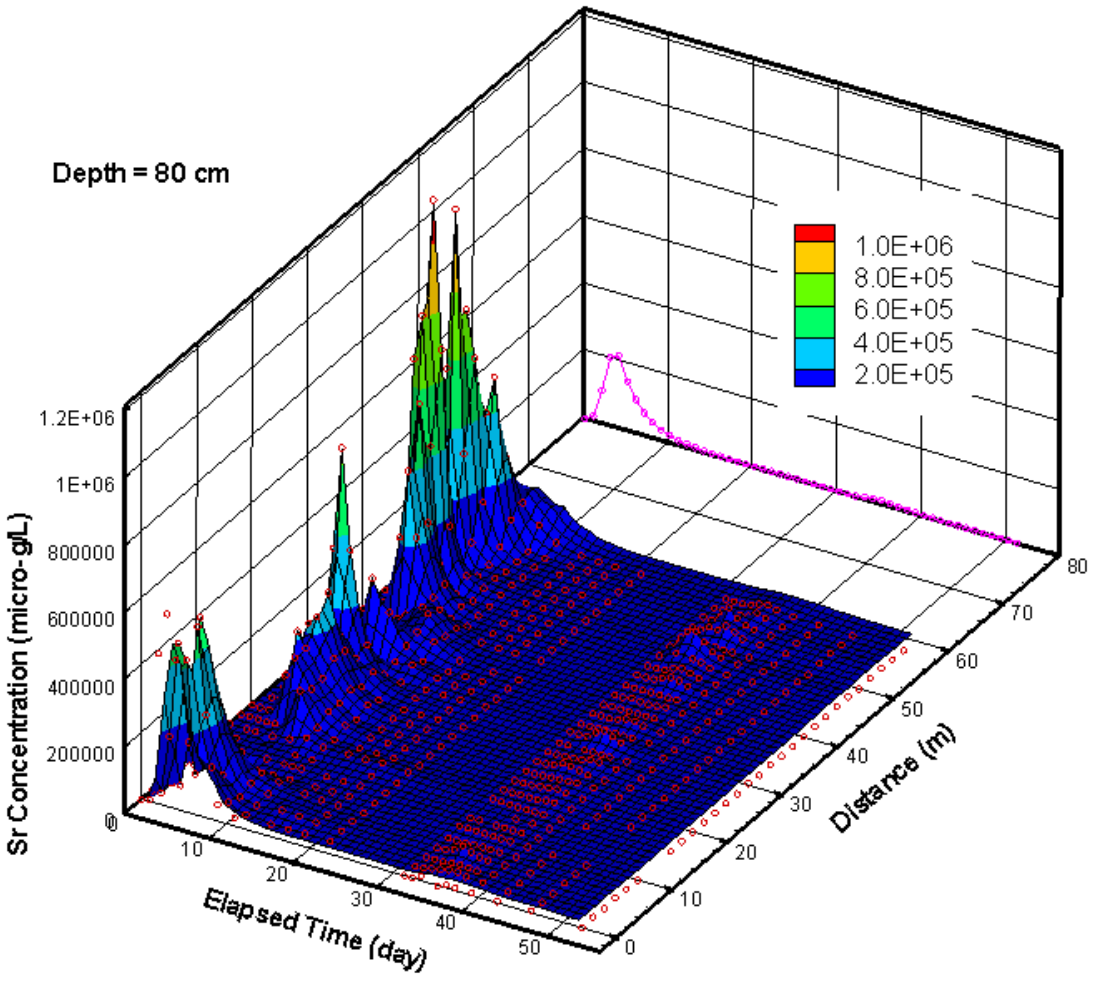

Figure 2.65. Measured Pore Water Strontium Concentration as a Function of Spatial Location and Time at the 80-cm (31.5-in.) Observation Depth at the Army Loop Road Dike Test Site. The field-scale averaged distribution is shown at 80 along the distance axis.

Unlike column experiments in which several pore volumes can be eluted to displace the initial exchange species, the design of the field experiment was constrained by limits on the total amount of water and solutes that could be injected. The compromise was a design based on a pulse input of tracer. Although such a design could not be expected to give rise to the typical retarded fronts observed in laboratory columns, it was expected to provide a realistic field-scale data set obtained under controlled boundary conditions at a well characterized site for use in model calibration. The observed cation breakthrough curves are reflective of ion exchange processes occurring in the porous medium and the nature of the boundary condition. Figure 2.60 through Figure 2.65 show the breakthough of cations.

Table 2.3 shows the transport parameters fitted using a variety approaches, including the convective dispersive equation, the convective lognormal transport equation, and temporal moment analysis.

Table 2.3. Fitted Transport Parameters for Field-average Breakthrough Curves from the Field Transport Experiments

		Depth (m)									
		0.40	**0.80**	**0.40**	**0.80**	**0.40**	**0.80**	**0.40**	**0.80**	**0.40**	**0.80**
Analysis	**Parameter**	**Cl^-**		**Ca^{2+}**		**Mg^{2+}**		**K^+**		**Sr^{2+}**	
1-D CDE	v ($m\ d^{-1}$)	0.038	0.115	0.073	0.062	0.082	NA	0.033	0.031	0.076	0.129
	D ($m^2\ d^{-1}$)	$4.40 \cdot 10^{-3}$	$1.62 \cdot 10^{-2}$	0.003	0.000	0.005	NA	0.000	0.000	0.002	0.007
	α (m)	0.117	0.141	0.040	0.003	0.057	NA	0.010	0.014	0.030	0.058
	T_{mean} (d)	10.645	6.965	10.959	12.903	9.756	NA	24.242	25.806	10.526	6.202
CLT	σ	0.684	0.561	0.311	0.091	0.397	NA	0.157	0.186	0.272	0.370
	μ	2.091	1.775	6.255	6.465	6.149	NA	7.100	7.155	6.233	5.666
Moments	T_{mean} (d)	11.994	10.921	12.903	13.559	14.545	NA	23.529	22.222	10.667	6.349
	v ($m\ d^{-1}$)	0.036	0.081	0.062	0.059	0.055	NA	0.034	0.036	0.075	0.126
	D ($m^2\ d^{-1}$)	$6.20 \cdot 10^{-3}$	0.038	0.005	0.002	0.006	NA	0.000	0.001	0.002	0.010
	α (m)	0.1705	0.466	0.083	0.039	0.101	NA	0.007	0.027	0.032	0.081
2-D CDE	v_z ($m\ d^{-1}$)	0.049	0.132	0.078	0.071	0.114	NA	0.034	0.001	0.083	0.139
	v_y ($m\ d^{-1}$)	0.037	0.086	0.014	0.007	0.012	NA	0.000	0.003	0.014	0.026
	D_z ($m^2\ d^{-1}$)	$9.77 \cdot 10^{-3}$	0.018	0.005	0.000	0.020	NA	0.000	0.109	0.005	0.019
	D_y ($m^2\ d^{-1}$)	$6.41 \cdot 10^{-3}$	0.119	0.000	0.000	0.000	NA	0.000	0.000	0.000	0.000
	α_z (m)	0.199	0.14	0.064	0.005	0.175	NA	0.011	101.77	0.059	0.137
	α_y (m)	0.174	1.383	0.020	0.004	0.025	NA	5.049	0.024	0.012	0.018

CDE—Convective Dispersive transport model
CLT—Convective Lognormal transport model
Moments—Time moment Analysis

V = mean pore water velocity
D = dispersion coefficient
α = dispersivity

μ = mean travel time
σ = travel time variance

Figure 2.60 and Figure 2.61 show the distribution of calcium, Ca^{2+}, at 0.4 and 0.8 m (1.3 and 2.6 ft), respectively. No calcium was added to the tracer, so the Ca^{2+} in the pore water is composed of calcium from the river water used in the infiltration test, calcium released from the sediments by ion exchange, and perhaps the dissolution of calcite ($CaCO_{3(s)}$). The Ca^{2+} front shows distinct differences in peak concentrations between the dike and sand matrix at both depths. These differences may be related to the different flow networks that led to spatially variable velocities. With the influx of tracer containing large amounts of Mg^{2+} as well as Sr^{2+}, the Mg^{2+} exchanged for Ca^{2+} at the leading edge of the tracer and a Ca^{2+} peak arrived slightly ahead of the Cl^- peak. Results also showed an increase in Ca^{2+} peak concentration with depth. The occurrence of the Ca^{2+} slightly in advance of the Cl^- peak and the similarity in Ca^{2+} peaks at the three depths suggest that Ca^{2+} in solution is Ca^{2+} liberated from the exchange sites by Mg^{2+}. The liberated Ca^{2+} continued to move through the profile liberating other cations (e.g., K^+, Na^+) in its path. The C^{2+} breakthrough curves are mostly tri-modal, perhaps a reflection of the timing of the three main infiltration events. The occurrence of higher Ca^{2+} concentrations in the sandy regions relative to the dike is indicative of a lower cation exchange capacity and higher pore water velocities relative to the dike region. These observations have important implications for modeling field-scale reactive transport. Calcite could precipitate, depending on the concentration of the amount of excess Ca^{2+} and the CO_3^- concentration, and calcite would exert control on the precipitation and mobility of other minerals

(e.g., strontianite, magnesite) through competition for exchange sites. The assumption of 1-D flow in a clearly 3-D flow environment would clearly impact the behavior of a calcite front and ultimately the precipitation behavior of other minerals. Assumptions of uniform distributions of calcite and a single mean cation exchange capacity would also have a significant impact on model predictions and the interpretation of reactive transport behavior. The effect of ignoring these small-scale variations is quite clear in the field-scale average curves plotted at 80 m (262 ft) along the horizontal axis. Using transport and ion-exchange parameters obtained from the average curves, or from homogenized Hanford sediments, are unlikely to match field-scale observations of reactive transport processes. Nevertheless, the behavior of Ca^{2+} is consistent with the column observations, which is only exacerbated by the multidimensional nature of the flow field.

Figure 2.62 and Figure 2.63 show distribution of the magnesium ion, Mg^{2+}, in solution, resulting from the second experiment in FY 2003. Unlike Ca^{2+}, Mg^{2+} was added to the tracer in the form of magnesium chloride to enhance the competition with strontium, Sr^{2+}, and potentially increase the mobility of Sr^{2+}. The general trend in Mg^{2+} breakthrough is in good agreement with expectations and pre-injection simulations of the experiments. A marked preference of the system for Mg^{2+} over Ca^{2+} resulted in a Ca^{2+} breakthrough identical to that of Cl^- but an Mg^{2+} that was slightly delayed. Peak Mg^{2+} concentrations and mass recovery considerably lower than the input pulse amounts are also indicative of a preference for Ca^{2+} over Mg^{2+} and are consistent with ion exchange. Some of the Mg^{2+} entering system liberated Ca^{2+} from the exchange sites while the remainder continued to move through the system. Mg^{2+} could be expected to be adsorbed as it moved deeper into the profile as shown in the column experiment. These data show considerable spatial variability in Mg^{2+} concentration that is related to the multidimensional flow field and the heterogeneous nature of the sediments. These phenomena appear to have had different effects at the two depths with zones of higher concentrations changing from the 0.4-m (1.31-ft) to the 80-cm (2.6-ft) depths. The field-scale average Mg^{2+} curves are shown at the 80-m (262-ft) horizontal location in plots. These curves show a considerable increase on Mg^{2+} at the 80-cm (2.6-ft) depth. These results reflect the combined effects of physical and geochemical heterogeneities and the preferential sorption of Mg^{2+} in a much more complicated flow field than possible in a 1-D column, which will require the numerical model for complete interpretation.

Figure 2.64 and Figure 2.65 show the measured concentrations for Sr^{2+}. The marked preference of the system for Sr^{2+} over Ca^{2+} resulted in a Sr^{2+} breakthrough identical to that of Cl^-. The similarity in breakthrough of Mg^{2+}, Sr^{2+}, and Cl^- is consistent with the column experiments and is also expected, given that Mg^{2+} was added to alter the behavior of Sr^{2+}. The low concentration of Sr^{2+} relative to the input value also suggests that Sr^{2+} was involved in the ion exchange reactions and the liberation of Ca^{2+} from the exchange complex. In fact, the behavior of Sr^{2+} was very much like that of Mg^{2+}. However, there were notable differences from the column experiments. There was significant spatial variability in the behavior of Sr^{2+} and an apparent increase in the peak Sr^{2+} and mass recovered as the depth increased. As with the other cations, these results reflect the interplay of physical and geochemical heterogeneities in a complex flow field but provide a dataset appropriate for model calibration.

2.10.2 Synopsis and Implications

The synopsis of findings in the study of field-scale coupled reactive transport and their implications are as follows:

- Ion exchange parameters derived from batch and column flow-through experiments are widely used as the basis for modeling reactive transport in homogeneous sediments under experimental conditions but may not adequately describe field-scale transport in heterogeneous systems.

- Field-scale observations of coupled flow and transport performed under well-controlled boundary conditions are useful for calibrating mechanistic models and to determine the relationship between laboratory-measured exchange capacity and the effective values needed to describe field behavior. Such data were collected in experiments at the Army Loop Road site.

- Although using a pulse input of tracers did not allow displacement of the initial exchange species and the chromatographic separation of cations, the response of the system to the tracer injection can be used to test the multicomponent ion exchange model for field-scale applications in heterogeneous sediments.

- In general, the sediments showed a preference for magnesium and strontium at the expense of calcium, and calcium was liberated from the exchange complex. In the presence of a high magnesium concentration, strontium mimicked the behavior of the conservative chloride, showing essentially no sorption. However, these ion exchange processes were influenced by the complicated flow field that controlled access to reactive sites that led to highly variable concentrations and breakthrough.

- Results show a complex interplay of physical, hydrologic, and geochemical heterogeneities in a complex flow field that provides a dataset for model calibration.

2.11 A Robust Model for Saturation-Dependent Anisotropy

Major discrepancies often persist between measured and predicted subsurface distributions of moisture and solutes, even in well-controlled intermediate-scale and field-scale experiments. These discrepancies are the consequence, in part, of the difficulty in accounting for permeability distributions, connectivity between sedimentary facies, and the extent of lateral spreading observed in the field. Contaminant plumes in the Hanford vadose zone often show extensive lateral spreading with splitting along flow paths and multiple zones of high-contaminant concentrations, even in sediments that appear homogeneous and isotropic at the regional scale. Lateral spreading is commonly attributed to anisotropy in the hydraulic conductivity tensor, **K**, caused by local-scale textural and permeability contrast between sedimentary facies. Variable or saturation-dependent anisotropy, an extreme of nonlinear behavior, can subdue and/or predict migration rates, depending on local stratigraphy; it can also enhance non-equilibrium flow and limit access to reactive surfaces.

An anisotropy ratio, C, is defined simply as the ratio of the hydraulic conductivity parallel to the bedding plane (K_p) and normal to bedding (K_N). Numerical studies and circumstantial evidence suggest that the anisotropy ratio in heterogeneous porous media depends on saturation (Yeh et al. 1985; Mantoglou and Gelhar 1987; Polmann et al. 1991; McCord et al. 1991). Thus, the quantification of C and its dependence on saturation is of major practical importance. Several approaches have been used to describe the state-dependent anisotropy, and each approach gives rise to a different relationship (Figure 2.66). These approaches have ranged from the assumptions of isotropic systems (i.e., C=1 [Stephenson and Freeze 1974]), to a constant anisotropy independent of saturation (i.e., C > 1

[Philip 1987; Boger 1998]), to the state-dependent factors introduced in the early 1980s (Zaslavsky and Sinai 1981; Mualem 1984). The Mualem (1984) model provides some insight into state-dependent C, but the assumption of perfect stratification limits its applicability to real soils. In a more recent study, Friedman and Jones (2001) reported measurements of pore-scale directional electrical conductivity as a function of saturation, a proxy for K, and showed a completely different relationship (Figure 2.66).

The infiltration and redistribution of the water in the subsurface depends on anisotropy; thus, the spatial patterns in moisture distribution will depend on the underlying assumptions and the method of calculating C. The objectives of this study were to investigate the factors contributing to lateral spreading at the field scale and to develop an approach to better quantify variable anisotropy across spatial scales.

It is hypothesized that anisotropy in macroscopic hydraulic properties is caused by fundamental differences in the longitudinal and transverse tortuosity that results from the preferential alignment of particles. During sedimentation, aggregation, and compaction, the stable equilibrium configuration for irregularly shaped particles with three axes of symmetry is with the large axis oriented horizontally (Lamb 1945, pp. 177–178). This preferential alignment of particles results in a microscale structure that renders the porous medium anisotropic in their resistance to the flow of mass and energy at the pore scale. Second, in natural sedimentary systems, particle deposition under water is typically subjected to flow currents, shearing, scouring, and interaction because of high particle concentrations that affect the pore-scale structure. In such depositional environments, asymmetric particles such as disks and rods form laminates with their long side parallel to the flow direction, but with their axis parallel to the shear planes. Disks often orient themselves with their flat sides in the plane of shear. Also shear forces from flow and

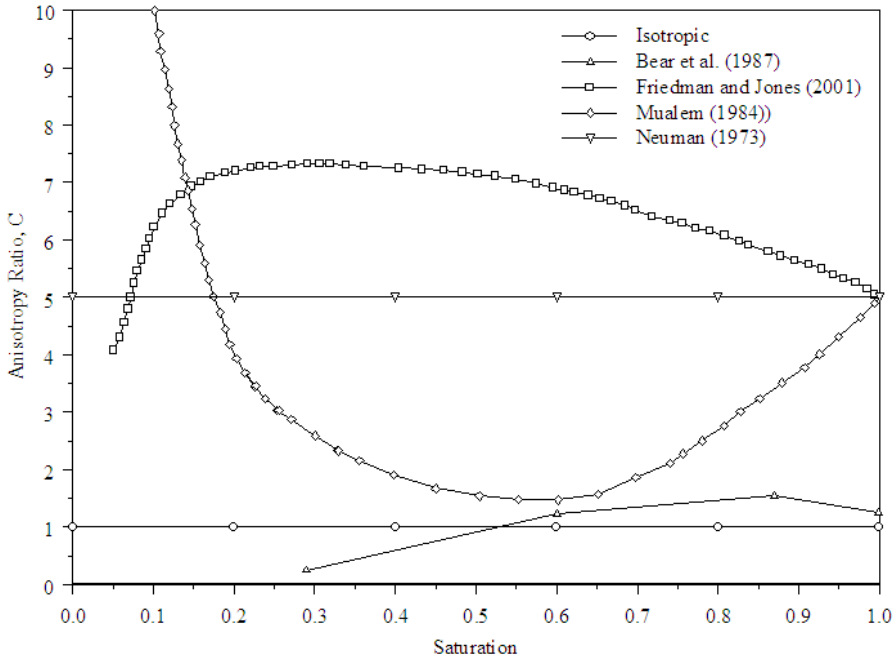

Figure 2.66. A Schematic Description of Possible State-Dependent Anisotropy Relationships. The different functional dependences of C on saturation result in different water-flow patterns (after Friedman and Jones 2001).

particle interaction can also cause imbrication of grains, while scouring often leads to cross-bedding. The net result of these phenomena is a macroscale layering and heterogeneity manifested as directionally dependent correlation lengths and anisotropic intrinsic properties. Sediments formed from the deposition of spherical or rounded particles, such as sands, would tend to show similar connectivity, tortuosity, and hydraulic conductivity in all directions, i.e., they would tend to be isotropic at the pore scale. In contrast, soils formed from the settling of flat particles and rods, which settle with their long axes horizontal, would tend to be anisotropic. Because of the higher degree of tortuosity and smaller degree of connectivity normal to the long axes, one might expect the conductivity normal to bedding, K_n, to be less than parallel to the long axes, i.e., the hydraulic conductivity parallel to bedding, K_p. It is now recognized that these microstructures and their manifestation as layers at the megascopic-scale may also control the subsurface spreading of contaminant (Gelhar and Axness 1983; Dagan 1988). The description of the anisotropy function is then reduced to defining the directional connectivity at the scale of interest.

To test this concept, a number of soils with specified connectivity were generated using geostatistical methods (Ward et al. 2002). The soils were subjected to numerical multi-step numerical experiments in which cubes were allowed to desaturate under constant-head boundary conditions imposed on the top and bottom boundaries. Each numerical experiment started at saturation after which the soil was dewatered gradually in 32 steps of pressure heads from 0 to 2.0 m (0 to 6.6 ft). The head values at the top and bottom boundaries were kept the same at a specific time so that gravity was the only driving force, i.e., flow occurred under a unit hydraulic-gradient condition. After steady-state conditions were reached at a given pressure, the pressure heads at the two boundaries were adjusted to new values. Flow in the synthetic soils was simulated using STOMP-W. After determining the unsaturated hydraulic conductivity in the direction normal to the soil strata, $K_n(h)$, the cube was rotated through 90°, and the simulations were rerun to determine the conductivity in the direction parallel to the soil strata, $K_p(h)$. After all the numerical experiments were completed, the mean values of h and θ over the whole 1×1 m (3.3×3.3 ft) soil domain were calculated for each step. In all, there were 64 pairs of $h(\theta)$, 32 pairs of $K_p(h)$, and 32 pairs of $K_n(h)$ data for each soil. For this study, we chose to use the van Genuchten (1980) model to describe the soil water-retention curve. The 64 pairs of $h(\theta)$ data were used to optimize the effective value of α, α_e, and the effective value of n, n_e, whereas parameters θ_s and θ_r were fixed. The parameters in the direction parallel to the soil strata, K_{sp} and L_p, were then optimized with the $K_p(h)$ data using the already optimized α_e and n_e as constants. Similarly, the parameters in the direction normal to soil strata, K_{sn} and L_n, were optimized to the $K_n(h)$ data.

2.11.1 Results

Results of the numerical experiments show that the water-retention curves were independent of flow direction, which is consistent with the current definition of the water retention for a representative elementary volume (Figure 2.67). However, the water-retention curve of a heterogeneous soil is dependent on the degree of heterogeneity. The value of α_e is positively correlated with variance of the natural log of the hydraulic conductivity, σ_Y^2, whereas the value of n_e is negatively correlated with σ_Y^2. The dependence of α_e and n_e on soil heterogeneity is caused by the nonlinear relationship between θ and h. Figure 2.67 shows that both α_e and n_e are functions of soil heterogeneity but essentially independent of soil anisotropy. This has important ramifications for characterization of Hanford sediments where a limited number of samples are typically used to predict the hydraulic properties for large domains without consideration for heterogeneity. Furthermore, hydraulic properties are typically

measured by first sieving out the < 2-mm size fraction, thereby ignoring the contribution of gravel, an important contributor to heterogeneity.

The effects of flow direction on unsaturated hydraulic conductivity are shown in Figure 2.68a–d. In an isotropic soil (R = 1), the unsaturated hydraulic conductivity at a given *h* in the direction parallel to soil strata, $K_p(h)$, was the same as that normal to soil strata, $K_n(h)$, as expected (Figure 2.68a). As R became larger, $K_p(h)$ became larger while $K_n(h)$ became smaller (Figure 2.68b–d) than the values of K(h) of the isotropic soil with nearly the same heterogeneity (Figure 2.68a). The ratio of $K_p(h)$ and $K_n(h)$ became larger as h became more negative. For example, for soil #11 with $\sigma_Y^2 = 1.717$ and R = 50 (c), when the soil was saturated, the saturated hydraulic conductivities parallel and normal to stratification were 1.56×10^{-4} and 5.08×10^{-5} m s^{-1}, respectively, giving an anisotropy ratio of $K_{sp}/K_{sn} = 3.1$. At a pressure head of -2.0 m (-6.6 ft), the hydraulic conductivities parallel and normal to stratification were 7.36×10^{-9} and 1.88×10^{-10} m s^{1}, respectively, resulting in $K_p/K_n = 39.2$. This means that unsaturated hydraulic conductivity is more anisotropic when the soils become drier. These results are consistent with the findings of previous studies (e.g., Stephens and Heermann 1988; McCord et al. 1991).

In general, anisotropy in the unsaturated hydraulic conductivity function is well described by an equation of the form:

$$K_i(S_e, K_{si}, L_i, \beta, \gamma) = K_{si} S_e^{L_i} A(S_e, \beta, \gamma) \tag{2.13}$$

where A is given by

$$A(S_e, \beta, \gamma) = \left[\frac{\int_0^{S_e} \left(\frac{dS_e}{h^\beta} \right)}{\int_0^1 \left(\frac{dS_e}{h^\beta} \right)} \right]^\gamma \tag{2.14}$$

In Equation (2.13),

- i = 1, 2, or 3, which denotes the direction parallel or normal to soil strata
- S_e = effective saturation
- K_{si} = saturated hydraulic conductivity in direction i
- L_i = connectivity-tortuosity coefficient in direction I, where L is a lumped parameter that accounts for pore connectivity and tortuosity and hence is called the connectivity-tortuosity coefficient
- β and γ = constants.

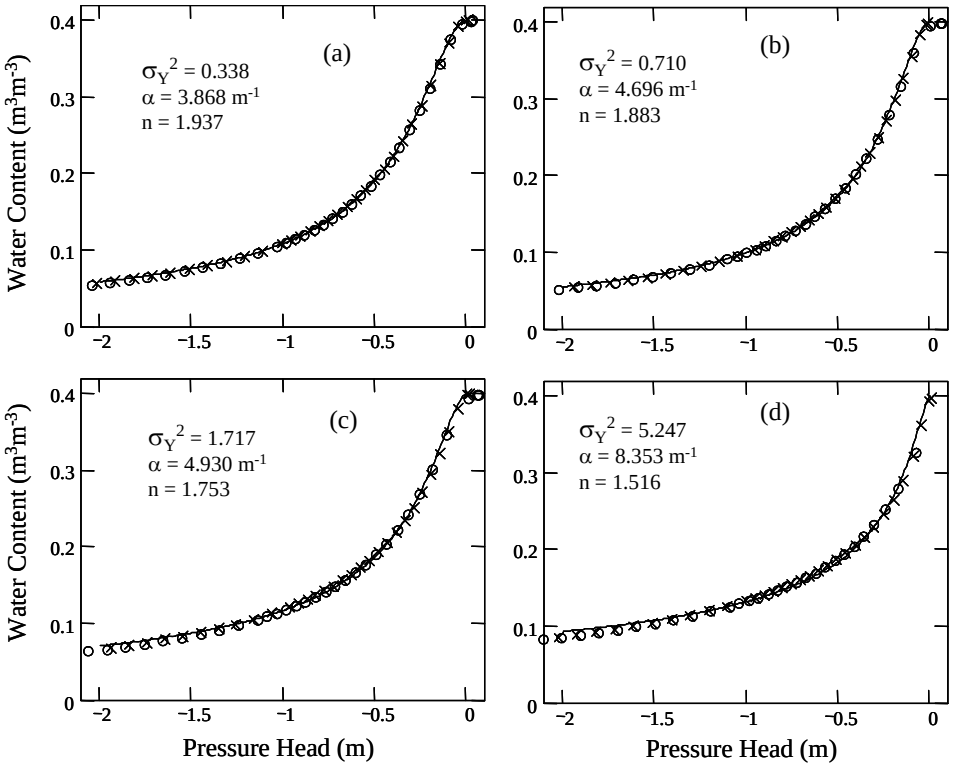

Figure 2.67. Water retention Curves of Anisotropic Soils with Different Levels of Heterogeneities and R = 50. Lines: best-fits; cross: parallel to soil strata; and circle: normal to soil strata. Variable: R is the ratio of correlation length at the direction parallel to soil strata and that normal to soil strata; α is the inverse macroscopic capillary length; n is the pore-size distribution parameter; $Y = \ln(K_s)$ with K_s being the saturated hydraulic conductivity; and σ_Y^2 is the variance of Y.

Equation (2.13) reduces to the Burdine (1953) relationship when $\beta = 2$ and $\gamma = 1$ and to the Mualem (1976) relationship when $\beta = 1$ and $\gamma = 2$. The L tensor describes all the effects on the effective hydraulic conductivity caused by soil heterogeneity and spatial correlations, which need to be specified in the stochastic method (Polmann et al. 1991). The widely used hydraulic functions (e.g., Burdine 1953; Mualem 1976) can be easily extended by allowing L to take different values for the three-principle orthogonal coordinate directions of flow. Hence, the connectivity-tortuosity (TCT) concept can be easily combined into commonly used relative permeability functions for use in numerical solutions of the flow equation.

An optimized L is actually a lumped parameter that accounts not only for flow path tortuosity and pore connectivity, but for pore configuration as well (Zhang et al. 2003b). Fitting for L showed that in the soils with different levels of heterogeneity and anisotropy, L decreased linearly as the ratio of the correlation length in the direction parallel to flow and normal flow increased. Larger values of L are indicative of less connected pores and/or more tortuous flow paths. Thus, L was smaller when flow was parallel to soil strata than when flow was normal to the soil strata. The effect of stratification on L was also stronger in more anisotropic soils, which means that the difference between L_p and L_n becomes larger

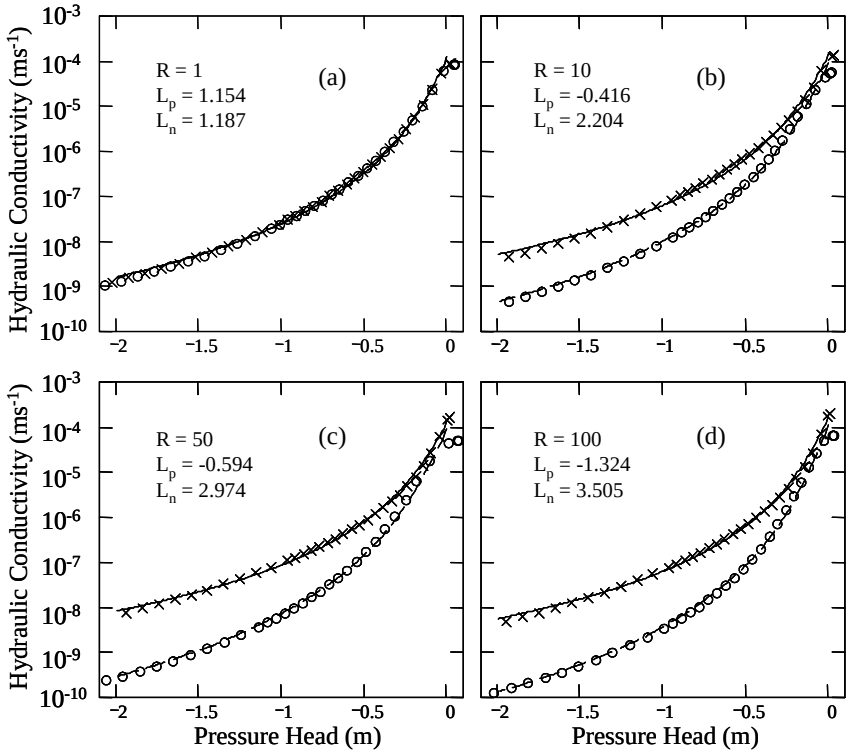

Figure 2.68. The Unsaturated Hydraulic Conductivity of Anisotropic Heterogeneous Soils with the σ_Y^2 = 2.0. Lines: best-fits; cross: parallel to soil strata; and circle: normal to soil strata. Variables: L_p is the connectivity-tortuosity coefficient at the direction parallel to the strata and L_n at the direction normal to strata; R is the ratio of correlation length at the direction parallel to strata and that normal to strata; $Y = \ln(K_s)$ with K_s being the saturated hydraulic conductivity; and σ_Y^2 is the variance of Y.

as a soil becomes more stratified. A number of researchers have found that the parameter L can be negative (e.g., Schuh and Cline 1990; Kosugi 1999; de Vos et al. 1999; Schaap and Leij 2000).

A negative L may be explained by the expected difference between the configuration of real soil pores and the ideal cylindrical pores whose lengths are proportional to their radii as assumed by Mualem (1976). The L tensor describes all the effects on the effective hydraulic conductivity caused by soil heterogeneity and spatial correlations, which need to be specified a priori in the stochastic method (Polmann et al. 1991). The widely used hydraulic functions can be easily extended by allowing L to take different values for the three-principle orthogonal coordinate directions of flow. Hence numerical solutions of the Richards' equation can be easily modified to include the TCT concept. A major advantage of using the connectivity tensor is that the L tensor can be easily determined by measuring the hydraulic functions in different directions using direct methods, or it can be optimized using inverse methods.

In the following definition in which the $\mathbf{K}(S_e)$ uses the tensorial TCT concept, the mathematics were formalized, assuming that the principal axes coincided with those of the hydraulic conductivity tensor at saturation. Raats et al. (2004) showed that a relative connectivity-tortuosity tensor can be defined as

$\mathbf{T}(S_e, L_i)$, with principal components, $T_i = S_e^{L_i} = \left(S_e^{L_1}, S_e^{L_2}, S_e^{L_3}\right)$, where S_e is the effective saturation. Thus, $\mathbf{K}(S_e)$ is shown to be the product of a saturation-dependent scalar variable, the tortuosity-connectivity tensor $\mathbf{T}(S_e, L_i)$, and a saturated hydraulic conductivity tensor, $\mathbf{K}_s$. In unsaturated anisotropic soils, $\mathbf{K}$ is then a product of a scalar variable, the symmetric connectivity tortuosity tensor, and the $\mathbf{K}_s$ tensor at saturation. The influence of saturation on $\mathbf{K}$ is illustrated below for four of the synthetic soils used by Zhang et al. (2003b) through radial plots of the hydraulic conductivity scalar as a function of saturation. As can be expected, the resulting curves are all ellipses in which the eccentricity of the ellipses reflects the degree of anisotropy of the soil at a given saturation (Figure 2.69). This is the first time that this concept has been demonstrated for unsaturated heterogeneous sediments.

2.11.2 Synopsis and Implications

The synopsis of findings in the development of a saturation-dependent anisotropy model for heterogeneous sediments and their implications are as follows:

- Infiltration and redistribution of the water in the subsurface strongly depends on anisotropy; thus, the spatial patterns in moisture distribution will depend on the underlying assumptions and the method of calculation of the anisotropy ratio, C.

- We hypothesize that anisotropy in soil properties arises from pore-scale heterogeneity caused by the alignment of aspherical soil particles, and the description of anisotropy reduces to the problem of quantifying the tortuosity and connectivity along the axis of interest. Pore connectivity is treated as a tensor, and anisotropic hydraulic properties can be described by extending existing hydraulic functions, e.g., the Burdine and the Mualem models, such that the connectivity-tortuosity coefficient (L) is a tensor.

- Numerical experiments in synthetic coarse-textured soils show that soil-water-retention curves of anisotropic soils are independent of the observation direction but dependent on soil heterogeneity. With this approach, the unsaturated hydraulic conductivity of anisotropic soils can differ by several orders of magnitude, depending on the observation direction. Furthermore, the anisotropy in hydraulic conductivity increases as the soil desaturates. This approach to modeling variable anisotropy has been incorporated into the STOMP code and is now being used for unsaturated flow modeling.

- The developments described in this paper have important implications for pore-scale modeling of flow and transport. Pore fabric geometry is clearly a key feature of sedimentary rocks and soils that impacts flow and transport of water and solutes. The increased tortuosity caused by flow around the aspherical particles causes a reduction in specific discharge and a decrease in permeability relative to a capillary bundle model for a given pressure gradient.

- At the local scale, pore morphology and connectivity can render sediments anisotropic in their resistance to the flow of water and solutes. Thus, anisotropy can affect access to reactive sites controlling sorption and natural attenuation. Understanding the nature and extent of anisotropy is important for improving our prediction capability for water and reactive solutes moving through the vadose zone, particularly at low water contents.

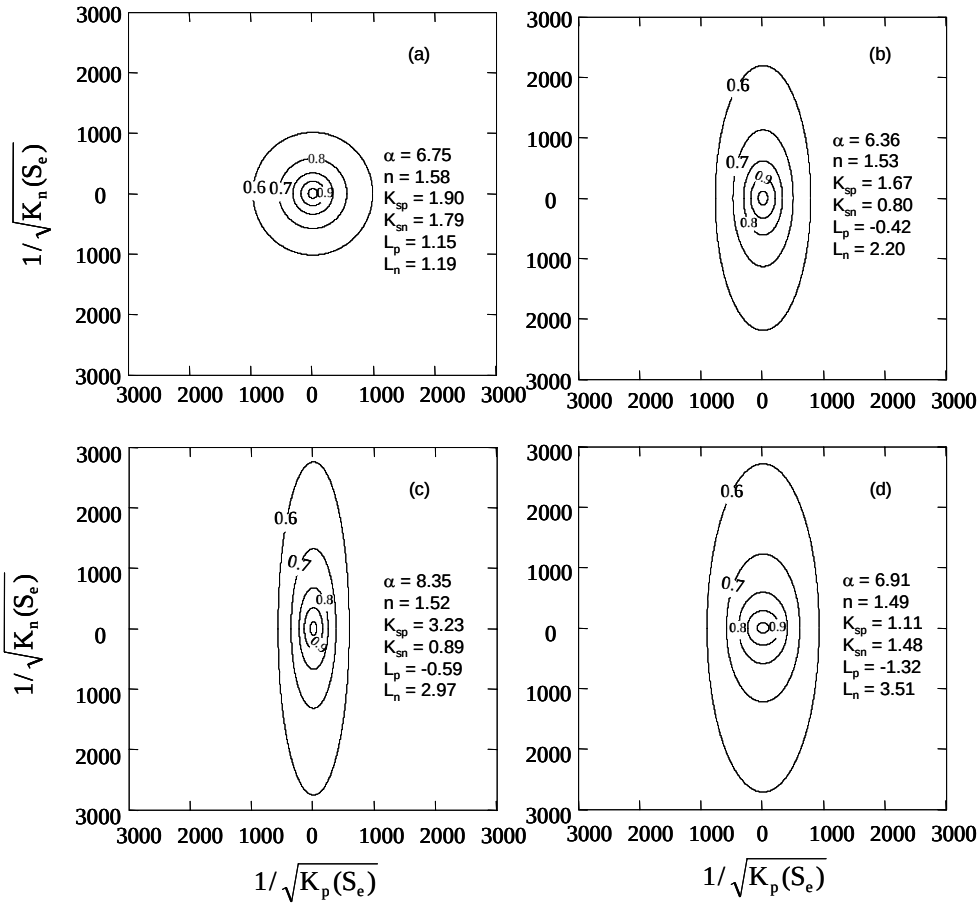

Figure 2.69. Contour Plots of $1/\sqrt{k_{\mathbf{n}}(S_e)}$, with K_n Being the Hydraulic Conductivity Scalar at Direction n, as a Family of Ellipses at Different Saturations for the Four Soils of Zhang et al. (2003) in Their Figures 4a-d. The numbers on the ellipses are saturations.

- In scaling permeability from the capillary tube model to actual sediments, consideration must then be given to treating tortuosity-connectivity as a tensor rather than a scalar quantity. Furthermore, the analysis of this fabric could provide the means of relating the tortuosity-connectivity parameter and anisotropy to pore fabric shape and orientation. Such an analysis could also be extended to the anisotropy of other related intrinsic properties as well as physical properties such as mechanical strength.

- Perhaps the most significant implication of this work is the ability to account for the effects of anisotropy in both the saturated and unsaturated hydraulic conductivity. It also provides a methodology for transforming the scalar water retention function into the hydraulic conductivity tensor.

2.12 Reduction of Parameter Dimension by Parameter Scaling

Several numerical models have been developed to predict infiltration and redistribution of water and dissolved contaminants in the subsurface. However, a remaining challenge is the parameterization of these models, particularly when the sediments of interest are heterogeneous with spatially varying hydraulic properties. One consequence of spatial variability is that the properties of a soil are a function of the size of soil samples, and hydraulic properties measured in the laboratory using small soil cores are usually not directly applicable to the field scale. Inverse methods have been proposed as one approach to estimate field-scale hydraulic properties, but a potential problem in heterogeneous sediments is that the parameter estimates may be non-unique, causing some of the parameters to be unidentifiable. The non-uniqueness problem becomes worse as the number of parameters to be estimated becomes larger.

Increased model complexity typically accompanies the incorporation of multi-scale heterogeneities, thereby increasing the parameter dimension and constraining traditional optimization methods. Global optimization algorithms have gained popularity for complex non-convex problems and highly dimensional parameter estimation problems typical of subsurface characterization. Nevertheless, these methods have been mostly limited to synthetic heterogeneous structures with low (12–20) dimensional parameters when in fact the typical unsaturated flow parameterization problem is one of with moderate (20–100) to high (> 150) dimensional parameters. A remaining challenge is therefore one of reducing parameter dimension in the inverse problem of field-scale unsaturated flow in heterogeneous anisotropic sediments.

Parameter dimension may be reduced by scaling the hydraulic properties with a technique like similar-media scaling (Miller and Miller 1956). The similar-media scaling technique scales soil water retention curves and the unsaturated hydraulic conductivity functions of multiple soils with similar pore geometry to those of a reference soil. The similar-media scaling allows a single solution of the Richards equation to suffice for numerous specific cases of flow in unsaturated soils. However, a fundamental assumption in the use of this method is that the soils are vertically uniform. In an attempt to incorporate vertical heterogeneity, Shouse et al. (1992) scaled soil water content (θ) with depth-dependent scaling factors with the assumption that the scaled unsaturated hydraulic conductivity is depth-independent. Using the scaled θ with a scaled form of the Richards equation allowed heterogeneous soil hydraulic properties to coalesce into unique functions for both $\theta(h)$ and $K(\theta)$, where h is pressure head and $K(\theta)$ is unsaturated hydraulic conductivity. A major limitation in this approach is that the need to determine the scaled depth for each observation must be determined using the depth-dependent scaling factors which are themselves dependent on both the observed and scaled water contents.

A layered formation composed of M different sediments with each texture can be assumed to be characterized by a set of hydraulic parameters, $\boldsymbol{\beta}$ (Figure 2.70a). A single sediment texture is selected as a reference and described by a set of reference parameters, $\tilde{\boldsymbol{\beta}}$. The j^{th} parameter of the i^{th} texture, β_{ij}, are related to the reference parameters through a set of mutually independent linear scaling factors, γ_{ij}, for I = 1 to M textures, i.e.,

$$\beta_{ij} = \gamma_{ij} \tilde{\beta}_j \tag{2.15}$$

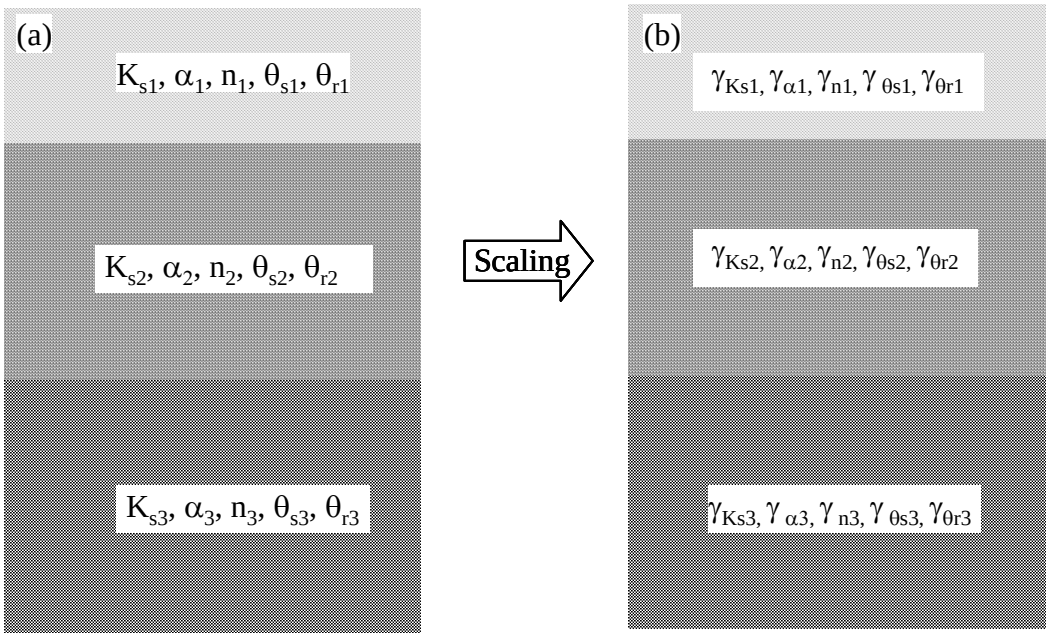

Figure 2.70. An Illustration of the Parameter Scaling in a Three-Layered Soil Using the van Genuchten (1980) Model: (a) Parameters Before Scaling and (b) Scaling Factors Reference to $(\tilde{K}_s, \tilde{\alpha}, \tilde{n}, \tilde{\theta}_s, \tilde{\theta}_r)$

Herein lies a major difference between this approach and traditional scaling; in this approach, we scale the soil hydraulic parameters of the hydraulic functions rather than the hydraulic properties. The total number of scaling factors is the same as the number of soil parameters (Figure 2.70b). For example, if the hydraulic functions of a three-layered soil are described by the van Genuchten (1980) model, then as shown in Figure 2.70, there are 15 parameters associated with the three layers (Figure 2.70a). These parameters can be described by 15 scaling factors (Figure 2.70b) and one set of reference parameter values. While selecting a different reference texture will produce different values of γ_{ij}, the actual parameter values and flow properties will not change. For a layered soil, the scaling factors reflect the effects of soil layering, and the reference parameter values reflect the effects of spatial scale. The problem reduces to one of estimating the scaling factors, and the solution is illustrated using the permeability.

An effective permeability, k_e, corresponding to a statistically isotropic field may be defined as

$$k_e = k_g \exp\left[\sigma^2\left(\frac{1}{2} - \frac{1}{D}\right)\right] \tag{2.16}$$

where k_g is the geometric mean permeability, σ^2 is the variance of log (k), and D is flow dimensionality. The validity of Equation (2.16) has been proven mathematically for the 1-D and 2-D cases, and its validity for the 3-D case has been demonstrated numerically for σ^2 up to 7.0. The effective permeability of a heterogeneous formation can be thought of as the field-scale permeability while k_g is the mean local-scale value. In this context, local scale means the range represented by an individual observation, and

field scale is the 3-D range of an experimental site. If we apply Equation (2.16) to two soils, A and B, that have similar degrees of heterogeneity (i.e., similar σ^2), the field-scale permeabilities of the materials will be proportionally larger or smaller than the local-scale values under the same flow condition, i.e., $k_e^A / k_e^B \approx k_g^A / k_g^B$. By definition, k_e^A / k_e^B is the scaling factor at field scale, and k_g^A / k_g^B is the scaling factor at local scale. This means that the scaling factors in Equation (2.15) are similar at the field- and local-scales. Hence, we assume that local-scale values of γ_{ij} are equal to those at the field-scale for all the parameters, i.e.,

$$\gamma_{ij}^{LS} = \gamma_{ij}^{FS} \tag{2.17}$$

where the superscript LS denotes local-scale, and FS denotes field-scale. Equation (2.17) essentially means that the relationship between the parameters of different textures is scale invariant. For example, if at the local-scale, the saturated hydraulic conductivity, K_s^{LS}, of the i^{th} texture is $10 \cdot \tilde{K}_s^{LS}$, we expect that the field-scale value, K_s^{LS}, of the i^{th} texture will be approximately $10 \cdot \tilde{K}_s^{FS}$ as well. This assumption is consistent with the published derivations of the effective hydraulic conductivity from a 3-D steady-state infiltration in statistically isotropic unsaturated porous media. It has been shown that the effective hydraulic conductivity is linearly proportional to the mean value of the local-scale hydraulic conductivity for given soil variability and correlation length. Thus, the scaling factors can be determined with Equation (2.15) using the parameter values measured at the local scale or in the laboratory. A variety of physico-empirical methods and empirical methods have also been proposed to estimate soil hydraulic properties using easily obtainable data (e.g., particle size distribution, bulk density). Scaling factors may also be determined with these methods using some easily obtainable information. Although there may be errors in the estimated hydraulic parameter values, it is expected that such error would be systematic and therefore cancel when the parameter values are used to calculate the scaling factors. Detailed discussions of this approach have been described previously (Zhang et al. 2002a,b; 2004a,b; Ward et al. 2006).

The parameter scaling concept was incorporated into the STOMP simulator, and the method was evaluated by applying it to a field experiment conducted in a layered sediment at Hanford's grass site in the 300 Area. The instantaneous profile experiment was conducted by Rockhold et al. (1988). The water content, θ, was monitored using neutron probe, and the pressure head, ψ, was monitored by tensiometers placed at 0.15- to 0.30-m-depth increments, down to 1.8 m. Ponding was facilitated by using planking installed in narrow trenches around which the soil was thoroughly compacted. The hydraulic functions were described by the van Genuchten (1980) model. STOMP was modified to allow the input of the scaling factors and the reference parameter values and coupled with UCODE (Poeter and Hill 1998) to permit parameter estimation by inverse modeling. Observations of both θ and ψ, made in 10 to 15 minute intervals, were used in the inverse model. The local-scale parameter values of α, n, θ_s, and θ_r at each soil depth were obtained by fitting soil water retention functions to measured ψ and θ. In both cases, we arbitrarily selected the parameter values of the topmost soil layer as the reference from which to calculate the scaling factors of the four parameters using Equation (2.15). The scaling factors for K_s were determined using the best fits of the remaining four parameters (i.e., α, n, θ_s, and θ_r) for each layer and the steady-state observations of θ and ψ. Five super parameters $(\tilde{K}_s, \tilde{\alpha}, \tilde{n}, \tilde{\theta}_s, \tilde{\theta}_r)$ describing the reference layer are optimized by inverse modeling after which they are back transformed to the full domain using scaling parameters determined a priori.

2.12.1 Results

Table 2.4 summarizes the local parameter values used as initial conditions for the inverse model and the scaling factors used in the inverse model. Using these parameters, the five super parameters describing the reference layer were inversely estimated. The resulting parameters and their corresponding 95% linear confidence intervals (LCIs) are given in Table 2.5. Because parameters $\tilde{K}_s$, $\tilde{\alpha}$, and $\tilde{n}$ were log-transformed for estimation, their 95% LCIs are expressed as the mean values multiplied or divided (×/÷) by a factor that has the minimum value of unity. The 95% LCIs for $\tilde{K}_s$ have the largest uncertainty, varying by as much as 1.57. The 95% LCIs for parameters $\tilde{\alpha}$ and $\tilde{n}$ vary with a factor less than 1.18. Both $\tilde{\theta}_s$ and $\tilde{S}_r$ have relatively small 95% LCIs that are equal or less than ± 0.011. An analysis of the correlation between the super parameters shows strong correlations between $\tilde{K}_s$ and $\tilde{\alpha}$ with a coefficient (R) of 0.934. The absolute values of the remaining coefficients were ≤ 0.78. A value of R less than 0.95 suggests that non-uniqueness is not a problem. Thus, the estimates of the super parameters obtained by this method can be considered to be unique.

Table 2.4. Values of the Local-Scale Hydraulic Parameters at the Calculated Scaling Factors Reference to the Layer 1

Parameter	**Layer 1**	**Layer 2**	**Layer 3**	**Layer 4**
K_s (m s^{-1})	1×10^{-5}	4.29×10^{-7}	2.56×10^{-7}	1.05×10^{-7}
α (m^{-1})	8.41	7.85	12.72	13.13
n (-)	1.232	1.236	1.355	2.054
θ_s (m^3 m^{-3})	0.264	0.199	0.153	0.146
θ_r (m^3 m^{-3})	0.043	0.022	0.017	0.031
S_r†(-)	0.163	0.111	0.111	0.212
γ_{Ks}	1	0.0429	0.0256	0.0105
γ_α	1	0.933	1.512	1.561
γ_n	1	1.003	1.100	1.667
$\gamma_{\theta s}$	1	0.754	0.580	0.553
γ_{Sr}	1	0.681	0.681	1.301
† $S_r = \theta_r / \theta_s$				

Table 2.5. Inversely Determined Reference Values of the Hydraulic Parameters, the 95% LCIs, and the Composite Scaled Sensitivities (CSSs) at Field Scale

Parameters	Mean with 95% LCI	CSS
$\tilde{K}_s$	2.787×/÷1.57 (10^{-3} m s^{-1})	8.25
$\tilde{\alpha}$	11.27×/÷1.18 (m^{-1})	9.19
$\tilde{n}$	1.214×/÷1.04	8.23
$\tilde{\theta}_s$	0.258±0.011 (m^3 m^{-3})	2.30
$\tilde{S}_r$	0.213±0.039	1.35
$\tilde{\theta}_r$	0.055† (m^3 m^{-3})	-
† $\theta_r = S_r\theta_s$.		

The scaling factors in Table 2.4 were used to back-transform the optimized super parameters to obtain the field-scale hydraulic parameters (Table 2.6) for each soil layer using Equation (2.15). These parameters were then used to simulate the actual experiment using STOMP-W. The relationship between the predicted and observed values using the local-scale parameter values is shown in Figure 2.71. With a

Table 2.6. Mean Values of the Hydraulic Parameters of Individual Layers

Soil Depth (m)	K_s (m s^{-1})	α (m^{-1})	n (-)	θ_s (m^3 m^{-3})	S_r (-)	θ_r[(a)] (m^3 m^{-3})
0–0.225	2.79×10^{-3}	11.3	1.214	0.258	0.213	0.055
0.225–0.375	1.20×10^{-4}	10.5	1.218	0.195	0.145	0.028
0.375–0.525	7.13×10^{-5}	17.0	1.336	0.150	0.145	0.022
0.525–1.800	2.93×10^{-5}	17.6	2.024	0.143	0.277	0.040
(a) $\theta_r = S_r\theta_s$						

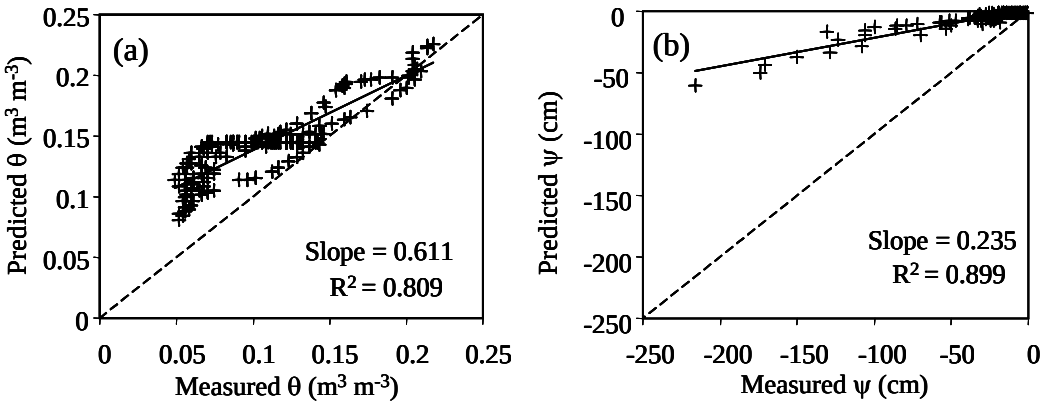

Figure 2.71. Comparison of the Observations and the Predictions of Water Content and Pressure Head Using the Local-Scale Parameter Values

perfect correlation between the predictions and observations, a zero intercept of a slope of unity would be expected, but this is clearly not the case. Figure 2.71 shows that the both the water contents and the pressure heads were overestimated with the local-scale values. Using the field-scale parameter estimates (Table 2.5) led to a significant reduction in error. The sum of the squared weighted residual (SSWR) decreased by 96% from 15484 to 604. Figure 2.72 shows the relationship between the predicted and observed values based on the field-scale parameter values. The slopes of the plots range from 0.903 to 0.997, which are much closer to unity than in with the local-scale values in Figure 2.71.

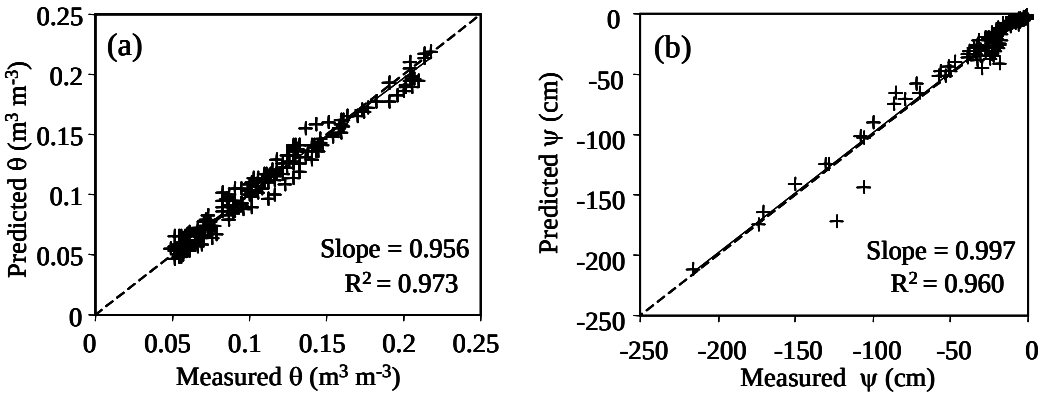

Figure 2.72. Comparison of the Observations and the Predictions of Water Content and Pressure Head Using the Field-Scale Parameter Values Based on the Parameter Scaling Concept

2.12.2 Synopsis and Implications

The synopsis of findings in the development of a method for reducing the parameter dimension for flow in heterogeneous sediments and their implications are as follows:

- Current approaches that can reduce parameter dimensions are based on the similar-media concept that requires the variables to be scaled in the horizontal and vertical directions. Difficulties in obtaining vertical-scale factors limits using property scaling in heterogeneous soils.

- The concept of parameter scaling proposed as a method to account for vertical heterogeneity is based on the scaling of the hydraulic parameters of different soil textures to a single set of reference values. Applying parameter scaling at the local- or field-scale provides a way to link the observations at different spatial scales, given the assumption that the values of the scaling factors are invariant across spatial scales. These factors can be estimated for readily available data like grain-size statistics or core measurements.

- Super parameters describing the reference texture are obtained by the inverse model and are back-transformed using the scale factors to derive the field-scale parameters for individual textures. This approach was successfully applied to the 299-E24-111 field site to achieve a reduction in parameter dimension from 24 to 6. Reference hydraulic parameters were successfully estimated by inverse modeling of the field experiments.

- Parameter scaling does not require that the soil materials to be geometrically similar. After scaling, the values of the parameters of all the soil textures reduce to the reference values, and the spatial variability of each hydraulic parameter can be expressed by the scaling factors.

- Global optimization algorithms are increasing in popularity for complex non-convex and highly dimensional parameter estimation problems typical of subsurface characterization. Thus far, these methods have been limited to synthetic heterogeneous structures with low (12–20) dimensional parameters. The proposed approach reduces the number of parameters in a formation with M textures by a factor of M and reduces simulation time by M^2. This approach has potential for use in parameter estimation in cases of moderate (20–100) to high (> 150) dimensional parameters.

2.13 Surface-Based Ground Penetrating Radar

Surface-based GPR is a geophysical method based on the transmission and reflection of high frequency (1 MHz to 1 GHz) EM energy that is seeing wider use for shallow subsurface characterization (Daniels et al. 1988; Davis and Annan 1989). In the typical surface-based GPR survey, data are acquired by transmitting an EM energy pulse into the subsurface and recording reflected energy at the surface with a receiver antenna. The recorded energy is displayed as the reflections seen in a radar section. The velocity of the EM wave through porous media is controlled by a dielectric constant, which is in turn governed by the relative amounts of water, air, and solid materials present. The dominant factors controlling the dielectric constant of a material are the water content, the volume fraction of clay, and the geometry of the solid phase (Topp et al. 1980). The large contrast between the dielectric constant of water (80) and that of air (1) and commonly-occurring mineral components (typically 3 to 12) has resulted in the widespread use of TDR methods to measure water content in soils to estimate volumetric water content, θ. A number of studies have shown that surface GPR can be used to map soil moisture content (Du and Rummel 1994; Chanzy et al. 1996; Huisman et al. 2001; Clement and Ward 2006) and the spatial correlation structure of flow variables (Rea and Knight 1998); it can also be used to estimate hydraulic properties (Knoll et al. 1995). Although GPR is routinely used at the Hanford Site, it is used mostly to locate buried objects and utilities rather than for characterization of porous media.

The objective of this study was to investigate the feasibility of using surface-based GPR to measure spatial distributions of moisture and to estimate the spatial correlation structure of texture and related hydraulic properties controlled by small-scale heterogeneities. No surface-based GPR measurements were made during the FY 2000 and FY 2001 injection tests at the 299-E24-111 test site. GPR surveys were limited to crosswell measurements in four PVC access tubes spaced about 4 m (13 ft) apart (Ward and Gee 2000; Majer et al. 2001). Surface-based GPR was used at the Army Loop Road test site during the FY 2002 and FY 2003 transport experiments. In these tests, GPR surveys were conducted using two approaches to determine the velocity of water in the subsurface.

A series of common offset surveys were conducted along the length of the 60-m (197-ft) transect at predetermined times during the course of the experiments. During each survey, common midpoint surveys were also conducted at different locations along the transect to determine air-wave and ground-wave velocities. Each field campaign consisted of common offset profiles and common midpoints (CMPs). Measurements were typically made in a west-to-east direction (left to right in Figure 2.73). The common offset profiles were collected parallel to the drip line and within the shallow trench excavated for

this line. Two lines were typically collected for each frequency with the following parameters. In the first profile, data were collected at 450 MHz at a 5-cm (2-in.) interval whereas in the second profile, data were collected at 225 MHz with a 10-cm (4-in.) spacing. The first profile was collected parallel to the drip line with an 80-cm (31.5-in.) spacing between the center of the antenna and the line source. The second profile was also measured parallel to the line source, but at a distance of 30 cm (12 in.) between the center of the antenna and the line source. The CMPs were made at 450 MHz and typically followed the common offset profiles with measurements at x = 8 m (26 ft) and 20 m (65.6 ft) along the transect.

Radar data were collected as a measurement of signal amplitude versus time, and conversion to permittivity and water content required knowledge of the ground-wave velocity. Calculating θ was a three-step process. The data were processed using a combination of ground-wave analysis and normal move out (NMO) analysis of the reflections (Yilmaz 1987, p. 526). The first survey was conducted on May 14, 2002, at the Army Loop Road site with a Geophysical Survey Systems, Inc. (GSSI) SIR10A Model 5106 GPR system. The 300-MHz antenna was attached to a 40-m (131-ft) antenna cable and was pulled by hand. Data were collected as discrete points with a point collected every 5 cm (2 in.) in a 150-ns window. The sample rate was 512 samples per scan in 16 BIT format. The data gain was fixed at 10 db, and filtering was via a low-pass filter 2/50 and a high-pass filter 2/4. Data were collected in two 60-m (197-ft) sections starting at the west end of the transect and moving east (Figure 2.73). There was no data stacking. Subsequent surveys were conducted with a PulseEKKO^{TM} 1000 GPR system using a 200 V transmitter (Sensors and Software, Mississauga, Ontario, Canada) with two sets of antennae with center frequencies of 225 and 450 MHz (Williams et al. 2002).

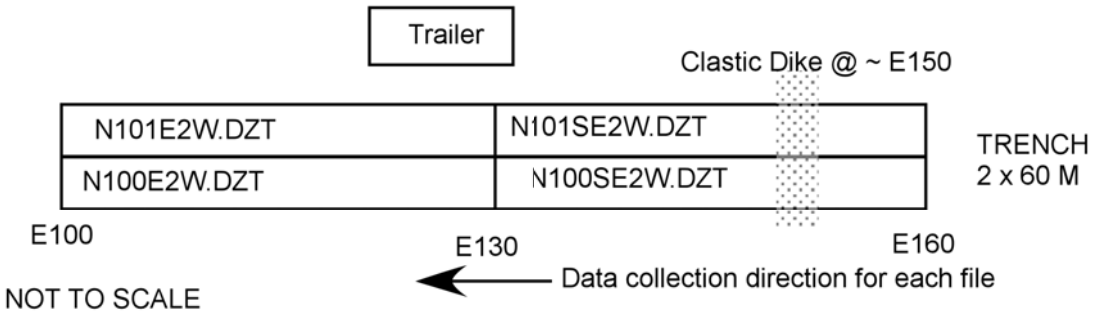

Figure 2.73. Schematic of Transect Showing Direction of Data Collection with Surface GPR

2.13.1 Results

Figure 2.74 shows the baseline common offset profile collected parallel to the line source at the Army Loop Road site on May 21, 2002, using the GSSI system with a 300-MHz antenna. Data were acquired every 5 cm (2 in.) at a distance of 0.8 m (2.6 ft) between the mid point of the antenna and the 1.0-m (3.3-ft) TDR probes. Data acquisition started at the northwestern end of the transect, and an example of a common offset profile is shown in Figure 2.75. A series of strong reflectors were apparent in the baseline data occurring at times ranging from 10 to 20 ns. These reflectors persisted for the duration of the

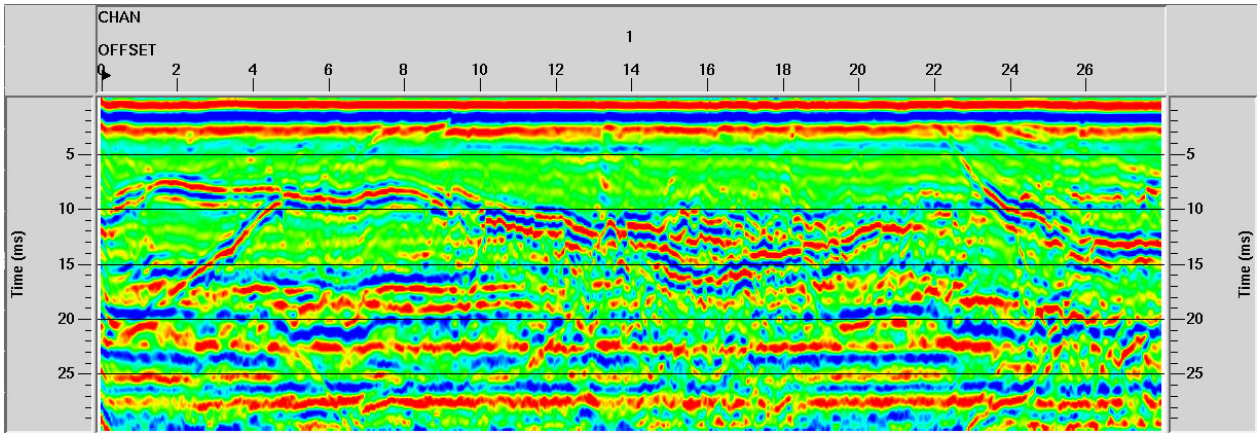

Figure 2.74. Common Offset GPR Data Collected 0.8 m (0.26 ft) from the Line Source at the Clastic Dike Site on May 21, 2002

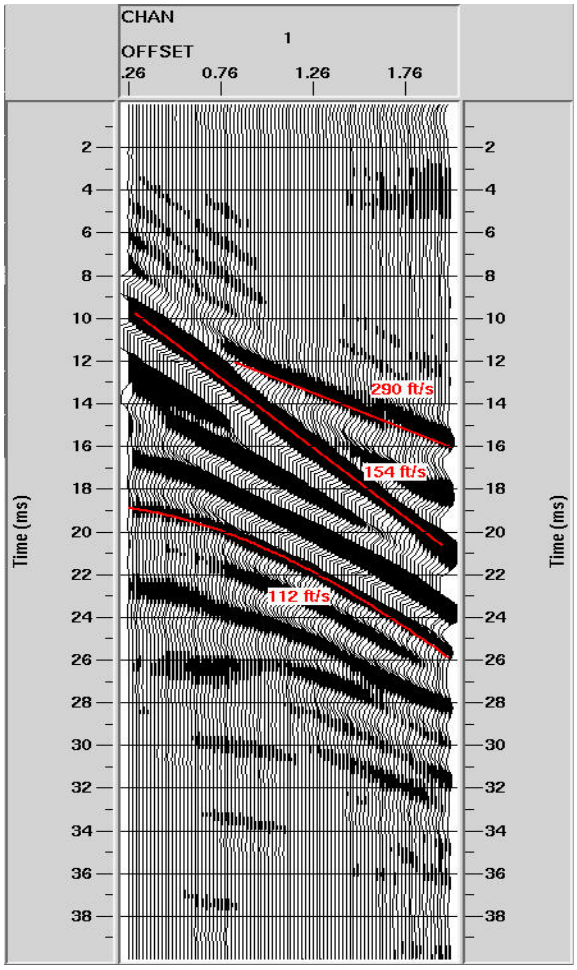

Figure 2.75. Example of Common Mid-Point Data at Position E140 at the Clastic Dike site with Arrivals Labeled

experiment with the only change being a gradual decrease in the signal-to-noise ratio as the total fluid volume injected increased. Similar profiles were collected for the duration of the experiment and were used to identify a variety of subsurface reflectors. The arrival times to these reflectors varied from 10 to 20 ns in the baseline, but changed as the experiment progressed. Arrival times showed a gradual increase with time, indicative of an increase in moisture as well as a decrease in the signal-to-noise ratio as the cumulative volume of injected water increased. Eight reflectors were designated as follows: red1, red3, red4, red5a, red7, red8, red9, and blue2. These eight reflectors formed the basis for the subsequent moisture content calculations.

High electrical conductivity in the clastic dike increased the dielectric loss of the signal, resulting in reduced strength of the reflections, as can be seen near x = 52 m (170 ft). The most obvious effect of the dike itself is the diffractions observed near the surface and a loss of coherence in the underlying reflector. The diffractions often define the edges of the dikes. They also disrupted or weakened the continuity of underlying reflections. Several coherent reflections are obvious from the data. In the upper 1 m (3.3 ft) on the south side of the transect, a rising event is seen from 2 to 10 m (6.6 to 33 ft). This is one of the strongest reflectors at the site and can be clearly seen between 7 and 15 ns, initially curving upward and then dipping downward as the distance along the transect increases. This reflector could be a bounding surface separating two different units or could very well be the sill observed near the dike in CPT Tubes CPT 7 and 8. Additional strong reflections are also easily observed from this profile and were confirmed during the excavation of the trench at the end of the experiment.

Upon review of the common offset GPR data from the Army Loop Road site, it became evident that the quality of the 225 MHz was inadequate to permit accurate calculations (Williams et al. 2002). Because of its lower frequency content, the 225 MHz data were initially expected to provide some information on that portion of the sediment sequence deeper than ~1.5 m (~4.9 ft). However, the signal-to-noise ratio of the 225-MHz data was particularly poor in this depth range (especially as the injection progressed), and the resolution in the upper 1.0 m (3.3 ft) was worse in comparison to the 450-MHz data. As such, only the 450-MHz data were used for this investigation. Excellent data quality over the duration of the experiment verified that a variety of reflectors, spanning a range of depths from 0.20 m (0.7 ft) to 1.20 m (4 ft), could consistently be picked from one field campaign to the next.

As shown in Figure 2.76, a series of strong reflectors were apparent in the baseline data occurring at times ranging from 10 to 20 ns. These reflectors were shown to be present over the *duration* of the experiment with the only change being a gradual decrease in the signal-to-noise ratio as the total fluid volume injected increased. Given the confidence that a consistent series of reflectors could be identified over the duration of the experiment, eight reflectors were designated as follows: red1, red3, red4, red5a, red7, red8, red9, and blue2. These eight reflectors formed the basis for the subsequent moisture content calculation (Williams et al. 2002). The depth to each of the eight reflectors observed at the Army loop Road site is shown in Figure 2.76. The depths covered by the survey ranged from roughly 0.25 m (0.82 ft) to 1.20 m (3.9 ft) below ground surface. This large range allowed the downward migration of the moisture front to be tracked as the infiltration progressed.

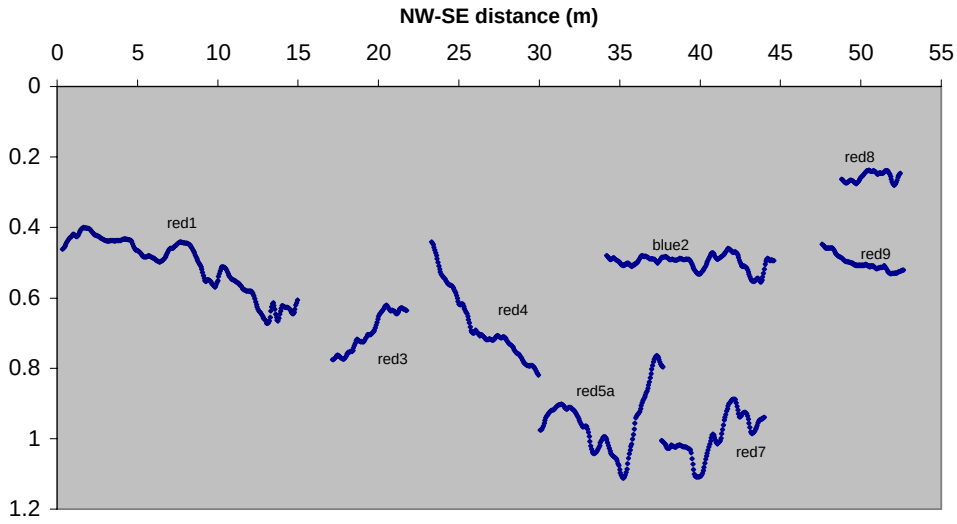

Figure 2.76. Map Showing the Spatial Location of each of the Eight Reflectors

The resulting time-lapse changes in travel time were monitored with the corresponding changes in θ_v computed and displayed in Figure 2.77 through Figure 2.80. The transect is broken to smaller sections to improve visualization. These figures show the θ (x) values calculated for individual reflectors for a given acquisition date. The notation used in the legend for each plot refers to the date of acquisition and the reflector under consideration (e.g., 66_red1 represents the θ(x) calculated for reflector "red1" on 06/06/02). Recall that the mean baseline value of θ was 0.129 m^3 m^{-3} and that it was assumed to be constant along the entire length of the profile. For this reason, it is only included on the first of the eight graphs.

For the most part, each of the plots of θ(x) as a function of time for the Army Loop Road experiment exhibits the same general trend. As expected, the changes in moisture content were iterative with increases in θ(x) of approximately 0.05 m^3 m^{-3} per 3-week interval. Of the eight reflectors, "red8" and "red9" were the shallowest. In considering the results for these two reflectors (Figure 2.79 and Figure 2.80), it appears likely that the influence of the other near-surface arrivals, such as the direct ground wave, contributed to a decreased capability to obtain good, repeatable travel time picks. This is especially true for the case of "red8" which, at 0.25 m (0.82 ft) below ground surface, shows an almost random set of changes in θ_v over the course of the investigation. If the data for "red9" are considered more closely, it is evident that there may be a bit of coherence to the wetting story. The data initially imply wetting over the first weeks of the experiment followed by a cycling of drying and then wetting and drying. Whereas this may seem to indicate nothing more than the spurious picking of travel times, the neutron-probe data collected in this area (the eastern side of the clastic dike) indicate a similar cyclical change in θ_v. While an adequate explanation is still elusive, conversations with other project investigators suggest that the influence of a nearby high matric potential sill may be at work acting as a wick to drive moisture migration away from the drip line. It should also be pointed out that the presence of the clastic dike along this portion of the GPR profile might have contributed to the observed anomalous effects. Comparison with the TDR data in this area may ultimately help determine whether the θ_v values determined around the clastic dike are of value.

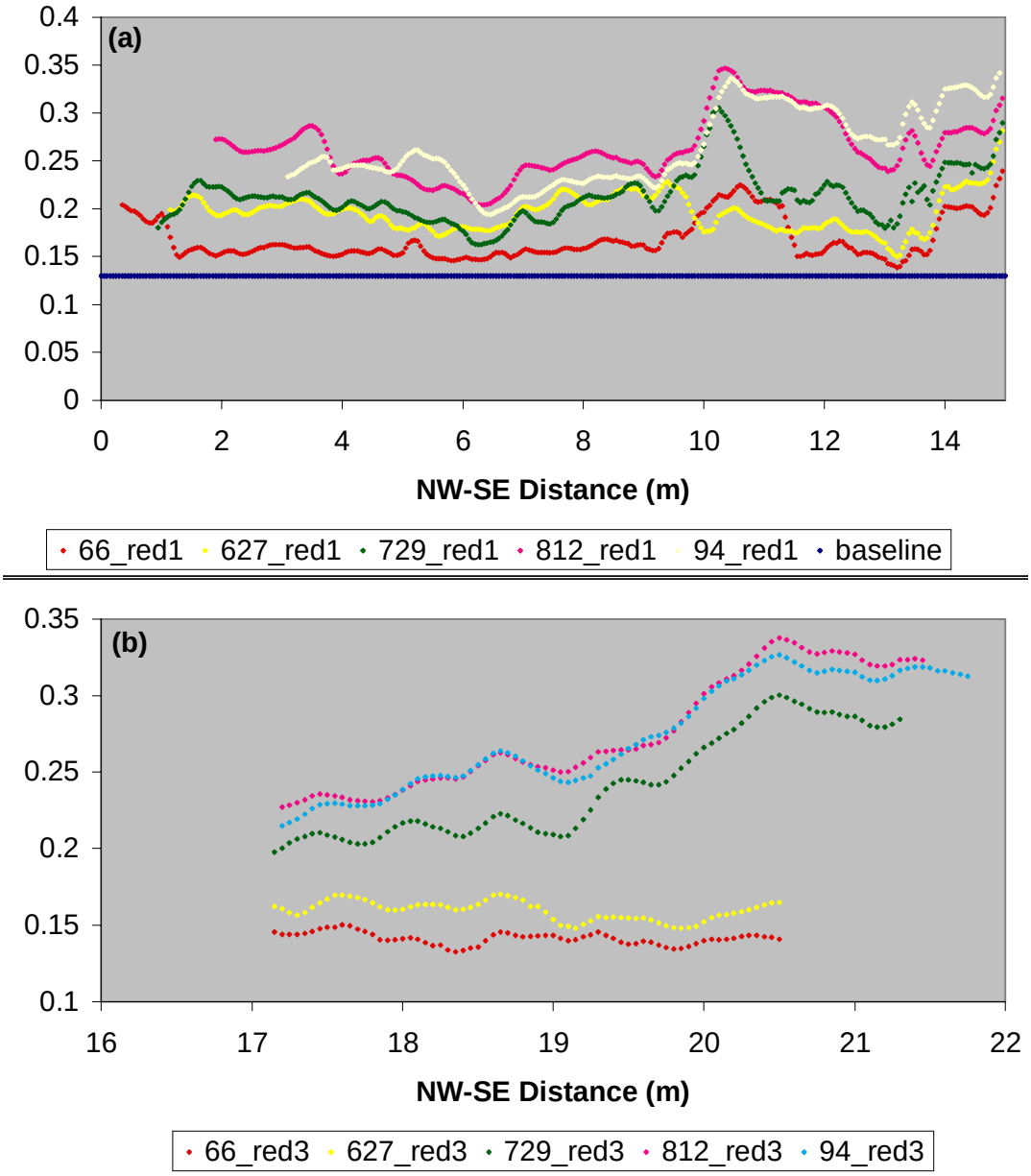

Figure 2.77. Change in θ(x) of Sediment Overlying Reflector over 3-Month Period of the Experiment at the Army Loop Road Site, (a) "red1" and (b) "red3"

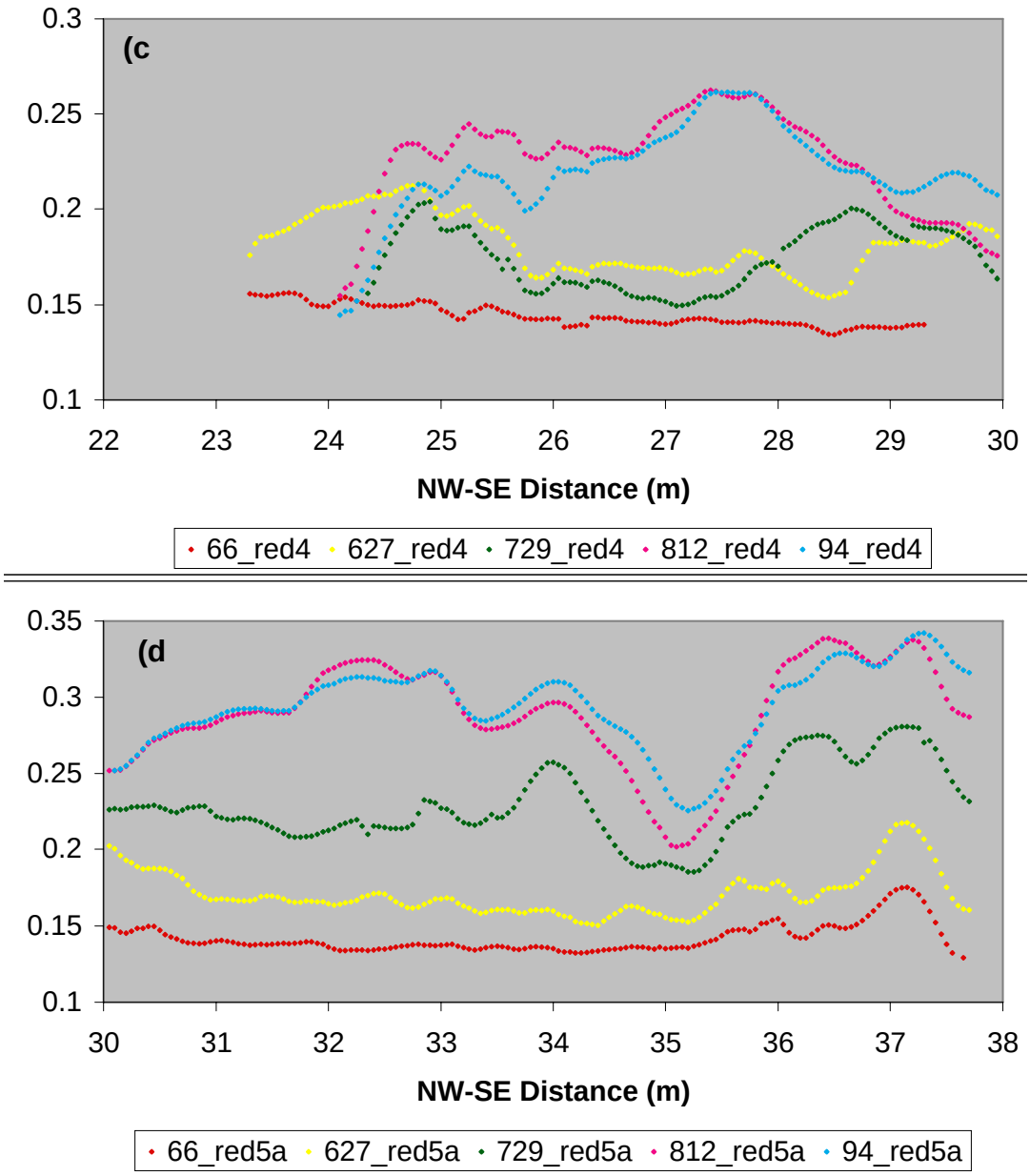

Figure 2.78. Change in θ(x) of Sediment Overlying Reflector During a 3-Month Period of the Experiment at the Army Loop Road Site (a) "red4" and (b) "red5a"

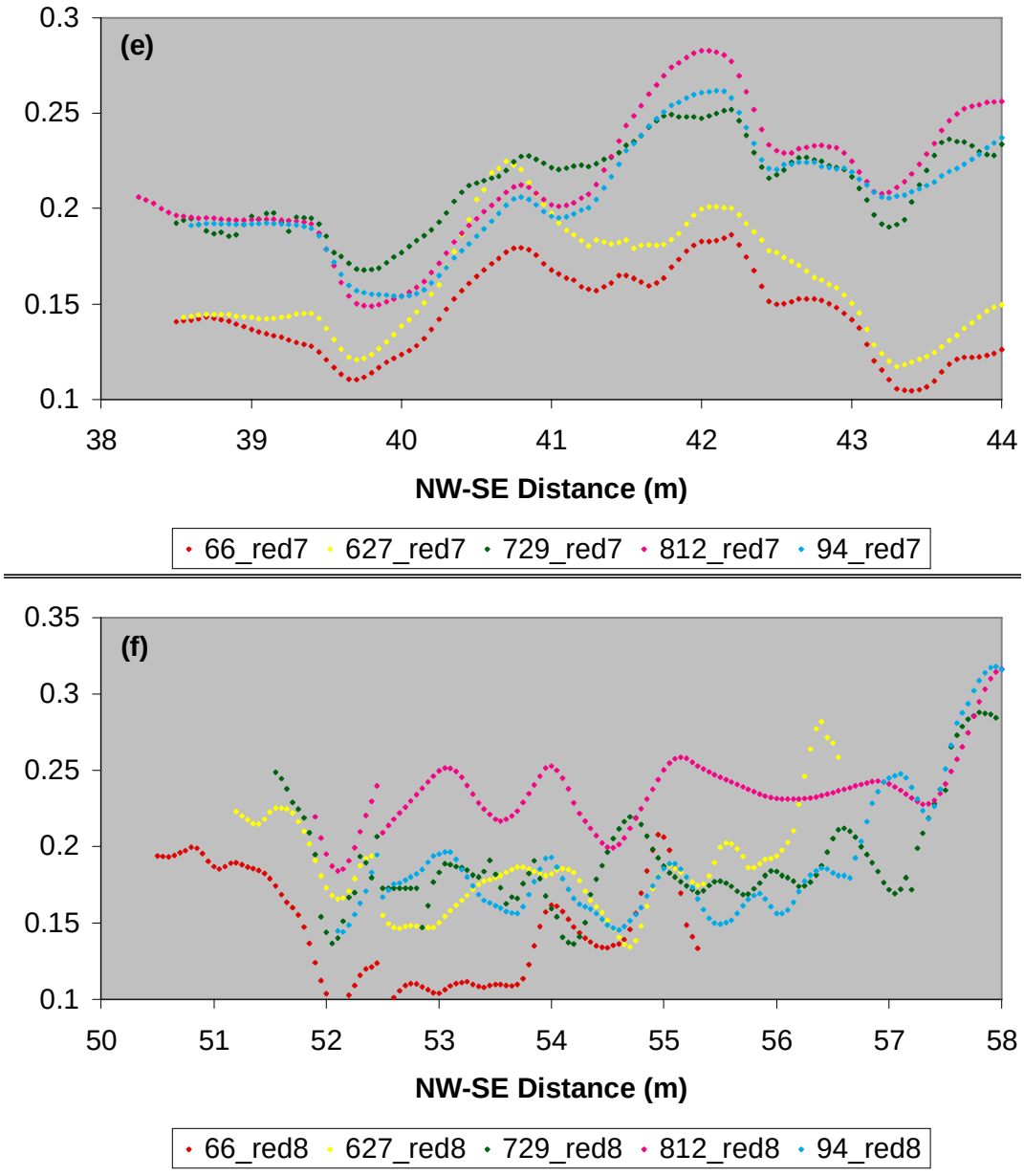

Figure 2.79. Change in θ(x) of Sediment Overlying Reflector During a 3-Month Period of the Experiment at the Army Loop Road Site, (a) "red7" and (b) "red8"

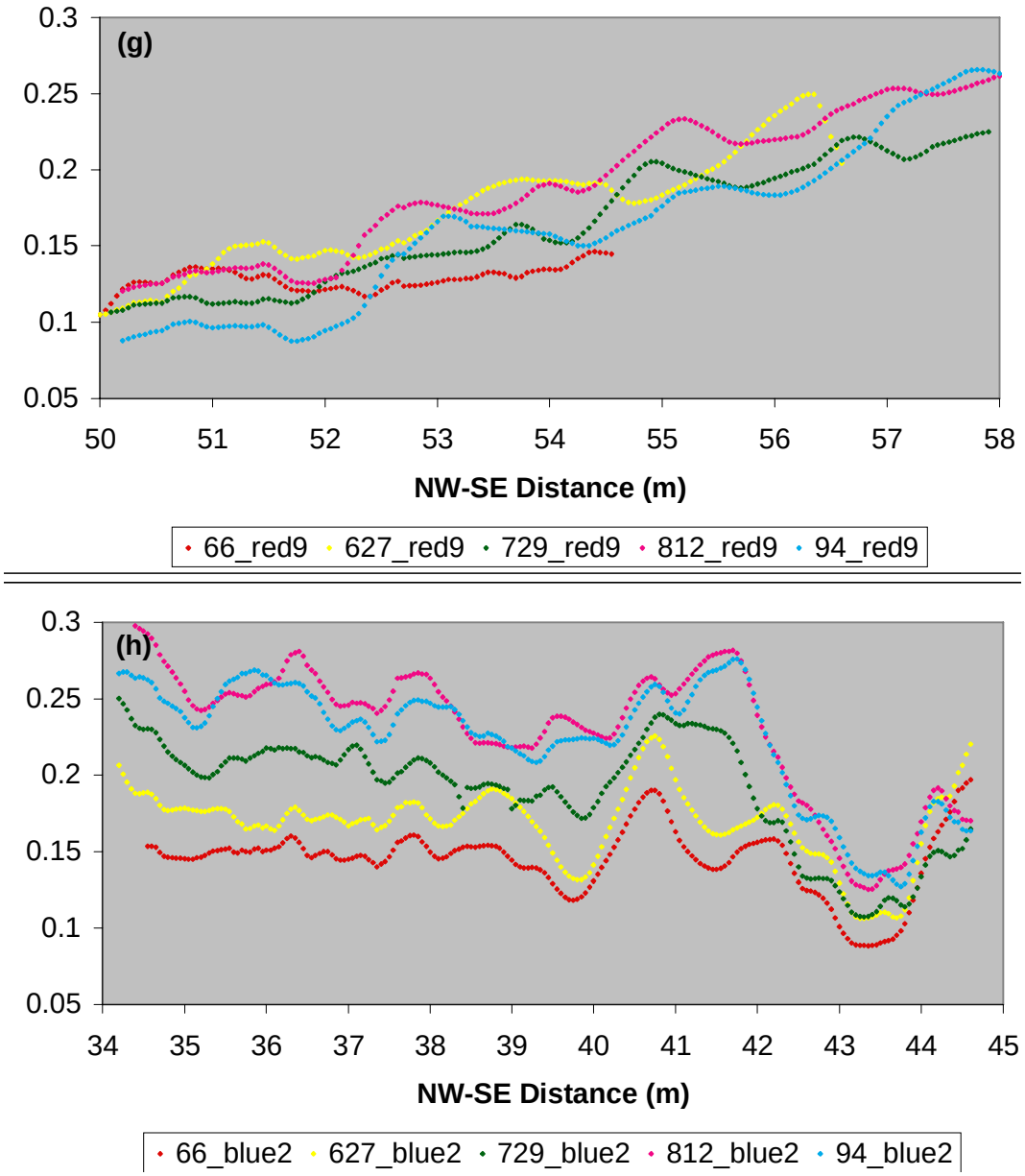

Figure 2.80. Change in θ(x) of Sediment Overlying Reflector During a 3-Month Period of the Experiment at the Army Loop Road Site, (a) "red9" and (b) "blue2"

These examples are in clear contrast to the data shown for the remaining reflectors at the Army Loop Road site, each of which illustrates quite clearly the progressive wetting of the sediment overlying them. Taking as examples reflectors "red5a" and "blue2" (Figure 2.78b and Figure 2.80b, respectively), one can see the progressive increase in θ(x) over time—reaching a maximum of nearly 0.35 m^3m^{-3} in some cases. These two reflectors occupy distinct levels within the sedimentary sequence with "red5a" being at an average depth of 0.90 m (3 ft) whereas "blue2" is at a mean depth of 0.45 m (1.5 ft). As one might anticipate, the time taken for the sediment overlying the deeper reflector (red5a) to reach a near steady-state value of θ(x) is longer than for the shallow reflector. The data shown for the other reflectors exhibit a similar pattern, reaching steady-state conditions by mid-August (or roughly 10 weeks after the

infiltration started). After this time, the sediment in the near surface (less than 1.0 m [3.3 ft] deep) would be at or near field capacity under conditions of gravitational drainage. As more water was released into the sequence, no additional infilling of the pore volume would have occurred, and drainage to deeper regions of the sequence would have occurred. The 450-MHz data definitely appear to bear this out. Unfortunately, the limited depth of investigation of these antennas provided little or no information on those depths greater than about 1 m. For that, we must turn to the borehole radar data obtained between the boreholes located near the southeastern end of the profile in the region of the clastic dike.

Some mention should also be made regarding the perceived accuracy of the surface reflection methodology, especially as it relates to the fidelity and repeatability of both the acquisition methodology and the picking of travel times. With respect to the acquisition methodology, it became clear early on that the start and stop positions of the profiles were not being exactly repeated. This can be seen in the θ_v data presented above. The prominent peaks and troughs evident in data collected during one visit are phase-shifted from those occurring at later dates. As these peaks and troughs likely represent "fixed" stratigraphic effects, they would not be expected to change lateral position over the course of the experiment. So the only plausible explanation is that the start/stop position of the GPR unit was slightly variable over the course of the investigation and that perhaps some data points were skipped because of a variety of causes during the operation. This does not diminish the overall utility of the methodology; it merely forces the data to be interpreted a bit more qualitatively. In other words, a given position (e.g., 23.5 m [77 ft] from the start) may not correspond precisely each time to the corresponding TDR (or similar) measurement. With respect to the accuracy of the travel time picking, it is helpful to consider the following example. From experience, it appears that the accuracy of the picks is likely to be on the order of ±0.5 ns. If one then uses this to assess the accuracy of the computed $\theta(x)$ values, then it can be found that the error in $\theta(x)$ is $\pm$ 0.0188. Smoothing and averaging of the travel time picks probably verifies better accuracy (or at least improved repeatability) of the data, and assuming the error is reduced to $\pm$ 0.2 ns, the corresponding error in $\theta(x)$ is $\pm$ 0.0075.

The surface GPR measurements demonstrate that there is a strong amount of spatial variability in the degree of wetting. More importantly, the changes in $\theta(x)$ over time determined for *each* of the reflectors exhibited some degree of spatial dependence. In the case of reflector "red1," there are several small ($\leq$ 2.0-m [$\leq$ 6.6-ft]) sections of the profile that appear to be preferentially wetting at a greater rate (as evidenced by the rate of $\theta(x)$ increase) and to a greater degree as reflected in the absolute values of $\theta(x)$. Clear evidence for lateral movement within a thin sill ($\leq$0.25 m [$\leq$0.82 ft] thick) was found within the trench that matches these region zones of elevated $\theta(x)$ and the increased rate of wetting. A similar effect was observed in any number of the other reflectors but is especially obvious in the data for reflectors "red5a" and "red7." In these cases, not only are there large differences in both the rate of change of $\theta(x)$ and the degree of wetting along the lines, but also these changes occur over even shorter spatial scales than for "red1." The data associated with these two reflectors exhibit change over scales of $\leq$ 1.0 m ($\leq$ 3.3 ft). It should be pointed out, however, that this might be partly (or even largely) an artifact associated with the uniform baseline $\theta(x)$ assumption. By including the TDR data to obtain a more realistic baseline, it should be possible to determine whether those regions that imply a greater degree of wetting simply started off with greater values of $\theta(x)$.

2.13.2 Synopsis and Implications

The synopsis of findings in the application of surface GPR to map moisture contents and subsurface structure and their implications are as follows:

- A series of surface GPR surveys were conducted at the Army Loop Road site to assess the utility of this method for characterizing the relationship between multiscale heterogeneities and moisture distribution patterns.

- GPR provided insight into the nature of fluid flow in and around the unique geology of a clastic dike. Whereas the neutron logging was helpful in elucidating some of these features, its limited inter-well coverage would have hampered identifying some of these features without excavation.

- The ability to interrogate large areas with high spatial resolution, along with the relatively low infrastructural support needed for the surface radar technique and the information it provides, clearly demonstrated the utility of GPR investigations and the potential to generate information from which the spatial correlation structure could be determined.

- These studies have given rise to a data set that could be used in the investigation of relationships between GPR response and multiscale hydraulic properties through pedotransfer functions as well as the joint inversion of GPR response and hydrologic measurements.

- There is evidence that GPR data may represent the correlation structure of flow variables and hydraulic properties. This technology could be invaluable for characterizing structure between boreholes, allowing the extension of borehole lithologic and hydraulic property data to the uncored regions. This type of information would be useful to identify the spatial correlation structure of hydraulic and transport properties and forms the basis of methodologies to regionalize local-scale property measurements. Surface GPR is non-invasive and can be used to rapidly cover large areas.

2.14 Seismic Crosshole Tomography

Multiscale spatial variability of physical and hydraulic properties in Hanford sediments renders the characterization of subsurface transport properties difficult using conventional vadose zone techniques. Geophysical techniques offer an opportunity to interrogate larger volumes of sediment while providing constraints on lithostratigraphy. However, many of the relationships relating geophysical response to physical and hydraulic properties are still not well understood in the heterogeneous unconsolidated sediments typical of Hanford's vadose zone. SCT is a well-established geophysical method that can provide valuable information about near-surface lithologic properties at and between wells in consolidated porous media. These data can be used to generate detailed images of subsurface structure but has had limited application in the unconsolidated sediments at Hanford.

SCT is based on the measurement of the travel times of seismic ray paths between two or more boreholes to derive a map of seismic velocity in the intervening sediments. Data are typically collected using one hole for the seismic source or transmitter while measuring first-arrival times using strings of hydrophones in adjacent wells. Energy is transmitted at multiple positions in the transmitter well and

received in the receiver well(s) with either single or multiple receivers. In practice, a three-component wall-locking geophone and a directional down-hole seismic source are initially lowered to the bottom of two boreholes. The two probes are then moved together in intervals of 30 to 60 cm (11.8 in. to 23.6 in.) so that a near horizontal ray path is maintained between them. The result is a network of overlapping ray paths that are then used to describe the average shear (S) and compressional (P) wave velocities. The resulting velocity image, known as a tomogram, can then be used to identify anomalous velocity zones lying between the boreholes as well as imaging individual velocity layers. These tomograms can be used to inferred lithology, bed geometry and continuity, fracture and fault properties, porosity, and, in some cases, the fluid distribution.

Early successes in SCT have come mostly from environments in which velocity heterogeneity was neither excessive nor layered. Where data from crosshole surveys in sedimentary environments have been acquired, they have often been difficult to interpret, analyze, and invert. In layered unconsolidated sediments, crosshole data are certain to contain arrivals from multiple paths, guided wave modes, super critical reflections, and mode conversions. Thus, the objective of this study was to investigate the feasibility of using SCT to delineate subsurface structure at the 299-E24-111 test site.

Crosshole seismic measurements were made at the 299-E24-111 test site after all of the infiltration tests were completed. The boreholes were sealed with inflatable packers so that they could be filled with water. Water-filled wells are often used to improve seismic coupling. Four different seismic crosswell sections were obtained from three high-resolution sections and one long offset section using a distant 15-cm (6-in.) steel-cased hole for a source hole. The steel-cased hole was also closed with an inflatable packer and filled with water. The three high-resolution sections were collected by placing a 24-element hydrophone array in Well X4, which was filled with water. A 3.8-cm (1.5-in.) diameter by 10-cm (4-in.) long piezoelectric cylindrical seismic source was then used successively in Wells X3, X2, and X1 (Figure 1.4). To make the necessary measurements, a three-component wall-locking geophone and a directional downhole seismic source were initially lowered to the bottom of two boreholes. The data were collected as tomographs at 0.25-m (0.82-ft) intervals for both source and receiver. The piezoelectric source energy output ranged from 1 to 10 kilohertz. The long offset section was obtained by leaving the hydrophone array in Well X4 and placing an orbital vibrator source in Well 2E-24-110, which was also filled with water, approximately 19 m (62 ft) away from X4. The purpose of this was to see how far seismic energy could be transmitted in the vadose zone. The orbital vibrator is a much stronger source than the piezoelectric source, but puts out lower frequencies, in the 50- to 300-hertz range. Average shear (S) and compressional (P) wave velocity values were obtained by calculating wave travel times between the source and receiver boreholes. Based on the assumption of a spatial resolution on the order of ¼ wavelength, and velocities on the order of 700 m (2297 ft) s^{-1}, the spatial resolution of measurements was estimated to be on the order of 10 cm (3.9 in.) for the piezoelectric data (assuming a frequency of 2000 Hz). A similar analysis resulted in a resolution on the order of 60 cm (23.6 in.) for the orbital source (assuming a 300-Hz orbital source). Details of the monitoring protocol, data collection, and processing are summarized in the test plan of Ward and Gee (2000) and the data report of Majer et al. (2001). The resulting data were processed and the travel times inverted to obtain the seismic velocity structure using an algorithm developed for inverting radar data.

2.14.1 Results

Figure 2.81 shows a sample wiggle trace display from the long-offset seismic test. This is a composite of the different levels and shows good P-wave and S-wave energy. Majer et al. (2001)

reported good energy transmission up to 300 hertz for this site. These results are very encouraging given the distance of propagation of such a high frequency in a vadose zone environment and suggest that this technique could be easily applied at the field scale for characterization of waste management areas.

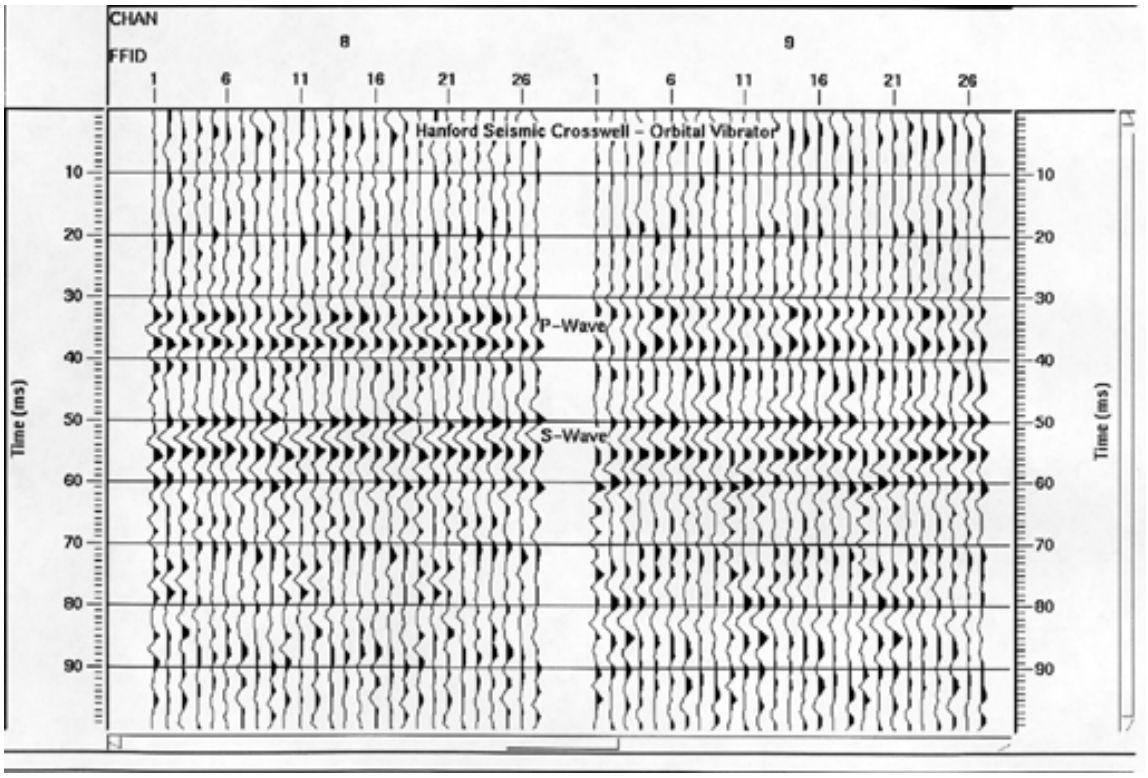

Figure 2.81. Sample Wiggle Trace Plot at 19 m (62 ft) Using a Seismic Source in the Range of 50 to 300 Hz

Although many seismic velocity tomograms have been reported in the literature, the reliability of the images, especially away from the boreholes, can rarely be examined because of the lack of independent measurements. One source of validation data available for this site was from crosshole radar tomography. Radar tomography uses the travel-times of high-frequency EM waves to reconstruct radar velocity panels whereas SCT uses the travel-times of elastic waves transmitted between sources and receivers to reconstruct a P-wave velocity profile of the subsurface. Because of the high frequency of the source and the short spacing between source and receiver locations in radar tomography, these panels can be used to resolve features 1 m (3.2 ft) or less, thereby providing detailed images of the subsurface from which lithostratigraphy can be derived.

Figure 2.82 compares the structure in subsurface heterogeneity derived from the seismic and radar measurements in the X1-X4 borehole pair (Figure 1.4) at the 299-E24-111 test site. The most striking observation is that the seismic velocities are quite low (550 to 750 m [1804 to 2461 ft] s^{-1}), just above the velocity in air (330 m [1083 ft] s^{-1}). Seismic velocities resolve the same stratigraphy as the radar-velocity estimates, but because radar and seismic waves sample the subsurface differently, there may be scaling issues to be resolved. Nevertheless, the high-radar-velocity layers coincide with the low-seismic-velocity layers and vice versa. This is most likely because EM velocities are high in air, whereas the acoustic-

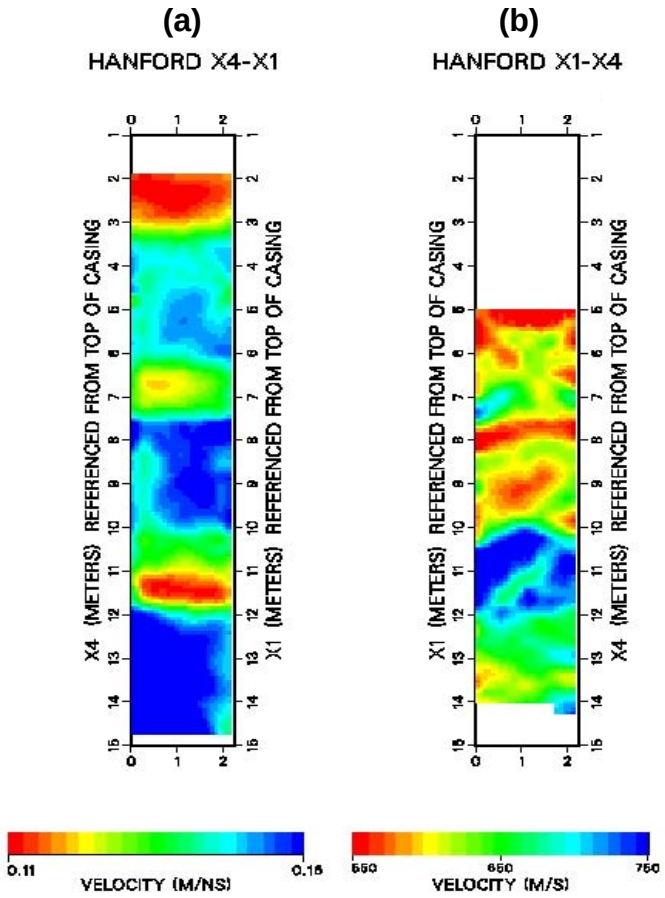

Figure 2.82. Subsurface Structure Inferred From (a) Crosshole Radar and (b) Cross Hole Seismic

wave velocities are low. Therefore, in unsaturated sediments, the seismic waves should travel slowest in high-porosity zones whereas EM waves should travel fastest. This interpretation is supported by the velocity tomograms in Figure 2.82.

The EM velocity measured by radar is related to the dielectric constant of the sediments. Water has a dielectric constant of around 80, air has a value of 1, and most geologic materials have dielectric constants between 3 and 12. Thus, water content may be determined from the dielectric constant using petrophysical models. Average velocities range from 0.140 m ns^{-1} in unsaturated sediments to around 0.080 m ns^{-1} in saturated sediments; thus, the lower velocities in Figure 2.82a correspond to wetter sediments. In these sediments, higher water contents are usually associated with fine-textured sediments ranging from silt to fine sand. Seismic velocities range from 330 m s^{-1} (1083 ft s^{-1}) and 600 to 1850 m s^{-1} (1968 to 6070 ft s^{-1}) in sand to 1100 to 2500 m s^{-1} (3609 to 8202 ft s^{-1}) in clay. Thus, seismic velocities are higher in finer-textured sediments, which, because they are wetter, show lower radar velocities. Overall, the seismic results are quite good, and the range of velocities shown in Figure 2.82b suggest sediments composed of fine to coarse sand. At the time of design of the experiments, there was some uncertainty about the capability of the seismic method to penetrate the unsaturated sediments and resolve the structure. The seismic results indicate that at a frequency of several hundred Hz, waves could propagate over 20 m (66 ft) and possibly 30 m (98 ft) to give relatively high-resolution characterization data. Resolutions of least 0.25 m (0.82 ft) appear feasible for delineating lithology. Until this set of

experiments, experience had shown that it was difficult to collect high-resolution seismic data (in the kHz range) in the vadose zone. This is because partial saturation greatly attenuates seismic energy. In fact, until this experiment, there had been no published reports of high-frequency seismic tomographs collected at this scale in any vadose-zone environment. Another advantage is that the seismic and radar data are complementary. The radar responds primarily to changes in moisture content whereas seismic velocity is controlled by the stiffness of the geologic materials and is therefore sensitive to differing pore space geometry, providing a measure of changes in porosity. Thus, time lapse tomograms collected with the two different modalities during an infiltration test would provide complementary information on the effects of lithology on moisture distribution. The spatial distribution of the antecedent moisture is controlled mostly by texture. Thus, measurements if antecedent moisture with radar could also be used to infer texture and hence porosity. A comparison of porosity estimates derived from seismic with crosshole radar tomography panels and neutron porosity logs in the same wells could provide insight into the value of these data for inverse modeling and characterization of structure. Differences in the support scales of the different modalities may also be useful for interpreting issues related to upscaling.

2.14.2 Synopsis and Implications

The synopsis of findings in the investigation of SCT for characterizing subsurface structures and their implications are as follows:

- Geophysical techniques offer an opportunity to interrogate larger volumes of sediment while providing constraints on lithostratigraphy, but many of the relationships relating geophysical response to physical and hydraulic properties are still not well understood.

- SCT is a well-established geophysical method that can provide valuable information about near-surface lithology but has not been widely used in unconsolidated porous media.

- Four different seismic crosswell sections were obtained from three high-resolution sections and one long offset section at the 299-E24-111 test site. Seismic velocities were quite low (550 to 750 m s^{-1} [1230 to 1678 mph]), just above the velocity in air (330 m s^{-1} [738.2 mph]), suggesting the presence of mostly sand and fine sands. Crosshole radar measurements, which are complementary to SCT, confirm these findings.

- These results represent the first of their kind for high-frequency seismic tomographs collected at this scale in any vadose-zone environment. SCT was able to delineate lithology at 0.25 m (0.82 ft) resolution with a penetration distance of over 20 m (66 ft) with a possibility of up to 30 m (98 ft).

- SCT can be used in waste management areas with existing infrastructure. Although water-filled wells were used to enhance seismic couple, they are not necessary. Combined use of crosshole seismic, radar, and neutron probe would provide complementary information about the effects of lithology on moisture distribution as well as upscaling relationships.

2.15 Crosshole Ground Penetrating Radar

Crosshole radar tomography is also a well-established geophysical method that can provide valuable information about near-surface lithologic properties at and between wells in porous media. Crosshole radar is analogous to the seismic reflection technique, except that EM waves (microwaves) are used rather than acoustic waves. The primary information obtained is the variation of dielectric properties of the subsurface. Because of the large contrast in the dielectric constant between water (80), most earth materials (3–5), and air (1), volumetric water contents can be easily inferred from radar data. Information about lithology and the distribution of different sediment types can also be inferred using established petrophysical relationships as the antecedent moisture content in an equilibrated profile is controlled by sediment texture. Radar tomography uses the travel-times of high frequency EM waves to reconstruct a radar velocity panel. Because of the high frequency of each source and the closely spaced source and receiver positions, these panels can be used to resolve sub-meter (25-cm [9.8-in.] or less resolution) features and are therefore useful for providing detailed subsurface images of sedimentary environments. The objective of this study was to investigate the feasibility of using crosshole radar tomography to delineate subsurface structure in Hanford's vadose zone and to track the movement of wetting fronts emanating from subsurface and near surface leaks. Crosshole radar measurements were made at both of the field test sites during the course of the field studies.

The radar campaigns at the 299-E24-111 test site consisted of repeated crosswell tomographic measurements collected between six possible well pairs: X1-X2, X2-X3, X3-X4, X1-X2, X1-X3, and X2-X4 (Figure 1.4). Data were collected using a Sensors & Software, Inc. PulseEKKO 100 GPR system using the 200-MHz center frequency antennas. The step size for data collection between well pairs X1-X2, X2-X3, and X3-X4 was 0.125 m (0.41 ft). Data were collected on four different occasions. The first was a pre-injection dataset (PRE) on May 25, 2000, during which the baseline condition was recorded. A second dataset (POST1) was collected on June 13, 2000, whereas a third (POST3) was collected on July 14. A fourth dataset (POST2) was collected on June 28 that consisted of nearly continuous data acquisition between well pair X1-X2 during an injection test. This was done in an attempt to map any changes in moisture distribution over the duration of a single injection (Majer et al. 2000).

At the Army Loop Road Site, the test area was defined by a 60-m (197-ft) long transect. Crosshole radar data were also acquired using a Sensors and Software, Inc. PulseEKKO100 GPR system equipped with both 100-MHz and 200-MHz antennas. The 100-MHz antennas were used for those well pairs in which the signals traversed the clastic dike (well pairs 1-3 and 4-8) whereas the 200-MHz antennas were used for all the remaining well pairs (well pairs 1-2, 2-8, 3-4, and 4-5) as shown in Figure 2.83. An important question in this study was the influence of the clastic dike that crossed the drip line.

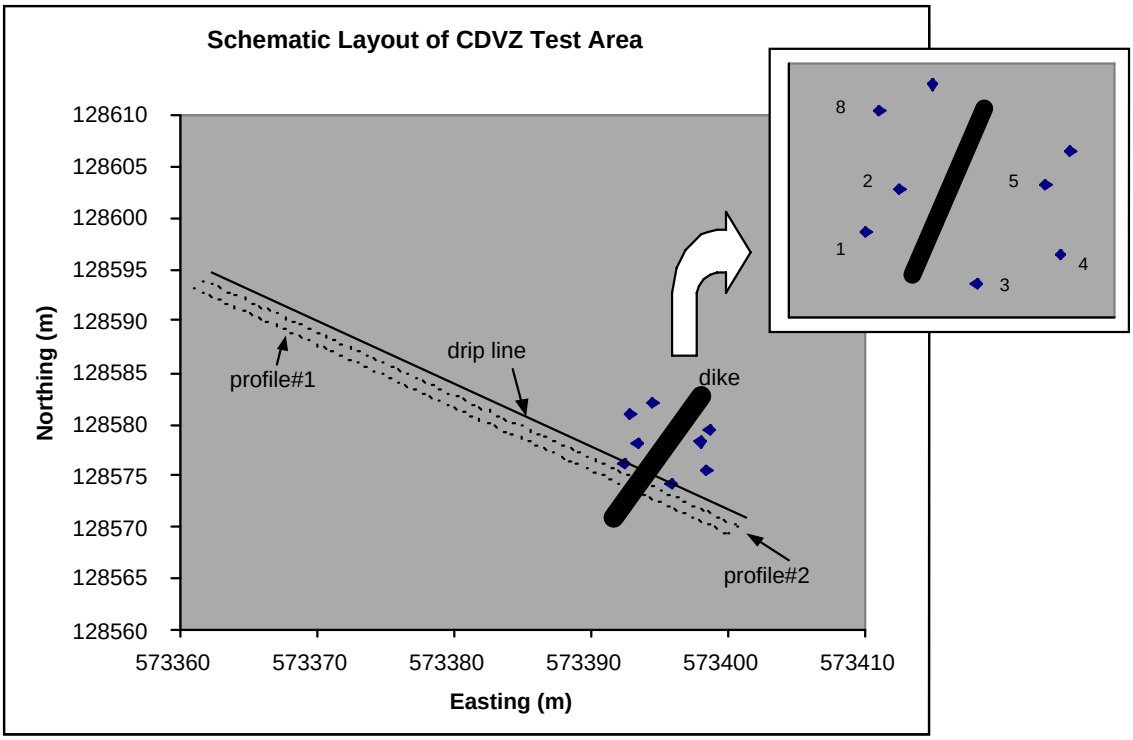

Figure 2.83. Schematic Layout Showing Common Offset Profiles and Borehole Radar Locations at the Army Loop Road Site

2.15.1 Results

Figure 2.84 shows the EM velocities obtained between the six well pairs, collected before the infiltration tests at the 299-E24-111 test site. A velocity pixel dimension of 0.25 × 0.25 m (0.8 × 0.8 ft) was used for the image inversion. These data were used to delineate the lithostratigraphy in the vicinity of the tomographic profiles. The EM propagation velocity range of 0.11 to 0.16 m (0.36 to 0.52 ft) ns^{-1} is typical for unsaturated, unconsolidated sands. The tomograms suggest the presence of at least six distinct velocity layers, each continuous across the length of the tomogram and ranging in thickness from 0.25 to 3.5 m (0.8 to 11.5 ft). The layers alternate between high and low velocities with the shallowest layer having low velocities (< 0.11 m [0.36 ft] ns^{-1}) and extending from the surface to a depth of about 3.0 m (9.8 ft). The next deepest layer had a higher velocity (~0.14 m [~0.46 ft] ns^{-1}) and extended about 3.0 to 3.5 m (9.8 to 11.5 ft) below this first layer to a depth of ~6.5 m (~21.3 ft). Lateral heterogeneities in velocity were also observed in this layer. The third layer was about 0.25 to 0.50 m (0.8 to 1.6 ft) thick with low EM velocities typically associated with fine sand or silt fine sand. Whereas this layer appeared mostly horizontal, there was some evidence of thickening and/or splitting near borehole X1. The fourth layer was about 0.25 to 0.50 m (0.8 to 1.6 ft) thick and consisted of higher velocity sediment, suggesting a coarser texture, and is best seen in the X3-X2 tomogram. Velocities in this layer were just slightly higher than the layer below. The fifth layer was about 3.0 m (9.8 ft) thick with similar velocities to those of the second layer, suggesting a similar texture. The sixth layer was about 0.50 to 0.75 m (1.6 to 2.5 ft), somewhat similar in thickness to the third layer in thickness and velocity. A seventh layer is evident with velocities over 0.16 m (0.52 ft) ns^{-1}. These seven layers were continuous across all of the radar profiles,

suggesting lateral continuity over an area of at least 4 m^2, and are consistent with the lithologic descriptions of Last et al. (2001). Based on the geologist's description of undisturbed split spoon samples obtained at boreholes S1, S2, and S3, the sediments were grouped into five distinct lithostratigraphic units as follows:

1) 3 to 6 m (9.8 to 19.7 ft). Poorly laminated slightly silty medium sand
2) 6 to 7 m (19.7 to 23 ft). Well stratified slightly silty to silty coarse to medium sand
3) 7 to 10 m (23 to 33 ft). Weakly stratified medium sand
4) 10 to 12 m (33 to 39 ft). Highly stratified slightly silty to silty coarse sand
5) 12 to 17 m (39 to 56 ft). Sand to slightly silty sand.

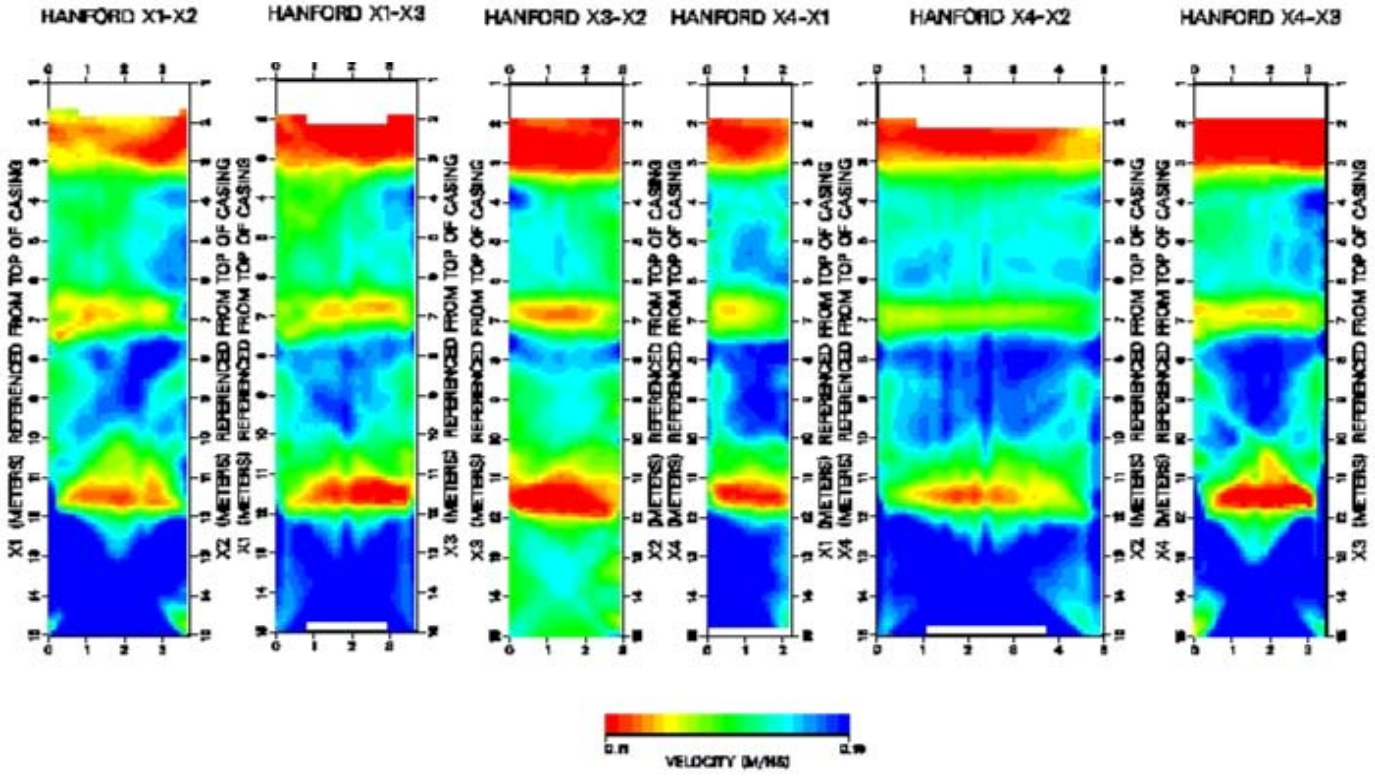

Figure 2.84. Electromagnetic Velocities Derived from the Pre-injection Crosshole GPR Measurements Between the Different Well Pairs at the 299-E24-111 site.

The EM velocities were converted to dielectric constants and finally volumetric water contents using the method of Topp et al. (1980). The resulting water-content tomograms were compared to neutron-probe-measured water contents in wells adjacent to the crosshole radar access tubes. Figure 2.85 compares GPR water content derived from the X3-X2 tomogram with a neutron-probe-measured moisture content contour between Wells H2 and H6 (Figure 1.4). Not only were the crosshole radar measurements effective in identifying the fine-textured, high-moisture zones identified by the neutron probe, but they also highlighted other regions of heterogeneity missed by the neutron logs. The spatial sensitivity of the neutron probe varies from about 0.15 m (0.49 ft) to 0.30 m (0.98 ft) in these sediments and was

interpolated between wells by kriging, whereas the radar moisture is based on actual velocity measurements between the two wells.

In addition to being able to identify the effects of small-scale heterogeneity on the distribution of antecedent moisture, differences in radar tomograms can provide near real time images of the infiltration process. This was demonstrated by calculating the difference in travel times obtained in the first post-injection tomograms from the baseline tomograms. Because the geology remains constant, observed changes in the dielectric constant can be attributed solely to the change in moisture as the wetting front passes the monitored domain.

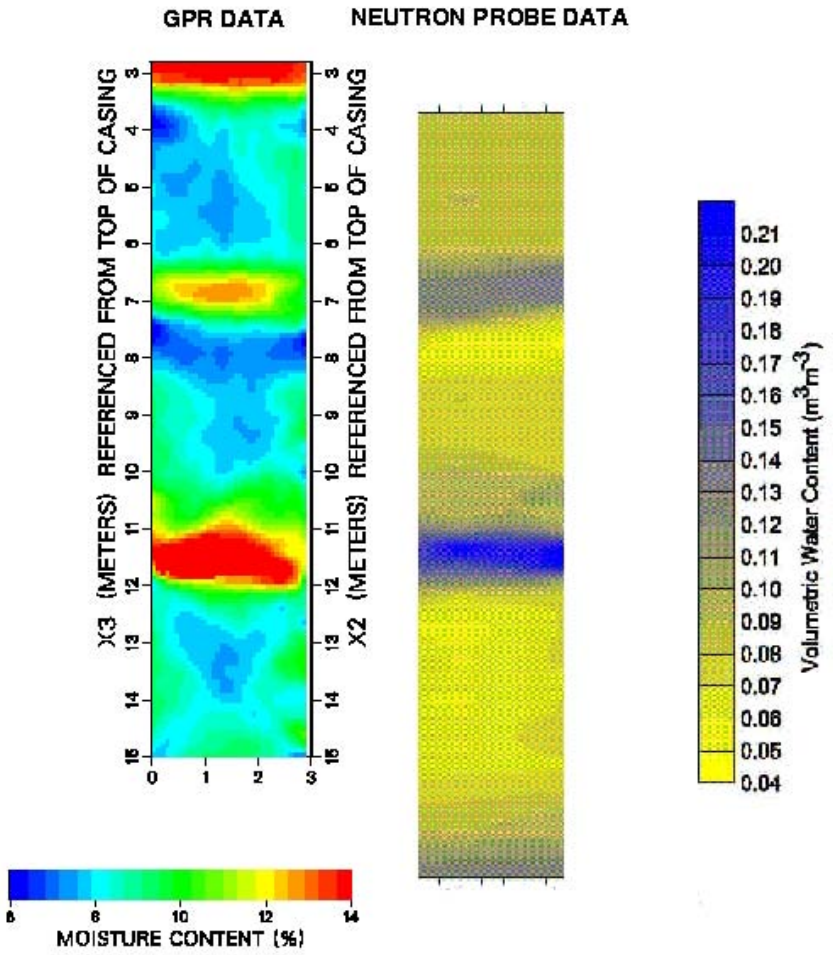

Figure 2.85. Moisture Content Derived from Radar Tomograms Between Wells X2 and X3 Compared to Moisture Content Data in the same Region Derived From Neutron-Probe Measurements Between Wells H2 and H6 at the 299-E24-111 Test Site

Figure 2.86 shows the changes in moisture content for three of the well pairs associated with POST1, the first set of measurements following the injection. The results indicate that the greatest changes in moisture occurred just above the low-moisture zone at a depth of 6.5 m (21.3 ft) in Layer 3 and just above the low moisture feature at a depth of 10 m (33 ft) in Layer 6. In fact, no changes in moisture were evident below the 10 m (33 ft) depth. At the time the first post-injection measurements were made, only a

small amount of water had reached the area interrogated by the X4-X3 well pair, which is about 3.5 m (11.5 ft) laterally from the injection point. As shown in Figure 2.87, the resulting water contents are in good agreement with the distribution of moisture content measured by neutron probe. Although the neutron-probe values are not "differenced" for this comparison, the areas of high moisture determined by neutron-probe data are co-located with the changes determined from the crosshole tomogram.

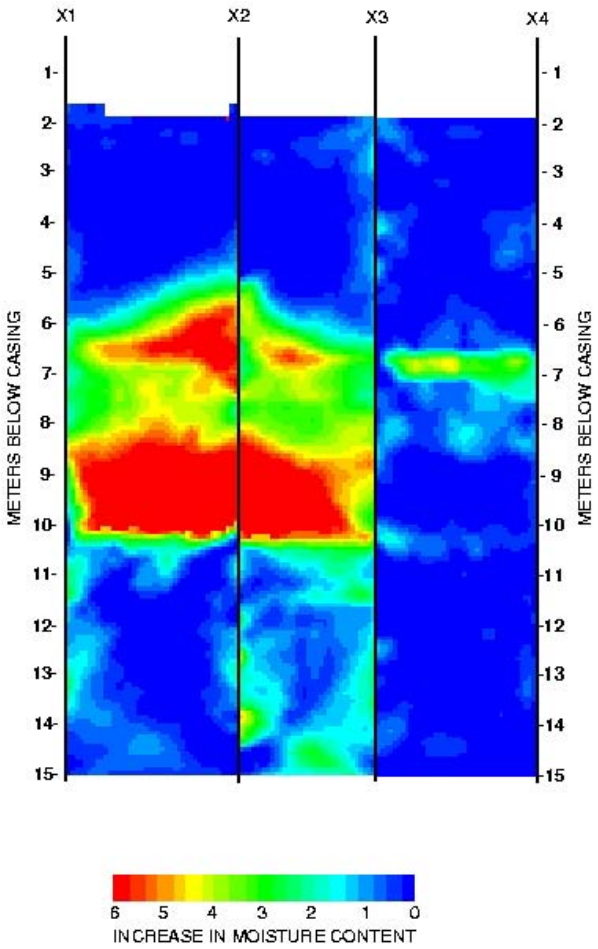

Figure 2.86. POST1 Changes in Water Content after the First Injection at the 299-E24-111 Test Site

Figure 2.88 shows the tomograms for POST2 data acquired during the fifth injection. These data were collected in a time lapse mode in an attempt to track an active injection. Data were acquired only between well pairs X2-X1, the well pair closest to the injection point. Three complete data sets were acquired between these well pairs at discreet intervals after approximately 568 L (150 gal), 1514 L (400 gal) and 3407 L (900 gal) were injected. Moisture contents were calculated from the data and subtracted from the baseline distribution acquired the previous afternoon before the injection. These data clearly show the fluid spreading laterally above the low-moisture zone in Layer 3 with little or no change in moisture occurring in or below this layer for the duration of monitoring. These observations are consistent with the neutron-probe measurements and spatial moment analyses of the changes in water content.

Crosshole radar was also able to detect differences in flow paths caused by changes in fluid properties. As part of a study to determine the effects of fluid properties, crosshole radar data from water and saline injections were compared for the 299E24-111 test site. Radar results indicate that the flow paths of the hypersaline sodium thiosulfate solution were different from those of salt-free water. The denser, more viscous sodium thiosulfate appears to have mixed less with the *in situ* fluids, suggesting that transport may have been influenced by the density differences. Figure 2.89 compares tomographs from the FY 2000 salt-free and FY 2001 thiosulfate injection between Wells X1 and X2 at the 299-E24-111 test site. Following the thiosulfate injection, the wetting front showed a significantly different path than observed with the same well pairs in FY 2000. The injection point was approximately 1 m (3.3 ft) behind the plane of these two wells at 5 m (16.4 ft) depth and 1.5 m (5 ft) from Well X1.

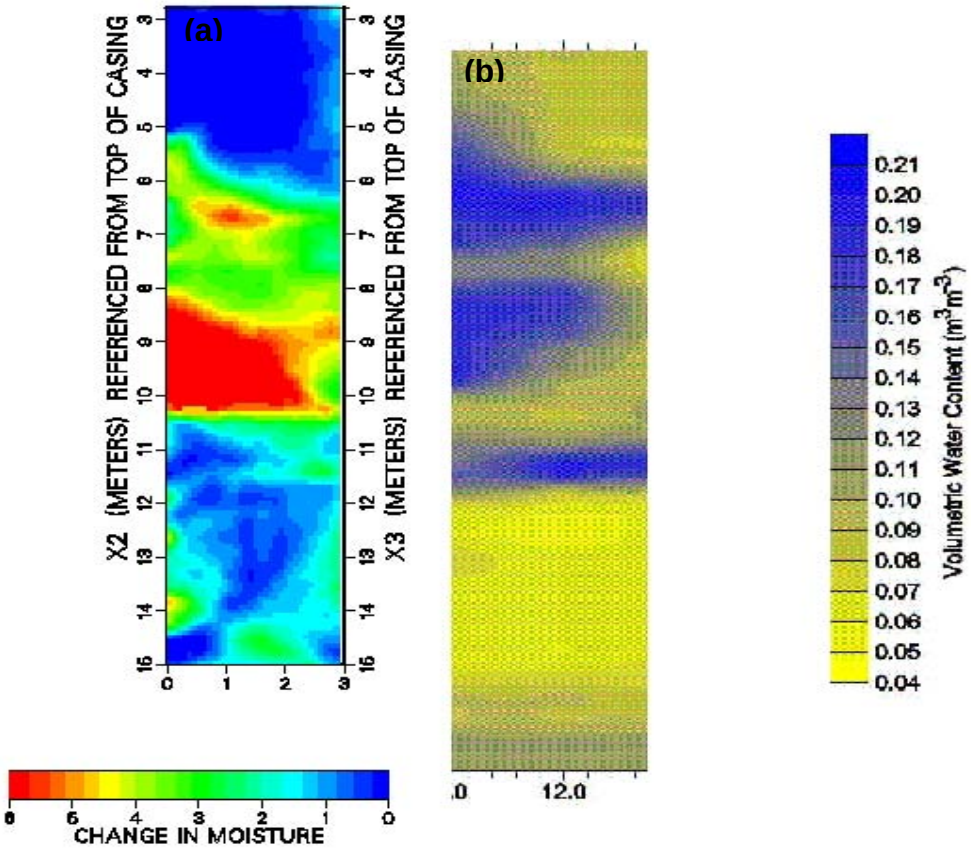

Figure 2.87. Distribution of Moisture Content after the Second Injection (a) Moisture Change from Crosshole Radar on June 13, 2000, and (b) Absolute Moisture from Neutron Probe on June 9, 2000

At the Army Loop Road site, crosshole radar showed the development of a relatively uniform wetting front beneath the drip line with little horizontal spreading perpendicular to the line. However, heterogeneity along the length of the drip line had a strong impact on the moisture distribution. The largest changes in water content occurred between boreholes 1 and 3 (Figure 2.83) that were oriented parallel to the drip line. The well pairs located to the north of the drip line showed only small changes in moisture. The dike was essentially a low-velocity vertical structure with unknown horizontal thickness, and the overall decrease in velocity in this structure was smeared across the velocity tomogram.

Nevertheless, changes in moisture that appeared to be impacted by the dike and sill were observed and corroborated by the borehole neutron data. The tomography results indicated that distances separated by 0.5 m (1.6 ft) or less showed strongly variable changes in water content. Especially encouraging were the observations of similar scales of variability within the trench to the north of the drip line. Clear evidence for lateral migration of water in a thin sill (≤0.25 m [0.82 ft] thick) was found within the trench that matches a similar region of elevated water content in the well pairs traversing this region. Changes in moisture that appeared to be impacted by the dike and sill were observed and corroborated by the borehole neutron data. The tomography results indicated that distances separated by 0.5 m (1.6 ft) or less showed strongly variable changes in water content. Especially encouraging were the observations of similar scales of variability within the trench to the north of the drip line. Clear evidence for lateral dispersion within a thin sill (≤0.25 m [0.82 ft] thick) was found within the trench that matches a similar region of elevated water content in the well pairs traversing this region.

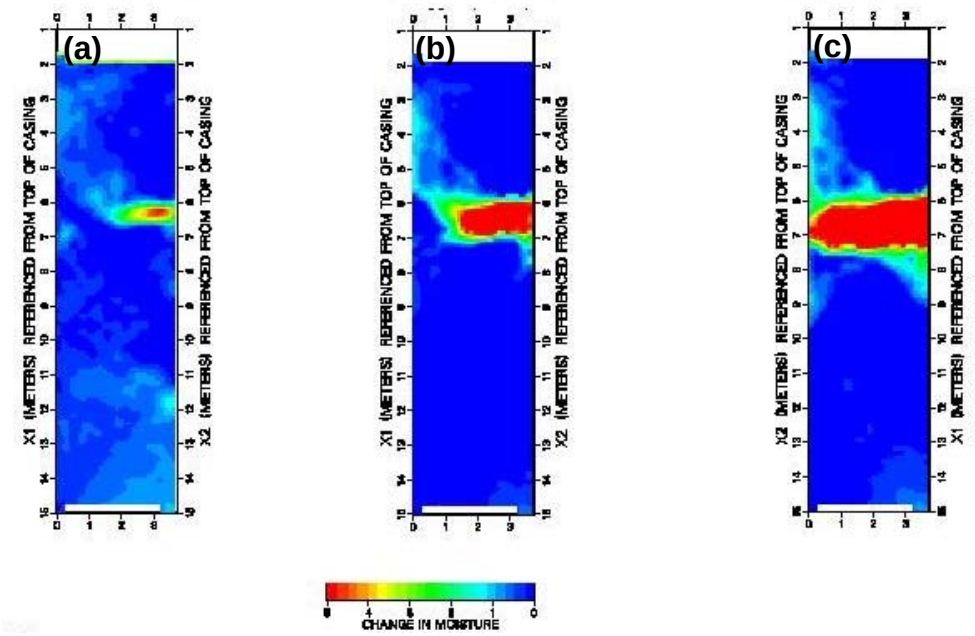

Figure 2.88. POST2 Changes in Moisture During the Fifth Injection at the 299-E24-111 Test Site, (a) After 568 L (150 gal), 1514 L (400 gal), and 3407 L (900 gal) Were Injected

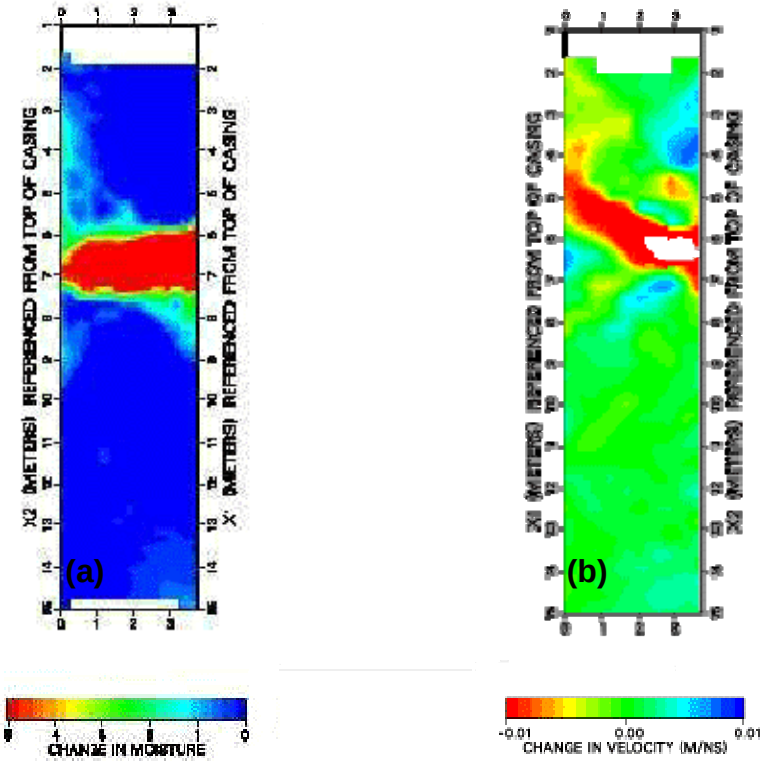

Figure 2.89. Radar Tomograms Between X1 and X2 After the Injection of 1893 L (500 gal) of (a) Water in the FY 2000 Test, (b) Sodium Thiosulfate in FY 2001

Figure 2.90 shows the base- and post-infiltration velocity tomograms from the Army Loop Road site. Several characteristics of the tomograms remain constant throughout the infiltration experiment. Tomograms 5-4 and 4-3 (i.e., the tomograms formed by well pairs 5-4 and 4-3) showed relatively uniform velocity to a depth of 6.0 m (20 ft) with a value of about 0.14 m (0.46 ft) ns^{-1}. Tomograms 1-2 and 2-8 show significantly decreased velocity in the upper 2 m (6.6 ft) relative to the lower regions. The tomograms traversing the clastic dike (3-1 and 8-5) showed significant reductions in velocity relative to the surrounding tomograms. However, the velocities are not consistent with those in the neighboring tomograms. This is caused by a combination of higher moisture content and the higher electrical conductivity of the dike. Both planes formed between well pairs 1-3 and 8-5 encompass the clastic dike, confirmed by a surface outcrop. Furthermore, the average velocity value was lower in well pair 1-3 than in well pair 8-5. This is consistent with the fact that the drip line is closer to well pair 1-3, making this a potentially wetter region with a lower EM velocity. Distributions of moisture content derived from the velocity tomograms are shown in Figure 2.91 compared against the neutron-probe data. A low-velocity region was evident at all times, before and after infiltration, near the surface between well pairs 1-2 and 2-8, suggesting pre-existing elevated moisture content. Nevertheless, changes in moisture content were observed in this region during the course of the experiment.

Figure 2.92 shows the changes from a) Base to Post 1, b) Post 1 to Post 2, c) Post 2 to Post 3, and d) Base to Post 3. Changes in moisture content were relatively constant through much of the region (between ±2%). However, there were notable exceptions. For example, the tomogram straddling the clastic dike nearest to the drip line (well pair 1-3) showed significant *wetting* (dark blue) in the upper

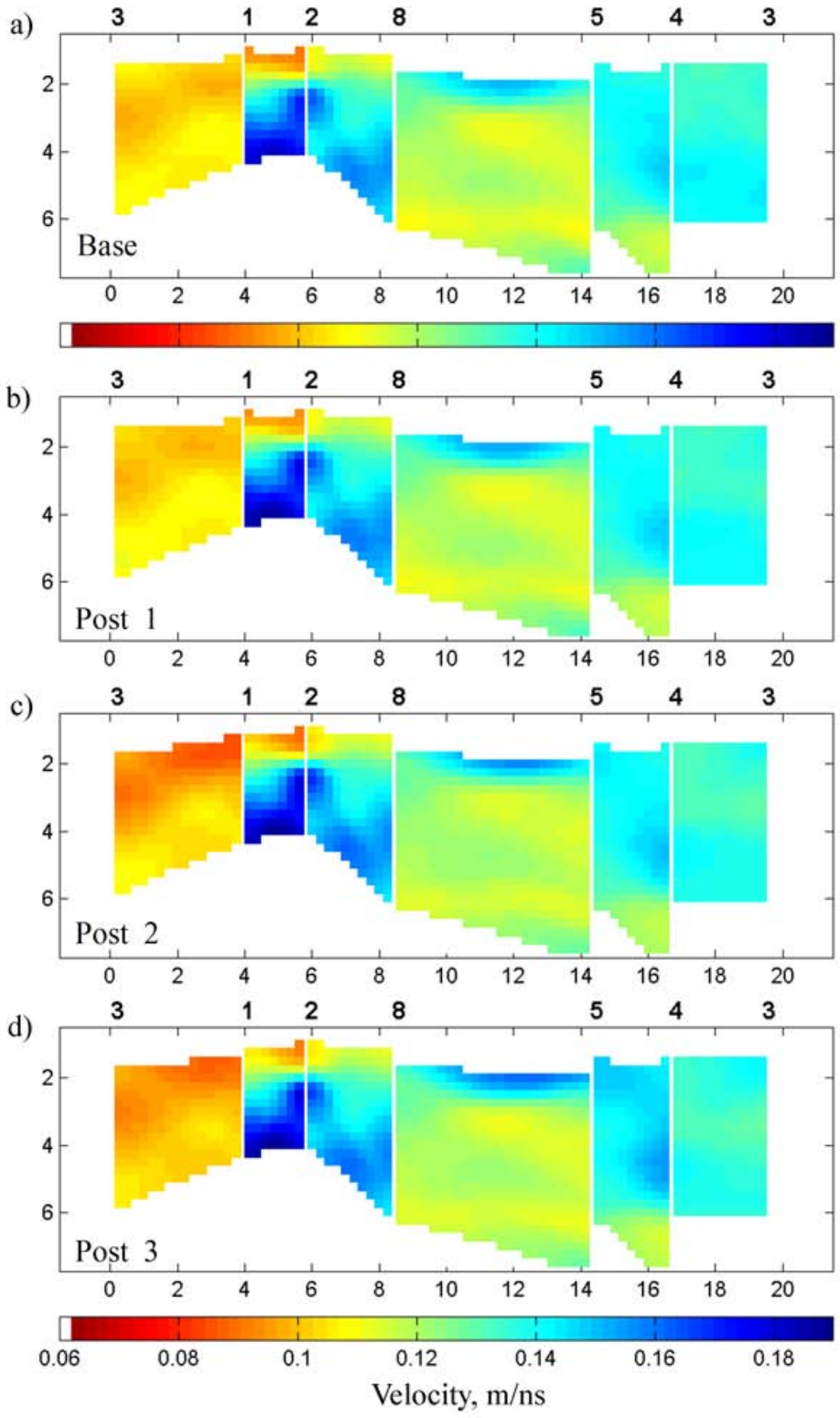

Figure 2.90. Crosshole Velocity Tomograms (a) Before and (b-d) During Infiltration Experiment at the Army Loop Road Site. Well numbers are listed across the top.

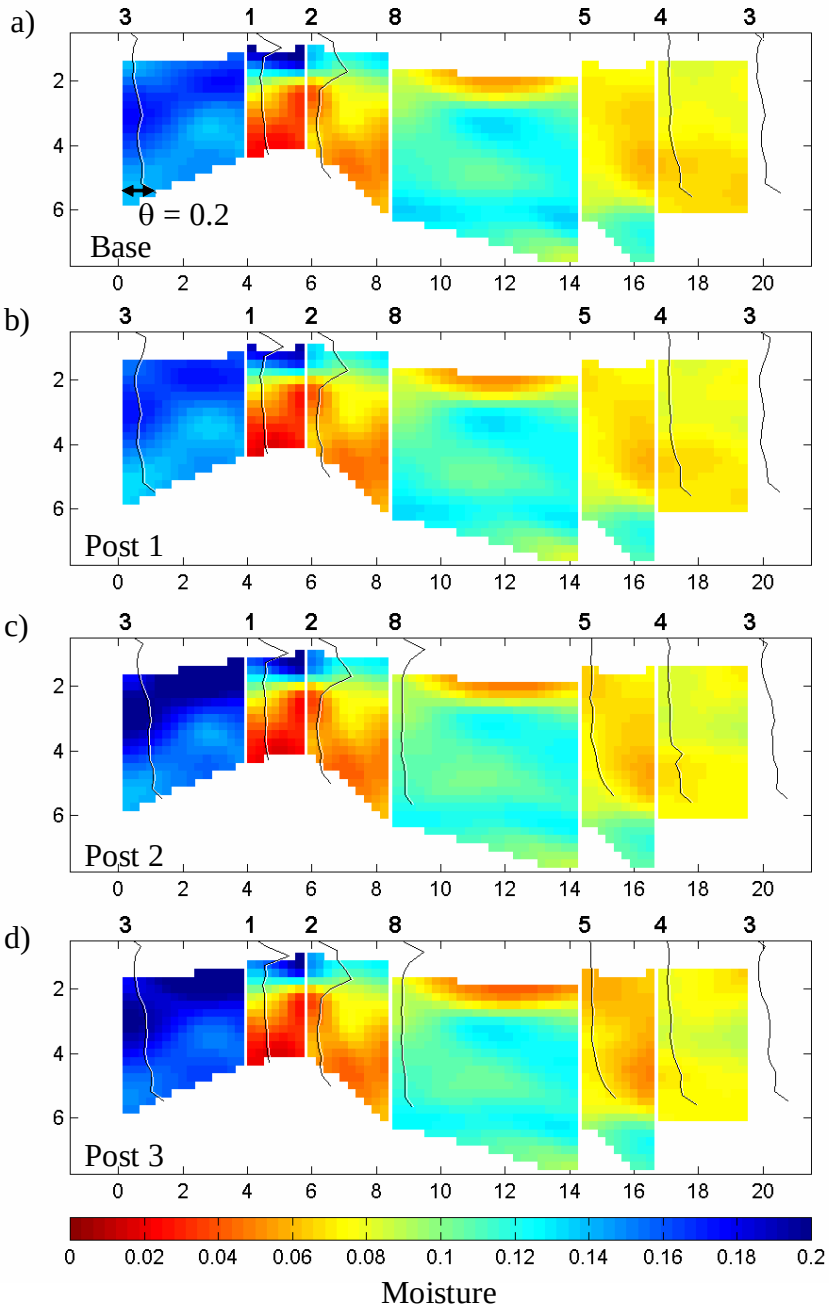

Figure 2.91. Comparison of Moisture Content Derived from GPR Travel-Time Tomography and Neutron-Probe Measurements at the Army Loop Road Site. Well numbers are listed across the top.

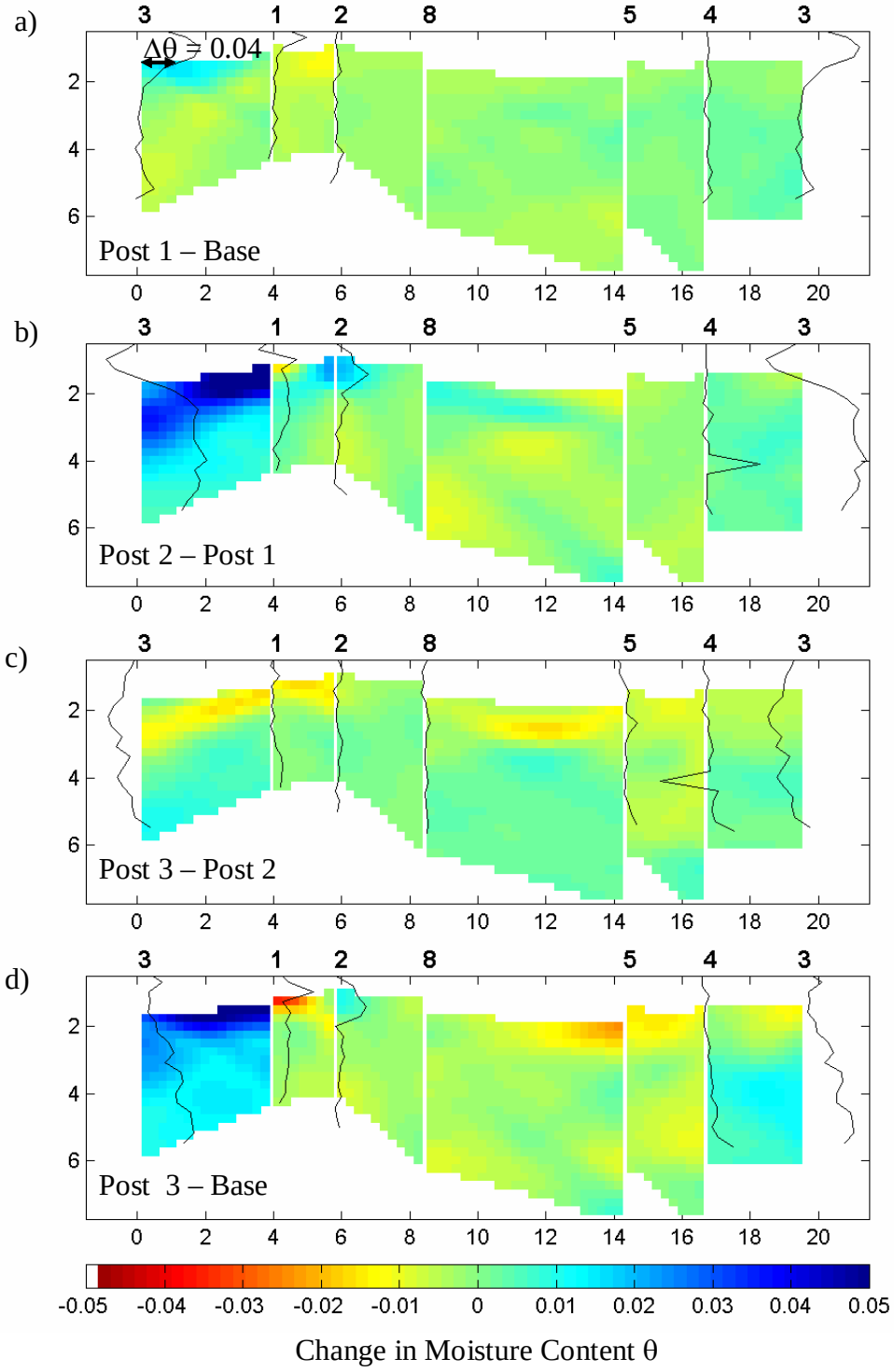

Figure 2.92. Changes in Moisture Content Derived from GPR Travel-Time Tomography and Neutron-Probe Measurements at the Army Loop Road Site. Well numbers are listed across the top.

region from Post 1 to Post 2—although it was expected that horizontal smearing caused by the low-velocity dike would be present. Interestingly, there was evidence of a slight drying (yellow to red) from Post 2 to Post 3 in this same region. Similarly, wetting was evident in the upper regions of the 1-2 and 2-8 well-pair tomograms from Post 1 to Post 2, followed by slight drying in the same regions from Post 2 to Post 3. Significant overall wetting (light blue) was seen from Base to Post 3 in the tomogram corresponding to well pair 4-3. The relevant neutron data are shown for each well are shown next to the tomograms. The moisture content range was on the order of -5% to +5%, and through most of the tomograms changes of only ±2% were typically observed. This change is approaching the accuracy limit of crosshole measurements, so the GPR-inferred changes in moisture content are minimal.

Wells 3, 4, and 5 showed clear evidence of the onset of infiltration. Before the injections, the moisture content in Well 3 remained relatively constant, ranging from 0.05 and 0.10 $m^3 m^{-3}$ above the depth of 4.0 m (13 ft), below which the moisture content increased only slightly. After the onset of infiltration, the moisture content increased to 0.15 $m^3 m^{-3}$ and higher while the region above 2.0 m (6.6 ft) remained at a lower moisture content (0.05 to 0.10 $m^3 m^{-3}$). Wells 4 and 5 showed similar behavior to Well 3 before infiltration; nearly constant moisture content values (ranging between 0.05 and 0.1 $m^3 m^{-3}$) were evident to a depth of about 4.0 m (13 ft) with higher values below this depth. These observations are consistent with a predominantly vertical migration of the wetting front that eventually started to move laterally to reach Well 3 at a depth of about 2.0 m (6.6 ft). The wetting front, however, did not reach Wells 4 or 5, perhaps because of the larger distance from the line source.

2.15.2 Synopsis and Implications

The synopsis of findings in the investigation of crosshole radar tomography for monitoring infiltration and characterizing subsurface structure and their implications are as follows:

- Crosshole radar offers advantages beyond neutron logs and vadose zone characterization typically used to monitor the moisture dynamics in the vadose zone, but many of the relationships relating the radar response to physical and hydraulic properties are not well understood.

- Crosshole radar provided new insight into the effects of subsurface heterogeneity at both test sites of the VZTFS. In particular, the borehole measurements provided a range of coverage outside of those typically obtained from neutron probe and other moisture sensors.

- At the 299-E24-111 test site, radar proved capable of showing the spatial continuity of fine-textured layers that could not be inferred from neutron logs because of the limited spatial sensitivity. At the Army Loop Road site, an extensive fine-textured layer was also shown to be responsible for the lateral movement of water movement away from the drip line. Unlike at the 299-E24-111 test site, a trench was excavated adjacent to the water source, providing visible confirmation of moisture movement in the sill. Such information could be obtained from neutron logging only when the access tube directly intersected the wetting front whereas the crosshole coverage allowed by the borehole radar technique allowed those regions not sampled by boreholes to be investigated.

- Results show that crosshole radar could easily interrogate distances of 5 m (16 ft) and perhaps as high as 10 m (33 ft) between boreholes at 200 MHz and even farther (up to 20 m [65.6 ft]) at

50 MHz. Crosshole radar was capable of delineating lithologic layers of 0.25 to 3.5 m (0.82 to 11.5 ft) thick with 0.25-m (0.82-ft) resolution. The technique proved capable of delineating moisture content and dynamics with a spatial resolution of 0.25 m (0.82 ft). Furthermore, results were in good agreement with neutron-probe measurements.

- A major hurdle to overcome in applying crosshole radar onsite is the need for non-conductive (e.g., PVC) well casings rather than the steel casing that is pervasive at Hanford. Non-conductive wells are highly recommended for new facilities being developed.

- Radar travel times are sensitive to temporal and spatial variations in water-content distributions, which are controlled by sediment texture. Crosshole radar can potentially be used to estimate field-scale hydraulic properties.

2.16 Crosshole Electromagnetic Induction

Traditionally, electromagnetic induction (EMI) logging has been used for direct measurement of electrical resistivity surrounding uncased wells in the petroleum industry. CEMI systems were originally developed for hard rock applications and tunnel detection based on high frequency (> 20 MHz) measurements and using ray tomography for data interpretation. Petroleum ("soft rock") applications and applications to unconsolidated sediments in hydrogeology were limited because high-frequency signals cannot propagate over distances of more than a few meters because of the poor coupling and severe attenuation caused by the low-resistivity elastic sediments. Low frequency CEMI has since been developed, extending borehole induction logging to the region between wells. The system operates like the traditional logging tool, except the transmitter and receiver are deployed in separate boreholes. The technique can provide high-resolution images of the subsurface between existing wells up to 1000 m (3280 ft) apart. The optimum operating frequency depends on borehole separation and background resistivity, but generally the frequency ranges between 40 Hz and 100 kHz. A frequency that is too low limits the resolution whereas one too high limits the range of the measurement.

Low frequency CEMI data are complementary to other modalities like seismic methods. Whereas CEMI is sensitive to variations in the pore fluid composition and surface charge of the porous medium, seismic velocity and attenuation respond to variations in porosity of the medium. The CEMI data are interpreted by inverse modeling to produce a tomogram. The objective of this study was to determine the feasibility of using EMI technology for environmental site characterization.

Two types of EMI surveys were conducted at the 299-E24-111 test site during the FY 2000 injection test: 1) surface EMI and 2) surface to borehole EMI (Hoversten and Gee 2000). In the surface EMI mode, an EM transmitter was located on the surface and EM impedance (i.e., the complex ratio of electric field divided by orthogonal magnetic field) measurements were made on a line across the expected path of the migrating fluid during the injection tests. For both the surface and surface-to-borehole systems, the transmitter was one capable of generating vertical and horizontal magnetic dipole moments on the order of 1000 amp-turn-m. The magnetic field was measured in the boreholes using vertical magnetic field receivers. The surface technique employed a commercial system from EMI, called the "IMAGEM" system, to profile one transect across the site. Two types of magnetic field sensors were used. EMI type BF4 coils were used in the steel cased boreholes because they have their maximum sensitivity below 1 KHz. The system was operated at four frequencies, 280, 488, 8727, and 20,000 Hz. A second slim-

hole coil was used for the PVC-cased wells because its maximum sensitivity occurs at 20 KHz, the upper end of the transmitted signal frequency range.

2.16.1 Results

Figure 2.93 shows the locations of the transmitters, the wells surveyed, and the surface line at the 299-E24-111 test site. For the surface line, the transmitter was located 94.6 m (310.4 ft) to the southwest, in line with the survey profile. This distance was chosen such that the EM fields would approximate plane waves at the receiver sites. With this configuration, the data could be interpreted without the complicating factors of finite source dimensions. The data could also be interpreted with full 3-D finite source inversion codes. The two types of surveys were conducted three times, once before the start of the experiment to obtain a baseline, once just after the first 3785 L (1000 gal.) of water had been injected, and once after the injections had been

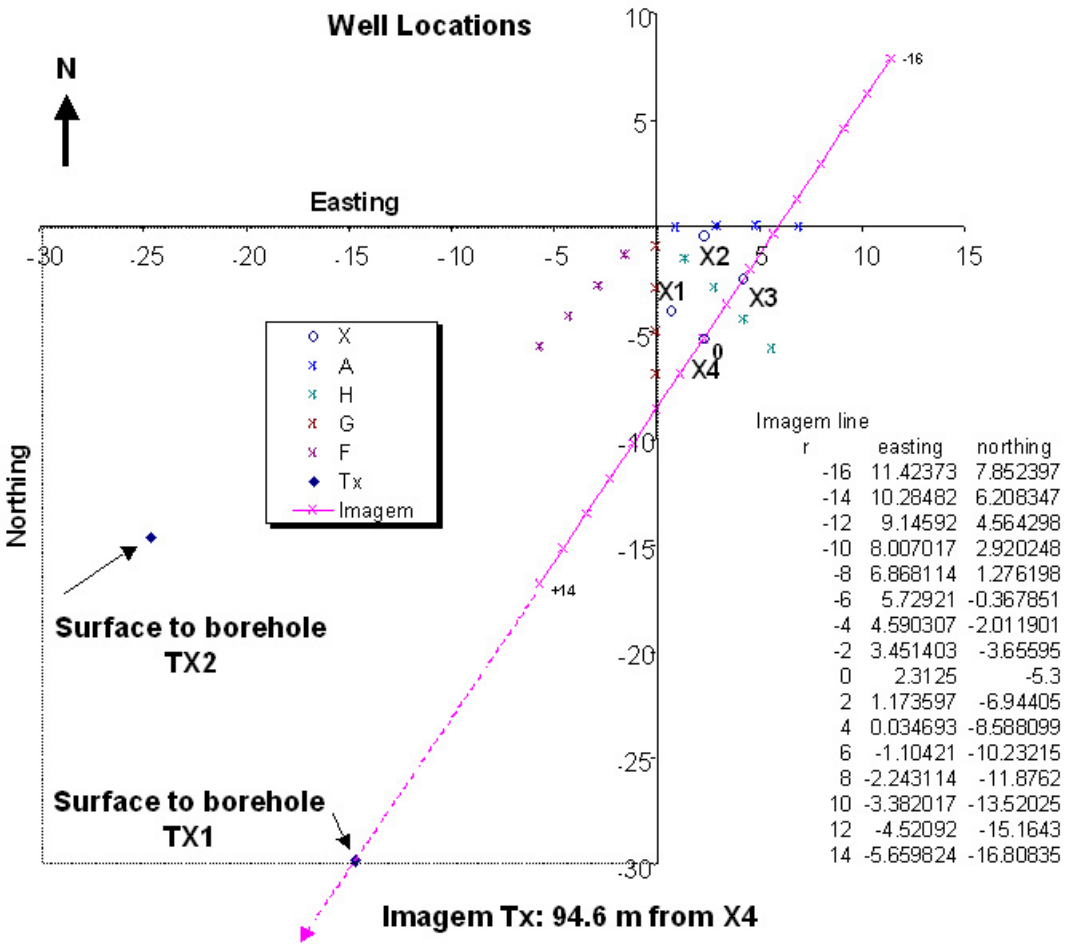

Figure 2.93. Transmitter Locations Relative to Center of Well Field at the 299-E24-111 Test Site. PVC wells (X1- X4) and steel cased wells (A,H,G,F) shown were used in the surface-to-borehole survey. The surface "IMAGEM" line is shown in pink. The transmitter for the IMAGEM survey was located 94.6 m (310.4 ft) to the southwest, in-line with the survey sites.

completed. The transects were measured May 23, 2000, June 5, 2000, and July 13, 2000, using frequencies between 1 KHz and 66 KHz. The objective was to map electrical conductivity changes in the top 20 m (65.6 ft) of the vadose zone that might have resulted from introducing the fluids into the subsurface.

For the surface-to-borehole measurements, the 8727 Hz data had the highest signal-to-noise ratio of the four frequencies collected. To interpret the observed data, a finite difference grid for inversion was built to include the transmitter and receiver areas, extending several hundred meters in each direction from the transmitter-receiver midpoint. The 3-D inversion was based on the scheme described by Newman (1995). The starting model was a half space in which the resistivity was derived from the average of the CPT resistivity logs collected during installation of the ERT electrodes. Data from the four transmitters were inspected and compared to the predictions of the 3 D forward models. The 3-D inversions were run on each data set to obtain a conductivity model. The models were then differenced to produce a 3-D conductivity difference model. Two differences are considered, one between the initial condition on May 23, 2000, and the first injection on June 5, 2000, and the other between the final injection on July 23, 2000, and the initial condition on May 23, 2000. Figure 2.94 shows nine depth slices through the first difference model for the 299-E24-111 test data set. When interpreting the 3-D inversion models, the volume of the model that the data are sensitive to must be considered. In general, this volume forms an ellipsoidal region between the source and receiver (Spies and Habashy 1995; Hoversten et al. 2001). The implication for the 3-D inversion models is that the appearance of a spatially confined feature does not necessarily mean that the total extent of the feature is known.

The 3-D difference model showed a near-surface region of decreased conductivity to the southwest of the X wells and a deeper area of increased conductivity centered on the X wells (Figure 1.4). This is consistent with the southeasterly movement of the plume observed with other geophysical logging modalities. To compare the 3-D conductivity difference models with the measured water-content changes in the steel-cased wells, vertical sections approximately coincident with the H wells were extracted from the models. The transect on which the H wells fall runs approximately through the middle of the X wells at N45W. Figure 2.95 shows the conductivity difference at the 299-E24-111 test site between June 5 and May 23, 2000. This plot is compared with changes in moisture between June 9, 2000, and May 5, 2000. The conductivity increase shown in Figure 2.96 lies just below the zone of maximum water-content change. The lateral extent of the zone of increased conductivity appears to terminate near Well H4 as does the water-content increase. This observed increase in conductivity is indicative of high conductivity pore water overlain by a more resistive fluid.

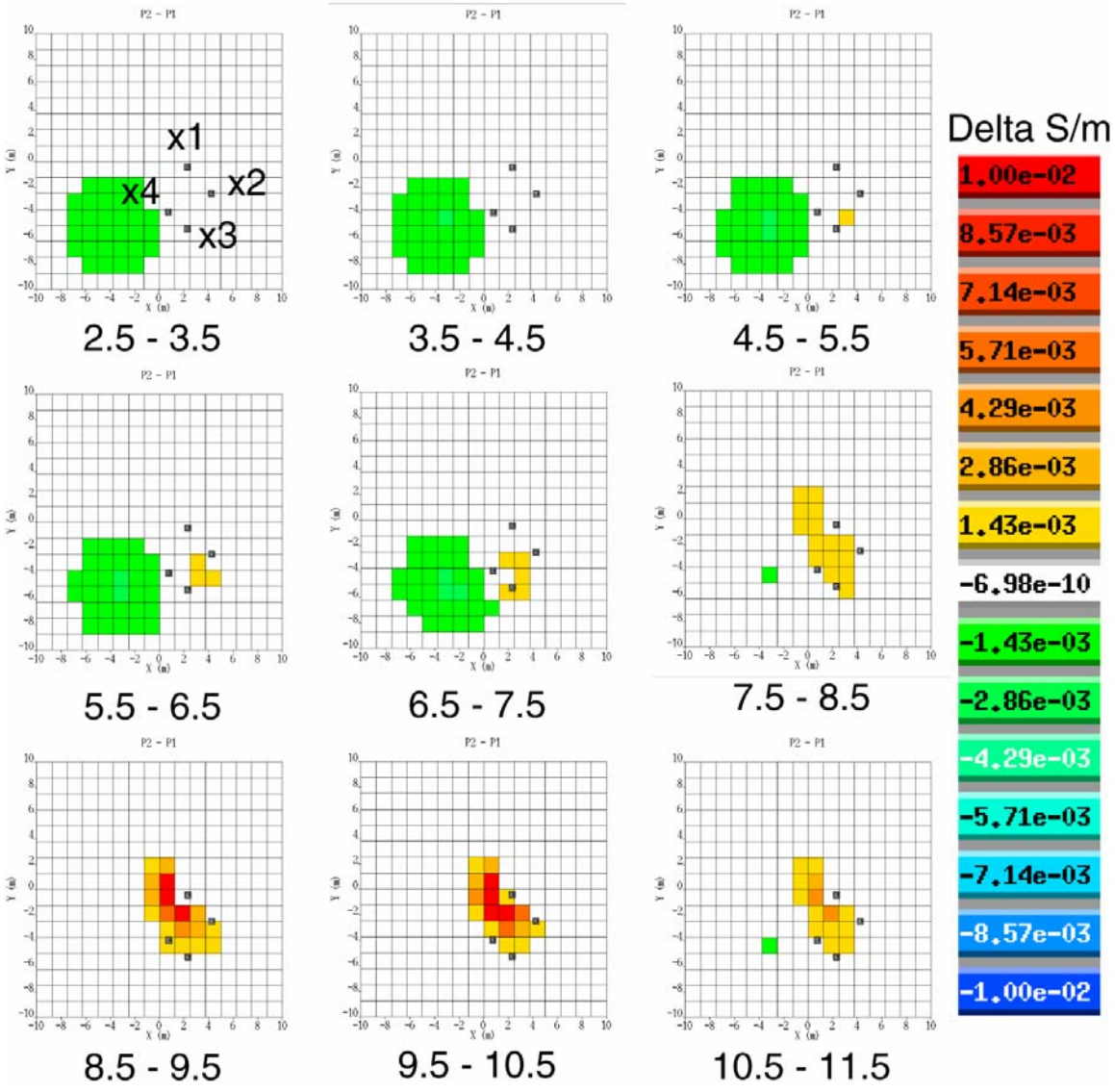

Figure 2.94. Plan Views of Conductivity Difference Between June 5 and May 23, 2000, for the Area Around PVC Wells X1 Through X4 at the 299-E24-111 Test Site. The area covers ± 10 m (± 32.8 ft) with the origin center of the steel well pattern.

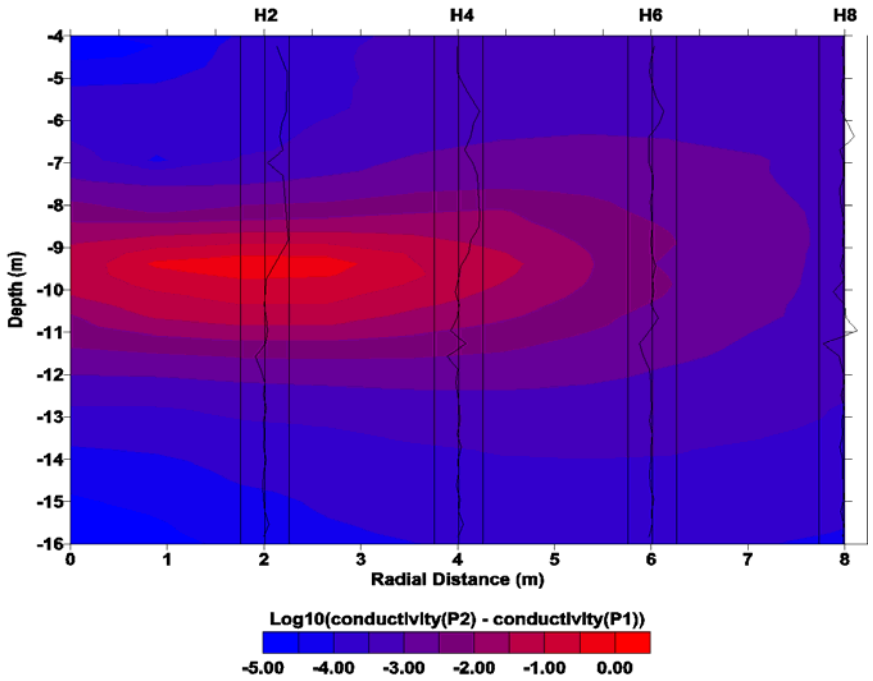

Figure 2.95. Conductivity Difference Between June 5, 2000, and May 23, 2000, Based on Data from Horizontal Magnetic Dipole at TX2 at the 299-E24-111 Test Site. Overlays are the water-content changes between June 9 and May 5, 2000, which showed a range of ± 0.10 m^3 m^{-3}.

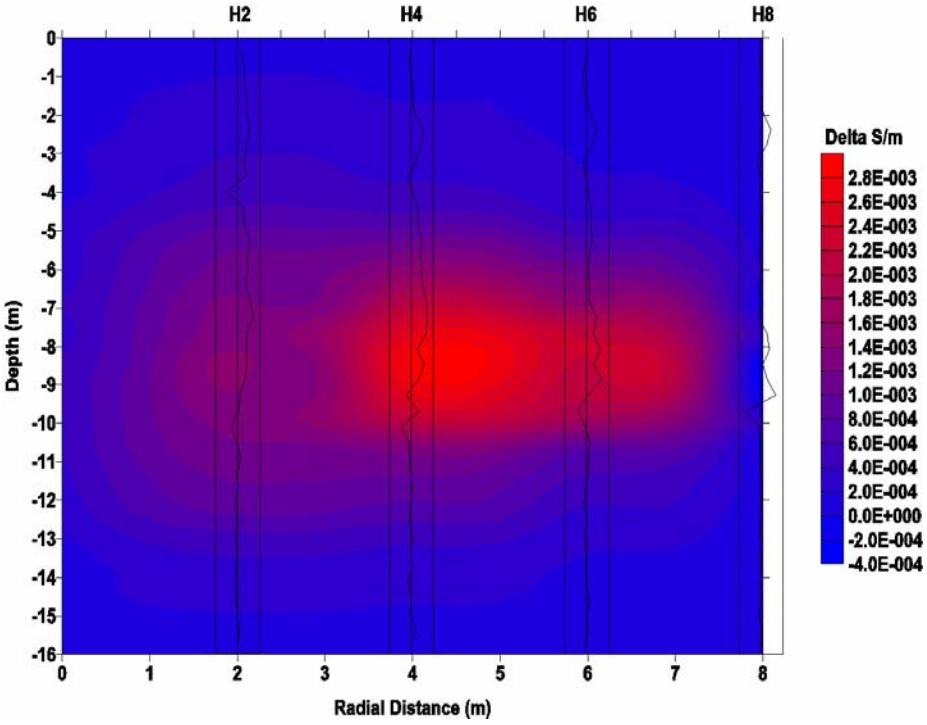

Figure 2.96. Conductivity Difference Between July 13, 2000, and May 23, 2000, Based on Data from Horizontal Magnetic Dipole at TX2 at the 299-E24-111 Test Site. Overlays are the water-content changes between June 9 and May 5, 2000, which showed a range of ± 0.10 m^3 m^{-3}.

Figure 2.97 shows the conductivity difference between July 13, 2000, and May 23, 2000, along the same profile. The maximum positive increase in conductivity had moved down and out from the injection point. In this case, the maximum conductivity difference is more coincident with the maximum water-content changes, although there are still some differences. An attempt was made to enhance the vertical resolution of the images by incorporating lithologic information from the borehole logs. Interpolations were made using the ERT data and CPT resistivity logs from Wells X2 and X3 to identify the major textural breaks. The interpolated surfaces were located near 2.5, 6.5, and 11 m (8.2, 21.3, and 36 ft) in depth and were used in the 3-D inversions as tears in the smoothing functions. This allowed the conductivity to change abruptly across these interfaces as it would in reality. Figure 2.97 shows the inversion of the same data shown in Figure 2.96 with discontinuities incorporated. The effects of the discontinuities can be seen at depths of 2.5, 6.6, and 11 m (8.2, 21.7, and 36 ft). Whereas the image may better represent known sharp boundaries, it placed the maximum increase in conductivity too far away from the injection point (compared to the water-content changes). In addition to the surface-to-borehole EM measurements, the EMI "IMAGEM" system was used to profile one transect across the site. This transect was imaged on May 23, 2000, June 5, 2000, and July 13, 2000. Frequencies between 1 KHz and 66 KHz were acquired. The three data sets were inverted for 2-D resistivity (Mackie et al. 1997) and then differenced to show changes in resistivity below the profile. In general, the data quality was good. Figure 2.98 shows the resistivity differences. Between June 5 and May 23, there was a general decrease in near-surface resistivity accompanied by an increase at depth. The increase at depth is consistant with

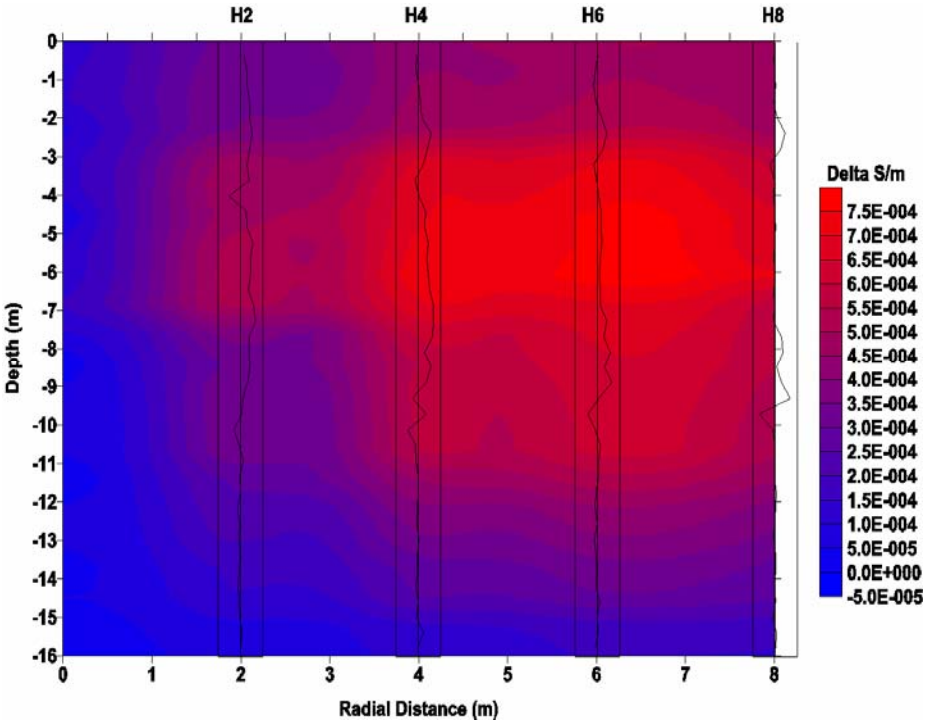

Figure 2.97. Conductivity Difference Between July 13, 2000, and May 23, 2000, Based on Data from Horizontal Magnetic Dipole at TX2 at the 299-E24-111 Test Site. Overlays are the water-content changes between June 9 and May 5, 2000 that showed a range of ± 0.10 m^3 m^{-3}. Three structural surfaces at 2.5-, 6.5-, and 11-m (8.2-, 21.3-, and 36-ft) depths were used to break the vertical smoothing.

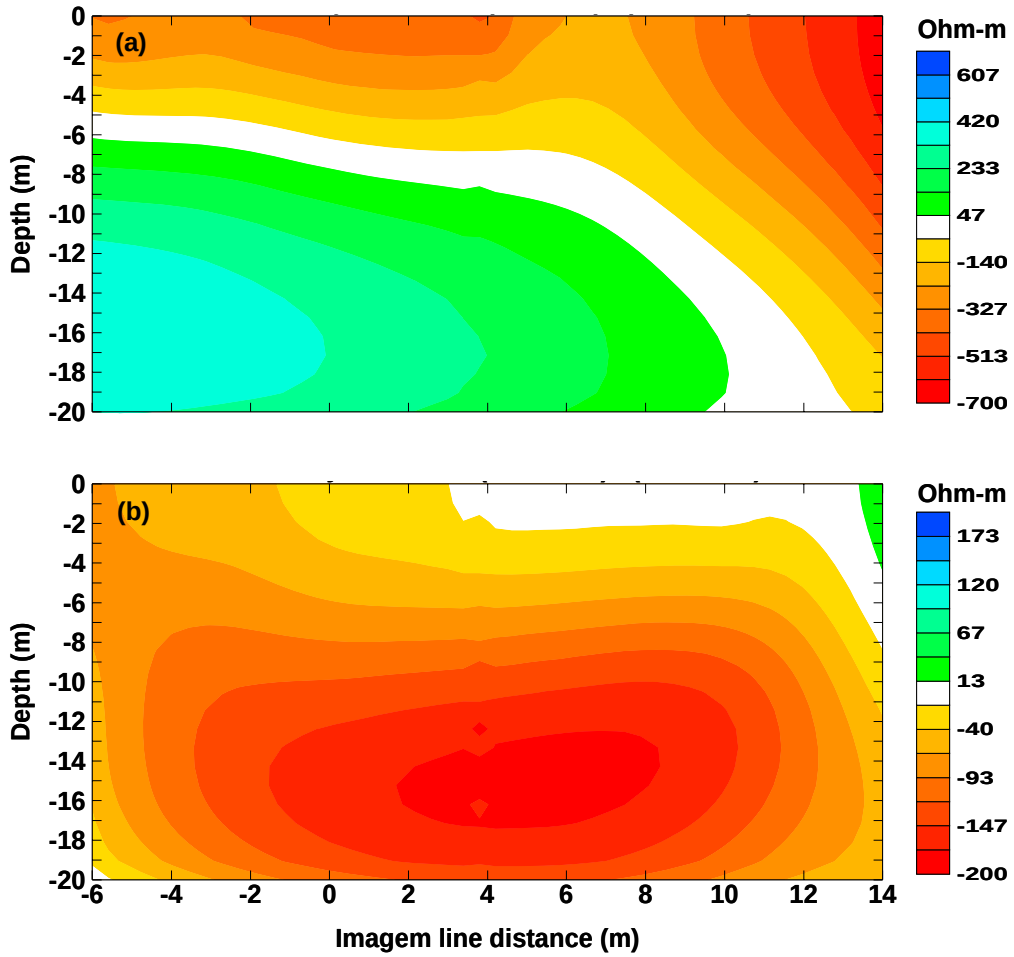

Figure 2.98. Resistivity Difference from Surface EMI Surveys at the 299-E24-111 Test Site, (a) Difference Between June 5, 2000, and May 23, 2000 and (b) Difference Between July 13, 2000, and May 23, 2000

observations made during the HRR survey. Between July 13, 2000, and May 23, 2000, the main difference is a decrease in resistivity centered around Well X3. The depth of the resistivity decrease is greater than observed in the water-content logs but has approximately the correct spatial extent.

2.16.2 Synopsis and Implications

The synopsis of findings in the investigation of EM induction for monitoring infiltration and characterizing subsurface structure and their implications are as follows:

- Low frequency CEMI systems have been developed extending borehole induction logging to the region between wells and have found applications in environmental characterization. The technique can provide high-resolution images of the subsurface between existing wells up to 1000 m (3280 ft) apart.

- Results of the 3-D inversions were encouraging and illustrated the capabilities of the surface-to-borehole EMI technique but were not as conclusive as those obtained with the other electrical

modalities. Inversions were performed using a single transmitter, but up to four transmitters could be modeled for each date of acquisition. Further improvements in the results could also come from using multiple transmitters and possibly other frequencies.

- The surface impedance IMAGEM survey operated at too low a frequency to give detailed images of the upper 15 m (49 ft). Data quality was good and suggested that a higher frequency system would be a good tool for near-surface imaging.

- To image the top 15 m (49 ft) in greater detail using only surface measurements would require higher frequencies than the IMAGEM system can currently generate. Systems now exist that are capable of frequencies up to 1 MHz, which would be more sutible for imaging the top few meters.

- The general pattern of resistivity changes is consistent with the movement of water downward and outward to the southeast from the release point over time. In addition, the behavior seems to be consistent with observations made in the surface DC resistivity array. Further modeling and comparison of different inversion algorithms on these data could be performed to access the causes of the increase in resistivity deep in the profile. Structural information in the inversions may be useful to determine whether such information that is readily obtained from crosshole GPR, seismic, and CPT can be used to improve the accuracy of the inversion.

2.17 High-Resolution Resistivity

The HRR technique is an extension of the conventional direct current (DC) electrical resistivity survey, which is based on the capacity of geologic materials to conduct an electrical current. In principle, a DC resistivity survey measures the voltage generated by the transmission of current between electrodes installed in the ground. The concept of resistivity or conductivity surveys for characterization of lithology or heterogeneities and monitoring is based on the mapping changes or distortions in an imposed electrical field that result from heterogeneities in the subsurface. Dry geologic materials are typically resistive, but in the presence of water and solutes can become electrically conductive. Changes in soil texture cause changes in the electrical conductivity of the sediments, whereas changes in moisture and/or pore fluid solute concentrations cause changes in the fluid-phase conductivity. These phenomena combine to cause distortions in an imposed electric field, which can be measured from the ground surface, with buried electrodes, in boreholes, or with a combination of the three. Changes in conductivity are measured using various electrode geometries of which the four-electrode Wenner and Schlumberger configurations are the most popular. In these configurations, current is driven by self-contained batteries with the two outer electrodes acting as the current source and sink. The two inner electrodes are potential electrodes and sense the electrical potential while current is flowing between the outer electrodes. The measured electrical potential varies with electrode spacing in a predictable fashion but is also dependent on sediment surface charge, hence lithology, as well as the conductivity of pore fluids.

The HRR technique is optimally based on the pole-pole electrode geometry but may be derived from any array of electrical sensors, including steel well casings. It differs from the conventional DC survey only in the procedures for data acquisition and processing (Fink 1980, 1994, 2000). The HRR technique has been applied to mapping the distribution and time-dependent changes of moisture and conductive contaminants in the subsurface. Two modes of operation are common 1) depth sounding and 2) profiling.

In the depth sounding mode, all four electrodes are initially placed in the ground with a very short spacing between adjacent electrodes. A reading is taken, and then the array is reset with an incremental increase in spacing. Another reading is taken, and the array is, in turn, progressively expanded in this manner until the maximum depth to be investigated is reached. The current and potential sense progressively deeper layers as the array is expanded. Two electrodes are used to inject current into the subsurface around a target while measuring the resulting potential field with a dense grid of electrodes on the surface. The linear surface arrays are used only to measure potential fields—their effect on the method is to provide additional horizontal distribution information and to provide depth correction/information. In the profiling mode, a constant electrode spacing is selected that senses the subsurface geology to the depth of interest, and this constant array is alternated along a line to measure lateral variations along the profile that have geologic meaning. In areas where steel-cased wells are present, these wells can be used as both a source of current and as a potential field measurement electrode.

The objectives of the study were to evaluate the use of HRR for characterizing the subsurface heterogeneities, detecting a simulated subsurface leak, and delineating the plume emanating from such leaks, all in the presence of conductive infrastructure, such as steel-cased wells. A 2-D electrode array was installed on the surface of the 299-E24-111 test site for surface-only measurements. The 2-D grid was laid out for an HRR survey and centered on the original injection well (Figure 2.99). In addition, the 32 existing steel cased wells were used as electrodes by connecting cables to the tops of the casings and by installing electrodes at the bottom of each well. Potential measurements were made using various combinations of the surface and down-hole electrodes (Figure 2.100). These included 1) measurements between steel casings, which consisted of electrically energizing an individual steel casing and measuring the resultant potentials on all other steel casings, 2) measurements between an electrode in the injection well and steel casings, which consisted of electrically energizing the electrode placed at the bottom of the injection well and measuring the resultant potentials on all 32 steel casings, 3) measurements between fabricated electrodes placed at the bottoms of all casings, which consisted of electrically energizing individual electrodes placed at the bottom of each steel casing and measuring the resultant potentials at all other bottom-hole electrodes, 4) measurements between the fabricated bottom-hole electrodes and steel casings, consisting of electrically energizing individual bottom-hole electrodes and measuring the resultant potentials at all the steel casings, other than the one containing the energized electrode, 5) measurements between the PVC injection-well electrode and bottom-hole electrodes, consisting of electrically energizing the injection-well electrode and measuring the resultant potentials at all 32 bottom-hole electrodes, and 6) surface measurements between electrodes. Electrical contact with the grounded steel casings was made at a stainless steel bolt threaded into each casing near the top of the casing.

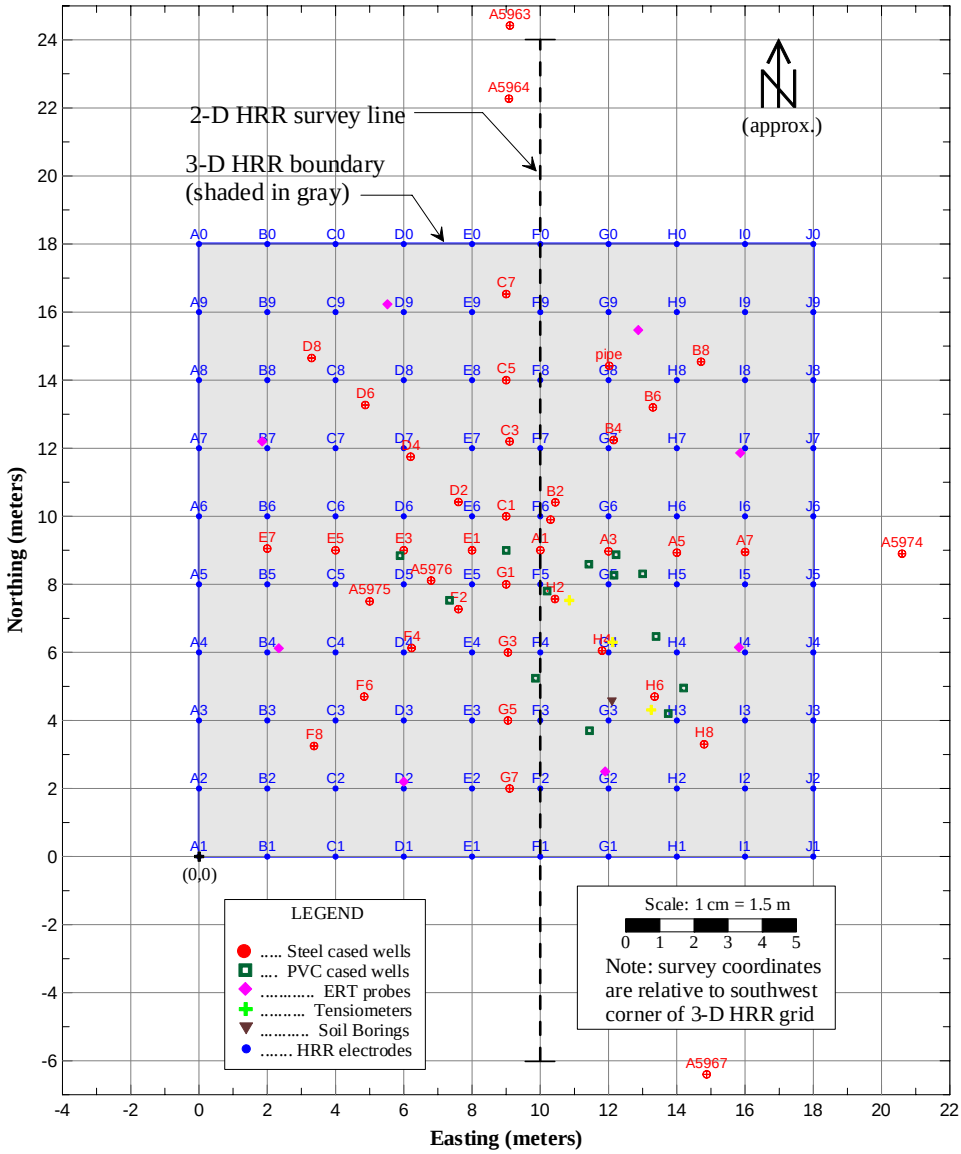

Figure 2.99. Location and Feature Map for HRR Measurements. Each electrode was approximately 0.46 m (18 in.) long and driven into the ground.

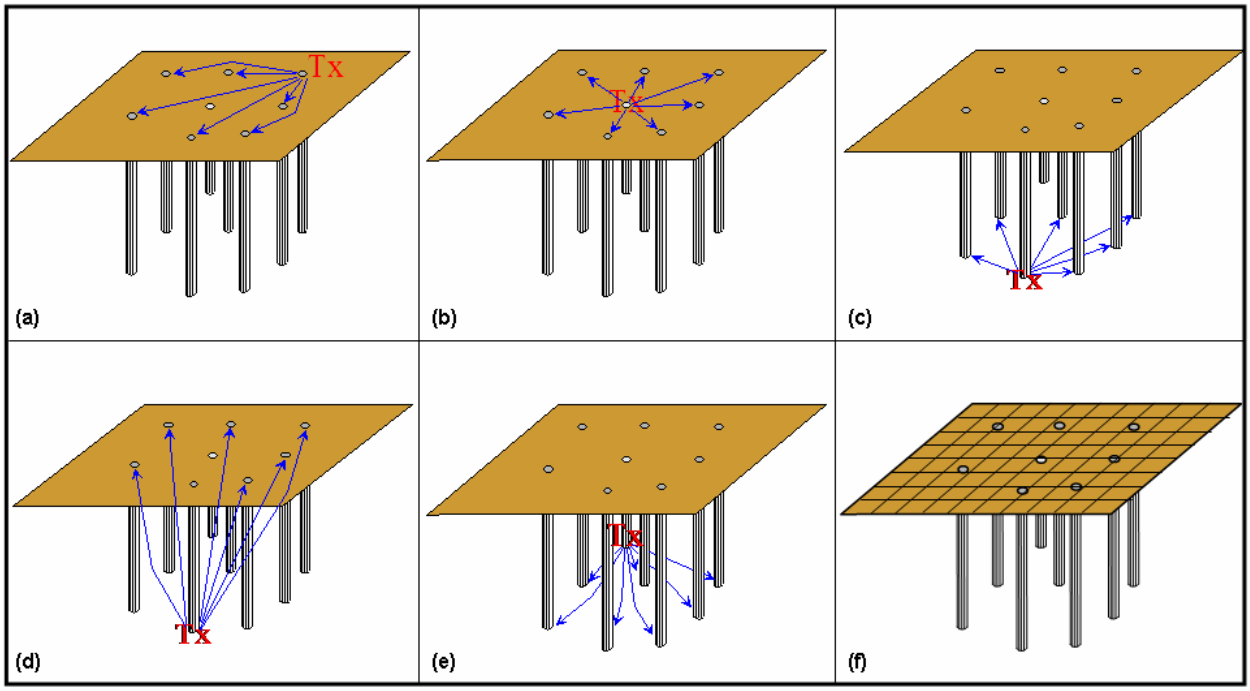

Figure 2.100. Six Electrode Configurations Used for HRR Data Acquisition (a) Between Steel Casings, (b) Between an Electrode in the Injection Well and Steel Casings, (c) Between Fabricated Electrodes Placed at the Bottoms of all Casings, (d) Between the Fabricated Bottom-Hole Electrodes and Steel Casings, (e) Between the Injection-Well Electrode and Bottom-Hole Electrodes, and (f) Between Surface Electrodes

The surveys focused on the 32-well study area configured as a series of concentric circles and were completed at various times before, during, and after two of the five completed injections in the FY 2000 experiments. Data acquisition was completed during two periods: May 24th through 31st and June 19th through 26th of 2000. The initial period was performed to establish a background data set before any injection. The second period spanned the fourth injection. Nineteen surface data sets and two casing data sets were acquired during the two site visits. Most of the data sets were acquired during the second visit when the data-acquisition system was programmed to make scans approximately every 2 hours. All electrical measurements were made using either the pole-pole electrode array or some two-electrode variation of the pole-pole array. Well-casing measurements consisted of simple voltage measurements made at the top of each casing because of an "injected" electrical current at the bottom of the injection well. Within the survey grid area, electrode spacing varied from 2 m (6.6 ft) minimum to 18 m (59 ft) maximum. The surveys were conducted with the OYO Corporation McOHM-21, a DC-powered electrical resistivity instrument. Two units were combined, thereby allowing the simultaneous connection of up to 96 electrodes over the standard 32 provided by the individual systems. The units were used in conjunction with OYO scanners and individual wires to the casings.

2.17.1 Results

Twenty-three complete data sets, totaling over 25,793 data points, were acquired during two field campaigns. Apparent resistivity values at the 299-E24-111 test site ranged from 150 to 600 ohm-meters. In general, higher resistivity values represent drier soil conditions, which are generally indicative of

coarse-grained sediments. Typical values for undisturbed geologic media range from less than 10 ohm-meters for clays to tens of ohm-meters for silts and sands, to several hundred ohm-meters for very dry alluvium and bedrock. The presence of the steel well casings limited the approaches available for processing the data. The most meaningful way to evaluate the HRR method was to examine the differences between data sets acquired before and after injection. In this way, the effects of the steel casings were minimized, and the changes in apparent resistivity would be emphasized.

Figure 2.101 compares temporal changes in electrical potential with the injected volume of fluid and the electrical conductivity during the course of the FY 2001 injections. The stepped green line is the cumulative volume of injected solution; the blue line is the solution conductivity (mostly off scale); and the red line is the observed potential between the injection well and casing A1. The solution conductivity showed an appropriate decrease when the river water replaced the tracer solutions at the end of the injections, but the in-ground conductivity (red line) continued to increase.

Potentials ranged from a few milliohms to tens of ohms, a spread of approximately five orders of magnitude. Such a large range of data values, in itself, suggests a high probability of feature recognition and characterization. This large range is due entirely to the high electrical conductivity of the injected solution and its effect on the bulk electrical conductivity. The system is very sensitive to changes in the conductivity of the injected fluid; the injection of river water following the low concentration tracer injection resulted in a measurable increase in bulk electrical conductivity. The HRR technique showed a clear response to the fluid injections, and a qualitative relationship is evident between the measured potentials and injected volume. Continuous monitoring of the site might have produced a more robust relationship. This suggests that the HRR technique may have potential for use as a leak detection system, even in environments with steel casings.

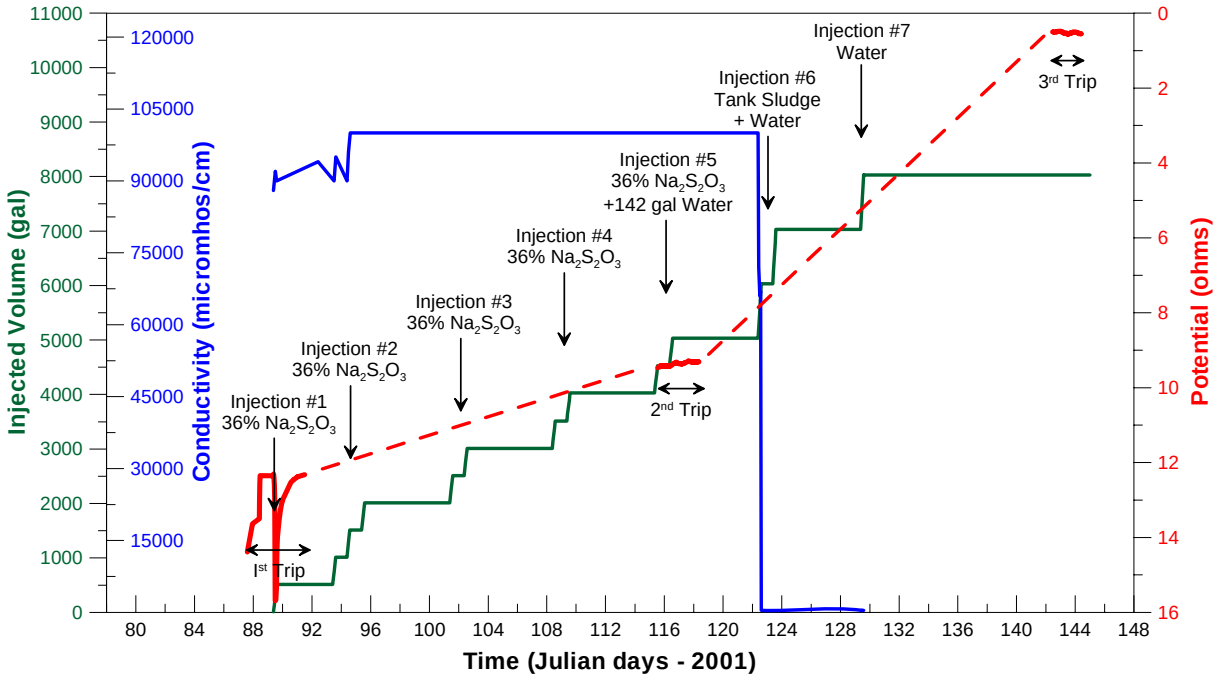

Figure 2.101. Temporal Changes in Electrical Potential Compared to Injected Water Volume and Electrical Conductivity

Casing-to-casing measurements (Figure 2.100a) consisted of simple voltage measurements made at the top of each casing in response to an injected electrical current from another casing. At least one measurement was made between every casing pair. The results are illustrated in Figure 2.102 using electrical potentials measured while well H2 was energized. This well was selected because it is located closest (within ½ meter) to the point of injection. Figure 2.102a shows the pre-injection measurements made one day before the initial injection. These data were treated as background data for subsequent processing. Figure 2.102b shows the observed data acquired immediately between 1 and 3 hrs after the completion of the first injection. Figure 2.102c shows the measurements made 1 day after the injection to observe changes caused by continued infiltration. Figure 2.102d shows the 1-hour post-injection data processed by subtracting the background. Figure 2.102e shows the 1-day post injection data processed by subtracting the background. The primary fields, Figure 2.102a,b,c show the expected circular pattern centered on well H2 with essentially no evidence of distortion caused by the presence of the other steel casings. The strong dipolar character of the residual data shown in Figure 2.102d,e is indicative of a conductive body at the inflection between the high and low closures. The difference between Figure 2.102d and e is caused by continued migration of the injected volume and a change in shape and location of the volume.

All of the casings were used as sources, and data analysis shows that proximity to the injection well is not required to produce diagnostic information. In all cases, the primary field consisted of circular contours centered on the source well. Correction for the background condition revealed a dipolar character in the residuals, which is attributed to the presence of a conductive body, in this case the injected fluid, located at the inflection between the high and low closures. The character of the dipolar feature was independent of the location of the excitation source with low potentials always on the source side of the conductive feature and the high opposite side of the feature. The casing-to-casing method appears capable of producing information on the dynamics of plume migration as well as volume estimates. The system, as demonstrated, was capable of detecting an 1893 L (500 gal.) leak, although one controlling factor appears to be the distance from source to leak. Although the method accurately located the lateral extent of a leak, the vertical resolution was poor.

Measurements using the electrode at the bottom of the PVC injection well and the steel casings (Figure 2.100b) also produced a measurable response, although the results appear inconsistent with expectations. Potentials were monitored at all casings as a function of time for the initial injection. Figure 2.103 shows stacked profiles of electrical potential measured in the four wells closest to the injection well. Time increases from left to right, the potential increases upwards, and the distance from the injection well decreases going away from the x-axis. The abscissa scale is labeled “Adjusted Time (Julian days)” to reflect this compression. The first two data points on the left side of each time series are background measurements. The remaining data points were acquired either during or after the injection. The most striking observation is the high potentials observed for the wells nearest the injection well. This result was counter intuitive as an injected tracer solution would normally be expected to reduce the potentials in the vicinity of the injection well. These data showed an increase in potential near the injection well and immediate but opposite responses in the two nearest wells. Well H2 showed an increase in potential immediately following the injected of the first 20-30 L (5-8 gal.). Well A1, the next closest well, showed an immediate decrease in potential. A similar decrease was observed in all other wells, although at decreasing amplitudes as distance from the injection well increased.

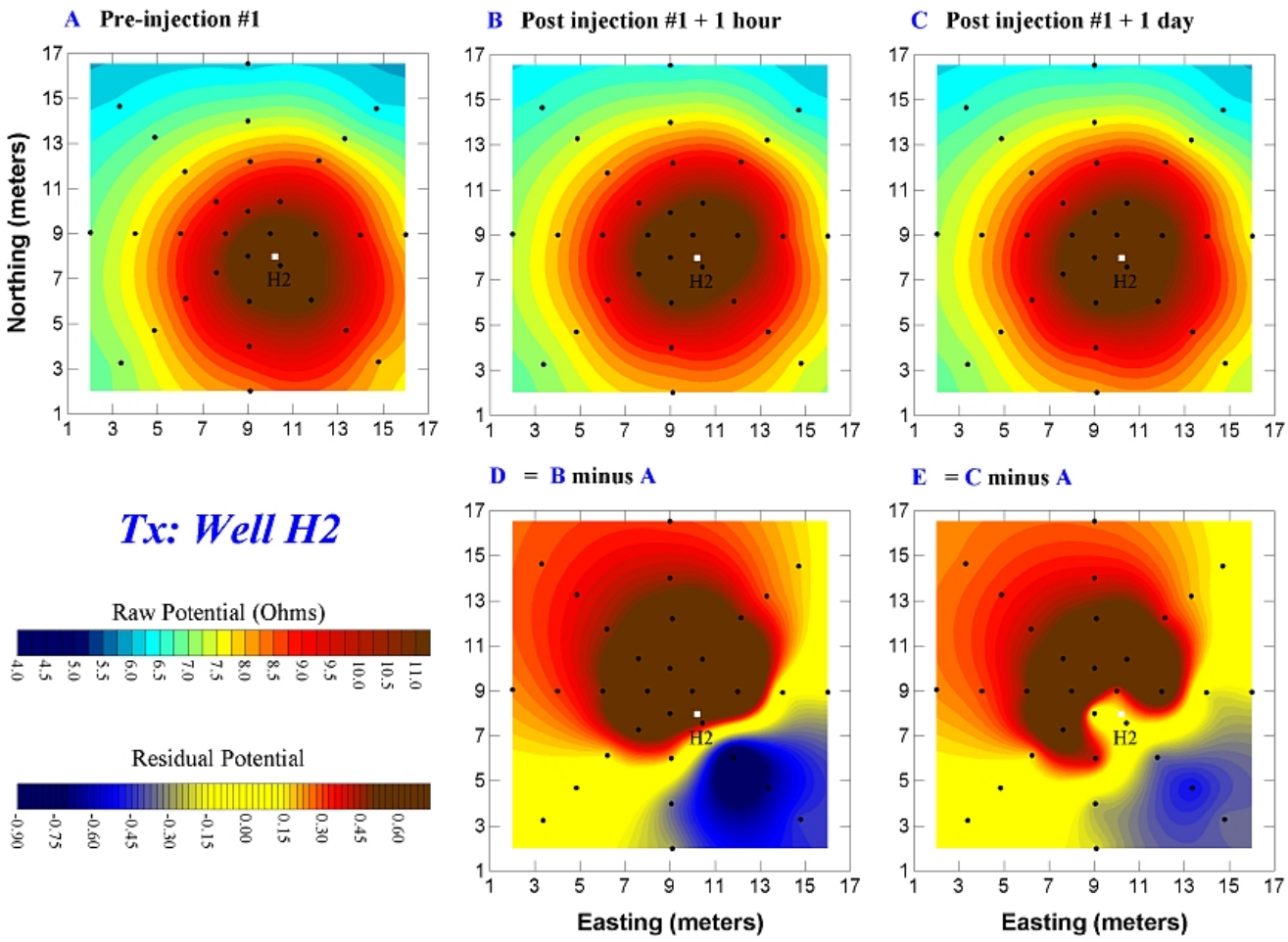

Figure 2.102. Distribution of Electrical Potential During Casing-to-Casing HRR Measurements in Which Well H2 was Energized

The characteristic response is caused by changes in the nature of the potential as the fluid approaches the electrode (casing). As the conductive fluid encroaches the casing, the potential increases sharply until the fluid makes contact. As the fluid contacts the casing, a narrow plateau in potential is formed, after which the potential decreases as the continued expansion of the plume increases the wetted surface area of the casing. Using this reasoning, it was postulated that the volume of injected solution could be estimated based on the distance between the injection well and the various affected casings. Application of this procedure to estimate injected volumes over the range of 2086 to 3036 L (551 to 8020 gal.) resulted in errors ranging from -30% (underestimation) to 70% (overestimation), suggesting the need for further analysis.

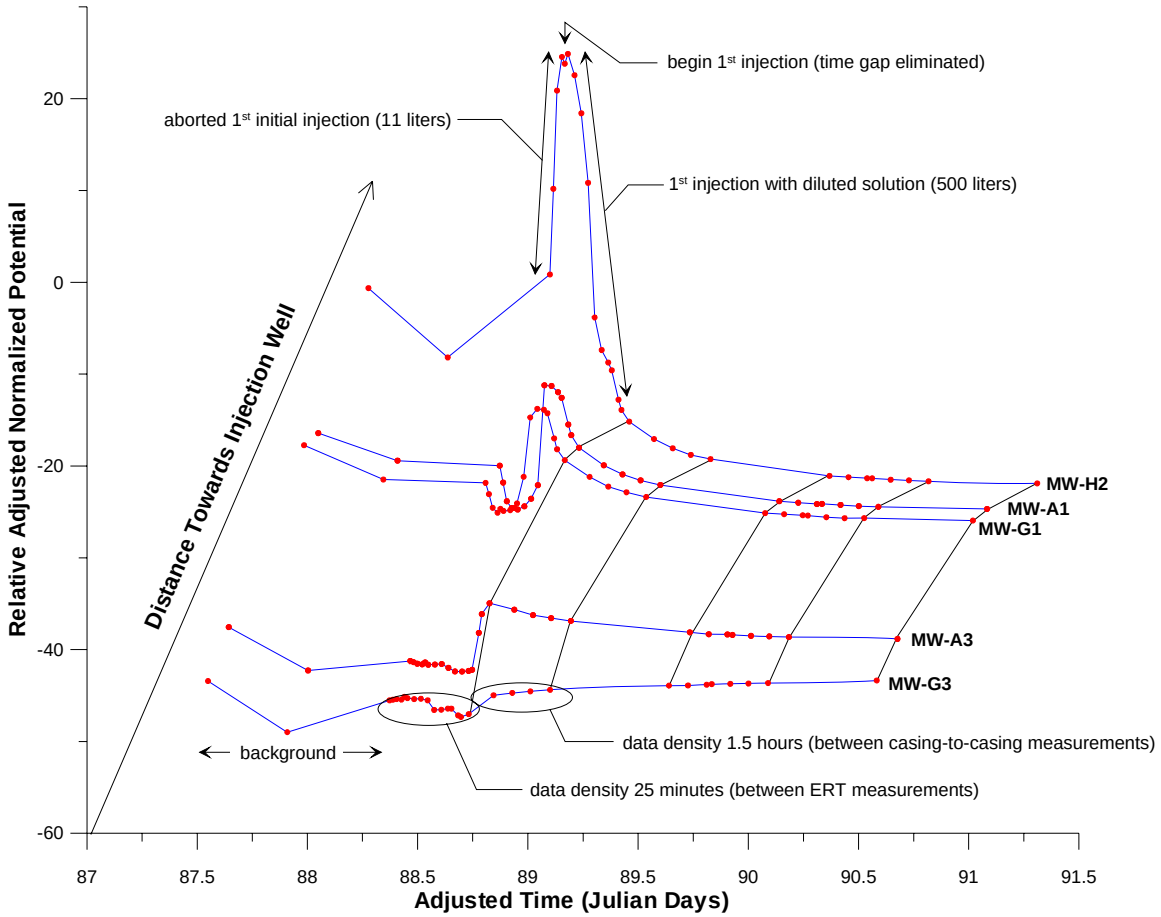

Figure 2.103. Stacked Profiles of Electrical Potential at the Four Wells Closest to the Injection Well

Nevertheless, this approach appears promising for monitoring leaks. The onset of increase in potential can be determined accurately, especially during continuous monitoring. The transition from increasing potential at a casing to a peak value can also be determined rapidly, and when combined with the time to onset, can be used to estimate an effective travel time between adjacent electrodes regardless of volume. The measured time for well H2 was about 48 minutes, and at a distance of 0.66 m (2.2 ft) from the injection well, the fluid was moving at an estimated effective velocity of 32 m (105 ft) d^{-1}. Although this configuration is not ideal for unplanned leaks, it may have application in monitoring field-scale injection experiments. An electrode in the injection well allowed immediate detection of the commencement of injection. The sequence of measurements was rapid because of the limited number of possibilities (only 32 measurements, one per casing), and the rapid sequence of measurements allowed accurate transit times from casing to casing to be estimated. Having an electrode in the injection well is conceptually similar to the mise-a-la-masse method that has been used extensively for mapping conductive bodies and monitoring tracer migration. This configuration proved to be highly sensitive for the transition from an initial condition to the onset of a leak. However, after a leak had occurred, detection of a subsequent leak showed a smaller response as the sensitivity appeared to have decreased.

Measurements between bottom-hole electrodes (Figure 2.100c) are analogous to the casing-to-casing measurements except that the measurements originate from the bottoms of the casings and results were quite similar. Measurements between bottom-hole electrodes and steel casings (Figure 2.100d) using the

bottom-hole electrodes as current sources and the tops of the casings for potentials were also similar to casing-to-casing measurements.

Figure 2.104 shows a 3-D plot of the inverted surface HRR data from the 299-E24-111 test site as differences in apparent resistivity. It was expected that the injected water with dissolved tracers would lower the apparent resistivity in the vicinity of the injection well and this was indeed the case. However, an interesting observation was an unexpected increase in resistivity at the top of the injection zone, contrary to the anticipated decrease.

The increase in resistivity may be the result of more resistive river water displacing less resistive antecedent moisture, or a release of colloidal particles because of the change in ionic strength of the pore water following the addition of the river water. Deviations in the resistivity differences are color-coded; yellow represents a negative change (lower than background), and purple represents a positive change (higher than background). Features of interest included the large resistive zone around the injection point (i.e., above the very top of the injected water column) and a relatively conductive, northeasterly dipping, near-surface zone. The resistive feature, which showed a northeasterly trend, did not appear to be a result of the injected water. It could be related to an earlier disturbance of the surface soil as there is an unused crib, north of the test site, running in a north-south direction. The location of the injection was still detectable from the surface with the non-invasive HRR method. Resistivity changes were largest near the injection well, as could be expected. The distribution also appeared to be anisotropic with the maximum range occurring in a northeasterly direction.

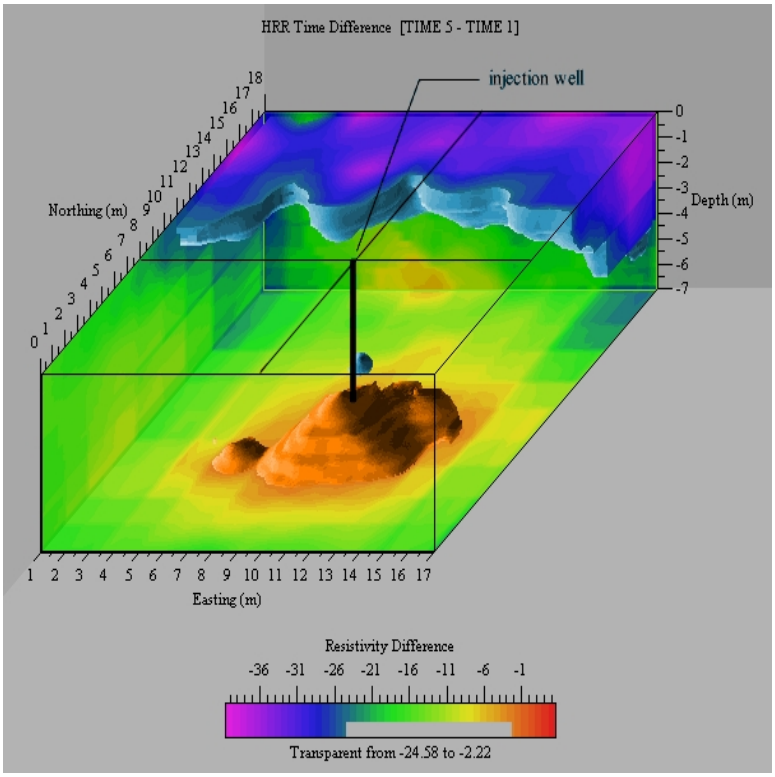

Figure 2.104. Volume Plot of Apparent Resistivity Differences at the 299-E24-111 Test Site

Figure 2.105 shows the resistivity distribution inferred from casing measurements at the 299-E24-111 test site, with a pattern similar to that in Figure 2.104. However, the lateral distribution of potential is not a smooth function of distance from the injection well. The lobed character is caused by the location of the well casings and the selected value of potential difference. Figure 2.106 shows the neutron-probe data from June 9, 2000. Data were restricted to the upper portion of the borehole to match the well-casing electrical data (Figure 2.106). The two data sets show good agreement, not only in general shape, but with respect to many of the small lobes.

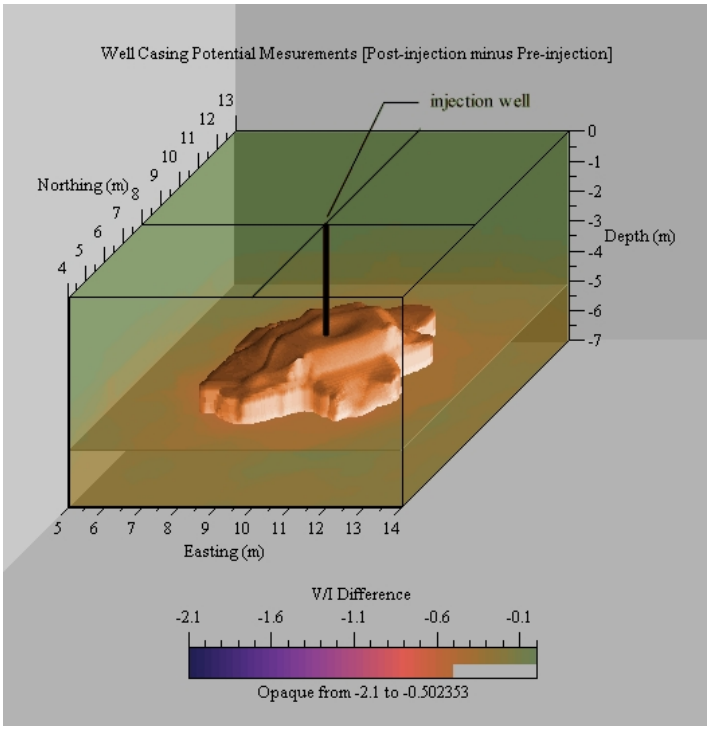

Figure 2.105. Plot of Well-Casing Apparent Resistivity at the 299-E24-111 Test Site

However, there was discrepancy in flow direction inferred from the neutron-probe data and HRR method. This may be a consequence of the nature of the two methods. The neutron probe was calibrated to give volumetric water content, and the measurements showed movement of the wetting front in a southeasterly direction. Under these conditions, resistivity changes were smallest in the direction of movement because water content, hence plume resistivity, was similar. The largest resistivity changes were in a direction perpendicular to the plume where the change in water content and resistivity would be large over a relatively short distance.

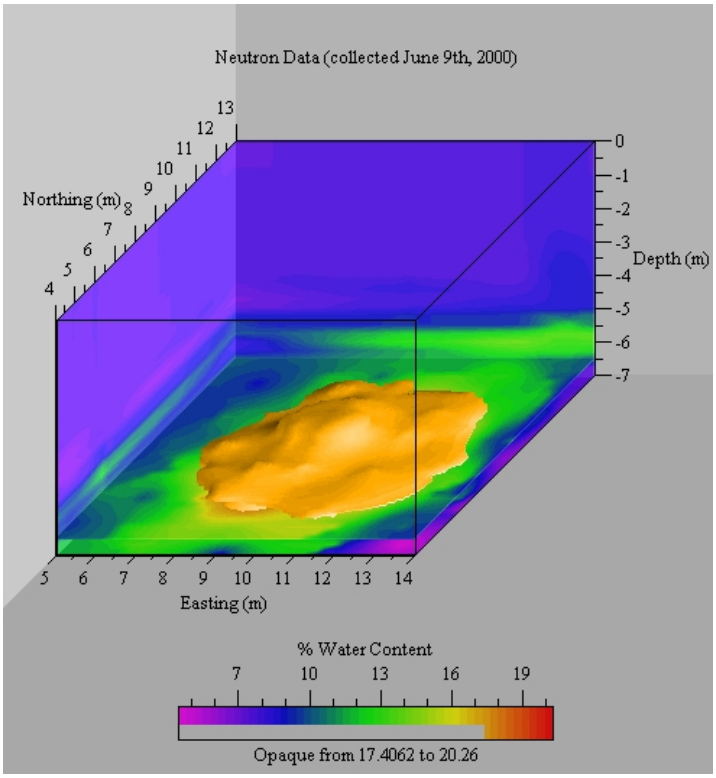

Figure 2.106. Water Content Derived from Neutron-Probe Measurements Made on June 9, 2000, at the 299-E24-111 Test Site. The cut-off is at 0.17 m^3 m^{-3}.

2.17.2 Synopsis and Implications

The synopsis of findings in assessing the feasibility of using HRR for plume delineation and leak detection and their implications are as follows:

- The HRR technique showed a clear response to experimental fluid injections, and a qualitative relationship was evident between the measured potentials and injected fluid volume. Results suggest that the HRR technique may have potential for use as a leak detection system, even in environments with steel casings.

- The casing-to-casing method appears capable of producing information on the dynamics of plume migration as well as volume estimates. The system as demonstrated showed a good minimum sensitivity, although one controlling factor appears to be the distance from energized well to leak. Although this method can accurately locate the lateral extent of a leak, vertical resolution is very poor. Measurements between bottom-hole electrodes and between bottom-hole electrodes and steel casings using the bottom-hole electrodes as current sources and the tops of the casings for potentials were all similar to casing-to-casing measurements.

- The HRR method effectively monitored the injection test at the 299-E24-111 test site where it was able to map the plume and confirm the presence of an electrically resistive flushed zone at

the base of the injection well. It was able to provide positive leak indications within minutes of the onset of injection as well as quantitative volumetric leak estimates.

- Subsurface leak detection is a complicated problem and not many technologies are available to permit near-real time detection, especially in contaminated areas. Based on these tests, the HRR technology was adapted to other vadose zone investigations at the Hanford Site (leak detection monitoring, BC cribs and trenches characterization, and currently for tank farm characterization). The leak-detection results for HRR provided the best volume estimates (within 30%) of the solution injected into the subsurface as well as relatively accurate leak rates in real-time. The technology has since been successfully applied at the BC trench field and BC cribs to delineate a ^{99}Tc plume associated with nitrate (Rucker and Sweeney 2004). The technique is also being deployed at T-Tank Farm, also with the goal of delineating subsurface conductive plumes. Although HRR shows significant potential for the potential delineation of electrically conductive plumes, it should be noted that it measures only the bulk electrical conductivity, which is a function of soil surface charge, pore water electrical conductivity (caused by the presence of contaminants), and soil volumetric water content. Information about specific contaminants cannot be determined from the surveys, and at most, it may be possible to calculate only the distribution of total dissolved solids in the absence of simultaneous measurements with other geophysical modalities.

2.18 Electrical Resistance Tomography

The ERT technique is also an extension of the conventional DC electrical resistivity survey in which measurements are made of voltage generated by the transmission of current between electrodes installed in the ground. The classical interpretation of DC resistivity surveys for identifying resistivity anomalies is based on an assumption of a homogeneous medium. As a result, conventional DC resistivity surveys have limited success in characterizing and monitoring heterogeneous anisotropic sediments in which anomalies are complex with nested scales of heterogeneity. The ERT method was designed to overcome some of these limitations and accomplishes this by making multiple groups of measurements of electrical current and electric potential multiple dimensions using numerous electrode pair combinations. The tomogram is developed through the joint inversion of the independent measurements.

ERT has been demonstrated to be a useful characterization tool, capable of providing details of the lithostratigraphy between wells (e.g., Newmark et al. 1994), subsurface processes such as fluid infiltration (Daily et al. 1992), steam injection, and ohmic heating (Ramirez et al. 1993, 1995) by mapping the spatial and temporal changes in soil resistivity resulting from changes in liquid saturation and temperature. Because process wastes at Hanford were generally of a high ionic strength, it was hypothesized that resistivity could be an ideal surrogate for locating difficult-to-detect contaminants. In general, ERT has been conducted using across-borehole geometry, using multiple electrically isolated electrodes placed in vertical arrays. This geometry has the potential to produce relatively high-quality, high-resolution images when the aspect ratio of vertical to horizontal spacing is equal to or greater than 1.5:1.0. Typical electrode installations involve multiple electrodes assembled on nonconductive casing (e.g., plastic or fiberglass) in conventionally installed boreholes, or as instrumentation strings installed using cone penetrometers. Both designs have been effective in shallow to moderate depths (most recently over 395 m [1296 ft]), but deeper installations require significant and more costly modifications. The methods

for data collection and processing have been described in detail by Ramirez and his colleagues (e.g., Ramirez et al. 1995). LaBrecque et al. (1996) describe the forward and inverse modeling codes.

The ERT technique was used during the FY 2000 and FY 2001 injection tests at the 299-E24-111 test site. The objectives of the ERT surveys were to assess the feasibility for detecting subsurface leaks, monitor infiltration processes, delineate lithologic units; and use steel casings as electrodes. Measurements were made using two different configurations. Multiple electrodes were assembled onto PVC casings to form VEAs for use in a point electrode configuration. Eleven electrode arrays with a total of 165 electrodes were installed by cone penetrometer to verify that each electrode was in good contact with the surrounding sediment (Figure 1.4). This configuration was used to conduct detailed 3-D surveys of the test site between depths of 5 and 19 m (16 and 62 ft) (Ramirez et al. 2001). In addition to the point electrode configuration, 30 of the well steel casings already at the site were used as "long electrodes" for ERT measurements. This configuration was expected to only produce 2-D images of horizontal plume structure as there is no sensitivity to vertical structure. The region sampled by these long electrodes extended from 0 to 19 m (0 to 62 ft).

2.18.1 Results

During the FY 2000 tests, fluid injections consisted of low ionic strength river water (resistivity of 70 ohm-m). The water released during the first two injection tests infiltrated soil partially saturated with low ionic strength solution (estimated at 30 ohm-m). The third spill in FY 2000 released a moderate ionic strength potassium bromide (KBr) tracer with a resistivity of 4 ohm-m. The KBr tracer invaded soil that had previously received 7900 L (2087 gal) of 70 ohm-m water. In contrast, the first five spills of FY 2001 released high ionic strength river water (resistivity of 0.3 ohm-m); the first two spills infiltrated soil partially saturated with low ionic strength solution (estimated at 70 ohm-m).

Figure 2.107 compares the changes in resistivity caused by similar volumes of released fluids having vastly different ionic strengths that were injected at the 299-E24-111 test site. Figure 2.107a shows the changes in resistivity at the 299-E24-111 test site resulting from the injection of 7900 liters of 70 ohm-m river water into a pore space partially saturated with pore water of an estimated 30 ohm-m resistivity. The water injection caused the resistivity to decrease by about a factor of about 2 to 3. Figure 2.107b shows the changes observed after a similar volume (7570 liters) of a 0.3 ohm-m sodium thiosulfate solution had infiltrated the soil. The thiosulfate injection caused a more significant decrease in resistivity, a factor of 10 to 100 in this case. Whereas the water injection resulted in a plume extending from 5 to around 10 m (16 to around 33 ft) deep, the injection of a similar volume thiosulfate solution resulted in a plume that extended beyond the 12-m (39-ft) fine-grained layer to a depth of 19 m (62 ft). The columnar shape of the plume suggests that the fluid is moving preferentially in the vertical direction, suggesting that some kind of a fingering mechanism at work.

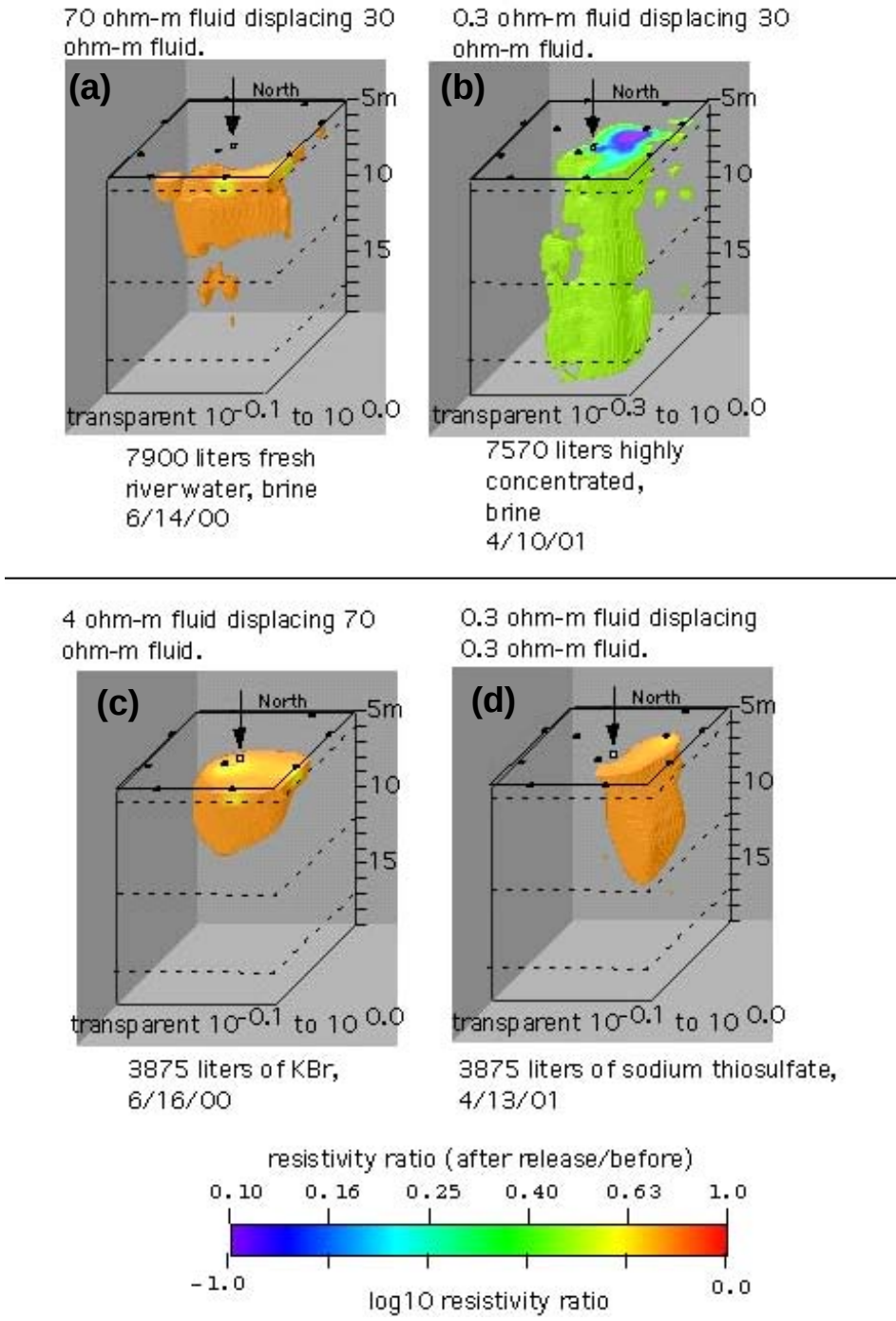

Figure 2.107. Comparisons of Tomographs Representing the FY 2000 and FY 2001 Injections. The FY 2000 Test injected low ionic strength fluids, and the FY 2001 test injected high ionic strength fluids.

Figure 2.107c and Figure 2.107d compare the low-ionic strength and high ionic strength distributions at the 299-E24-111 test site after a similar magnitude of resistivity decrease (about a 30% decrease). Such a comparison minimizes the uncertainty in estimates of plume dimensions associated with comparisons of tomographs showing vastly different resistivity changes. Figure 2.107c includes the effects of the KBr tracer injected in FY 2000. The response in Figure 2.107c is there because of the displacement of very low ionic strength pore water from the river water injection 1 week earlier by a low-ionic-strength KBr tracer solution. In this case, the observed resistivity change is caused by a combination of changes in pore fluid salinity and in saturation. The KBr injection created a bowl-shaped plume that extended from 5 to about 9 m (16 to around 30 ft) with a maximum width of about 7 m (23 ft) in the north-south and east-west directions. The shape of the plume showed very little evidence of anisotropy. Figure 2.107d shows the resistivity change resulting from the third sodium thiosulfate injection in FY 2001. Here, the response was caused by the displacement of a high-ionic-strength solution from soil that is relatively flowing and an earlier injection of 7570 L (2000 gal) salt solution. The change in resistivity in this case was caused primarily by changes in saturation as the ionic strength of the displacing and displaced fluids was similar. Adding 3875 L (1024 gal) of solution created a fingerlike, vertically oriented region extending from 5 to about 12 m (16 to around 40 ft) whereas the maximum width was about 7 m (23 ft) in the north-south direction and 3 m (10 ft) in the east-west direction. The shape of the plume suggested that significant anisotropy occurred, although the flow appeared to be primarily in the vertical direction. Whereas the movement of the low-ionic strength plume was mildly anisotropic with a preferential movement in the horizontal direction, the movement of the high-ionic strength plume was predominantly vertical along discrete, localized, vertical flow paths.

Figure 2.108 shows the time history of resistivity changes resulting from the injection of the high ionic strength fluid. This sequence shows the evolution of resistivity change as a function of the volume released. Figure 2.108a through Figure 2.108e show volume renderings, and all voxels with resistivity ratios between 1.0 and 0.5 ($10^{0.00}$ to $10^{-0.03}$) are transparent. Figure 2.108f through Figure 2.108j show the same data, but with horizontal and vertical slices through the tomographs.

During the FY 2000 water and dilute tracer injection at the 299-E24-111 test site, a bulbous wetting front developed beneath the injection point and gradually moved to the southeast. Some of the tracer may have been lost to the image block to the southeast, but the data show that most of the fluid was retained inside the image block. Almost all of the tracer volume remained above the 12-m (39.4-ft) depth. The resistivity change tomographs compare reasonably well with neutron differences that show the plume was contained above the 12-m (39.4-ft) layer. The initial pore water had a higher electrical conductivity (ionic concentration) than the tracer water in Releases 1 and 2. During the KBr release, the original pore fluid was largely replaced by the tracer fluid directly below the injection point, but this effect decays rapidly away from the injection point.

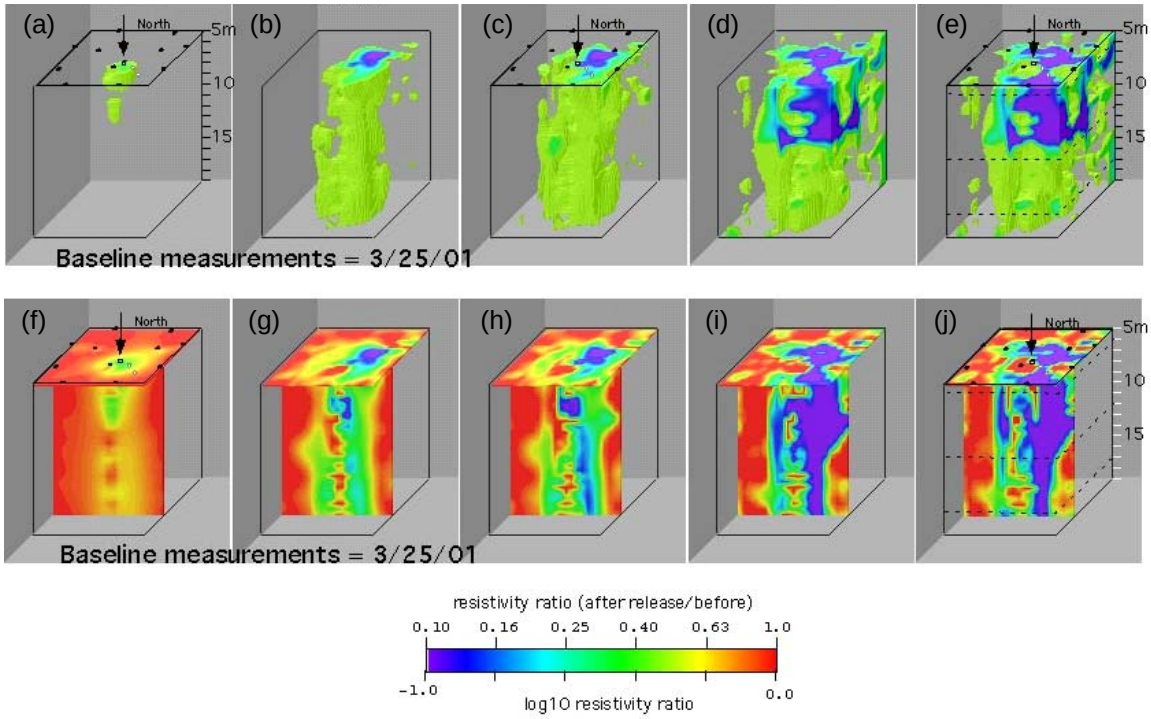

Figure 2.108. Changes in Resistivity of the Whole Test Region as a Function of Time and Injected Fluid Volume at the 299-E24-111 Test Site

During the FY 2001 field experiment at the 299-E24-111 test site, the sodium thiosulfate solution moved deeper and faster than the low-ionic-strength fluid observed in the FY 2000 test. When the saline solution was injected, there was less lateral spreading of the plume when compared to plumes of relatively fresh water. Plumes of relatively fresh water did not display evidence of fingering but showed considerable lateral spreading. The tomographs suggest that the fine-grained layers located at 6- and 12-m (19.7- and 39.4-ft) depths are penetrated by the highly concentrated brine. The relatively fresh water plumes did not penetrate the 12-m (39.4 ft) silt layer. These data show resistivity decreases that can be attributed primarily to changes in pore water electrical conductivity. However, unlike the results from the neutron probe and crosshole radar logs, this time sequence suggests that the plume moved mostly downward from the release point with relatively little lateral spreading. Figure 2.108h through Figure 2.108i show the development of localized regions of preferential flow with a low resistivity developing in the southwest corner of the 299-E24-111 test site near Well H6. These data show the plume penetrating the fine-textured layer at the 12-m (39.4-ft) layer after an injection of only 7570 L (2000 gal) of thiosulfate solution on April 10, 2001, and these data are consistent with observations from neutron-probe measurements (Ward et al. 2002).

Figure 2.109 compares an ERT tomograph with changes in moisture content derived from neutron-probe measurements in boreholes H2, H4, and H6 at the 299-E24-111 test site. Figure 2.109a shows a diagonal slice through the tomograph, along the D-H transect. The black dots on top of the tomograph indicate the location of the electrode arrays whereas the white ellipses indicate the location of the steel-cased wells used for neutron measurements. The dotted lines show the approximate location of fine-grained units. Figure 2.109b, c, and d show three profiles of water-content differences relative to the initial condition. The resistivity tomograph shows a region of large resistivity decreases (small resistivity

ratios indicated by the blue and purple colors) that extend over the entire monitoring depth of 5 to 19 m (16 to 62 ft). Above the fine-textured layer at 12 m (39.4 ft), the region of large decrease is somewhat wider than at locations deeper in the profile. Below the layer, the region of strong changes suggests a vertically oriented fingerlike zone. The neutron logs show a large increase in moisture above the 12-m (39.4-ft) layer on May 04, 2001 (Figure 2.109b) and smaller increases on May 11, 2001 (Figure 2.109c). Below the 12-m (39.4-ft) layer, the neutron profiles of 5/11/01 suggest large saturation increases that are not present in the measurements made on May 04, 2001 (Figure 2.109d). The increase in water content below the 12-m (39.4-ft) confining layer on May 11, 2001, is consistent with the fingerlike anomaly observed in the tomographs below 12 m (39.4 ft) and confirms the penetration of this layer.

There is a need for caution when comparing ERT and neutron probe results as the two geophysical modalities respond to different flow variables. The dominant mechanism affecting the neutron response is the change in water content within a relatively small region around the access tube. The dominant

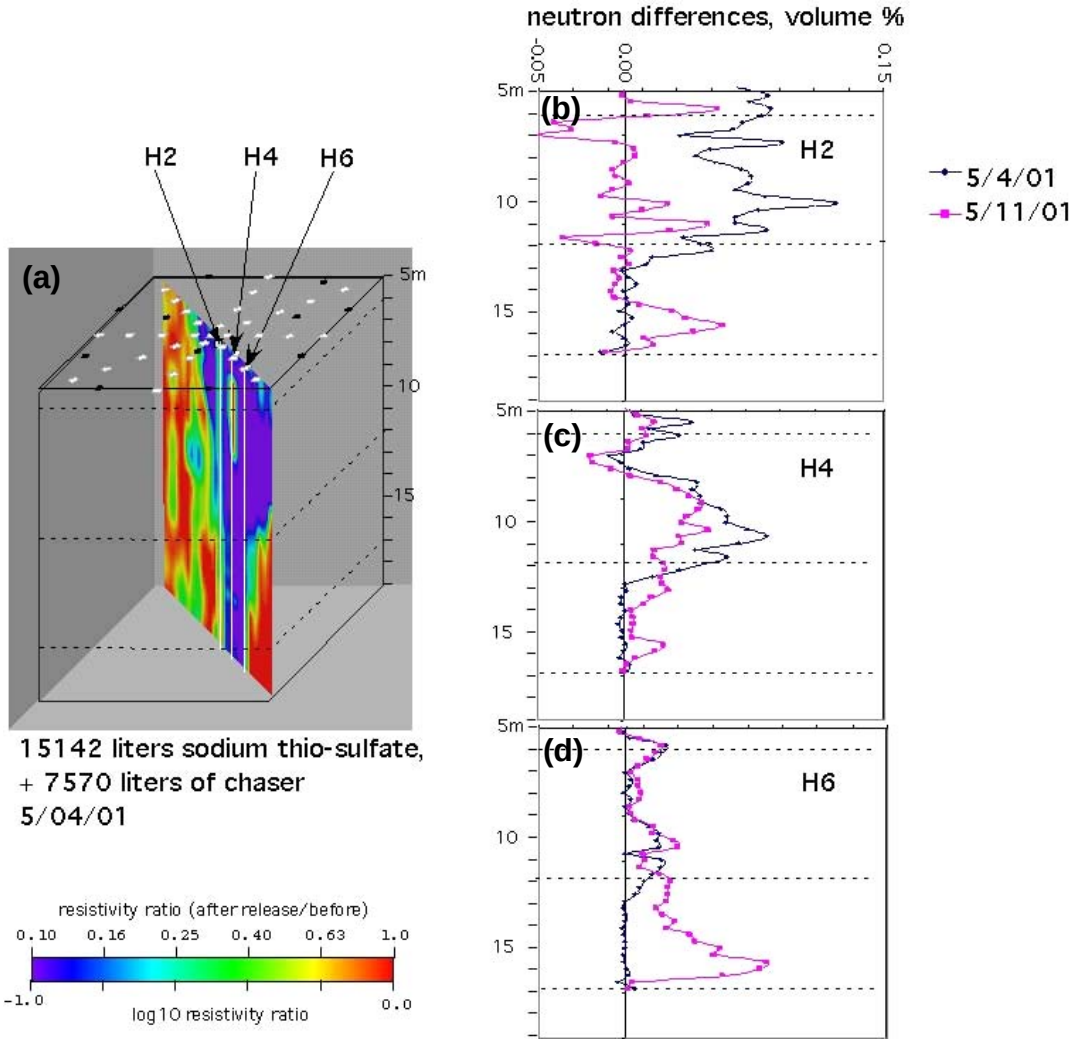

Figure 2.109. Comparison of a Tomograph of the Whole Test Site with Neutron Log Differences Along Boreholes H2, H4, and H6 at the 299-E24-111 Test Site

mechanism causing changes in resistivity is the changing salinity of the pore fluid, but a much larger volume of soil can be interrogated compared to the neutron probe. In areas were saturation changes are small, it is difficult to detect such changes with the neutron probe, especially if the changes are occurring more than 0.30 m (0.98 ft) away from the access tube. However, such small changes in saturation caused by the movement of a salt solution would cause large changes in pore water conductivity results in large resistivity decreases. The large changes in resistivity observed in Figure 2.109 are therefore quite possible even though the neutron probe shows little or no change in saturation because the sodium thiosulfate causes large changes in pore fluid conductivity. Under such circumstances, ERT would be much more sensitive to small changes in fluid content than the neutron probe.

As part of the VZTFS, the feasibility of using the steel well casings as electrodes to delineate a subsurface plume was explored using the long-electrode configuration. Figure 2.110 shows the tomographs resulting from measurements made with the long-electrode configuration at the 299-E24-111 test site. These data were derived from measurements made on April 10, 2001, after the injection of 7570 L of sodium thiosulfate solution. Figure 2.110a shows the tomograph resulting from 11 VEAs consisting of 165 point electrodes to serve as a reference. Figure 2.110b shows the tomograph based on a combination of point-electrode and long-electrode measurements. Data were collected using 8 of the 11 arrays along the perimeter of the site coupled with the 30 steel casings. In the combined data set, measurements using electrodes in the interior arrays were removed to simulate the case where no electrode arrays are installed within a tank farm. This approach is similar to what could be done if electrode arrays were installed outside a waste management area, and the dry wells were used as electrodes inside the waste management area. Figure 2.110c shows the tomograph calculated using only data from the long electrode configuration and is representative of a survey that might result from measurements in a tank farm.

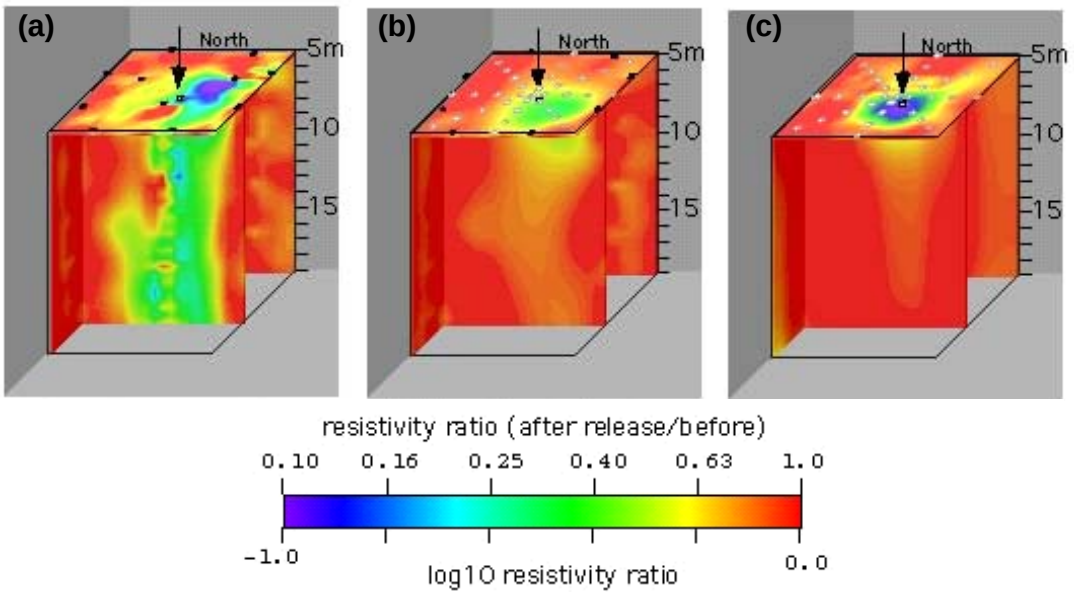

Figure 2.110. A Comparison of Tomographs Based on ERT Measurements with Different Electrode Configurations of Long-Electrode Measurements After the Injection of 7570 L (2000 gal.) of Sodium Thiosulfate Solution, (a) 165 Point Electrodes, (b) 120 Point Electrodes Combined with 30 Long Electrodes, and (c) 30 Long Electrodes Using Steel Cased Wells

Both of the tomographs based on long-electrode measurements show a conductive anomaly near the surface that is consistent with the known longitudinal and transverse horizontal extent of the plume directly below the release point (Figure 2.110b and c). The vertical extent of the anomaly in Figure 2.110b is most likely real because the data collected with the point electrode arrays provide vertical resolution. However, the vertical extent of the anomaly in Figure 2.110c is most likely a processing artifact related to the conductivity assumed for the steel casings in the numerical model. Therefore, there is no relation to the vertical extent of the plume. Thus, only a crude image of the plume is obtained. The results demonstrate that steel casings may be useful in detecting the presence of subsurface plumes as well as delineating the lateral extent of the plume. A combination of VEAs around the perimeter of the domain of interest with dry wells improved the resolution, suggesting that it should be possible to map the vertical and horizontal extent of conductive plumes in such environments.

2.18.2 Synopsis and Implications

The synopsis of findings in the investigation of ERT for monitoring infiltration and characterizing subsurface structure and their implications are as follows:

- Conventional electrical resistivity surveys have had limited hydrogeologic applications where electrical resistivity anomalies are complex with nested scales of heterogeneities. ERT is an extension of the conventional method designed to overcome these limitations by making multiple measurements using various electrode combinations from which a tomograph is generated by the joint inversion of all the individual measurements.

- The deployment of ERT during the FY 2000 and FY 2001 field studies at the 299-E24-111 test site successfully generated tomographs of the developing plumes. Measurements were made using VEAs installed by cone penetrometer as well as with steel casings in a long electrode configuration.

- Data acquisition is relatively fast, depending on the number of electrodes and the monitoring protocol. Generating the tomographs by jointly inverting the measurements is computationally intensive with the typical 3-D problem requiring anywhere from a few hours to several days, which could limit use for real time leak detection and monitoring.

- The best electrode configuration for subsurface leak detection and monitoring is one in which the region of interest is completely surrounded with electrodes. This could be a potential limitation in contaminated areas where the cost-installing electrodes could be prohibitive. Tests conducted using existing steel casings as long electrodes were able to delineate the plume but showed poor vertical resolution.

- Comparisons of ERT tomographs with neutron-probe moisture data and the associated mass balances show relatively good agreement. Both the point-electrode and long-electrode configurations have since been tested at the mock tank site as a potential technology for leak detection and monitoring to support tank retrieval operations (Barnett et al. 2003), but the technology was not selected for implementation.

2.19 Statistical and Spatial Correlation Structure of Flow Variables

Upscaling of local-scale estimates of physical, hydraulic, and geochemical parameters and regionalization to larger domains requires information on the spatial correlation structure of these parameters or appropriate surrogates. It has been shown that local-scale predictions based on pedotransfer functions can be regionalized for terrestrial ecosystems simply by coupling the pedotransfer functions with information on the spatial correlation structure derived from geostatistical methods (Scheinost et al. 1997). Upscaling methods for flow have been developed based on a spectral solution of the first-order stochastic perturbation equation in which the variance of capillary pressure head and the anisotropy ratio increases with decreasing saturation (Yeh et al. 1985; Polmann 1990). Using the resulting equations requires information on the correlation lengths in the vertical, λ_z, and horizontal, λ_z, directions. However, except for one experimental site at Hanford where K_s measurements were made at a horizontal spacing Δx=0.3 m and to a depth of 18 m, most measurements have been made at sampling intervals too coarse to yield accurate estimates of the correlation lengths. Thus, literature values of correlation lengths are often used for flow and transport simulations with the assumption that the same values are applicable (Khaleel and Connelly 2004).

The objective of this study was to quantify the correlation structure of various parameters needed to simulate flow and transport. The configuration of the 299-E24-111 test site was such that information on the vertical correlation structure could be obtained but because of the horizontal spacing, features occurring at spatial scales less than 2 m (6.6 ft) would be missed. This was an important consideration in the design of the experiments at the Army Loop Road site where a 60-m (197-ft) long transect was instrumented at 0.5-m (1.6-ft) intervals to allow determination of the horizontal correlation lengths. Soil properties and flow variables are usually not random in space, but tend to have spatial continuity with correlation over some distance because of the depositional environments. Geostatistical techniques are useful for estimating the effects of the depositional environment on the 3-D flow field, especially when the 2- or 3-D heterogeneous flow field has spatial continuity (Delhomme 1979; Desbarats and Bachu 1994). A number of researchers have shown that variogram modeling can be used to quantify the spatial covariance structure and to characterize heterogeneities of the subsurface in two or more dimensions. The semivariogram chosen to identify the spatial covariance structure of flow variables and transport properties is defined as (Deutsch and Journel 1998)

$$\gamma(h) = \frac{1}{2N(h)} \sum_{i=1}^{N(h)} \left[p(x_i) - p(x_i + h) \right]^2 \tag{2.18}$$

where h is the spatial separation distance known as the lag, N(h) is the number of data pairs separated by a vector h, and $p(x_i)$ denotes the observation at a location. The semi-variogram provides a good measure of environmental structure and can be modeled with various approaches using shape parameters, such as the range (A_0), nugget (C_0), and the sill ($C_0 + C$). One commonly used model is the spherical model expressed by

$$\gamma(h) = \begin{cases} C_0 + C_1 \left[1.5(d/a) - 0.5(h/a)^3 \right], & d \le a \\ C_0 + C_1, & d > a \end{cases} \tag{2.19}$$

where C_0 = nugget variance
C_1 = a constant
$C_0 + C_1$ = limiting value called sill
a = range value for d where the sill occurs.

The range determines the extent of the zone of influence of an experimental point. Equation (2.20) may be standardized to the total variance as

$$\gamma_s(h) = \begin{cases} B_0 + B_1\left[1.5(d/a) - 0.5(h/a)^3\right], & d \le a \\ 1, & d > a \end{cases} \tag{2.20}$$

where $B_0 = C_0/(C_0 + C_1)$ is the standardized nugget variance, and $B_1 = C_1/(C_0 + C_1)$ is a constant. The conventional opinion exists that at some distance, the semi-variance between neighboring observations becomes random and reaches a plateau, commonly known as the sill in the semivariogram. However, the range at which the plateau is reached and the magnitude of variance at the plateau often depends on the sampling scale itself as well as the size of the sampling area (Journel and Huijbregts 1978).

The variogram may also be expressed by the autocorrelation function:

$$r(h) = 1\text{-}\gamma_s(h) \tag{2.21}$$

Often the spatial autocorrelation of a parameter is expressed by the correlation scale or the integral scale, λ, defined as (Russo and Bresler 1981)

$$\lambda = \left[2\int_0^\infty h\, r(h)\, dh\right]^{1/2} \tag{2.22}$$

Distribution tests, correlations, multiple regressions, and nonlinear regressions were conducted using a combination of in-house tools and commercial software packages. Variograms and ordinary kriging were performed with the Geostatistical Software Library (GSLIB) software package (Deutsch and Journel 1998). For the FY 2000 and 2001 data from the 299-E24-111 test site, the correlation structure of the flow variables and anisotropy ratios were determined by fitting models to the experimental variograms. Omni-directional variograms were fitted to the transverse vertical, longitudinal, and transverse horizontal directions by in 22.5-degree increments from 0 degrees to 157.5 degrees. Fitted parameters and flow variables from the FY 2002 and FY 2003 experiments at the Army Loop Road site were also analyzed to determine the correlation structure. Flow and transport parameters optimized by inverse modeling of data from the Army Loop Road site were analyzed in a similar fashion to determine the correlation structure.

2.19.1 Results

The summary statistics of the neutron-probe data collected during the 8 neutron-probe logging campaigns in FY 2000 are summarized in Table 2.7. The summary statistics for the 13 neutron-probe logging campaigns time steps in FY 2001 are summarized in Table 2.8 and Table 2.9. For FY 2000, the sample mean θ increased over the period May 05, 2000 to June 23, 2000 and then decreased gradually

until the end of the experiment on July 31, 2000. For FY 2001 data, the sample mean θ increased from March 22, 2001 to May 10, 2001 after which it decreased gradually until the end of the experiment on August 14, 2001. These trends are consistent with the spatial moment analysis over time that showed a loss of water mass by lateral migration out of the monitored domain.

Table 2.7. Descriptive Statistics of the FY 2000 Neutron-Probe Water-Content Data for Surveys 1 Through 8

FY00 Water Content (%)	05/05	06/02	06/09	06/16	06/23	07/07	07/17	07/31
Mean	3.42	3.67	3.83	3.98	4.08	3.97	3.88	3.82
Standard Error	0.04	0.05	0.06	0.06	0.06	0.05	0.05	0.05
Median	3.09	3.15	3.21	3.23	3.3	3.31	3.32	3.35
Standard Deviation	1.42	1.83	2.05	2.20	2.24	1.97	1.83	1.74
Sample Variance	2.03	3.34	4.19	4.86	5.04	3.87	3.33	3.03
Kurtosis	17.49	7.80	4.73	3.99	2.62	4.54	5.70	7.49
Skewness	3.18	2.48	2.12	1.99	1.74	1.80	1.91	2.10
Range	14.49	14.69	14.13	14.61	13.09	15.06	14.61	14.52
Minimum	1.69	1.68	1.53	1.67	1.64	1.64	1.53	1.67
Maximum	16.18	16.37	15.66	16.28	14.73	16.70	16.14	16.19
Count	1376	1376	1376	1376	1376	1376	1376	1376
Confidence Level (95.0%)	0.08	0.10	0.11	0.12	0.12	0.10	0.10	0.09

Table 2.8. Descriptive Statistics of the FY 2001 Neutron-Probe Water-Content Data for Surveys 1 Through 7

FY01 Water Content (%)	03/22	03/30	04/06	04/12	04/19	04/26	05/03
Mean	3.51	3.56	3.87	4.12	4.19	4.12	4.32
Standard Error	0.04	0.04	0.05	0.06	0.06	0.06	0.07
Median	3.17	3.13	3.25	3.33	3.36	3.28	3.28
Standard Deviation	1.48	1.66	2.02	2.18	2.27	2.25	2.67
Sample Variance	2.19	2.74	4.09	4.76	5.16	5.07	7.12
Kurtosis	13.15	10.67	6.00	3.31	3.12	2.98	3.24
Skewness	2.73	2.66	2.23	1.75	1.71	1.74	1.83
Range	13.95	15.07	14.17	14.25	15.33	14.59	16.30
Minimum	1.62	1.62	1.77	1.76	1.80	1.72	1.64
Maximum	15.57	16.69	15.94	16.01	17.13	16.31	17.94
Count	1376	1376	1376	1376	1376	1376	1376
Confidence Level (95.0%)	0.08	0.09	0.11	0.12	0.12	0.12	0.14

Table 2.9. Descriptive Statistics of the FY 2001 Neutron-Probe Water-Content Data for Surveys 8 Through 13

FY01 Water Content (%)	5/10	5/17	5/23	6/6	6/22	8/14
Mean	4.34	4.23	4.23	3.93	3.92	3.74
Standard Error	0.07	0.06	0.06	0.05	0.05	0.04
Median	3.45	3.55	3.49	3.47	3.49	3.35
Standard Deviation	2.43	2.11	2.25	1.82	1.74	1.64
Sample Variance	5.91	4.47	5.04	3.32	3.04	2.69
Kurtosis	2.78	4.82	7.27	6.81	8.33	10.95
Skewness	1.62	1.77	2.12	1.95	2.11	2.39
Range	16.75	17.59	19.75	16.52	16.55	16.28
Minimum	1.58	1.72	1.63	1.66	1.65	1.51
Maximum	18.33	19.31	21.38	18.18	18.20	17.79
Count	1376	1376	1376	1376	1376	1376
Confidence Level (95.0%)	0.13	0.11	0.12	0.10	0.09	0.09

In stratified sediments, the extent to which an asymmetric flow field develops is controlled by the geometry, scale and continuity of textural contrasts that give rise to heterogeneity in the permeability field. To gain insight into the underlying structure controlling wetting front migration and the distribution of moisture, the in situ 3-D spatial correlation structure of the moisture distribution was determined by calculating the traditional variograms and correlograms for each measurement. Because a drift was suspected to exist in the plume and there might be a trend present in the data, it was decided to model the spatial continuity using the correlograms. The correlograms were visualized as variograms by subtracting their values from 1.0. The experimental variograms and models for measured θ (x,y,z;t) from the two experiments are shown in Figure 2.111 through Figure 2.115.

The parameters of the directional correlogram models of the water-content data from the time steps in FY 2000 salt-free and FY 2001 hypersaline experiments at the 299-E24-111 test site are listed in Table 2.10 and Table 2.11, respectively. Because of an apparent difference in correlation structure for the vertical and horizontal planes, a nested model was used to fit the experimental correlograms. As can be expected, the structure of the variogram and the spatial continuity of θ(x;t) varied with time during the water injections. From Figure 2.111, Figure 2.112, and Table 2.10 the correlogram behaviors of the eight surveys in FY 2000 appear to be separated into four groups: (1) May 5; (2) June 2 and 9; (3) June 16 and 23; and (4) July 7, 17, and 31. The correlogram structures are very similar within the groups, with similar ranges, sills, and ratios of anisotropy. From Figure 2.113, Figure 2.114, Figure 2.115, and Table 2.11, similar partitioning can be found in the models of θ(x;t) from the FY 2001 hypersaline injection. Four groups were also apparent and included: (1) March 22, 30, and April 6; (2) April 12, 19, 26, and May 3 and 10; (3) May 17, and 23; and (4) June 6, 26 and August 14. The nature of this grouping is unclear but may be related to the moisture status and the temporal persistence of a correlation structure. The change in variance and range over time is a reflection of the changing degree of heterogeneity affecting flow and is consistent with the published findings. Wendroth et al. (1999) observed that the variance of soil water pressure head was large under wet conditions. With decreasing soil water pressure head the variance decreased to a critical value, for which the spatial correlation structure disappeared. With further drying, the variance increased again and a spatial range of correlation existed.

Table 2.10. Correlogram Models of the FY 2000 Neutron-Probe Water-Content Data for Surveys 1 Through 8

FY 2000 Survey Date	Nugget	Model	Sill	Range (m)		
				Deg = 22.5	Deg=112.5	Vertical
5-5-00	0	Spherical	0.34	2.2	2.7	0.6
		Spherical	0.66	70	20	1.4
6-2-00	0.02	Spherical	0.51	6.5	6	1.2
		Spherical	0.47	120	24	2.6
6-9-00	0	Spherical	0.6	6	5.5	1.3
		Spherical	0.4	150	32	4.7
6-16-00	0.02	Spherical	0.6	6.8	5.3	1.4
		Spherical	0.38	100	25	9.0
6-23-00	0	Spherical	0.6	6.5	6	1.4
		Spherical	0.4	100	25	9.0
7-7-00	0	Spherical	0.42	7	6.5	0.9
		Spherical	0.58	100	22	3.4
7-17-00	0	Spherical	0.42	7	7	0.7
		Spherical	0.58	200	23	2.8
7-31-00	0	Spherical	0.38	6	6	0.6
		Spherical	0.62	200	22	2.4

During drying, temporally stable variation patterns also developed. In our data, increasing $\theta(x;t)$ led to an increase in variance to a critical value, almost double the initial value, and a spatial correlation structure became evident. The fitted peak value of the variance coincided with the point at which water started to leave the system because of lateral flow. Beyond this point, there was a gradual decrease in variance and a loss of correlation structure. In contrast, the second sill showed a decrease with time, reaching a minimum when mass started to leave the system, after which it increased.

The fact that the boundary of the monitoring domain for the 299-E24-111 test site was only 16 m across may raise questions about the validity of the modeled range. In fact, the absence of a stable sill can be expected in strongly layered systems in which the horizontal range exceeds the boundary of the sampling domain. These data show an increase in the range over time, also reaching a maximum just prior to the loss of mass. In fact, the fitted range of correlation increased from around 70 m (230 ft) to over 100 m (328 ft) in the direction of maximum continuity. These values appear quite reasonable for the depositional environment. Weber (1982) presented data for five major depositional environments, including marine, deltaic, barrier, delta fringe, delta plain, distribution channel, and coarse point bars. The median length of continuity varied from over 600 m (1968 ft) in the marine depositional environment, to 150 m (492 ft) for a delta fringe, to less than 15 m (49 ft) for point bars. The depositional environment of Hanford's 200 East Area is best classified as a distribution channel (George Last, personal communication). The median length of continuity for fine-textured intercalations in a distribution channel is between 60 and 100 m (197 and 328 ft). The similarity of sediments deposited under similar conditions suggests that the results of this study can be used as the basis for the design of stratigraphic, anisotropic models for sites with relatively few data. Thus, it is expected that these results will be invaluable in the development of conceptual models for sites that are too heavily contaminated to characterize the stratigraphic model or hydrologic properties.

Table 2.11. Correlogram Models of the FY 2001 Neutron-Probe Water-Content Data for Surveys 1 Through 13

FY 2001 Survey Date	Nugget	Model	Sill	Range (m)		
				Deg = 22.5	Deg=112.5	Vertical
3/22/01	0	Spherical	0.27	2.8	2.8	0.4
		Spherical	0.73	55	18	1.55
3/30/01	0	Spherical	0.45	3	3	0.7
		Spherical	0.55	60	18	2.3
4/6/01	0	Spherical	0.45	4.5	4.5	1
		Spherical	0.55	50	18	3.6
4/12/01	0	Spherical	0.5	6	6	1.2
		Spherical	0.5	65	20	7
4/19/01	0.02	Spherical	0.5	6	5	1.3
		Spherical	0.48	50	18	9
4/26/01	0.03	Spherical	0.5	6.5	6	1.3
		Spherical	0.47	50	20	7.5
5/3/01	0.02	Spherical	0.58	7	6	2.1
		Spherical	0.4	30	20	11
5/10/01	0	Spherical	0.55	7	6	1.5
		Spherical	0.45	45	18	10
5/17/01	0.03	Spherical	0.38	7	7	0.9
		Spherical	0.59	70	16	4.2
5/23/01	0	Spherical	0.5	7.5	7.5	1
		Spherical	0.5	100	16	7
6/6/01	0	Spherical	0.37	6	7	0.7
		Spherical	0.63	80	17	2.8
6/26/01	0	Spherical	0.4	5.8	7	0.6
		Spherical	0.6	120	17	2.4
8/14/01	0	Spherical	0.37	5.5	7	0.6
		Spherical	0.63	120	17	1.8

The variograms are clearly anisotropic and in all cases show significant differences in anisotropy from initial conditions. The anisotropy ratios (both horizontal to vertical and within horizontal) of the directional correlograms were examined by modeling the correlograms in the vertical direction and horizontally in 22.5-degree increments from 0 degrees to 157.5 degrees. The directions of maximum and minimum continuity were determined to be 22.5 degrees and 112.5 degrees, respectively. In the direction of maximum horizontal continuity, the variograms were much simpler than in the vertical direction. There is clear evidence of pseudo periodicity in the vertical direction because of the layering, giving rise to a sinusoidal (hole) effect. Repetitive structures, such as parallel sedimentary layers, typically give rise to hole effects perpendicular to the layers. The wavelength of the oscillation is approximately equal to that of the structure causing the effects. The hole at 5 m (16 ft) coincides with the depth of the first fine-textured layer.

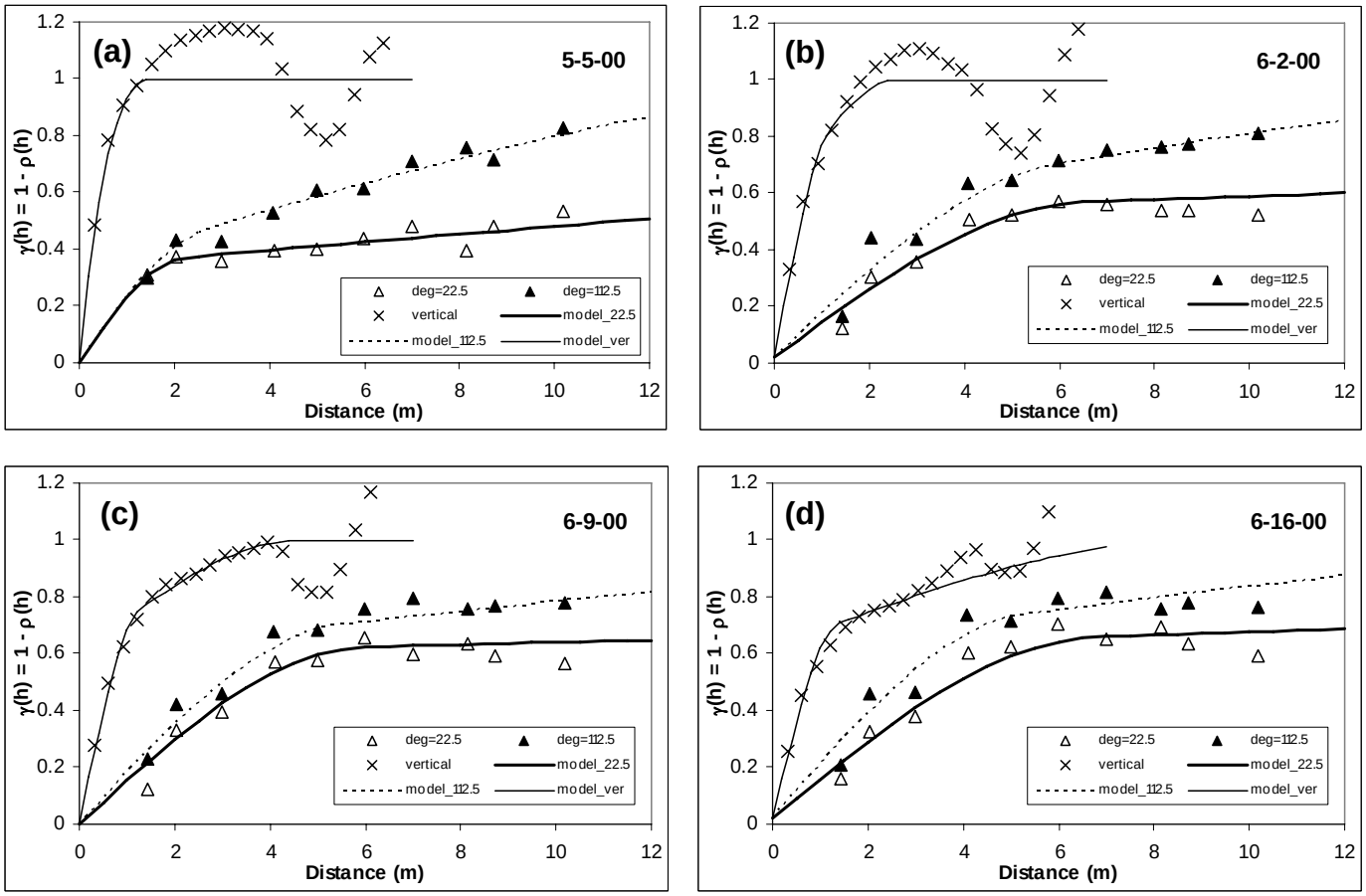

Figure 2.111. Semivariograms and Models of the FY 2000 Neutron-Probe Water Contents for Surveys 1 (May 05, 2000) Through 4 (Jun 16, 2000)

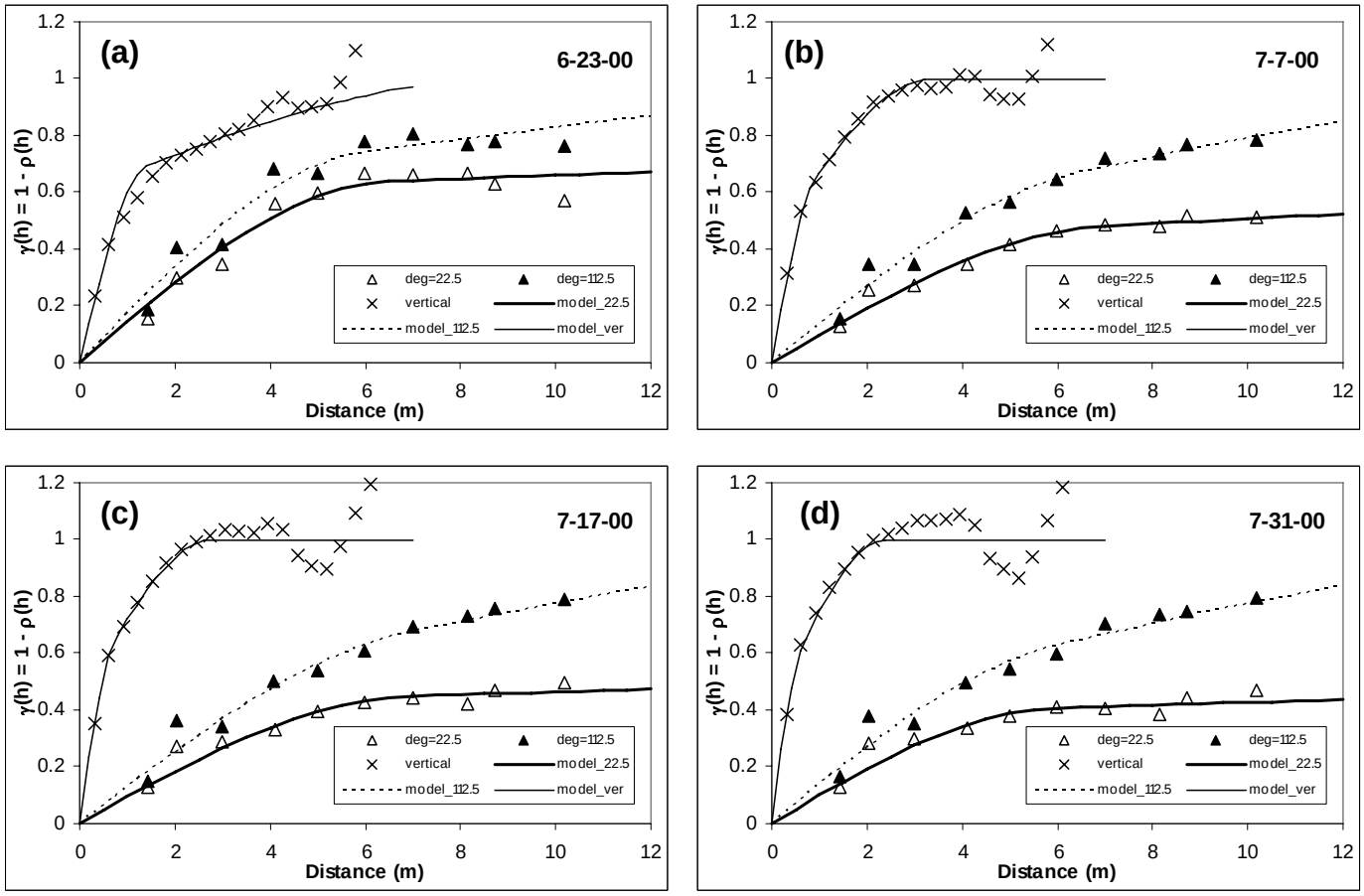

Figure 2.112. Semivariograms and Models of the FY 2000 Neutron-Probe Water Contents for Surveys 5 (Jun 23, 2000) Through 8 (Jul 31, 2000)

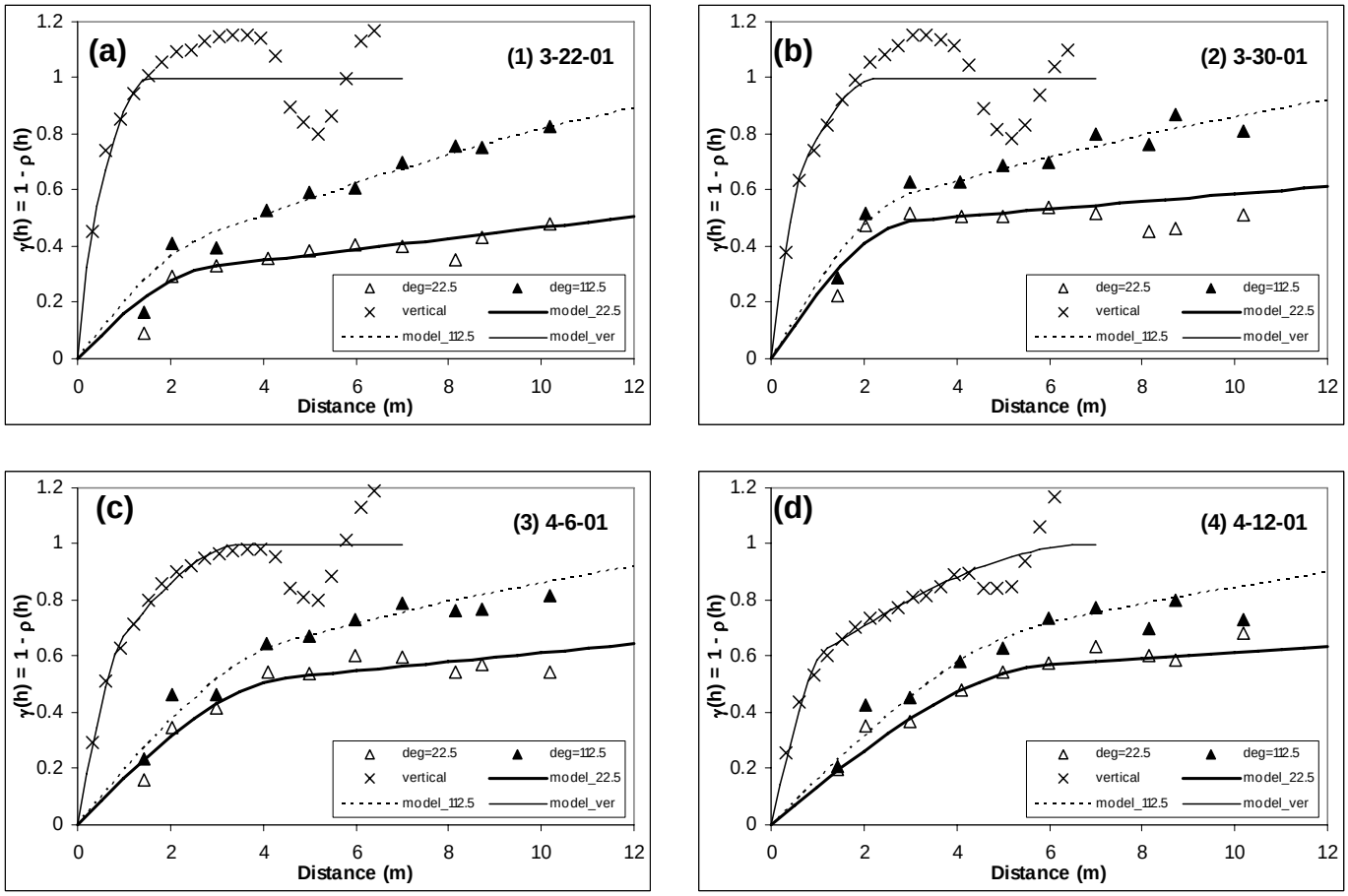

Figure 2.113. Semivariograms and Models of the FY 2001 Neutron-Probe Water Contents for Surveys 1 (Mar 22, 2001) Through 4 (Apr 12, 2001)

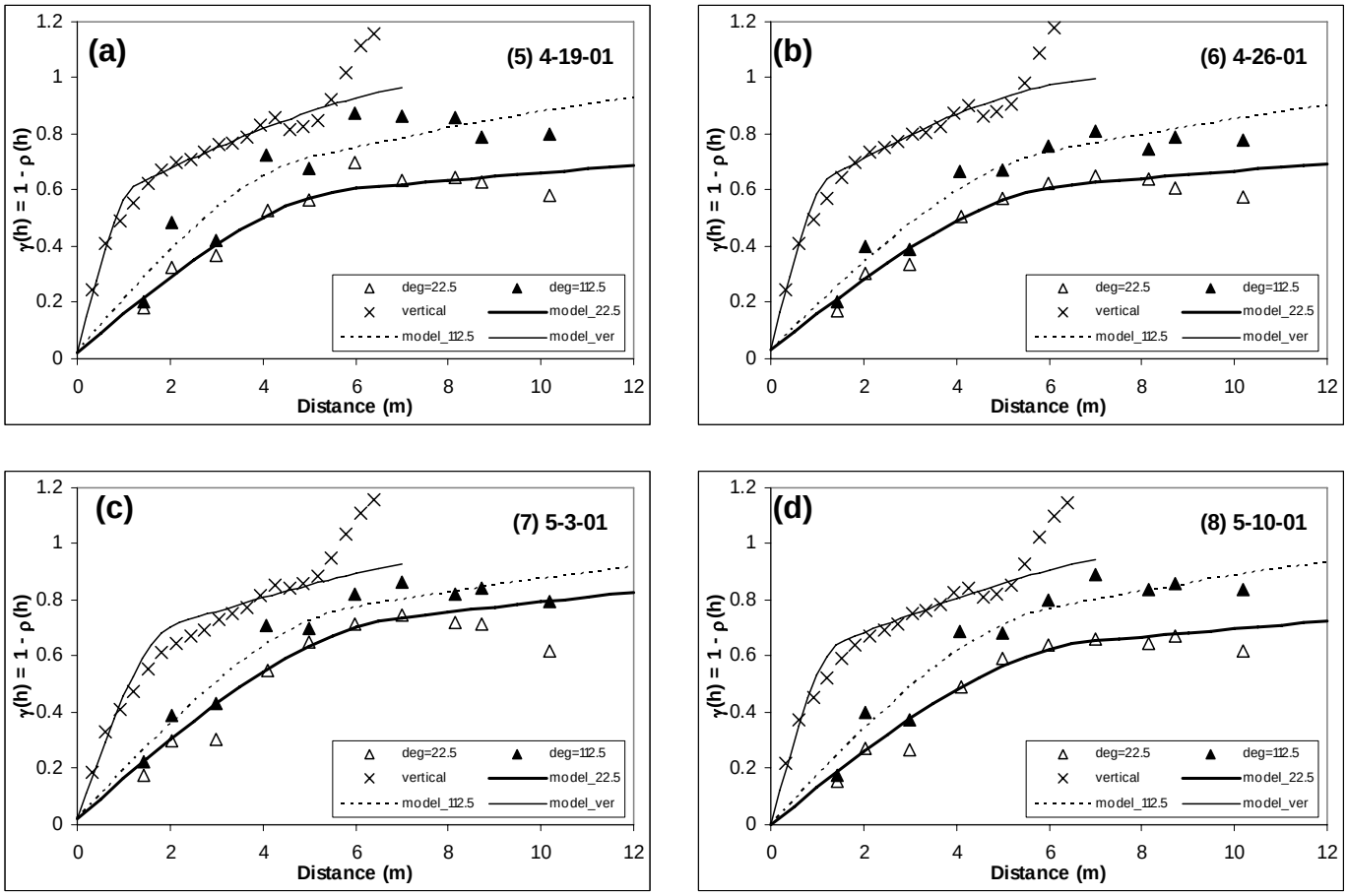

Figure 2.114. Semivariograms and Models of the FY 2001 Neutron-Probe Water Contents for Surveys 5 (Apr 19, 2001) Through 8 (May 10, 2001).

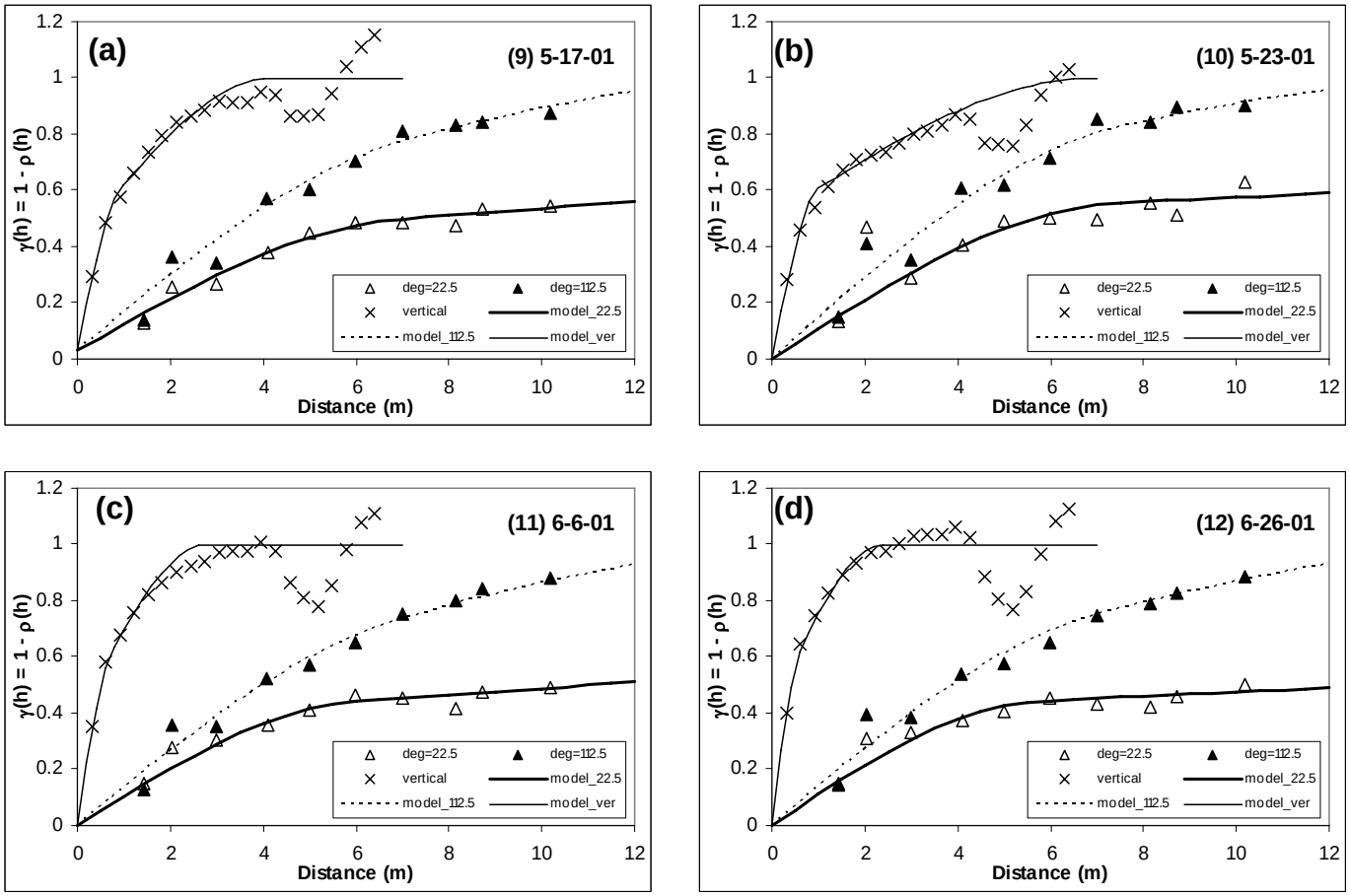

Figure 2.115. Semivariograms and Models of the FY 2001 Neutron-Probe Water Contents for Surveys 1 (Mar 22, 2001) Through 4 (Apr 12, 2001).

For a better perspective on anisotropy structure and changes over time at the 299-E24-111 test site, a series of vertical variogram surface maps were developed for four well transects in FY 2000 using the initial condition data (May 05, 2000) and the data from Jul 07, 2000. These variogram surface maps are shown in Figure 2.116 and Figure 2.117. There were significant differences in anisotropy between the two sampling times. The minimum horizontal continuity appears to be in the NW-SE direction, with the maximum continuity perpendicular to this direction (i.e., NE-SW). In the direction of maximum horizontal continuity, the variogram map is simpler, suggesting a simple layered system with some pseudo periodicity in the vertical direction because of the layering of beds of different texture and water-holding capacity.

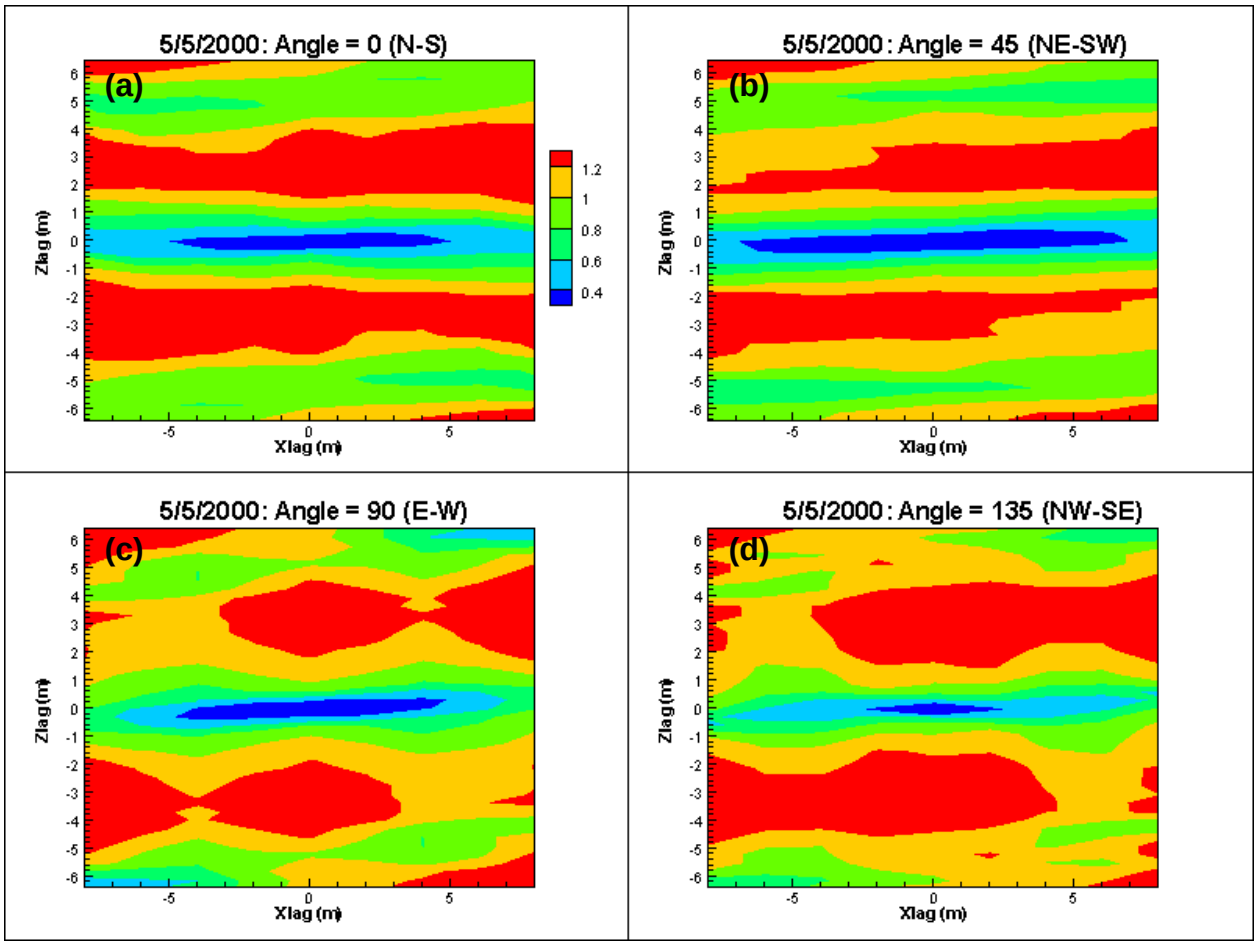

Figure 2.116. Semivariograms and Models of the FY 2001 Neutron-Probe Water Contents for Surveys 5 (May 17, 2001) Through 8 (Jun 26, 2001)

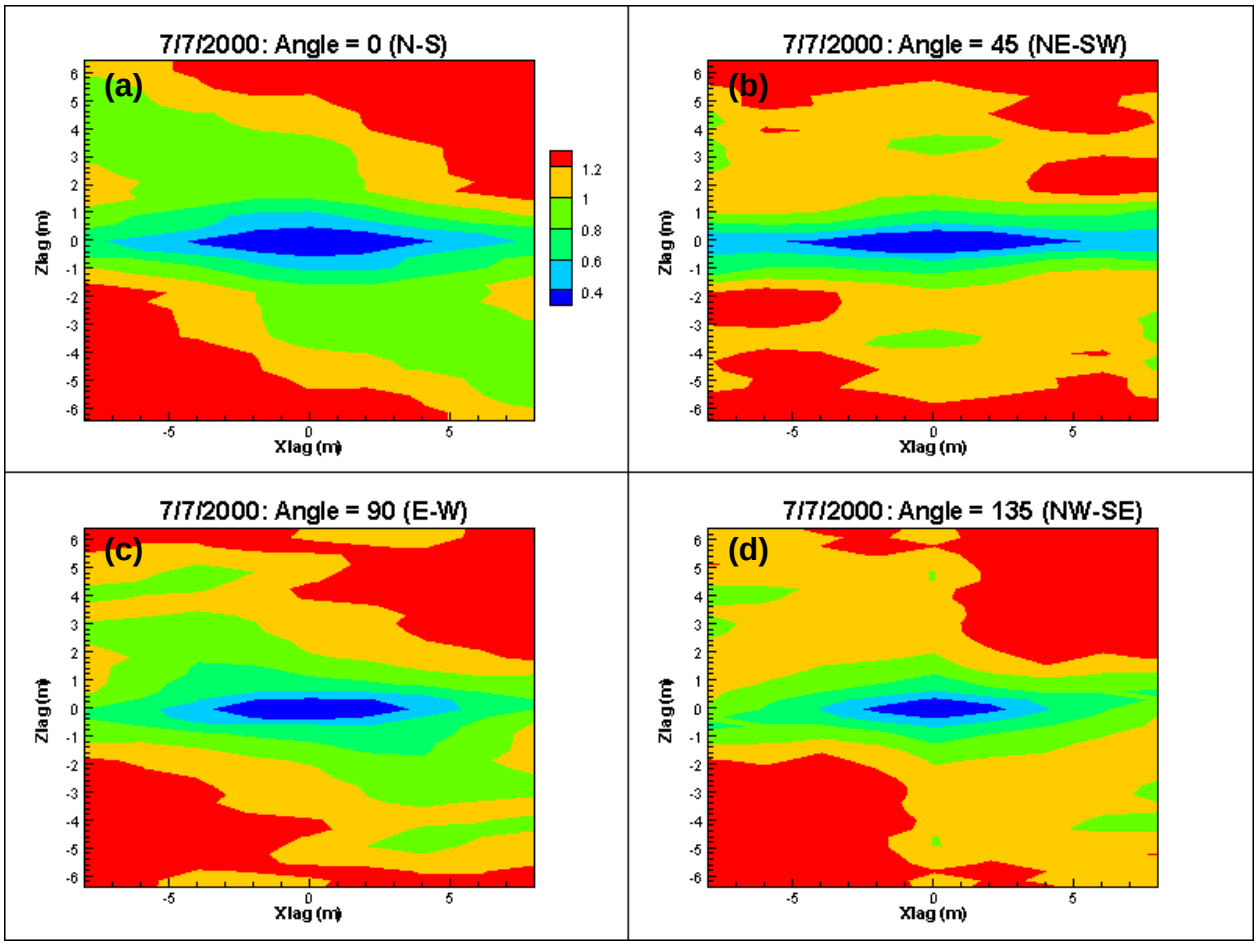

Figure 2.117. Semivariograms and Models of the FY 2001 Neutron-Probe Water Contents for Surveys 5 (May 17, 2001) Through 8 (Jun 26, 2001)

There is a suggestion of directional anisotropy at the 299-E24-111 test site within the variogram surface in the minimum continuity direction (NW-SE), with slightly greater continuity of moisture in moving from the upper left quadrant (NW) in Figure 1.4 to the lower right quadrant (SE). On the moisture map for that transect for the initial conditions, there was evidence of sedimentary structures that could be responsible for this anisotropy. Those structures would direct moisture laterally in a southeasterly direction as the moisture content increased. In fact, as the moisture content increased from the initial condition to July 07, 2000, the moisture distributions changed significantly, and this is reflected in the variogram surface maps. The most striking observation is the weakening of the strong horizontal anisotropy structure that was prominent in the variogram map of the initial condition (Figure 2.116). A diagonal anisotropy structure evolved to replace the vertical structure, reflecting the transport of moisture downward, and to the south and east of the experimental plot.

The impact of heterogeneity on subsurface moisture distributions and correlation structure was also evident at the Army Loop Road site. Field measurements of water content and solute concentrations were inverted using the STOMP-UCODE to estimate the local-scale hydraulic parameters at 59 locations along the 60-m (197-ft) transect. The spatial variations of the parameters are shown in Figure 2.118. A 2-m

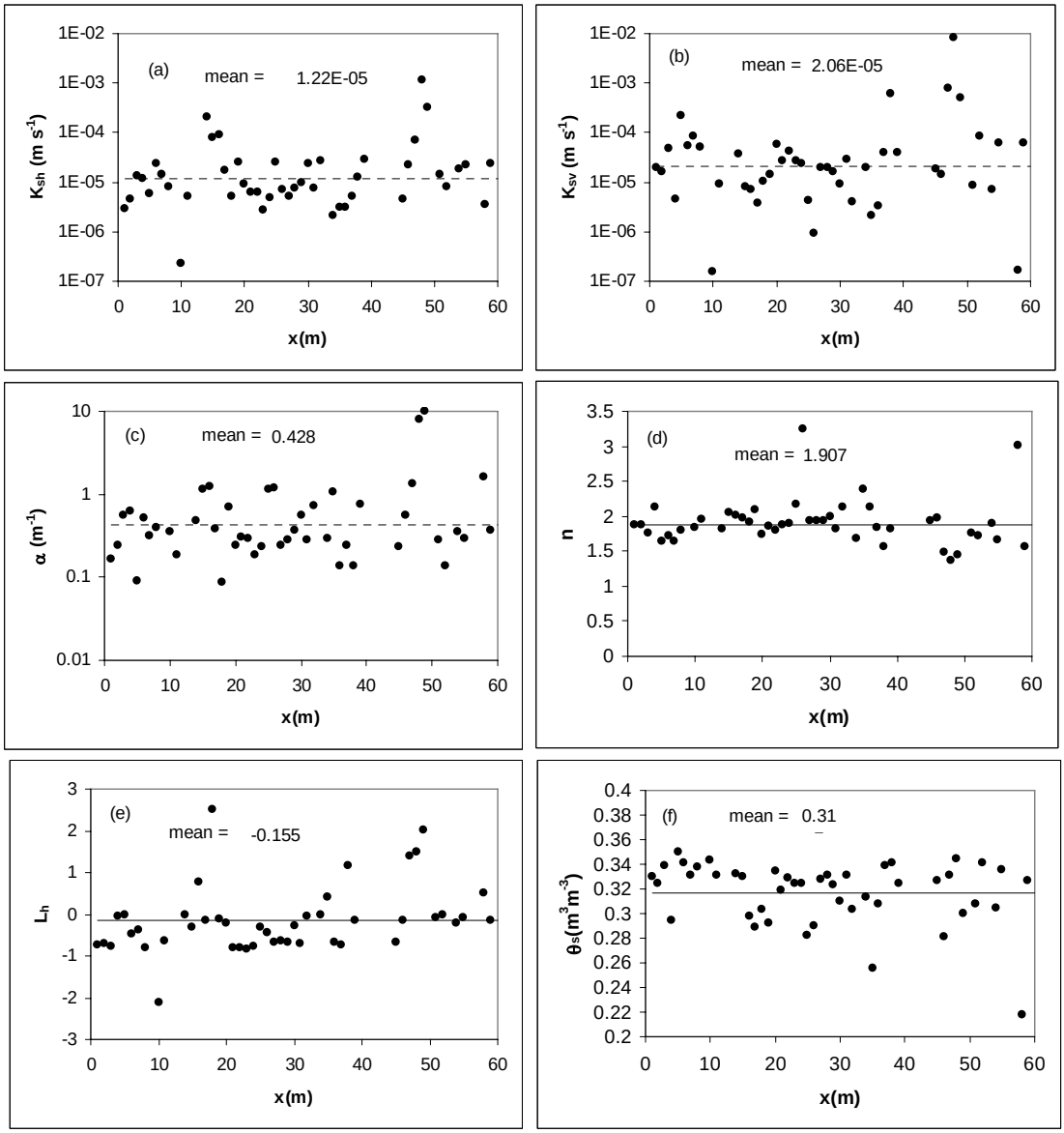

Figure 2.118. Spatial Variability of the Soil Hydraulic Parameters at the Army Loop Road Dike. Symbols: local parameter values; dashed line: geometric mean; solid line: arithmetic mean.

(6.6-ft) wide dike was located at around 10 m (33 ft) and as a result, low values of saturated horizontal hydraulic conductivity, K_{sh}, and the vertical saturated hydraulic conductivity, K_{sv}, were observed (Figure 2.118a,b). However, there was no clear trend of hydraulic properties at the Army Loop Road site.

The symmetry of a distribution can be characterized by calculating the skewness (C_{sk}), which measures the degree of asymmetry of a distribution around its mean. Positive skewness indicates that the right tail is more pronounced than the left tail. The skewness should be near zero for samples from a normal distribution. The calculated C_{sk} suggests that parameters K_{sh} (C_{sk} = 0.693) and K_{sv} (C_{sk} = 0.214) were log-normally distributed, which is consistent with published observations. The parameter α was closer to a log-normal distribution, also consistent with published results. Parameter *n* was closer to a

log-normal distribution (C_{sk} = 1.26) than a normal distribution (C_{sk} = 2.19), also consistent with published results. The reason that parameters K_{sh}, K_{sv}, α, and n are all closer to log-normal distributions is that each of these four parameters has a lower bound, i.e., K_{sh}, K_{sv}, and α can only take positive values whereas n can only take values larger than 1.0 but with no upper bound. Parameter θ_s was closer to a normal distribution, and the horizontal pore connectivity, L_h , was also close to normally distributed. Note that parameter L_h cannot be log-transformed because its value can be negative. The probability distributions of the hydraulic parameters with (K_{sh}, K_{sv}, α, and n) or without (θ_s, and L_h) log-transformation are shown by histograms in Figure 2.119. These histograms are similar to normal

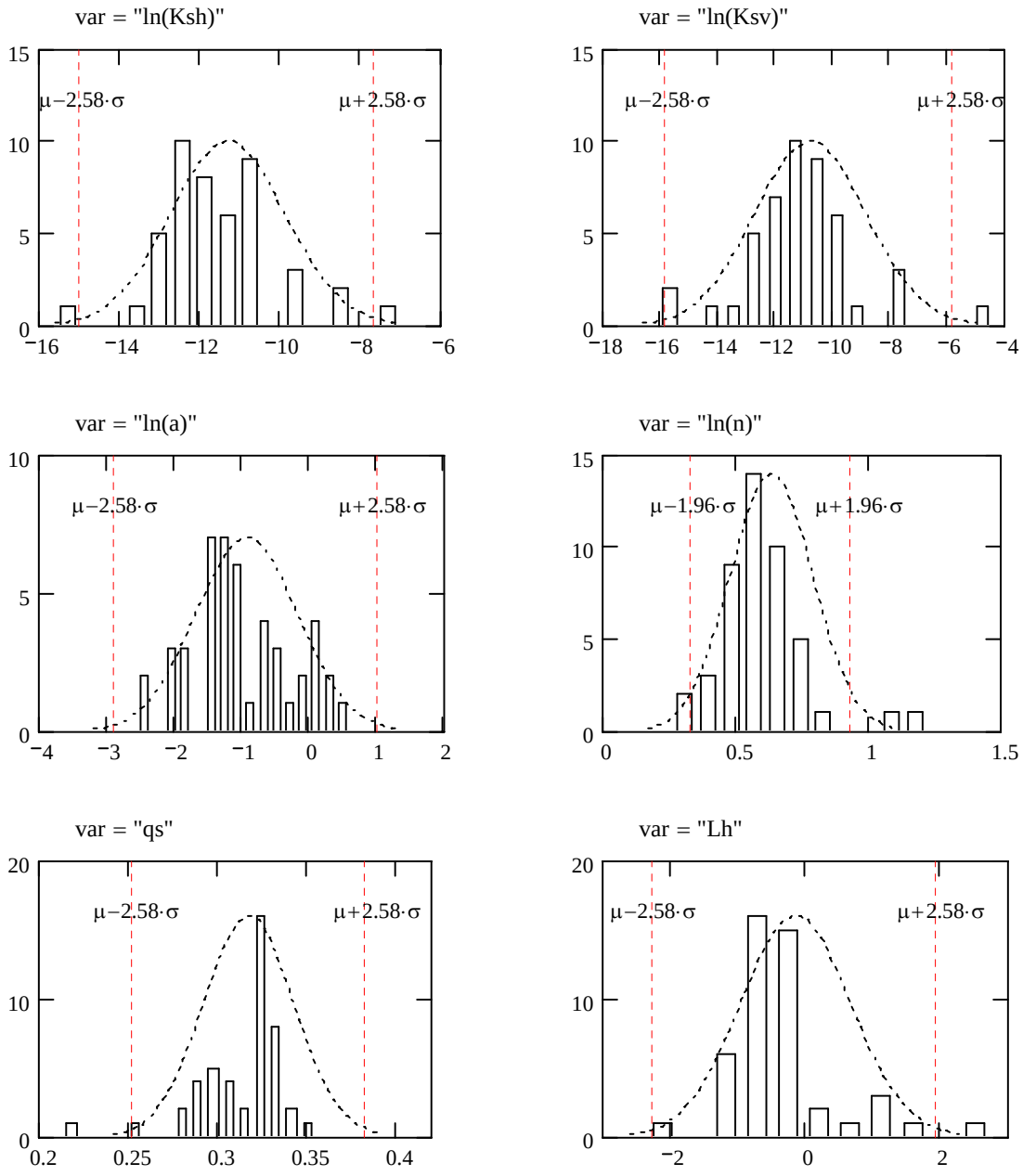

Figure 2.119. Histograms of Soil Hydraulic Parameters for the Army Loop Road Site

distributions, as suggested by the skewness values. The range between the two vertical dashed lines in each plot in Figure 2.119 shows the 95% confidence interval (CI) of the probability distribution of the corresponding parameter. A larger confidence interval indicates larger spatial variability. At the Army Loop Road site, parameters K_{sh} and K_{sv} varied by factors of 16.2 and 45.1, respectively, and had the largest spatial variability among all the parameters. Parameter α varied by a factor of 6.7 and had the medium variability. Parameters n, θ_s, and L_h had the smallest variability. This degree of variability emphasizes the importance of collecting an adequate number of samples to verify that the resulting properties are representative of the field-scale values at the site of interest. The number of samples required will increase as the degree of variability increases.

Soil hydraulic properties typically show spatial continuity with correlation over some distance determined by the depositional environment. Knowledge of the spatial correlation structure is necessary to develop multivariate probability density functions, which are often used to predict the mean and variance of flow or transport properties in heterogeneous soils. Neglecting the cross correlation between parameters may cause significant error unless the correlation is nearly zero. The cross-correlation coefficients, R_s, between the parameters of the test site are given in Table 2.12. Note that the four parameters closer to being log-normally distributed were log-transformed. The absolute values of the correlation coefficient, |R|, range from near 0 to 0.824. Parameters K_{sh} and K_{sv} are correlated, but the correlation coefficient (0.557^{**}) is much smaller than one. This indicates that, in addition to the textural effects on K_{sh} and K_{sv}, the difference in soil structure (e.g., stratification) at the horizontal and vertical also plays a very important role. The positive correlation ($R = 0.665^{**}$) between K_{sh} and α agrees with the findings of previous research. However, there is barely any correlation (R = 0.109) between K_{sv} and α. A possible reason is that the existence of macropores (e.g., cracks, root channels) has a strong effect on K_{sv} but not much effect on α. Parameter L, although used to describe the tortuosity-connectivity coefficient, seems to be a reflection of flow path connectivity under unsaturated conditions. Larger L indicates less flow connectivity. Generally, under unsaturated conditions, coarser soils tend to have lower flow connectivity than finer soils, and hence, coarser soils tend to have larger L values than finer soils. This may explain why L_h is positively correlated with K_{sh}, K_{sv}, and α, which are generally larger in coarser soils. However, some of the correlations are difficult to explain. For example, parameter n is negatively correlated with all of the other parameters. This is different from the relationships observed in the UNSODA database. Nevertheless, these results show that the correlations between most parameter pairs were in the medium correlation range. However, none were low enough to be neglected or high enough to be used to estimate one from the other.

Table 2.12. The Autocorrelation Coefficients, R_s, for Hydraulic Parameters at the Army Loop Road Site

	$\ln(K_{sv})$	**$\ln(\alpha)$**	**$\ln(n)$**	**θ_s**	**L_h**
$\ln(K_{sh})$	$0.557^{(b)}$	$0.665^{(b)}$	$-0.341^{(a)}$	0.030	$0.572^{(b)}$
$\ln(K_{sv})$		0.109	$-0.824^{(b)}$	$0.6^{(b)}$	$0.415^{(b)}$
$\ln(\alpha)$			-0.281	-0.106	$0.549^{(b)}$
$\ln(n)$				$-0.707^{(b)}$	-0.229
θ_s					-0.256

(a) Significant at 95% level.
(b) Significant at 99% level.

The standardized semivariograms of the hydraulic parameters of the Army Loop Road site are shown in Figure 2.120. Four of the six parameters, i.e., K_{sh}, K_{sv}, α, and L_h, shown, respectively, in Figure 2.120a, b, c, and f, showed strong spatial correlations. These parameters had standardized nugget variances between 0.0 and 0.4 with a fitted range between 2.4 and 4.6 m (7.9 and 15 ft). Parameters n and θ_s showed evidence of spatial correlation. The presence of a nugget variance suggests that the correlation range is smaller than the spacing of the instruments. In these experiments, instruments were placed at 0.5 m (1.6 ft) spacing, but measurements were made at a 1-m (3.28-ft) spacing. Transforming the variogram model shown in Figure 2.120 to an autocorrelation function yielded horizontal integral scales of 1.8 m (5.9 ft) for K_{sh}; 1.4 m (4.6 ft) for K_{sv}; 1.0 m (3.3 ft) for α; and 0.8 m (2.6 ft) for L_h. These results question the validity of the assumption of identical correlation lengths for all hydraulic parameters that is often used in variably saturated flow models.

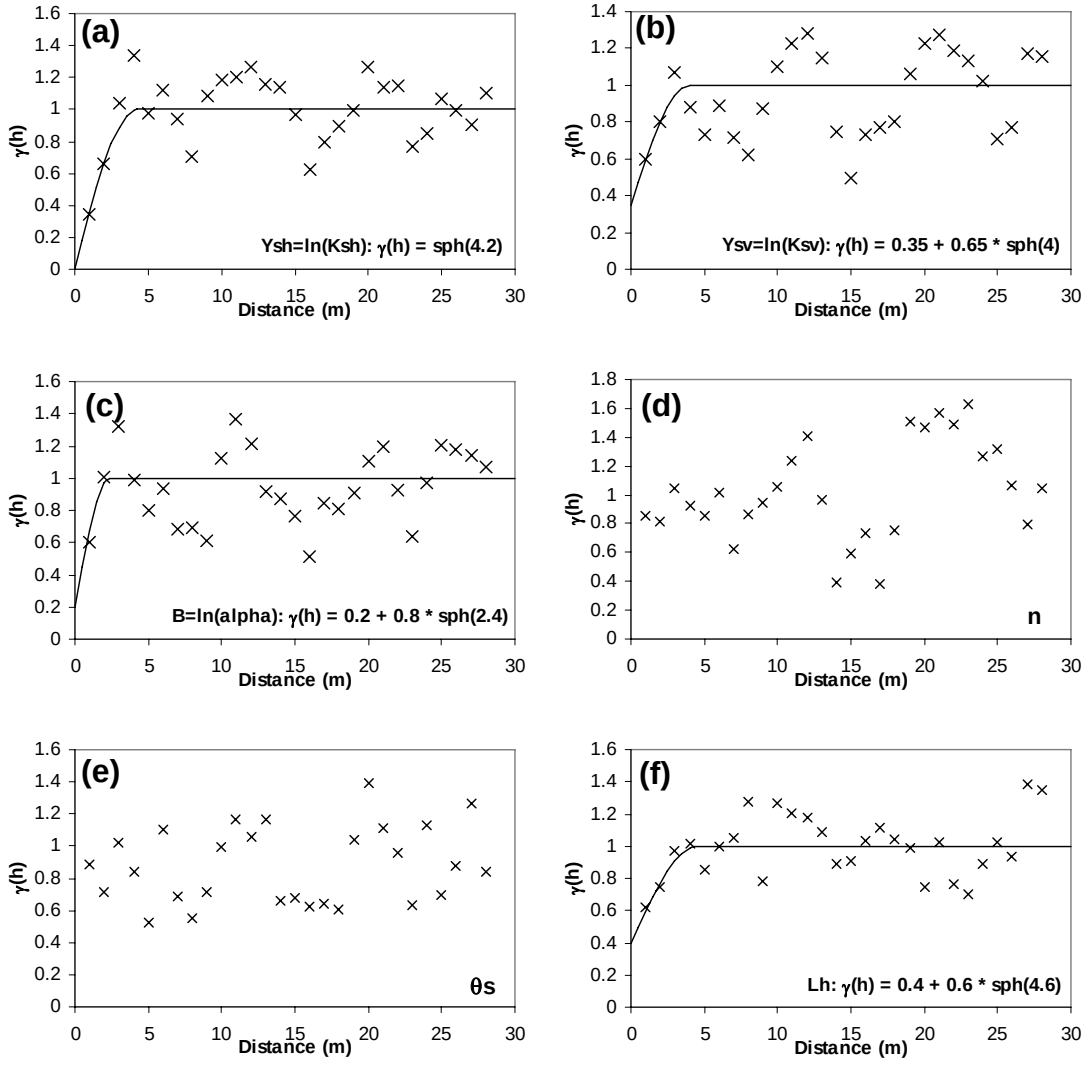

Figure 2.120. Semivariograms and Models of the Hydraulic Parameters at the Army Loop Road Site, (a) ln K_{sh}, (b) ln K_{sv}, (c) ln α, (d) n, (e) θ_s, and (f) L_h

2.19.2 Synopsis and Implications

The synopsis of findings in the analysis of the statistical and spatial correlation structure and their implications are as follows:

- Soil hydraulic properties, and thus flow variables, typically show spatial continuity with correlation over some distance determined primarily by the depositional environment. These properties and variables may also show autocorrelation.

- Knowledge of the autocorrelation and the spatial correlation structure are used to 1) develop multivariate probability density functions and predict the mean and variance of flow or transport properties in heterogeneous soils, 2) calculate upscaled values for input into field-scale numerical models, and 3) extend characterization information to uncharacterized sites with similar depositional environments.

- The analysis of variograms of moisture data collected over time showed changes in the variance, range, and anisotropy structure over time, reflecting a change in the degree of heterogeneity affecting flow over time. In general, the variance in moisture was larger under wetter conditions, and during drying, temporally stable variation patterns developed.

- Changes in the anisotropy structure with saturation is consistent with the recently developed model for saturation-dependent anisotropy in hydraulic conductivity, which can lead to large amounts of lateral spreading of contaminants parallel to layering.

- Measurements at the 299-E24-111 test site fitted correlation length ranging from 70 m (230 ft) to over 100 m (328 ft) in the direction of maximum continuity. These values are reasonable for the depositional environment, which can be classified as a distribution channel. Published values for the median length of continuity for fine-textured intercalations in a distribution channel are between 60 and 100 m (197 and 328 ft).

- Variograms were clearly anisotropic, and directions of maximum and minimum continuity were determined to be 22.5 degrees and 112.5 degrees, respectively. In the direction of maximum horizontal continuity, variograms were much simpler than in the vertical direction. Vertical variograms showed evidence of pseudo periodicity, most likely caused by layering, as the wavelength of the oscillation was approximately equal to the depth of a major textural change.

- Experiments at the Army Loop Road site provide insight into the horizontal correlation structure and the relationship among flow parameters. The vertical saturated hydraulic conductivity, K_{sv}, was the most variable, with the horizontal saturated hydraulic conductivity, K_{sh}, being the second most variable parameter. Parameter α showed medium variability whereas parameters n, θ_s, and L_h showed the smallest variability. Parameters K_{sh}, K_{sv}, α, and n were closer to being log-normally distributed than normally distributed whereas θ_s and L_h were closer to a normal distribution.

- The horizontal correlation lengths of parameters K_{sh}, K_{sv}, α, and L_h were between 2.4 and 4.6 m (7.8 and 15 ft). None of the parameters showed the same correlation lengths. Parameters n and

θ_s did not show any spatial autocorrelation. The cross correlation between parameter pairs was significant at the 95% level; none were low enough to ignore or high enough to be used to estimate one from the other.

- The implication is that heterogeneity and anisotropy should be represented in vadose zone flow and transport models at Hanford. Hydraulic properties of the Hanford vadose zone are spatially variable and anisotropic with varying degrees of autocorrelation. Determining the field-scale hydraulic properties, their spatial variability, and correlation structure is therefore useful for predicting flow and contaminant transport. Anisotropy is an important mechanism, and observed changes in the anisotropy structure with saturation emphasize the importance of modeling this phenomenon with a robust model that accounts connectivity. All the correlation lengths were different for hydraulic parameters, which impacts the assumption of identical correlation lengths for all hydraulic parameters needed for upscaling with other methods.

2.20 Inverse Modeling of Field-Scale Unsaturated Flow

Most of the waste within the DOE complex resides in the vadose zone, requiring knowledge of the unsaturated hydraulic conductivity field to describe flow and transport. Under variably saturated conditions typical of these sites, inverse modeling must address multi-fluid, multi-physics flow as well as consider multi-component reactive transport (Section 2.21). Because of the depositional environment (Figure 1.1, Figure 1.2) it is also important to account for multi-scale heterogeneity and anisotropy structures and the varying degrees of connectivity that may exist among these structures. Inverse procedures are now routinely used in the laboratory to parameterize capillary pressure-saturation [$P_c(S_e)$] and relative permeability-saturation [$k_r(S_e)$] functions in flow columns (Mishra and Parker 1989). Applied models for two- and three-phase flow and transport, which incorporate constitutive models of varying complexity subject to various assumptions using different numerical methods, have also been developed (Kaluarachchi and Parker 1989; Parker et al. 1994). In contrast, there have been few applications of inverse modeling for field-scale characterization of variably-saturated sediments, mostly because of the nonlinear transport functions, the high-dimensional parameters, and the large difference between the number of parameters and the typical number of data points.

Predictions of flow and reactive transport are needed to interpret distributions of contaminants that cannot be described by equilibrium distribution coefficient models and to evaluate remedial options. The currently accepted method for predicting moisture and contaminant distributions is to use numerical models to solve the Richards' equation for water flow and the convective-dispersion equation for solute transport. These equations are typically solved using laboratory-measured flow-and-transport properties. However, uncertainty is introduced with spatial variability and the disparity in measurement and modeling scales. To determine the overall accuracy of model predictions, field data must be compared directly to model predictions. A useful method for model comparisons with field data is inverse modeling, which uses the nonlinear regression methods to estimate the effective hydraulic parameters at the scale of the observations.

A number of laboratory and field applications (van Dam et al. 1992; Parkin et al. 1995; Simunek and van Genuchten 1996; Lehmann and Ackerer 1997; Abbaspour et al. 2000; Inoue et al. 2000; and Zhang et al. 2000) have shown the potential of inverse techniques for improving the design and analysis of vadose zone flow-and-transport experiments. Increased model complexity will accompany the

incorporation of multi-scale heterogeneities, thereby increasing parameter dimension and further constraining traditional optimization methods. As more parameters are added to the inverse model, convergence becomes more difficult to attain, and, in some cases, the system converges to a local minimum in the multi-dimensional parameter space. As a result, tools for the automatic inversion of field-scale unsaturated flow experiments in heterogeneous sediments are limited. Global optimization algorithms have gained popularity for complex non-convex problems and high-dimensional parameter estimation problems typical of subsurface characterization. They can also yield estimates of prediction confidence limits using estimates of the parameter joint probability density function conditioned on a calibration process (Vrugt et al. 2003). Nevertheless, using these methods has been mostly limited to synthetic heterogeneous structures with low (12 to 20) dimensional parameters (Vrugt et al. 2003). Thus, there is a need for a general framework for computationally efficient estimation of intermediate (20 to 150) and high (> 150) dimension parameters in complex environmental models.

One of the first tasks undertaken in the VZTFS was to develop a tool for automatic inversion of unsaturated flow and transport in heterogeneous soils and sediments. To facilitate inverse modeling of flow and transport of dilute non-reactive tracers in variably saturated systems, the STOMP simulator (White and Oostrom 2000) was coupled with the USGS-developed inverse modeling program UCODE (Poeter and Hill 1998). STOMP is designed to solve a variety of nonlinear, multiple-phase, flow-and-transport problems for unsaturated porous media. STOMP requires one text input file. Modifications were made to the STOMP code and the format of the input file to simplify coupling with UCODE (Zhang et al. 2002b).

Running UCODE requires an application model, which in this case is STOMP. The STOMP code was modified to automatically generate two of the UCODE input files, i.e., the *out_uc1.uni* and *out_uc1.ext* files. A new output file, *out_uc1.sto*, is produced after each run of STOMP. The *out_uc1.sto* file includes the simulated values corresponding to all the observations. The inverse version of STOMP also requires two additional cards, i.e., the *UCODE control card* and the *observed data card*, in the input file. To have these functions take effect, at the first line of the *solution control card*, the phrase "w/inverse" is needed before the last comma. Prior information on estimated parameters can be included in the regression. Sensitivities needed for the method are calculated approximately by forward or central differences. Statistics are calculated for use in 1) diagnosing inadequate data or identifying parameters that probably cannot be estimated with the available data, 2) evaluating uncertainty of the estimated parameter values, 3) evaluating the model representation of the actual processes, and 4) quantifying the uncertainty of model simulated values. A powerful aspect of using nonlinear regression is the parameter statistics, which are generated by UCODE. The statistics presented can be used diagnostically to measure the amount of information provided by the data and to identify model error (bias), or to infer the uncertainty with which values are calculated. UCODE performs different functions by specifying different PHASE values (Table 2.13) in the universal file. It is best to begin with PHASE = 1 and proceed to 2 and/or 22, and then 3. PHASE = 33, 44, and 45 generally are run only using a satisfactorily calibrated model. Phase 11 produces values that can be used to create a sum-of-squared, weighted residuals contour graph. Zhang et al. (2002b) provided a full description of the input files required for running the coupled STOMP/UCODE model.

Table 2.13. The Functions of each PHASE of UCODE

PHASE	Function
1	Forward modeling using the starting parameter values.
11	Performs a forward model run and calculates the sum-of-squared, weighted residuals of the objective function.
2	Locates sensitivities at starting parameter values.
22	Locates sensitivities and parameter variance, covariance, and correlations at starting parameter values.
3	Performs inverse procedure to find the best-fit parameter values.
33	Calculates the modified Beale's measure of model linearity.
44	Calculates predictions and their linear confidence and prediction intervals.
55	Calculates differences and their linear confidence and prediction intervals.

The STOMP/UCODE combination was applied to inverse modeling during the first two injections of the previous infiltration experiment of Sisson and Lu (1984). The Cartesian coordinate system was used, and the origin was set at the lower southwest corner. Principle directions of anisotropy were assumed to be aligned with the Cartesian coordinate system so that cross components of the saturated hydraulic conductivity tensor are zero. Hysteresis was not considered in this analysis, and the calibration curves reported by Fayer et al. (1995) were used to calculate observed water content.

2.20.1 Results

The first application of the inverse model was based on a 2-D simulation of flow in a small section of the 299-E24-111 test site during the test by Sisson and Lu (1984). This section includes four observation wells marked by H2, H4, H6, and H8, respectively. A 2-D cylindrical coordinate system was used with the origin at the depth of 15.24 m (50 ft) directly below the injection well. Non-uniform cell sizes were assigned and varied from 0.1 m (0.3 ft) to 0.5 m (1.6 ft) at the radial (r) direction and from 0.1524 m (0.5 ft) to 0.3048 m (1 ft) at the vertical direction (z). The 519 observations from the first two injections were used to inversely estimate the field-scale soil hydraulic parameters. The observations about 3 months before the start of the experiment were taken as the initial values. Zero-flux top boundary and unit-gradient lower boundary were assigned to the surface of the soil and at the depth of 15.24 m (50 ft), respectively. Five constitutional soil materials (Table 2.14) with different textures were assigned to the region to be simulated. We assume that the 1) soil layers are horizontal, 2) soil materials are anisotropic and each of them has a unique set of hydraulic parameters, 3) scaling factors associated with K_{sh} and K_{sv} are the same, where K_{sh} and K_{sv} are the horizontal and vertical saturated hydraulic conductivity, respectively, and 4) source strength to the H section is equal to the average source strength.

The laboratory-scale parameter values were measured using the cores described in Last and Caldwell (2001). The soil zonation was taken according to the K_s values of these cores. The soil materials are classified into five texture groups, whose laboratory-scale hydraulic parameter values and their occurrence depths are listed in Table 2.14.

Table 2.14. The Soil Materials and the Corresponding Laboratory-Measured Hydraulic Parameter Values of the H-Section of the 299-E24-111 Test Facility

	Material Number				
	B	**C**	**D**	**E**	**F**
Soil Depth (ft)	18.0–19.5, 22.0–23.0, 31.0–32.0, 32.5–33.0, 36.0–38.5	0.0–12.0, 19.5–20.0, 29.0–30.0, 32.0–32.5, 33.0–33.5, 34.536.0	12.0–18.0, 20.0–20.5, 21.0–22.0, 23.0–25.5, 33.5–34.5	20.5–21.0, 26.0–29.0, 30.0–31.0, 38.5–39.0, 40.0–50.0	25.5–26.0, 39.0–40.0
K_s (ms^{-1})	1.78×10^{-5}	5.05×10^{-5}	1.99×10^{-4}	4.90×10^{-4}	1.05×10^{-3}
α (m^{-1})	4.7	8.6	8.9	6.9	20.0
n (-)	2.063	1.995	2.958	3.739	3.05
θ_s(m^3m^{-3})	0.338	0.364	0.368	0.373	0.41
θ_r(m^3m^{-3})	0.036	0.035	0.033	0.027	0.02

The field-scale parameter values are listed in Table 2.15. Comparisons of the predicted and observed soil water contents for the cases are shown in Figure 2.121. When the laboratory-scale parameter values were used to predict the flow (Figure 2.121a), there was a very low correlation between the predictions and observations ($R^2 = 0.28$). When the field-scale parameter values were obtained by applying the non-similar media (NSM) scaling, the correlation between the predictions and observations ($R^2 = 0.45$) was improved (Figure 2.121b). For the 3-D inversions, geophysical logging data reported by Fayer et al. (1995) were used to infer the lithology of the sediments. Because most observations were taken at the depth between 10 ft (3.05 m) and 50 ft (15.24 m), the focus was on the soil domain within this range. To determine the correlations between the site lithology and θ_{ss}, ϕ, and γ, the observations were interpolated using the kriging method and the cylindrical coordinate system at the radial spacing of 0.25 m (0.8 ft), azimuthal angle of $\pi/16$, and vertical spacing of 0.25 ft (0.0762 m). Three-dimensional distributions, θ_{ss}, ϕ, and γ, are then plotted using the TecPlot® software package.

Table 2.15. The Field-Scale Hydraulic Parameter Values of the H-Section of the 299-E24-111 Test Facility

	Material Number				
	B	**C**	**D**	**E**	**F**
K_{sh} (ms^{-1})	4.01×10^{-5}	1.14×10^{-4}	4.48×10^{-5}	1.10×10^{-3}	2.37×10^{-3}
K_{sv} (ms^{-1})	1.46×10^{-5}	4.14×10^{-5}	1.63×10^{-4}	4.01×10^{-4}	8.60×10^{-4}
$\alpha^{(a)}$ (m^{-1})	4.7	8.6	8.9	6.9	20.0
n (-)	1.934	1.870	2.773	3.504	2.859
θ_s(m^3m^{-3})	0.338	0.364	0.368	0.373	0.41
θ_r(m^3m^{-3})	0.036	0.035	0.033	0.027	0.02
(a) α was fixed because of the high correlation between α and K_{sh}.					

Figure 2.122 shows the 3-D distribution of the steady-state water content. The θ_{ss} values vary from 1.8% to 10.1%. There are two layers, at the depths of about 7 and 12 m (23 and 39 ft), respectively, with higher θ_{ss} values than the adjacent soils. The thicknesses of the two layers vary from position to position and are between approximately 0.5 and 2 m (1.6 and 6.6 ft). Figure 2.123 shows the spatial distribution

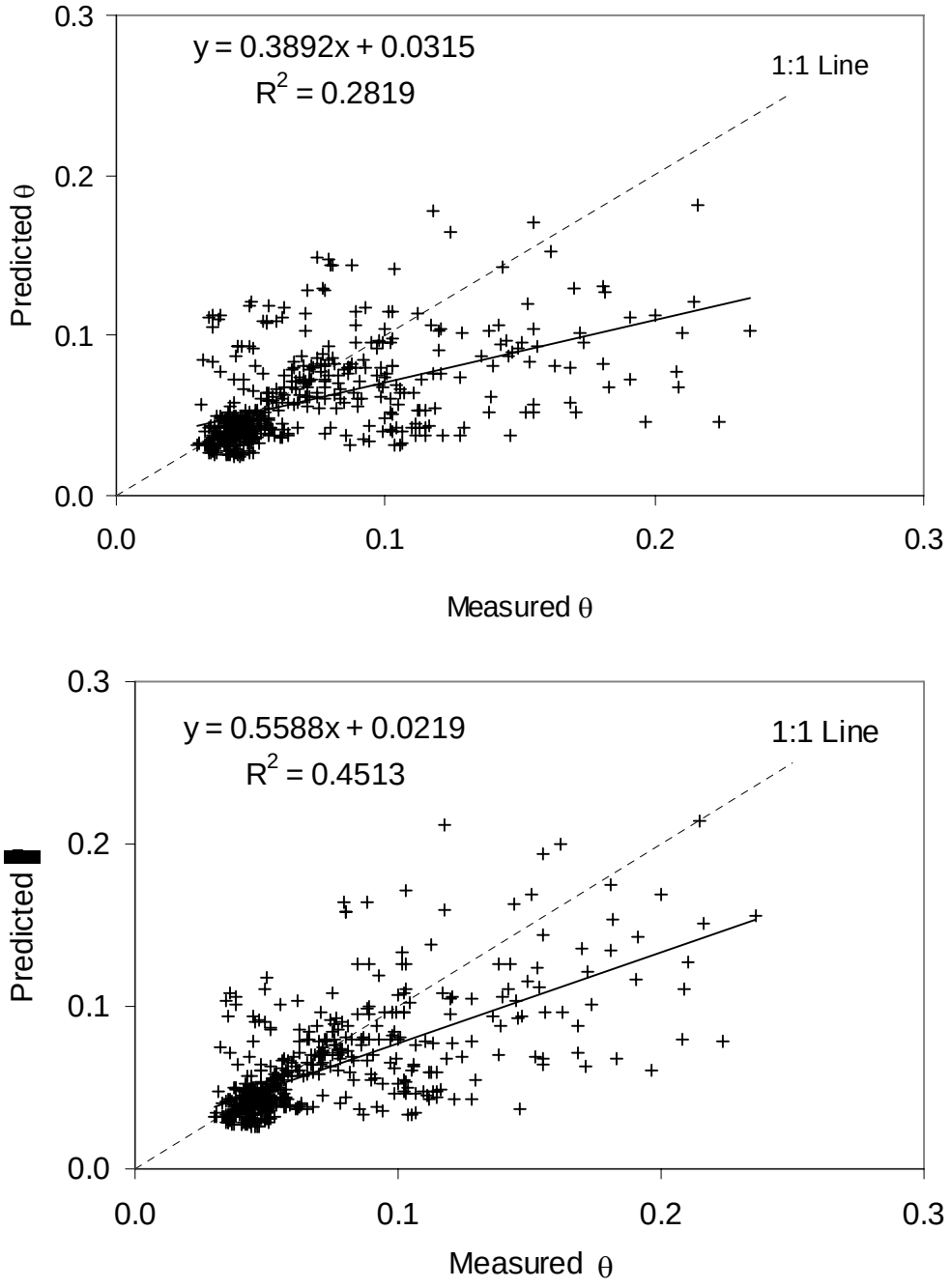

Figure 2.121. Comparison of the Predicted and Observed Soil Water Contents at the H-Section of the Injection Experiment Described in Sisson and Lu (1984). Parameter values for each case are listed in Table 2.15. The number of observations is N = 519. Parameterizations: (a) laboratory-scale parameter values and (b) field-scale parameter values. Dashed lines: the 1:1 line. Solid lines: linear regression line.

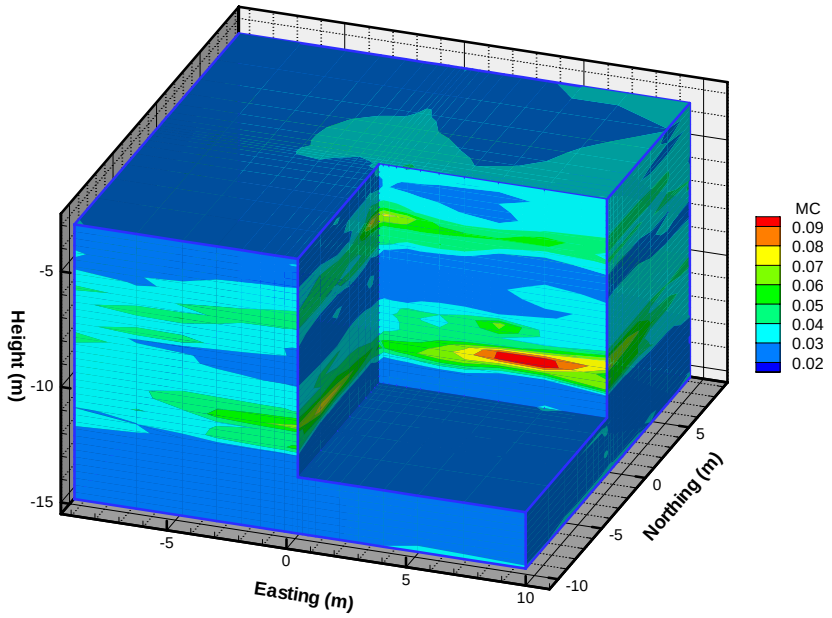

Figure 2.122. The Distribution of Steady-State Water Content of the 299-E24-111 Test Facility

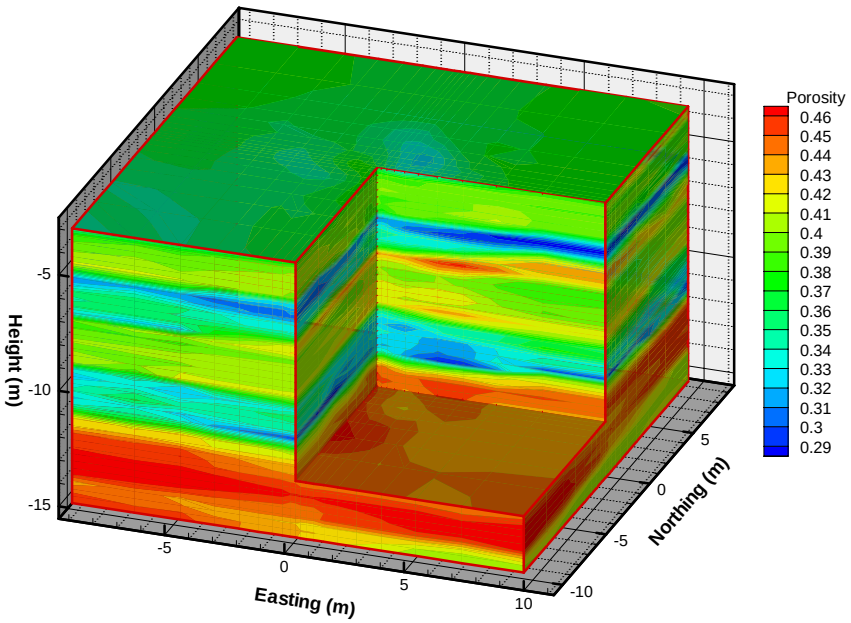

Figure 2.123. The Distribution of Soil Porosity of the 299-E24-111 Test Facility

of porosity, which ranges between 27.8% and 47.6%. There is more evidence of heterogeneity in the porosity, ϕ, (Figure 2.123) than in the steady-state water content (Figure 2.122).

Figure 2.124 shows a scatter plot between θ_{ss} and ϕ. There is an inverse correlation between θ_{ss} and ϕ. The lower θ_{ss} values generally correspond to the higher ϕ values, and the soils with these values are coarser generally and have higher permeability. This suggests that we may use ϕ only variables for texture classification. Because the plot of ϕ (Figure 2.124) shows the soil stratification better than the plot of θ_{ss}, ϕ estimates were used to determine soil textures. Previous studies using soil coring data have found that the soil at this site may be classified into seven textures (e.g., Smoot 1995). Thus, we also classified the soil into seven material types (Table 2.16) according to the values of ϕ.

For the flow simulations, the Cartesian coordinate system was used, and the origin was set at the lower southwest corner. Principle directions of anisotropy were assumed to be horizontal and vertical. Hysteresis was not considered. The size of the simulation domain was (x, y, z) = (40.7 m [133.5 ft], 40.7 m [133.5 ft], 12.2 m [40 ft]). The depth range of the simulation domain was from 10 ft (3.048 m) to 50 ft (15.24 m). The simulation domain was gridded with a variable horizontal cell step (Δx and Δy) and a constant vertical cell step (Δz). The minimum values of Δx and Δy were 0.2 m (0.7 ft), which were at the center of the domain. The values of Δx and Δy increased by a factor of 1.3 as the distance to the center of the domain increased. The value of Δz was 0.3048 m (1 ft). The source was placed at the center of the x-y plane and at the depth from 4.57 m (21.6 ft) to 4.88 m (16 ft). The top boundary condition was zero-flux and the bottom unit gradient. The four sides had zero-flux boundary conditions. Note that the zero-flux side boundary conditions were not met because of lateral flow movement. However, when the horizontal scale of the simulation domain is large enough, the zero-flux side boundary conditions are reasonable approximations.

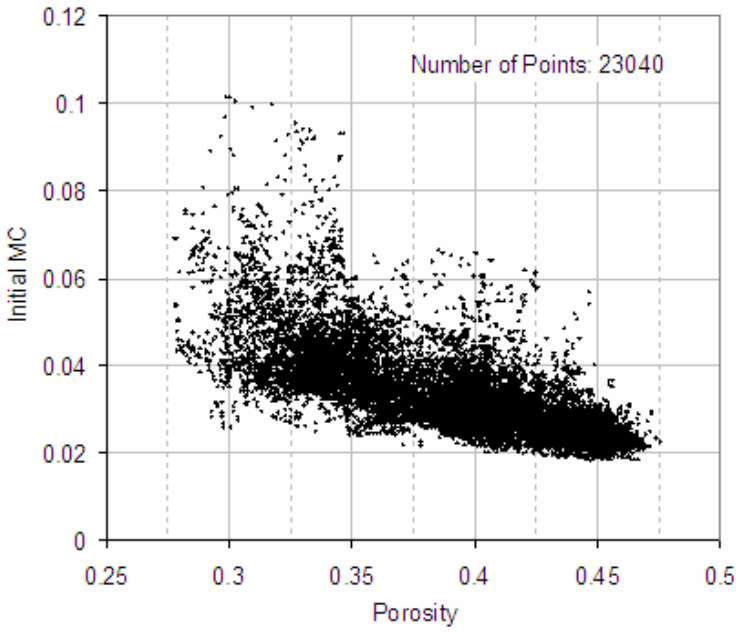

Figure 2.124. A Cross Plot of Porosity and Steady-State Water Content for the 299-E24-111 Test Facility

Table 2.16. Soil Classification of the 299-E24-111 test Site Using Porosity and Steady-State Water Content

Soil	Porosity (ϕ)
T1	≥0.450
T2	0.425–0.449
T3	0.400–0.424
T4	0.375–0.399
T5	0.350–0.374
T6	0.325–0.349
T7	<0.325

The seven soil textures used for classification were assumed to correspond to the seven textures of Smoot (1995) with Texture 1 being the coarsest and Texture 7 the finest with the hydraulic properties of each texture described by six parameters. Then, the local-scale values of parameters K_{sv}, α, and n were approximated using the parameter values of Smoot (1995) where K_{sv} is the K_s at vertical direction. Values of θ_s were estimated as 0.9 ϕ. The value of θ_r of a texture was approximated by the minimum value of the observed steady-state water content of this texture. We also assumed that $K_{sh} = 5K_{sv}$, where K_{sh} is the K_s at horizontal direction. The field-scale values of the hydraulic parameters were inversely estimated using the UCODE/STOMP combination and the parameter scaling method (Zhang et al. 2002b). Considering the simulation time in the inverse modeling, we used the 6241 observations of injections #1, #5, and #9 rather than the observations of all the 11 injections.

The inversion for 42 parameters simultaneously was difficult because of convergence problems in UCODE. These convergence problems resulted from physically unrealistic parameter values between perturbations that caused the forward model to fail. After applying parameter scaling using the local-scale values of the hydraulic parameters, the number of parameters to be estimated reduced to the six parameters of the reference textures. Analyses showed that the flow was not very sensitive to parameters and θ_s and θ_r; hence, these two parameters were not estimated during the inverse modeling. The estimated field-scale values of hydraulic parameters of the reference texture are listed in Table 2.16. The relatively low correlation coefficients indicate that these parameters were not significantly correlated. The converted hydraulic parameter values for the seven material types are listed in Table 2.17. Using the field-scale parameter values in Table 2.17 and the values of θ_s and θ_r in Table 2.14, the flow was simulated. As a comparison, the flow was also simulated using the local-scale parameter values in Table 2.14. When the local-scale parameter values were used, the overall standard error (σ) of water content was 0.038 $m^3\ m^{-3}$, and the coefficient of determination (R^2) was 0.34. When the field-scale parameter values were used, the value of σ decreased by 42% to 0.024 $m^3\ m^{-3}$ and $R^2 = 0.61$. Comparisons between the simulated and observed water contents for each of the seven textures also show good agreement (Zhang et al. 2004a). The results show that the simulated water content in all the textures was significantly improved after applying parameter scaling and inverse modeling.

Table 2.17. The Mean Values of the Hydraulic Parameters of each Texture of the 299-E24-111 test Site Soil

	K_{sh} (m s^{-1})	K_{sv} (m s^{-1})	α (m^{-1})	n (-)
T1	1.328×10^{-2}	2.624×10^{-3}	4.026×10^{-1}	1.910
T2	4.428×10^{-3}	8.748×10^{-4}	7.664×10^{-2}	2.034
T3	2.657×10^{-3}	5.249×10^{-4}	2.844×10^{-1}	1.824
T4	1.230×10^{-3}	2.430×10^{-4}	1.310×10^{-1}	2.390
T5	6.568×10^{-5}	1.298×10^{-5}	2.240×10^{-2}	3.449
T6	6.568×10^{-5}	1.298×10^{-5}	2.240×10^{-2}	3.449
T7	2.829×10^{-5}	5.589×10^{-6}	4.454×10^{-2}	1.910

2.20.2 Synopsis and Implications

The synopsis of findings for the inverse modeling of variably saturated field-scale flow problems and their implications are as follows:

- The STOMP simulator was coupled with UCODE to allow estimation of field-scale values of soil hydraulic parameters based on the various injection experiments performed at the 299-E24-111 test site. Parameter scaling, which relates the hydraulic parameter values measured at different spatial scales for different soil textures, was used to reduce the parameter dimension. The inverse technique was applied to a case of 2-D flow and 3-D flow in a heterogeneous soil.

- Results show that simulation errors were significantly reduced after applying parameter scaling and inverse modeling. When compared to the use of local-scale parameters, parameter scaling reduced the sum of squared weighted residue by 93 to 96% for the relatively smaller scale (~2 m [6.6 ft]) 1-D flow and 59% for the much more complex 299-E24-111 test site, which has a spatial scale of about 18 m (59 ft).

- Although there was good agreement between the observed and predicted water contents, not all of the observations were matched with the forward STOMP model. The local-scale parameter values had errors, and hence the calculated scaling factors also had errors. For a more accurate determination of the local-scale values, different methods are needed to estimate the local-scale values of the hydraulic parameters. Another possible source of error was the error in the determination of the soil texture distribution. Soil porosity was used as a criterion for texture classification. However, the difference in steady-state water contents suggests that some of the textures may contain different material types. Thus, some of the seven texture types could be further divided into sub-groups according to steady-state water content for a more detailed description of texture distribution.

- Routine application of these methods could benefit from using existing data or measurements that are relatively easy to obtain, such as particle-size distribution information and advanced monitoring techniques that can increase the number of experimental observations relative to the geophysical logs and advanced techniques.

- These preliminary studies highlight a number of challenges in the application of inverse modeling to field-scale unsaturated flow. While model-independent estimation packages like UCODE provide much needed flexibility for inverse modeling, they are constrained by computational demands, particularly when dealing with non-steady flow in heterogeneous systems.

2.21 Inverse Modeling of Multicomponent Reactive Transport

Natural soils contain a variety of different minerals and materials of varying texture. Because different minerals can have different types of cation exchange sites exhibiting different exchange selectivities, they are chemically heterogeneous. This surface heterogeneity may explain the commonly observed "non-ideal" behavior of cation exchange in soils, where exchange selectivities or exchange capacities may vary with solution conditions and spatial location. Reactive transport modeling can provide insight into movement in these complex environments, and some of the most well known models for reactive transport have been developed for use in the DOE complex (e.g., Lichtner 2001; Steefel and Yabusaki 1996). However, application of these models to field-scale transport problems remains limited by the effects of multiscale heterogeneities, the nonlinear nature of transport properties, and the scale dependence of hydrogeological and reaction processes. A significant challenge remains in the development of field-scale parameters that accurately represent the combined influence of physical and chemical heterogeneities (Davis et al. 1998). It is becoming more common to use reactive transport models to predict contaminant migration from nuclear and chemical waste disposal sites and investigate the evolution of vadose zone and groundwater chemistry (Glynn and Brown 1996). Often parameters relevant to contaminant mobility and solute transport, such as reaction kinetics and ion exchange capacities in heterogeneous systems, are unknown.

Inverse modeling provides a means to estimate these unknown scale-dependent parameters and to develop a mechanistic understanding of coupled hydrological and chemical processes. Inverse modeling has been used extensively in hydrogeology for conceptual model identification and to estimate unknown model parameters. Inverse procedures have been used extensively to estimate flow and transport parameters at various spatial scales ranging from laboratory experiments to regional aquifers (Mishra and Parker 1989; Poeter and Hill 1998; Šimůnek et al. 1998; Carrera et al. 2005). In contrast, there have been few applications of inverse modeling for field-scale characterization of variably-saturated sediments, mostly because of the nonlinear transport functions, the high-dimensional parameters, and the large difference between the number of parameters and the typical number of data points. Recently developed parameter scaling techniques and the coupling of the STOMP simulator with UCODE now permits inverse modeling of field-scale variably saturated flow problems (Zhang et al. 2003a, 2004a,b; Ward et al. 2006). Although inverse modeling has been used in reactive transport studies, it has been traditionally applied to static geochemical models that do not consider transport. Applications to transport have focused mostly on conservative and weakly reactive solutes in saturated systems. Although these applications can yield insights into the evolution of subsurface chemistry, different mineral assemblages may be predicted to form in the absence of transport (Freedman et al. 2003). Furthermore, if the flow system is not well understood, an inverse simulation may prove impractical, particularly if the geochemical samples are not hydraulically connected.

The objective of this study was to develop an inverse modeling methodology for multiphase reactive transport in multi–dimensional heterogeneous porous media. The scope was to extend the work that coupled STOMP and UCODE to include the CRUNCH multicomponent transport model to allow

simultaneous determination of hydraulic, transport, and ion exchange parameters from the laboratory and field-scale observations of reactive transport. The parameters of interest include dispersivity, CEC, selectivity coefficients, and possibly initial concentrations of Na^+, K^+, Ca^{2+}, Mg^{2+}, Sr^{2+} and boundary concentrations of these cations. Because STOMP and CRUNCH are not fully coupled, the approach is to determine optimum parameter estimates by solving the inverse problem of water flow and reactive solute transport in a two-step procedure. In the first step, steady-state observations of water content and matric potential are inverted to determine the distribution of hydraulic properties. In the next step, the best-fit transport parameters are determined by minimizing the weighted sum of squares, which is a function of the differences between the experimental, calculated adsorbed amounts and the sequential breakthrough of the pore water cations. The parameters to be estimated in this step are the dispersivities, CECs, and cation selectivity coefficients as well as kinetic reaction parameters such as specific surface of minerals, apparent activation energy, and rate constants.

For this study, the reactive transport code, CRUNCH (Steefel and Yabusaki 1996), was coupled to UCODE (Poeter and Hill 1998), a non-linear parameter estimation code. CRUNCH is a computer code that simulates multicomponent reactive transport in porous media. There are two transport modes in CRUNCH. One transport mode is Operator Splitting 3-Dimensional Reactive Transport (OS3D), which simulates reactive transport by splitting the reaction and transport steps in time. The other transport mode is Global Implicit Multicomponent Reactive Transport (GIMRT), which simulates 2-D reactive transport by solving both reaction and transport equations simultaneously (Steefel and Yabusaki 1996). Both transport modes are based on a continuum representation of transport and reaction in porous media. The codes solve the nonlinear set of partial differential equations for reaction and transport using the finite difference method. Aqueous chemical reactions are represented as equilibrium reactions, whereas aqueous-solid phase reactions are kinetic. Ion exchange and surface complexation may also be performed with CRUNCH. CRUNCH does not currently solve for flow. However, a velocity field calculated externally with the STOMP code can be used. Although a steady-state flow field can be used, CRUNCH is also capable of reading transient flow field data, as well as transient saturations, porosities, and densities.

Modifications were made to the CRUNCH code so that it permits the creation of the necessary UCODE input files. The modified code is referred to as CRUNCH-UCODE. CRUNCH-UCODE is configured so that the creation of the UCODE files is invisible to the user. That is, the user only needs to input the required information into the CRUNCH input file, and CRUNCH will create the appropriate files for UCODE execution. On start-up, CRUNCH reads an input file that provides the chemical and physical data needed for a run. The CRUNCH input file is organized as a series of blocks that are identified by keywords. Within each block, keywords for parameters are used to define parameter values. Keyword blocks may appear anywhere in the input file, and keyword parameters may appear anywhere within a particular block (Steefel 2004).

To demonstrate the CRUNCH-UCODE capabilities, two inverse simulations were performed. The first was based on a hypothetical study in a 50-cm (19.7-in.) long column packed with a soil with a porosity of 0.151 and discretized into 1-cm (0.4-in.) grid cells. Although calcite, brucite, aragonite, strontianite, gypsum, and magnesite are considered as potential precipitates, only 1% of calcite is initially present in the column. The soil is assumed to have a single exchanger site, and flow within the column is steady at 5.83 cm (2.3 in.) d^{-1}. At time greater than zero, a solution of 5.0% $MgCl_2$ and 0.5% $SrCl_2$ enters at the top of the column and continues to enter the column until the simulation terminates after 16.5 days.

In the model, this situation is simulated as a flux boundary condition where the entire column has been initialized to the initial condition, and transport is carried out using the OS3D mode.

In the second application, reactive transport parameters were identified for the field-scale cation migration experiment that was performed at the Army Loop Road test site. This experiment focused on reactive transport of stable strontium (as a surrogate for ^{90}Sr) in heterogeneous unsaturated sediments, with a design based on water flow from a surface line source. Under an assumption that at the local scale, flow was steady with 2-D convection and dispersion, the objective of the field infiltration experiment was to measure steady-state distributions of matric potential, water content, and tracer concentrations and travel times beneath a surface line source (Ward and Gee 2002). The experiments were conducted on a 60-m (197-ft) long transect at the Army Loop Road. Twin-rod TDR probes were installed at 0.5-m (1.6-ft) intervals along the transect to depths of 1.0 m (3.3 ft), 0.8 m (2.6 ft), 0.4 m (1.3 ft), and 0.2 m (0.7 ft). Probes were spaced 0.15 m (0.5 ft) apart perpendicular to the transect. The longest (1 m [3.3 ft]) probe was installed along the mid line of the transect, near the line source, with probes of decreasing length installed with increasing distance from the line-source increase (Figure 2.53). At the outer edge of the transect, a second set of 1-m (3.3-ft) long probes were installed to capture any deeper lateral movement from the line source. These probes were installed on a 2-m (6.6-ft) interval along the transect. Apart from monitoring matric potential, the probes also collected pore-water samples for tracer analysis. Chemical analyses were performed for samples taken at 40-cm (15.7-in.) and 80-cm (31.5-in.) depths. Concentrations were measured on the pore water samples using ion chromatography for anion analysis and the inductive coupled plasma technique for cation analysis.

The infiltration experiment was conducted using constant-flux surface boundary conditions. Water was applied as a line source to the transect with an average application rate of 485 L d^{-1} (128 gpd). The tracers consisted of 4.7 g l^{-1} strontium chloride and 47.5 g l^{-1} magnesium chloride. Household bleach (6% sodium hypochlorite) was also present at a concentration of 102 ppm to control algal growth. The injection occurred over a 2-day period and at the same rate as the irrigation water that was applied once the pulse injection stopped. Tracers were applied only after steady-state flow conditions were attained in the profile. Application to the experimental plot remained steady throughout the experiments, averaging 476.6 L d^{-1} (125.9 gpd). A total of 730 L (193 gal) of tracer solution was applied to the transect before the application line was switched back over to tracer-free water.

2.21.1 Results

The column data were based on a hypothetical study; therefore, a data set was first synthesized with a forward run of CRUNCH. In this way, the capability of UCODE to obtain the correct parameter estimates could be assessed because the true values of the parameters are known. In the first test case, the inverse problem was run with the observations to verify that UCODE is capable of identifying the true parameter values when the starting values for the regression analysis are equal to their true values. Aqueous concentrations at 20 cm (7.9 in.) and 40 cm (15.7 in.) from the outlet of the column were obtained from the simulated data and were then used as observed data for the inverse run. Total concentrations of Ca^{2+}, Mg^{2+}, Sr^{2+}, Na^{+} and K^{+} were used for comparing observed and simulated data. The CEC, the solid solution ratio, and the kinetic reaction rates for all of the minerals are parameters that are optimized for the hypothetical column study and are shown in Table 2.18.

Although all the minerals were considered in the reactive transport simulations, aragonite, gypsum, and brucite remain under saturated and do not precipitate during the simulation. As the solution traveled

through the column, calcite was dissolved, and magnesite precipitates ahead of a strontianite precipitation front. At the end of the simulation, magnesite began to undergo dissolution as well, and the rate of strontianite precipitation increased. At the same time, Ca^{2+}, Mg^{2+}, Sr^{2+}, Na^{+}, and K^{+} competed for exchange sites.

Table 2.18. True Values of Parameters Used in the Synthetic Data Case

Parameter	Symbol	Value	Lower Bound	Upper Bound
Cation exchange capacity	CEC	1.E-06	1.E-08	1.E-04
Solid solution ratio	ss_ratio	3000	1000	5000
Calcite rate	rate	-6.0	-20.0	-4.0
Magnesite rate	rate	-6.0	-20.0	-4.0
Aragonite rate	rate	-6.0	-20.0	-4.0
Strontianite rate	rate	-6.0	-20.0	-4.0
Brucite rate	rate	-6.0	-20.0	-4.0
Gypsum rate	Rate	-6.0	-20.0	-4.0

A second simulation was run in which the initial parameter values for the cation exchange capacity and solid solution ratio were set at their lower bounds, 1.e-08 equiv g^{-1} soil and 1000 g kg^{-1} H_2O, respectively. Mineral reaction rates were set at -12.0, which represents an intrinsic kinetic rate constant of 1×10^{-12} mol kg^{-1} H_2O per year. The resulting parameter estimates, which were obtained after six iterations, are shown in Table 2.19. These results demonstrate that there is considerable parameter interaction, especially with respect to mineral reaction rates. Because aragonite, brucite, and gypsum did not precipitate, their rate constants remained unchanged because they had no effect on the final concentration estimates. However, none of the intrinsic rate constants for the three reactive minerals approached the true value of -6.0. The rate constant for magnesite was 24 orders of magnitude smaller (~ -30) than the true value, and the rate constant for calcite was 5.5 orders of magnitude higher (~ -5.5). The parameter estimate for strontianite was closest to its true value of -6.0 at ~ -9.3 (or $1 \times 10^{-9.3}$ mol kg^{-1} H_2O per year).

Table 2.19. Parameter Estimates for Synthetic Data Cases for Different Initial Values, Cases 1 and 2

			Case 1		Case 2	
Parameter	Symbol	True Value	Initial Value	Parameter Estimate	Initial Value	Parameter Estimate
Cation exchange capacity	CEC	1.00E-06	1.00E-06	1.01E-06	1.00E-08	6.42E-08
Solid solution ratio	ss_ratio	3000	3000	2887.5	1000	3482.3
Calcite rate	Rate	-6.00	-6.00	-5.95	-12.0	-0.5891
Magnesite rate	Rate	-6.00	-6.00	-6.00	-12.0	-30.698
Aragonite rate	Rate	-6.00	-6.00	-6.00	-12.0	-12.0
Strontianite rate	Rate	-6.00	-6.00	-6.00	-12.0	-12.0
Brucite rate	Rate	-6.00	-6.00	-6.00	-12.0	-12.0
Gypsum rate	Rate	-6.00	-6.00	-6.00	-12.0	-12.0

Parameter estimates for the ion exchange parameters were closer to their true values than the mineral intrinsic rate constants. Although the final parameter estimate for the cation exchange capacity was more than six times larger than the initial value, it was 93.6% of its true value. Whereas the parameter estimate

for the solid surface ratio was 3.5 times greater than the initial value, the estimate was only 16% greater than its true value of 3000 g kg^{-1} H_2O. These results demonstrate that not only is there interaction among the ion exchange parameters, but interaction also occurs among the exchange and intrinsic rate parameters, and non-uniqueness of the calibrated parameters exists. This result is not surprising because species that are incorporated into mineral precipitates then become unavailable for exchange sites, and vice-versa. Moreover, the constant source input to the column means that the concentrations approach steady-state, and the concentrations are not distinct enough to discern a reactive transport front. A pulse source, one of limited duration, may yield a data set with better information on the processes controlling the reactive transport front. Because of parameter non-uniqueness, it may not be possible to estimate both parameter types in the same inverse simulation. More importantly, initial parameter estimates need to be constrained as much as possible to measurements or data from literature.

Two additional simulations were performed so that exchange and rate constant parameters were estimated separately. In test Case 3, the initial parameter values for the cation exchange capacity and solid solution ratio were set to values closer to their true values because test Case 2 demonstrated the importance of constraining the initial parameter estimates. The cation exchange capacity starting value is set to 7.7E-07 equiv g^{-1} soil and the solid surface ratio to 3500 g kg^{-1} H_2O. Mineral reaction rate constants were set to their true values and eliminated from the regression analysis. The resulting parameter estimates shown in Table 2.20, which were obtained after a single iteration, do not differ from their initial estimates by a large measure, only by 10% and 1% for the cation exchange capacity and the solid surface ratio, respectively. To test the sensitivity of the final parameter estimates to the initial parameter values, other inverse runs were performed with different starting values. All of the runs yielded similar results. The final estimates of the exchange parameters were within 10% of the initial estimate, even when the tolerance that describes parameter convergence was lowered.

Table 2.20. Parameter Estimates for Synthetic Data Cases for Different Initial Values, Cases 3 and 4

			Case 3		Case 4	
Parameter	**Symbol**	**True Value**	**Initial Value**	**Parameter Estimate**	**Initial Value**	**Parameter Estimate**
Cation exchange capacity	CEC	1.00E-06	7.700E-07	6.95E-07	1.00E-08	N/A
Solid solution ratio	ss_ratio	3000	3500	3477.2	1000	N/A
Calcite rate	rate	-6.00	-6.00	N/A	-12.0	-1.288
Magnesite rate	rate	-6.00	-6.00	N/A	-12.0	-5.419
Aragonite rate	rate	-6.00	-6.00	N/A	-12.0	N/A
Strontianite rate	rate	-6.00	-6.00	N/A	-12.0	-6.349
Brucite rate	rate	-6.00	-6.00	N/A	-12.0	N/A
Gypsum rate	rate	-6.00	-6.00	N/A	-12.0	N/A

In the 2-D inversion, the focus of the application was on a 2-D slice at a distance of 22 m along the 60-m (197-ft) transect. The reactive transport inverse calibration was performed using data collected from both the 80-cm (31.5-in.) and 40-cm (15.7-in.) depth for Cl^-, Ca^{2+}, Mg^{2+}, Sr^{2+}, and Na^+. Using optimized hydraulic parameters obtained from a previous calibration effort, steady-state simulations were run to obtain the necessary input data to CRUNCH. Although the volumetric flow rate at Meter 22 could be estimated at 7.94×10^{-5} m^3 d^{-1} (476.6 L d^{-1} [126 gal d^{-1}]/60,000 cm [23,622 in.]), the flux density at the boundary was unknown because the flux area was also unknown. Consequently, the calibration of

velocities to the non-reactive tracer data was required and yielded an estimated area of 1.985 cm^2. At the field site, $MgCl_2$ and $SrCl_2$ tracers mixed with river water were applied to the transect surface.

Once these components entered the subsurface, calcite ($CaCO_{3(s)}$) underwent dissolution, and strontianite ($SrCO_{3(s)}$) and magnesite ($MgCO_{3(s)}$) that formed as carbonate (CO_3^{2-}) became available in the system. In addition to mineral precipitation and dissolution, ion exchange also occurred during the experiment. Ions involved in these exchange reactions included Mg^{2+}, Ca^{2+}, Sr^{2+}, K^+, and Na^+. In the CRUNCH simulator, the rate of exchange was described using mass action expressions whose selectivity coefficients and b-dot parameters were determined based on a Hanford sediment column study (Steefel 2004). Only four parameters were included in the inverse simulation. These parameters included the solid solution ratio and the kinetic reaction rate parameter for calcite, magnesite, and strontianite (mol m^{-2} s). Because of parameter interactions and subsequent identifiability problems, the CEC parameter was fixed at the measured value of 3.8670 meq $(100\ g)^{-1}$.

There is evidence of multi-region dispersivity from the non-reactive tracer breakthrough curves. Longitudinal and transverse dispersivities at 80 cm (31.5 in.) were estimated to be 8 cm (3 in.) and 0.85 cm (0.33 in.), respectively. At 40-cm (15.7-in.) depth, the longitudinal dispersivity was estimated at 12 cm (4.7 in.), and the transverse dispersivity at 1.3 cm (0.5 in.). Figure 2.125 shows results of this calibration. Final estimates of these parameters appear in Table 2.21 for the inverse simulations at the two different depths. Figure 2.126 and Figure 2.127 show breakthrough curves indicating the observed and simulated values of the total concentrations for Ca^{2+}, Mg^{2+}, Sr^{2+}, K^+, and Na^+. Estimated parameter values are shown in Table 2.21 and are the same for both cases except for a slightly smaller reaction rate estimated for strontianite at the 40-cm (15.7-in.) depth. For both sets of breakthrough curves, similar behavior is shown in the ability to match the observed and simulated data. For example, a good match between simulated and observed total Ca^{2+} concentrations occurred in both cases. A good match between observed and simulated data also occurred for Na^+ and K^+, ions that were involved in the exchange reactions. The total concentration of Mg^{2+}, however, was overestimated in both cases.

Table 2.21. True Values of Parameters Used in the Synthetic Data Case

Parameter	Symbol	Value	Lower Bound	Upper Bound
Cation exchange capacity	CEC	1.E-06	1.E-08	1.E-04
Solid solution ratio	ss_ratio	3000	1000	5000
Calcite rate	rate	-6.0	-20.0	-4.0
Magnesite rate	rate	-6.0	-20.0	-4.0
Aragonite rate	rate	-6.0	-20.0	-4.0
Strontianite rate	rate	-6.0	-20.0	-4.0
Brucite rate	rate	-6.0	-20.0	-4.0
Gypsum rate	Rate	-6.0	-20.0	-4.0

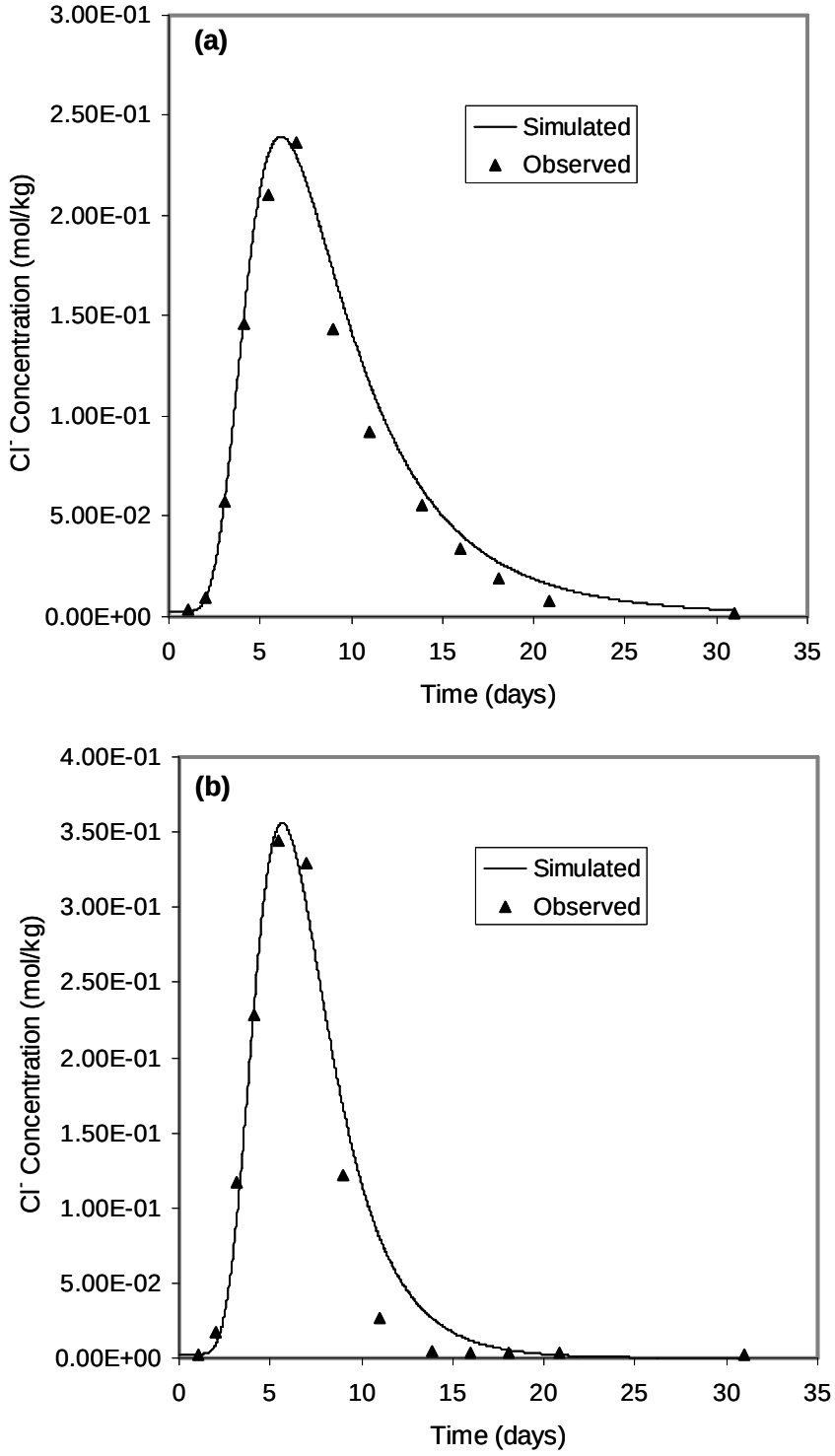

Figure 2.125. Observed and Simulated Cl- Concentrations Using (a) a Longitudinal Dispersivity of 8.0 cm (3.1 in.) and a Transverse Dispersivity of 0.85 cm (0.33 in.) at the 80-cm (31.5-in.) Depth and (b) a Longitudinal Dispersivity of 12.0 cm (4.7 in.) and a Transverse Dispersivity of 1.3 cm (0.5 in.) at the 40-cm (15.7-in.) Depth

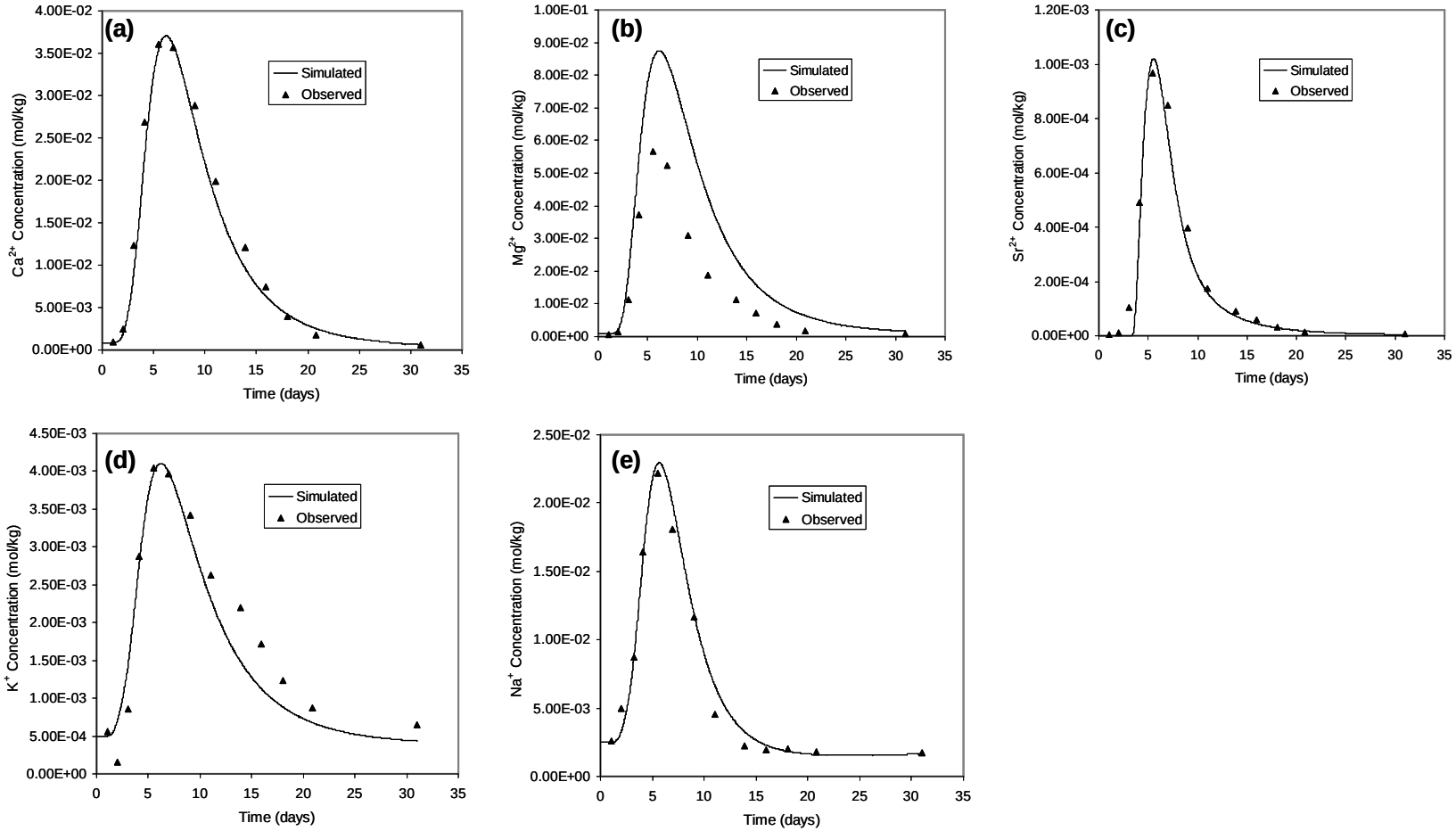

Figure 2.126. Observed and Simulated Concentrations for Reactive Constituents Ca^{2+}, Mg^{2+}, Sr^{2+}, K^{+}, and Na^{+} at 40-cm (15.7-in.) Depth

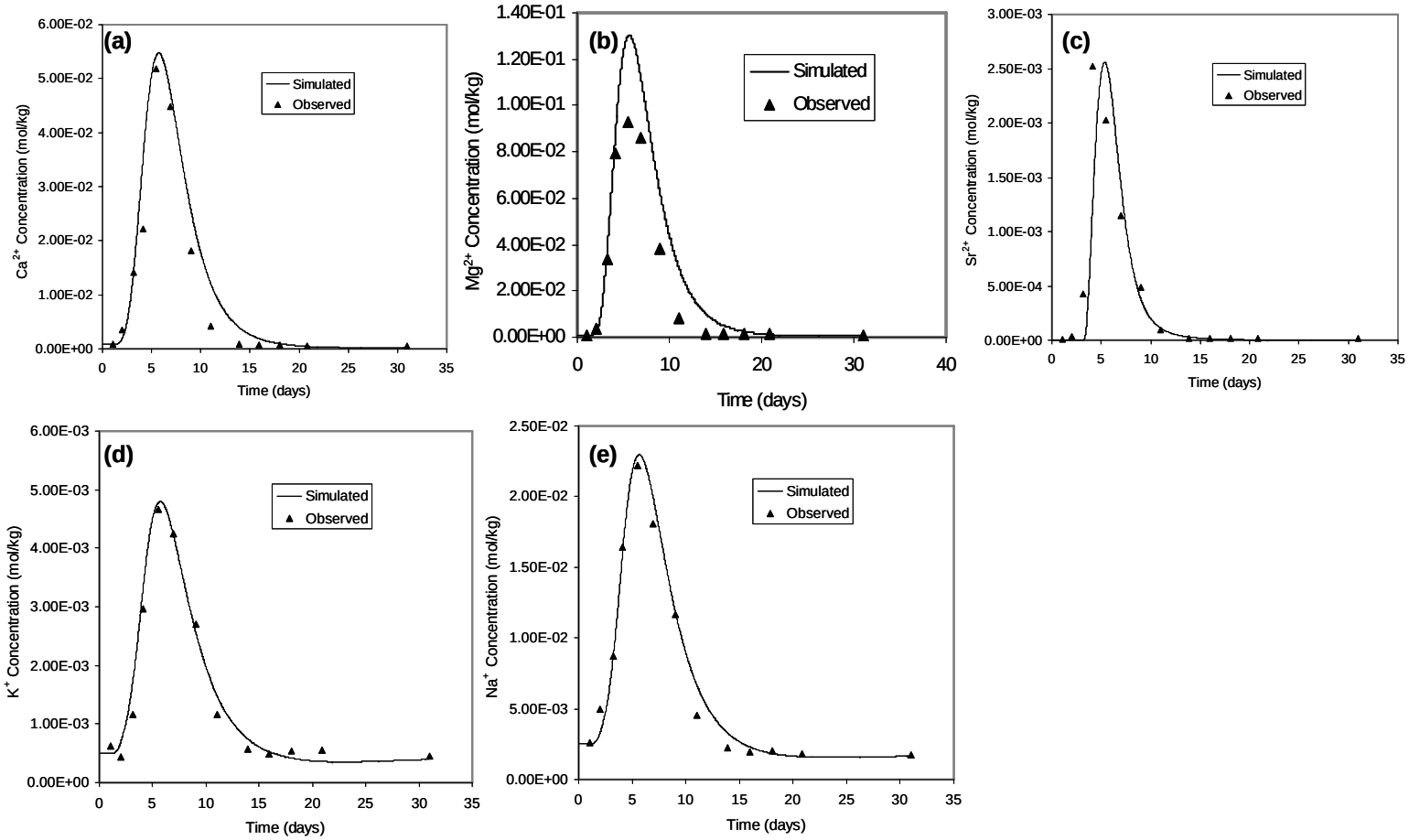

Figure 2.127. Observed and Simulated Concentrations for Reactive Constituents Ca^{2+}, Mg^{2+}, Sr^{2+}, K^{+}, and Na^{+} at 80-cm (31.5-in.) Depth

Figure 2.128 shows the final predicted total exchange concentration distributions for (a) Sr^{2+} and (b) Mg^{2+} at 31 days. Simulations show that at 31 days, the area of magnesite distribution was more limited than the 2-D distribution of strontianite (Freedman et al. 2004). This result is attributed to the preferential exchange of Mg^{2+} (Figure 2.128a). Given that strontianite formed first in the system, magnesite precipitation was largely limited by the availability of carbonate, which in turn, was dependent upon calcite dissolution. Although the final estimate for the rate of magnesite precipitation was high (~10^{-4}), the rate of formation was insensitive to the reaction rate because of the limitation of carbonate in the system. A time delay also occurred for the simulated total concentrations of Sr^{2+} in both inverse simulations. Although exchange is an important process in the system, the inverse simulations demonstrated that the magnitude of the total concentration of Sr^{2+} and magnesite in the system was controlled more by the rate of precipitation than the solid solution ratio parameter. The peak arrival time, however, was controlled more by the solid solution ratio parameter than the strontianite rate of reaction. Although the magnesite precipitation rate had little impact on the total Mg^{2+} in the system, by contrast, the strontianite kinetic reaction rate was far more sensitive. This occurred because the magnesium in the tracer solution was 10 times higher than that of the strontium, and magnesium dominated the exchange reactions.

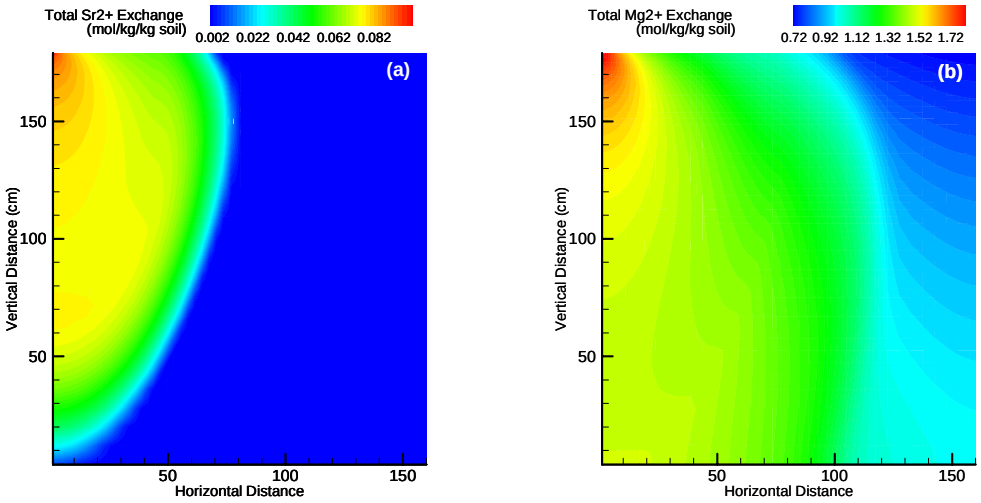

Figure 2.128. Final Predicted Total Exchange Concentration Distributions for (a) Sr^{2+} and (b) Mg^{2+}

An important result of this inverse analysis is the insensitivity of the system to the rate of magnesite precipitation and the over prediction of the total magnesium concentration. Because the solid solution ratio does not have a significant impact on the total concentration of magnesium, these results imply that the selectivity coefficient and b-dot parameters used to describe the competitive adsorption behavior for ion exchange are not appropriate for this site. To improve the match between simulated and observed total concentrations, the inverse problem may need to consider the selectivity coefficients and/or b-dot parameters assumed known in this analysis. Although these parameters are usually determined experimentally, the absence of empirical data may warrant their inclusion in the optimization scheme. Other improvements to matching observed and simulated concentration data may be accomplished using different weighting schemes or normalizing the residuals in the UCODE analysis. This is an important factor given that the concentration data have peaks that range over three orders of magnitude.

In general, a good fit resulted for all species, except that Mg^{2+} was over predicted. The model also predicted a delay in Sr^{2+} and slightly under predicted K+ at the 40-cm (15.7-in.) depth. Results suggest that the concentration of Sr^{2+} is affected more by the strontianite precipitation rate than by the solid-solution ratio. The resulting strontianite reaction rate parameter differed slightly between the 40-cm (15.7-in.) (3.02×10^{-9} mol m^{-2} s) and 80-cm (31.5-in.) depth ($3.39 \times$ 10-9 mol m^{-2} s). The magnesite precipitation rate was insensitive because it was limited by the availability of CO_3^-. In general, the reversible multicomponent ion exchange model developed by Steefel (2004) for the S-SX Tank Farm proved to be applicable for these sediments despite the differences in solid and solution chemistry. The model was developed to evaluate the effect on strontium migration of multiple competing cations, including Na^+, K^+, Ca^{++}, and Mg^{++}. Whereas this model represents the most recent attempt to predict strontium migration in the presence of multiple competing cations, including Na^+, K^+, Ca^{2+}, and Mg^{2+}, its applicability to other waste sites and different sediments has not be established. These results suggest that to improve the model fit, site-specific data on selectivity coefficients and b-dot parameters may be needed or perhaps included in the optimization scheme.

2.21.2 Synopsis and Implications

The overall goal of this study was to develop a reliable method for model identification describing transport when multicomponent ion exchange occurs in variably saturated flow problems. The synopsis of findings for the inverse modeling of multicomponent reactive transport subsurface and their implications are as follows:

- An improved understanding of field-scale flow, transport, and reaction processes that addresses multi-scale heterogeneities was achieved by history-matching of state variables such as water contents, pressure heads, and chemical concentrations.

- In the typical inverse model application, there are insufficient geochemical and physical data at the field scale to perform the inverse modeling task, and transport parameters are usually treated separately from the geochemical parameters. In contrast, at the laboratory scale, measurements are often used to estimate relevant parameters.

- The methodology for performing automatic inverse simulations with CRUNCH-UCODE was developed and tested. Currently, parameters that describe kinetic reaction rates and cation exchange capacities can be used in the inverse methodology, as shown in the example simulations. However, additional parameters, both chemical and physical, need to be added to diversify CRUNCH-UCODE capabilities.

- For the synthetic data set that was simulated, the calibrated parameters were non unique. Non-uniqueness can be avoided by constraining the model as much as possible to measurements or data from literature, or by designing an experiment so that the measured concentrations yield information on the processes controlling the reactive front. Parameter non-uniqueness may mean that estimates do not necessarily need to be considered as fixed values. A range of parameter values may be more appropriate for the parameter estimates as in a Monte Carlo analysis.

- For the inverse analysis of the field experiment at the Army Loop Road site, results demonstrate that the parameters describing the mass action relationships for ion exchange limit the ability to

obtain a good fit between simulated and observed total magnesium concentrations. An optimization scheme that includes these parameters in the analysis may be required, though the identifiably of these parameters has not yet been investigated.

- Currently, only two data types in CRUNCH can be used for the observations. Observations must either be aqueous concentrations or ion exchange concentrations. Although few datasets are likely to contain ion exchange concentration data, this option was primarily set as a placeholder for the addition of future options. The incorporation of other types of data, such as mineral data, would also be useful additions.

- These preliminary studies highlight a number of challenges in the application of inverse modeling to joint inversions of field-scale hydrogeophysical data. While model-independent estimation packages like UCODE provide flexible inverse modeling capabilities, they are computationally constrained when dealing with multiphase reactive transport in heterogeneous systems.

- A general methodology for inverse reactive transport modeling will require a thorough investigation of methods to simultaneously account for differences in model structure and reaction processes; robust weighting schemes, and methods for normalizing the concentration data residuals. Utilities must also be implemented to identify parameter sensitivities before performing the analysis. In this way, insensitive parameters can be eliminated from the inverse so that reasonable parameter estimates can be obtained.

- Because CRUNCH does not simulate water flow, velocity fields and moisture content distributions must be first be obtained from STOMP. To gain a better understanding of the multiscale reactive transport process and the effects of heterogeneity, a numerical simulator is needed with comprehensive process capabilities for chemically reactive non-isothermal flow of multiphase fluids.

2.22 Field-Scale Hydraulic Properties from Spatial Moments

Predictions of field-scale transport in unsaturated anisotropic soils often show discrepancies compared to field observations, partly because of the heterogeneity within the hierarchy of scales and partly because of the saturation dependence of anisotropy. Models often under-predict lateral spreading in the vadose zone. Because of the high level of detail that would be required to model these structures across multiple scales, determination of effective hydraulic properties continues to be an important goal in hydrogeology. Upscaling procedures are often employed to facilitate simulation over large spatial scales, and a number of techniques have been proposed for determining effective properties for use in heterogeneous, anisotropic systems. However, some upscaling methods may smooth descriptions of hydraulic functions and not capture the fine-scale heterogeneities determined to be important during the field injection experiments at the 299-E24-111 and Army Loop Road test sites.

When considering unsaturated systems, there are two major difficulties to overcome. First is the non-linear, scale-dependent nature of the constitutive properties, e.g., the permeability ($\boldsymbol{k}$), saturation (S), and capillary pressure (P_c) relationships. It has been shown that averaging of individual fine-scale relationships to derive effective properties can lead to under prediction of lateral spreading (Ferrand and Celia 1992). Second is the difficulty in making multiple measurements of the state variables needed to

describe flow, e.g., water contents and matric potential over large spatial scales. Although matric potential measurements continue to be quite difficult to perform, recent advances in vadose zone monitoring technologies have seen increased use of automated sensors for point measurements of water content. Similar advances in hydrogeophysics have resulted in more widespread use of geophysical techniques to monitor moisture contents over large spatial scales. Thus, it is now possible to monitor the evolution of a water plume from a scale of point sensors to the scale of hundreds of meters and even kilometers.

The goal of this study was to investigate or develop methods that could be used to obtain quick estimates of field-scale or effective hydraulic properties from easily acquired measurements such as the spatiotemporal evolution of a wetting front. A simple phenomenological approach was used based on the analysis of the temporal changes in the spatial moments of an evolving subsurface water plume (Ward et al. 2006). In this approach, the heterogeneous porous medium is conceptually homogenized and replaced by an effective medium whose hydraulic properties are described in terms of effective parameters. The method takes advantage of the similarity between the moisture-based Richards' equation and the convective-dispersive equation, CDE (Barry et al. 1991; Barnes 1986), to derive hydraulic parameters from temporal changes in the spatial moments of an infiltrating water plume. There are comparable expressions for θ and concentration C; the convective velocity is analogous to $dK/d\theta$; and D is analogous to the dispersion tensor. However, because of the strong dependence of K and D on θ, Equation (2.21) is strongly nonlinear. Nevertheless, these similarities are useful for estimating effective properties from temporal changes in the field-scale spatial moments. The relationship between spatial moments of the concentration and the parameters of the convection-dispersion equation has been derived and is now widely used for estimating field-scale transport properties (Freyberg 1986; Garabedian et al. 1991).

The continuity equation for 3-D transient water flow in an unsaturated homogeneous or equivalent homogenous, porous medium may be expressed in two forms:

(1) the water content- or θ-based form as

$$\frac{\partial \theta}{\partial t} = \nabla D(\theta) \nabla \theta - \frac{dK(\theta, K_s, \alpha, n, L)}{d\theta} \frac{\partial \theta}{\partial z} \tag{2.21}$$

(2) the pressure- or h-based form as

$$\frac{\partial \theta}{\partial t} = \nabla \cdot \left[K(h, K_s, \alpha, n, L) \nabla h \right] - \frac{\partial K(h, K_s, \alpha, n, L)}{\partial z} \tag{2.22}$$

where θ = volumetric water content
t = time
∇ = Laplacian in physical-space coordinates
$D(\theta) = K(\theta)/C(\theta)$ = soil-water diffusivity (Klute 1952)
$K(\theta)$ = soil hydraulic conductivity
z = vertical distance from the soil surface
$C(\theta) = d\theta/dh$ = specific water-holding capacity with h being the soil water pressure head.

The water retention function for each equivalent homogeneous medium may be defined as (van Genuchten, 1980)

$$\theta(h, \alpha, n, \theta_s, \theta_r) = \theta_r + (\theta_s - \theta_r)\left[1 + \alpha \mid h \mid^n\right]^{(1/n-1)} \tag{2.23}$$

Combining (2.23) with the statistical pore size model of Mulaem (1976) yields the hydraulic conductivity function for an equivalent homogenous medium as:

$$K(h, K_s, \alpha, n, L) = K_s \frac{\left\{1 - (\alpha \mid h \mid)^{n-1}\left[1 + (\alpha \mid h \mid)^n\right]^{(1/n-1)}\right\}^2}{\left[1 + (\alpha \mid h \mid)^n\right]^{L(1-1/n)}} \tag{2.24}$$

where θ_s = Saturated water content
θ_r = Residual water content
h = Pressure head
n = pore-size distribution parameter
α = fitting parameter that is inversely proportional to the pressure head at air-entry
$K(\theta)$ = soil hydraulic conductivity
L = pore connectivity-tortuosity parameter

Equation (2.21) is applicable to a homogeneous or equivalent homogeneous medium but not suited to heterogeneous sediments because of discontinuities in θ profiles. This form of the flow equation degenerates under fully saturated conditions.

The gravity term of the flow equation, which is analogous to the vertical convective velocity in the CDE, is determined from the temporal evolution of the plume centroid along the vertical coordinate, allowing calculation of an upscaled vertical conductivity, $K_z(\theta_e)$ as a function of effective water content. As with the dispersion tensor in the CDE, the rate of change of the second spatial moment in 3-D space is used to calculate the water diffusivity tensor, $D(\theta_e)$, from which the upscaled longitudinal and traverse horizontal hydraulic conductivity functions, $K_x(\theta_e)$ and $K_y(\theta_e)$, respectively, are calculated. The final requirement to implementing this approach is a method for estimating the various components of (2.21). As suggested by Ward et al. (2002), these terms can be estimated from temporal changes in spatial moments.

Spatial moments arise naturally in the parameterization of flow and transport models (Freyberg 1986). For a 3-D water-content distribution, measured at time *t*, the ijkth plume-scale moment is defined as

$$M_{ijk}(t) = \int_{-\infty}^{\infty}\int_{-\infty}^{\infty}\int_{-\infty}^{\infty} \theta(x,y,z,t)\, x^i, y^j, z^k \, dx\, dy\, dz \tag{2.25}$$

where $\theta(x,y,z; t)$ is the water-content field above background, and $\theta(x,y,z;t_0)$ and x, y, z are the spatial coordinates. For this study, values of the superscripts *i, j, k* are limited to 0, 1, or 2, representing the zeroth and the first and second moments, respectively. The zeroth moment is unique in that, under conditions when it exists, its value is proportional to the total mass contained in the system. Thus, from (2.25), the mass of water in the plume at time *t* is calculated as $\rho_w \cdot M_{000}(t)$ where ρ_w is the fluid density. In a closed system, $\rho_w \cdot M_{000}(t)$ should be equal to the injected mass of water at time *t*. The first central spatial moment describes the position of the plume centroid as a function of time $[x_c(t), y_c(t), z_c(t)]$ in response to gravity and is calculated as

$$x_c(t) = \frac{M_{100}(t)}{M_{000}(t)};\;\; y_c(t) = \frac{M_{010}(t)}{M_{000}(t)};\; z_c(t) = \frac{M_{001}(t)}{M_{000}(t)} \tag{2.26}$$

The second central moment defines the spatial covariance tensor, $\boldsymbol{\sigma_{ij}}$, in which the components of the main diagonal are defined as

$$\sigma_{xx}(t) = \frac{M_{200}(t)}{M_{000}(t)} - x_c^2;\;\; y_c(t) = \frac{M_{010}(t)}{M_{000}(t)} - y_c^2;\; z_c(t) = \frac{M_{001}(t)}{M_{000}(t)} - z_c^2 \tag{2.27}$$

The second moments in (2.27) are physically related to the spread of the water plume about the center of mass in response to matric potential gradients. Thus, the time history of the spatial moments may be useful for describing the behavior of the infiltrating plume without any assumptions about the flow process. The innovation is relating the spatial moments to the hydraulic parameters in (2.21) in the proposed homogenization approach.

To estimate effective vertical conductivity, $K_z(\theta_e)$, some simplifying assumptions about flow must be made. Under unit gradient conditions, at large time, the vertical flux density of water, *q*, near the source is a direct measure of the unsaturated hydraulic conductivity, $K_z(\theta_e)$, at the effective moisture content, θ_e. The simultaneous measurement or estimation of *q* and θ_e for injection rates less than K_s, therefore, provides a direct measure of the $K(\theta_e)$ function (Youngs 1964). In direct analogy with the CDE, the vertical convective velocity, $V = dK(\theta)/d\theta$, in (2.21) from which the vertical hydraulic conductivity at θ_e is calculated as

$$K_z(\theta_e) = \int V(\theta_e) d\theta_e = \int \frac{dz_c(t)}{dt}\, d\theta_e \tag{2.28}$$

In Equation (2.28), the relationship $z_c(t)$ is related to θ_e through the dependence of θ_e on time, i.e., $t = f(\theta_e)$. The term $dz_c(t)/dt$ is obtained directly from the spatial moments as the time rate of change in the first spatial moment calculated in Equation (2.26).

Unlike the CDE where the velocity tensor describes convection along the three principle coordinates, here it applies only to the vertical component of flow because it is derived from the gravitational component of the total potential. In contrast, the diffusivity term in Equation (2.21) describes the flow of water in response to the matric potential gradient and is applicable to both vertical and horizontal flow components. In the CDE, the dispersion coefficient describes the dispersive spreading of the solute plume and the variance of an initially highly localized plume after time t is 2Dt. The time derivative of the spatial covariance of the solute distribution, when used in conjunction with the CDE, allows definition of the dispersion coefficient as one half of the change in the covariance tensor σ_{ij} with time (Freyberg 1986; Garabedian et al. 1991). The expressions for dispersion and diffusivity are comparable, so in a similar fashion, D in Equation (2.21) is estimated from the time rate of change of the second spatial moment of the water-content distribution, i.e.,

$$D_{ij}(\theta_e) = \frac{1}{2}\frac{\partial \sigma_{ij}^2(t)}{\partial t} \tag{2.29}$$

To determine $K_{ij}(\theta_e)$ from $D_{ij}(\theta_e)$, we first recall from (Klute 1952) that

$$D_{ij}(\theta) = K(\theta)\frac{dh}{d\theta} \tag{2.30}$$

where $dh/d\theta$ is recognized as the reciprocal of the soil water capacity, $C(\theta)$. At the effective water content, we can write Equation (2.30) in terms of θ_e. Substituting Equation (2.30) for $D_{ij}(\theta_e)$ in Equation (2.29) gives rise to an expression for $K_{ij}(\theta_e)$ in terms of the time rate of change of the covariance tensor

$$K_{ij}(\theta_e)\frac{dh}{d\theta_e} = \frac{1}{2}\frac{\partial \sigma_{ij}^2(t)}{\partial t} \tag{2.31}$$

The right hand side of Equation (2.31) is calculated directly from Equation (2.27), but $dh/d\theta_e$ is unknown. In the absence of simultaneous plume-averaged h and θ_e, solving Equation (2.31) for $K_{ij}(\theta_e)$ would be difficult. This potential difficulty can be avoided in one of two ways. First, $dh/d\theta_e$ can be determined from Equations (2.29) and (2.30) as

$$\frac{dh}{d\theta_e} = \frac{1}{2K_{ij}(\theta_e)}\frac{\partial \sigma_{ij}^2(\theta_e)}{\partial t} \tag{2.32}$$

Because only $K_z(\theta_e)$ is known at this point, $dh/d\theta_e$ could be determined from Equation (2.31) using Equation (2.28). This provides the means for estimating the effective water-retention function. Integrating Equation (2.32) with respect to θ_e gives the effective or plume-scale water-retention function, $\theta(h)$. In the second approach, the calculation of $dh/d\theta_e$ is avoided by first defining the anisotropy ratio as

the ratio of Equation (2.28) to Equation (2.31). Equation (2.31) may be expanded and rearranged to give $K_{ij}(\theta_e)$ simply in terms of $K_z(\theta_e)$ as

$$K_{ij}(\theta_e) = \frac{K_{ij}(\theta_e) \cdot dh/d\theta_e}{K_z(\theta_e) \cdot dh/d\theta_e} K_z(\theta_e) \tag{2.33}$$

By substituting Equation (2.30) into the numerator and denominator of the first term in Equation (2.33), Equation 2.33 is rewritten in terms of the water diffusivity and the vertical hydraulic conductivity,

$$K_{ij}(\theta_e) = \frac{D_{ij}(\theta_e)}{D_z(\theta_e)} K_z(\theta_e) \tag{2.34}$$

Finally, on substituting Equation (2.29) for $D(\theta_e)$ in Equation (2.34) and simplifying, an expression is obtained for the horizontal component of conductivity strictly in terms of the time dependence of the covariance tensor and the vertical conductivity. As in Equation (2.285), the time dependence of the covariance tensor may be expressed in terms of θ_e because $t = f(\theta_e)$. Thus, Equation (2.34) may be rewritten as

$$K_{ij}(\theta_e) = \frac{\partial\sigma_{ij}^2(\theta_e)/\partial t}{\partial\sigma_{zz}^2(\theta_e)/\partial t} K_z(\theta_e) \tag{2.35}$$

The effective hydraulic conductivity for the longitudinal direction is determined from Equation (2.35) as $K_{xx}(\theta_e)$ whereas the effective conductivity for the transverse horizontal direction is determined as $K_{yy}(\theta_e)$. The resulting $K_{xx}(\theta_e)$, $K_{yy}(\theta_e)$, and $K_{zz}(\theta_e)$ are then fitted to Equation (2.24) to obtain the upscaled or effective parameters whereas their ratios allow a description of the saturation-dependent anisotropy.

2.22.1 Results

Analysis of the trajectory of the centroid provides more insight into the hypothesis of mass leaving the monitored domain and provides the basis for estimating the field-scale parameters using the proposed homogenization approach. For this study, we focused on the FY 2000 hyposaline injections. Figure 2.129 shows the vertical trajectory of the plume centroid as a function of elapsed time. The vertical centroid showed a nonlinear dependence on elapsed time that was best described by a power function. The decline in $z_c(t)$ with time resulted in a decrease in the vertical velocity that may be caused by two factors. First, as the injection progressed at a constant rate, the injected water had to wet larger and larger volumes of soil so the rate of advance of the wetting front would decrease. Second, the deeper fine-textured layer present appears to have imposed a limit on the maximum depth of penetration. The time dependence of the plume variance is needed to quantify movement caused by matric potential gradients. Figure 2.130 shows that initially the transverse horizontal variance increased slowly with a nonlinear dependence on elapsed time.

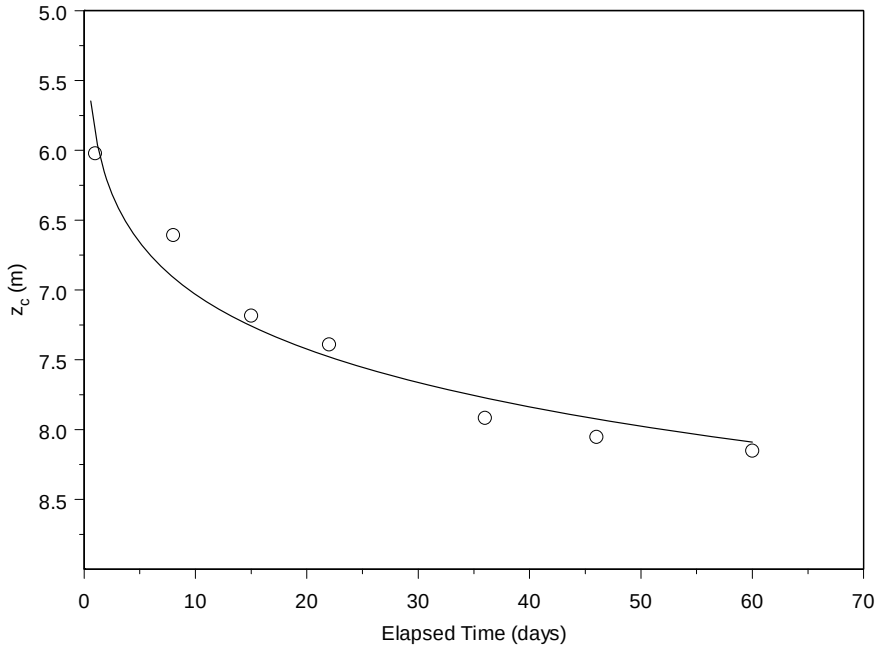

Figure 2.129. Measured Vertical Displacement of the Centroid of the Water Plume Versus Time. The Solid Line Represents the Least Squares Regression with $z_c(t)= 5.8718\ t^{0.0783}$; $R^2 = 0.953$.

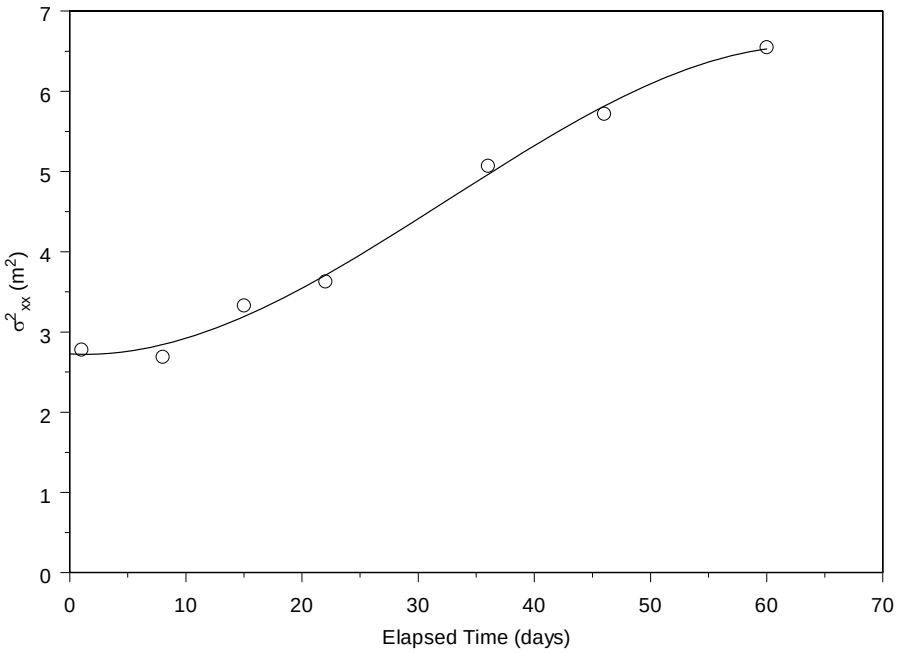

Figure 2.130. Transverse Horizontal Variance of the Water Plume Versus Time. The Solid Line Represents the Least Squares Regression with $\sigma^2_{xx} = -3{\cdot}10^{-5}\ t^3 + 0.0031\ t^2 - 0.009\ t + 2.7305$; $R^2 = 0.995$.

As seen in Figure 2.131, the behavior of σ^2_{yy} is remarkably similar to σ^2_{xx}, which might suggest an effective medium that is isotropic or only mildly anisotropic in the horizontal plane. In both cases, the rate of change started to decrease after about 35 days. This may be expected because, as the plume moved laterally, it continued to encounter heterogeneity. In contrast, σ^2_{zz} showed an initial rapid increase but slowed significantly after about 10 days (Figure 2.132). Closer observation of σ^2_{zz} as a function of travel distance suggests that the initial slowing may have been caused by a delay in water entering the coarser sand underlying the fine-textured layer at 5 m.

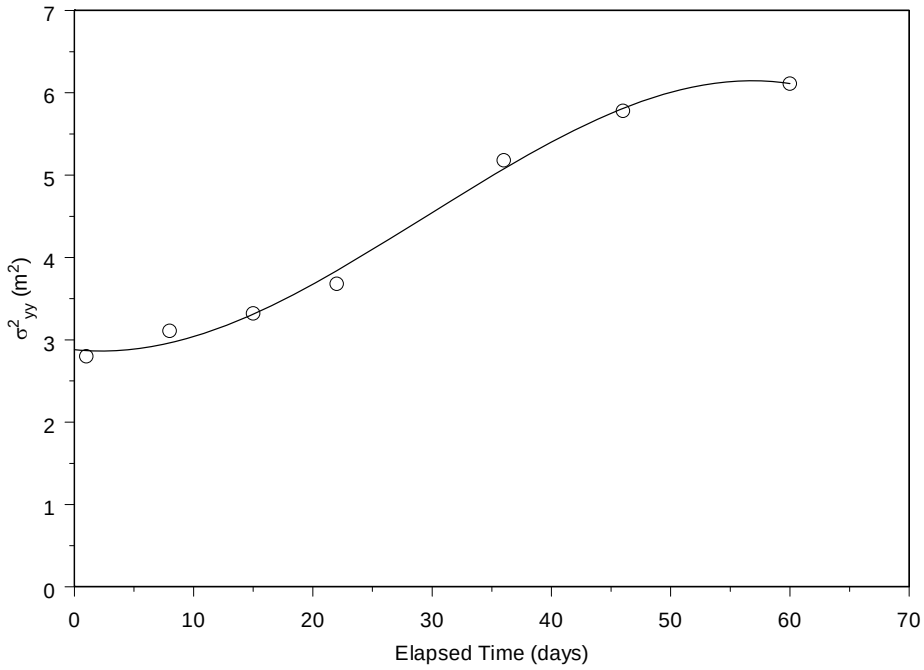

Figure 2.131. Longitudinal Variance of the Water Plume Versus Time. The Solid Line Represents the Least Squares Regression with $\sigma^2_{yy} = -4{\cdot}10^{-5}\, t^3 + 0.0036\, t^2 - 0.065\, t + 2.8851$; $R^2 = 0.994$.

Table 2.22 summarizes the parameters derived from the homogenizing approach. The predicted $K_x(\theta_e)$, $K_y(\theta_e)$ and $K_z(\theta_e)$ curves were simultaneously fitted to the saturation form of the van Genuchten-Mualem hydraulic conductivity model to estimate the α and n parameters and the pore connectivity-tortuosity tensor, $L_i = (L_x, L_y, L_z)$. Given that the approach only provides the means for estimating the upscaled $\mathbf{K}(\theta_e)$, a full description of the water-retention parameters would require prior information on θ_s and θ_r predict actual water contents. In this case, we used the average values of the measured local-scale parameters from Zhang et al. (2004b) as estimates for the homogenization method. The resulting $\mathbf{K}(\theta_e)$ showed saturation-dependent anisotropy. Table 2.22 also shows the anisotropy coefficients of the saturated hydraulic conductivity for the effective medium. The system appears only mildly anisotropic in the horizontal plane with an anisotropy ratio (K_{sx}/K_{sy}) of only 1.28. The fitted K_s in the x-direction, however, was over 4 times K_s in the z-direction; the fitted K_s in the y- direction was just over 3 times that in the z-direction.

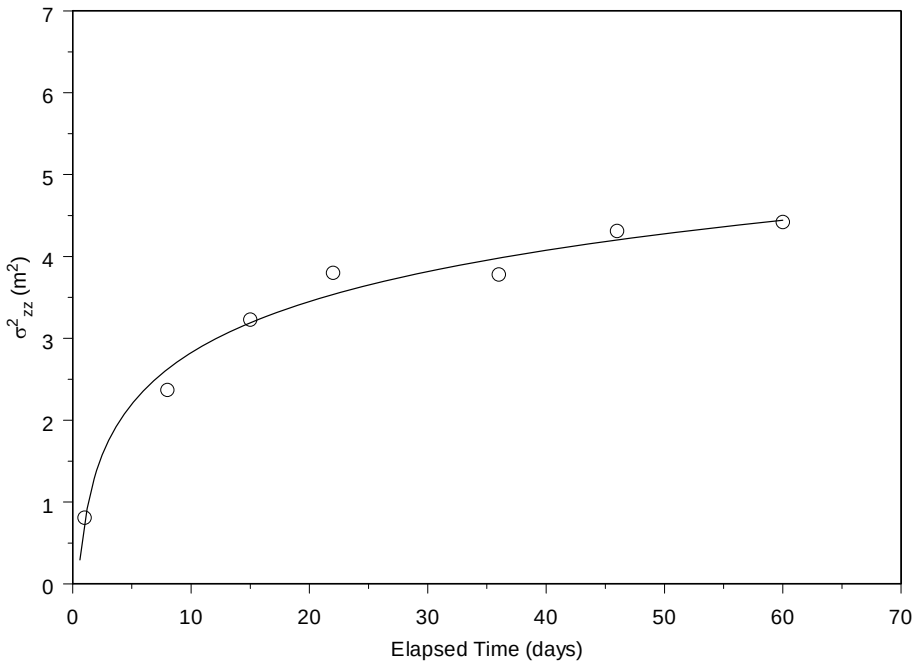

Figure 2.132. Vertical Variance of the Water Plume Versus Time. The Solid Line Represents the Least Squares Regression with $\sigma^2_{zz} = 0.9035 \ln(t) + 0.7452$; $R^2 = 0.981$.

The fitted value of α is remarkably similar to the geometric mean of the local-scale α (Zhang et al. 2004b). However, the fitted *n* is more than 3 times larger than the geometric mean of the local-scale n. The directional dependence of the fitted pore connectivity is consistent with the asymmetric wetting fronts observed in field data and the proposed theory of a connectivity tensor. The local-scale parameters were derived from core measurements in which no attempts were made to measure directional properties; thus, *L* is treated as a scalar quantity.

The resulting parameters were used in the STOMP simulator to predict $\theta(\mathbf{x},t)$, which is expected from the infiltration tests at times equivalent to the monitoring times in the FY 2000 field experiment at the 299-E24-111 test site. Figure 2.133 compares the observed water contents with those simulated using the upscaled parameters derived from spatial moments. In general, using the calculated parameters resulted in underestimating the water content, which was expected, given the value of the n parameter. Nevertheless, the sum of squared residual (SSR) with these parameters was 40.3, almost twice the 22.8 reported in Zhang et al. (2004b) for the same simulation using the local-scale parameters. The predicted distributions matched the centroid locations reasonably well, although the effects of the small-scale stratification on lateral spreading were lost. In stratified sediments, the extent to which an asymmetric flow field develops is controlled partly by geometry, scale, and the continuity of textural contrasts that give rise to heterogeneity in the conductivity field. This upscaling approach does capture some of these effects, given the resulting **K** and **L** tensors. However, the resulting parameters may not adequately capture the full effects of correlated regions of high conductivity or anisotropy and therefore may under-predict the extent of lateral movement. These results can be expected given the phenomenological basis of the approach and the assumption that the θ-based flow equation can be treated as a nonlinear form of

the CDE. Nevertheless, it does provide insight into the average behavior of the plume without the need for complex models.

Table 2.22. Upscaled Parameters of an Effective Homogenous Medium (EHM) based on the Homogenization Method

Soil	θ_s ($m^3\ m^{-3}$)	K_{sx} ($m\ s^{-1}$)	K_{sy} ($m\ s^{-1}$)	K_{sz} ($m\ s^{-1}$)	α (m^{-1})	n (-)	L_x (-)	L_y (-)	L_z (-)	θ_r ($m^3\ m^{-3}$)	K_{sx}/K_{sz}
EHM	0.345	7.90E-04	6.15E-04	1.89E-04	4.421	10.657	3.079	1.991	0.192	0.03	4.18

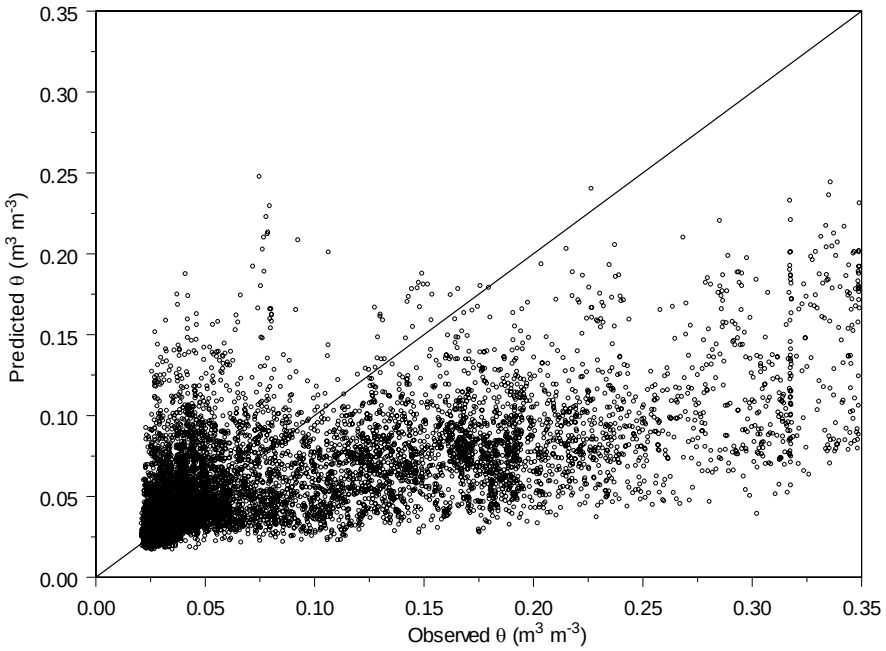

Figure 2.133. Comparisons of Simulated and Observed Water Contents using Upscaled Values of Hydraulic Parameters Derived from the Phenomenological Method based on Spatial Moment Analysis. The mean square residual error was 4.87×10^{-3}.

2.22.2 Synopsis and Implications

The synopsis of findings for this study and their implications are as follows:

- We developed a simple homogenization approach that takes advantage of the broad similarity between the θ-based flow equation and the CDE to estimate the upscaled water retention and the unsaturated hydraulic conductivity tensor.

- The resulting K(θ) was essentially isotropic in the horizontal direction but strongly anisotropic in the vertical direction. Effective anisotropy ratios based on temporal changes in the spatial moments of the water plume ranged from 1 to 4.

- Forward simulations with the resulting parameters predicted the location of the center of mass reasonably well but were unable to adequately capture the effects of lateral spreading.

2.23 The Combined Parameter Scaling Inverse Technique for Upscaling Flow

Determining a large number of soil hydraulic parameters for heterogeneous soils remains a challenge because inverting for too many parameters can lead to parameter values that are non-unique. The non-uniqueness problem becomes worse as the number of parameters to be estimated becomes larger. Furthermore, when large numbers of parameters are inverted, large numbers of observations are required and very long simulation times will be needed because the simulation time increases quadratically with the number of parameters to be estimated. Some researchers have shown that the number of parameters to be estimated can be reduced by similar-media scaling, which scales soil water-retention curves and the unsaturated hydraulic conductivity functions of multiple soils with similar pore geometry to those of a reference soil. The similar-media scaling allows a single solution of the Richards' equation to suffice for numerous specific cases of flow in unsaturated soils. However, this approach does not address vertical heterogeneity, which is a significant source of concern for most DOE sites. Previous attempts to incorporate the effects of vertical heterogeneity have only been partially successful (Shouse et al. 1992; Vogel et al. 1991; Eching et al. 1994). As part of this study, a combined parameter scaling and inverse technique (CPSIT) was developed to overcome these problems and to allow upscaling of hydraulic parameters from the local to the field scale.

The CPSIT approach includes two steps: 1) parameter scaling and 2) inverse modeling, and it reduces the number of parameters to be estimated (Zhang et al. 2002b, 2004b). Parameter scaling has the following characteristics: 1) unlike property scaling, parameter scaling does not require the soil materials to be geometrically similar, 2) after taking parameter scaling, the values of the hydraulic parameters of all the soil textures perfectly reduce to the reference values, 3) the spatial variability of each hydraulic parameter can be expressed by the scaling factors, 4) the flow equation can always be expressed in real time and space regardless of the soil heterogeneity, and hence the parameters may be estimated inversely, and 5) when the parameters are to be estimated by an inverse procedure, the number of unknown variables is reduced by a factor of the number of textures (M), and the simulation time is reduced approximately by a factor of M^2.

In the CPSIT approach, a heterogeneous soil is conceptualized as a composition of multiple EHMs whose hydraulic properties are scale-dependent. The local-scale properties are typically measured in the laboratory using small soil cores and must be upscaled before application to field-scale predictions. We extend the parameter-scaling concept by coupling it with the inverse modeling approach described in the previous section to upscale hydraulic parameters. The CPSIT only estimates the hydraulic parameters of the reference EHM and hence has the advantages of both the scaling and inverse techniques: the number of parameters to be estimated is reduced by a factor of the number of EHMs, and the field-scale parameter values are optimized. Because of reducing the number of parameters, the CPSIT requires fewer observations to identify all of the hydraulic parameters and suffers less than other methods from non-uniqueness. More importantly, the relationship between parameter values at the local and field scales of the reference EHM may be transferable to other untested sites with soils of similar variability hierarchy.

The CPSIT method was tested by applying it to field-scale injection two different tests conducted over a scale of about 16 m (52.5 ft) horizontally and 18 m (59 ft) vertically at the 299-E24-111 test site.

Flow was simulated using STOMP, and the field observations were inverted using the coupled STOMP/UCODE as previously described. Prior information on the parameters α and L was used because of the relatively low sensitivity of flow to these parameters. Because the soil has a dominant layered structure, the principle directions of anisotropy were assumed to be horizontal and vertical. The pre-injection water contents were used to define the initial condition. Because of the large injection volume and small precipitation during the experimental period, a no-flow boundary condition was used at the top of the simulation domain. No-flow boundary conditions were also applied to the four sides, and a unit gradient condition was imposed at the bottom. To reduce the effects of the side boundaries, the horizontal scale of the modeling domain was set to 40.7 × 40.7 m (133.5 × 133.5 ft), which is much larger than the horizontal observation scale of 16 × 16 m (52.5 × 52.5 ft). The depth of the simulation domain extended from 3.05 m (10 ft) to 15.24 m (50 ft), which is the region within which most of the observations were taken. A Cartesian coordinate system was used, and the origin was set at the lower southwest corner. The simulation domain was subdivided into a grid with a variable horizontal spacing step (Δx and Δy) and a constant vertical spacing step (Δz). The minimum values of Δx and Δy were 0.2 m (0.66 ft), which were at the center of the domain. The values of Δx and Δy increased by a factor of 1.3 as the distance to the center of the domain increased. The value of Δz was 0.3048 m (1 ft). The numbers of nodes at x, y, z directions were 24, 24, and 40, respectively. The source was placed at the center of the x-y plane and over a vertical range of 4.57 to 4.88 m (15 to 16 ft). For the earlier injections, the plume was a smaller size, and monitoring of water content was restricted to the immediate vicinity of the injection well.

2.23.1 Results

Soil textures of the site were characterized using data from the three boreholes, S1, S2, and S3, installed during the 2000 and 2001 field campaigns (Last and Caldwell 2001). The vertical heterogeneity of the various geologic strata was evaluated by visually inspecting the strata, which were classified into five units, summarized in Table 2.23 (Last et al. 2001):

Table 2.23. Geologist's Description of the Main Sediment Facies at the 299-E24-111 Experimental Site

Facies	Depth (m)	Description
A	3–6	Poorly laminated slightly muddy medium sand
B	6–7	Well stratified slightly muddy to muddy coarse to medium sand
C	7–10	Weakly stratified medium sand
D	10–12	Highly stratified slightly muddy to muddy coarse sand
E	12–17	Sand to slightly muddy sand

These five material types were treated as five distinct EHMs for the sediments at the experimental site. At Hanford, all the waste tanks are buried a few meters below the soil surface, so the hydraulic properties of the soil materials around and below the leak impact the flow and transport of contaminants, whereas the material above the leak have little effect. Hence, the hydraulic properties of the materials below the 3-m (9.8-ft) depth were investigated whereas those above 3 m (9.8 ft) were not. The mean

hydraulic parameters of the five material types, derived from measurements by Schaap et al. (2003), are listed in Table 2.24. The average values of K_{sh}, θ_s, and θ_r are the arithmetic means, those of α and n are the geometric means, and that of K_{sv} is the harmonic mean, where K_{sh} is the value of K_s at the horizontal direction, and K_{sv} is the value of K_s at the vertical direction.

After identifying the different EHMs and their spatial distribution and measuring their local-scale hydraulic parameters, Material C was arbitrarily chosen as the reference EHM. The scaling factors of each parameter (Table 2.25) were calculated as described by Zhang et al. (2004b) using Table 2.24. The field-scale values of the hydraulic parameters were inversely estimated using the combined parameter scaling and inverse technique. Because parameters with low sensitivities are typically not identifiable in an inverse analysis without additional information, a sensitivity analysis, which is described below, was performed on the parameters of the reference EHM before optimization. After parameter scaling was completed, the number of unknowns was reduced by a factor equal to the number of material types (i.e., 5 in this case) from 35 to 7. Because $\tilde{\theta}_r$ was set as a constant, six of the seven parameters were then estimated inversely using UCODE and STOMP.

Table 2.24. The Average Values of the Hydraulic Parameters at Local Observation Scale (the average values of K_{sh}, θ_s, and θ_r were the arithmetic means and those of K_{sv}, α, and n, the geometric means) and the Number of Samples, N

Materials	**θ_s**	**K_{sh}**	**K_{sv}**	**α**	**n**	**θ_r**	**L**	**N**
	m^3m^{-3}	$m\ s^{-1}$	$m\ s^{-1}$	m^{-1}	-	m^3m^{-3}	-	-
A	0.317	1.02E-05	8.53E-06	3.45	4.20	0.0353	-0.222	3
B	0.348	8.11E-06	1.09E-06	5.25	2.29	0.0250	0.065	10
C	0.341	1.58E-05	4.24E-06	4.44	3.33	0.0367	0.835	18
D	0.337	4.21E-06	1.00E-06	4.17	2.49	0.0411	0.634	15
E	0.383	1.89E-05	8.70E-06	5.87	3.01	0.0288	0.558	5

Table 2.25. The Calculated Scaling Factors Reference to Material C Using the Local-Scale Parameter Values Given in Table 2.24

Materials	**θ_s**	**K_{sh}**	**K_{sv}**	**α**	**n**	**θ_r**	**L**
A	0.930	0.645	2.013	0.779	1.262	0.963	-0.266
B	1.022	0.515	0.257	1.182	0.688	0.682	0.078
C	1.000	1.000	1.000	1.000	1.000	1.000	1.000
D	0.990	0.267	0.237	0.941	0.748	1.120	0.759
E	1.125	1.199	2.054	1.323	0.904	0.785	0.668

Table 2.26 lists the upscaled FS hydraulic parameter values for the five materials. These results also show that the anisotropy coefficients (K_{sh}/K_{sv}) of the saturated hydraulic conductivity for the materials at the 299-E24-111 test site were between 4.0 and 24.7. These values are larger than those in Table 2.24, which were determined by taking the arithmetic and harmonic means using local-scale parameter values. The classic inverse technique estimates all the parameters simultaneously and hence is referred to as simultaneous inversion (SI). The SI approach is often used to estimate the field-scale hydraulic parameters. Simultaneously inverting a large number of parameters will encounter problems, such as

model divergence, extremely long simulation time, and non-uniqueness of results. For the injection tests at the 299-E24-111 site, there were 30 parameters, and attempts to simultaneously invert them using estimated values or even parameter values measured in the laboratory led to divergence of the problem and difficulty in obtaining results. If the solution converged, it would have taken about 2 months to complete the simulation. After a few attempts, the simultaneous inversion was found to converge only if 1) the parameter estimates obtained using CPSIT (Table 2.26) were used as the starting values, and 2) prior information was applied to θ_s, α, n, and L. Because these starting values were very close to the final values, the SI after CPSIT took only eight iterations to converge. Compared with CPSIT alone, the inclusion of simultaneous inversion decreased SSR by 26% from 3.24 to 2.40. The comparison of the parameter estimates using CPSIT and SI indicates that CPSIT treated a parameter of all the textures (e.g., K_{sh} for the five textures) as a whole whereas SI treated them as independent parameters. Consequently, some parameters (e.g., K_{sh} and K_{sv} for D and E) using SI may not be estimated well because of the lack of observations or very small changes within a material, whereas they may be well estimated using CPSIT.

Table 2.26. The Effective Parameters of Individual Materials Using the Combined Parameter Scaling and Inverse Technique

Materials	θ_s ($m^3\ m^{-3}$)	K_{sh} ($m\ s^{-1}$)	K_{sv} ($m\ s^{-1}$)	α (m^{-1})	n (-)	L (-)	θ_r ($m^3\ m^{-3}$)	K_{sh}/K_{sv}
A	0.321	9.88E-04	2.50E-04	2.683	4.366	-0.311	0.039	4.0
B	0.353	7.88E-04	3.18E-05	4.075	2.381	0.091	0.027	24.8
C	0.345	1.53E-03	1.24E-04	3.446	3.461	1.169	0.040	12.3
D	0.342	4.09E-04	2.94E-05	3.241	2.588	0.888	0.045	13.9
E	0.388	1.84E-03	2.55E-04	4.560	3.130	0.781	0.031	7.2

Figure 2.134 compares the simulated and observed water contents. Results show that the simulated water contents improved significantly after applying parameter scaling and inverse modeling. When the local-scale parameter values were used, the MSR of water content was 3.99×10^{-3} (Figure 2.134a). The water contents of most observations were significantly overestimated when the local-scale parameter values were used to simulate flow (Figure 2.134a). When the upscaled field-scale parameter values were used, the MSR value decreased by 83.2% to 6.71×10^{-4} (Figure 2.134b). The same experiment was simulated by Sisson and Lu (1984), Lu and Khaleel (1993), Smoot and Lu (1994), and Smoot and Williams (1996) using different types of models. Rockhold et al. (1999) conducted simulations of the same experiment using a conditional simulation and upscaling method. They reported a root-mean-squared-error in predicted water content of 0.0335 and 0.0280 for two simulations of flow in a single day. Simulations based on the proposed CPSIT and using the upscaled parameters produced an RMSE of 0.0259 for a period of 123 days. Thus, CPSIT is a robust and effective approach for upscaling flow parameters from the local-scale to field scale. Compared to the traditional simultaneous inversion, CPSIT has the advantages of 1) reducing the number of unknowns to be inversely estimated by a factor of the number of EHMs (M), 2) reducing the simulation time by a factor of about M^2, 3) requiring fewer observations and suffering less non-uniqueness problems, and 4) using both the local- and field-scale data to determine the FS hydraulic parameters.

A potential problem identified with the CPSIT is that any error in the local-scale parameter values may be compounded through the upscaling process to the field-scale results. This is because the local-scale parameter values are used to calculate scaling factors, and the values of the scaling factors are fixed during the upscaling process. This limitation can be minimized or virtually eliminated by taking more samples and perhaps using more advanced laboratory methods for characterization. Another potential limitation is that in a given simulation, the hydraulic properties of all the EHMs must be described using the same type of hydraulic function, e.g., either the Brooks and Corey (1966) or the van Genuchten (1980) model, but cannot be mixed. However, this should not limit the use of the model because a consistent approach for describing constitutive functions is typically used during flow modeling.

Whereas there has been significant progress in developing upscaling methodologies for flow parameters, very little has been done in terms of upscaling transport parameters, particularly for reactive transport. There is significant potential for the CPSIT method to be applied to field-scale transport problems for field-scale hydraulic properties and to the estimation of reactive transport properties. There is also a need for further evaluation of approaches for estimating scaling factors using readily available or easily measured data like grain-size distributions. The relationships between grain-size statistics and sorption parameters described in previous sections may very well form the basis of a method for scaling reactive transport parameters for heterogeneous sediments.

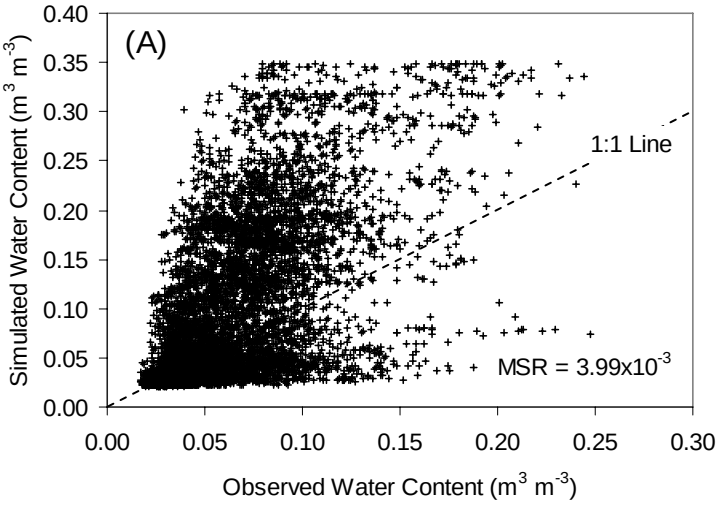

Figure 2.134. Comparisons of Simulated and Observed Water Contents of the 299-E24-111 Experiment (Sisson and Lu 1984) During Injections #2 (days 7 to 14), #6 (days 35 to 42), and #10 (days 63 to 123) using (A) the Local Scale and (B) the Field-Scale Values of Hydraulic Parameters. There were 10,583 observations.

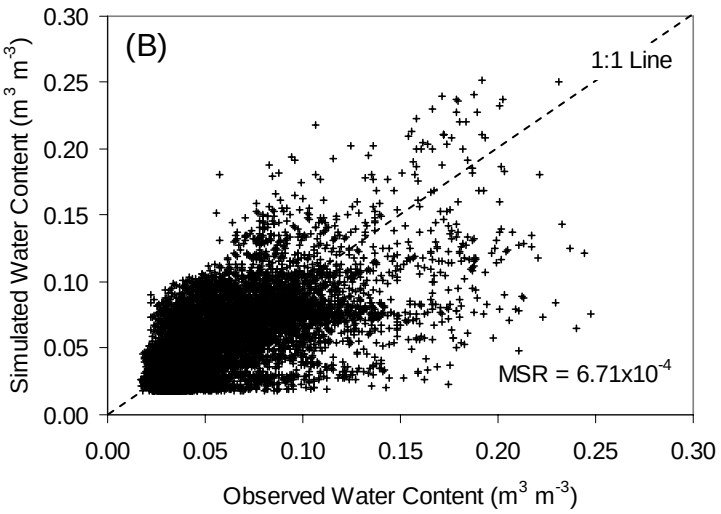

Figure 2.134 (Contd)

2.23.2 Synopsis and Implications

The synopsis of findings in the development of the parameter scaling inverse technique and their implications are as follows:

- Estimating the large number of parameters needed to describe unsaturated flow in heterogeneous anisotropic sediments remains a challenge because simultaneous inversion for too many parameters can lead to problems with non-identifiability and non-uniqueness. The non-uniqueness problem typically worsens as the number of parameters to be estimated becomes larger. This study was aimed at developing methods overcome these problems to allow inversion of field-scale flow problems.

- A two-step CPSIT approach is proposed that combines parameter scaling with inverse modeling to reduce the number of parameters to be estimated. The heterogeneous medium is conceptualized as multiple EHM. After the spatial distribution of soil textures and the local-scale parameter values of each of the EHMs are determined, scaling factors that relate the parameters of each EHM to a set of super parameters for a reference texture are determined. In the inversion step, the super parameters are optimized after which the values for each EHM are determined by a back transformation using the scale factors.

- The CPSIT approach has several advantages over the tradition simultaneous inversion for estimating parameters for a porous medium with M different than EHM. This approach: (1) reduces the number of unknowns to be inversely estimated by a factor of M and is therefore a novel way to reduce the parameter dimension, (2) reduces the simulation time by a factor of about M^2, (3) requires fewer observations and is less susceptible to non-uniqueness problems, and (4) uses both the local- and field-scale data to determine the field-scale hydraulic parameters.

2.24 A Comparison of Upscaling Methods for Hanford Sediments

Subsurface flow and transport in natural formations is strongly influenced by phenomena occurring at scales ranging from the molecular to kilometers. In unsaturated sediments, the multi-scale effects are compounded by non-linearities inherent to the transport processes, e.g., the capillary pressure-saturation [$P_c(S_e)$], relative permeability-saturation [$k_r(S_e)$], and saturation-dependent anisotropy [$C(S_e)$] functions. The simulation of fluid flow in these complex formations is of considerable practical importance for decisions related to remedial actions and long-term stewardship. Of particular interest in these formations are the embedded fine-scale features and how they impact field-scale flow and transport. The support scale of hydrogeologic properties is typically smaller than the scale of parameterization and resolution of corresponding hydrogeologic models. A realistic simulation of unsaturated flow sediments demands discretization of the domain, at least at the support scale, and the assignment of hydraulic properties to each grid cell. However, traditional vadose zone characterization methods provide parameters measured at the laboratory scale.

A more common approach is to define an equivalent homogeneous medium with upscaled flow properties and predict the mean flow behavior at the field scale using upscaled parameters. The goal of upscaling is to average the fine-scale properties such that flow simulations using the upscaled parameters provide a solution as close as possible to the one that could have been calculated in a high-resolution simulation of measured parameter values. The objective of this study was to compare different approaches for upscaling that are currently being used for unsaturated flow simulations. In this study, STOMP-W was used predict the field-scale temporal and spatial distribution of water content at the 299-E24-111 test site using three different upscaling approaches: 1) conditional simulation with similar media scaling (Rockhold et al. 1999), 2) the combined parameter scaling inverse modeling approach developed as part of the VZTFS that explicitly accounts for connectivity (Zhang et al. 2004b; Ward et al. 2006), and 3) stochastic macroscopic anisotropy based on a small perturbation solution (Yeh et al. 1985).

In the conditional simulation method of Rockhold et al. (1999), the water retention $P_c(S_e)$ function was described by the Brooks-Corey model with $\theta_r = 0$ (Brooks and Corey 1964). The unsaturated hydraulic conductivity function was predicted from K_s, $k_r(S_e)$ and the $P_c(S_e)$ parameters using the Burdine (1953) model. Similar media scaling was used to estimate hydraulic properties for the entire domain from a set of scale mean parameters and measured distributions of porosity and initial water content. Model parameters were essentially those used by Rockhold et al. (1999). In the CPSIT approach method, parameter scaling with inverse modeling was used to obtain the upscaled flow parameters (Zhang et al. 2004b, Ward et al. 2006). Model parameters were those reported by Ward et al. (2006). In the stochastic macroscopic anisotropy method of Yeh et al. (1985), the derivation of upscaled flow parameters and saturation-dependent anisotropy was based on a spectral solution to the linearized Richards' flow equation (Polmann 1990). Model parameters were those typically used to describe the gravelly sand H1 facies, the material most consistent with the designations used by Khaleel and Connelly (2004).

The subsurface domain was discretized into identical 3-D grids for the three different simulation approaches. The simulation domain was subdivided into a grid with a variable horizontal spacing step (Δx and Δy) and a constant vertical spacing step (Δz). The minimum values of Δx and Δy were 0.2 m, which were at the center of the domain around the injection point. The values of Δx and Δy increased by a factor of 1.3 as the distance from the center of the domain increased. The value of Δz was 0.3048 m. The numbers of nodes at x, y, z directions were 24, 24, and 40, respectively. The source was placed at the

center of the x-y plane and over a vertical range of 4.57 to 4.88 m. Parameters for the models were derived from the analysis of the recent injection experiments at the 299-E24-111 test site, but data for the 1980 injection tests at the 299-E24-111 test site reported in Sisson and Lu (1984) were used to test the models. The test of interest included two injections of 227 L of water used to test the injection system followed by another eleven injections with an average volume of 3790 L, each occurring over a 12-hour period. Of these injections, ten occurred at weekly intervals whereas the eleventh occurred 3 months later. Sisson and Lu (1984) monitored water-content distributions by neutron probe.

2.24.1 Results

Figure 2.135 compares the measured spatial distribution of soil water content with the simulated distributions along an east-west transect 54 days after the start of the 1980 injections. By this time, 34,338 L (9071 gal) of water had been injected. The measured water content shows an asymmetric distribution beneath the injection point (Figure 2.135a). This observation was similar to that for the FY 2000 and 2001 injection tests and is attributed to the layered anisotropic nature of the sediments at the site (Ward et al. 2002, 2003). An analysis of the 3-D distribution of the wetting front showed that water moved preferentially in a southeasterly direction. The largest changes in θ occurred in the southeastern quadrant (Ward et al. 2006). This preferential movement is evident in the increased lateral spreading along the east-west transect (Figure 2.135a) relative to that along the north-south transect. As the injection progressed, water eventually penetrated the coarse layer beneath the injection point and started

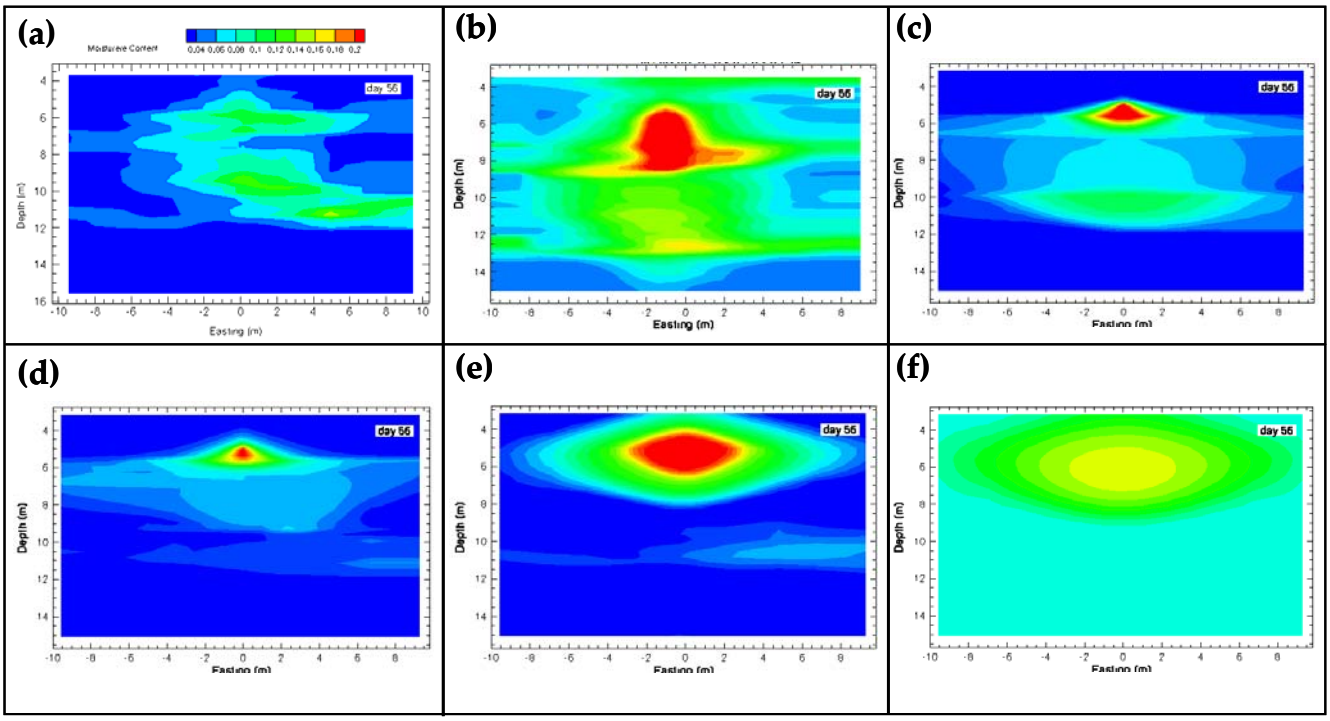

Figure 2.135. Observed and Predicted Water-Content Distributions Along an East-West Transect (a) Observed for the 1980 Injection Test of Sisson and Lu (1984), (b) Conditional Simulation, (c) Layered with Constant Anisotropy, (d) Heterogeneous with Connectivity Tensor, (e) Stochastic Perturbation with Measured Initial Water Content, (f) Stochastic Perturbation with Mean Initial Water Content

to spread in and above the deeper fine-textured layer. Injections were discontinued after adding 39,411 L (10,411 gal) of water. Up to this point, none of the injected water had penetrated the lower fine-textured layer. The absence of any significant accumulation of water in the domain suggested that water left the monitored domain by some other mechanism.

Figure 2.135b shows the water-content distribution predicted with the conditional simulation method of Rockhold et al. (1999) and a similar medium scaling approach along the east-west transect. The general shape of the simulated plume and the variations are caused by the larger architectural elements, particularly those caused by two fine-textured layers at 6 and 12 m (20 and 40 ft); these are in good agreement with the experimentally determined distributions. The north-south section of the plume showed considerably less spreading than the east-west transect and even appeared somewhat more symmetric. This profile also shows the effects of differences in local-scale anisotropy structures that result from the multi-scale heterogeneities such as those shown in Figure 1.1. However, the predicted amount of vertical movement of water through the lower fine-textured layer does not match the observed amount. This could be caused by either an under prediction of lateral movement in and above this layer or an underestimation of the bubbling pressure of the underlying coarse-textured layer. The upscaling procedure resulted in smoothing of the initial saturations that propagated through to the hydraulic property estimates and the resulting predictions of water content. Thus, the heterogeneities introduced by the resulting spatial structure of the parameter fields reflect the true heterogeneity only in a rough statistical sense with evidence of connectivity across scales. As a result, the effects of the fine-scale heterogeneities may not be adequately represented by this approach (Rockhold et al. 1999). Other investigators (Ferrand and Celia 1992) have shown that simple averaging of individual fine-scale relationships to derive effective relationships may not be adequate. The approach of Rockhold et al. (1999) yields reasonable estimates of the principle components of the K tensor at the scale of the model grid cells but may be limited in cases where a full K tensor is needed. Rockhold et al. (1999) reported root-mean-squared-error values for water content of 0.0335 and 0.0280 for two 1-day simulations of flow using this method. For the 133-day simulation in this study, the root-mean-squared-error for water-content predictions was 0.04.

Figure 2.135c shows the water-content distributions predicted with the CPSIT method using a five-layer perfect stratification model with anisotropy that is independent of saturation. The simulated plume reflects the effects of the larger architectural elements with lateral spreading in and around fine-textured layers at 6 and 12 m (20 and 40 ft). The intervening coarse-textured zone also shows less spreading, which is in general agreement with the experimentally determined distributions (Figure 2.135a). An east-west transect shows a dip in the lower fine-textured layer with increased movement of water to the east. However, the effects of the fine-scale heterogeneity are largely absent because the fine-scale effects are not included in a stratigraphic model based on a collection of five effective homogeneous media. Even though the detailed effects of fine-scale heterogeneities are not captured, the effects of the local connectivity and anisotropy structures are still reasonably well represented. This approach also represented the capability of the lower fine-textured layer to minimize flow into the underlying coarse layer. Using this approach reduced the mean squared residual error by 83.2% relative to the case when the local-scale parameters were used (Zhang et al. 2004b). The root-mean-squared-error for water-content predictions was only 0.0259, based on a 133-day simulation, compared to a value of 0.035 using the conditional simulation approach.

Figure 2.135d shows the water-content distributions predicted with the CPSIT method using a heterogeneous model with anisotropy and connectivity modeled via the tortuosity connectivity tensor. The five major facies were used to represent the domain as in the layered model, but these were assigned to individual grid cells based on the distribution of physical properties and initial water contents. Each cell was assigned a set of hydraulic properties with unique anisotropy and connectivity structures defined via the tortuosity-connectivity tensor. This approach captured the main features of the distribution as well as the finer scale effects and preferential movement. The local-scale capillary breaks that enhance lateral flow were also well represented. Despite using only five facies to describe the range of properties, this approach captured the effects of the multi-scale heterogeneities. In contrast to the conditional simulation and the perfectly stratified case, there was a smaller accumulation of water in the top 9 m (30 ft) and the intervening coarse layers between the two fine-textured layers. There was no evidence of penetration of water beneath the fine-textured layer at 12 m (40 ft). The smaller accumulation of moisture reflects improvement in connectivity and saturation-dependent anisotropy, which improved the prediction of water mass leaving the monitored domain. Using this approach reduced the mean squared residual error by 90.4% relative to the case when the local-scale parameters were used (Ward et al. 2006). The root-mean-squared-error for water-content predictions was only 0.0187 based on a 133-day simulation.

Figure 2.135e shows the predicted water contents along the east-west transect using the stochastic macroscopic anisotropy approach of Yeh et al. based on the Polmann (1990) model with measured initial water contents. The simulated plume matches the depth of penetration predicted with the method of Rockhold et al. (1999) and provides evidence of the underlying heterogeneity in the initial water-content distribution in the 10 to 12 m (33 to 40 ft) depth (Figure 2.135e). In contrast to the other methods, using the stochastic macroscopic anisotropy approach to represent $K(\psi)$ smoothes out the fine-scale details in θ and ψ distributions.

The effect of heterogeneity and anisotropy on lateral spreading was examined in more detail by calculating the time dependence of the spatial moments of the water plume. Ward et al. (2002, 2006) have shown that the time-dependence of 3-D spatial moments can be used to characterize an infiltrating water plume. Here the discussion is to the zeroth moment, which is related to the mass of water in the domain of interest. Figure 2.137 through Figure 2.140 compare the time dependence of the experimentally injected and recovered water mass with the simulated mass recovery based on the three different upscaling methods. In general, all of the methods show an increase in mass recovery over time, which also reflects the periodic injections.

Figure 2.137 compares the recovery predicted using the approach of Rockhold et al. (1999) based on a conditional simulation and similar media scaling. The simulated recovery also shows the characteristic saw-tooth pattern observed in the field data. The simulated recovery is also similar to the injected mass and observed recovery up until around 30 days. After 30 days, the simulated recovery was smaller than the injected mass but still higher than the measured recovery. This observation also suggests a much larger storage capacity in the porous medium and a lower predicted anisotropy in that simulated water contents were higher than the observed contents, and water was predicted to leave the system much later. The slower initial rate of water loss was caused by water leaving the monitored domain via vertical flow rather than laterally. The simulated recovery also shows the characteristic saw-tooth pattern observed, but unlike the field observation, the general slope is relatively constant, although it is somewhat less than that of the injection. Water loss by lateral movement predicted with the Rockhold et al. (1999) method started around 65 days.

Figure 2.138 compares the recovery predicted using the perfectly stratified CPSIT model with the experimental observations. The simulated recovery also shows the characteristic saw-tooth pattern observed, but unlike the field observation, the general slope is relatively constant, although it is somewhat less than that of the injection. The predicted and measured curves became indistinguishable after around 40 days with a rapid decline starting around 65 days as water exited the monitored domain. Figure 2.136 shows a similar plot for the heterogeneous CPIT model, also with a tortuosity-connectivity tensor. The response is almost identical to the perfectly stratified case except that the decline in recovered mass starts about 5 days earlier. In both cases, the rate of decline is very similar to the measured rate. The lower almost linear slope in the models with the connectivity tensor suggests that the overall storage with the current parameterization may be larger than the experimental system or that the connectivity described by the model may be larger than that in the field, leading to more lateral flow. Figure 2.139 shows a similar plot for the stochastic approach based on the measured initial water-content distribution. The measured mass injected and simulated mass recoveries were strongly correlated. An important difference between the stochastic approach and the previously discussed approaches, however, is the smaller predicted loss of water mass from the system. Figure 2.139 shows that the recovered mass reached a plateau that is essentially equivalent to the injected mass when the measured initial water content is used. However, use of an average water content derived from a steady-state simulation at a fixed recharged rate results in larger differences (Figure 2.140).

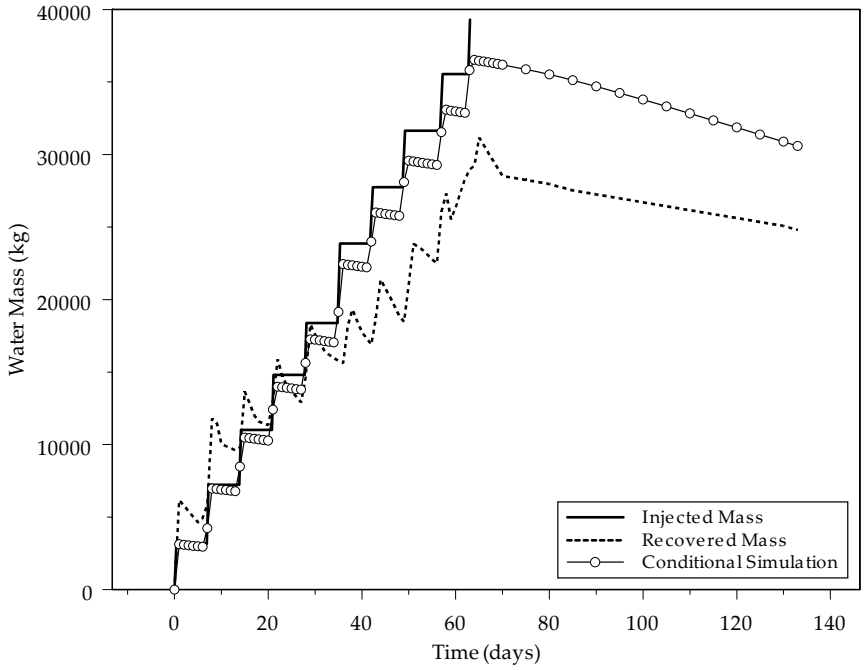

Figure 2.136. Comparison of Experimentally Injected and Recovered Water Mass With Predicted Recovery Based on a Conditional Simulation with Similar Media Scaling

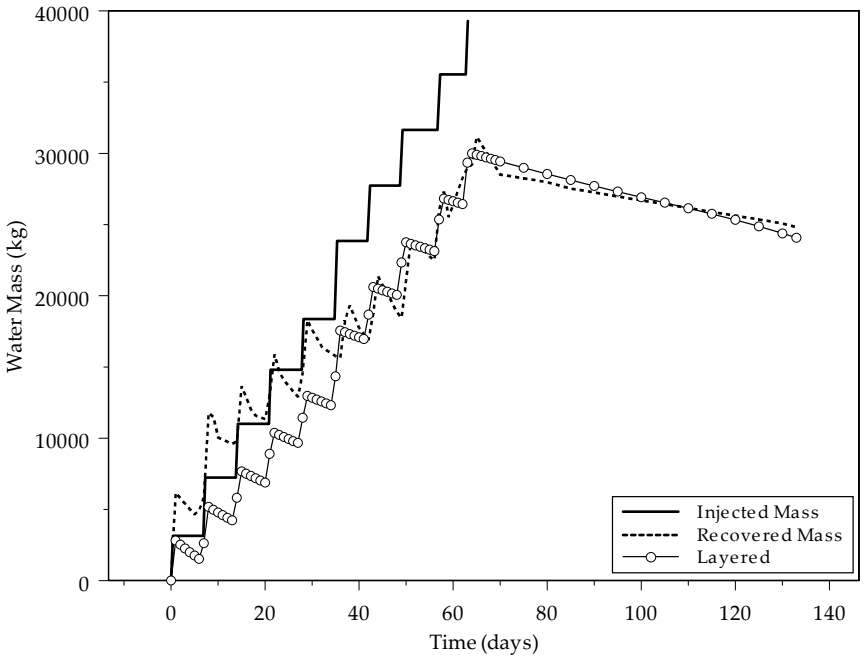

Figure 2.137. Comparison of the Experimentally Injected and Recovered Water Mass with Predicted Recovery Based on Perfect Stratification with Constant Anisotropy

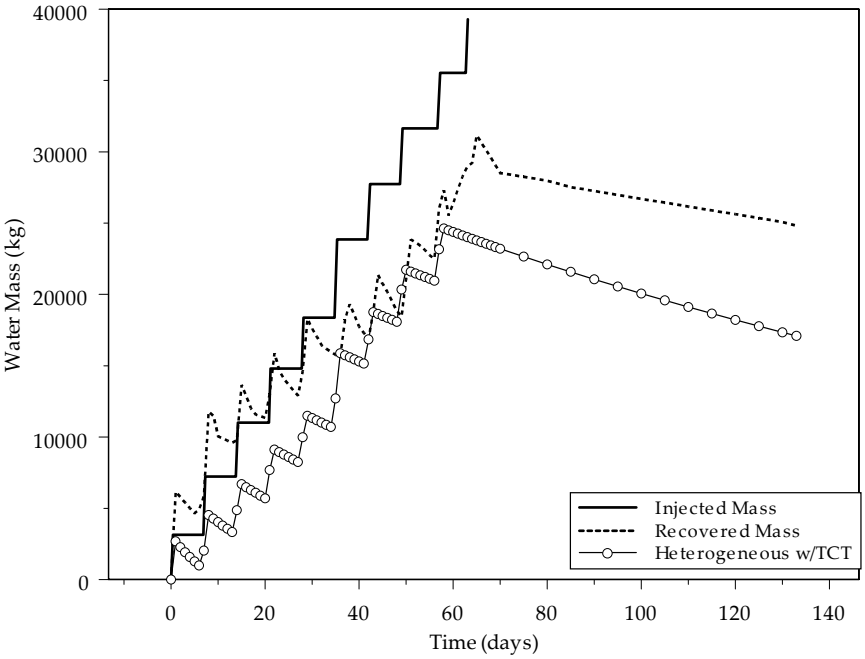

Figure 2.138. Comparison of Experimentally Injected and Recovered Water Mass With Predicted Recovery Based on a Heterogeneous Model with variable Connectivity

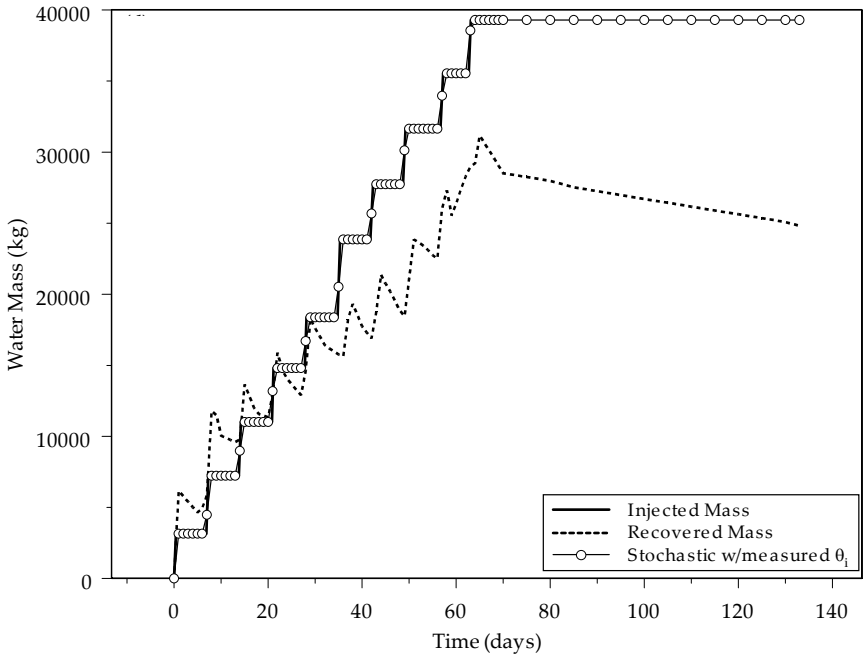

Figure 2.139. Comparison of Experimentally Injected and Recovered Water Mass With Predicted Recovery Based on Stochastic Upscaling and the Measured Initial Moisture Content

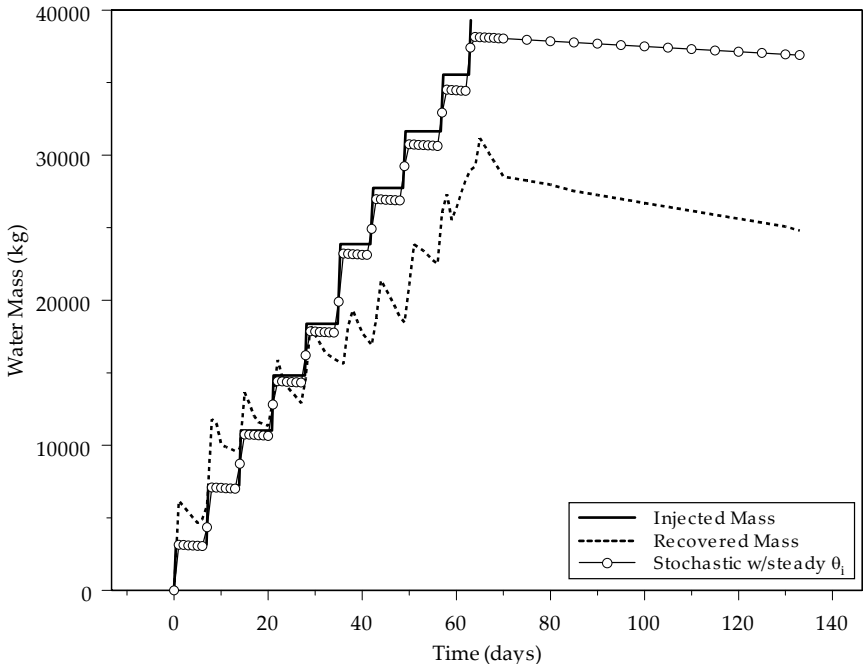

Figure 2.140. Comparison of Experimentally Injected and Recovered Water Mass With Predicted Recovery Based on Stochastic Upscaling and a Uniform Initial Moisture Content

2.24.2 Synopsis and Implications

The synopsis of findings in the comparison of upscaling methods for Hanford sediments and their implications are as follows:

- Three different upscaling approaches were compared: 1) conditional simulation with similar media scaling, 2) combined parameter scaling inverse modeling that explicitly accounts for connectivity, and 3) stochastic macroscopic anisotropy based on the small perturbation solution. The methods all converged to different results with respect to moisture distributions and mass recovery. Methods that accounted for fine-scale heterogeneity and the connectivity of regions of similar conductivities matched both spatial and temporal distributions of water mass.

- The implications of this study are significant. Accounting for small-scale heterogeneities and the connectivity of regions of similar conductivity in highly heterogeneous anisotropic sediments is important for matching the impacts of fine-scale features on lateral spreading of moisture and contaminants. The final selection of a parameterization and simulation method is controlled to some extent by the intended use of the results. If the end use is to determine water or contaminant flux to a compliance plane, the overall flow behavior is more important than detailed flow paths resulting from small-scale heterogeneities, and all three methods may be sufficient. If the interest is in the distribution of moisture and contaminants over time, then the other methods that account for the fine-scale heterogeneities and local anisotropy structures may be more appropriate to use.

3.0 Conclusions

A series of field experiments were conducted at the Hanford Site, near Richland, Washington, from FY 2000 through FY 2003 at two different locations to develop data sets to test models of flow and transport in the vadose zone. The field studies were also done to investigate the use of advanced monitoring techniques for evaluating flow-and-transport mechanisms and delineating contaminant plumes in the vadose zone at the Hanford Site. The studies were conducted as part of the Groundwater/Vadose Zone Integration Project Science and Technology Project, now known as the Remediation and Closure Science Project, managed by PNNL and supported by DOE, Richland Operations Office. This report summarizes the key findings from the field studies and demonstrates how data collected from these studies are being used to improve conceptual models and develop numerical models of flow and transport in Hanford's vadose zone. Results from the field studies and associated analysis have appeared in more than 50 publications generated over the past 4 years. These publications include test plans and status reports in addition to numerous technical notes and papers.

Two major field campaigns were performed, one at a well injection test site previously developed and tested and a second at clastic dike test facility. Both field studies have resulted in field-scale transport parameters for Hanford conditions useful for improving predictions of subsurface flow and transport at the Hanford Site. In addition, advanced geophysical methods, including HRR measurements, were successfully tested and are now being deployed at Hanford for subsurface investigations and tank retrieval detection. The most useful information gained from these studies has been a better understanding of the vadose zone, specifically related to the impact of small-scale stratigraphic features (e.g., sediment layering) on water flow and contaminant transport. Conceptual models have been developed that take into account the lateral spreading of water and contaminants observed in the field studies. Numerical models of unsaturated flow and transport have been revised to account for lateral spreading of subsurface contaminant plumes.

The key results from these studies include:

1) Greater understanding of the complexity of plume migration in the vadose zone at Hanford. Fine-scale geologic heterogeneities, including grain fabric and lamination, were observed to have a strong effect on the large-scale behavior of contaminant plumes, primarily through increased lateral spreading resulting from anisotropy.

2) Observations of anion exclusion in Hanford sediments. Anion exclusion is a mechanism by which negatively charged ions are repelled from the surfaces of negatively charged soil particles, thereby increasing their velocity. Thus, the travel time of ions like pertechnetate, the stable form of ^{99}Tc found in oxidized environments, may decrease over that of unsaturated water flow.

3) Development of large datasets of coupled flow and transport behavior for both conservative and reactive solutes that reflect the complex interplay of physical, hydrologic, and geochemical heterogeneities in very complex flow fields that are needed for model calibration.

4) Development of a new and robust model for describing saturation-dependent anisotropy in strongly heterogeneous soils. This model is based on the concept that key pore geometrical factors, such as shape, size distribution, and tortuosity, all interact to produce what is effectively a directional-

dependent pore connectivity. This tensorial connectivity gives rise to permeability contrasts that are direction dependent. The concept of a connectivity tensor has been incorporated into PNNL's STOMP simulator, which is currently being used to understand plume behavior at a number of sites where lateral spreading may have dominated waste migration.

5) Development of inverse modeling capabilities for time-dependent, subsurface, variably saturated flow using an automated optimization algorithm. This was accomplished by coupling STOMP with the non-linear parameter estimation code UCODE.

6) Development of a parameter scaling methodology for incorporating the effects of layering into model parameterization. This technique allows layered soils to be described by a single set of reference parameters and scale factors and has made it possible, for the first time, to invert field-scale unsaturated flow in layered soils.

7) Development of a CPSIT technique for calculating field-scale hydraulic parameters that are needed to describe subsurface flow in heterogeneous soils and sediments. Applying this technique to the analysis of the injection test significantly reduced the simulation time needed for inverse modeling and resulted in a notable improvement in predictions of infiltration and redistribution of water in the subsurface.

8) Development of inverse modeling capabilities for time-dependent, subsurface, reactive transport with transient flow fields using an automated optimization algorithm. This was accomplished by coupling the reactive transport code, CRUNCH, with the non-linear parameter estimation code UCODE. Currently, four reactive transport parameters, including cation exchange capacity, solid solution ratio, kinetic rate constant for mineral reaction, and the exponent representing species dependence on the far-from-equilibrium reaction rate, can be estimated with CRUNCH-UCODE.

9) Development of two new upscaling approaches for estimating field-scale hydraulic properties. The first approach falls into the category of volume averaging or homogenization techniques and estimates the plume-scale hydraulic properties from temporal differences in the spatial moments of an infiltrating water plume. The second approach combines the newly developed parameter scaling, which overcomes the problem of scaling vertical heterogeneity with inverse modeling to estimate field-scale parameters that are implicitly anisotropic.

10) Development of pedotransfer functions for describing fine-scale hydrologic and geochemical heterogeneity and for incorporating this heterogeneity into reactive transport models. This approach is based on grain-size statistics and can be used to describe heterogeneity in hydraulic properties and sorption properties such as the cation exchange capacity and the specific surface area of Hanford sediments.

11) Confirmation of recharge estimates needed for transport calculations by evaluating long-term drainage records. Water fluxmeters and lysimeters provide both short- and long-term estimates of recharge at waste sites, particularly those that have been kept free of vegetation.

12) Demonstration of advanced vadose-zone monitoring techniques for providing high-resolution information of the subsurface to support plume delineation and detailed information on the subtle changes in lithology and bedding surfaces. HRR is now being used for detecting saline plumes at several waste sites at Hanford.

4.0 Related Publications

1. DePaolo DJ, ME Conrad, K Maher, and GW Gee. 2004. "Evaporation effects on O and H isotopes in deep vadose zone pore fluids at Hanford, Washington: Implications for recharge and horizontal fluid movement." *Vadose Zone J.* 3:220–232.
2. Fayer MJ, and GW Gee. 2004. "Soil Water Measurement by Neutron Scattering." Paper 505 In *Encyclopedia of Soils in the Environment.* (Ed D Hillel) pp. 6-12, Elsevier Ltd., Oxford, U.K.
3. Freshley MD, AL Bunn, GW Gee, TJ Gilmore, CT Kincaid, RE Peterson, AL Ward, SB Yabusaki, and JM Zachara. 2002. *Groundwater Protection Program Science and Technology Summary Description.* PNNL-14092, Pacific Northwest National Laboratory, Richland, WA.
4. Gee GW, AL Ward, TG Caldwell, and JC Ritter. 2002. "A vadose-zone water fluxmeter with divergence control." *Water Resour. Res. 38 (8)* 1141, doi:10.1029/2001WR000816.
5. Gee GW, AL Ward, ZF Zhang and A Anandacoomaraswamy. 2004. "Use of Water Fluxmeters to Measure Drainage." pp. 321–331. *In: Drainage VIII. Proceedings of the 8th International Drainage Symposium*. RA Cooke (ed), Mar. 21–24, Sacramento, CA. ASAE, St. Joseph, MI.
6. Gee GW, AL Ward, ZF Zhang, GS Campbell, and J Mathison. 2002. The influence of hydraulic non-equilibrium on pressure plate data. *Vadose Zone J*. 1:172–178.
7. Gee GW, and AL Ward. 2001. "Hanford vadose zone transport field studies." Page 9. *In: WM 01 Conference Proceedings*, Feb. 25–March 2, 2001. Tucson, Arizona (electronic only). url address: www.wmsym.org. U. of Arizona Press, Tucson, AZ.
8. Gee GW, and AL Ward. 2001. *Vadose Zone Transport Field Study: Status Report.* PNNL-13679, Pacific Northwest National Laboratory, Richland, WA.
9. Gee GW, and AL Ward. 2002. "Estimation of Net Infiltration of Meteoric Water at the SX Tank Farm." Appendix D.8.2, pp. D356–D365. *In:* AJ Knepp. 2002. *Field Investigation Report for Waste Management Area S-SX*. RPP-7884, Rev. 0, CH2M HILL Hanford Group, Inc., Richland, WA.
10. Gee GW, and AL Ward. 2002. "Hanford Vadose Zone Transport Field Experiments." Appendix D.8.1, p. D347–D355. *In:* AJ Knepp. 2002. *Field Investigation Report for Waste Management Area S-SX*. RPP-7884, Rev. 0, CH2M HILL Hanford Group, Inc., Richland, WA.
11. Gee GW, and AL Ward. 2002. "Predicting deep drainage using soil hydraulic properties and soil texture data." *In: Transaction of the 17th World Congress of Soil Science*. Bangkok, Thailand, August 2002, http://www.ldd.go.th/Wcss2002/pages/SA/Sym_04.htm (electronic).
12. Gee GW, and AL Ward. 2002. "Vadose Zone Transport Field Studies." Sec. 7.3.2, pp. 7.25–7.26. *In: Hanford Site Environmental Report 2001*. PNNL-13910, Pacific Northwest National Laboratory, Richland, WA.
13. Gee GW, and AL Ward. 2002. "Vadose Zone Transport Field Studies." Sec. 3.3.2 pp. 3.57–3.59. *In: Hanford Site Groundwater Monitoring for Fiscal Year 2001*. PNNL-13788, Pacific Northwest National Laboratory, Richland, WA.

14. Gee GW, and AL Ward. 2003. "Vapor transport in dry soils." pp. 1012–1016. *In: Encyclopedia of Water Science*. BA Stewart and TA Howell (eds.), Marcel Dekker, New York.

15. Gee GW, PD Meyer, and AL Ward. 2004. "Nuclear Waste Disposal." In *Encyclopedia of Soils in the Environment* (Ed D Hillel) pp. 56-63, Elsevier Ltd., Oxford, U.K.

16. Gee GW, ZF Zhang, and AL Ward. 2003. "A modified vadose-zone fluxmeter with solution collection capability." *Vadose Zone J.* 2:627–632.

17. Gee GW, ZF Zhang, and AL Ward. 2004. "Vadose Zone Water Fluxmeter Improvements and Tests." Sec. 3.3.2, pp. 3.3–4, 5, 13. *In: Hanford Site Groundwater Monitoring for Fiscal Year 2003.* PNNL-14548, Pacific Northwest National Laboratory, Richland, WA.

18. Gee GW. 2004. "Texture." In *Encyclopedia of Soils in the Environment.* (Ed D Hillel) pp. 149-155, Elsevier Ltd., Oxford, U.K.

19. Gee GW, and AL Ward. 2002. *Predicting Deep Drainage Using Soil Hydraulic Properties and Soil Texture Data*. Sec. 7.3.6, p. 7.31-7.33. *In:* Hanford Site Environmental Report 2001. PNNL-13910, Pacific Northwest National Laboratory, Richland, WA.

20. Gee GW. 2005. Comments on "Improvements to Measuring Water Flux in the Vadose Zone" (K.C. Masarik, J.M. Norman, K.R. Brye, and J.M. Baker; J. Environ. Qual. 33:1152–1158). *J. Environ. Qual.* 34(2):408-409.

21. Gee GW, JM Keller, and AL Ward. 2005. "Measurement and prediction of deep drainage from bare sediments at a semiarid site." *Vadose Zone J.* 4(1):32-40.

22. Gee GW, ZF Zhang, SW Tyler, WH Albright, and MJ Singleton. 2005. "Chloride mass balance: Cautions in predicting increased recharge rates." *Vadose Zone J.* 4(1):72-78.

23. Hoversten GM. 2000. *Preliminary Report. Surface to Borehole and Surface Electromagnetic Surveys at the Hanford Leak Experiment.* PNNL-13793. Pacific Northwest National Laboratory, Richland, WA.

24. Hunt AG, and G W Gee. 2002. "Application of critical path analysis to fractal porous media: Comparison with examples from the Hanford Site." *Adv. Water Resour.* 25(2): 129-146.

25. Hunt AG, and GW Gee. 2002. "Water-retention estimates using continuum percolation theory: Test of Hanford Site soils." *Vadose Zone J.* 1:252–260.

26. Hunt AG, and GW Gee. 2002. "Water retention of fractal soil models using continuum percolation theory: Tests of Hanford Site Soils." *Vadose Zone J.* 1:252–260.

27. Hunt AG, and GW Gee. 2003. "Wet-end deviations from scaling of the water retention characteristics of fractal porous media." *Vadose Zone J.* 2:759–765.

28. Last GV, and TG Caldwell. 2001. *Core Sampling in Support of the VZTFS*. PNNL-13454, Pacific Northwest National Laboratory, Richland, WA.

29. Last, GV, TG Caldwell, and AT Owen. 2001. *Sampling of Borehole WL-3A through 12 in support of the VZTFS.* PNNL-13631, Pacific Northwest National Laboratory, Richland, WA.

30. Majer EL, JE Peterson, KH Williams, and TM Daley. 2000. *High Resolution Imaging of Vadose Zone Transport Using Crosswell Radar and Seismic Methods*. PNNL-13791, Pacific Northwest National Laboratory, Richland, WA.

31. Murray CJ, DG Horton, AL Ward, and GW Gee. 2002. "Hydrogeologic Influence of Clastic Dikes on Vadose Zone Transport." Sec. 7.3.3, pp. 7.26–7.29. *In: Hanford Site Environmental Report 2001*. PNNL-13910. Pacific Northwest National Laboratory, Richland, Washington.

32. Murray CJ, DG Horton, AL Ward, and GW Gee. 2002. "Hydrogeologic Influence of Clastic Dikes on Vadose Zone Transport." Sec. 3.3.4, pp. 3.64–3.67, 3.82–3.86. *In: Hanford Site Groundwater Monitoring for Fiscal Year 2001*. PNNL-13788, Pacific Northwest National Laboratory, Richland, WA.

33. Raats PAC, ZF Zhang, AL Ward, and GW Gee. 2004. "The relative connectivity-tortuosity tensor for conduction of water in anisotropic unsaturated soils." *Vadose Zone J*. 3:1471-1478.

34. Ramirez A, W Daily, and A Binley. 2001. *Final Report- FY 2001 for the 200 E. Vadose Zone Test Site, Hanford, Washington.* PNNL-13794, Pacific Northwest National Laboratory, Richland, WA.

35. Schapp MG, PG Shouse, and PD Meyer. 2003. *Laboratory Measurements of the Unsaturated Hydraulic Properties at the Vadose Zone Transport Field Study Site.* PNNL-14284, Pacific Northwest National Laboratory, Richland, WA.

36. Singleton MJ, EL Sonnenthal, ME Conrad, DJ DePaolo, and GW Gee. 2004. "Multiphase reactive transport of stable isotope fractionation in unsaturated zone pore water and vapor: Application to seasonal infiltration events at the Hanford Site, WA." *Vadose Zone J*. 3:775-785.

37. Sisson JB, GW Gee, JM Hubbell, WL Bratton, JC Ritter, AL Ward, and TG Caldwell. 2002. "Advances in tensiometry for long-term monitoring of soil water pressures." *Vadose Zone J*. 1:310–315.

38. Ward AL, and GW Gee. 2000. *Vadose Zone Transport Field Study: Detailed Test Plan for Simulated Leak Tests.* PNNL-13263. Pacific Northwest National Laboratory, Richland, WA.

39. Ward AL, and GW Gee. 2001. *Vadose Zone Transport Field Study: FY2001 Test Plan.* PNNL-13451, Rev. 1, Pacific Northwest National Laboratory, Richland, WA.

40. Ward AL, and GW Gee. 2002. "Effects of Accelerated Movement Due to Surface Tension and Contact Angle Effects in Hypersaline Fluids Transported in Unsaturated Sediments." Appendix D.8.3, pp. D366–D368. *In:* AJ Knepp. 2002. *Field Investigation Report for Waste Management Area S-SX*. RPP-7884, Rev. 0, CH2M HILL Hanford Group, Inc., Richland, WA.

41. Ward AL, and GW Gee. 2002. *Vadose Zone Transport Field Study: FY 2002 Test Plan.* PNNL-13857, Pacific Northwest National Laboratory, Richland, WA.

42. Ward AL, and GW Gee. 2003. *Vadose Zone Transport Field Study: FY 2003 Test Plan.* PNNL-14240. Pacific Northwest National Laboratory, Richland, WA.

43. Ward AL, CJ Murray, G W Gee, Y Xie, and ZF Zhang. 2004. "Impact of Clastic Dikes on Vadose Zone Flow." Sec. 3.3.7, pp. 3.3–10. *In: Hanford Site Groundwater Monitoring for Fiscal Year 2003.* PNNL-14548, Pacific Northwest National Laboratory, Richland, WA.

44. Ward AL, GW Gee, and ZF Zhang. 2002. "Hydrologic Tests of Lateral Flow and Transport in the Hanford Vadose Zone." Appendix D.4.1 (D-223–D233). *In: Field Investigation Report for Waste Management Area B-BX-BY.* AJ Knepp (ed), RPP-10098, Rev 0, CH2MHILL Hanford Group, Inc., Richland, WA.

45. Ward AL, GW Gee, ZF Zhang, and JM Keller. 2002. *Vadose Zone Transport Field Study: FY 2002 Status Report.* PNNL 14150, Pacific Northwest National Laboratory, Richland, WA.

46. Ward AL, TG Caldwell, and GW Gee. 2000. *Vadose Zone Transport Field Study: Soil Water Content Distributions by Neutron Moderation*. PNNL-13795, Richland, WA.

47. Ward AL, ZF Zhang, and GW Gee. 2005. "Upscaling Unsaturated Hydraulic Parameters for Flow through Heterogeneous Anisotropic Sediments." *Adv. Water Resour.* (In Press).

48. Zhang ZF, AL Ward, and GW Gee. 2002. A Parameter Scaling Concept for Estimating Field-Scale Hydraulic Functions of Layered Soils. p. 103–107. *In: Proceedings of the 2002 International Groundwater Symposium,* AN Findkakis (ed.), Lawrence Berkeley National Laboratory, Berkeley, CA, March 2002.

49. Zhang ZF, AL Ward, and GW Gee. 2002. *Estimating Field-Scale Hydraulic Parameters Using a Combination of Parameter Scaling and Inverse Methods.* PNNL-14109, Pacific Northwest National Laboratory, Richland, WA.

50. Zhang ZF, AL Ward, and GW Gee. 2003. "A Tensorial Connectivity-Tortuosity Concept to Describe the Unsaturated Hydraulic Properties of Anisotropic Soils." *Vadose Zone J.* 2:313–321.

51. Zhang ZF, AL Ward, and GW Gee. 2003. "Estimating soil hydraulic parameters of a field drainage experiment using inverse techniques." *Vadose Zone J.* 2:201-211.

52. Zhang ZF, AL Ward, and GW Gee. 2004. "A parameter scaling concept for estimating filed-scale hydraulic functions of layered soils." *J. Hydraulic Res.* 42:93-103.

53. Zhang ZF, AL Ward, GW Gee. 2004. "A combined parameter scaling and inverse technique to upscale the unsaturated hydraulic parameters for heterogeneous soils." *Water Resour. Res.* 40(8): Art. No. W08306.

5.0 Conference Presentations

1. Fayer MJ, CJ Murray, DG Horton, PD Long, GW Gee, AL Ward, J Wilson, and W Clement. 2000. "Hydrogeological Measurements and Hydrofacies Models of Clastic Dikes at the Hanford Site, Southcentral Washington." *Eos Trans. AGU, 81* (48), Fall Meet. Suppl., Abstract H51C-07.

2. Fink JB, AL Ward, and GW Gee. 2001. "Vadose Zone Injection Monitoring with Electrical Geophysics Using Steel Casings as Electrodes." *Eos Trans. AGU, 82*(47), Fall Meet. Suppl., Abstract H31C-0246.

3. Fink JB, MT Levitt, and GW Gee. 2002. "Steel Casing Resistivity Technology (SCRT): Innovative Applications of Electrical Methods for Buried Tank Leak Detection." *Eos Trans. AGU, 82*(47), Fall Meet. Suppl., Abstract H61A-0749.

4. Freedman V, AL Ward, and GW Gee. 2004. "Estimating Transport Parameters for Field-Scale Cation Migration in the Vadose Zone." *SSSA Annual Meeting Abstracts*, Oct. 31–Nov. 4, Seattle, WA.

5. Gee GW, and AL Ward. 2000. "Contaminant Plume Studies in the Vadose Zone at the Department of Energy's Hanford Site, Richland, Washington." *Eos Trans. AGU, 81* (48), Fall Meet. Suppl., Abstract H51C-05.

6. Hunt AG, and GW Gee. 2001. "Critical Path Analysis of the Hydraulic Conductivity of Fractal Soils at the US DOE Hanford Site." *Eos Trans. AGU, 82*(47), Fall Meet. Suppl., Abstract H21F-12.

7. Kapsi KA, GW Gee, and CS Simmons. 2001. "Water-Budget Analysis of Landfill Covers Using Simplified Models." *Eos Trans. AGU, 82*(47), Fall Meet. Suppl., Abstract H12F-117.

8. Keller JM, AL Ward, ZF Zhang, and GW Gee. 2003. "A Method for Correcting Cable Length Effects on TDR-measured Electrical Conductivity." *SSSA Annual Meeting*, Denver, CO, November 2-6.

9. Keller JM, AL Ward, ZF Zhang, and GW Gee. 2003. "A Method For Correcting Diurnal Fluctuations In Electrical Conductivity Inferred From TDR Measurements In The Field." *Unsaturated Zone Interest Group Meeting*, Richland, Washington, October 8-10.

10. Keller JM, AL Ward, ZF Zhang, and GW Gee. 2004. "Predicting Soil-Water Retention Functions of Hanford Soils From Particle Size Distribution Data." *SSSA Annual Meeting*, Seattle, WA, November 1-4.

11. Kowalsky MB, SA Finsterle, JE Peterson, S Hubbard, Y Rubin, EL Majer, AL Ward, and GW Gee. 2004. "Estimating Field-Scale Soil Hydraulic Properties Through Joint Inversion of Cross-Borehole GPR Travel Times And Hydrological Measurements." Paper No. 128-4.

12. Kowalsky MB, SA Finsterle, JE Peterson, Y Rubin, EL Majer, AL Ward, and GW Gee. 2004. "Estimating field-scale soil hydraulic properties and petrophysical models through joint

GPR/hydrological measurement inversion." *Eos Trans. AGU, 85*(47), Fall Meet. Suppl., Abstract H23A-1101.

13. Mann FM, and GW Gee. 2000. "Radioactive and Mixed Waste in the Vadose Zone I." *Eos Trans. AGU, 81* (48), Fall Meet. Suppl.

14. Murray CJ, AL Ward, JL Wilson, PE Long, BJ Lechler, WP Clement, PK Kannberg, and GW Gee. 2001. "The Effects of Clastic Dikes on Vadose Zone Transport at the Hanford Site, Southcentral Washington." *Eos Trans. AGU, 82*(47), Fall Meet. Suppl., Abstract H52A-0370.

15. Myers DA, and GW Gee. 2000. "Moisture Distribution in Hanford's SX Tank Farm." *Eos Trans.* AGU, 81 (48) Fall Meet. Suppl., Abstract H51C-03.

16. Pervizpour M., C Ochola, X Mo, H Moo-Young, and AL Ward. 2004. "A centrifuge study of unsaturated flow and contaminant transport in anisotropic heterogeneous media." *SSSA Annual Meeting Abstracts*, Oct. 31–Nov. 4, Seattle, WA.

17. Rector DR, ML Stewart, and AL Ward. 2004. "A Study of the Effect of Microstructure on the Anisotropy of Hydraulic Conductivity Using the Lattice-Boltzmann Method." *SSSA Annual Meeting Abstracts*, Oct. 31–Nov. 4, Seattle, WA.

18. Rucker DF, JB Fink, DR Glaser, GW Gee, and MK Sweeney. 2004. "Comprehensive Geophysical Investigation over a Former Radioactive Waste Site, Hanford, Washington." *Eos Trans. AGU, 85*(47), Fall Meet. Suppl., Abstract H23A-1115.

19. Selker JA, Ward, M Niemet, N Weisbrod, and C Cooper. 2000. "Field Observations of Transport of High Concentration Solutions in Unsaturated Sedimentary Materials." *Eos Trans. AGU, 81* (48), Fall Meet. Suppl., Abstract H61A-01.

20. Sisson JB, and GW Gee. 2001. "Estimating Recharge from Soil Water Tension Data." *Eos Trans. AGU, 82*(47), Fall Meet. Suppl., Abstract H32G-08.

21. Sisson, JB, and GW Gee. 2000. "Water Potentials in Sands and Gravels at Hanford, Washington." *Eos Trans. AGU, 81* (48), Fall Meet. Suppl., Abstract H51C-06.

22. Ward AL, MD White, GW Gee, and J Selker. 2000. "Incorporating the Effect of Fluid Constitution on Surface Tension and Equilibrium Contact Angle into Predictions of Hypersaline Fluid Migration in Unsaturated Soils." *Eos Trans. AGU, 81* (48), Fall Meet. Suppl., Abstract H61A-02.

23. Ward AL, JM Keller, ZF Zhang, and GW Gee. 2004. "Hydrostratigraphic Characterization Using High-resolution Borehole Moisture Logs and Grain-size Distribution Statistics." *Eos Trans. AGU, 85*(47), Fall Meet. Suppl., Abstract H23A-1110.

24. Ward AL, and ZF Zhang. 2005. "Upscaling unsaturated hydraulic parameters for flow through heterogeneous anisotropic sediments: A comparison of two methods." *European Geosciences Union, Geophysical Research Abstracts, Vol. 7*, 05898, EGU05-A-05898.

25. Ward AL, MD White, G Gee, and J Selker. 2000. "Incorporating the Effect of Fluid Constitution on Surface Tension and Equilibrium Contact Angle into Predictions on Hypersaline Fluid Migration in Unsaturated Soils." EOS p. F411. *American Geophysical Union*, Washington, D. C.

26. Ward AL, MD White, G Gee, and J Selker. 2000. "Incorporating the Effect of Fluid Constitution on Surface Tension and Equilibrium Contact Angle into Predictions on Hypersaline Fluid Migration in Unsaturated Soils." EOS p. F411. *American Geophysical Union*, Washington, D. C.

27. Ward AL, ZF Zhang, and GW Gee. 2004. "A Comparison of State-dependent Anisotropy Models for Strongly Heterogenous Porous Media." *SSSA Annual Meeting Abstracts*, Oct. 31–Nov. 4, Seattle, WA.

28. Ward AL, GW Gee, and ZF Zhang. 2001. "The Effect of Fluid Properties on Field-Scale Anion Transport During Intermittent Unsaturated Flow." *Eos Trans. AGU, 82*(47), Fall Meet. Suppl., Abstract H31C-0265.

29. White MD, and AL Ward. 2001. "Numerical Investigations of Vadose Zone Transport of Saturated Sodium Thiosulfate Solutions." *Eos Trans. AGU, 82*(47), Fall Meet. Suppl., Abstract H12F-06.

30. Yabusaki S, FM Mann, GW Gee, and J Zachara. 2000. "Radioactive and Mixed Waste in the Vadose Zone III." *Eos Trans. AGU, 81* (48), Fall Meet. Suppl., Abstract H61A-07.

31. Zhang ZF, AL Ward, GW Gee, MD White, and JM Keller. 2004. "Quantifying Saturation-Dependent Anisotropy." *Eos Trans. AGU*, 85(47), Fall Meet. Suppl., Abstract H23A-1109.

32. Zhang ZF, AL Ward, and GW Gee. 2001. "Estimating Soil Hydraulic Properties From Field-Scale Experiments Using the Inverse Model UCODE With the STOMP Simulator." *Eos Trans. AGU, 81* (48) Fall Meet. Suppl., Abstract H11F-11.

33. Zhang ZF, AL Ward, and GW Gee. 2004. "Estimating the Hydraulic Properties of Soils with Saturation-Dependent Anisotropy in Hanford." *SSSA Annual Meeting Abstracts*, Oct. 31–Nov. 4, Seattle, WA.

6.0 VZTFS Reports

1. Ward AL, and GW Gee. 2003. *Vadose Zone Transport Field Study: FY 2003 Test Plan.* PNNL-14240, Pacific Northwest National Laboratory, Richland, WA.

2. Ward, AL and GW Gee. 2002. *Vadose Zone Transport Field Study: FY 2002 Test Plan.* PNNL-13857, Pacific Northwest National Laboratory, Richland, WA.

3. Ward AL, and GW Gee. 2001. *Vadose Zone Transport Field Study: FY 2001 Test Plan.* PNNL-13451, Rev. 1, Pacific Northwest National Laboratory, Richland, WA.

4. Ward AL, and GW Gee. 2000. *Vadose Zone Transport Field Study: Detailed Test Plan for Simulated Leak Tests*. PNNL-13263, Pacific Northwest National Laboratory, Richland, WA.

5. Ward AL, GW Gee, ZF Zhang, and JM Keller. 2002. *Vadose Zone Transport Field Study: FY2002 Status Report.* PNNL-14150, Pacific Northwest National Laboratory, Richland, WA.

6. Ward AL, TG Caldwell, and GW Gee. 2000. *Vadose Zone Transport Field Study: Soil Water Content Distributions by Neutron Moderation*. PNNL-13795, Pacific Northwest National Laboratory, Richland, WA.

7. Ramierz A, W Daily, A Binley, and GW Gee. 2001. *Final Report, FY 2001, 200 East Vadose Test Site Hanford, Washington, Electrical Resistance Tomography*. PNNL-13794, Pacific Northwest National Laboratory, Richland, WA.

8. Hoversten GM, and GW Gee. 2000. *Preliminary Report: Surface-to-Borehole and Surface Electromagnetic Surveys at the Hanford Leak Experiment*. PNNL-13793, Pacific Northwest National Laboratory, Richland, WA.

9. Majer EL, KH Williams, JE Peterson, and GW Gee. 2001. *High Resolution Imaging of Vadose Zone Transport Using Crosswell Methods.* PNNL-13792, Pacific Northwest National Laboratory, Richland, WA.

10. Majer EL, JE Peterson, KH Williams, TM Daley, and GW Gee. 2000. *High Resolution Imaging of Vadose Zone Transport Using Crosswell Radar and Seismic Methods*. PNNL-13791, Pacific Northwest National Laboratory, Richland, WA.

11. Gee, GW, and AL Ward. 2001. *Vadose Zone Transport Field Study: Status Report.* PNNL-13679, Pacific Northwest National Laboratory, Richland, WA.

12. Gee, GW, AL Ward, JC Ritter, JB Sisson, JM Hubbell, and H Sydnor. 2001. *Installation of a Hydrologic Characterization Network for Vadose Zone Monitoring of a Single-Shell Tank Farm at the U. S. Department of Energy Hanford Site*. PNNL-13712, Pacific Northwest National Laboratory, Richland, WA.

13. Last GV, and TG Caldwell. 2001. *Core Sampling in Support of the VZTFS.* PNNL-13454, Pacific Northwest National Laboratory, Richland, WA.

14. Last, GV, TG Caldwell, and AT Owen. 2001. *Sampling of Boreholes WL-3A through 12 in support of the VZTFS*. PNNL-13631, Pacific Northwest National Laboratory, Richland, WA.

15. Zhang, FZ, AL Ward, and GW Gee. 2002. *Estimating Field-Scale Hydraulic Parameters of Heterogeneous Soils Using A Combination of Parameter Scaling and Inverse Methods*. PNNL-14109, Pacific Northwest National Laboratory, Richland, WA.

7.0 References

Abbaspour KC, R Kasteel, and R Schulin. 2000. "Inverse Parameter Estimation in a Layered Unsaturated Field Soil." *Soil Sci.* 165(2):109-123.

Amrhein C, and DL Suarez. 1990. "Procedure for Determining Sodium-Calcium Selectivity in Calcareous and Gypsiferous Soils." *Soil Sci. Soc. Am J.* 54(4):999-1007.

Banin A, and A Amiel. 1969. "A Correlative Study of the Chemical and Physical Properties of a Group of Natural Soils of Israel." *Geoderma* 3:185-198.

Barnes CJ. 1986. "Equivalent Formulations for Solute and Water Movement in Soils." *Water Resour. Res.* 22:913-918.

Barnett DB, GW Gee, MD Sweeney, MD Johnson, VF Medina, DP Mendoza, BG Fritz, F Khan, WD Daily, JB Fink, MT Levitt, and AM Binley. 2003. *Results of Performance Evaluation Testing of Electrical Leak-Detection Methods at the Hanford Mock Tank Site--FY 2002-2003*. PNNL-14192, Pacific Northwest National Laboratory, Richland, WA.

Barry DA, GC Sander, and IR Phillips. 1991. "Modelling Solute Transport, Chemical Adsorption and Cation Exchange." Pages 913-918, *Proc. Int. Hydrol. Water Resour. Symposium,* Institution of Engineers, Perth, Australia 2-4 October, 1991.

Baumgartner N, GW Parkin, and DE Elrick. 1994. "Soil Water Content and Potential Measured by Hollow Time Domain Reflectometry Probe." *Soil Sci. Soc. Am. J.* 58:315-318.

Berglund S, and V Cvetkovic. 1996. "Contaminant Displacement in Aquifers: Coupled Effects of Flow Heterogeneity and Nonlinear Sorption." *Water Resour. Res.* 32(1):23-32 (95WR02767).

Biggar JW, and DR Nielsen. 1962. "Miscible displacement: II. Behavior of tracers." *Soil Sci. Soc. Am. Proc*. 26:125–128.

Bjornstad BN, KR Fecht, and AM Tallman. 1987. *Quaternary Stratigraphy of the Pasco Basin, South Central Washington*. RHO-BW-SA-563A, Rockwell Hanford Operations, Richland, WA.

Boger M. 1998. "Three-Dimensional Analytical Solutions for the Unsaturated Seepage Problem." *J. Hydrol. Eng*. 3:193-202.

Bouma J, and JAJ Van Lanen. 1987. "Transfer functions and threshold values: From soil characteristics to land qualities." In: *Quantified land evaluation*. KJ Beek et al. (Editors). Proc. Worksh. ISSS and SSSA, Washington, DC. Apr. 27–May 2, 1986. Int. Inst. Aerospace Surv. Earth Sci. Publ. no. 6. ITC Publ., Enschede, The Netherlands, pp. 106-110.

Brooks RH, and AT Corey. 1966. "Hydraulic Properties of Porous Media Affecting Fluid Flow." *Proc. ASCE J. Irrig. Drain. Div.* 92:61-88.

Brooks RH, and AT Corey. 1964. "Hydraulic properties of porous media." Hydrol. Paper 3. Colorado State University, Fort Collins, CO.

Bruch JC. 1970. "Two-dimensional dispersion experiments in a porous medium." *Water Resour. Res.* 6(3):791-800.

Burdine NT. 1953. "Relative Permeability Calculations from Pore-Size Distribution Data." *Trans. AIME* 198:71-77.

Campbell GS. 1974. "A simple method for determining unsaturated conductivity from moisture retention data." *Soil Sci.* 117:311-314.

Campbell GS, and S Shiozawa. 1992. "Prediction of Hydraulic Properties of Soils Using Particle Size Distribution and Bulk Density Data," p. 317-328. *In Proceedings of an International Workshop on Indirect Methods for Estimating the Hydraulic Properties of Unsaturated Soils*. Univ. of California Press, Berkeley, CA.

Carrera J, A Alcolea, A Medina, J Hidalgo, and LJ Slooten. 2005. "Inverse problem in hydrogeology." *Hydrogeol J*. 13:206–222.

Chanzy A, A Tarussov, A Judge, and F Bonn. 1996. "Soil Water Content Determination Using a Digital Ground-Penetrating Radar." *Soil Sci. Soc. Am J*. 60:1318-1326.

Clement WP, and AL Ward. 2006. "Using Ground Penetrating Radar to Measure Soil Moisture Content." Book Title: *Handbook of Agricultural Geophysics*. Editors: BJ Allred (USDA/ARS-SDRU), JJ Daniels (Ohio State University), and M Reza Ehsani (University of Florida), CRC Press.

Cushman JH, LS Bennethum, and BX Hu. 2002. "A Primer on Upscaling Tools for Porous Media." *Adv. Water Resour*. 25(8-12):1043-1067.

Dagan G. 1988. "Time Dependent Macrodispersion for Solute Transport in Anisotropic Heterogeneous Aquifers." *Water Resour. Res.* 24:1491-1500.

Dagan G. 1989. *Flow and transport in porous formations*. Berlin, Springer-Verlag.

Dagan G. 1990. "Transport in Heterogeneous Porous Formations: Spatial Moments, Ergodicity, and Effective Dispersion." *Water Resour. Res.* 26:1281-1290.

Daily W, A Ramirez, D Labrecque, and J Nitao. 1992. "Electrical-Resistivity Tomography of Vadose Water-Movement." *Water Resour. Res.* 28(5):1429-1442.

Daniels DJ, DJ Gunton, and HF Scott. 1988. "Introduction to Subsurface Radar." *IEEE, 135,* (F4), 278-320.

Davis JA, GP Curtis, and JD Randall. 1998. *Application of Surface Complexation Modeling to Describe Uranium(VI) Adsorption and Retardation at the Uranium Mill Tailings Site at Naturita, Colorado*. NUREG/CR-6820, U.S. Nuclear Regulatory Commission, Washington, DC.

Davis JL, and AP Annan. 1989. "Ground Penetrating Radar for High Resolution Mapping of Soil and Rock Stratigraphy." *Geophys. Prospecting* 37:531-551.

Delhomme JP. 1979. "Spatial Variability and Uncertainties in Groundwater Flow Parameters: A Geostatistical A`pproach." *Water Resour. Res. 15*(2):269-280.

de Marsily G, F Delay, J Goncalves, P Renard, V Teles, and S Violette. 2005. "Dealing with spatial heterogeneity." *Hydrogeol J.* DOI 10.1007/s10040-004-0432-3, 13:161–183.

Desbarats A. 2001. "Geostatistical Modeling of Regionalized Grain-Size Distributions Using Min/Max Autocorrelation Factors." *In: geoENV III - Geostatistics for Environmental Applications Series: Quantitative Geology and Geostatistics*. Vol. 11, P Monestiez, D Allard, and R Froidevaux (Eds.).

Desbarats AJ, and S Bachu. 1994. "Geostatistical Analysis of Aquifier Heterogeneity from the Core Scale to the Basin Scale: A case study." *Water Resour. Res.* 30(3): 673-684.

Deutsch CV, and AG Journel. 1998. *GSLIB Geostatistical Software Library and User's Guide*, 2nd edition, Oxford University Press, NY.

de Vos JA, J Simunek, PAC Raats, and RA Feddes. 1999. "Identification of the Hydraulic Characteristics of a Layered Silt Loam," pp. 783-798. *In* M.Th. van Genuchter, Leij, and L. Wu (eds.) *Characterization and Measurement of the Hydraulic Properties of Unsaturated Porous Media, Part 1*. University of California, Riverside, CA.

DOE, see U.S. Department of Energy.

Dreimanis A, and M Rappol. 1997. "Late Wisconsian Sub-Glacial Clastic Intrusive Sheets Along Lake Erie Bluffs, at Bradville, Ontario, Canada." *Sedimen. Geol.* 111:225-2487.

Du S, and P Rummel. 1994. "Reconnaissance Studies of Moisture in the Subsurface with GPR." *Proceedings of the Fifth International Conference on Ground Penetrating Radar*, GPR '94, 1241-1248.

Eching SO, JW Hopmans, and O Wendroth. 1994. "Unsaturated Hydraulic Conductivity from Transient Multistep Outflow and Soil Water Pressure Data." *Soil Sci. Soc. Am. J.* 58:687-695.

Ewing, RE. 1998. "Upscaling issues in parameter estimation of models for flow in porous media." In: *Proceedings of Inverse Problem, Control, and Shape Optimization* Carthage, Tunisia, April 8-10, 1998, 1-6.

Fayer MJ, JB Sisson, WA Jordan, AH Lu, and PR Heller. 1993. *Subsurface Injection of Radioactive Tracers: Field Experiment for Model Validation Testing.* NUREG/CR-5996, U.S. Nuclear Regulatory Commission, Washington, D.C.

Fayer MJ, RE Lewis, RE Engleman, AL Pearson, CJ Murray, JL Smoot, RR Randall, WH Wegener, and AH Lu. 1995. *Reevaluation of a Subsurface Injection Experiment for Testing Flow and Transport Models.* PNNL-10860, Pacific Northwest National Laboratory, Richland, WA.

Fecht KR, KA Lindsey, BN Bjornstad, DG Horton, GV Last, and SP Reidel. 1998. *Clastic Injection Dikes of the Pasco Basin and Vicinity.* BHI-01003, Draft A, Bechtel Hanford Inc., Richland, WA.

Fecht KR, KA Lindsey, BN Bjornstad, D Horton, GV Last, and SP Reidel. 1999. *Clastic Injection Dikes of the Pasco Basin and Vicinity.* U.S. Department of Energy, Geologic Atlas Series, BHI-01103.

Ferrand, L. A., M.A. Celia. 1992. "The effect of heterogeneity on the drainage capillary pressure-saturation relation." *Water Resour. Res.* 28(3):859-870.

Fink JB. 1980. "Logarithmic Pseudosections for IP and Resistivity." Presented at the *50th Ann. Int. Mtg., Soc. Expl. Geophys.*

Fink JB. 1994. "A Unified Method of Plotting DC Resistivity and Induced Polarization Data." Presented at the *John S. Sumner Memorial International Workshop on Induced Polarization (IP) in Mining and the Environment*, Tucson, AZ.

Fink JB. 2000. "High Resolution Resistivity: Applications and Case Histories." Presented at the *Advanced Vadose Zone Characterization Workshop*, Richland, WA.

Freedman VL, KP Saripalli, and PD Meyer. 2003. "Influence of Mineral Precipitation and Dissolution on Hydrologic Properties of Porous Media in Static and Dynamic Systems." *Applied Geochemistry* 18:589-606.

Freedman V, AL Ward, and GW Gee. 2004. "Estimating Transport Parameters for Field-Scale Cation Migration in the Vadose Zone." *SSSA Annual Meeting Abstracts,* Oct. 31-Nov. 4, Seattle, WA.

Freyberg DL. 1986. "A Natural Gradient Experiment on Solute Transport in a Sand Aquifer, 2, Spatial Moments and the Advection and Dispersion of Nonreactive Tracers." *Water Resour. Res.* 22(13):2031-2046.

Friedman SP, and SB Jones. 2001. "Measurement and Approximate Critical Path Analysis of the Pore-Scale-Induced Anisotropy Factor of an Unsaturated Porous Medium." *Water Resour. Res.* 37:2929-2942.

Garabedian SP, DR LeBlanc, LW Gelhar, and MA Celia. 1991. "Large-Scale Natural Gradient Tracer Test in Sand and Gravel, Cape Cod, Massachusetts." *Water Resour. Res.* 27(5):911-924.

Gautier Y, MJ Blunt, and MA Christie. 1999. "Nested gridding and streamlined-based simulation for fast reservoir performance prediction." *Computational Geosciences* 3:295-320.

Gelhar LW, and CL Axness. 1983. "Three-Dimensional Stochastic Analysis of Macrodispersion in Aquifers." *Water Resour. Res.* 19:161-180.

General Accounting Office (GAO). 1989. *DOE's Management ofSsingle-Shelled Tanks at Hanford, Washington*. GAO/RCED-89-157, Washington, D.C.

Glynn P, and J Brown. 1996. "Reactive Transport Modelling of Acidic Metal-Contaminated Ground Water at a Site with Sparse Spatial Information." *In: Reactive Transport in Porous Media, Review in Mineralogy*. Vol. 34 (Lichtner et al., eds.). The Mineralogical Society of America, Washington D.C.

Hammel K, and K Roth. 1998. "Approximation of Asymptotic Dispersivity of Conservative Solute in Unsaturated Heterogeneous Media with Steady State Flow." *Water Resour. Res.* 34(4):709-716.

Han NW, J Bhakta, RG Carbonell. 1985. " Longitudinal and Lateral Dispersion in Packed Beds: Effect of Column Length and Particle Size Distribution." *AIChE Journal* 31(2):277-288.

Harleman DRF, and RR Rumer. 1963. "Longitudinal and lateral dispersion in an isotropic porous medium." *Fluid Mech.* 16:385-394.

Hayashi T. 1966. "Clastic Dikes in Japan (I)." *Japanese Journal of Geology and Geography*, Transactions and Abstracts 37:1-20.

Hills RG, PJ Wierenga, DB Hudson, and MR Kirkland. 1991. "The Second Las Cruces Trench Experiment: Experimental Results and Two-Dimensional Flow Predictions." *Water Resour. Res.* 27:2707-2718.

Hoversten MG, and GW Gee. 2000. *Surface-to-Borehole and Surface Electromagnetic Surveys at the Hanford Leak Experiment.* PNNL-13793, Pacific Northwest National Laboratory, Richland, WA.

Hoversten GM, GA Newman, HF Morrison, E Gasperikova, and JI Berg. 2001. "Reservoir Characterization Using Crosswell EM Inversion: A Feasibility Study for the Snorre Field, North Sea." *Geophysics* 66:1177-1189.

Huisman JA, C Sperl, W Bouten, JM Verstraten. 2001. "Soil Water Content Measurements at Different Scales: Accuracy of Time Domain Reflectometry and Ground-Penetrating Radar." *J. Hydrol.* 245:48-58.

Inoue M, J Simunek, S Shiozawa, and JW Hopmans. 2000. "Simultaneous Estimation of Soil Hydraulic and Solute Transport Parameters from Transient Infiltration Experiments." *Adv. Water Res.* 23:677-688.

Jacobs Engineering Group, Inc. 1997. *Engineering Calculations for the Supplement Analysis for the Tank Waste Remediation System Decision Assessment*. Richland, WA.

Jacobs Engineering Group, Inc. 1998a. *Final AX Tank Farm Vadose Zone Screening Analysis for the Retrieval Performance Evaluation Criteria Assessment*. Richland, WA.

Jacobs Engineering Group, Inc. 1998b. *Final SX Tank Farm Vadose Zone Screening Analysis for the Retrieval Performance Evaluation Criteria Assessment.* Richland, WA.

Journel AG, and CJ Huijbregts. 1978. *Mining Geostatistics.* Academic Press, NY.

Kachanoski RG, C Hamlin, and IJ van Wesenbeeck. 1990. "Spatial Variability of Water and Solute Flux in a Layered Soil," p 31-41. *In Field-Scale Water and Solute Flux in Soils*. Ed. K Roth, H Fluhler, WA Jury, and JC Parker, 294 pp. Birkhäuser Publ., Basel, Switzerland.

Kaluarachchi JJ, and JC Parker. 1989. "An efficient finite element method for modeling multiphase flow." *Water Resour. Res.* 25:43-54.

Khaleel R and MP Connelly. 2004. *Modeling data package for an initial assessment of closure for S-SX Tank Farms*. RPP-17209 Revision 0, CH2M Hill Hanford Group, inc. Richland WA.

King PR. 1989. "The Use of Renormalization for Calculating Effective Permeability." *Transport in Porous Media* 4:37-58.

Klute A. 1952. "Some Theoretical Aspects of the Flow of Water in Unsaturated Soils." *Soil Sci. Soc. Proc*. 16:144-148.

Knoll M, R Knight, and E Brown. 1995. "Can Accurate Estimates of Permeability be Obtained from Measurements of Dielectric Properties?" *In Proceedings of the Symposium on the Application of Geophysics to Engineering and Environmental Problems* (SAGEEP95- April 23-26, 1995, Orlando, FL, 25-35), Environmental and Engineering Geophysical Society, Wheat Ridge, CO.

Kosugi K. 1999. "General Model for Unsaturated Hydraulic Conductivity for Soils with Lognormal Pore-Size Distribution." *Soil Sci. Soc. Am. J.* 63:270-277.

Krupp HK, JW Biggar, and DR Nielsen. 1972. "Relative flow rates of salt and water in soil." *Soil Sci. Soc. Am. Proc*. 36:412–415.

LaBrecque DJ, M Milleto, W Daily, A Ramirez, and E Owen. 1996. "The Effects of Noise on Occam's Inversion of Resistivity Tomography Data." *Geophysics* 61:538-548.

Lamb H. 1945. *Hydrodynamics*. 6th ed. Dover, New York.

Last GV, and TG Caldwell. 2001. *Core Sampling in Support of the Vadose Zone Transport Field Study*. PNNL-13454, Pacific Northwest National Laboratory, Richland, WA.

Last GV, TG Caldwell, and AT Owen. 2001. *Sampling of Borehole WL-3A through -12 in Support of the Vadose Zone Transport Field Study*. PNNL-13631, Pacific Northwest National Laboratory, Richland, WA.

Lehmann F, and P Ackerer. 1997. "Determining Soil Hydraulic Properties by Inverse Method in One Dimensional Unsaturated Flow." *J. Environ. Qual.* 26:76-81.

Lichtner PC. 2001. *FLOTRAN User Manual*. LA-UR-01-2349, Los Alamos National Laboratory, Los Alamos, NM.

Lieser KH, and C Bauscher. 1987. "Technetium in the hydrosphere and in the geosphere. I. Chemistry of technetium and iron in natural waters and influence of the redox potential on the sorption of technetium." *Radiochim. Acta*. 42:205-213.

Lotspeich FB, and FH Everest. 1981. *A New Method for Reporting and Interpreting Textural Composition of Spawning Gravel*, USDA Forest Service. Pacific Northwest Forest and Range Experiment Station Research Note.

Lu AH, and R Khaleel. 1993. "Calibration/Validation of VAM3D Model Using Injection Test Data at Hanford." *In Vadose Zone Modeling Workshop Proceedings*, March 29-30, 1993. R Khaleel (ed.), WHC-MR-0420, Westinghouse Hanford Company, Richland, WA.

Mackie RL, DW Livelybrooks, TR Madden, and JC Larsen. 1997. "A Magnetotelluric Investigation of the San Andreas Fault at Carrizo Plain, California." *Geophys. Res. Letters* 24:1847-1850.

Majer EL, JE Peterson, KH Williams, TM Daley, and GW Gee. 2000. *High Resolution Imaging of Vadose Zone Transport Using Crosswell Radar and Seismic Methods*. PNNL-13791, Pacific Northwest National Laboratory, Richland, WA.

Majer EL, KH Williams, and JE Peterson. 2001. "High Resolution Imaging of Vadose Zone Transport Using Crosswell Methods." PNNL-13792, Pacific Northwest National Laboratory, Richland, WA.

Mangerud J, E Sønstegaard, HP Sejrup, and S Haldorsen. 1981. "A Continuous Eemian-Early Weichselian Sequence Containing Pollen and Marine Fossils at Fjøsanger, Western Norway." *Boreas* 10:137-208.

Mantoglou A, and LW Gelhar. 1987. "Stochastic Modeling of Large-Scale Transient Unsaturated Flow." *Water Resour. Res.* 23:37-46.

McCord JT, DB Stephens, and JL Wilson. 1991. "Hysteresis and State Dependent Anisotropy in Modeling Unsaturated Hillslope Hydrologic Processes." *Water Resour. Res.* 27:1501–1518.

McHenry JR. 1957. *Properties of Soils of the Hanford Project.* HW-53218, Hanford Atomic Products Operation, Richland, WA.

Miller EE, and RD Miller. 1956. "Physical theory for capillary flow phenomenon." *J. Appl. Phys.* 27:324-332, 1956.

Mishra S, and JC Parker. 1989. "Parameter estimation for coupled unsaturated flow and transport." *Water Resour. Res.* 25:385–396.

Mualem Y. 1976. "A New Model for Predicting the Hydraulic Conductivity of Unsaturated Porous Media." *Water Resour. Res.* 12:513-522.

Mualem Y. 1984. "Anisotropy of Unsaturated Soils." *Soil Sci. Soc. Am. J.* 48:505-509.

Murray CJ, AL Ward, JL Wilson, PE Long, BJ Lechler, WP Clement, PK Kannberg, and GW Gee. 2001. "The Effects of Clastic Dikes on Vadose Zone Transport at the Hanford Site, Southcentral Washington." *In: EOS Trans. AGU,* 82(47), Fall Meet. Suppl., Abstract H52A-0370.

Murray CJ, AL Ward, and JL Wilson, III. 2003. *Influence of Clastic Dikes on Vertical Migration of Contaminants in the Vadose Zone at Hanford.* PNNL-14224, Pacific Northwest National Laboratory, Richland, WA.

Murray CJ, AL Ward, and JL Wilson, III. 2003. *Influence of Clastic Dikes on Vertical Migration of Contaminants in the Vadose Zone at Hanford*. PNNL-14224, Pacific Northwest National Laboratory, Richland, WA.

National Research Council (NRC). 2000. *Seeing into the Earth. Noninvasive Characterization of the Shallow Subsurface for Environmental and Engineering Application.* National Academy Press, Washington, D.C.

Newman GA. 1995. "Crosswell Electromagnetic Inversion Using Integral and Differential Equations." *Geophysics* 60:899-911.

Newmark RL, S Boyd, W Daily, R Goldman, R Hunter, D Kayes, K Kenneally, A Ramirez, K Udell, and M Wilt. 1994. "Using Geophysical Techniques to Control In Situ Thermal Remediation." *In Proceedings of the Symposium on the Application of Geophysics to Engineering and Environmental Problems (SAGEEP) '94*, Boston, Massachusetts, March 27-31, pp. 195-211.

Newsom FJ. 1903. "Clastic Dikes." *Geol. Soc. Amer. Bull.* 14:227-268.

Pachepsky YA, DJ Timlin, and LR Ahuja. 1999. "Estimating saturated hydraulic conductivity using water retention data and neural networks." *Soil Sci.* 164(8):552-560.

Parker JC, JL Zhu, TG Johnson, VJ Kremesec, and EL Hickman. 1994. "Modeling free product migration and recovery at hydrocarbon spill sites." *Ground Water* 32:119-128.

Parkin GW, DE Elrick, RG Kachanoski, and RG Gibson. 1995. "Unsaturated Hydraulic Conductivity Measured by TDR Under a Rainfall Simulator." *Water Resour. Res.* 31(3):447-454.

Perfect E, MC Sukop, and GR Haszler. 2002. "Prediction of dispersivity for undisturbed soil columns from water retention parameters." *Soil Sci. Soc. Am. J.* 66(3), 696-701.

Peterson GL. 1968. "Flow structures in sandstone dikes." *Sedimentary Geology* 2:177-190.

Petersen LW, P Moldrup, OH Jacobsen, and DE Rolston. 1996. "Relations Between Specific Surface Area and Soil Physical and Chemical Properties." *Soil Sci.* 161:9-21.

Philip JR. 1987. "Steady Three-Dimensional Absorption in Anisotropic Soils." *Soil Sci. Soc. Amer. J.* 51:30-35.

Poeter EP, and MC Hill. 1998. *Documentation of UCODE, a Computer Code for Universal Inverse Modeling*. U.S. Geological Survey, Water-Resources Investigations Report 98-4080.

Pogue KR. 1998. "Earthquake-Generated Structures in Missoula Flood Slackwater Sediments (Touchet Beds) of Southeastern Washington." *Geological Society of America Abstracts with Programs*, 30:398-399.

Polemio M, and JD Rhoades. 1977. "Determining Cation Exchange Capacity: A New Procedure for Calcareous and Gypsiferous Soils." *Soil Sci. Soc. Am. J.* 41:524-528.

Polmann DJ. 1990. *Application of Stochastic Methods to Transient Flow and Transport in Heterogeneous Unsaturated Soils.* Ph.D. Thesis, Massachusetts Institute of Technology, Cambridge, MA.

Polmann DJ, D McLaughlin, S Luis, LW Gelhar, and R Ababou. 1991. "Stochastic Modeling of Large-Scale Flow in Heterogeneous Unsaturated Soils." *Water Resour. Res.* 27:1447-1458.

Raats PAC, ZF Zhang, AL Ward, and GW Gee. 2004. "The Relative Connectivity-Tortuosity Tensor for Conduction of Water in Anisotropic Unsaturated Soils." *Vadose Zone J.* 3(4):1471-1478.

Ramirez A, W Daily, DJ LaBrecque, E Owen, and D Chestnut. 1993. "Monitoring an Underground Steam Injection Process Using Electrical Resistance Tomography." *Water Resour. Res.* 29:73-87.

Ramirez A, W Daily, and RL Newmark. 1995. "Electrical Resistance Tomography for Steam Injection Monitoring and Process Control." *J. Environ. Eng. Geophysics* 0(1):39-51.

Ramirez A, W Daily, A Binley, and GW Gee. 2001. *Final Report, FY 2001, 200 East Vadose Test Site Hanford, Washington, Electrical Resistance Tomography*. PNNL-13794, Pacific Northwest National Laboratory, Richland, WA.

Rawls WJ and Brackensiek. 1982. "Estimating soil water retention from from soil properties." *J. Irrig. and Drainage Div. ASCE* 108: 166-171.

Rea J, and R Knight. 1998. "Geostatistical Analysis of Ground Penetrating Radar Data: A Means of Describing Spatial Variation in the Subsurface." *Water Resour. Res.* 34:329–339.

Reidel SP, and DG Horton. 1999. *Geologic Data Package for Immobilized Low-Activity Waste 2001 Performance Assessment*. PNNL-12257, Pacific Northwest National Laboratory, Richland, WA.

Renard P, and G de Marsily. 1997. "Calculating equivalent permeability: A review." *Advances in Water Resources* 20:253-278.

Rockhold ML, MJ Fayer, and GW Gee. 1988. *Characterization of Unsaturated Hydraulic Conductivity at the Hanford Site*. PNL-6488, Pacific Northwest Laboratory, Richland, WA.

Rockhold ML, RE Rossi, and RG Hills. 1996. "Application of similar media scaling and conditional simulation for modeling water flow and tritium transport at the Las Cruces Trench Site." *Water Resour. Res*. 32:595-609.

Rockhold ML, CJ Murray, and MJ Fayer. 1999. "Conditional Simulation and Upscaling of Soil Properties." *In Proceedings of the International Workshop on Characterization and Measurement of the Hydraulic Properties of Unsaturated Porous Media,* M Th van Genuchten, FJ Leif, and L Wu (eds.), pp. 1391-1402. University of California, Riverside, CA.

Romano N, and M Palladino. 2002. "Prediction of soil water retention using soil physical data and terrain attributes." *J. Hydrol.* (Amsterdam) 265:56–75.

Roth K, WA Jury, H Flühler, and W Attinger. 1991. "Transport of Chloride Through an Unsaturated Field Soil." *Water Resour. Res.* 27:2533-2541.

Rouston RC, and KR Fecht. 1979. *Soil (Sediment) Properties of Twelve Hanford Wells with Geologic Interpretation*. RHO-LD-82, Rockwell Hanford Operations, Richland, WA.

Rucker DF, and MD Sweeney. 2004. *Plume Delineation in the BC Cribs and Trenches Area*. PNNL-14948, Pacific Northwest National Laboratory, Richland, WA.

Russo D. 1993. "Stochastic Modeling of Macrodispersion for Solute Transport in a Heterogeneous Unsaturated Porous Formation." *Water Resour. Res.* 29:383–397.

Russo D, and E Bresler. 1981. "Soil Hydraulic Properties as Stochastic Processes: I. An Analysis of Field Spatial Variability." *Soil Sci. Soc. Am. J.* 45:682-687.

Russo D, and M Bouton. 1992. "Statistical Analysis of Spatial Variability in Unsaturated Flow Parameters." *Water Resour. Res.* 28:1911-1925.

Sanchez-Vila X, JP Girardi, and J Carrera. 1995. "A Synthesis of Approaches to Upscaling of Hydraulic Conductivities." *Water Resour. Res. 31*(4):867-882.

Schaap MG, and W Bouten. 1996. "Modeling Water Retention Curves of Sandy Soils Using Neural Networks." *Water Resour. Res.* 32:3033-3040.

Schaap MJ, and FJ Leij. 2000. "Improved Prediction of Unsaturated Hydraulic Conductivity with the Mualem-van Genuchten Model." *Soil Sci. Soc. Am. J.* 64:843-851.

Schaap MG, PJ Shouse, and PD Meyer. 2003. *Laboratory Measurements of the Unsaturated Hydraulic Properties at the Vadose Zone Transport Field Study Site*. PNL-14284, Pacific Northwest National Laboratory, Richland, WA.

Scheinost AC, W Sinowski, and K Auerswald. 1997. "Regionalization of Soil Water Retention Curves in a Highly Variable Soilscape, I. Developing a New Pedotransfer Function." *Geoderma* 78:129-143.

Schroeder NC, D Morgan, DJ Rokop, and J Fabryka-Martin. 1993. "Migration of technetium-99 in the alluvial aquifer at the Nevada Test Site, Nevada, USA." *Radiochim. Acta* 60:203-209.

Schuh WM, and RL Cline. 1990. "Effect of Soil Properties on Unsaturated Hydraulic Conductivity Pore-Interaction Factors." *Soil Sci. Soc. Am. J.* 54:1509-1519.

Schulin R, PJ Wierenga, H Flühler, and J Leuenberger. 1987. "Solute Transport Through a Stony Soil." *Soil Sci. Soc. Am. J.* 51: 36-42.

Serne RJ, GV Last HT Schaef, DC Lanigan, CW Lindenmeier, CC Ainsworth, RE Clayton, VL LeGore, MJ O'Hara, CF Brown, RD Orr, IV Kutnyakov, TC Wilson, KB Wagnon, BA Williams, and DS Burke. 2002. *Characterization of Vadose Zone Sediment: Borehole 41-09-39 in the S-SX Waste Management Area.* PNNL-13757-3, Pacific Northwest National Laboratory, Richland, WA.

Shouse PJ, JB Sisson, TR Ellsworth, and JA Jobes. 1992. "Estimating In Situ Unsaturated Hydraulic Properties of Vertically Heterogeneous Soils." *Soil Sci. Soc. Am. J.* 56:1673-1679.

Shrock RR. 1948. *Sequence in Layered Rocks*. McGraw-Hill Book Co., NY.

Šimůnek J, and MT van Genuchten. 1996. "Estimating Unsaturated Soil Hydraulic Properties from Tension Disc Infiltrometer Data by Numerical Inversion." *Water Resour. Res.* 32:2683-2696.

Šimůnek J, MT Van Genuchten, MM Gribb, and JW Hopmans. 1998. "Parameter estimation of unsaturated soil hydraulic properties from transient flow processes." Soil & Tillage Research 47(1-2):27-36.

Sisson JB, and AH Lu. 1984. *Field Calibration of Computer Models for Application to Buried Liquid Discharges: A Status Report*. RHO-ST-46P, Rockwell Hanford Operations, Richland, WA.

Smoot JL. 1995. *Development of a Geostatistical Accuracy Assessment Approach for Modeling Water Content in Unsaturated Lithologic Units*. Ph.D. Dissertation, University of Idaho, Moscow, ID.

Smoot JL, and AH Lu. 1994. "Interpretation and Modeling of a Subsurface Injection Test, 200 East Area, Hanford Washington." *In: Thirty-third Hanford Symposium on Health and the Environment*. GW Gee, and NR Wing (eds.). In-situ Remediation: Scientific Basis for Current and Future Technologies, November 7-11, 1994, Richland, WA, Battelle Press, Columbus, OH.

Smoot JL, and RE Williams. 1996. *A Geostatistical Methodology to Assess the Accuracy of Unsaturated Flow Models*. NUREG/CR-6411, U.S. Nuclear Regulatory Commission, Washington, D.C.

Spies BR, and TM Habashy. 1995. "Sensitivity Analysis of Cross-Well Electromagnetics." *Geophysics* 60:834-845.

Steefel CI. 2004. "Evaluation of the Field-Scale Cation Exchange Capacity of Hanford Sediments." *11th International Symposium on Water-Rock Interaction*, Saratoga Springs, NY.

Steefel CI, and SB Yabusaki. 1996. *OS3D/GIMRT Software for Modeling Multicomponent-Multidmensional Reactive Transport User Manual & Programmer's Guide*. PNNL-11166, Pacific Northwest National Laboratory, Richland, WA.

Steefel CI, S Carroll, PH Zhao, and S Roberts. 2003. "Cesium Migration in Hanford Sediment: a Multisite Cation Exchange Model Based on Laboratory Transport Experiments." *J. Contam. Hydrol.* 67(1-4):219-246.

Stephens DB, and S Heermann. 1988. "Dependence of Anisotropy on Saturation in a Stratified Sand." *Water Resour. Res*. 24(5):770-778.

Stephenson GR, and RA Freeze. 1974. "Mathematical Simulation of Subsurface Flow Contributions to Snowmelt Runoff, Reynolds Creek Watershed, Idaho. *Water Resour. Res*. 10:284-294.

Stewart ML, AL Ward, and DR Rector. 2006. "Study of Pore Geometry Effects on Anisotropy in Hydraulic Permeability Using the Lattice-Boltzmann Method." *Advances in Water Resources Advances in Water Resources* 29(3): (In press).

Tietje O, and M Tapkenhinrichs. 1993. "Evaluation of pedo-transfer functions." *Soil Sci. Soc. Am. J.* 57:1088-1095.

Topp GC, JL Davis, and AP Annan. 1980. "Electromagnetic Determination of Soil Water Content: Measurements in Coaxial Transmission Lines." *Water Resour. Res.* 16:574–582.

U.S. Department of Energy (DOE). 1996. *SX Tank Farm Report*. DOE/ID/12584-268. Grand Junction Projects Office, Grand Junction, CO.

U.S. Department of Energy (DOE). 1998a. *Groundwater/Vadose Zone Integration Project Specification.* DOE/RL-98-48, Richland Operations Office, Richland, WA.

U.S. Department of Energy (DOE). 1998b. *Removal Performance Evaluation for the AX Tank Farm*. DOE/RL-98-72, Draft A, Richland Operations Office, Richland WA.

van Dam JC, JNM Stricker, and P Droogers. 1992. "Inverse Method for Determining Soil Hydraulic Functions from One-Step Outflow Experiments." *Soil Sci. Soc. Am. J.* 56:1042-1050.

van Genuchten, M Th. 1980. "A Closed Form Equation for Predicting the Hydraulic Conductivity of Unsaturated Soils." *Soil Sci. Soc. Am. J.* 44: 892-989.

van Wesenbeeck IJ, and RG Kachanoski. 1991. "Spatial Dependence of In Situ Solute Transport." *Soil Sci. Soc. Am. J.* 55:3-7.

van Wesenbeck I, and G Kachanoski. 1994. "Effect of Variable Horizon Thickness on Solute Transport." *Soil Sci. Soc. Am. J.* 58:1307-1316.

Vogel T, M Cislerova, and JW Hopmans. 1991. "Porous Media with Linearly Variable Hydraulic Properties." *Water Resour. Res.* 27: 2735-2741.

Vrugt J, H Gupta, W Bouten, and S Sorooshian. 2003. "A shuffled complex evolution Metropolis algorithm for optimization and uncertainty assessment of hydrologic model parameters." *Water Resources Research*. 39(8), SWC1:1-1:16.

Ward AL, and GW Gee. 2000. *Vadose Zone Transport Field Study: Detailed Test Plan for Simulated Leak Tests.* PNNL-13263. Pacific Northwest National Laboratory, Richland, WA.

Ward AL, and GW Gee. 2002. *Vadose Transport Field Study: FY 2002 Test Plan.* PNNL-13857, Pacific Northwest National Laboratory, Richland, WA.

Ward AL, GW Gee, and MD White. 1997. *A Comprehensive Analysis of Contaminant Transport in the Vadose Zone Beneath Tank SX-109.* PNNL-11463, UC-702, Pacific Northwest National Laboratory. Richland, WA.

Ward AL, TG Caldwell, and GW Gee. 2000. *Vadose Zone Transport Field Study: Soil Water Content Distributions by Neutron Moderation*. PNNL-13795, Pacific Northwest National Laboratory, Richland, WA.

Ward AL, GW Gee, ZF Zhang, and JM Keller. 2002. *Vadose Zone Transport Field Study: FY 2002 Status Report.* PNNL 14180, Pacific Northwest National Laboratory, Richland, WA.

Ward AL, GW Gee, ZF Zhang, and JM Keller. 2003. *Vadose Zone Transport Field Study: FY 2002 Status Report*. PNNL-14150, Pacific Northwest National Laboratory, Richland, WA.

Ward AL, GW Gee, ZF Zhang, and JM Keller. 2004. *Vadose Zone Contaminant Fate-and-Transport Analysis for the 216-B-26 Trench*. PNNL-14907, Pacific Northwest National Laboratory, Richland, WA.

Ward AL, ZF Zhang, and GW Gee. 2006. "Upscaling unsaturated hydraulic parameters for flow through heterogeneous anisotropic sediments." *Adv. Water Resour*. 29:268-280.

Weber KJ. 1982. "Influence of common sedimentary structures on fluid flow in reservoir models." *J. Pet. Tech*. March: 665-672.

Wendroth O, PS Koszinski, H Rogasik, CJ Ritsema, and DR Nielsen. 1999. "Spatio-temporal patterns and covariance structures of soil water status in two Northeast-German field sites." *J. Hydrol*. 215:38-58.

White MD, and M Oostrom. 2000. "STOMP Subsurface Transport Over Multiple Phases: Theory Guide." PNNL-11216, Pacific Northwest National Laboratory, Richland, WA.

White MD, and AL Ward. 2001. "Numerical Investigations of Vadose Zone Transport of Saturated Sodium Thiosulfate Solutions." *Eos Trans. AGU, 82*(47), Fall Meet. Suppl., Abstract H12F-06.

White MD, M Oostrom, and MD Williams. 2001. *Initial Assessments for S–SX Field Investigation Report (FIR): Simulations of Contaminant Migration with Surface Barriers.* PNWD-3111, Pacific Northwest National Laboratory, Richland, WA.

Wierenga PJ, DB Hudson, RG Hills, I Porro, J Vinson, and MR Kirkland. 1990. *Flow and Transport Experiments at the Las Cruces Trench Site: Experiments 1 and 2*. NUREG/CR-5607, Nuclear Regulatory Commission, Washington, D.C.

Wierenga PJ, DB Hudson, and MR Kirkland. 1991. "The Second Las Cruces Trench Experiment: Experimental Results and Two-Dimensional Flow Predictions." *Water Resources Research* 27:2707-2718.

Wierenga PJ, and MTh van Genuchten. 1989. "Solute transport through small and large unsaturated soil columns." *Ground Water* 27:35–42.

Williams KH, MB Kowalsky, EL Majer, JE Peterson, and SS Hubbard. 2002. *High Resolution Imaging of Vadose Zone Transport Using Surface and Crosswell Ground Penetrating Radar Methods.* Pacific Northwest National Laboratory, Richland, WA.

Wood BD. 2000. *Review of Upscaling Methods for Describing Unsaturated Flow.* PNNL-13325. Pacific Northwest National Laboratory, Richland, WA.

Wood TR, and GT Norrell. 1996. *Integrated Large-Scale Aquifer Pumping and Infiltration Tests, Ground Water Pathways OU 7-06.* Rep. INEL-96/0256, Lockheed Martin Idaho Technologies Company, Idaho Falls, ID.

Wösten JHM, YaA Pachepsky, and WJ Rawls. 2001. "Pedotransfer functions: bridging the gap between available basic soil data and missing soil hydraulic characteristics." *J. Hydrol.* 251:123–150.

Yabusaki SB, and AL Ward. 2004. "High-Resolution Modeling Studies of Vadose Zone Reactive Transport." (Invited Paper No. 217-7) *Geological Society of America Abstracts with Programs.* 35(6):531, September 2003.

Yeh T-C J, LW Gelhar, and AL Gutjahr. 1985. "Stochastic Analysis of Unsaturated Flow in Heterogeneous Soils 1. Statistically Isotropic Media." *Water Resour. Res.* 21: 447-456.

Yilmaz Ö. 1987. *Seismic Data Processing.* Society of Exploration Geophysicists, Tulsa, OK.

Young MH, PJ Wierenga, and CF Mancino. 1996. "Large Weighing Lysimeters for Water Use and Deep Percolation Studies." *Soil Science.* 161:491-497.

Youngs EG. 1964. "An Infiltration Method of Measuring the Hydraulic Conductivity of Unsaturated Porous Materials." *Soil Sci.* 97:307-311.

Youngs EG. 1991. "Infiltration Measurements—A Review." *Hydrological Processes* 5(3):309-320.

Zachara JM, SC Smith, and C Liu. 2002. "Ion Exchange Studies." RPP-10098, River Protection Project, Richland, WA. Appendix D.2.2. *In:* Knepp AJ. 2002. *Field Investigation Report for Waste Management Area B-BX-BY. RPP-10098. Rev. 0.* CH2M HILL Hanford Group, Inc., Richland, WA.

Zaslavsky D, and G Sinai. 1981. "Surface Hydrology: IV. Flow in Sloping Layered Soil." *J. Hydraul. Div., Am. Soc. Civ. Eng.* 107:1-93.

Zhang ZF, RG Kachanoski, GW Parkin, and B Si. 2000. "Measuring Hydraulic Properties Using a Line Source: II. Field Test." *Soil Sci. Soc. Am. J.* 64:1563-4569.

Zhang ZF, AL Ward, and GW Gee. 2002a. "Parameter Estimation for Unsaturated Layered Soils Through a Combination of Non-similar Media Scaling and Inverse Flow Modeling." *In: IAHR International Groundwater Symposium "Bridging the Gap between Measurement and Modeling in Heterogeneous Media."* International Groundwater Symposium, Berkeley, California, pp. 103-107, published by IAHR, Madrid, Spain.

Zhang ZF, AL Ward and GW Gee. 2002b. *Estimating Field-Scale Hydraulic Parameters of Heterogeneous Soils Using a Combination Parameter Scaling and Inverse Methods.* PNNL-14109, Pacific Northwest National Laboratory, Richland, WA.

Zhang ZF, AL Ward, and GW Gee. 2003a. "Estimating Soil Hydraulic Parameters of a Field Drainage Experiment Using Inverse Techniques." *Vadose Zone Journal* 2:201-211.

Zhang ZF, AL Ward, and GW Gee. 2003b. "A Tensorial Connectivity-Tortuosity (TCT) Concept to Describe the Unsaturated Hydraulic Properties of Anisotropic Soils." *Vadose Zone Journal* 2:313-321.

Zhang ZF, AL Ward, and GW Gee. 2004a. "A Parameter Scaling Concept for Estimating Field-Scale Hydraulic Functions of Layered Soils." *J. Hydraulic Research* 41(extra):93-103.

Zhang ZF, AL Ward, and GW Gee. 2004b. "A combined parameter scaling and inverse technique to upscale the unsaturated hydraulic parameters for heterogeneous soils." *Water Resour. Res.* 40(8), W08306, doi:10.1029/2003WR002925.

Zhuang HE, JS Zeng, and LY Zhu. 1988. "Sorption of radionuclides technetium and iodine on minerals. *Radiochim. Acta* 44/45:143-145.

Distribution

No. of Copies

ONSITE

9 **DOE Richland Operations Office**

BL Charboneau	A6-33
RD Hildebrand	A6-38
JG Morse	A6-38
KM Thompson	A6-38
AC Tortoso	A6-38
Public Reading Room (2)	H2-53
Administrative Record (2)	H6-08

1 **DOE Office of River Protection**

RW Lober	H6-60

1 **CH2M Hill Hanford**

CD Wittreich	H6-62

4 **CH2M Hill Hanford Group Inc.**

FJ Anderson	H6-03
M Connelly	E6-35
FM Mann	H0-22
DA Myers	H0-22

3 **Fluor Hanford Inc.**

MW Benecke	E6-35
TW Fogwell	E6-35
BH Ford	E6-35

2 **Washington State Department of Ecology**

J Caggiano	H0-57
Ecology Library	H0-57

No. of Copies

ONSITE

12 **Pacific Northwest National Laboratory**

MD Freshley	K9-33
GV Last	K6-81
EC Sullivan	K6-81
AL Ward (4)	K9-33
SB Yabusaki	K9-36
JM Zachara	K8-96
ZF Zhang	K9-33
Information Release (2)	K1-06